

SCDAP/RELAP5/MOD3.1 Code Manual Volume V: Developmental Assessment

Contributing Authors:

**C. M. Allison
G. A. Berna
S. M. Bourdon^a
E. W. Coryell
K. L. Davis
D. T. Hagrman
J. K. Hohorst
L. J. Siefken**

Editors:

**J. K. Hohorst
E. C. Johnsen**

**Manuscript Completed:
December 1993**

**Idaho National Engineering Laboratory
EG&G Idaho, Inc.
Idaho Falls, Idaho 83415**

**Prepared for the
Division of Systems Research
Office of Nuclear Regulatory Research
U. S. Nuclear Regulatory Commission
Washington, DC 20555
Under DOE Contract No. DE-AC07-761D01570
FIN W6095**

a. Institute for the Protection of Nuclear Safety, Cadarache Nuclear Center, France.

ABSTRACT

The SCDAP/RELAP5 code has been developed for best estimate transient simulation of light water reactor coolant systems during a severe accident. The code models the coupled behavior of the reactor coolant system, the core, fission product released during a severe accident transient as well as large and small break loss of coolant accidents, operational transients such as anticipated transient without SCRAM, loss of offsite power, loss of feedwater, and loss of flow. A generic modeling approach is used that permits as much of a particular system to be modeled as necessary. Control system and secondary system components are included to permit modeling of plant controls, turbines, condensers, and secondary feedwater conditioning systems.

This volume contains detailed code-to-data calculations performed using SCDAP/RELAP5/MOD3.1, as well as comparison calculations performed with earlier code versions. The results of full plant calculations which include Surry, TMI-2, and Browns Ferry are described. The results of a nodalization study, which accounted for both axial and radial nodalization of the core, are also reported.

EXECUTIVE SUMMARY

The specific features of SCDAP/RELAP5/MOD3.1 are described in this five volume set of manuals covering the theory, use, and assessment of the code for severe accident applications. This set replaces the SCDAP/RELAP5/MOD3 Code Manual, NUREG/CR-5273.

The SCDAP/RELAP5 computer code is designed to describe the overall reactor coolant system (RCS) thermal-hydraulic response, core damage progression, and in combination with VICTORIA^a, fission product release and transport during severe accidents. The code is being developed at the Idaho National Engineering Laboratory (INEL) under the primary sponsorship of the Office of Nuclear Regulatory Research of the U.S. Nuclear Regulatory Commission (NRC).

The code is the result of merging the RELAP5/MOD3^b and SCDAP models. The RELAP5 models calculate the overall RCS thermal hydraulics, control system interactions, reactor kinetics, and the transport of noncondensable gases. Although previous versions of the code have included the analysis of fission product transport and deposition behavior using models derived from TRAP-MELT, this capability is being replaced through a data link to the detailed fission product code, VICTORIA, as a result of an effort to reduce duplicative model development and assessment.

The SCDAP code models the core behavior during a severe accident. Treatment of the core includes fuel rod heatup, ballooning and rupture, fission product release, rapid oxidation, zircaloy melting, UO₂ dissolution, ZrO₂ breach, flow and freezing of molten fuel and cladding, and debris formation and behavior. The code also models control rod and flow shroud behavior.

The RELAP5 code is based on a nonhomogeneous and nonequilibrium model for the two-phase system that is solved by a fast, partially implicit numerical scheme to permit economical calculation of system transients. The objective of the RELAP5 development effort from the outset was to produce a code that includes important first order effects necessary for accurate prediction of system transients but is sufficiently simple and cost effective such that parametric or sensitivity studies are possible. The development of SCDAP/RELAP5 has this same focus.

The code includes many generic component models from which general systems can be simulated. The component models include fuel rods, control rods, pumps, valves, pipes, heat structures, reactor point kinetics, electric heaters, jet pumps, turbines, separators, accumulators, and control system components. In addition, special process models are included for effects such as form loss, flow at an abrupt area change, branching, choked flow, boron tracking, and noncondensable gas transport.

The development of the current version of the code was started in the spring of 1992. This version contains a number of significant improvements to the SCDAP models since the last versions of the code, SCDAP/RELAP5/MOD2.5 and SCDAP/RELAP5/MOD3, were released. These improvements include the

a. T. Heames et al., *VICTORIA: A Mechanistic Model of Radionuclide Behavior in the Reactor Coolant System Under Severe Accident Conditions*, NUREG/CR-5545, SAND90-0756, Rev. 1, December 1992.

b. C. M. Allison, C. S. Miller, N. L. Wade (Eds.) *RELAP5/MOD3 Code Manual*, Volumes I through IV, NUREG/CR-5535, EGG-2596, June 1990.

addition of several new models to describe the earlier phases of a severe accident, changes in the late phase models to provide more “physically intuitive” behavior for full plant calculations, and changes to improve the overall reliability and usability of the code. The improvements in the early phase models include the addition of models to treat (a) the effects of grid spacers including the effects of Inconel spacer grid-zircaloy cladding material interactions, (b) BWR B₄C control blade-zircaloy channel box material interactions, and (c) accelerated heating, melting, and hydrogen generation during the reflood of damaged fuel rods. An extension to the molten pool models to treat the sporadic growth of the boundaries of the molten pool into adjacent regions of relatively intact assemblies or rubble debris beds is the most significant change to the late phase models. Improvements in overall reliability and usability of the code for plant calculations include changes in the overall code numerics to reduce the likelihood of numerical instabilities or code failures and changes in the codes input/output processors. The most noticeable of these for the code users is the conversion of the SCDAP input to a form more compatible with the RELAP5 style. In addition to these modeling and coding changes, SCDAP/RELAP5/MOD3.1 has also been subjected to (a) an intensive effort of verification testing to identify and resolve outstanding code errors and (b) a systematic assessment of the code to quantify the uncertainties in the predicted results.

This volume, Volume V, contains the developmental assessment of SCDAP/RELAP5/MOD3.1. The assessment results, including calculations performed with earlier code versions, encompass both full plant verification problems and code-to-data comparisons. The results of a nodalization study, which accounted for both axial and radial nodalization of a BWR and PWR core, are also reported. The code-to-data calculations were performed for the following experiments including CORA-7, CORA-13, DF-4, SFD 1-4, SFD 1-3, SFD 1-1, SFD ST, LOFT LP-FP-2, and PHEBUS B9+. The verification problems were comprised of Surry, TMI-2, and Browns Ferry full plant calculations.

Results from this assessment of SCDAP/RELAP5/MOD3.1 and assessments of earlier versions of the code indicate a significant increase in the code’s capabilities and usability. This version is more reliable and easier to use than earlier release versions. The number of code failures, during a calculation, due to water property (thermodynamic phase) errors have decreased significantly. The change to RELAP5 free format card number input in the SCDAP module significantly decreased the time needed to develop an input deck. This input change also gave the user the ability to change some SCDAP variables on restart, decreasing the time needed to perform a series of sensitivity studies. Improved numerics, time smoothing and time step repetition significantly lower the cpu-time needed to perform a calculation. SCDAP/RELAP5/MOD3.1 is a faster running, more reliable version of the code than any previously released version.

The code-to-data comparisons for SCDAP/RELAP5/MOD3.1 indicated that there were no major inconsistencies between these comparisons and those performed as part of the assessment of earlier versions of the code. In addition no systematic biases appear in the results that can be directly attributed to the changes in RELAP5 numerics and thermal-hydraulic models. The results of the early phase of simulated experimental accidents, show that the variation between the calculated and measured behavior was typically less than ~20%. The plant calculations indicated the importance of the improvements in the late phase model. The nodalization studies for Browns Ferry for a Large Break Loss-of-Coolant Accident and Surry for a high pressure, station blackout, ignoring surge line failure include no systematic problems with time and spatial nodalizations. Results appear to converge asymptotically as the number of axial nodes and radial channel increased. It was determined for the Browns Ferry calculations for early phase analyses, that a minimum of 7 flow channels, 3 representative assemblies, and 8 axial nodes should be

used. It was recommended for Surry that a minimum of 5 flow channels, 5 representative assemblies, and 10 axial nodes should be used.

ACKNOWLEDGMENTS

Development of a complex computer code such as SCDAP/RELAP5 is the result of a team effort. Acknowledgments are made to those who made significant contributions to the earlier versions of SCDAP/RELAP5 in particular for the contributions of G. H. Beers, E. R. Carlson, and T. M. Howe. Acknowledgment is also made of E. C. Johnsen for her work in code configuration control, and to B. D. Reagan for her support in preparing figures and correcting equations. The authors also acknowledge the RELAP5 development team, specifically R. J. Wagner, R. A. Riemke, and C. S. Miller for their contributions to SCDAP/RELAP5.

The SCDAP/RELAP5 Program is indebted to the technical monitors responsible for directing the overall program: Dr. Y. Chen of the U. S. Nuclear Regulatory Commission and Mr. W. H. Rettig of the Department of Energy Idaho Operations Office. Finally, acknowledgment is made of those many code users who have been very helpful in stimulating correction of code deficiencies with special appreciation to Dr. T. J. Haste and L. Nilsson for the many hours of technical review they provided.

CONTENTS

ABSTRACT	iii
FIGURES.....	xi
TABLES	xxvii
EXECUTIVE SUMMARY	xxix
ACKNOWLEDGMENTS	xxxiii
1. INTRODUCTION.....	1-1
1.1 General Code Capabilities.....	1-1
1.2 Relationship to Other NRC-Sponsored Software.....	1-2
1.3 Quality Assurance	1-2
1.4 Organization of the SCDAP/RELAP5 Manuals.....	1-3
1.5 Organization of Volume V.....	1-3
2. REVIEW OF NEW MODELS AND CODE IMPROVEMENTS.....	2-1
2.1 Summary of RELAP5 Related Thermal-Hydraulic Improvements	2-1
2.1.1 Interphase Heat Transfer Model.....	2-1
2.1.2 Wall Condensation Model	2-1
2.1.3 Effect of Noncondensables.....	2-1
2.1.4 Steam Injection Model	2-2
2.1.5 Time Smoothing	2-2
2.1.6 Umbrella Model	2-2
2.2 Summary of Changes and Improvements in the SCDAP Module	2-2
2.2.1 Inconel Grid Spacer/Zircaloy Interaction Model	2-2
2.2.2 Reflood and Vapor Limited Diffusion of Steam.....	2-3
2.2.3 BWR Control Blade/Channel Box Model.....	2-3
2.2.4 Late Phase Modeling	2-4
2.2.5 Lower Head Modeling (COUPLE)	2-5
2.2.6 User Conveniences and Improved Capabilities.....	2-5
2.3 The Effects of Changes made to SCDAP/RELAP5	2-6
3. SCDAP/RELAP5/MOD2.5, MOD3 AND MOD3.1 COMPARISON	3-1
3.1 CORA	3-1
3.1.1 CORA-7 Test Comparisons.....	3-1
3.1.2 CORA-13 Test.....	3-2
3.2 ACRR DF-4 Experiment	3-4
3.3 Full-Size Nuclear Power Plants.....	3-9
4. SCDAP/RELAP5/MOD3.1 ASSESSMENT.....	4-1
4.1 Estimate of Overall Model Uncertainties	4-1

4.1.1	Thermal Behavior.....	4-1
4.1.2	Onset of Rapid Oxidation and Hydrogen Production	4-7
4.1.3	Fuel Rod Ballooning	4-8
4.1.4	Early Phase Bundle Liquefaction.....	4-11
4.1.5	Late Phase Damage Progression	4-13
4.2	Model Assessment of SCDAP/RELAP5/MOD3.1	4-15
4.2.1	Control Material Behavior.....	4-15
4.2.2	Material Interactions and the Grid Spacer Model	4-18
4.2.3	Reflood Model.....	4-20
4.2.4	BWR Control Blade Channel Box	4-36
4.2.5	User Conveniences and Usability Improvements	4-37
5.	NODALIZATION STUDY	5-1
5.1	BWR Nodalization	5-1
5.1.1	Axial Nodalization Study	5-1
5.1.1.1	Results of the Axial Nodalization Study.....	5-3
5.1.2	Conclusions	5-7
5.1.3	Radial Nodalization.....	5-7
5.1.4	Results of the BWR Full Plant Radial Nodalization Study.....	5-7
5.1.5	Recommendations and Conclusions.....	5-12
5.2	PWR Nodalization.....	5-13
5.2.1	Axial Nodalization	5-13
5.2.1.1	Model Development.....	5-13
5.2.1.2	Description of the Axial Nodalization Study.....	5-13
5.2.1.3	Results of the PWR Axial Nodalization Sensitivity Study	5-15
5.2.2	Nodalization Sensitivity Study of Surry PWR during TMLB' Accident.....	5-22
5.2.2.1	Introduction	5-22
5.2.2.2	Plant Description and Nodalization	5-22
5.2.2.3	Boundary Conditions and Modeling Options	5-27
5.2.2.5	Description of Heatup of Reactor Core Before Surge Line Failure	5-34
5.2.2.6	Late Phase Damage Progression.....	5-39
5.2.2.7	Thermal Hydraulic Behavior and Heatup of Components n Reactor System	5-45
5.2.2.8	Conclusions	5-48
6.	CONCLUSIONS	6-1
7.	REFERENCES	7-1
A.1.	KfK EXPERIMENT CORA-13	A-4
A.1.1	Cora Facility And Test Conditions	A-4
A.1.1.1	Test Conditions.....	A-5
A.1.2	Changes to the Input Model	A-5
A.1.2.1	Lower Bundle Modeling Prior to and During Reflood.....	A-6
A.1.2.2	Heater Rod Electrode	A-7

A.1.2.3	Localized Hot Spots in Bundle.....	A-7
A.1.3	Results of the Calculations	A-7
A.1.3.1	Influence of the Material Interaction Model.....	A-7
A.1.3.2	Vapor Limited Diffusion of Steam in Zircaloy	A-8
A.1.3.3	Effects of the Reflood Model	A-11
A.1.3.3.1	Hydrogen Production	A-14
A.1.3.3.2	End-state of the Bundle.....	A-18
A.1.3.4	Impact of the New Style Input	A-18
A.1.4	Conclusions	A-18
A.2.	KfK EXPERIMENT CORA-7	A-20
A.2.1	Experiment Transient Model	A-20
A.2.2	Results	A-22
A.2.2.1	Base Case.	A-22
A.2.2.2	Nested Shroud Case.....	A-22
A.2.3	Code Performance	A-26
A.3.	ACRR EXPERIMENT DF-4.....	A-31
A.3.1	Experiment Transient Model	A-31
A.3.2	Results	A-32
A.3.2.1	DF-4 Base Case.	A-32
A.3.2.2	DF-4 Blade Case.	A-34
A.3.3	Code Performance	A-39
A.4.	PBF SFD 1-4 EXPERIMENT	A-41
A.4.1	Description of the SCDAP/RELAP5 Model	A-41
A.4.1.1	Nodalization	A-41
A.4.1.1.1	Initial Conditions.....	A-42
A.4.1.2	Boundary Conditions.....	A-42
A.4.2	Results	A-43
A.4.2.1	Thermal Behavior.....	A-43
A.4.2.2	Hydrogen Production	A-46
A.4.2.3	Metallic Material Relocation.....	A-47
A.4.2.4	Fission Product Releases	A-48
A.4.2.5	Code Performance	A-49
A.5.	PBF SFD 1-3 EXPERIMENT	A-50
A.5.1	Description of the SCDAP/RELAP5 Model	A-50
A.5.1.1	Nodalization	A-50
A.5.1.2	Initial Conditions	A-51
A.5.1.3	Boundary Conditions.....	A-51
A.5.2	Results	A-52
A.5.2.1	Thermal Behavior.....	A-53

A.5.2.2	Hydrogen Production	A-54
A.5.2.3	Metallic Material Relocation.....	A-56
A.5.2.4	Fission Product Releases	A-57
A.5.2.5	Code Performance	A-57
A.6.	PBF SFD 1-1 EXPERIMENT	A-58
A.6.1	Description of the SCDAP/RELAP5 Model	A-58
A.6.1.1	Nodalization	A-58
A.6.1.2	Initial Conditions	A-59
A.6.1.3	Boundary Conditions.....	A-59
A.6.2	Results	A-60
A.6.2.1	Thermal Behavior.....	A-60
A.6.2.2	Hydrogen Production	A-63
A.6.2.3	Metallic Material Relocation.....	A-64
A.6.2.4	Fission Product Releases	A-65
A.6.2.5	Code Performances.....	A-66
A.7.	PBF SCOPING TEST EXPERIMENT	A-67
A.7.1	Description of the SCDAP/RELAP5 Model	A-67
A.7.1.1	Nodalization	A-67
A.7.1.2	Initial Conditions	A-68
A.7.1.3	Boundary Conditions.....	A-68
A.7.1.4	Shroud Thermal Conductivity	A-69
A.7.2	Results	A-69
A.7.2.1	Thermal Behavior.....	A-69
A.7.3	Cladding Oxidation and Hydrogen Production	A-72
A.7.3.1	Metallic and Ceramic Material Relocation	A-73
A.7.3.2	Fission Product Releases	A-75
A.7.3.3	Code Performances.....	A-76
A.8.	PHEBUS B9+ EXPERIMENT.....	A-77
A.8.1	Description of the Test Train	A-77
A.8.2	Description of the Test Scenario.....	A-77
A.8.3	Description of the SCDAP/RELAP5 Model	A-78
A.8.3.1	Nodalization	A-78
A.8.3.2	Initial Conditions	A-79
A.8.3.3	Boundary Conditions.....	A-79
A.8.4	Results	A-80
A.8.4.1	Thermal Behavior.....	A-80
A.8.4.1.1	Thermal Behavior in the Steam Phase	A-80
A.8.4.1.2	Thermal Behavior in the Helium Phase	A-80
A.8.4.2	Cladding Oxidation and Hydrogen Production	A-81
A.8.4.3	Metallic Material Relocation.....	A-82
A.8.4.4	Bundle Blockage	A-85

A.8.4.5 Code Performances.....	A-85
A.9. OECD LOFT LP-FP-2.....	A-86
A.9.1 Input Model	A-86
A.9.1.1 Primary Coolant System Model	A-86
A.9.1.2 Core Model.....	A-87
A.9.1.3 Initial Conditions.....	A-89
A.9.1.4 Boundary Conditions.....	A-90
A.9.2 Transient Analysis	A-91
A.9.2.1 System Thermal Hydraulic Behavior	A-91
A.9.2.2 Key Transient Parameters.....	A-96
A.9.2.3 Transient Damage Progression.....	A-97
A.9.3 Assessment Summary.....	A-100
A.10. SURRY PLANT TRANSIENT RESULTS	A-102
A.10.1 Plant Transient Model	A-102
A.10.2 General Results for Surry TMLB' Calculation	A-105
A.10.2.1Power Generation.	A-106
A.10.2.2Thermal-Hydraulic Response.....	A-106
A.10.2.3Hydrogen Production.....	A-115
A.10.2.4Damage Progression Response.....	A-116
A.10.2.5Lower Plenum Response.	A-116
A.10.3 Code Performance	A-117
A.10.3.1Code Reliability Improvements.....	A-118
A.10.3.2New Style Input.	A-120
A.10.3.3CPU Usage.	A-121
A.10.3.4SCDAP/RELAP5/MOD3 and SCDAP/RELAP5/MOD3.1 Comparison	A-121
A.11. TMI-2.....	A-123
A.11.1 Plant Transient Model	A-123
A.11.2 Results	A-129
A.11.3 Power Generation.	A-131
A.11.4 Code Performance	A-134
A.12. Browns Ferry	A-137
A.12.1 Plant Transient Model	A-137
A.12.2 Results	A-138
A.12.2.1Power Generation.	A-139
A.12.2.2Hydrogen Production.....	A-151
A.12.3 Code Performance	A-153
A.13. REFERENCES	A-161

B.1.	INTRODUCTION	B-3
B.2.	CALCULATED BEHAVIOR FOR BASE CASE ANALYSIS	B-7
B.3.	RADIAL AND AXIAL NODALIZATION SENSITIVITY STUDY	B-20
B.4.	CONCLUSIONS	B-38

FIGURES

Figure 3-1.	Calculated and measured fuel rod temperatures at the 750 mm using SCDAP/RELAP5/MOD2.5 and SCDAP/RELAP5/MOD3	3-1
Figure 3-2.	Calculated and measured fuel rod temperatures at the 750 mm elevation using SCDAP/RELAP5/MOD3.1	3-2
Figure 3-3.	End-state figure of the CORA-7 comparisons	3-3
Figure 3-4.	Artist's rendition of a representative cross-section of the CORA-7 damaged bundle	3-3
Figure 3-5.	Comparison of calculated fuel rod temperatures for CORA-13 from SCDAP/RELAP5/MOD3 and SCDAP/RELAP5/MOD3.1 with measured at 750 mm elevation.....	3-4
Figure 3-6.	Artist rendition of the CORA-13 bundle showing the calculated and measured end-state.....	3-5
Figure 3-7.	Comparison of calculated fuel rod temperatures for DF-4 using the same version of the code and the two control blade models at the 0.096 m elevation.....	3-6
Figure 3-8.	Comparison of calculated fuel rod temperatures for DF-4 at the 0.258 m elevation using the two control blade models and the same version of the code.....	3-6
Figure 3-9.	Comparison of calculated fuel rod temperatures for DF-4 at the 0.368 m elevation using the two control blade models with the same version of the code.....	3-7
Figure 3-10.	Predicted fuel rod temperatures for DF-4 at the 0.96 m elevation from 3 versions of the code compared to the measured	3-7
Figure 3-11.	Predicted fuel rod temperatures for DF-4 at the 0.258 m elevations using 3 versions of the code compared to the measured	3-8
Figure 3-12.	Predicted temperatures for the channel box for DF-4 at the 0.258 m elevation using both control blade models compared to the measured	3-9
Figure 4-1.	Calculated and measured core dry-out time as a function of elevation for LOFT LP-FP2	4-2
Figure 4-2.	Calculated and measured collapsed liquid level for the PBF SFD1-3 experiment	4-3
Figure 4-3.	Calculated and measured collapsed liquid level for the PBF-SFD 1-4 experiment	4-3
Figure 4-4.	Calculated and measured heating rates as a function of temperature for the CORA-7, CORA-13 and DF-4 experiments.....	4-4
Figure 4-5.	Calculated versus measured heating rates for the CORA-7, CORA-13 and DF-4 experiments.....	4-5
Figure 4-6.	Calculated versus measured heating rates in the 0.0 to 1.0 K/s range for the CORA-7, CORA-13, and DF-4 experiments.....	4-5
Figure 4-7.	Comparison of calculated versus measured time shifts for the CORA-7, CORA-13, and DF-4 experiments	4-6

Figure 4-8.	CORA-13 calculated versus measured temperatures for the unheated fuel rod, heated fuel rod and control rod	4-7
Figure 4-9.	Predicted hydrogen production rates for CORA-7	4-9
Figure 4-10.	Comparison of CORA-15 temperature data with predicted values and ballooning turned on with double-sided oxidation	4-10
Figure 4-11.	Comparison of CORA-15 temperature data with predicted values with no ballooning modeled.....	4-10
Figure 4-12.	Comparison of CORA-15 temperature data with predicted values with ballooning and single sided oxidation	4-11
Figure 4-13.	CORA-7 Calculated and measured absorber rod temperatures at the 750 mm elevation using SCDAP/RELAP5/MOD3.1	4-12
Figure 4-14.	Calculated and measured control rod temperatures for CORA-13 at the 550 and 750 mm elevations	4-12
Figure 4-15.	End-state figure of the CORA-7 comparisons	4-13
Figure 4-16.	Artist rendition of the bundle showing the calculated and measured end-state4-14	
Figure 4-17.	Core condition after reflood.....	4-14
Figure 4-18.	Calculated late phase damage progression	4-15
Figure 4-19.	Calculated and measured absorber temperatures for the CORA-7 experiment at the 750 mm elevation in the bundle using SCDAP/RELAP5/MOD3.1	4-16
Figure 4-20.	CORA-7 calculated and measured absorber rod temperatures at the 750 mm elevation using SCDAP/RELAP5/MOD3.....	4-17
Figure 4-21.	Calculated and measured absorber temperatures for the CORA-13 experiment at the 550 and 750 mm elevation in the bundle using SCDAP/RELAP5/MOD3.1	4-17
Figure 4-22.	Calculated temperature histories at the 0.4 m elevation for cases of Inconel and zircaloy grid spacer for a PWR bundle at the 0.63 m elevation4-19	
Figure 4-23.	Calculated accumulated hydrogen production for cases of Inconel and zircaloy grid spacer for a PWR bundle at the 0.63 elevation.....	4-19
Figure 4-24.	Printed output showing core degradation events	4-20
Figure 4-25.	Calculated fuel rod cladding temperature response for LOFT LP-FP-2 during reflood.....	4-22
Figure 4-26.	Calculated LOFT LP-FP-2 fuel rod reflood response at the 42 inch elevation in the central fuel module.....	4-22
Figure 4-27.	Calculated hydrogen production rates from the steamed starved and vapor diffusion limited cases for CORA-13	4-23
Figure 4-28.	Calculated LOFT LP-FP-2 cumulative hydrogen production during reflood	4-23
Figure 4-29.	CORA-7 comparison of maximum bundle temperature.....	4-24
Figure 4-30.	CORA-7 comparison of hydrogen generation rate	4-25
Figure 4-31.	CORA-7 comparison of hydrogen generation rate	4-26

Figure 4-32.	CORA-7 comparison of integral hydrogen production	4-26
Figure 4-33.	CORA-7 comparison of fuel rod temperatures at the 550 mm elevation.....	4-27
Figure 4-34.	CORA-7 comparison of fuel rod temperatures at the 750 mm elevation.....	4-27
Figure 4-35.	CORA-7 comparison of fuel rod temperatures at the 950 mm elevation.....	4-28
Figure 4-36.	CORA-7 comparison of control rod temperatures at the 750 mm elevation.....	4-28
Figure 4-37.	CORA-7 calculated and measured temperatures at the 350 mm elevation - vapor diffusion and steamed starved limitations	4-29
Figure 4-38.	Calculated and measured temperatures at the 550 mm elevation - vapor diffusion and steamed starved limitations.....	4-29
Figure 4-39.	Calculated and measured temperatures at the 750 mm elevation - vapor diffusion and steamed starved limitations	4-30
Figure 4-40.	Hydrogen production rates from the steamed starved and vapor diffusion limited cases	4-30
Figure 4-41.	Calculated and measured temperatures at the 350 mm elevation when reflood and hot spots in the bundle are modeled using a ZrO_2 failure temperature of 2,250 K.....	4-31
Figure 4-42.	Calculated and measured temperatures at the 550 mm elevation when reflood hot spots in the bundle are modeled using a ZrO_2 failure temperature of 2,250 K.....	4-31
Figure 4-43.	Calculated and measured temperatures at the 750 mm elevation when reflood and hot spots in the bundle are modeled using a ZrO_2 failure temperature of 2,250 K.....	4-32
Figure 4-44.	Calculated and measured temperatures at the 950 mm elevation when reflood and hot spots in the bundle are modeled using a ZrO_2 failure temperature of 2,250 K.....	4-32
Figure 4-45.	CORA-13 hydrogen production in the bundle when reflood and the hot spots in the bundle are modeled using a ZrO_2 failure temperature of 2,250K	4-33
Figure 4-46.	CORA-13 calculated and measured temperatures at the 350 mm elevation when reflood and the hot spots in the bundle are modeled using a ZrO_2 failure temperature of 2,450 K.....	4-33
Figure 4-47.	CORA-13 calculated and measured temperatures at the 550 mm elevation when reflood and the hot spots in the bundle are modeled using a ZrO_2 failure temperature of 2,450 K.....	4-34
Figure 4-48.	CORA-13 calculated and measured temperatures at the 750 mm elevation when reflood and the hot spots in the bundle are modeled using a ZrO_2 failure temperature of 2,450 K.....	4-34
Figure 4-49.	CORA-13 calculated and measured temperatures in the bundle at the 950 mm elevation when reflood and hot spots in the bundle are modeled using a failure temperature of 2,450 K	4-35

Figure 4-50.	CORA-13 calculated and measured hydrogen production rates when reflood and the hot spots in the bundle are modeled using a ZrO_2 failure temperature of 2,450 K	4-36
Figure 5-1.	RELAP5 nodalization of the core region of the Browns Ferry Nuclear Power Plan	5-2
Figure 5-2.	SCDAP nodalization used to represent the reactor core for the axial nodalization study	5-2
Figure 5-3.	Maximum bundle temperature comparison of the original executable which allowed at maximum of 10 nodes in the core and the executable which allowed 30 axial nodes for core modeling	5-3
Figure 5-4.	Axial division of the core for the 5, 8, 10, 20, and 24 node models used in the study	5-4
Figure 5-5.	Predicted maximum bundle temperatures from the 5, 8, 10, 20, and 24 axial node representation of the bundle	5-5
Figure 5-6.	Predicted hydrogen generation rate for the 5, 8, 10, 20, and 24 node representations of the bundle	5-5
Figure 5-7.	Predicted integral hydrogen production for the 5, 8, 10, 20 and 24 node axial representations of the bundle.....	5-6
Figure 5-8.	CPU time needed to run the 5, 8, 10, 20 and 24 axial node representations of the bundle to completion	5-6
Figure 5-9.	RELAP5 nodalization of the Browns Ferry nuclear reactor.....	5-8
Figure 5-10.	Predicted nuclear heat generation for 3, 5, and 7 channel radial representation of the Browns Ferry core using the ORNL blade model and a 7 channel representation using the old model	5-9
Figure 5-11.	Predicted maximum bundle temperatures for the 3, 5, and 7 channel representation of the Browns Ferry core using the ORNL blade model and a 7 channel representation using the old control blade model	5-9
Figure 5-12.	Predicted maximum bundle temperatures for the three radial representations of the core using the ORNL control blade/channel box model	5-10
Figure 5-13.	Predicted CPU time for the 3, 5, and 7 channel radial representation of the Browns Ferry core and a 7 channel representation using the old control blade model	5-10
Figure 5-14.	Predicted control blade temperatures near the axial center of the bundle for all radial nodalization schemes	5-11
Figure 5-15.	Predicted fuel rod temperatures near the axial center of the bundle for all radial nodalization schemes	5-11
Figure 5-16.	Predicted rate and integral hydrogen values for each 3, 5, and 7 radial representations of the Browns Ferry nuclear core	5-12
Figure 5-17.	Predicted rate of hydrogen produced for the 3, 5, and 7 radial representations of the Browns Ferry nuclear core with smoothing using a running average	5-12

Figure 5-18.	Ten axial node RELAP5 nodalization used to study PWR nodalization effects	5-13
Figure 5-19.	Single Surry fuel assembly used for the axial nodalization study	5-14
Figure 5-20.	Axial core divisions used to determine the effect of the number of axial divisions on PWR core behavior	5-15
Figure 5-21.	Predicted maximum bundle temperatures using 5 different axial divisions of the core	5-16
Figure 5-22.	Predicted hydrogen generation rates using 5 different axial divisions of the core	5-16
Figure 5-23.	Predicted integral hydrogen production using 4 different axial divisions of the core	5-17
Figure 5-24.	Predicted temperatures in the upper bundle.....	5-18
Figure 5-25.	Predicted hydrogen generation rates.....	5-18
Figure 5-26.	Predicted damage level	5-19
Figure 5-27.	Maximum bundle temperatures comparing calculations using courant limit and forced time step size	5-19
Figure 5-28.	CPU time comparing calculations using Courant limit and forced time step size.....	5-20
Figure 5-29.	Comparison of CPU time using the nearly and semi-implicit numerical schemes.....	5-21
Figure 5-30.	Comparison of maximum bundle temperatures using the nearly and semi-implicit numerical schemes.....	5-21
Figure 5-31.	Nodalization of primary system loop.....	5-23
Figure 5-32.	Axial cross section of reactor core showing nodalization of core for 5x10 case	5-24
Figure 5-33.	Axial cross section of reactor core and vessel for 5x10 case.....	5-25
Figure 5-34.	Radial cross section of reactor vessel showing nodalization of core.....	5-26
Figure 5-35.	Layout of fuel rods and control rods in fuel assembly	5-27
Figure 5-36.	Reactor power history from 0.0 to 100 seconds	5-31
Figure 5-37.	Reactor power history from 0.0 to 10,000 seconds	5-31
Figure 5-38.	Collapsed liquid level in reactor vessel	5-32
Figure 5-39.	Pressure history of primary coolant system.....	5-32
Figure 5-40.	History of maximum core temperature	5-33
Figure 5-41.	History of maximum temperature at midplane of lower head of reactor vessel.....	5-34
Figure 5-42.	Accumulated production of hydrogen	5-35
Figure 5-43.	Temperature history of fuel rods at several elevations in the center channel for 5x10 case	5-36
Figure 5-44.	Temperature history of fuel rods at several elevations in the center channel for 5x20 case	5-36
Figure 5-45.	Temperature history of fuel rods at 2.7 m elevation for each channel for 5x10 case	5-37

Figure 5-46.	Temperature and oxide thickness histories at 2.7 m elevations for center and periphery outer flow channels for 5x10 case.....	5-37
Figure 5-47.	Temperature history of fuel rods in bottom half of center fuel channel for 5x10 case.....	5-38
Figure 5-48.	Temperature history of fuel rods in bottom half of center fuel channel for 5x20 case.....	5-38
Figure 5-49.	Heat generation in reactor core from oxidation and decay heat	5-39
Figure 5-50.	Rate of hydrogen production	5-39
Figure 5-51.	Thermal response of reactor core during reflood and late phase damage progression	5-40
Figure 5-52.	Radial distribution in temperature of reactor core during reflood and late phase damage progression	5-41
Figure 5-53.	Core degradation map after reflood for 5x10 case.....	5-42
Figure 5-54.	Core degradation map after reflood for the 5x20 case.....	5-42
Figure 5-55.	Effective radius of molten pool for 5x10 and 5x20 cases.....	5-43
Figure 5-56.	Map of core degradation for 5x10 case	5-44
Figure 5-57.	Map of core degradation for 5x20 case	5-44
Figure 5-58.	History of maximum temperature at midplane of lower head of reactor vessel.....	5-45
Figure 5-59.	History of maximum temperature of debris in lower head of reactor vessel.....	5-46
Figure 5-60.	Variation in radial direction of velocity of steam at top of core for 5x10 case	5-46
Figure 5-61.	Variation in radial direction of velocity of steam at top of core for 5x20 case	5-47
Figure 5-62.	Volume fraction of liquid at midplane of center channel of reactor core.....	5-47
Figure 5-63.	Temperature of steam at top of core at three radial locations for 5x20 case.....	5-48
Figure 5-64.	Temperature history of structures in lower part of upper plenum region of reactor vessel	5-49
Figure 5-65.	Temperature history of surge line	5-49
Figure 5-66.	History of rate of flow of steam through break in surge line	5-50
Figure 5-67.	Accumulated flow of steam through break in surge line	5-50
Figure A-1.	Schematic of the CORA facility test section and the test bundle	A-4
Figure A-2.	Argon and steam flow rates used during the CORA-13 experiment	A-6
Figure A-3.	Comparison of calculated fuel rod temperatures from SCDAP/RELAP5/MOD3 and SCDAP/RELAP5/MOD3.1 with measured at 750 mm elevation	A-8
Figure A-4.	Severe Accident Nuclear Plant Analyzer representation of the bundle end-state with grid spacer model in code.....	A-9

Figure A-5.	Artist rendition of the bundle showing the calculated and measured end-state.....	A-10
Figure A-6.	Calculated and measured temperatures at the 350 mm elevation - vapor diffusion and steamed starved limitations	A-10
Figure A-7.	Calculated and measured temperatures at the 550 mm elevation - vapor diffusion and steamed starved limitations	A-11
Figure A-8.	Calculated and measured temperatures at the 750 mm elevation - vapor diffusion and steamed starved limitations	A-11
Figure A-9.	Hydrogen production rates from the steamed starved and vapor diffusion limited cases	A-12
Figure A-10.	Calculated and measured temperatures at the 350 mm elevation when reflood and hot spots in the bundle are modeled using a ZrO_2 failure temperature of 2,250 K.....	A-12
Figure A-11.	Calculated and measured temperatures at the 550 mm elevation when reflood hot spots in the bundle are modeled using a ZrO_2 failure temperature of 2,250 K	A-13
Figure A-12.	Calculated and measured temperatures at the 750 mm elevation when reflood and hot spots in the bundle are modeled using a ZrO_2 failure temperature of 2,250 K.....	A-13
Figure A-13.	Calculated and measured temperatures at the 950 mm elevation when reflood and hot spots in the bundle are modeled using a ZrO_2 failure temperature of 2,250 K.....	A-14
Figure A-14.	Hydrogen production with reflood and the hot spots in the bundle are modeled using a ZrO_2 failure temperature of 2,250 K	A-15
Figure A-15.	Calculated and measured temperatures at the 350 mm elevation when reflood and the hot spots in the bundle are modeled using a ZrO_2 failure temperature of 2,450 K	A-15
Figure A-16.	Calculated and measured temperatures at the 550 mm elevation when reflood and the hot spots in the bundle are modeled using a ZrO_2 failure temperature of 2,450 K	A-16
Figure A-17.	Calculated and measured temperatures at the 750 mm elevation when reflood and the hot spots in the bundle are modeled using a ZrO_2 failure temperature of 2,450 K	A-16
Figure A-18.	Calculated and measured temperatures in the bundle at the 950 mm elevation when reflood and hot spots in the bundle are modeled using a failure temperature of 2,450 K.....	A-17
Figure A-19.	Calculated and measured hydrogen production rates when reflood and the hot spots in the bundle are modeled using a ZrO_2 failure temperature of 2,450 K	A-17
Figure A-20.	Nodalization for the CORA-7 experiment.....	A-21
Figure A-21.	Total core power for the CORA-7 experiment	A-22
Figure A-22.	Surface temperature for the top half of the fuel rod component for the CORA-7 experiment	A-23

Figure A-23.	Surface temperature for the bottom half of the fuel rod component for the CORA-7 experiment	A-23
Figure A-24.	Surface temperature for the top half of the simulator rod component for the CORA-7 experiment	A-24
Figure A-25.	Surface temperature for the bottom half of the simulator rod component for the CORA-7 experiment.....	A-24
Figure A-26.	Surface temperature for the top half of the shroud component for the CORA-7 experiment	A-25
Figure A-27.	Surface temperature for the bottom half of the shroud component for the CORA-7 experiment	A-25
Figure A-28.	Surface temperature for the top half of the control rod component for the CORA-7 experiment	A-26
Figure A-29.	Surface temperature for the bottom half of the control rod component for the CORA-7 experiment	A-26
Figure A-30.	Total hydrogen production for the CORA-7 experiment.....	A-27
Figure A-31.	Surface temperature for the top half of the fuel rod component for the nested shroud model of the CORA-7 experiment.....	A-27
Figure A-32.	Surface temperature for the top half of the simulator rod component for the nested shroud model of the CORA-7 experiment	A-28
Figure A-33.	Surface temperature for the top half of the control rod component for the nested shroud model of the CORA-7 experiment	A-28
Figure A-34.	Surface temperature for the top half of the inner shroud component for the nested shroud model of the CORA-7 experiment	A-29
Figure A-35.	Surface temperature for the top half of the high-temperature shield shroud component for the nested shroud model of the CORA-7 experiment	A-29
Figure A-36.	CPU time for the CORA-7 experiment.....	A-30
Figure A-37.	Test train nodalization for the DF-4 experiment.....	A-33
Figure A-38.	Total core power for the DF-4 experiment	A-34
Figure A-39.	Surface temperature for the fuel rod component for the DF-4 experiment	A-35
Figure A-40.	Surface temperature for the shroud component representing the ZrO ₂ insulation for the DF-4 experiment	A-35
Figure A-41.	Surface temperature for the BWR control rod component for the DF-4 experiment	A-36
Figure A-42.	Total hydrogen production for the DF-4 experiment.....	A-36
Figure A-43.	Total core power for the DF-4 experiment using the ORNL blade model	A-37
Figure A-44.	Surface temperature for the fuel rod component for the DF-4 experiment using the ORNL blade model	A-37
Figure A-45.	Surface temperature for the shroud component representing the ZrO ₂ insulation for the DF-4 experiment using the ORNL blade model	A-38

Figure A-46.	Surface temperature for the control blade for the DF-4 experiment using the ORNL blade model	A-38
Figure A-47.	Surface temperature for channel box segment 1 for the DF-4 experiment using the ORNL blade model	A-39
Figure A-48.	Surface temperature for channel box segment 2 for the DF-4 experiment using the ORNL blade model	A-39
Figure A-49.	Total hydrogen production for the DF-4 experiment using the ORNL blade model	A-40
Figure A-50.	CPU time for the DF-4 experiment.....	A-40
Figure A-51.	Core representation for the SFD 1-4 experiment.....	A-42
Figure A-52.	Nodalization of test train for the SFD 1-4 experiment	A-43
Figure A-53.	Total core power for the SFD 1-4 experiment	A-44
Figure A-54.	Cladding temperatures at 0.55 m elevation. PC: Calculation using BE nuclear power. BC: Calculation using BE nuclear power + 20%	A-45
Figure A-55.	Cladding temperatures for the top half of the fuel rods for the SFD 1-4 experiment (BE calculation using BE nuclear power + 20%)	A-45
Figure A-56.	Cladding temperatures for the bottom half of the fuel rod components for the SFD 1-4 experiment (BE calculation using BE nuclear power + 20%).....	A-46
Figure A-57.	Core representation for the SFD 1-3 experiment.....	A-51
Figure A-58.	Nodalization of test train for the SFD 1-3 experiment	A-52
Figure A-59.	Total core power for the SFD 1-3 experiment	A-53
Figure A-60.	Cladding temperatures at 0.40 m elevation. PC: Calculation using BE nuclear power. BC: Calculation using BE nuclear power + 15%	A-54
Figure A-61.	Cladding temperatures for the top half of the fuel rods for the SFD 1-3 experiment (BE calculation using BE nuclear power + 15% after 1000 seconds)	A-55
Figure A-62.	Cladding temperatures for the bottom half of the fuel rod components for the SFD 1-3 experiment (BE calculation using BE nuclear power + 15% after 1,000 seconds).....	A-55
Figure A-63.	Core representation for the SFD 1-1 experiment.....	A-59
Figure A-64.	Nodalization of test train for the SFD 1-1 experiment	A-60
Figure A-65.	Total core power for the SFD 1-1 experiment	A-61
Figure A-66.	Cladding temperatures for the top half of the fuel rods for the SFD 1-1 experiment (BE calculation)	A-62
Figure A-67.	Cladding temperatures for the bottom half of the fuel rod components for the SFD 1-1 experiment (BE calculation).....	A-63
Figure A-68.	Axial profile of maximum fuel temperature (BE calculation).....	A-64
Figure A-69.	Nodalization and core representation of the test train for the SFD-ST experiment	A-68
Figure A-70.	Total bundle power for the SFD-ST experiment.....	A-69

Figure A-71.	Cladding temperatures for the top half of the fuel rods for the SFD-ST experiment. PC: preliminary calculation. RC: reference calculation	A-70
Figure A-72.	Collapsed liquid level in the bundle for the SFD-ST experiment. RC: reference calculation. SG-: calculation without spacer grid.....	A-71
Figure A-73.	Cladding temperatures for the top half of the fuel rods for the SFD-ST experiment. RC: reference calculation. SG-: calculation without spacer grid.....	A-72
Figure A-74.	Total hydrogen generation mass for the SFD-ST experiment. RC: reference calculation. SG-: calculation without spacer grid.....	A-74
Figure A-75.	Nodalization and core representation of the test train for the PHEBUS B9+ experiment	A-78
Figure A-76.	Total core power for the PHEBUS B9+ experiment.....	A-79
Figure A-77.	PHEBUS B9+ test cladding temperatures in the upper part of the bundle.....	A-81
Figure A-78.	PHEBUS B9+ test cladding temperatures in the lower part of the bundle.....	A-82
Figure A-79.	PHEBUS B9+ test cladding oxidation profile in the bundle	A-83
Figure A-80.	PHEBUS B9+ test total fuel dissolution in the bundle	A-84
Figure A-81.	SCDAP/RELAP5 nodalization diagram of LP-FP-2 reactor vessel	A-87
Figure A-82.	SCDAP/RELAP5 nodalization diagram of LP-FP-2 primary system	A-88
Figure A-83.	Radial core hydrodynamic nodalization	A-88
Figure A-84.	SCDAP center fuel module nodalization.....	A-89
Figure A-85.	Comparison of measured and calculated system pressure.....	A-92
Figure A-86.	Comparison of calculated and measured core dryout time.....	A-93
Figure A-87.	Calculated and estimated LPIS mass flow rate	A-93
Figure A-88.	Calculated and measured cladding temperature at the 10 inch elevation.....	A-94
Figure A-89.	Calculated and measured cladding temperature at the 27 inch elevation.....	A-94
Figure A-90.	Calculated and measured cladding temperature at the 42 inch elevation.....	A-95
Figure A-91.	Radial temperature profile across the center fuel module at 42 inch elevation.....	A-96
Figure A-92.	Calculated and measured outer shroud temperatures at the 42 inch elevation.....	A-97
Figure A-93.	Effect of oxidation rate limit on identical fuel rod components	A-98
Figure A-94.	Calculated hydrogen production.....	A-98
Figure A-95.	Calculated core end state prior to reflood	A-99
Figure A-96.	Cladding outer radii	A-100
Figure A-97.	Vessel nodalization for the Surry plant transient	A-104

Figure A-98. Pressurizer coolant loop for the Surry plant transient.....	A-105
Figure A-99. COUPLE mesh representing the lower reactor vessel head for the Surry plant transient.....	A-106
Figure A-100. Total core power for the Surry plant transient	A-108
Figure A-101. System pressure for the Surry plant transient	A-108
Figure A-102. Surface temperature for the top half of the inner channel fuel rod component for the Surry plant transient	A-109
Figure A-103. Surface temperature for the bottom half of the inner channel fuel rod component for the Surry plant transient	A-109
Figure A-104. Surface temperature for the top half of the inner channel control rod component for the Surry plant transient	A-110
Figure A-105. Surface temperature for the bottom half of the inner channel control rod component for the Surry plant transient	A-110
Figure A-106. Surface temperature for the top half of the middle channel fuel rod component for the Surry plant transient	A-111
Figure A-107. Surface temperature for the bottom half of the middle channel fuel rod component for the Surry plant transient	A-111
Figure A-108. Surface temperature for the top half of the middle channel control rod component for the Surry plant transient	A-112
Figure A-109. Surface temperature for the bottom half of the middle channel control rod component for the Surry plant transient	A-112
Figure A-110. Surface temperature for the top half of the outer channel fuel rod component for the Surry plant transient	A-113
Figure A-111. Surface temperature for the bottom half of the outer channel fuel rod component for the Surry plant transient	A-113
Figure A-112. Surface temperature for the top half of the outer channel control rod component for the Surry plant transient	A-114
Figure A-113. Surface temperature for the bottom half of the outer channel control rod component for the Surry plant transient.....	A-114
Figure A-114. Total hydrogen production for the Surry plant transient.....	A-116
Figure A-115. Damage progression map from SCDAP output for Surry plant transient.....	A-117
Figure A-116. Peak lower plenum debris bed temperature for the Surry plant transient.....	A-118
Figure A-117. Lower plenum debris height for the Surry plant transient	A-118
Figure A-118. Lower plenum debris and head axial temperature distribution for the 0.2 m elevation for the Surry plant transient.....	A-119
Figure A-119. Lower plenum debris and head axial temperature distribution for the 0.5 m elevation for the Surry plant transient.....	A-119
Figure A-120. Lower plenum debris and head axial temperature distribution for the 1.0 m elevation for the Surry plant transient.....	A-120
Figure A-121. CPU time for the Surry plant transient	A-121
Figure A-122. Nodalization of the TMI-2 reactor pressure vessel.....	A-125

Figure A-123. Nodalization of the TMI-2 coolant loop A	A-126
Figure A-124. Nodalization of the TMI-2 coolant loop B	A-127
Figure A-125. Nodalization of the TMI-2 pressurizer	A-128
Figure A-126. Nodalization of the TMI-2 coolant loop A steam generator.....	A-129
Figure A-127. Letdown mass flow rate used in the TMI-2 accident analysis.....	A-130
Figure A-128. Total core power for the TMI-2 plant transient	A-132
Figure A-129. Calculated maximum fuel bundle temperature for the TMI-2 plant transient.....	A-132
Figure A-130. Calculated and measured pressurizer liquid level for the TMI-2 plant transient.....	A-133
Figure A-131. Collapsed liquid level in the reactor vessel for the TMI-2 plan transient.....	A-133
Figure A-132. Calculated and measured pressures in the RCS, steam generator A, and steam generator B.....	A-134
Figure A-133. Mass flow rates in the Loop A and B hot leg for the TMI-2 plant transient.....	A-135
Figure A-134. Mass flow rates in the RCS PORV for the TMI-2 plant transient	A-135
Figure A-135. Nodalization for the Browns Ferry plant transient	A-139
Figure A-136. Total core power for the Browns Ferry plant transient.....	A-141
Figure A-137. System pressure for the Browns Ferry plant transient.....	A-142
Figure A-138. Surface temperatures for the top half of the Channel 1 fuel rod component for the Browns Ferry plant transient	A-143
Figure A-139. Surface temperatures for the bottom half of the Channel 1 fuel rod component for the Browns Ferry plant transient	A-143
Figure A-140. Surface temperatures for the top half of the Channel 1 water rod component for the Browns Ferry plant transient	A-144
Figure A-141. Surface temperatures for the bottom half of the Channel 1 water rod component for the Browns Ferry plant transient.....	A-144
Figure A-142. Surface temperatures for the top half of the Channel 1 shroud component for the Browns Ferry plant transient	A-145
Figure A-143. Surface temperatures for the bottom half of the Channel 1 shroud component for the Browns Ferry plant transient	A-145
Figure A-144. Surface temperatures for the top half of the Channel 2 fuel rod component for the Browns Ferry plant transient	A-146
Figure A-145. Surface temperatures for the bottom half of the Channel 2 fuel rod component for the Browns Ferry plant transient	A-146
Figure A-146. Surface temperatures for the top half of the Channel 2 water rod component for the Browns Ferry plant transient	A-147
Figure A-147. Surface temperatures for the bottom half of the Channel 2 water rod component for the Browns Ferry plant transient.....	A-147
Figure A-148. Surface temperatures for the top half of the Channel 2 shroud component for the Browns Ferry plant transient	A-148

Figure A-149. Surface temperature for the bottom half of the Channel 2 shroud component for the Browns Ferry plant transient	A-148
Figure A-150. Surface temperatures for the top half of the Channel 2 control rod component for the Browns Ferry plant transient	A-149
Figure A-151. Surface temperatures for the bottom half of the Channel 2 control rod component for the Browns Ferry plant transient.....	A-149
Figure A-152. Surface temperatures for the top half of the Channel 3 fuel rod component for the Browns Ferry plant transient	A-150
Figure A-153. Surface temperatures for the bottom half of the Channel 3 fuel rod component for the Browns Ferry plant transient	A-150
Figure A-154. Surface temperatures for the top half of the Channel 3 water rod component for the Browns Ferry plant transient	A-151
Figure A-155. Surface temperatures for the bottom half of the Channel 3 water rod component for the Browns Ferry plant transient.....	A-151
Figure A-156. Surface temperatures for the top half of the Channel 3 shroud component for the Browns Ferry plant transient	A-152
Figure A-157. Surface temperatures for the bottom half of the Channel 3 shroud component for the Browns Ferry plant transient	A-152
Figure A-158. Surface temperatures for the top half of the Channel 3 control rod component for the Browns Ferry plant transient	A-153
Figure A-159. Surface temperatures for the bottom half of the Channel 3 control rod component for the Browns Ferry plant transient.....	A-153
Figure A-160. Surface temperatures for the top half of the Channel 4 fuel rod component for the Browns Ferry plant transient	A-154
Figure A-161. Surface temperatures for the bottom half of the Channel 4 fuel rod component for the Browns Ferry plant transient	A-154
Figure A-162. Surface temperatures for the top half of the Channel 4 water rod component for the Browns Ferry plant transient	A-155
Figure A-163. Surface temperatures for the bottom half of the Channel 4 water rod component for the Browns Ferry plant transient.....	A-155
Figure A-164. Surface temperatures for the top half of the Channel 4 shroud component for the Browns Ferry plant transient	A-156
Figure A-165. Surface temperatures for the bottom half of the Channel 4 shroud component for the Browns Ferry plant transient	A-156
Figure A-166. Surface temperatures for the top half of the Channel 4 control rod component for the Browns Ferry plant transient	A-157
Figure A-167. Surface temperatures for the bottom half of the Channel 4 control rod component for the Browns Ferry plant transient.....	A-157
Figure A-168. Total heat transfer in the four fuel assembly channels for the Browns Ferry plant transient.....	A-158
Figure A-169. Total hydrogen production for the Browns Ferry plant transient	A-158
Figure A-170. CPU time for the Browns Ferry plant transient	A-159

Figure B-1.	Axial cross-section showing nodalization of reactor vessel and reactor core	B-4
Figure B-2.	Radial cross-section showing nodalization of reactor core	B-5
Figure B-3.	Layout of fuel rods and control rods in fuel assembly	B-6
Figure B-4.	Reactor power history from 0.0 to 100 seconds	B-9
Figure B-5.	Reactor power history from 0.0 to 30,000 seconds	B-9
Figure B-6.	Pressure history of primary coolant system.....	B-11
Figure B-7.	History of maximum core temperature.....	B-11
Figure B-8.	Temperature histories of fuel rods in each flow channel at 2.7 m elevation.....	B-12
Figure B-9.	Temperature histories of fuel rods in each flow channel at 2.0 m elevation.....	B-13
Figure B-10.	Accumulated production of hydrogen	B-14
Figure B-11.	Rate of hydrogen production due to oxidation of reactor core	B-14
Figure B-12.	Extent of oxidation of fuel rods in each flow channel at elevation of 2.7 m	B-15
Figure B-13.	Velocities of steam in each flow channel at top of reactor core.....	B-15
Figure B-14.	Steam temperatures in each flow channel at top of reactor core.....	B-16
Figure B-15.	Temperatures of structures in lower and upper part of upper plenum	B-17
Figure B-16.	Temperature history of surge line	B-17
Figure B-17.	Effective radius of molten pool.....	B-18
Figure B-18.	Accumulated amount of CPU time on CRAY X-MP/216 computer.....	B-19
Figure B-19.	Axial cross-section showing nodalization of vessel for case of five flow channels and ten axial node	B-21
Figure B-20.	Radial cross-section of nodalization for five channel case	B-22
Figure B-21.	Comparison of maximum core temperature for the 3x10, 5x10, and 5x20 cases	B-24
Figure B-22.	Comparison of temperatures at the 2.7 m elevation in the center flow channel for the three cases	B-25
Figure B-23.	Temperatures at 2.7 m elevation in outer flow channel for the 3x10, 5x10, and 5x20 cases	B-26
Figure B-24.	Temperatures at 2.0 m elevation in center flow channel for the 3x10 and 5x10 cases	B-26
Figure B-25.	Accumulated hydrogen production for the 3x10, 5x10, and 5x20 cases	B-27
Figure B-26.	Radial distribution in velocity of steam at top of core for 5x10 case	B-28
Figure B-27.	Radial distribution in velocity of steam at top of core for 5x20 case	B-28
Figure B-28.	Temperatures of structures in lower part of upper plenum for the 3x10, 5x10, and 5x20 cases	B-29
Figure B-29.	Temperature of surge line for the 3x10, 5x10, and 5x20 cases.....	B-29
Figure B-30.	Effective radius of molten pool for the 3x10, 5x10, and 5x20 cases.....	B-30

Figure B-31.	Evolution of melt progression for 3x10 case in period 14,372 to 20,000 seconds.....	B-31
Figure B-32.	Evolution of core degradation in 3x10 case for period from 22,000 to 30,000 seconds.....	B-32
Figure B-33.	Evolution of core degradation for 3x10 case for period from 31,000 to 36,000 seconds.....	B-33
Figure B-34.	Evolution of molten pool for 5x10 case from 14,500 to 20,000 seconds.....	B-34
Figure B-35.	Evolution of molten pool for 5x10 case from 22,000 to 30,000 seconds.....	B-35
Figure B-36.	State of core degradation for 5x10 case at 30,656 seconds	B-36
Figure B-37.	Evolution of core degradation for 5x20 case	B-37

TABLES

Table 1-1.	Information for code-to-data comparisons	1-5
Table 3-1.	Version comparison for the Surry calculations	3-10
Table 4-1.	Hydrogen Production	4-8
Table 4-2.	Sensitivity Study Comparison for Hydrogen Production	4-35
Table 5-1.	Summary of BWR Nodalization Studies	5-4
Table 5-2.	PWR Axial Nodalization Studies	5-15
Table 5-3.	Summary of Sensitivity Studies using 10 Axial Nodes	5-17
Table 5-4.	Radial power distribution.....	5-26
Table 5-5.	Comparison of timing of damage progression for 5x10 and 5x20 cases.....	5-29
Table A-1.	Sensitivity Study Comparison for Hydrogen Production	A-18
Table A-2.	Event table for the CORA-7 experiment	A-21
Table A-3.	Event table for the DF-4 experiment	A-32
Table A-4.	Simulated sequence of events for SFD 1-4 experiment.....	A-47
Table A-5.	Simulated sequence of events for SFD 1-3 experiment.....	A-56
Table A-6.	Simulated sequence of events for SFD 1-1 experiment.....	A-65
Table A-7.	Simulated sequence of events for SFD-ST experiment	A-75
Table A-8.	Simulated sequence of events for PHEBUS B9+ experiment	A-84
Table A-9.	Comparison of calculated and measured initial conditions	A-90
Table A-10.	SCDAP component placement and the number of representative rods for Surry NPP.....	A-103
Table A-11.	Event sequence and timing for Surry TMLB'	A-107
Table A-12.	Event sequence and timing for Surry TMLB'	A-115
Table A-13.	Version comparison for the SCDAP/RELAP5/MOD3 and SCDAP/RELAP5/MOD3.1 calculations	A-122
Table A-14.	Key events occurring during the TMI-2 accident.....	A-130
Table A-15.	Models and capabilities verified by TMI-2 calculation	A-136
Table A-16.	Key events in the Browns Ferry accelerated calculation.....	A-140
Table A-17.	Models and capabilities verified by Browns Ferry calculation.....	A-160
Table B-1.	Radial power distribution in reactor core	B-5
Table B-2.	Calculated progression of damage in Surry reactor during TMLB'	B-8
Table B-3.	Radial power distribution for five channel case.....	B-22
Table B-4.	Comparison of the timing of damage progression for the 3x10, 5x10, and 5x20 cases	B-23

SCDAP/RELAP5/MOD3.1 Code Manual

Volume V: Developmental Assessment

1. INTRODUCTION

The SCDAP/RELAP5 computer code is designed to describe the overall reactor coolant system (RCS) thermal-hydraulic response, core damage progression, and, in combination with VICTORIA¹, fission product release and transport during severe accidents. The code is being developed at the Idaho National Engineering Laboratory (INEL) under the primary sponsorship of the Office of Nuclear Regulatory Research of the U.S. Nuclear Regulatory Commission (NRC).

1.1 General Code Capabilities

The code is the result of merging the RELAP5/MOD3² and SCDAP³ models. The RELAP5 models calculate the overall RCS thermal hydraulics, control system interactions, reactor kinetics, and transport of noncondensable gases. Although previous versions of the code have included the analysis of fission product transport and deposition behavior using models derived from TRAP-MELT, this capability is being replaced through a data link to the detailed fission product code, VICTORIA, as a result of an effort to reduce duplicate model development and assessment. The SCDAP models calculate the damage progression in the core structures and the formation, heatup, and melting of debris.

SCDAP/RELAP5 is capable of modeling a wide range of system configurations from single pipes to different experimental facilities to full-scale reactor systems. The configurations can be modeled using an arbitrary number of fluid control volumes and connecting junctions, heat structures, core components, and system components. Flow areas, volumes, and flow resistances can vary with time through either user control or models that describe the changes in geometry associated with damage in the core. System structures can be modeled with RELAP5 heat structures, SCDAP core components, or SCDAP debris models. The RELAP5 heat structures are one-dimensional models with slab, cylindrical, or spherical geometries. The SCDAP core components include representative light water reactor (LWR) fuel rods, silver-indium-cadmium (Ag-In-Cd) and B₄C control rods and/or blades, electrically heated fuel rod simulators, and general structures. A two-dimensional, finite element model based upon the COUPLE⁴ code may be used to calculate the heatup of debris and/or surrounding structures. This model takes into account the decay heat and internal energy of newly fallen or formed debris and then calculates the transport by conduction of this heat in the radial and axial directions to the wall structures and water surrounding the debris. Perhaps the most important use of this model is to calculate the heatup of the vessel wall so that the time at which the vessel may rupture can be determined. Other system components available to the user include pumps, valves, electric heaters, jet pumps, turbines, separators, and accumulators. Models to describe selected processes, such as reactor kinetics, control system response, and tracking noncondensable gases, can be invoked through user control.

The development of the current version of the code was started in the spring of 1992. This version contains a number of significant improvements since the last versions of the code, SCDAP/RELAP5/MOD2.5 and SCDAP/RELAP5/MOD3, were released. These improvements include the addition of several new models to describe the earlier phases of a severe accident, changes in the late phase models to pro-

vide more “physically intuitive” behavior for full plant calculations, and changes to improve the overall reliability and usability of the code. The improvements in the early phase models include the addition of models to treat (a) the effects of grid spacers including the effects of Inconel spacer grid-zircaloy cladding material interactions, (b) BWR B₄C control blade-zircaloy channel box material interactions, and (c) accelerated heating, melting, and hydrogen generation during the reflood of damaged fuel rods. An extension to the molten pool models to treat the sporadic growth of the boundaries of the molten pool into adjacent regions of relatively intact assemblies or rubble debris beds is the most significant change to the late phase models. Improvements in overall reliability and usability of the code for plant calculations include changes in the overall code numerics to reduce the likelihood of numerical instabilities or code failures and changes in the codes input/output processors. The most noticeable of these for the code users is the conversion of the SCDAP input to a form more compatible with the RELAP5 style. In addition to these modeling and coding changes, SCDAP/RELAP5/MOD3.1 has also been subjected to (a) an intensive effort of verification testing to identify and resolve outstanding code errors and (b) a systematic assessment of the code to quantify uncertainties in the predicted results.

1.2 Relationship to Other NRC-Sponsored Software

SCDAP/RELAP5 and RELAP5 are developed in parallel and share a common configuration. Both codes share a common source deck. Separate codes are formed only prior to compilation, so changes made to the source deck are automatically reflected in both codes.

The development and application of the code is also related to several other NRC-sponsored software packages. Theoretical work associated with the development of PARAGRASS-VFP⁵ has resulted in model improvements for fission product release. A data link to the VICTORIA code will allow for the detailed treatment of phenomena such as fission product and aerosol transport, deposition, and resuspension. A link with PATRAN⁶ and ABAQUS⁷ provides the user with the means to calculate the details of lower head failure. Animated plant response displays are possible through links to the Nuclear Plant Analyzer (NPA)⁸ display software, which gives the user an efficient way of analyzing the large amount of data generated. Detailed plant simulations from accident initiation through release of fission products to the atmosphere are made available through links to the CONTAIN⁹ containment response and CRAC2¹⁰ or MACCS¹¹ atmospheric dispersion consequence codes.

1.3 Quality Assurance

SCDAP/RELAP5 is maintained under a strict code configuration system that provides a historical record of the changes made to the code. Changes are made using an update processor that allows separate identification of improvements made to each successive version of the code. Modifications and improvements to the coding are reviewed and checked as part of a formal quality program for software. In addition, the theory and implementation of code improvements are validated through assessment calculations that compare the code-predicted results to idealized test cases and experimental results.

1.4 Organization of the SCDAP/RELAP5 Manuals

The specific features of SCDAP/RELAP5/MOD3.1 are described in a five-volume set of manuals covering the theory, use, and assessment of the code for severe accident applications. Although Volume I describes (a) the overall code architecture, (b) interfaces between the RELAP5 system models, and (c) any system models unique to SCDAP/RELAP5, the code user is referred to the companion set of six volumes which describe the RELAP5² system thermal hydraulics and associated models.

Volume I presents a description of SCDAP/RELAP5/MOD3.1-specific thermal-hydraulic models (relative to RELAP5/MOD3), and interfaces between the thermal-hydraulic models and damage progression models.

Volume II contains detailed descriptions of the severe accident models and correlations. It provides the user with the underlying assumptions and simplifications used to generate and implement the basic equations into the code, so an intelligent assessment of the applicability and accuracy of the resulting calculation can be made.

Volume III provides the user's guide and code input for the severe accident modeling. SCDAP input was recently changed to be consistent with the free-form input used by RELAP5. User guidelines are produced specifically for the severe accident code. The user should also refer to the RELAP5/MOD3 Code Manual Volume V: User Guidelines, for a complete set of guidelines.

Volume IV describes the material property library, MATPRO. It contains descriptions of the material property subroutines available for severe accident analysis.

Volume V documents the assessment of SCDAP/RELAP5/MOD3.1 created in early 1993. It includes nodalization sensitivity studies and time-step sensitivity studies, assessments using standard PWR and BWR plant models, and assessment using code-to-data comparisons.

1.5 Organization of Volume V

Volume V of the manual contains the results of developmental assessment calculations. These calculations were performed to evaluate the effects of new models, error corrections, and usability improvements on predicted results.

Since 1983, different versions of the stand-alone SCDAP and integrated SCDAP/RELAP5 computer codes have been applied to early phase damage progression experiments, full plant natural circulation and direct containment heating (DCH) analyses, as well as the TMI-2 accident. The results of those calculations have been primarily reported in the open literature and test results reports. In 1990, a systematic effort to integrate those results was started. The results of that effort were reported in 1992.¹² Since that time SCDAP/RELAP5/MOD3.1 was created and many assessment calculations were repeated with this version of the code. Since MOD3.1 contains improvements to the numerics, new early phase and late phase damage progression models, error corrections, usability improvements, and user conveniences, assessment activities focused on seven main activities.

1. The evaluation of the impact of model additions and improvements on the

code-to-data comparisons starting with the early changes in the damage progression models. This evaluation is a continuation of previous work started in 1990 with the code extensions made possible by changes and extensions to the RELAP5 thermal-hydraulic models.

2. Perform a series of calculations to verify the effectiveness of the usability improvements, and that the changes in printed output were giving the user correct information.
3. Perform a series of code-to-data comparisons to evaluate the changes in the variances between calculated and observed behavior. Since new damage progression models, such as the grid spacer material interaction and reflood, were added to the code, some changes in hydrogen production, heatup rates, and blockage formation were expected.
4. Evaluate the effectiveness of the Oak Ridge National Laboratory control blade/channel box model for BWR analysis.
5. Evaluate the codes ability to predict core damage progression behavior up to and through lower head failure.
6. Evaluate axial and radial nodalization dependencies on predicted results for full size PWR and BWR nuclear power plants.
7. Identify any modeling deficiencies or errors that still exist in the code from the code-to-data comparisons.

Most of the experiments used for the assessment of SCDAP/RELAP5/MOD3.1 were used in earlier assessments of the code, with the exception of PHEBUS B9+. Predicted results for the PHEBUS B9+ test are contained in Appendix A. Table 1-1 summarizes the tests used for this assessment, the previous code versions used to analyze the tests, and the phenomena evaluated. Not all of these results are described in this report. In these instances, the code-to-data comparisons are described in experiment specific reports.

Volume V of the SCDAP/RELAP5/MOD3.1 code manual is organized in the following manner. Section 1 contains introductory remarks common to all volumes and a short description of assessment activities. Section 2 summarizes RELAP5 thermal-hydraulic improvements and the changes, new models, increased capabilities and error corrections in the SCDAP module. Section 3 focuses on version-to-version comparisons. Section 4 presents the results of the assessment calculations concentrating on modeling uncertainties and the effectiveness of the changes, new models, increased capabilities, and error corrections on predicting core behavior during the analysis of a severe accident. Section 5 presents the results of an axial and radial nodalization study for full size nuclear power plants. The Surry nuclear power plant was used for the PWR study and Browns Ferry for the BWR study. Section 6 contains the conclusions drawn from the code assessment and Section 7 is the references. Appendix A gives complete descriptions of the facilities, modeling, and the results of calculations performed for this code assessment. Appendix B contains the calculated behavior of the Surry PWR during a TMLB' accident.

Table 1-1. Information for code-to-data comparisons.

Experiment	Temperature	Ballooning	Oxidation/ hydrogen production	Fission product release	Damage progression
PBF SFD-ST	S-18, ^a SR-3	S-18, SR-3	S-18, SR-3	S-18	SR-3
PBF SFD 1-1	S-18, SR-3	S-18, SR-3	S-18, SR-3	S-18, SR-3	SR-3
PBF SFD 1-3	SR-2, SR-3	SR-2, SR-3	SR-2, SR-3	SR-2, SR-3	SR-2, SR-3
PBF SFD 1-4	SR-1, SR-3	SR-1, SR-3	SR-1, SR-3	SR-1, SR-3	SR-1, SR-5
PHEBUS B9+	SR-3	SR-3	SR-3	SR-3	SR-3
PHEBUS FPT0	SR-3	SR-3	SR-3	SR-3	SR-3
LOFT LP-FP2	SR-1, SR-3	SR-1, SR-3	SR-1, SR-3	SR-1, SR-3	SR-1, SR-3
CORA-7	SR-2, SR-2.5, SR-3	--	SR-2, SR-2.5, SR-3	--	SR-2, SR-2.5, SR-3
CORA-13	SR-2.5, SR-3		SR-2.5, SR-3		SR-2.5, SR-3
CORA-15	SR-2.5, SR-3	SR-2.5, SR-3	SR-2.5, SR-3	--	SR-2.5, SR-3
CORA-18	SR-2, SR-3	--	SR-2, SR-3	--	SR-2, SR-3
DF-4	SR-2, SR-2.5, SR-3	--	SR-2, SR-2.5, SR-3	--	SR-2, SR-2.5, SR-3
TMI-2	SR-1, SR-3	SR-1, SR-3	SR-1, SR-3	--	SR-1, SR-3
SURRY	SR-2, SR-2.5, SR-3	SR-2, SR-2.5, SR-3	SR-2, SR-2.5, SR-3	--	SR-2, SR-2.5, SR-3
BROWNS FERRY	SR-2.5, SR-3	SR-2.5, SR-3	SR-2.5, SR-3	--	SR-2.5, SR-3

- a.
- S-11 = SCDAP version 11
 - S-18 = SCDAP version 18
 - S-20 = SCDAP version 20
 - SR-1 = SCDAP/RELAP5/MOD1
 - SR-2 = SCDAP/RELAP5/MOD2
 - SR-2.5 = SCDAP/RELAP5/MOD2.5
 - SR-3 = SCDAP/RELAP5/MOD3

2. REVIEW OF NEW MODELS AND CODE IMPROVEMENTS

2.1 Summary of RELAP5 Related Thermal-Hydraulic Improvements

Under the direction of the U. S. Nuclear Regulatory Commission, an effort was undertaken by the developers of RELAP5 to improve the reliability and running time of RELAP5/MOD3.² During this effort, no new models were added to the code, however, enhancements were made to the existing models to improve their capabilities and reliability.¹³ Since these improvements are common to RELAP5 and SCDAP/RELAP5¹⁴, a brief description of these model enhancements, which improve both the running time and reliability of the code, is included in this section of the document. A complete description of all enhancements is contained in the RELAP5/MOD3 reference documents.

2.1.1 Interphase Heat Transfer Model

In previous versions of RELAP5 and SCDAP/RELAP5, the flow of nitrogen from accumulators into the system could not be modeled for large break analysis calculations. In these versions, nitrogen from the accumulators entered the system below the freezing point of water causing the code to fail. The only way to complete this type of analysis was to valve off the accumulator before nitrogen began flowing into the system. The lack of a model to account for direct heating between two phases in the presence of significant amounts of noncondensable gases and large temperature differences throughout the system was determined to be the cause of this deficiency. To correct this problem, changes were made to the basic RELAP5 interphase heat transfer models to account for direct heating between two phases in the presence of noncondensable gases by weighting the contribution of each heat transfer component according to a ratio of partial pressures (the partial pressure of water vapor/the partial pressure of the noncondensable gases). If no noncondensable gases are present, the code uses the old interphase heat transfer model.

2.1.2 Wall Condensation Model

Prior to enhancement of the wall condensation model, energy could be erroneously removed from the liquid phase under certain conditions. If the fluid temperature became cooler than the wall temperature, the wall heat transfer model was activated causing erroneous results and code failure. Changes were made in the RELAP5 wall condensation model so that the driving potential for the liquid heat flux is the difference between the wall temperature and the liquid temperature and the driving potential for the total flux is the difference between wall temperature and the saturation temperature. The vapor heat flux is then the difference between the total heat flux and the liquid heat flux. This change in logic prevents the code from calculating wall condensation when the temperature of liquid flowing through the system is considerably cooler than that of the wall.

2.1.3 Effect of Noncondensables

The RELAP5/MOD3 model did not calculate a major effect of noncondensables in a reactor system, a reduction in the rate of heat transfer. To correct this deficiency, the empirical rate of heat transfer model used in RELAP5/MOD2 was again implemented in the present version of the code. This model modifies the liquid side interfacial heat transfer coefficient (H_{if}) to account for the noncondensables in a subcooled liquid.

2.1.4 Steam Injection Model

RELAP5/MOD3 tended to calculate condensation and heat transfer rates that were too high when the injection of steam into subcooled water was simulated. The bubbly flow correlations and logic used in RELAP5/MOD2 give lower condensation and heat transfer rates and appear to be more applicable in the situation where steam is injected into a subcooled liquid. Until an adequate model can be developed, it is recommended that the MOD2 bubbly flow correlations be used.

2.1.5 Time Smoothing

The time smoothing/under relaxation technique for smoothing the interphase drag and interphase heat transfer terms used in RELAP5/MOD2 was reinstalled into the code. The RELAP5/MOD2 model contains empirical time constants that are, in some cases, sensitive to time step size but are considerably more reliable than the less empirical model developed for RELAP5/MOD3.

2.1.6 Umbrella Model

The umbrella model smoothly limits the liquid side interfacial heat transfer coefficient (H_{if}) when conditions of phase appearance/disappearance are being experienced. This model has now been implemented and is applied at low system pressures.

2.2 Summary of Changes and Improvements in the SCDAP Module

The changes made to the SCDAP module of the code since SCDAP/RELAP5/MOD2.5² was released consist of: (1) significant improvements in modeling for calculating the behavior of a reactor core during the early phases of a severe accident, (2) changes to the late phase models so that the predicted behavior will represent the late phase of a severe accident, and (3) changes to improve the overall reliability and usability of the code. Improvements to existing models, the new models, and the changes made to input processing are summarized in this section. A detailed discussion of all SCDAP models may be found in Volumes I and II.

2.2.1 Inconel Grid Spacer/Zircaloy Interaction Model

During the course of a severe accident, eutectic interactions occur between grid spacer Inconel and the zircaloy cladding of a fuel rod or a zircaloy guide tube. These interactions effect the temperatures at which core materials begin melting and relocating at the grid spacer locations. Results from previous CORA experiments and separate effects testing at Kernforschungszentrum Karlsruhe (KfK), show that contact of Inconel from a grid spacer, or the small Inconel tabs used to stabilize fuel rods when zircaloy grid spacers are employed, with zircaloy results in a chemical reaction that liquefies a fraction of the fuel rod cladding at temperatures well below the zircaloy melting point. A model, based on results from separate effects experiments performed by Garcia and Hofmann at KfK^{15,16,17}, was developed for use in the code. This model uses parabolic rate equations to analytically describe the transient growth of the reaction zone on both sides of the interface between Inconel and zircaloy. These reaction rate correlations, which are functions of temperature and oxide thickness, describe the effects of the protective oxide layer formed during early stages of zircaloy oxidation on the chemical interactions occurring between Inconel and zircaloy. The model calculates the initial fuel rod failure due to the formation of eutectics at

temperatures more representative of those observed during the course of an experiment, the drainage of absorber material to lower elevations in the bundle, and the accumulation of debris near a grid spacer location.

2.2.2 Reflood and Vapor Limited Diffusion of Steam

As observed in the LOFT LP-FP-2 test, two SFD (ST and 1-1) tests performed in the Power Burst Facility (PBF) at the INEL, and CORA-12 and CORA-13 reflood tests performed in the CORA facility at KfK, significant oxidation and hydrogen production occur during the reflood phase of a severe accident. In previous versions of the code, the increased oxidation and hydrogen production coincident with the addition of water to cool the core was not well represented. A new model that describes the events occurring in the reactor core during reflood was developed.

The reflood model in SCDAP/RELAP5/MOD3.1 incorporated RELAP5 thermal hydraulics, reflood correlations, and quenching equations. The model also considered a mass transfer coefficient calculated using a heat/mass transfer analogy based on vapor limited diffusion of steam to the zircaloy surface and the effects of argon or other noncondensable gases flowing through the core. For the oxidation of additional zircaloy to be predicted to occur during the reflood phase of a simulated accident, the oxide layer formed on the cladding surface is considered to shatter when the following criteria were satisfied: (1) a cooling rate in the bundle greater than 2 K/s, (2) a beta-zircaloy layer less than 0.1 mm thick, and (3) an oxide temperature less than or equal to 1,560 K. The calculation of the oxygen uptake by zircaloy uses a mass/heat transfer analogy based on mass flow rates, water vapor thermal conductivity, mass diffusivity, and viscosity that assume the Colburn j factors for heat and mass transfer to be equal. This model enhanced the heatup, hydrogen production, and melt relocation that occur ahead of the quench front.

2.2.3 BWR Control Blade/Channel Box Model

Prior to SCDAP/RELAP5/MOD3.1, the BWR control blade consisted of a simple model based on cylindrical geometry with the channel box walls represented by the SCDAP shroud model. A control blade/channel box model based on experiment-specific models developed for the CORA BWR tests and the ACRR DF-4 test under the Boiling Water Reactor Severe Accident Technology (BWRSAT) program at Oak Ridge National Laboratory (ORNL) was developed by ORNL for inclusion in SCDAP/RELAP5/MOD3.1. The BWR control blade/channel box model was designed as a separate SCDAP component to represent all geometries of interest, including full-size BWR cores and experimental facilities, so that it contained sufficient detail to account for all important phenomena occurring in a BWR core during a severe accident.

The BWR blade/box component is based on a nodal configuration that uses three radial temperature nodes to represent the control blade and two nodes to represent the channel box walls at each axial elevation in the core. At each axial elevation, the model interacts with two RELAP5 hydrodynamic volumes, one on the interstitial side of the component and the other on the fuel bundle side. The gap between the stainless steel rodlets and blade sheath is also modeled. This gap communicates with the coolant interstitial volume through a series of holes in the blade sheath and results in two additional surfaces on which stainless steel oxidation can occur. The model imposes an additional thermal resistance between the blade sheath and the rodlets. To calculate the interactions of the control blade and channel box within the reactor core during a severe accident, hydrodynamic parameters from RELAP5 are used. The

steam, hydrogen, and inert gas mass flow rates and fluid pressures from RELAP5 are used in the internal oxidation model to calculate the partial pressures of steam and hydrogen in the system. The RELAP5 fluid temperatures, convective heat transfer coefficients, and time step size are used to calculate heat transfer, and the hydrodynamic volume fluid void fractions are used by the internal radiation model to determine when a radiation heat transfer calculation to the interstitial side to the component should be performed. The radiation heat transfer rates, on the fuel-bundle side of the channel box, are obtained from the SCDAP radiation model. The model returns to RELAP5 weighted average wall temperatures of surface areas exposed to a coolant volume.

Damage progression of the control blade/channel box is calculated using an approximate solution method to solve the melting terms in the energy equation and to simulate the liquefaction of the B₄C/stainless steel and stainless steel/zircaloy eutectics. The B₄C and stainless steel or stainless steel and zircaloy material pairs, if present, are allowed to react using reaction kinetics developed by Hofmann.¹⁸ The relocation of molten material in the blade region is controlled by solidification rates. The relocation logic in the model allows for horizontal movement of molten material as well as a downward flow that continues until all material has solidified or moved past the bottom of the defined core. The relocation model is to some extent based on the results of CORA BWR experiments with an initial heatup rate of 1 K/s, which results in only a small extent of oxidation of the control blade prior to its melting. For initial heatup rates of less than 0.3 K/s, there will be considerably more oxidation of the control blade prior to its melting. In these cases, the extent of relocation may be overpredicted by the relocation model.

2.2.4 Late Phase Modeling

The late phase model improvements recently added to the code included models to represent the spreading of molten core material in radial and axial directions, the re-opening of a blocked region in the core as molten material relocates from the region, the formation of a cohesive debris region, and/or the formation of a rubble debris bed.

Previous versions of the code did not model the spreading of molten material in a radial direction and the axial spreading of molten material was modeled simplistically. The axial node in an earlier version would only contain molten material after the fuel cladding in that location was heated to the point of ceramic melting. The model in SCDAP/RELAP5/MOD3.1 includes extensions to the molten pool model to calculate the spreading of molten material. These extensions allowed the code to calculate a radial spreading rate as a function of (1) the temperature and size of the molten pool, (2) the flow rate and temperature of fluid flowing through the porous debris region adjacent to the molten pool, and (3) the porosity and particle size of the porous debris region adjacent to the molten pool. The model is based on the concept of a sporadically moving crust enveloping the molten pool with the crust experiencing repeated cycles of melting, flowing, and freezing.

A model that removes blockage areas at a specific location in the bundle once material slumps away was added to the code. This model removes a planar blockage region once material slumps away by changing the flow area of the junction from a value of zero, indicating a blocked region, to the flow area of the junction prior to the formation of the blockage. If a bulk blockage region relocates, the model restores all flow areas and activates the RELAP5 control volumes (that model fluid at that location) to their state prior to the formation of the blockage. The blockage model also models flow areas and volumes at all bundle locations to account for the compaction that takes place when porous debris melts.

Models to account for the formation and behavior of debris, cohesive and rubble, regions during a severe accident were added to the code. The model for cohesive, nonporous, debris considers the debris bed to be a solidified metallic melt consisting of control rod material and fuel rod cladding containing embedded intact fuel rods. The model calculates the heatup of the nonporous debris taking into account the axial heat conduction and the transfer of heat by convection and radiation from the upper and lower surfaces of the cohesive debris region and the internal heat generation from the embedded fuel rods. The rubble debris bed is modeled as a region of debris formed when a section of the core, embrittled by oxidation, shatters on contact with relatively cool reflood water. The model considers convective heat transfer between the debris particles and the fluid between debris particles to be the only mechanism that can remove heat from the debris region. Porous debris heat up is calculated by taking into account the heat of fusion for each material in the debris bed, decay heat in the debris particles, size of the debris bed, rate of heat transfer between the fluid and the debris particles, and the state of the debris (dryout, in process of being quenched or quenched).

2.2.5 Lower Head Modeling (COUPLE)

Improvements were made to a model based on COUPLE,⁴ a two-dimensional, finite element, steady state and transient heat conduction and advection code, used to calculate the heatup of the debris and/or surrounding structures such as the vessel wall to allow accurate calculation of damage to the lower head of a reactor. Modeling improvements have been made in (a) heat transfer rate at the surface of the COUPLE finite-element mesh, (b) interfaces to RELAP5 control volumes, (c) multiple COUPLE finite-element meshes, (d) natural convection of liquefied debris, and (e) heat transfer at the interface between debris and structure. Finally, an interface with PATRAN⁶ was developed. This interface allows a COUPLE finite element mesh to be generated by PATRAN and linked to SCDAP/RELAP5.

2.2.6 User Conveniences and Improved Capabilities

Many user conveniences, improved or new capabilities, and error corrections are in SCDAP/RELAP5/MOD3.1. These additions, changes, and/or improvements decreased the time needed to develop and debug an input deck, improved running time, removed oscillations due to numerical instabilities, corrected inconsistencies and redundancies, and added missing variables to the printed output.

The change from free format input to RELAP5 style card number along with the addition of range checking and error trapping routines in the SCDAP module simplified the building of an input deck, facilitated input checking, and decreased the time needed to debug the input deck. The change to card number input gave the user the ability to change SCDAP variables on restart and facilitated the performance of sensitivity studies.

Numerical oscillations, observed in earlier versions of the code when the time step exceeded a stability limit associated with the absorption of radiation heat in the fluid, were smoothed. The linear time smoothing algorithm that was applied to the radiation heat transfer calculation allowed a large relative time step to be used without significant numerical oscillations. Also, to increase the usability and reliability of the code, changes were made so that error estimates at the end of each time step were checked. If error estimates were too large, all variables were reset to their values before the start of the time step. The code then attempted to repeat the calculation using a smaller time step size. By using the time step repetition in

conjunction with the time smoothing option, significant improvements in numerical stability and efficiency were achieved.

2.3 The Effects of Changes made to SCDAP/RELAP5

The incorporation of error corrections and model enhancements resulted in significant improvements in code reliability and run time. Improvements in computation time ranged from twenty percent to nearly a factor of three with significantly smoother results for test problems, experimental analysis, and accident scenarios in full plants. The impact of these changes are described in detail in the remaining sections.

3. SCDAP/RELAP5/MOD2.5, MOD3 AND MOD3.1 COMPARISON

Several versions of the code, SCDAP/RELAP5/MOD2.5, MOD3, and MOD3.1 were used to analyze several experiments including the CORA-7 and CORA-13 tests, the ACRR DF-4 test and the Surry Nuclear Power Plant. Code version to code version comparisons for the two CORA experiments, DF-4, and the Surry Nuclear Power Plant will be discussed in this section. In addition to the version to version comparison for the CORA experiments, how well the calculated results from each version agree with the measured data from the experiment will also be discussed.

3.1 CORA

A series of bundle heating and melting experiments have been conducted in the CORA test facility at Kernforschungszentrum, Karlsruhe (KfK) to examine core damage progression under severe accident conditions. These steam-fed out-of-pile tests use a combination of electrically heated and unheated bundle components to simulate decay heating in a reactor core. A description of the facility and the experiments used in this assessment effort appears in Appendix A.

3.1.1 CORA-7 Test Comparisons

Throughout the development of SCDAP/RELAP5, the CORA-7 test has been used as an assessment tool. The CORA-7 test, a large PWR bundle containing 57 rods, 20 unheated fuel rods, 32 simulator rods and 5 control rods, was performed on February 22, 1990. Various versions of the code have been used to analyze this experiment, the first being Version 3f, the official transmittal of SCDAP/RELAP5/MOD2.5. Figures 3-1 and 3-2 show the measured temperatures on two different rods and predicted temperature responses using three versions of the code. These figures indicate that differences in predicted temperatures and damage progression behavior using the latest version of the code is consistent with earlier code versions and is within experimental and modeling uncertainties.

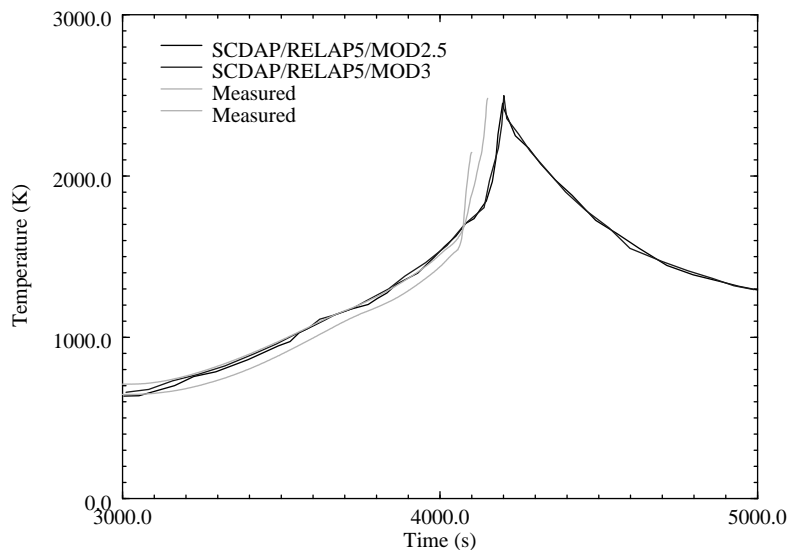


Figure 3-1. Calculated and measured fuel rod temperatures at the 750 mm using SCDAP/RELAP5/MOD2.5 and SCDAP/RELAP5/MOD3.

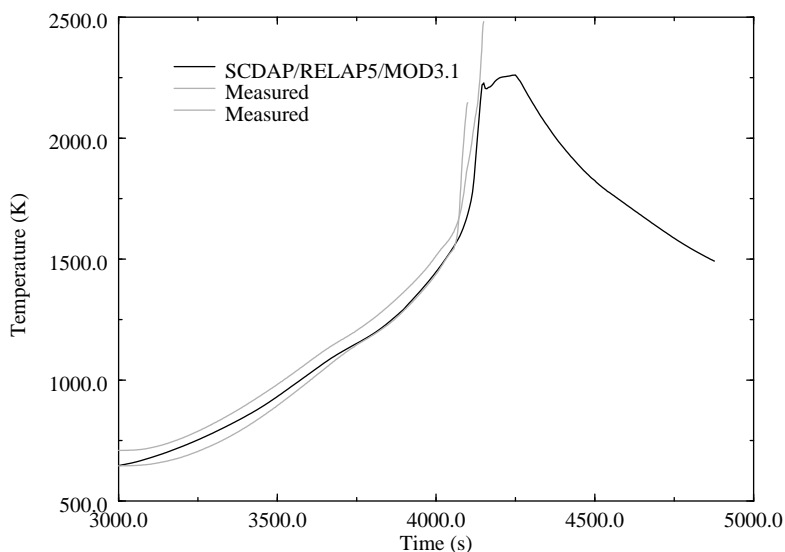


Figure 3-2. Calculated and measured fuel rod temperatures at the 750 mm elevation using SCDAP/RELAP5/MOD3.1.

There were no significant differences noted in the oxidation and hydrogen production behavior between SCDAP/RELAP5/MOD3 and earlier versions of the code that could not be attributed to the differences in predicted temperature response. Previous code versions as well as SCDAP/RELAP5/MOD3.1 predicted oxidation of the cladding and melt relocation to begin in the upper quarter of the bundle and progress upward into the upper plenum. However, the addition of the grid spacer model to SCDAP/RELAP5 with a preliminary model in SCDAP/RELAP5/MOD3 and the final model in SCDAP/RELAP5/MOD3.1 changed the predicted damage progression behavior downward toward the bundle bottom. Prior to the addition of the grid spacer model, relocating clad, fuel and/or control material flowed downward forming a blockage region near the bottom of the bundle. Once the grid spacer model was implemented, relocating liquefied cladding, fuel, or control material from the upper elevations slowed and began to solidify at the middle Inconel spacer location forming a blockage region. As a result, the location of the predicted blockage region is now more consistent with the location of the blockage region determined from the post-test metallurgical examination of the damaged bundle.¹⁹ Figure 3-3 shows a representation of the SCDAP/RELAP5 predicted end state as compared to the end state determined from the post test metallurgical examination. Figure 3-4 shows an artist's representation of a representative fuel rod showing core damage and blockage regions as compared to those determined from the post test metallurgical examination. The code predicted UO_2 fuel and cladding to liquify at 0.85 m. The liquified material flowed downward forming a large blockage region near the Inconel spacer grid. Similar behavior during the experiment was determined from the post-test metallurgical examination.

3.1.2 CORA-13 Test

CORA-13, which is International Standard Problem 31 and was performed at KfK on November 15, 1990, has been used primarily to assess SCDAP/RELAP5's ability to calculate the additional oxidation and hydrogen generation that occurs during reflood of a core. See Appendix A for a more detailed description of this test.

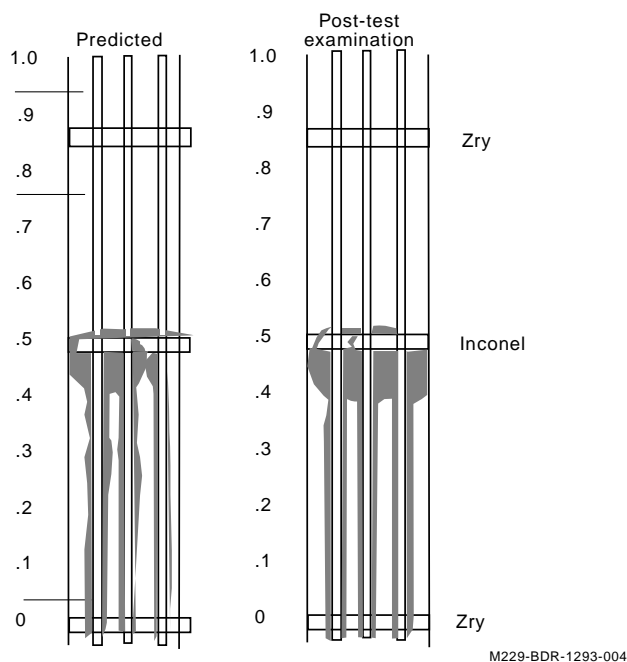


Figure 3-3. End-state figure of the CORA-7 comparisons.

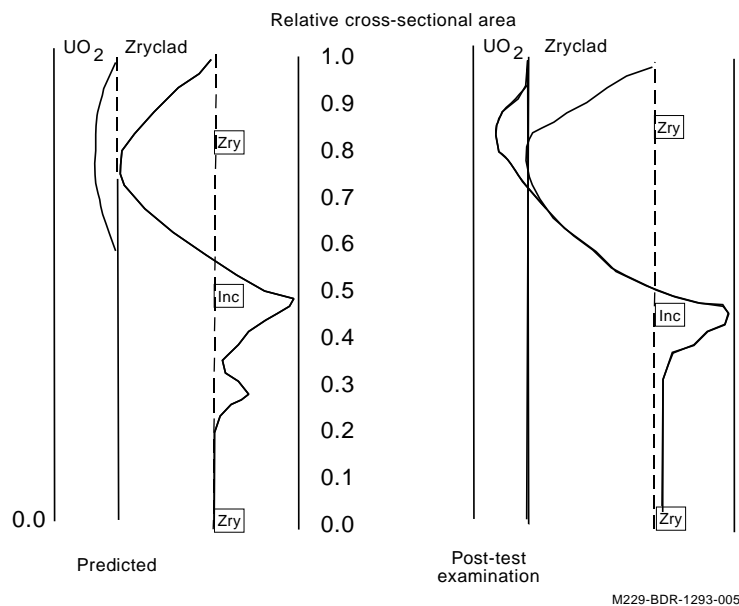


Figure 3-4. Artist's rendition of a representative cross-section of the CORA-7 damaged bundle.

Comparison of the results between different versions of the code indicated that the inclusion of the grid spacer/material interaction model impacted the calculated core damage progression in the following manner: (1) initial fuel rod clad failure occurred near the Inconel grid spacer at a temperature substantially lower than calculated in earlier versions of the code, (2) cladding began to liquefy at temperatures near 1,500 K due to eutectics being formed between Inconel from the grid spacer and the zircaloy fuel rod clad, and, (3) a blockage region consisting of accumulated melted debris formed near the location of the grid

spacer. Figure 3-5 compares the calculated unheated fuel rod temperature from an earlier calculation.^{20, 21} using SCDAP/RELAP5/MOD3 and SCDAP/RELAP5/MOD3.1 with the measured data at the 750 mm elevation. The figure shows that the calculated temperature response of the bundle components was not adversely effected by the addition of the grid spacer model. The most notable improvement in the calculated results was the formation of a large blockage region near the Inconel grid spacer. Figure 3-6 shows an artist's conception of the calculated and measured end-state of the bundle.²²

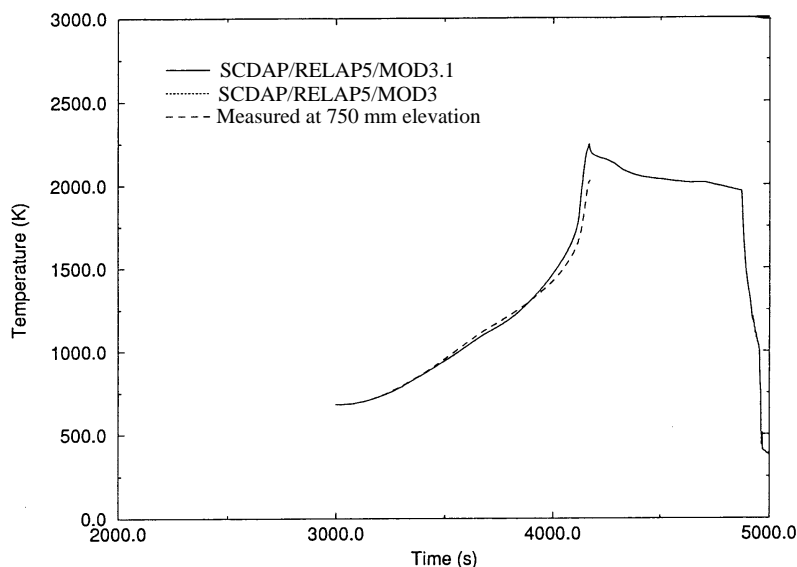


Figure 3-5. Comparison of calculated fuel rod temperatures for CORA-13 from SCDAP/RELAP5/MOD3 and SCDAP/RELAP5/MOD3.1 with measured at 750 mm elevation.

However, the inclusion of a model to treat the influence of reflood as discussed in Section 4 had the most dramatic impact on the results. When vapor limited diffusion of steam to the zircaloy surface was implemented in the code, heating rates in the bundle slowed considerably and the onset of hydrogen production was delayed several hundred seconds and occurred over a longer period than observed when steam starvation limits were imposed. In addition, models which accounted for the spalling or cracking of the protective oxide layer on the zircaloy in the bundle resulted in renewed heating and melting that was much more consistent with the data.

3.2 ACRR DF-4 Experiment

The Annular Core Research Reactor (ACRR) at Sandia National Laboratory (SNL) has been used for in-pile experiments investigating fuel behavior after coolant boiloff in simulated PWR and BWR severe accidents. The reactor features an annular core located at the bottom of a 10 m deep water-filled tank. For each test, the experimental fuel bundle and shroud is placed in a dry capsule in a central flux trap region of the driver core. The experimental bundle is heated by fission power. Steam from a superheater is injected into the test section of the capsule. A description of the ACRR test facility is contained in Appendix A.

The Debris Formation 4 (DF-4) experiment was performed in the ACRR at SNL in the late 1980s. The active core region containing the fuel bundle was 0.508 m in length. The fuel bundle consisted of a zircaloy-lined ZrO_2 thermal shroud, 14 PWR-type fuel rods, 0.508 m long, enriched to 10 wt% ^{235}U , and a zircaloy channel box containing a B_4C control blade.²³ The initial analysis of this experiment was

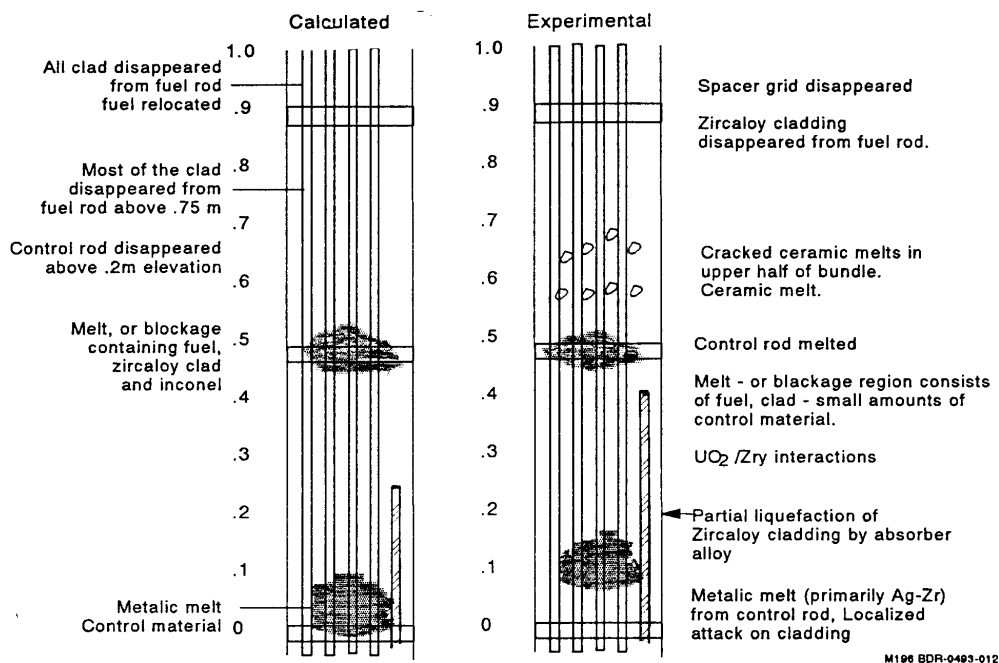


Figure 3-6. Artist rendition of the CORA-13 bundle showing the calculated and measured end-state.

performed using an early version of SCDAP/RELAP5/MOD2 in 1989.²⁴ New calculations were made of the experiment with each new release of the code, the last being made with SCDAP/RELAP5/MOD3 using the ORNL-developed control blade/channel box model.

The effect of the addition of the control blade/channel box model is shown in Figures 3-7 to 3-9. Using the same version of the code, SCDAP/RELAP5/MOD3 two calculations were performed, one using the ORNL model to model the control blade/channel box region of the experimental bundle, the other using the SCDAP shroud model to model the channel box and the cylindrical B_4C rod model to represent the control blade region. Results of these two calculations were compared with the measured data. The figures showing the predicted temperatures at three elevations, 0.096, 0.258, and 0.386 m, with the measured data, indicate that the new control blade/channel box model predicts fuel rod temperatures slightly hotter during the transient than those predicted by the old model. The older method of modeling the control blade region appears to predict temperatures closer to the measured data in the lower bundle, whereas middle bundle temperatures and relocation behavior predicted by the ORNL model are closer to measured values. Both models tend to successfully predict the damage progression trends taking place within the control blade channel.

Small differences in temperature response at various elevations in the bundle related to the differences in modeling the control blade/channel box in the input deck were observed. The introduction of the ORNL control blade/channel box model into the code, along with changes and error corrections to the heat transfer, and radiation heat transfer models made significant improvements in the code's prediction of bundle temperature response and damage progression events for a BWR severe accident scenario. As

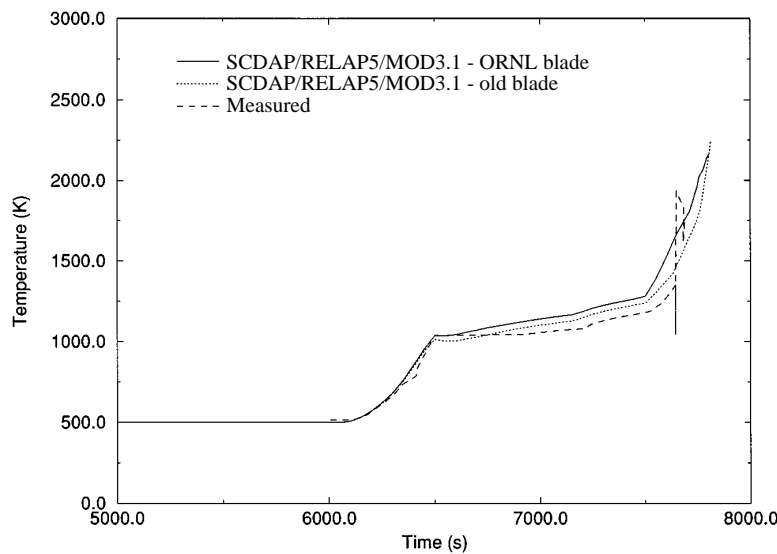


Figure 3-7. Comparison of calculated fuel rod temperatures for DF-4 using the same version of the code and the two control blade models at the 0.096 m elevation.

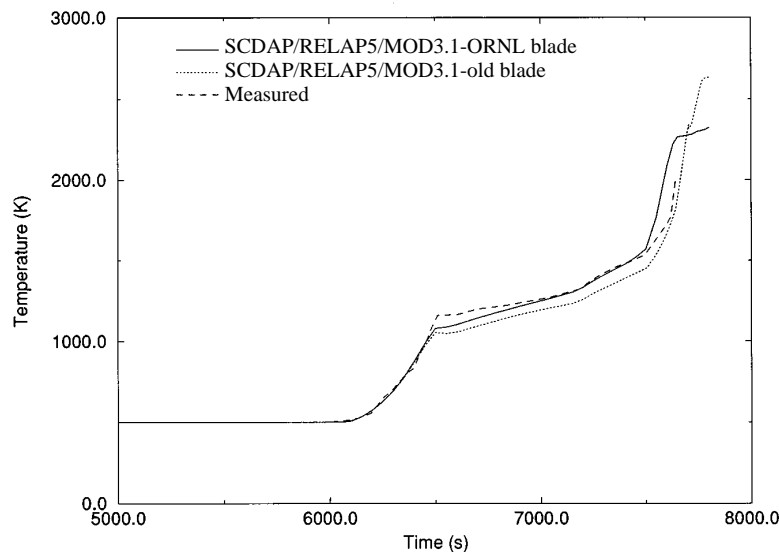


Figure 3-8. Comparison of calculated fuel rod temperatures for DF-4 at the 0.258 m elevation using the two control blade models and the same version of the code.

shown in Figures 3-10 and 3-11, predicted fuel rod temperature response during the early phases of the experiment using any version of the code agrees well with the measured data. Each code version, SCDAP/RELAP5/MOD3, and SCDAP/RELAP5/MOD3.1, predicts the temperature rise during the initial heating phase well, with MOD3.1 overshooting, by 50 K, the initial temperature at the start of the equilibration phase and earlier versions undershooting this temperature by about 50 K. Using SCDAP/RELAP5/MOD3.1, predicted temperatures during equilibration phase converged with the measured data within 500 seconds and duplicated the measured data until the onset of rapid oxidation, whereas earlier versions

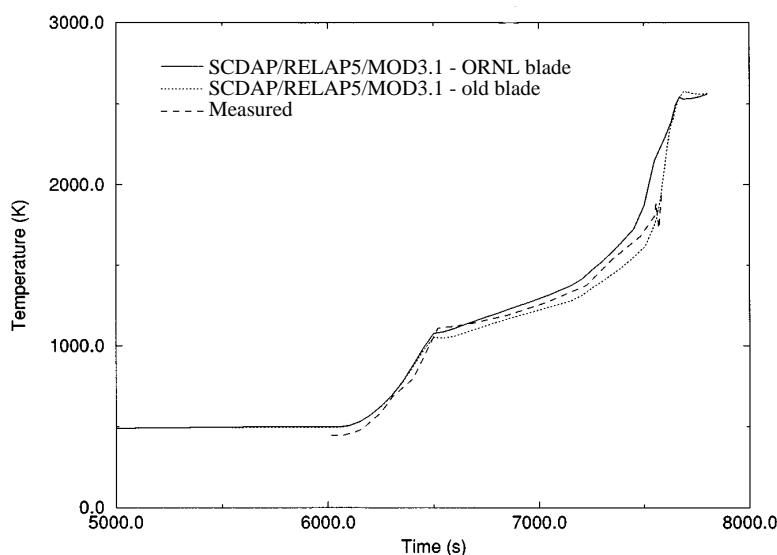


Figure 3-9. Comparison of calculated fuel rod temperatures for DF-4 at the 0.368 m elevation using the two control blade models with the same version of the code.

tended to consistently under predict temperatures by 50 K during this phase. SCDAP/RELAP5/MOD3.1 predicted the temperature at which rapid oxidation was observed to occur, although once oxidation began, this code version predicted an oxidation rate faster than observed. SCDAP/RELAP5/MOD3 and SCDAP/RELAP5/MOD3.1 predicted the onset rapid oxidation to occur at a temperature 100 K cooler and a time 100 seconds later than observed. This delay in the onset of rapid oxidation is due to consistently lower predicted temperatures during the equilibration and pre-transient phase of the experiment.

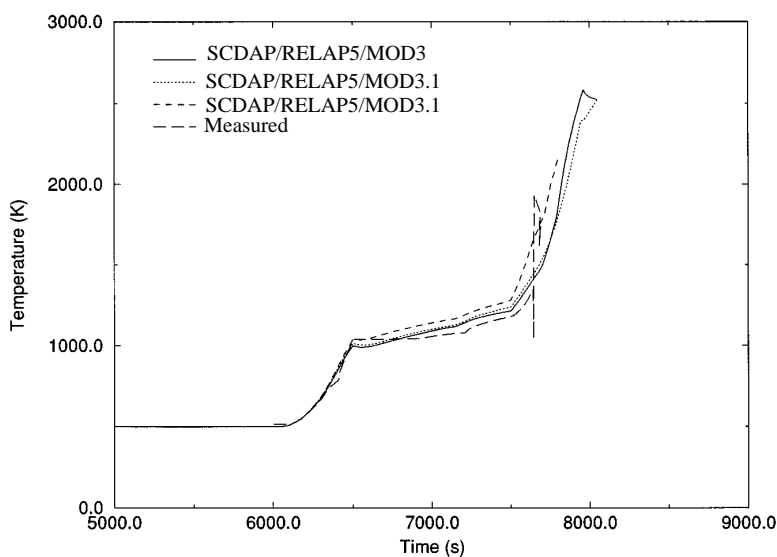


Figure 3-10. Predicted fuel rod temperatures for DF-4 at the 0.96 m elevation from 3 versions of the code compared to the measured.

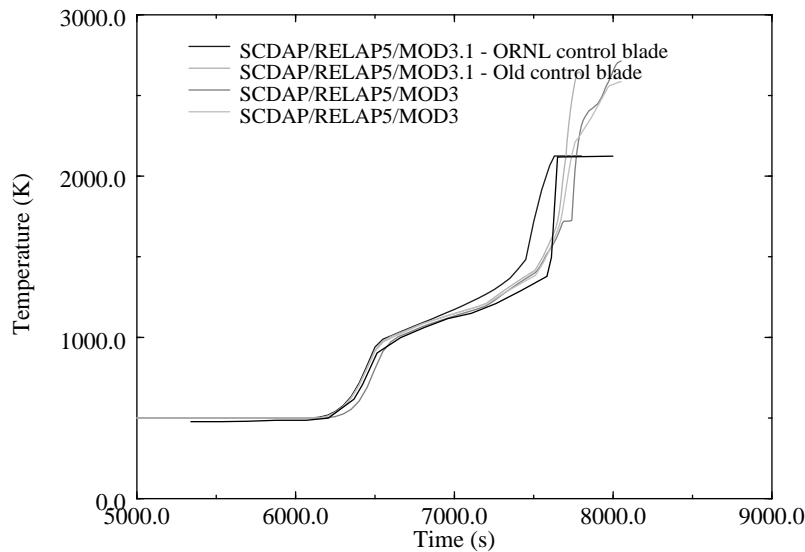


Figure 3-11. Predicted fuel rod temperatures for DF-4 at the 0.258 m elevations using 3 versions of the code compared to the measured.

During the equilibration phase of the DF-4 experiment, fuel rod and channel box temperatures tended to be slightly underpredicted when the control blade/channel box model developed by ORNL is used. As core equilibration continues during the experiment, the code predicted a heatup rate was more than was measured resulting in a channel box oxidation excursion occurring earlier and a temperatures slightly higher than the measured data. As shown in Figure 3-12, the predicted channel box temperatures, using the SCDAP shroud component to model the channel box and the cylindrical control blade model, are in good agreement with the measured data. Early equilibration phase temperatures are predicted equally well with either model. The ORNL model overpredicted temperatures during the later part of the equilibration phase and the oxidation excursion. The old control blade/channel box model overpredicts temperatures, but the overprediction is considerably less. Near the bottom of the bundle, the old control blade model predicts a temperature response closer to the measured data, whereas the ORNL model predicts temperatures closer to measured data in the upper bundle. The discrepancy between the predicted and measured temperature at the top of the bundle was attributed to reflux cooling occurring in the upper portion of the test train, which was not modeled by the code. In the middle regions of the bundle fissile zone (0.254 and 0.368 m elevations), the calculated heatup rate and peak bundle temperature agreed with the measured heatup rate and the PIE estimated peak bundle temperature.

The rapid oxidation of the fuel rod cladding and zircaloy channel box, calculated to begin when the temperature in the upper bundle exceeded 1,700 K and continuing until steam starvation occurred, agreed with what was observed during the experiment. The total quantity of hydrogen was predicted well with the measured value of 39 g and the calculated value of 35 g. The order and timing of key damage progression events agreed with the measured results, although commencing approximately 100 seconds early with the initiation of the rapid oxidation driven heatup phase of the experiment. The calculated relocation of the stainless steel control blade agreed quite well with the data. The calculated state of the bundle, at the time of complete blockage of the control blade flow channel appeared to be consistent with the post irradiation examination (PIE).

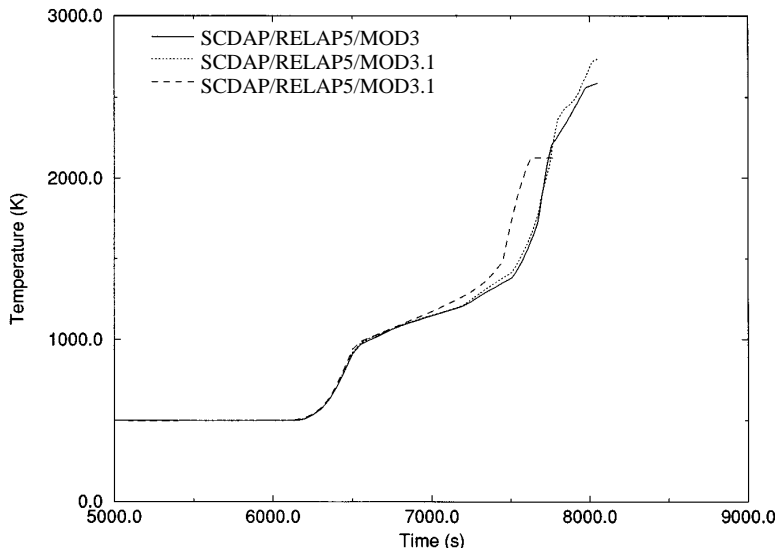


Figure 3-12. Predicted temperatures for the channel box for DF-4 at the 0.258 m elevation using both control blade models compared to the measured.

3.3 Full-Size Nuclear Power Plants

Extensive testing of the models in SCDAP/RELAP5 has been conducted using experiments performed in experimental facilities around the world. For the code to be used to analyze and predict events occurring during an accident in a commercial nuclear power plant, such as Surry, the effect of the addition of new models and error corrections, and usability improvements on predicted results needed to be assessed. The Surry Nuclear Power Plant was chosen for this assessment as numerous analyses over a number of years have been performed using several versions of RELAP5 or SCDAP/RELAP5 looking at the effects of code changes on several accident scenarios as a TMLB', depressurization, or LOCA pin failure.

Calculations of a TMLB' severe accident scenario in the Surry Nuclear Power Plant were performed with two different code versionse. The first set of results were for SCDAP/RELAP5/MOD3 as reported in the study for the potential of high pressure melt ejection by Knudson.²⁵ The second set of results were those reported in Appendix B for SCDAP/RELAP5/MOD3.1. The calculations for each version were performed with the same nodalization of the reactor core; the reactor core was divided into three flow channels with each flow channel divided into ten axial nodes. None of the two calculations modeled countercurrent natural circulation in the hot leg or leakage from the seals in the reactor coolant pumps. The calculations reported by Knudson were designed to minimize the time to failure of the lower head. In these calculations, user defined parameters that control the modeling of melt progression were assigned values that maximized the calculation of melt progression and thus maximized the calculation of core blockage. In the calculations described in Appendix B, the parameters that control the modeling of melt progression were assigned values for best estimate modeling, which are the default values. These three parameters were: (1) failure temperature of oxide shell on fuel rod cladding, (2) thickness at which oxide shell is durable and will then not fail until its temperatures exceeds the melting temperature of the oxide shell, and,

(3) minimum hoop strain for double-sided oxidation. In the MOD3 calculations, these three variables were assigned values of 2,400 K, 0.9 mm (100% oxidation of cladding), and 0.02 respectively. For the MOD3.1 calculations, these three variables had the default values of 2,600 K, 0.185 mm (30% oxidation of cladding), and 0.02, respectively.

The results of the calculations with the versions are compared in Table 3-1. The initial events and damage thresholds are similar for the two versions. These events and damage thresholds for which similar times are calculated include: (1) beginning of rupture of fuel rods, (2) rupture of surge line, and (3) rupture of hot leg with pressurizer. The calculated time for beginning of ceramic melting and thus the formation of a molten pool was significantly earlier with SCDAP/RELAP5/MOD3.1. The time for initial formation of the molten pool is 12,860 seconds with SCDAP/RELAP5/MOD3.1 and is 15,180 seconds for SCDAP/RELAP5/MOD3. This difference in results was due to differences between the two calculations in the values of user defined parameters for melt progression, which were discussed above. These differences in melt progression parameters make it useful to compare the calculations of the two versions of the code only out to the time of beginning of ceramic melting.

Table 3-1. Version comparison for the Surry calculations.

Event or damage threshold	SCDAP/ RELAP5/ MOD3	SCDAP/ RELAP5/ MOD3.1
	time (s)	time (s)
Liquid level drops below bottom of fuel rods	10,620	11,000
Beginning of rupture of fuel rods	12,360	11,950
Rupture of surge line	12,930	13,035
Rupture of hot leg with pressurizer	14,058	13,990
Beginning of ceramic melting (molten pool)	15,180	12,860

4. SCDAP/RELAP5/MOD3.1 ASSESSMENT

This section summarizes SCDAP/RELAP5/MOD3.1 specific assessment results. It includes (a) an estimation of overall model uncertainties based upon code-to-data comparisons for the early stages of a severe accident and (b) an assessment of the new models that are unique to this version of the code. There is also a brief discussion of the likely modeling uncertainties for the later stages of an accident. However, it is not yet possible to provide a quantitative estimate of the model uncertainties for these stages of the accident.

4.1 Estimate of Overall Model Uncertainties

The estimates of overall modeling uncertainties are based upon representative code-to-data comparisons using SCDAP/RELAP5/MOD3.1 as discussed in Appendix A. These experiments included a relatively wide range of thermal-hydraulic conditions from representative tests in the CORA, PBF, ACRR, PHEBUS, and LOFT facilities. The general trends and overall variation between the calculated and measured results are discussed, including (a) thermal response, (b) oxidation and hydrogen production, (c) fuel rod ballooning, and (d) the initial melting and relocation of core component materials.

It should be noted that overall variation between calculated and measured results discussed in this section is a conservative estimate of the modeling uncertainties since that variation includes both modeling and experimental uncertainties.^a Although a rigorous assessment of the relative contribution of the experimental uncertainties is beyond the scope of this report, previous sensitivity studies for the PBF SFD 1-3 and SFD 1-4 experiments indicate uncertainties in bundle power and heat losses resulted in a variation in bundle temperature comparable to the uncertainties in the test conditions.^{26, 27}

4.1.1 Thermal Behavior

Important measures of the ability of the code to predict thermal behavior during the early phases of an accident include (a) bundle dryout or changes in liquid level, (b) initial heating rates, (c) accelerated heating associated with rapid increase in Zircaloy oxidation, and (d) peak bundle temperatures. The assessment of dryout or changes in liquid level used the PBF SFD tests, where the water in the bundle was boiled down by an increasing fission power at a constant pressure, and the LOFT LP-FP-2 test, where the water in the Reactor Coolant System (RCS) and vessel was blown down through a break in the simulated Low Pressure Injection System (LPIS). Initial heating rates and accelerated heating rates were measured

a. The experimental uncertainties include both direct and indirect contributors. Examples of important direct measurement uncertainties are those for hydrogen production and peak bundle temperature. In the PBF SFD and LOFT LP-FP-2 tests where uncertainty estimates were provided, the uncertainty in total measured hydrogen production varied from a minimum of $\pm 12\%$ to a maximum of $\pm 36\%$. In addition, because direct measurements of temperature typically fail as zircaloy melting temperatures are reached, metallurgical examinations to establish peak bundle temperatures rely upon key melting or fuel morphology indicators. As a result, the experimental uncertainty in peak bundle temperature may be on the order of $\pm 15\%$. The indirect contributors are those associated with uncertainties in test boundary conditions that are used as input conditions for code calculations, or experiment-specific features that are not accurately represented in the code calculations. Examples from the PBF SFD tests include (a) bundle power with estimated uncertainties of $\pm 15\%$, (b) axial power profile, $\pm 25\%$ for tests without control rods, and (c) radial and axial heat losses, $\pm 25\%$ and $\pm 10\%$, respectively.

and compared for all of the tests, as described in Appendix A with additional analysis performed upon the CORA-7, CORA-13, and DF-4 tests as described in this section. Peak bundle temperatures were also compared for all of the experiments although the measurement uncertainties preclude any quantitative assessments.

Figure 4-1 shows a comparison of measured and calculated dryout times in the LOFT LP-FP-2 test. As shown on this figure, the calculated dryout, as the upper half of the core is uncovered, is in good agreement with that observed. As the water level drops below the midpoint of the core, the scatter in the data becomes larger and there is a larger variation between measured and calculated values. As discussed in Appendix A, the uncertainty in the estimated break flows during the experiment results in a bias in the initial core uncover time. However, once the initial core uncover time is established, the variation between the calculated and observed dryout, and the associated start of core heatup at a given elevation, varies from near zero at the top of the core to approximately 100 seconds at the bottom of the core. Such a variation is comparable to previous assessment results for LOFT using early versions of the code.^a

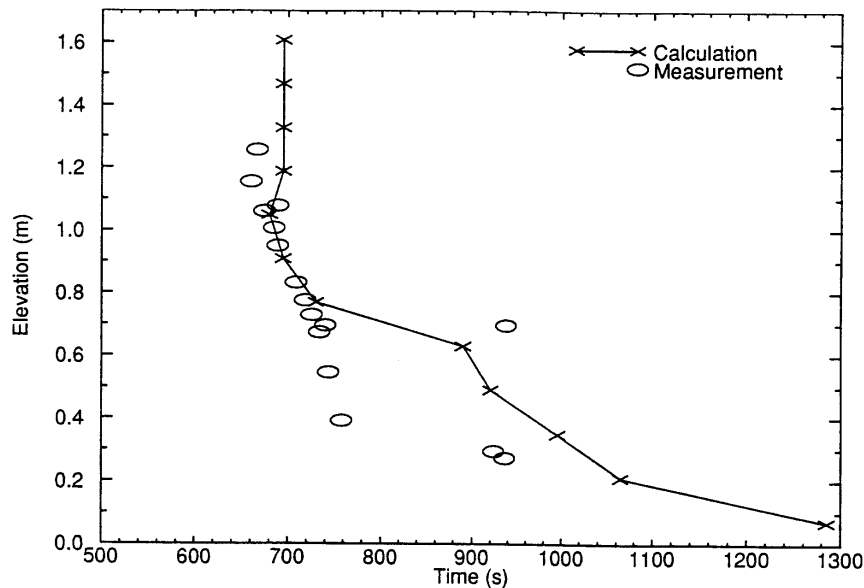


Figure 4-1. Calculated and measured core dry-out time as a function of elevation for LOFT LP-FP2.

Figures 4-2 and 4-3 show the calculated and measured collapsed liquid levels in two PBF SFD tests - SFD 1-3 and SFD 1-4. As shown on these figures the overall time for complete bundle uncover is matched relatively well although the calculated values show a step-wise change not apparent in the data. Although specific sensitivity studies were not performed to quantify the exact nature of the variations in the calculated and measured collapsed liquid level, these variations are likely caused by differences in actual and input axial power profiles. The actual axial power level in the SFD tests varies continuously with liquid level due to the moderating effect of the water on the fission power in the bundles. That power profile can vary as much as $\pm 25\%$ from the partially liquid filled to steam filled bundle (and $\pm 50\%$ as the Ag-In-Cd absorber material relocates in the SFD 1-4 test). However, the assessment calculations were

a. The assessment results are described in an informal report, EGG-SSRE-10098, *SCDAP/RELAP5/MOD3 Assessment: Assessment of Early Phase Damage Progression Models*, February 1992.

performed using three discrete changes in the axial power profile because of code input restrictions. The results for the SFD 1-3 test also demonstrates the influence of axial heat losses and experiment-specific features that can result in an increase in the variation between calculated and measured behavior. In this test, the water level actually drops below the bottom of the active fuel due to heat transfer from the bottom of the fuel to, and gamma heating of, the lower plenum of the test train. However, in the SFD 1-3 calculations, the axial heat losses and lower plenum structures were not modeled. As a result, it was impossible for the calculated water level to drop below the bottom of the active fuel.

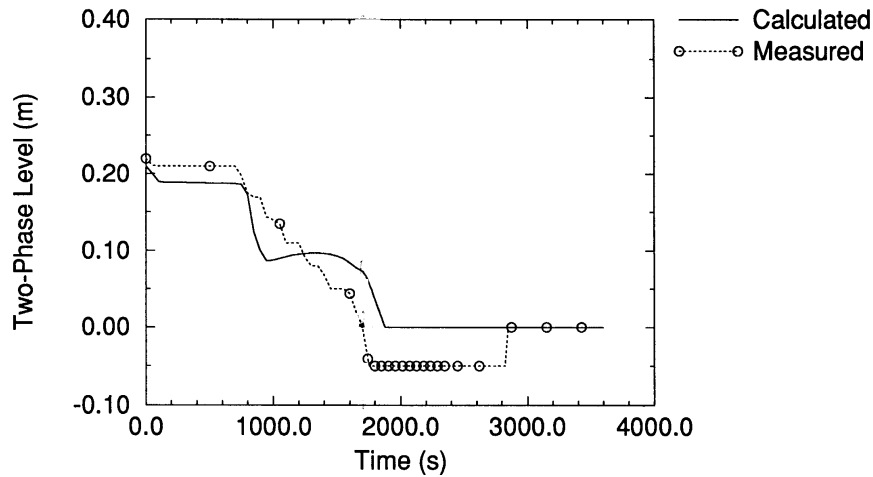


Figure 4-2. Calculated and measured collapsed liquid level for the PBF SFD1-3 experiment.

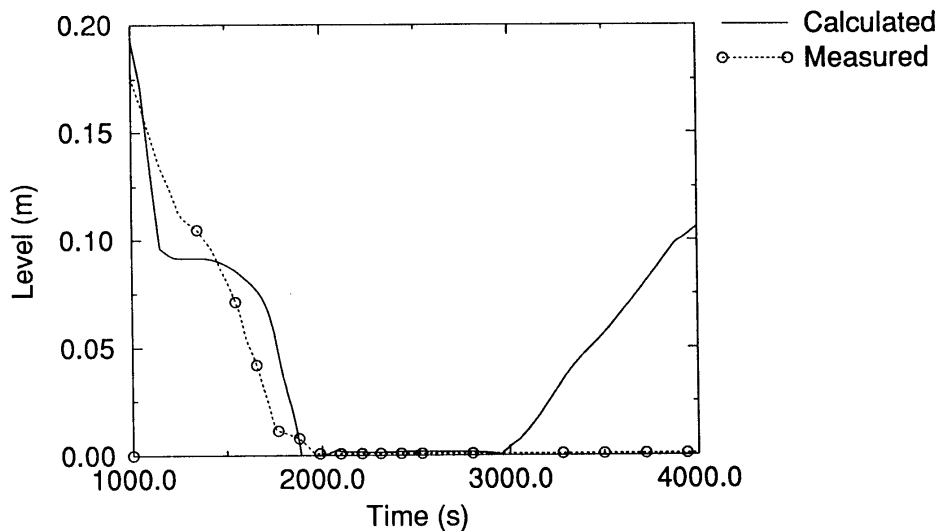


Figure 4-3. Calculated and measured collapsed liquid level for the PBF-SFD 1-4 experiment.

Although, as discussed in Appendix A, a comparison of the calculated and measured temperature responses show that the general trends of the initial heatup of the experimental bundles are predicted relatively well, an additional assessment of the overall variation between the calculated and measured heating rates and timing for the accelerated heating associated with rapid oxidation was performed for

three representative code-to-data comparisons, CORA-7, CORA-13, and DF-4. Figure 4-4 shows the calculated and measured heating rates as a function of temperature. For temperatures below 1,500 K the measured and calculated heating rates are closely clustered together. As the temperatures exceed 1,500 K, the heating rates start to increase and the scatter increases between (a) different tests and measurement locations in the experimental bundles and between (b) measured and calculated results. Figure 4-5 shows the calculated heating rates plotted versus the measured rates. At lower temperatures and heating rates from 0.5 to 1.0 K/s, the calculated and measured heating rates fall within $\pm 20\%$ with a few isolated points outside that range. At higher heating rates the scatter is larger with the primary outliers due to localized, at a thermocouple location, oxidation which is either calculated and not observed or vice versa. Figure 4-6 shows an expanded scale for heating rates below 1 K/s. Figure 4-7 shows a comparison of calculated versus measured time shifts in the temperature responses. That is, the figure represents the time required to reach a given temperature in the calculations versus that required in the experiment. Since the temperature is increasing with time in these experiments, increasing time on the figure also corresponds to increasing temperature. From this figure, it is clear that the majority of calculated and measured times to heat the experimental bundles to temperatures between 2,200 and 2,500 K falls within a range of 20%. It is also apparent for these three tests, that there is a systematic bias in that the average calculated temperatures lag the measured temperatures by about 10%.

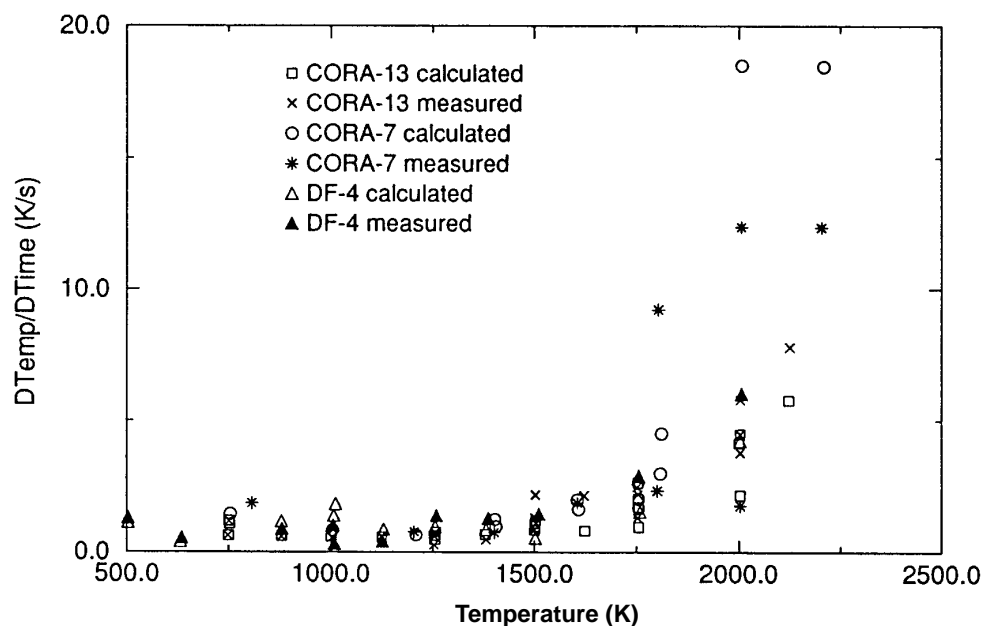


Figure 4-4. Calculated and measured heating rates as a function of temperature for the CORA-7, CORA-13 and DF-4 experiments.

If these results are compared against previous estimates of modeling uncertainties using earlier versions of the code, it is clear that the overall uncertainties in predicted heating rates up to a peak temperature between 2,200 and 2,500 K have not changed substantially. In those previous assessments it was concluded that the overall variation between measured and calculated temperature responses for a similar range of experiments was on the order of ± 20 to $\pm 30\%$.

If these results are compared to the expected uncertainty in bundle temperature associated with experimental uncertainties in power and heat losses, it is also clear that a variation of $\pm 20\%$ could result

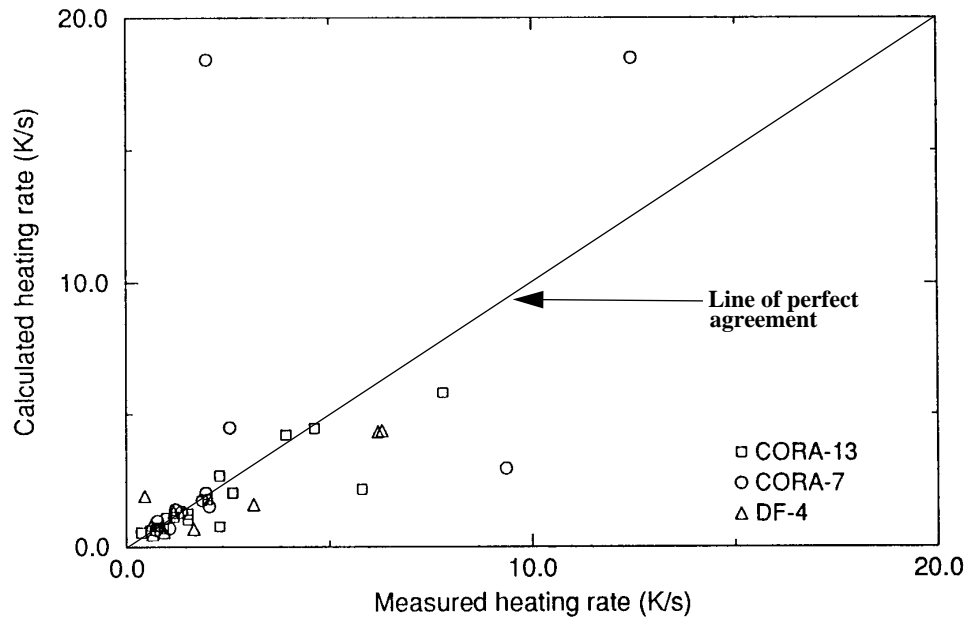


Figure 4-5. Calculated versus measured heating rates for the CORA-7, CORA-13 and DF-4 experiments.

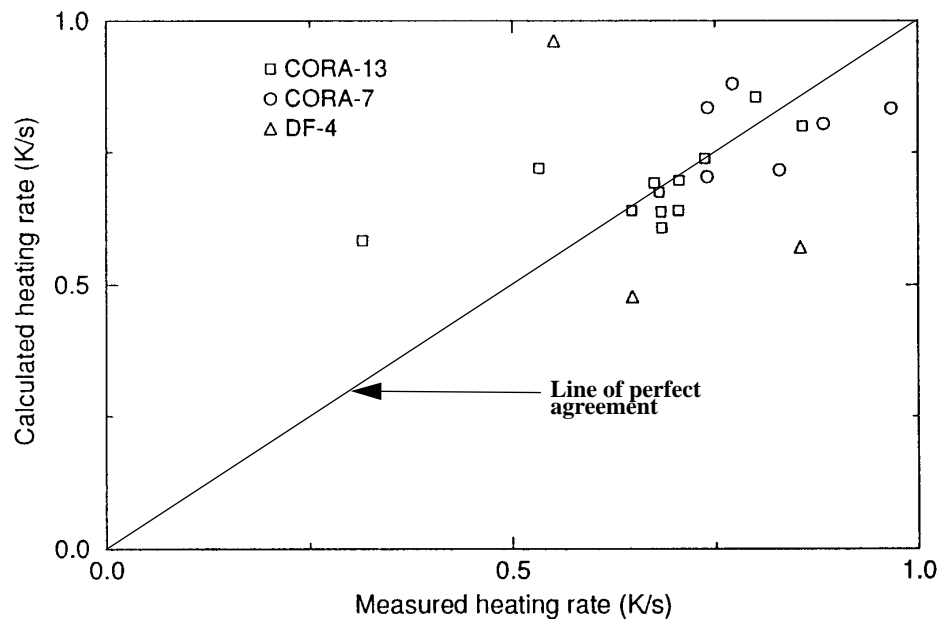


Figure 4-6. Calculated versus measured heating rates in the 0.0 to 1.0 K/s range for the CORA-7, CORA-13, and DF-4 experiments.

from the uncertainties in test conditions. As a result, it is unlikely that the overall variation between calculated and measured temperatures during the initial heating phase, heating rates on the order of 1 K/s or less, can be significantly reduced unless the uncertainties in test conditions are further reduced. On the other hand, at higher heating rates where the scatter is, in some cases, substantially greater than $\pm 20\%$, reductions in modeling uncertainties associated with the rapid heating due to oxidation is likely to reduce

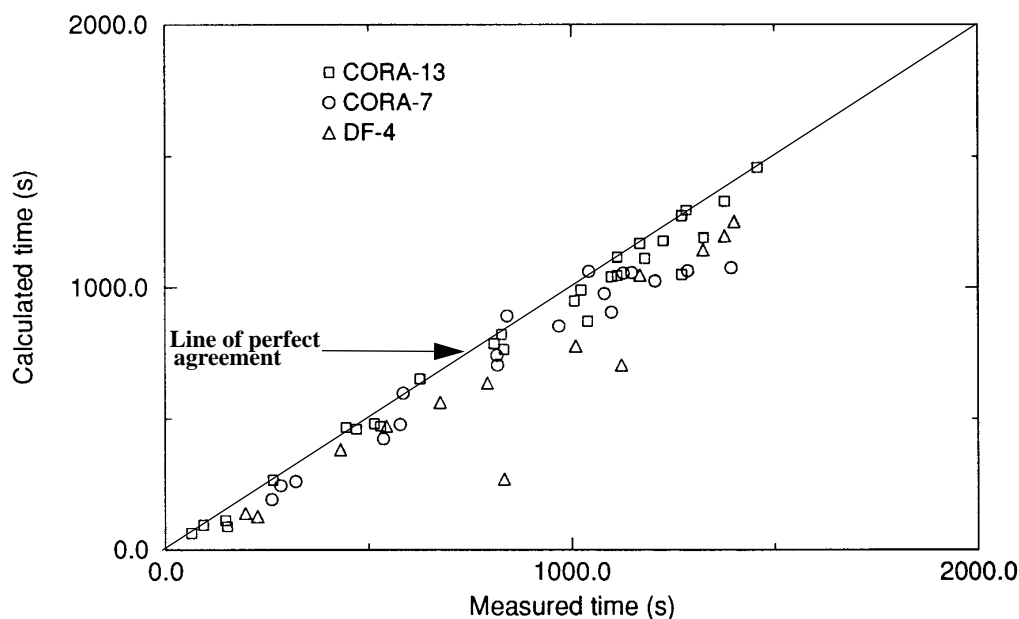


Figure 4-7. Comparison of calculated versus measured time shifts for the CORA-7, CORA-13, and DF-4 experiments.

the overall variation. The possible benefits of reducing the contributions due to indirect experimental uncertainties by the more thorough analysis of experimental-specific features and reductions in uncertainties in experimental boundary conditions can be demonstrated using the CORA-13 code-to-data comparisons. As discussed in Appendix A, this experiment was an international standard problem so the effort in quantifying experimental boundary conditions was more pronounced than in many other tests. In addition, the level of detail used to represent the experimental facility was substantially greater than in other assessment calculations. As a result, as shown on Figure 4-8, the overall variation between calculated and measured temperatures was decreased to approximately $\pm 10\%$.

It can also be seen in Figure 4-8 that the variation between calculated and measured temperatures for CORA-13 increases to a level of $\pm 20\%$ as temperatures exceed 2,000 K. This increase is also indicative of the observed behavior in the code-to-data comparisons. Although the increase in uncertainties at the higher temperatures is due in part to the accelerated heating rates due to oxidation, another significant contributor is the uncertainty associated with the melting or liquefaction of core materials. The direct experimental uncertainties are large due to the failure of most of the thermocouples near 2,000 K and the limitations of metallurgical examinations in determining bundle temperatures. The modeling uncertainties are also large, primarily as a result of the uncertainties in the temperatures and bundle conditions at the time of initial fuel rod material liquefaction and relocation. The most precise assessment of the peak temperature calculations arises from code-to-data comparisons for those experiments where ceramic melting temperatures are reached, since metallurgical key melt indicators are well defined. Of the experiments described in Appendix A, ceramic melting was clearly observed, and calculated by the code, for the PBF SFD and LOFT LP-FP-2 tests. In these experiments, the variation between calculated and measured peak temperatures varied from 1-10%. For the CORA tests, where the temperature remained below ceramic melting, the maximum temperature observed prior to thermocouple failure was about

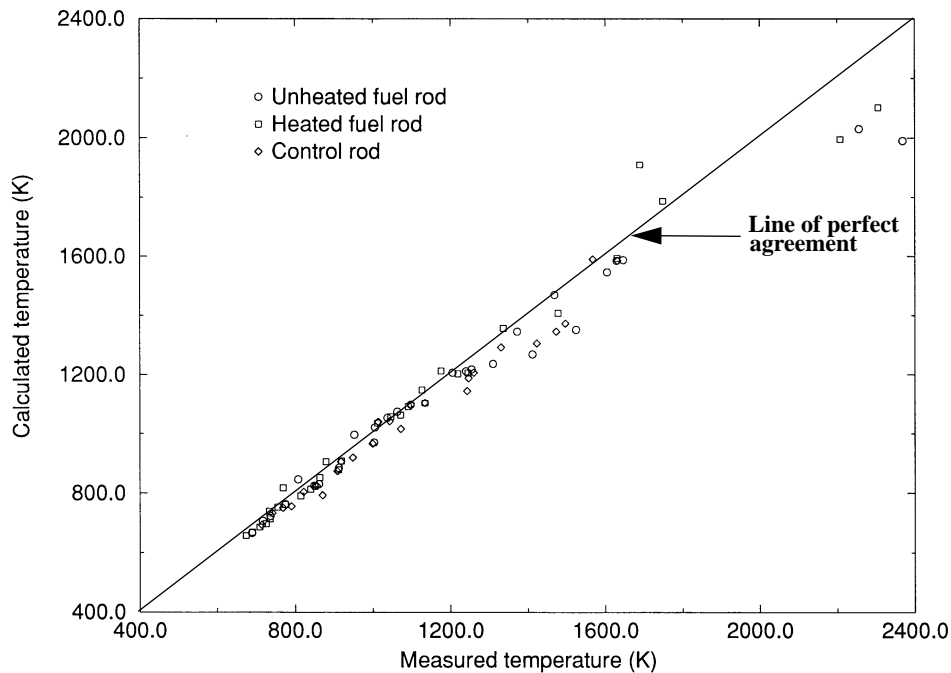


Figure 4-8. CORA-13 calculated versus measured temperatures for the unheated fuel rod, heated fuel rod and control rod.

2,200 K while the calculated peak temperatures were 100-200 K higher. Metallurgical estimates of peak bundle temperatures have not yet been established.

4.1.2 Onset of Rapid Oxidation and Hydrogen Production

Table 4-1 shows the calculated and measured total hydrogen production for the tests discussed in Appendix A. The average variation for those tests terminated by reflood, SFD-ST, CORA-13, and LOFT LP-FP-2, is 17% with a noticeable systematic underprediction for SFD-ST and CORA-13. Although this underprediction is substantially less than that predicted using earlier versions of the code, the new reflood model is still underpredicting the oxidation during reflood for these two tests by 40-50%. The average variation for the experiments that were not reflooded is 13% with the average heavily biased by the large variation for the SFD 1-1 test. If this test is excluded from the average, the variation in total hydrogen production for non-reflooded tests is well within the experimental uncertainty for the measurements. The discrepancy for SFD 1-1 has been attributed to the over prediction of the cladding temperatures in the upper half of the bundle as discussed in Appendix A.

As discussed in more detail in a later section describing the assessment of the new reflood model, there may be a relatively large systematic bias in the rate of hydrogen production for steam rich CORA experiments, resulting in an over-prediction in the hydrogen production rates during the accelerated heatup of the bundle and an underprediction once peak bundle temperatures are reached and fuel rod melt relocation is taking place. There are two, possibly related, sources for this bias. First, as shown in Figure 4-9, vapor diffusion has a strong limiting effect on the peak hydrogen productions rates in the CORA tests due to the presence of a large fraction of argon in the coolant. When the vapor diffusion limiting model is

Table 4-1. Hydrogen Production.

Test	Measured	Calculated SCDAP/ RELAP5/ MOD3.1	% Difference
SFD-ST	172 ± 40 g	81 g	52.9
SFD 1-1	64 ± 7	94 g	46.9
SFD1-3	59 ± 7g	66 g	11.9
SFD1-4	86 ± 12 g	89 g	3.5
DF-4	39 g	35 g	5.4
CORA-7	114 g	108 g	5.2
CORA-13	210 g	118 g	44.8
PHEBUS B9+	39 ± 8 g	33 g	15.4
LP-FP-2	1,024 ± 364 g	980 g	6.25

used for all of the fuel rods in the bundle, the calculated hydrogen production rates are in much better agreement with those measured. However, the peak heating rates are then significantly underpredicted. When a mix of hot rods, where vapor diffusion limits are ignored, and cold rods, where diffusion limits are considered, the code calculations give the best overall agreement for both peak heating and hydrogen production rates. This effect is not nearly as pronounced for the other experiments without argon. Second, there may be a systematic delay in the measured hydrogen production rates. Although systematic corrections have not been applied to all of the tests, these delays have been evaluated for CORA-13 resulting in a correction to the original data. However, there still is a bias in the CORA-13 comparisons even after the delay corrections and vapor diffusion limits are applied.

4.1.3 Fuel Rod Ballooning

Several experiments, LOFT LP-FP-2, the PBF SFD, and CORA-15 tests showed ballooning and rupture. In general, the calculated times and temperatures for rupture agree with that observed, within the uncertainty of the measurements. However, a more detailed assessment using CORA-15 indicated some biases in the results in terms of the predicted ballooning strains. CORA-15 was used for the more detailed assessment since it was specifically designed to study the effects of ballooning and rupture. In this experiment, an internal rod pressure was chosen to result in ballooning and rupture in the high alpha-phase of the zircaloy cladding (1,000-1,100K). The ballooning and rupture during this test, relative to other CORA tests without ballooning and rupture, (a) advanced the relative timing of the onset of rapid oxidation by 100-200 seconds, and, (b) markedly reduced the fuel damage in the lower half of the bundle.

The CORA-15 assessment calculations were performed in the United Kingdom using a version of SCDAP/RELAP5/MOD2.5 with error corrections and modifications that were subsequently incorporated into SCDAP/RELAP5/MOD3.1. Although these calculations have not been redone with SCDAP/

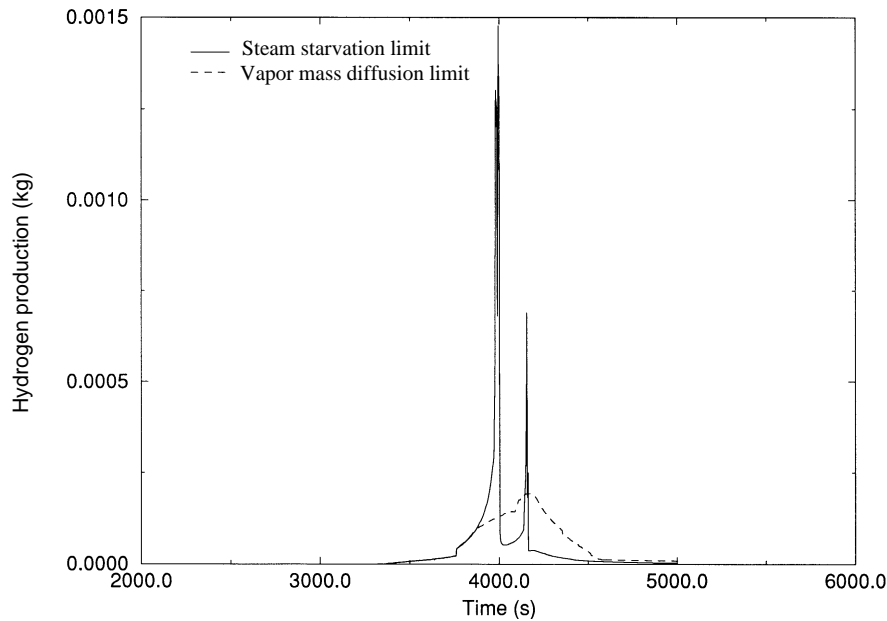
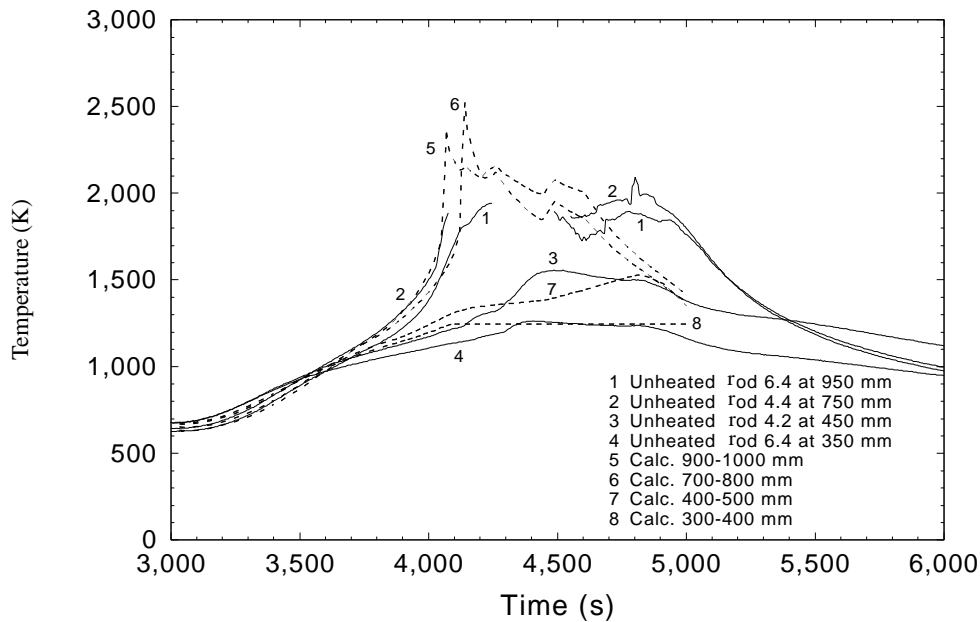


Figure 4-9. Predicted hydrogen production rates for CORA-7.

RELAP5/MOD3.1, the conclusions from the SCDAP/RELAP5/MOD2.5 study are considered to be valid for SCDAP/RELAP5/MOD3.1.

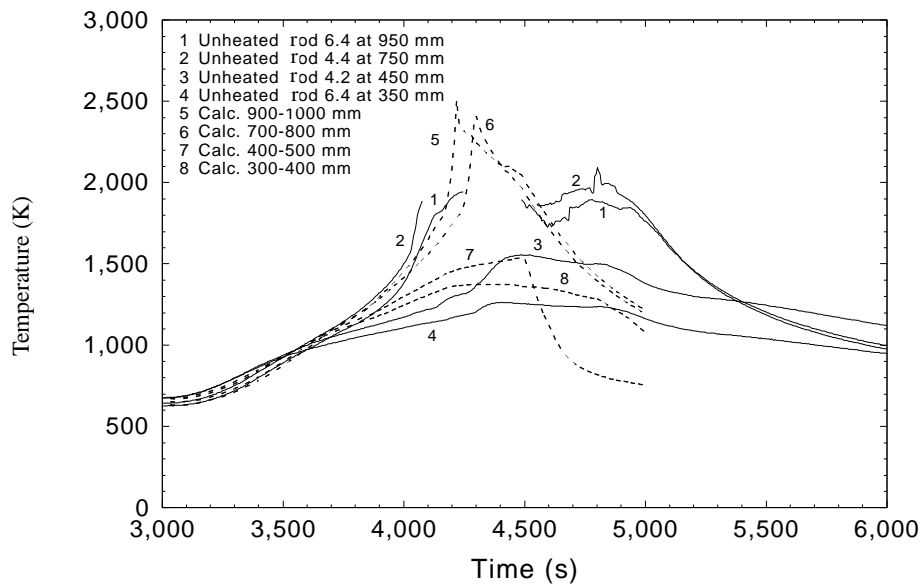
The effects of ballooning on the temperature excursion include the competing effects of (1) increased cladding surface area, promoting cooling of the cladding; (2) flow blockage, diverting flow into the bypass; and (3) double sided oxidation decreasing the heating rates. For example the ballooning model presently in SCDAP/RELAP5/MOD3.1 shows good agreement with measured data for the time and axial location of the oxidation excursion. Results from the assessment of the ballooning model are shown in Figures 4-10 to 4-12. As shown in Figure 4-10, the code predicted temperatures in the lower half of the bundle are considerably cooler than those in the upper half, consistent with post-test metallurgical examination results. Results plotted in Figure 4-11 with the ballooning model turned off show the oxidation excursion occurring too late, with the acceleration in the temperature ramp rate calculated to start at a temperature considerably higher than observed during the experiment. As shown in Figure 4-12, changing from single sided oxidation of the ballooned region to double sided oxidation shifts the onset of rapid heating by about 200 seconds (or in temperature by about 200 K). It should be noted that the assumption of unrestricted access to steam to the inner cladding surface, inherent in the SCDAP/RELAP5 model, is a limiting case, since in practice the burst opening will be of finite size. However for ballooning in the high alpha-phase region, the strains and rupture openings are likely to be large.²⁹

While the calculated time and axial extent of ballooning observed in CORA-15 are in reasonable agreement with the experiment, the code over-predicts cladding strain in experiments where the rod fill gas pressure was low (less than 0.6 MPa). For example in other calculations described in Reference 28, calculations for two other CORA tests show the strains are over-predicted. In CORA-12, where the internal pressure at the onset of cladding ballooning was 0.25 MPa (compared with a system pressure of 0.22 MPa), the code calculated strains in the range of 4-9%. In CORA-5, where internal pressure was 0.45 MPa for the



M554-WHT-492-01

Figure 4-10. Comparison of CORA-15 temperature data with predicted values and ballooning turned on with double-sided oxidation.



M554-WHT-492-02

Figure 4-11. Comparison of CORA-15 temperature data with predicted values with no ballooning modeled.

same pressure, and the code calculated strains over 20%. In neither experiment was there any evidence of ballooning. This discrepancy was attributed to the fact that the code is using creep/plasticity data relevant to zircaloy weaker than that used in the CORA facility for temperatures in the high alpha-phase region and at low stresses. It was also noted that oxidation strengthening of the cladding which restricts ballooning above 1,273 K is not modeled, therefore, ballooning calculated under these circumstances should be

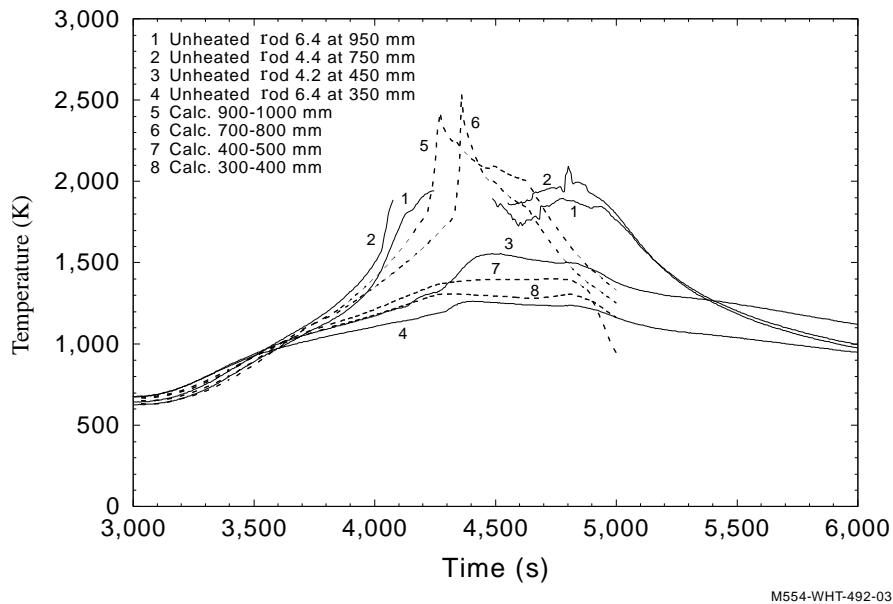


Figure 4-12. Comparison of CORA-15 temperature data with predicted values with ballooning and single sided oxidation.

limited. Such a limit is now incorporated in SCDAP/RELAP5/MOD3.1 even though the oxidation strengthening is not directly modeled.

The calculated ballooning behavior in the PBF SFD and LOFT LP-FP2 experiments was consistent with that reported in earlier assessments of the code.¹² However, it was also concluded that while, the predicted temperature of fuel rod rupture was consistent with experimental observations, the ability of the models to predict the axial extent and local strains for these experiments cannot be accurately assessed due to the uncertainties in the data. The trend in the data appears to be axially extended ballooning consistent with the codes “sausage” or axisymmetric ballooning model rather than the localized asymmetric model.

4.1.4 Early Phase Bundle Liquefaction.

The availability of measured PWR and BWR control material temperatures is limited. The CORA series of experiments measured the temperature response of Ag-In-Cd control rods in the PWR experiments, and of the control blade and channel box in the BWR experiments. Control blade and channel box temperatures measurements were also recorded during the ACRR DF-4 control blade/channel box experiment. Data from CORA-7 and CORA-13 was used to assess the codes ability to predict PWR control rod behavior during a severe accident. Data from DF-4 was used for the assessment of BWR control material models.

Measured absorber rod temperatures from the CORA-7 and CORA-13 experiments were used to evaluate modeling and experimental uncertainties in this assessment report. Figures 4-13 and 4-14 show calculated and measured absorber temperatures for the CORA-7 and CORA-13 experiments. As shown in these figures the predicted absorber temperatures for these experiments are within a few percent of the

measured in the upper bundle up to the predicted melting of control material. The predicted temperature and duration of control material melting is in good agreement with the measured. At the 550 mm elevation, for the CORA-13 experiment a temperature underprediction of about 10% was observed. Though, at this elevation, the melting temperature and the time over which absorber melting occurred were in good agreement with the measured. Predicted BWR control blade behavior was in good agreement with the measured as discussed in Section 4.2.4 and the appendices.

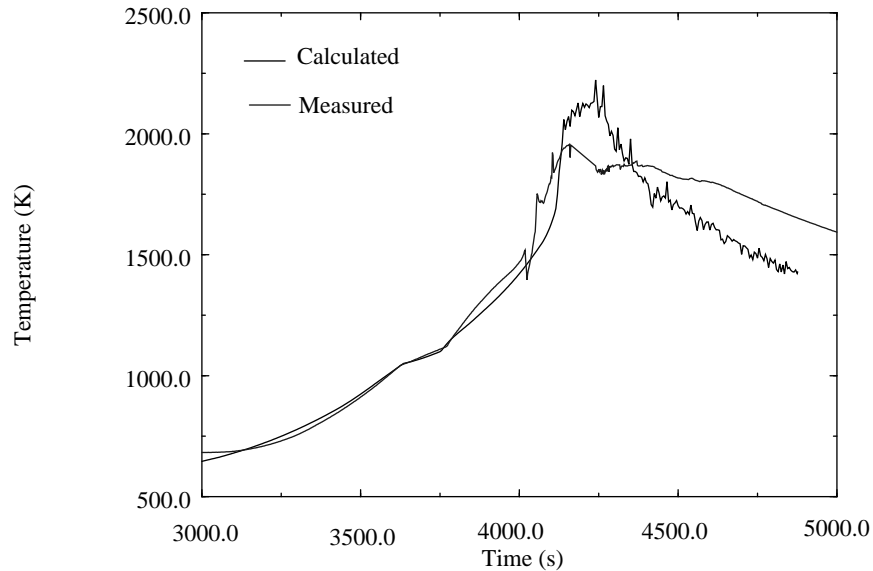


Figure 4-13. CORA-7 Calculated and measured absorber rod temperatures at the 750 mm elevation using SCDAP/RELAP5/MOD3.1.

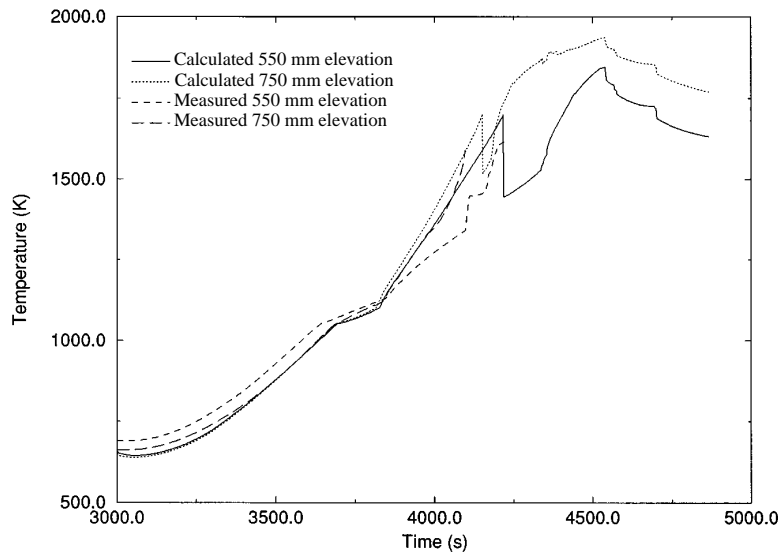


Figure 4-14. Calculated and measured control rod temperatures for CORA-13 at the 550 and 750 mm elevations.

Fuel rod liquefaction cannot be adequately assessed since very little metallurgical characterization data for assessment purposes has been published. Preliminary results from post-test bundle examinations of damaged bundles provide temperature estimates and some damage information for various bundle regions. From this information it was determined that the code is underpredicting fuel rod liquefaction in CORA. The code predicts liquefaction relatively well for the PBF and LOFT tests, (see Appendix A). For slow cooling tests, or test similar to PHEBUS B9+ where temperature was held at zircaloy melting temperature for a relatively long period, the dissolution model significantly overpredicts fuel rod liquefaction. This overprediction is discussed in the PHEBUS B9+ section of Appendix A.

Predicted and PIE determined end-states for the CORA-7 and CORA-13 experiments are shown in Figures 4-15 and 4-16. The predicted end-state for LOFT LP-FP-2 is shown in Figure 4-17. The CORA predicted end-states agree quite well with the measured. Blockage region is predicted to form near the inconel grid spacer for both tests, in good agreement with PIE determined values. The end-state predicted end-state after reflood of LOFT shows core damage. The predicted damage agrees quite well with metallurgical data and are discussed as part of the LOFT description in the appendix.

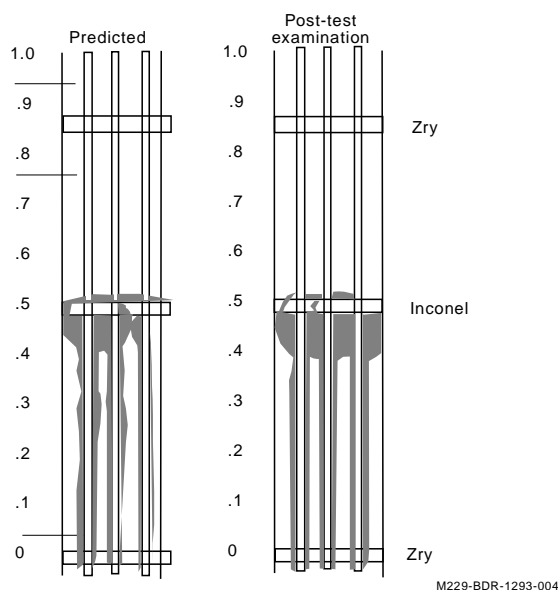


Figure 4-15. End-state figure of the CORA-7 comparisons.

4.1.5 Late Phase Damage Progression

The assessment of the late phase damage progression models is limited to an evaluation of the reasonableness of the behavior predicted by these models. This limitation in assessment is due to the lack of data for assessing the late phase damage progression models, that calculate the behavior of the core from the time of initial formation of a molten pool up to and through lower head failure. In a calculation of the behavior of the Surry reactor during a TMLB' severe accident, the code predicted the formation of a molten pool at a location with a temperature of 2,873 K. Figure 4-18 shows the SCDAP/RELAP5/MOD3.1 calculated progression of damage after the initial formation of a molten pool. The initial formation of the molten pool is predicted to occur at temperatures consistent with those determined from metallurgical examinations of the TMI-2 damaged core. An analysis of the Surry nuclear power plant as described in Appendix A was used in this assessment to evaluate the late phase models and the links between SCDAP/

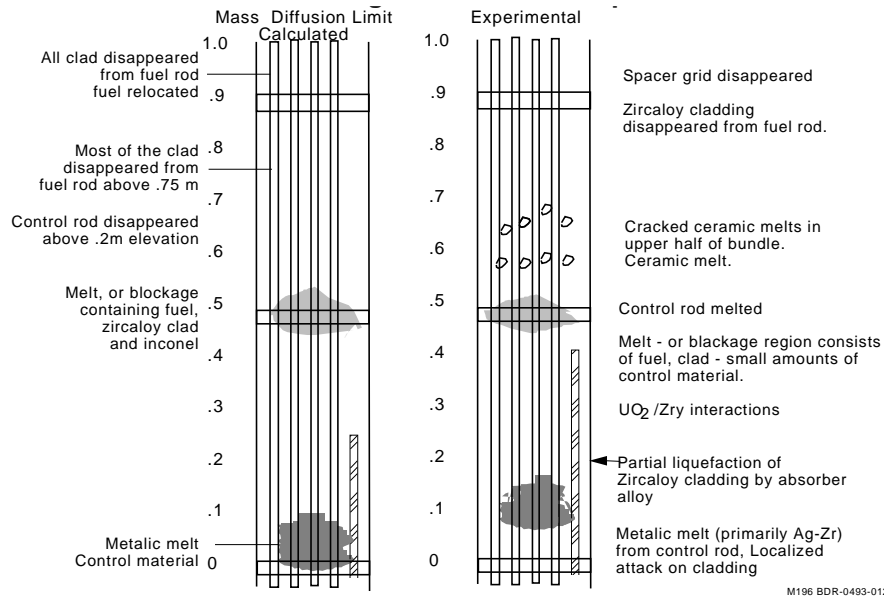


Figure 4-16. Artist rendition of the bundle showing the calculated and measured end-state.

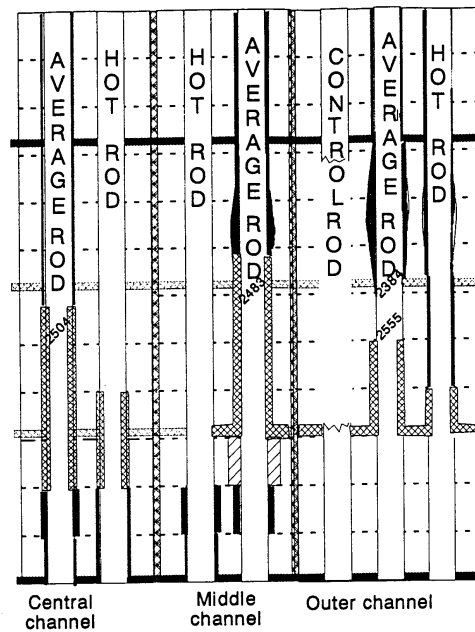


Figure 4-17. Core condition after reflood.

RELAP5/MOD3.1 and COUPLE. The linkage between the late phase model and COUPLE appears to work and give reasonable results. No assessment has been performed of lower head failure models.

core degradation map

I = intact fuel component underscore indicates
P = porous debris metallic or planar
M = molten or frozen ceramic pool blockage in volume at bottom
V = Relap fluid volume now void of fuel of indicated node

— I — x's indicate
— V — that total or bulk
xxPxx blockage occurs
xxMxx in the volume

conditions of in-core molten pool at time = 17675. sec

axial node #					
20	I	V	xxMxx	I	I
19	V	V	P	I	I
18	V	V	I	I	I
17	V	xxMxx	I	I	I
16	xxMxx	P	I	I	I
15	P	I	I	I	I
14	I	I	I	I	I
13	I	I	I	I	I
12	I	I	I	I	I
11	I	I	I	I	I
10	I	I	I	I	I
9	I	I	I	I	I
8	I	I	I	I	I
7	I	I	I	I	I
6	I	I	I	I	I
5	I	I	I	I	I
4	I	I	I	I	I
3	I	I	I	I	I
2	I	I	I	I	I
1	I	I	I	I	I

Relap vol. at bottom 111010000 114010000 112010000 115010000 113010000

conditions of in-core molten pool at time = 19675. sec

Axial node #					
20	I	V	V	I	I
19	V	V	V	I	I
18	V	V	V	I	I
17	V	V	xxMxx	V	I
16	V	V	xxMxx	V	I
15	V	xxMxx	xxMxx	V	I
14	xxMxx	xxMxx	P	xxMxx	I
13	xxMxx	xxMxx	I	xxMxx	I
12	xxMxx	P	I	P	I
11	P	I	I	I	I
10	I	I	I	I	I
9	I	I	I	I	I
8	I	I	I	I	I
7	I	I	I	I	I
6	I	I	I	I	I
5	I	I	I	I	I
4	I	I	I	I	I
3	I	I	I	I	I
2	I	I	I	I	I
1	I	I	I	I	I

Relap vol. at bottom 111010000 114010000 112010000 115010000 113010000

conditions of in-core molten pool at time = 21675. sec

Axial node #					
20	I	V	V	I	I
19	V	V	V	I	I
18	V	V	V	I	I
17	V	V	V	V	I
16	V	V	V	V	I
15	V	V	xxMxx	V	P
14	V	V	xxMxx	V	P
13	xxMxx	xxMxx	xxMxx	xxMxx	I
12	xxMxx	xxMxx	P	xxMxx	I
11	xxMxx	xxMxx	P	P	I
10	P	P	I	I	I
9	I	I	I	I	I
8	I	I	I	I	I
7	I	I	I	I	I
6	I	I	I	I	I
5	P	P	P	P	I
4	I	I	I	I	I
3	I	I	I	I	I
2	I	I	I	I	I
1	I	I	I	I	I

Relap vol. at bottom 111010000 114010000 112010000 115010000 113010000

Figure 4-18. Calculated late phase damage progression.

4.2 Model Assessment of SCDAP/RELAP5/MOD3.1

4.2.1 Control Material Behavior

During a verification process completed in May of 1993, several deficiencies and error related to PWR control rods were identified. These deficiencies relating to control rod meltdown, drainage of control material from a bundle location after melting, and heat conduction were resolved in SCDAP/RELAP5/MOD3.1. SCDAP/RELAP5/MOD3.1 also contains modeling improvements and error corrections to the PWR control rod model. The additions and corrections to the PWR control blade model were assessed

against the results from calculations using previously released versions of the code and measured data from the CORA experiments and PBF SFD 1-4. A complete description of the control material modeling is contained in Volume 2. In addition to improved PWR control material models and error corrections, SCDAP/RELAP5/MOD3.1 also contains the ORNL developed control blade/channel box model which more accurately represents control blade behavior during a severe accident in a BWR. This model was assessed against DF-4 results using SCDAP/RELAP5/MOD3.1, previously released versions of the code, and measured data.

Figure 4-19 shows the calculated and measured temperatures for the control rod at the 750 mm elevation for the CORA-7 large bundle PWR test. As shown in this figure, the code is predicting the control material to begin melting and relocating at 1,150 K in good agreement with the measured data. Melting of the control material, indicated by the flattening of the curve, is predicted to continue over a period of approximately 300 seconds again in good agreement with the measured data. The improvements and error corrections to the modeling of control material in the code greatly improved the code's ability to predict control material melting and relocation. Figure 4-20 shows predicted temperatures at the 750 mm elevation for CORA-7 as compared to the measured using SCDAP/RELAP5/MOD3. This version predicted the control material to begin melting earlier in time and at a slightly higher temperature than observed. Figure 4-21 shows the predicted and measured control rod temperatures for the CORA-13 experiment, which are in good agreement with the measured.

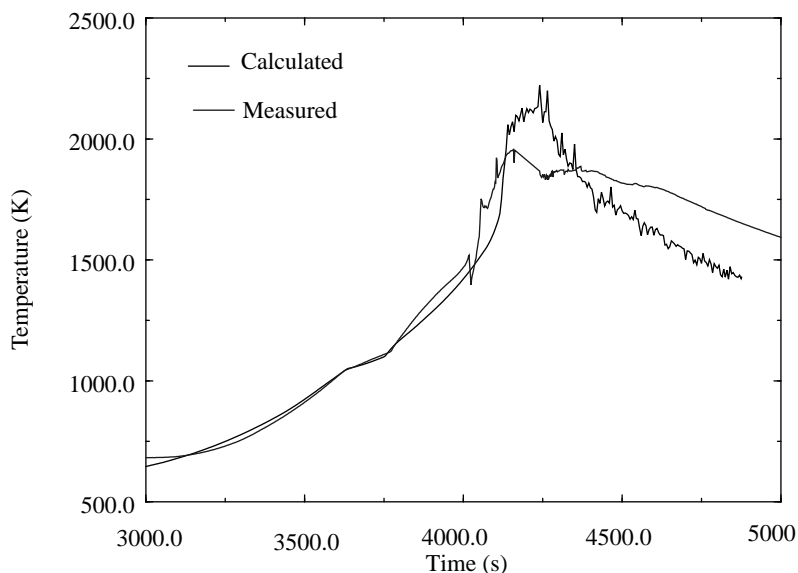


Figure 4-19. Calculated and measured absorber temperatures for the CORA-7 experiment at the 750 mm elevation in the bundle using SCDAP/RELAP5/MOD3.1.

The addition of the BWR control blade/channel box model into the code significantly changed predicted behavior in the blade region of an experimental bundle with little change to predicted fuel rod temperature response. For the BWR test DF-4, very little variation in predicted fuel rod temperature response was observed between earlier versions of the code using the cylindrical model inside a zircaloy shroud to represent the control blade/channel box region in the bundle and versions using the new model. The addition to the new model improved the predicted behavior for the control blade and channel box up to the relocation of control to the bottom of the channel box. Using the new model, BWR analysis can only be carried out up to the time a complete blockage forms in the channel box. Predicted channel box and control

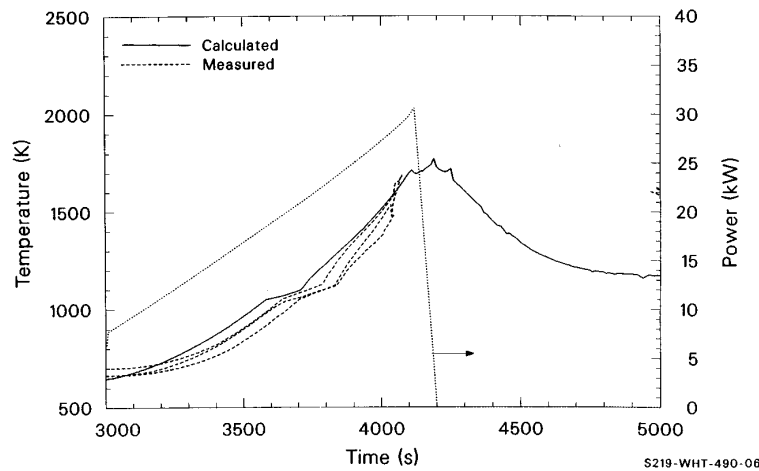


Figure 4-20. CORA-7 calculated and measured absorber rod temperatures at the 750 mm elevation using SCDAP/RELAP5/MOD3.

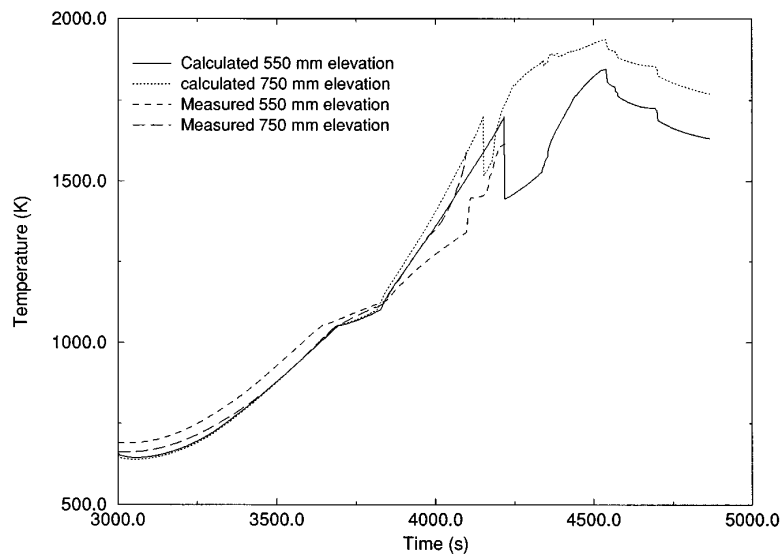


Figure 4-21. Calculated and measured absorber temperatures for the CORA-13 experiment at the 550 and 750 mm elevation in the bundle using SCDAP/RELAP5/MOD3.1.

blade temperatures more closely followed the experimental results up to the time of blade failure and relocation. Since the ORNL model considers oxidation of channel box zircaloy, the total quantity of hydrogen produced during the early phase of the experiment increased from 35 g using the old model to 43 g with the new model. Considering the uncertainty in the measurement of hydrogen during the experiment, the predicted quantity using the new blade/box model is closer to the experimental values than those obtained with the old model. A complete description of the DF-4 analysis using the ORNL control blade

model is contained in the Appendix A and code-to-data comparisons looking at temperature histories using various versions of the code and the different blade models are presented in Section 3.

4.2.2 Material Interactions and the Grid Spacer Model

The addition of models to replicate the eutectic interactions of Inconel, either as grid spacers or small rod stabilizing tabs on zircaloy grid spacers, with zircaloy fuel rod cladding improved considerably the code's ability to predict damage progression. The impact of modeling material interactions between grid spacers material and zircaloy on the relocation and freezing of liquefied material and relocation of loose debris was assessed using two CORA experiments, CORA-7, and CORA-13, PBF SFD 1-4, and a phenomenological problem based on the SFD 1-4 bundle. The model improved bundle oxidation, heatup, and the location of blockage regions in the core. Depictions of the bundle end-states, predicted and observed from the post-test metallurgical examination, for CORA-7 and CORA-13 are presented in Section 4.1.4. The new model predicts noticeable cladding liquefaction, due to chemical interactions occurring between Inconel and zircaloy, to begin at the location of an Inconel grid spacer as temperatures in that region near 1,500 K. Liquefaction can occur only if the clad oxide thickness is less than 100 microns. Also, since predicted bundle thermal behavior is more consistent with the measured behavior, relocating material from hotter regions in the upper bundle slows as it comes in contact with cooler material in the grid spacer location. As hot slumping material comes in contact with the cooler liquefied grid spacer material it freezes forming a blockage region. As shown in the CORA-7 and CORA-13 end-state representations in Section 4.1.4, the location of blockage regions are consistent with those observed in the test.

The model was also assessed using a test problem based on the PBF SFD 1-4 experiment. Using this problem, the behavior differences between Inconel and zircaloy grid spacers as modeled in the code were determined. The presence of an Inconel instead of zircaloy grid spacer had the effect of greatly accelerating the rate of heat up at the location (0.4 m) of the grid spacer located below the Inconel spacer. The results of this comparison are shown in Figure 4-22, where the predicted temperature histories at the 0.4 m elevation are shown for the cases of Inconel and zircaloy grid spacers at the 0.63 m elevation. As shown in the figure, the temperature at the 0.4 m elevation sharply increased when a mixture of liquefied cladding and grid spacer material came in contact with the grid spacer at the 0.4 m elevation. The sharp increase in temperature accelerated the rate of oxidation at this location, which in turn accelerated the heatup. The acceleration in the rate of oxidation is shown in Figure 4-23, where hydrogen produced by cladding oxidation is plotted as a function of time.

In general terms when SCDAP/RELAP5/MOD3.1 is used to analyze a PWR experiment containing Inconel grid spacers, the extent of liquefaction of cladding at the location of the Inconel grid spacer is more representative of that observed in experiments. The model predicts the Inconel grid spacer to begin liquefaction at temperatures near 1,600 K. The molten Inconel then begins reacting with the zircaloy cladding. Once the cladding was penetrated by the mixture of molten Inconel and zircaloy, liquefaction and slumping due to the chemical reaction between Inconel and zircaloy was predicted. The rate of heating at the grid spacer location was also more representative.

The changes to the modeling as well as the print out from the new models gives the user a clearer picture of the early phase damage progression events occurring in the bundle. Figure 4-24 shows a section of SCDAP/RELAP5/MOD3.1 output, illustrating the print out of damage progression events as they are

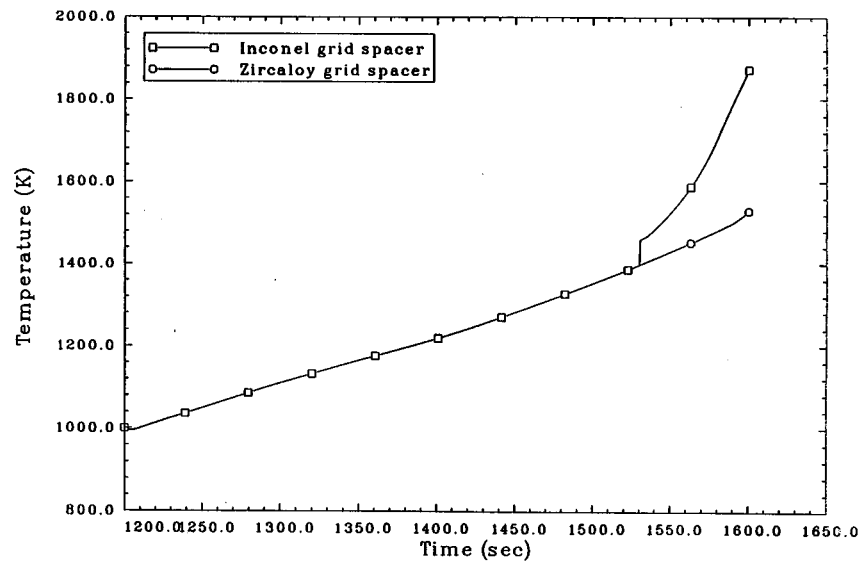


Figure 4-22. Calculated temperature histories at the 0.4 m elevation for cases of Inconel and zircaloy grid spacer for a PWR bundle at the 0.63 m elevation.

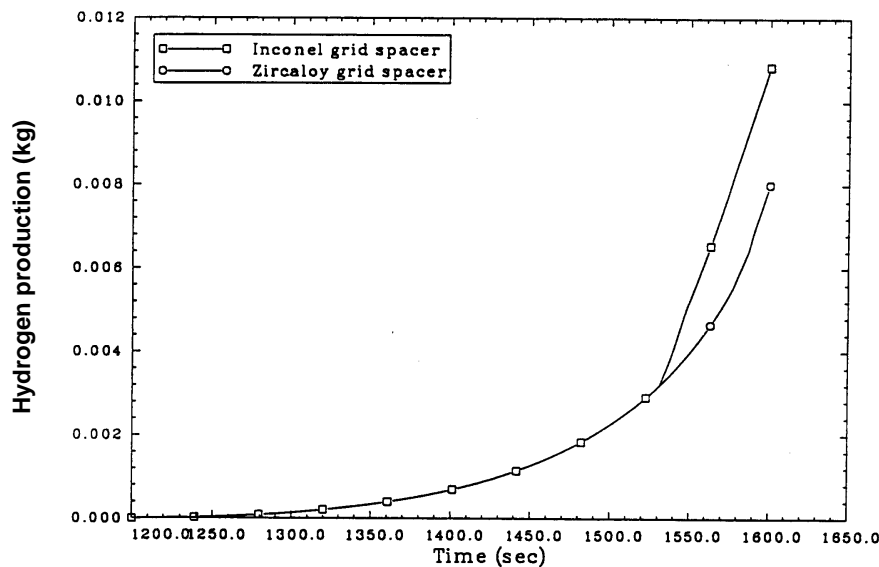


Figure 4-23. Calculated accumulated hydrogen production for cases of Inconel and zircaloy grid spacer for a PWR bundle at the 0.63 elevation.

predicted to occur by the code. As shown in Figure 4-24 the time, the axial node into which cladding slumps, component number, and energy at the time of the slumping are printed. Also the formation, location, and the time the slumping of a metallic crust occurred are indicated on the printout. The addition of printout which gives a clear indication of time, temperature, energy, and location of the damage events occurring in the bundle allows the code user to closely follow all events as they occur and compare these results with those observed during an experiment.

```

fuelan -----core degradation event-----
fuelan *** Cladding slumped into axial node      8
component no. 1 event time= 544.3250000    energy(j)=0.3498E+05
fuelan Total thermal energy in slumped material =0.4160E+05

Meltdown stops local oxidation
event time=0.5443E+03
comp # = 1
axial node = 10
mass zr removed=0.2883E-01
0*** for component 1 axial node 8
grid spacer mass =0.2000E-02 relocated Zr mass=0.2883E-01
grid spacer now considered Zr ***
in DISZRI Zircaloy grid spacer calculated to slump
Grid spacer slumping at axial node # 8 component # 1
thkave=0.1000E-02 rhozu=0.7274E+04 czu=0.3531E+03 hfus=0.2455E+06 tmelt0=0.1273
icomp= 1 nhrdpn= 8 irubpp= 0 kfail= 8 wfrzr=0.6900E+00 wfruo=0.3071E+00

fuelan -----core degradation event-----
fuelan *** Grid spacer has slumped
event time = 544.3500000    axial node = 8 elevation (m) =0.2926E+01 compone

fuelan -----core degradation event-----
fuelan *** Cladding slumped into axial node      6
component no. 1 event time= 544.3500000    energy(j)=0.1591E+05
fuelan Total thermal energy in slumped material =0.1591E+05
scdadv-----core degradation event-----
Slumping down of metallic crust for component 1. before slumping crust at ax
0*** for component 1 axial node 6
grid spacer mass =0.2000E-02 relocated Zr mass=0.3083E-01
grid spacer now considered Zr ***
in DISZRI Zircaloy grid spacer calculated to slump
Grid spacer slumping at axial node # 6 component # 1
thkave=0.1000E-02 rhozu=0.7263E+04 czu=0.3508E+03 hfus=0.2421E+06 tmelt0=0.1273
icomp= 1 nhrdpn= 6 irubpp= 0 kfail= 6 wfrzr=0.7042E+00 wfruo=0.2943E+00

fuelan -----core degradation event-----
fuelan *** Grid spacer has slumped
event time = 544.3625000    axial node = 6 elevation (m) =0.2195E+01 compone

fuelan -----core degradation event-----
fuelan *** Cladding slumped into axial node      5
component no. 1 event time= 544.3625000    energy(j)=0.1665E+05
fuelan Total thermal energy in slumped material =0.1665E+05
scdadv-----core degradation event-----
Slumping down of metallic crust for component 1. before slumping crust at ax
0*** for component 1 axial node 5
grid spacer mass =0.2000E-02 relocated Zr mass=0.3283E-01
grid spacer now considered Zr ***
in DISZRI Zircaloy grid spacer calculated to slump
Grid spacer slumping at axial node # 5 component # 1
thkave=0.1000E-02 rhozu=0.7243E+04 czu=0.3494E+03 hfus=0.2404E+06 tmelt0=0.1273
icomp= 1 nhrdpn= 5 irubpp= 0 kfail= 5 wfrzr=0.7167E+00 wfruo=0.2824E+00

fuelan -----core degradation event-----
fuelan *** Grid spacer has slumped
event time = 544.3750000    axial node = 5 elevation (m) =0.1829E+01 compone

fuelan -----core degradation event-----
fuelan *** Cladding slumped into axial node      4
component no. 1 event time= 544.3750000    energy(j)=0.1739E+05
fuelan Total thermal energy in slumped material =0.1739E+05
scdadv-----core degradation event-----
Slumping down of metallic crust for component 1. before slumping crust at ax
0*** for component 1 axial node 4
grid spacer mass =0.2000E-02 relocated Zr mass=0.3483E-01

```

Figure 4-24. Printed output showing core degradation events.

4.2.3 Reflood Model

The reflood model in SCDAP/RELAP5/MOD3.1 consists of two basic parts, vapor diffusion and oxide spalling or cracking. The code model for vapor diffusion was evaluated using data from both CORA-7 and CORA-13.

Earlier versions of SCDAP/RELAP5 did not predict the increased hydrogen production or core damage during the reflood phase of an experiment. Several possible sources were identified as the cause of

these deficiencies: (1) the lack of a model to calculate the oxidation of relocating material or material forming a cohesive debris bed, (2) an input density for the shroud insulation that was higher than the actual density, which resulted in lower predicted temperatures and less oxidation of the zircaloy shroud liner, (3) the lack of a model to calculate double sided oxidation of the shroud line, and, (4) the lack of a model to calculate phenomena occurring during reflood of the core. These deficiencies were corrected and assessed using LOFT LP-FP-2 and CORA-13.

These tests were used to assess the ability of SCDAP/RELAP5/MOD3 to model the core damage progression during the reflood phase of an experiment, or to predict core behavior if reflood cooling of the core was used in an attempt to terminate an accident in a nuclear power plant. In both experiments an oxidation excursion sufficient to drive temperatures up occurred upon core reflood. In LOFT, the temperature excursion was sufficient to drive fuel rod temperatures above the melting point of ceramic UO_2 (3,100 K) in the central fuel module. CORA-13 and LOFT both show increased zircaloy oxidation and hydrogen production during reflood.

The addition of the reflood model and a model limiting the vapor diffusion of steam to zircaloy, described in Section 2, dramatically improved the code's ability to model thermal hydraulic response during reflood and hydrogen generation. Through the use of oxide shattering criteria, the reflood model exposes additional fresh zircaloy to high temperature steam at the time of reflood. The exposure of additional cladding zircaloy to steam during reflood results in renewed oxidation, a temperature excursion, and increased hydrogen production typical of that observed during the experiments. Figure 4-25 shows the calculated LOFT LP-FP-2 fuel rod cladding temperature response to the oxidation excursion in the central fuel module during reflood. Reflood was initiated at 1,760 seconds, but the reflood did not reach the core until 1,775 seconds, at which time a series of oxidation excursion spikes were modeled across the core. Figure 4-26 shows the reflood response of a fuel rod in the central fuel module at the 42 inch elevation. As reflood water enters the core, oxide shattering exposes fresh zircaloy to steam, and an oxidation excursion begins. The excursion continues until all exposed zircaloy is exhausted at this location. The component begins to cool and the oxide shatter process begins elsewhere in the core. Predicted results now better replicate those observed during the experiment. Previous versions of the code predicted the oxidation of all available zircaloy prior to reflood. This deficiency was corrected in the reflood model which was assessed using LOFT and CORA-13, since measurements of hydrogen production during reflood exist for these experiments. These measurements indicated large quantities of hydrogen were produced as reflood water enters the core. These experimental measurements were compared with predicted hydrogen production values to assess the effectiveness of the relocation, debris formation, and metallic interaction models as well as the oxide shattering criteria in the reflood model on making new zircaloy available for oxidation upon the addition of water to the core. Figures 4-27 and 4-28 show the results of these comparisons. Figure 4-27 shows the calculated hydrogen production rate for CORA-13 and Figure 4-28 shows the integral hydrogen production for LOFT. These plots show the code is now predicting additional hydrogen production on reflood. Predicted CORA-13 hydrogen production, Figure 4-27, shows a large spike during reflood, which is in qualitative agreement with the data. The code predicted 980 g hydrogen to be produced during the analyses of LOFT LP-FP-2, 270 g during the transient phase of the simulated accident and 710 g during reflood. The predicted values are within the uncertainty of the measured values, 205 ± 11 g during the transient phase and a cumulative production of $1,024 \pm 364$ g.

The reflood model correctly predicts the shattering of the cladding oxide upon reflood, provides an oxidation excursion, and predicts additional generation of hydrogen. There is insufficient experimental

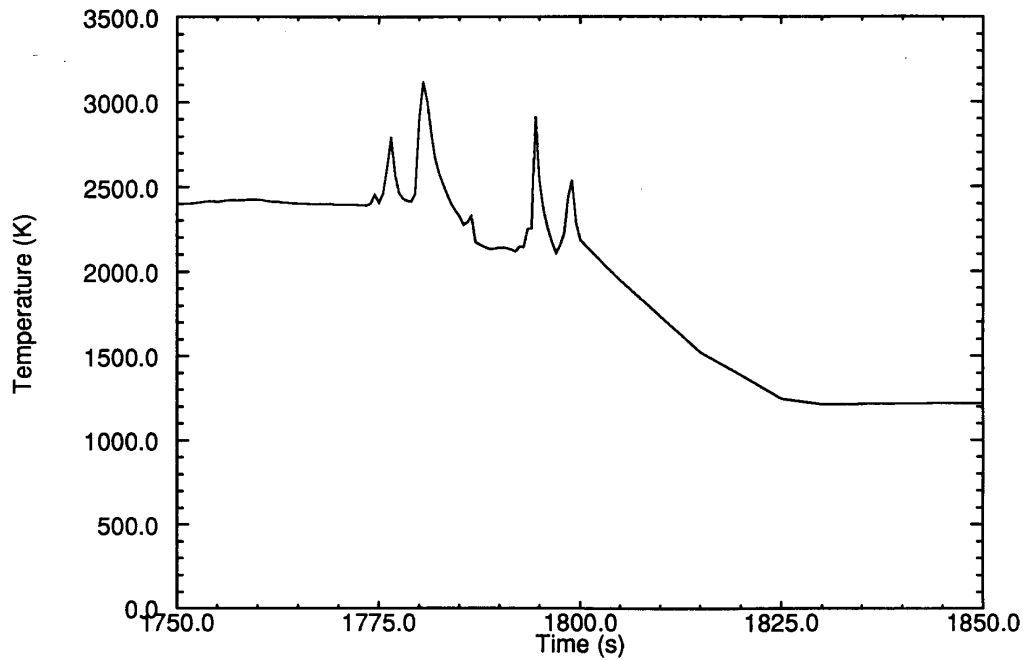


Figure 4-25. Calculated fuel rod cladding temperature response for LOFT LP-FP-2 during reflood.

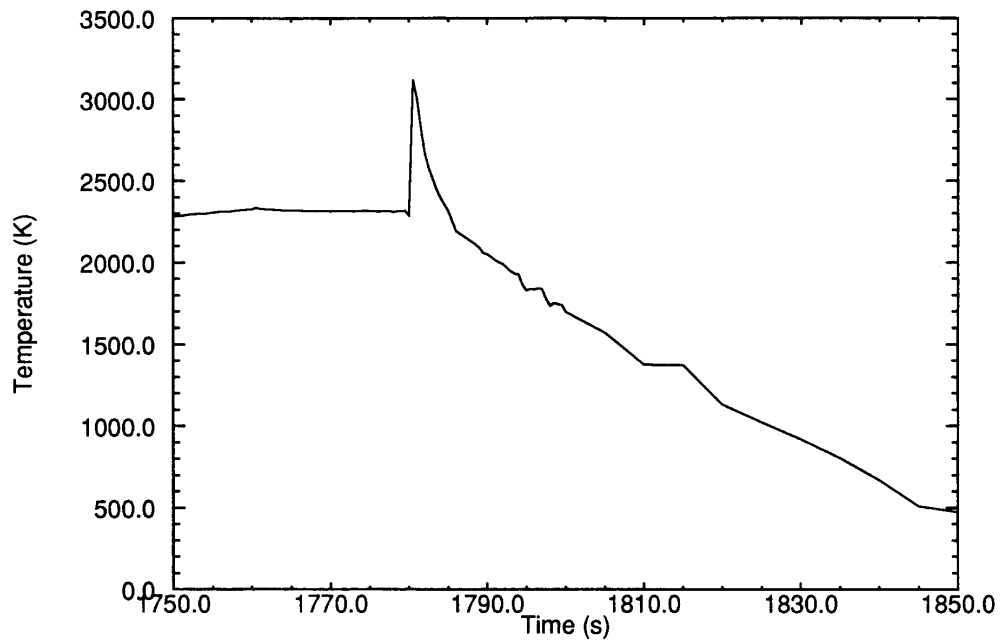


Figure 4-26. Calculated LOFT LP-FP-2 fuel rod reflood response at the 42 inch elevation in the central fuel module.

data to determine if the predicted oxidation excursions are typical of physical response, but the integral measurements, such as hydrogen production and debris formation appear to match measured quantities within experimental uncertainties.

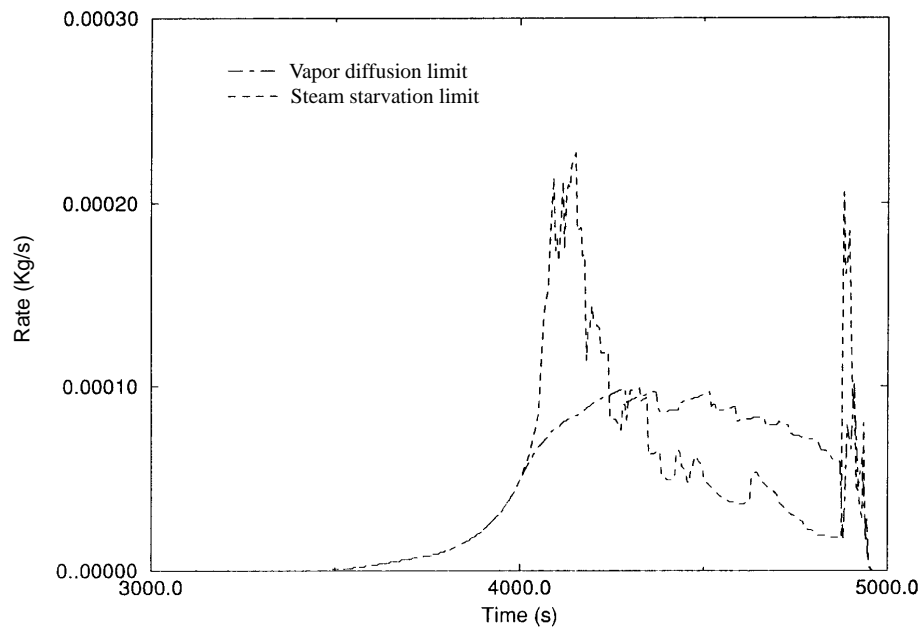


Figure 4-27. Calculated hydrogen production rates from the steamed starved and vapor diffusion limited cases for CORA-13.

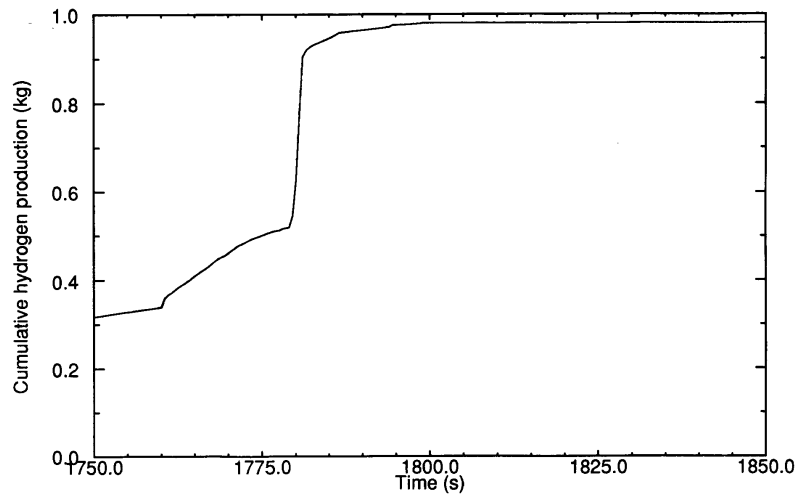


Figure 4-28. Calculated LOFT LP-FP-2 cumulative hydrogen production during reflood.

The impact of installing a vapor diffusion model, which limited the diffusion of steam to the zircaloy cladding, into SCDAP/RELAP5/MOD3 on hydrogen generation and core damage progression was assessed using CORA-7 and CORA-13. Preliminary investigations into the effect of this model indicated that the predicted hydrogen production rate and the onset time of hydrogen generation was representative of that measured during the experiment, though a rapid oxidation excursion was not predicted.²³⁻²⁷ It was determined that some areas in an experimental bundle tended to heat up faster than others, therefore, a method to model these hot spots was developed. A hot rod input model was developed where vapor

diffusion limits were ignored so that steam starvation was the limiting factor on cladding oxidation. The incorporation of the hot rod model into an input deck also improved the radial modeling of the temperature distribution through the bundle. Although representative fuel rods are intended to describe the average behavior of fuel rods in an experimental bundle, in reality, local hot spots may exist due to local inhomogeneities in power generation, heat transfer or flow rates. These hot spots may not significantly influence the overall behavior of the bundle or core, the local heat generation due to oxidation is strongly affected due to the exponential dependency of oxidation rates upon temperature.

To determine the effect of hot rods, four CORA-7 calculations were performed: 1 oxidation of all rods in the bundle was limited by vapor diffusion; 2 oxidation of all rods in the bundle was limited by steam starvation; 3 a steam starvation limit was applied to two simulator rods (the two hot rods); and 4 a steam starvation limit was applied to 20 unheated rods and two simulator rods (22 hot rods). Figures 4-29 to 4-32 show the predicted differences. Figure 4-29 shows the predicted peak bundle temperatures for each of these calculations. As shown in the figure, the steam starvation limited calculation predicts a rapid rise in temperature, indicating rapid oxidation to occur at 3,900 seconds, at a predicted onset temperature of 1,700 K. As the number of represented hot rods decreases, the onset time of the rapid oxidation phase is delayed. A gradual rise in bundle temperature, without a rapid oxidation phase is predicted when oxidation is limited for all zircaloy clad fuel rods by the vapor diffusion. Figure 4-30 compares predicted hydrogen production from the mass diffusion limited case with the steam starvation limited case. As shown in the figure, the time hydrogen production begins is identical for each calculation. Differences in the hydrogen generation rate begin to show at 3,900 seconds, when the maximum bundle temperature is 1,700 K.

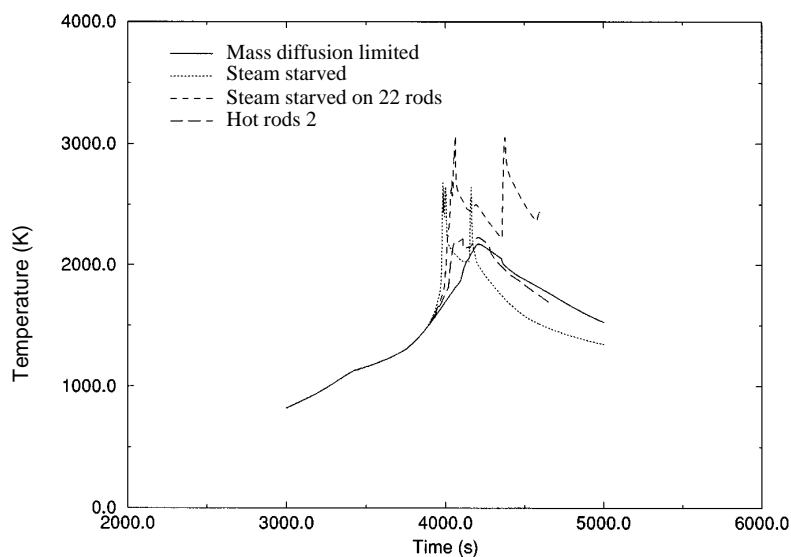


Figure 4-29. CORA-7 comparison of maximum bundle temperature.

The vapor diffusion limited calculation predicts a slow and gradual rise in hydrogen production, typical of the measured values during CORA-7 experiment, whereas the steam starvation limited calculation predicts a rapid rise in hydrogen production coinciding with the predicted onset of rapid oxidation. Figures 4-31 and 4-32 show the differences in hydrogen generation rates and integral hydrogen production for each investigated case. As the number of represented hot rods decrease, the rate of hydrogen generation tends to increase more slowly until the rapid oxidation onset temperature is reached. The 22 hot rod calculation shows rapid oxidation being delayed 50 seconds from the fully steam starved model and the

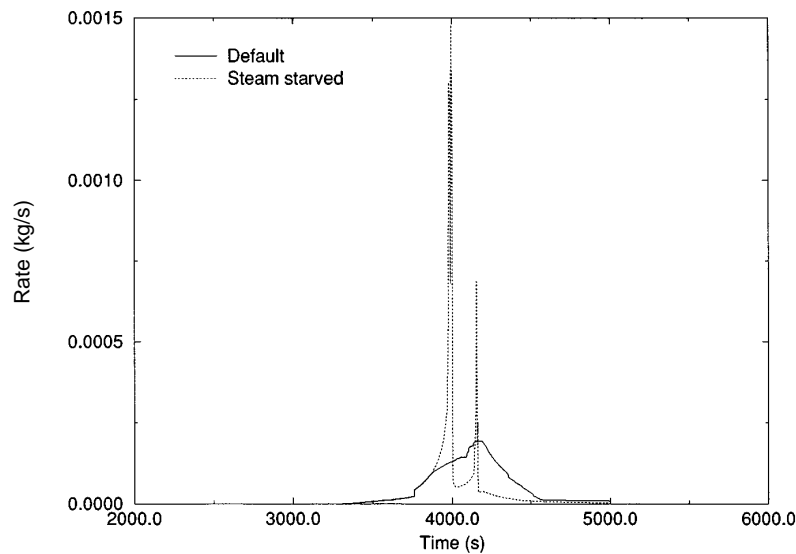


Figure 4-30. CORA-7 comparison of hydrogen generation rate.

2 hot rod calculation shows very little difference in hydrogen generation from the model limited fully by the vapor diffusion. This figure indicates that the number of hot rods used to represent bundle hot spots should be greater than 2 and less than 22 for the CORA-7 experiment. The predicted total hydrogen produced during the experiment, Figure 4-32, shows the steam starved calculation predicting the production of less hydrogen than any other representation of the bundle, and the 22 hot rod calculation the most. This result is consistent with the hydrogen generation rate results, since the 22 hot rod calculation shows a gradual rise in hydrogen production for a longer period of time and a broader hydrogen spike coinciding with the rapid oxidation phase, and the observation that the number of hot spots in the bundle should be greater than 2 and less than 22.

Figures 4-33 to 4-35 show temperatures measured during the experiment and the predicted temperatures for each oxidation limiting calculation for three different elevations. At the 550 mm elevation, Figure 4-33, the fuel rod and oxidation onset temperatures are over predicted for each bundle representation, oxidation beginning several hundred seconds early for the completely steam-starved case, and slightly later for the 22 hot rod case. The completely vapor diffusion limited case or the two hot rod case shows no oxidation transient at this elevation. At the 750 mm elevation, Figure 4-34, using 22 hot rods, the predicted fuel rod and oxidation onset temperatures are still over predicted. The two hot rod model and the completely vapor diffusion limited case, again do not predict an oxidation transient. At the 950 mm elevation, Figure 4-35, the two hot rod model predicts results closer to the measured data than any other core representation. These results again indicate the hot rod concept to model irregularities in bundle heating is correct, and the actual number of hot areas should be greater than two and less than 22. Figure 4-36 shows the predicted control rod temperatures for each representation. As shown in the figure, the representation of bundle hot spots has little effect on the predicted temperature response of the control material up to control rod failure. Predicted temperatures for each representation agree quite well with the measured data up until the time of control rod failure and relocation.

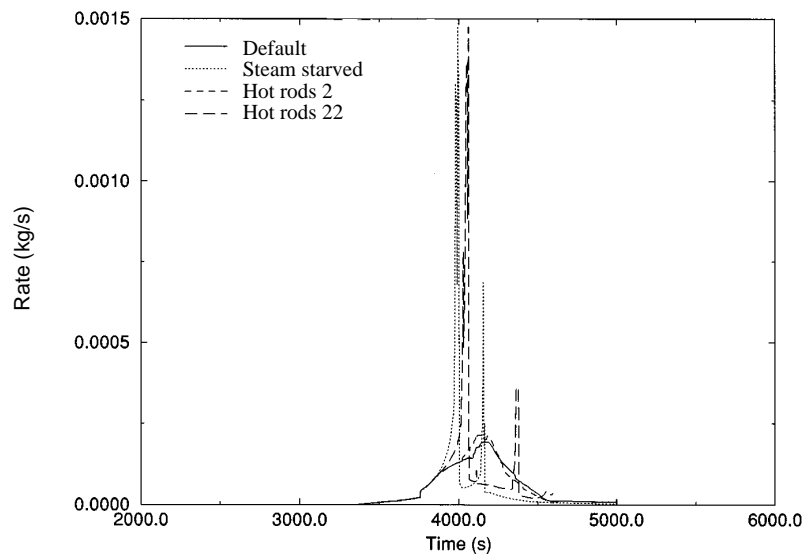


Figure 4-31. CORA-7 comparison of hydrogen generation rate.

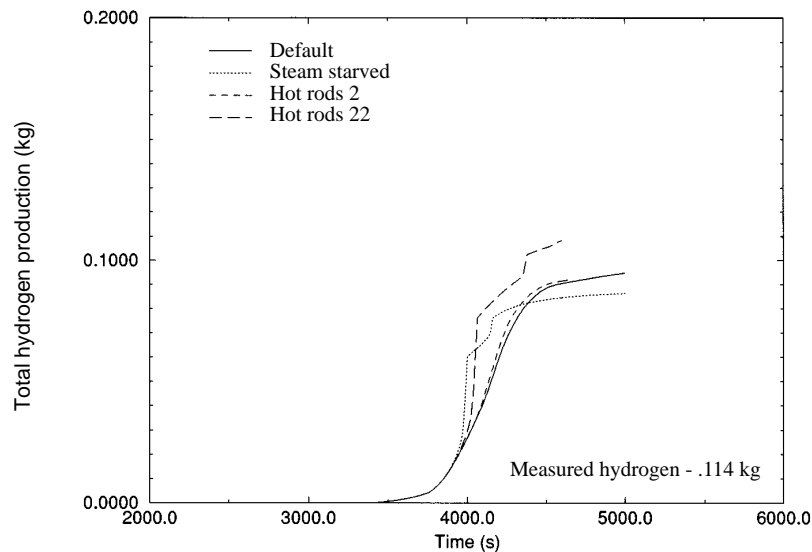


Figure 4-32. CORA-7 comparison of integral hydrogen production.

Figures 4-37 to 4-39 compare the results of the mass diffusion limited and steam starvation limited calculations with the measured data in the upper, middle, and lower regions of the bundle, and Figure 4-40 shows the rate of hydrogen production from both calculations. The predicted bundle heating when vapor diffusion limits on oxidation are used exclusively tend to be delayed considerably from the data in the upper bundle, whereas when steam starvation is used to limit oxidation, temperatures in the upper bundle agree well with the measured data, but component temperatures in the bottom half of the bundle are over predicted. All calculations were performed using a ZrO_2 failure temperature of 2,250 K.

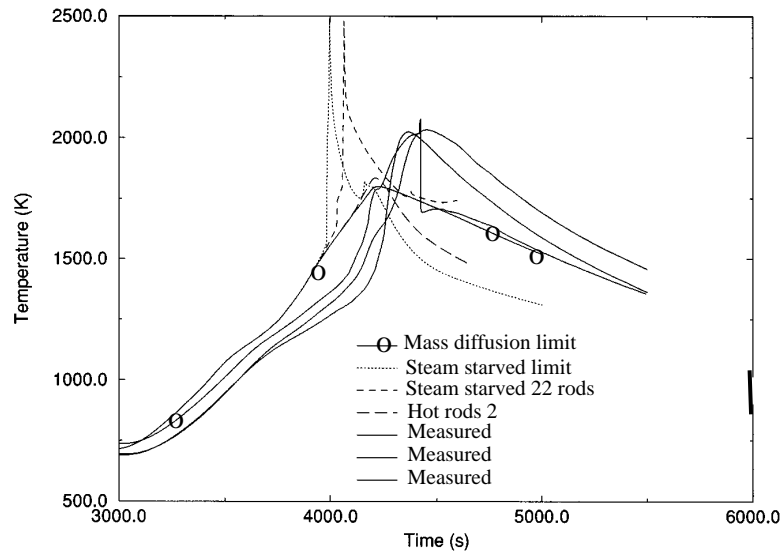


Figure 4-33. CORA-7 comparison of fuel rod temperatures at the 550 mm elevation.

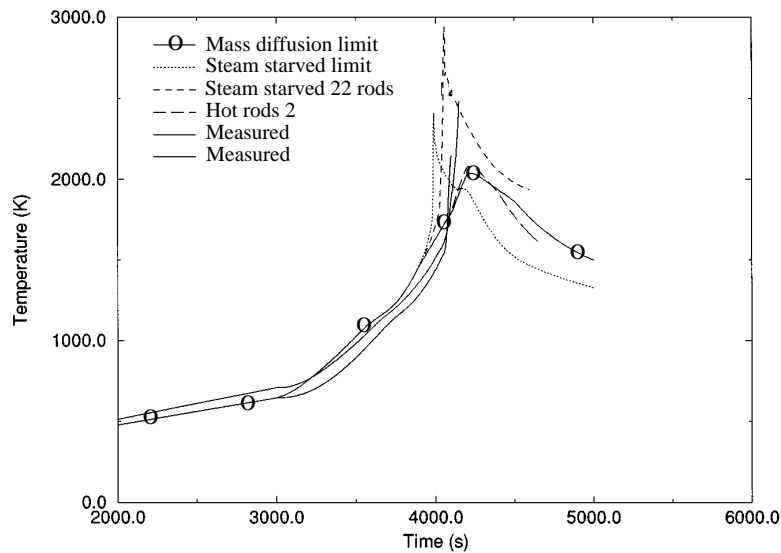


Figure 4-34. CORA-7 comparison of fuel rod temperatures at the 750 mm elevation.

For the CORA-13 calculation, a fuel bundle representation was tried that used one SCDAP fuel rod component to represent the local hot spots in the bundle, and another to represent the average rods in the same region. Oxidation of the rod representing the hot spots was limited by steam starvation, and the average rods by vapor diffusion. Code to data comparisons for a ZrO_2 failure temperature of 2,250 K of

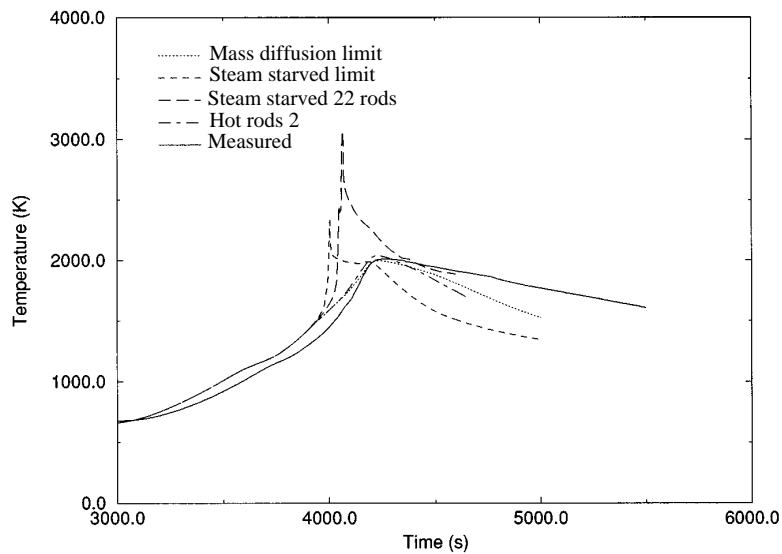


Figure 4-35. CORA-7 comparison of fuel rod temperatures at the 950 mm elevation.

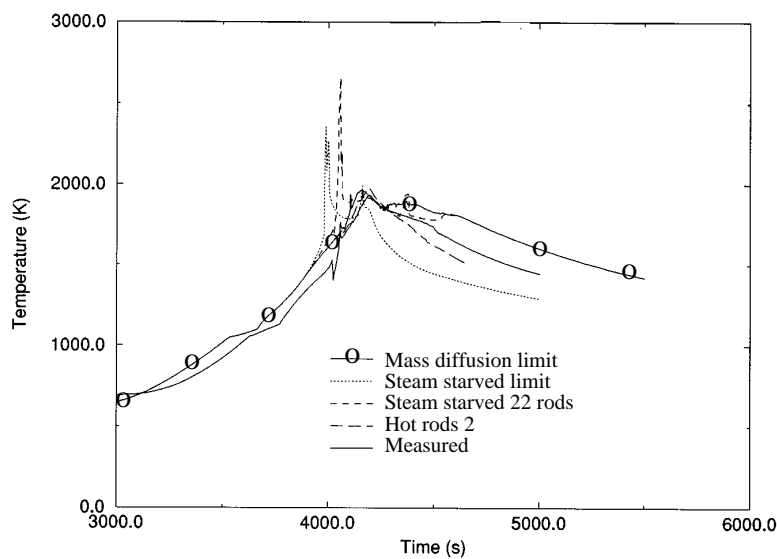


Figure 4-36. CORA-7 comparison of control rod temperatures at the 750 mm elevation.

unheated fuel rod temperatures at various elevations in the bundle are shown in Figures 4-41 to 4-44 and a comparison of predicted hydrogen production with the measured is shown in Figure 4-45.

Figures 4-46 to 4-49 show the calculated temperatures at four elevations in the bundle compared to the measured values at the same elevations when a failure temperature of 2,450 K was used and the lower plenum and quench tank was represented.

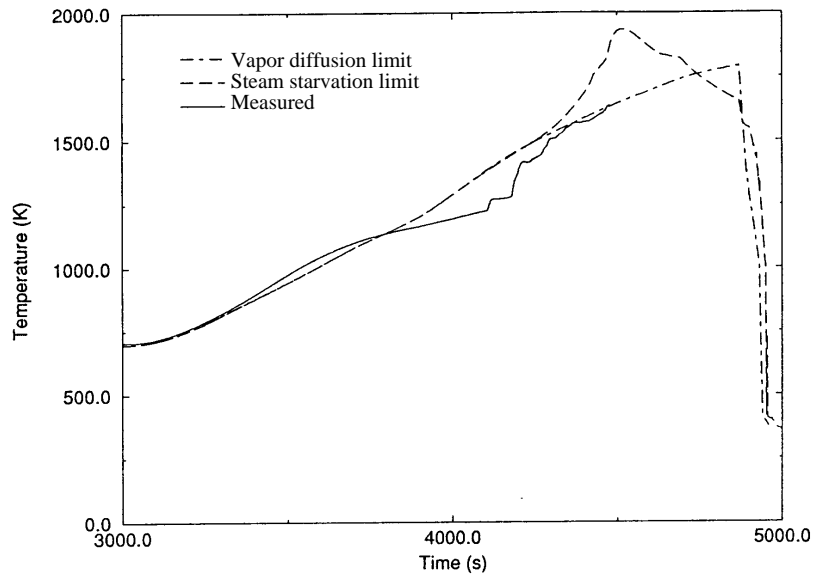


Figure 4-37. CORA-7 calculated and measured temperatures at the 350 mm elevation - vapor diffusion and steamed starved limitations.

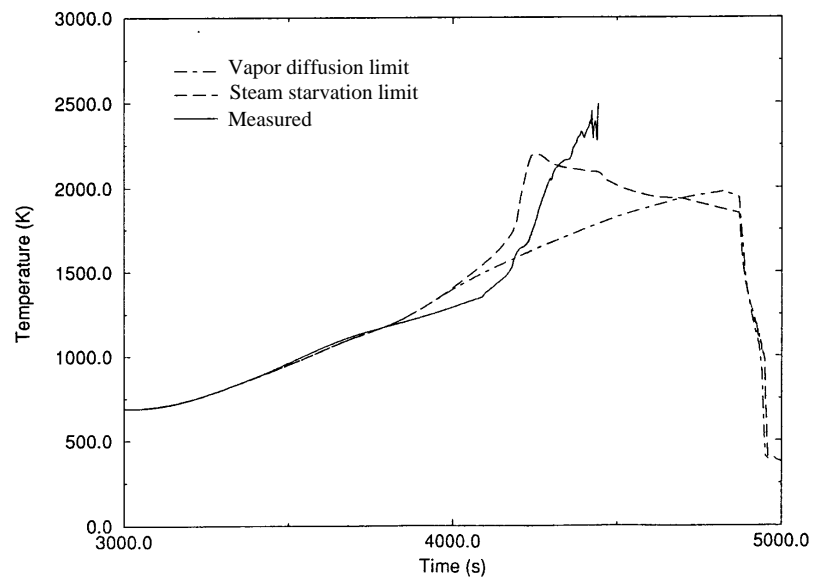


Figure 4-38. Calculated and measured temperatures at the 550 mm elevation - vapor diffusion and steamed starved limitations.

As shown in Figures 4-46 through 4-49, the predicted results showed improved agreement with the data. The temperature in the lower quarter of the bundle is still over predicted but is improved over previous results. The predicted temperatures in the upper three quarters of the bundle agree well with the data.

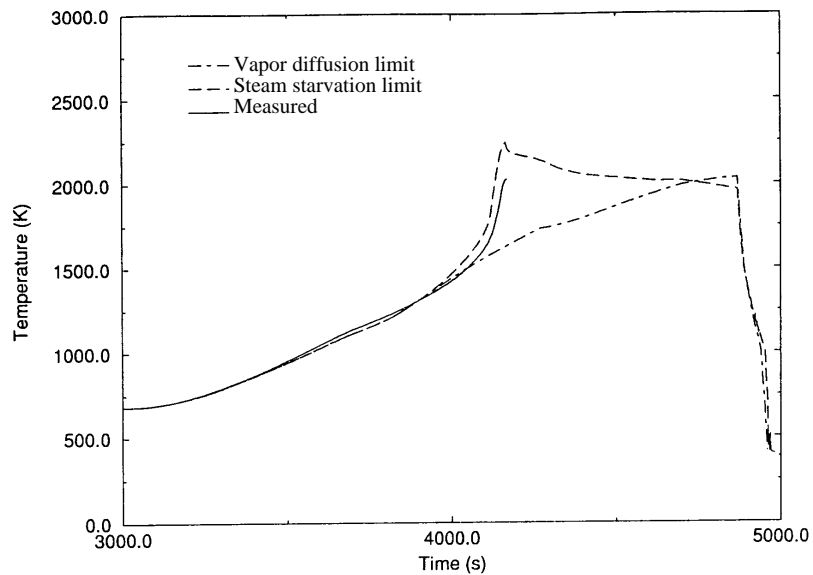


Figure 4-39. Calculated and measured temperatures at the 750 mm elevation - vapor diffusion and steamed starved limitations.

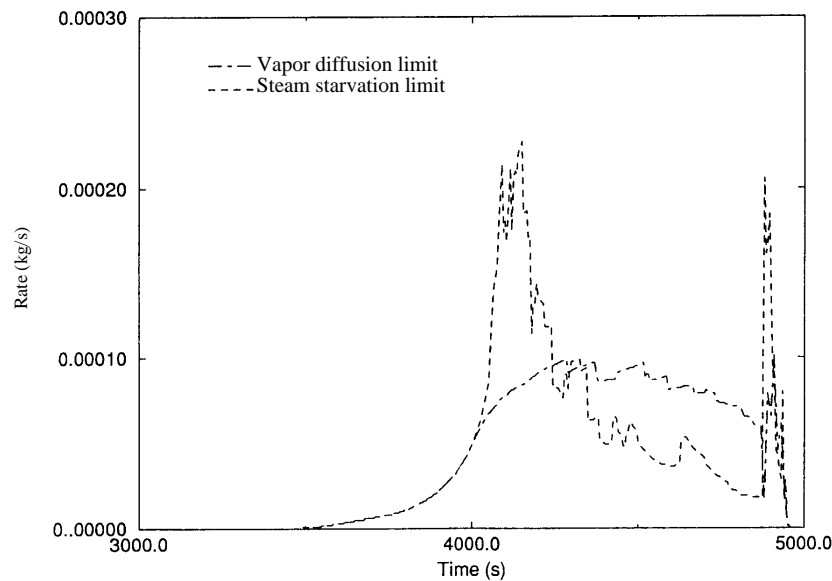


Figure 4-40. Hydrogen production rates from the steamed starved and vapor diffusion limited cases.

Figure 4-50 shows the predicted hydrogen production rate compared to the measured rate when the reflood model in the code has been activated, hot spots modeled, lower plenum and quench tank modeled, and the ZrO_2 failure temperature set to 2,450 K. The code more accurately predicts the hydrogen spike at reflood and the percent of the total predicted hydrogen produced during reflood. However, the total calculated amount produced during the experiment is still underpredicted. Table 4-2 shows the results of the studies performed using the reflood model.

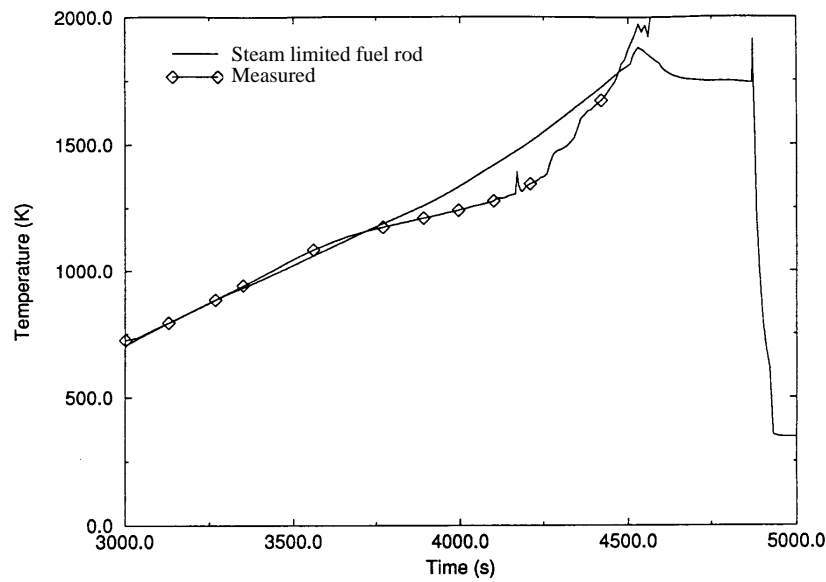


Figure 4-41. Calculated and measured temperatures at the 350 mm elevation when reflood and hot spots in the bundle are modeled using a ZrO_2 failure temperature of 2,250 K.

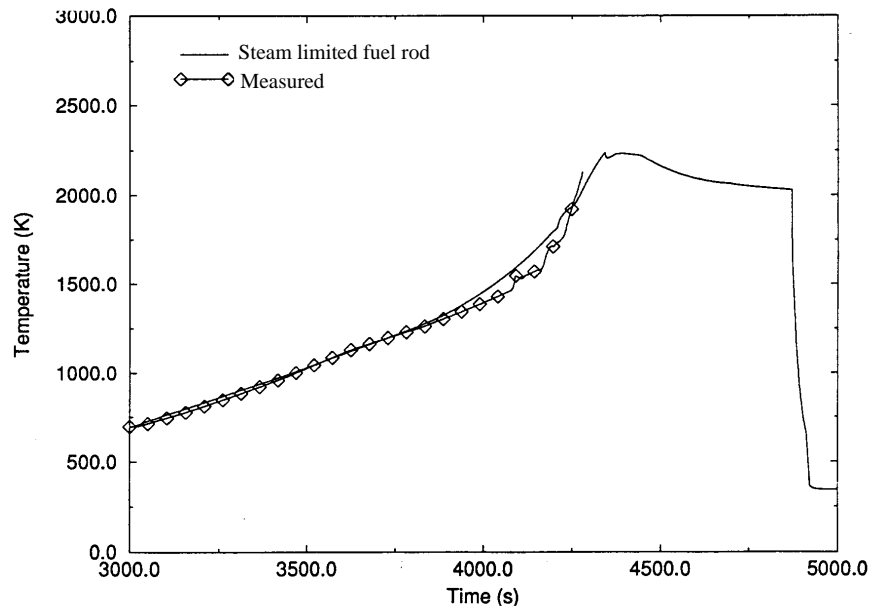


Figure 4-42. Calculated and measured temperatures at the 550 mm elevation when reflood hot spots in the bundle are modeled using a ZrO_2 failure temperature of 2,250 K.

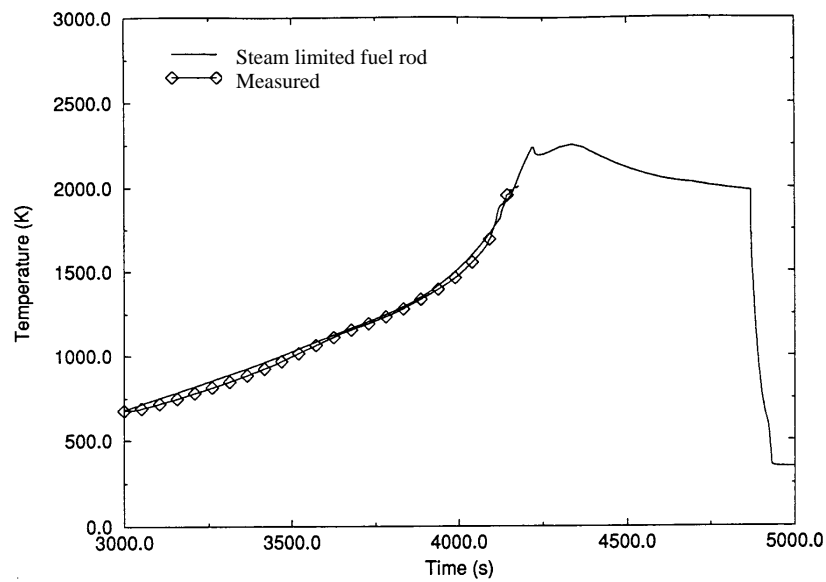


Figure 4-43. Calculated and measured temperatures at the 750 mm elevation when reflood and hot spots in the bundle are modeled using a ZrO_2 failure temperature of 2,250 K.

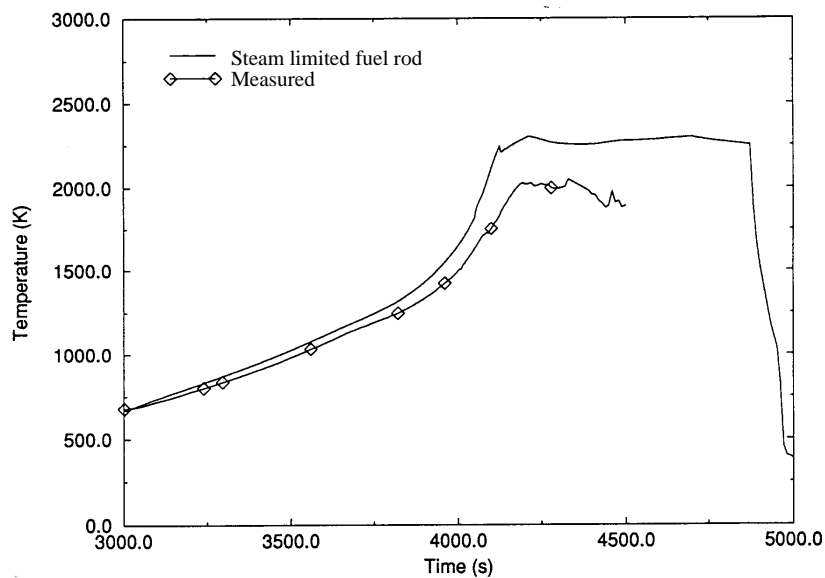


Figure 4-44. Calculated and measured temperatures at the 950 mm elevation when reflood and hot spots in the bundle are modeled using a ZrO_2 failure temperature of 2,250 K.

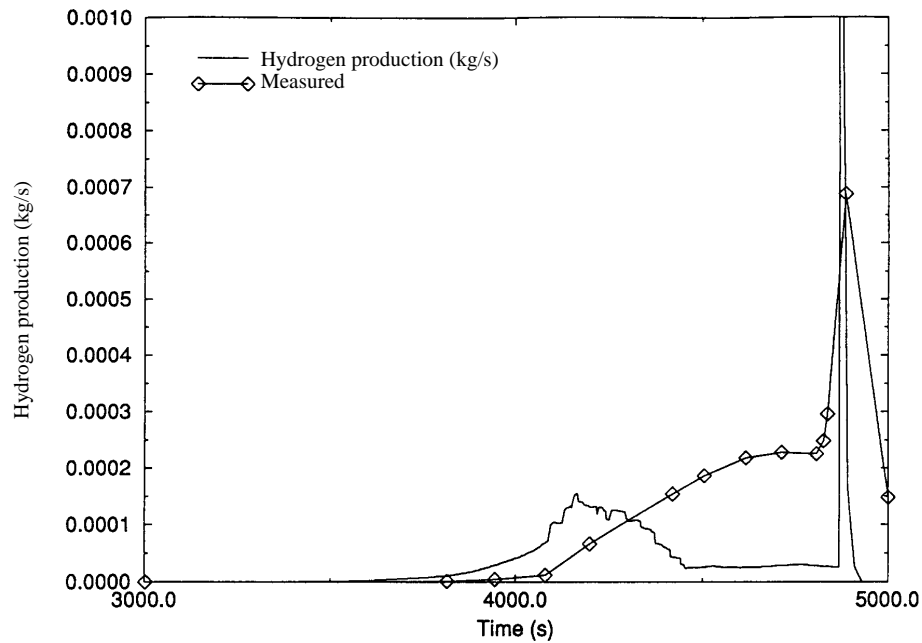


Figure 4-45. CORA-13 hydrogen production in the bundle when reflood and the hot spots in the bundle are modeled using a ZrO_2 failure temperature of 2,250K.

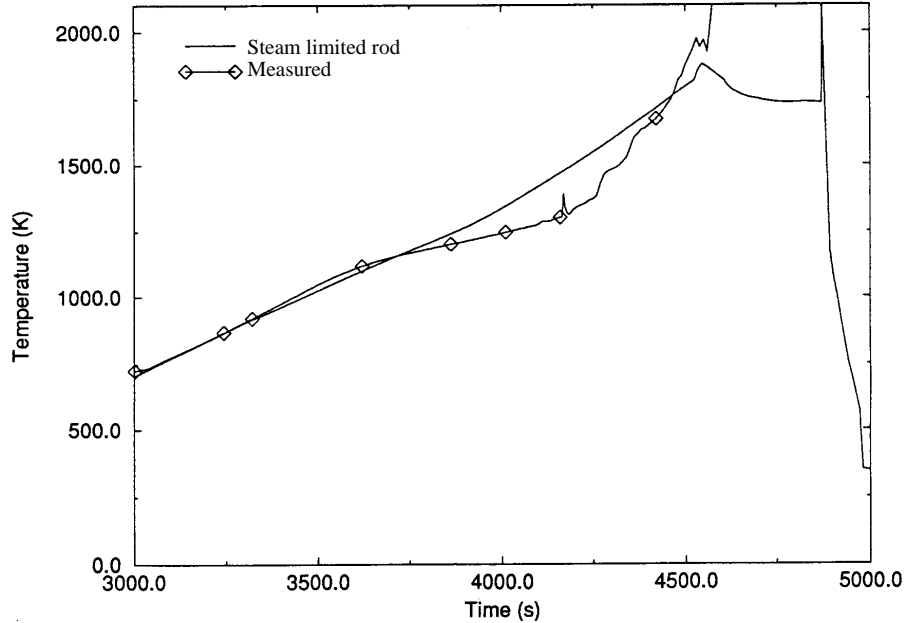


Figure 4-46. CORA-13 calculated and measured temperatures at the 350 mm elevation when reflood and the hot spots in the bundle are modeled using a ZrO_2 failure temperature of 2,450 K.

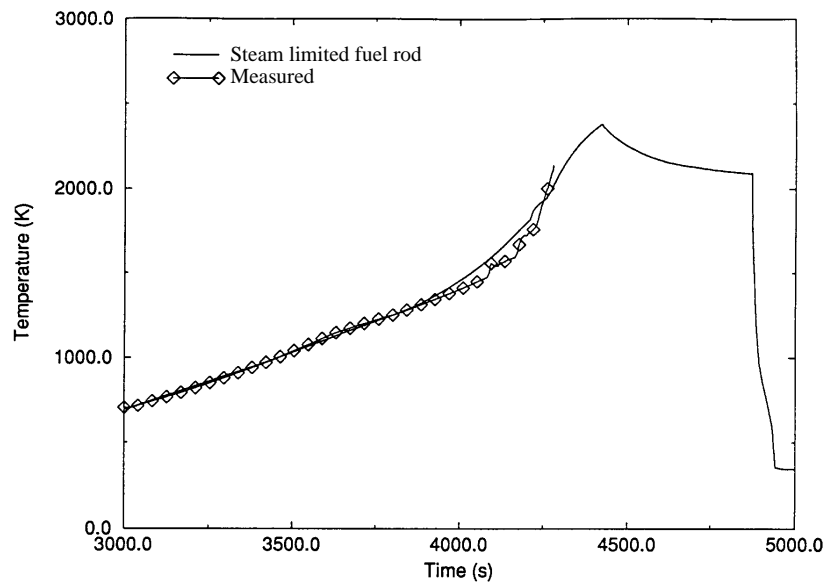


Figure 4-47. CORA-13 calculated and measured temperatures at the 550 mm elevation when reflood and the hot spots in the bundle are modeled using a ZrO_2 failure temperature of 2,450 K.

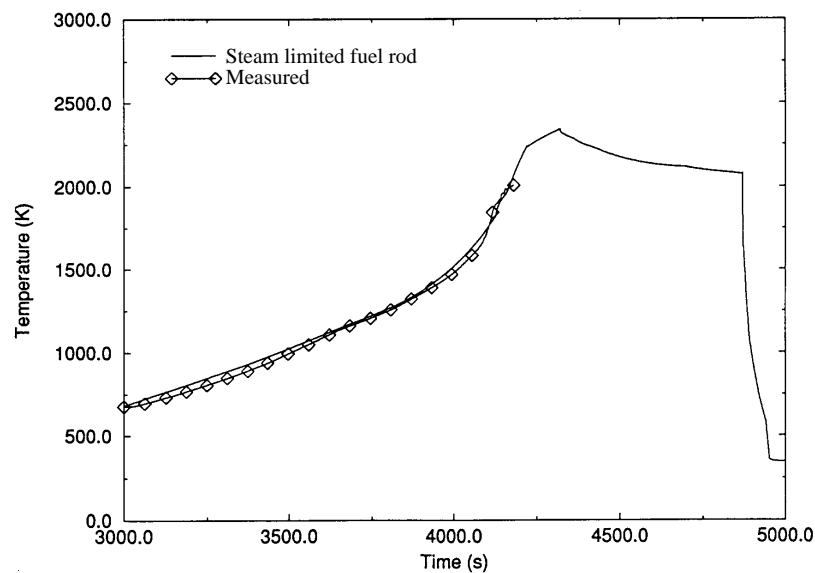


Figure 4-48. CORA-13 calculated and measured temperatures at the 750 mm elevation when reflood and the hot spots in the bundle are modeled using a ZrO_2 failure temperature of 2,450 K.

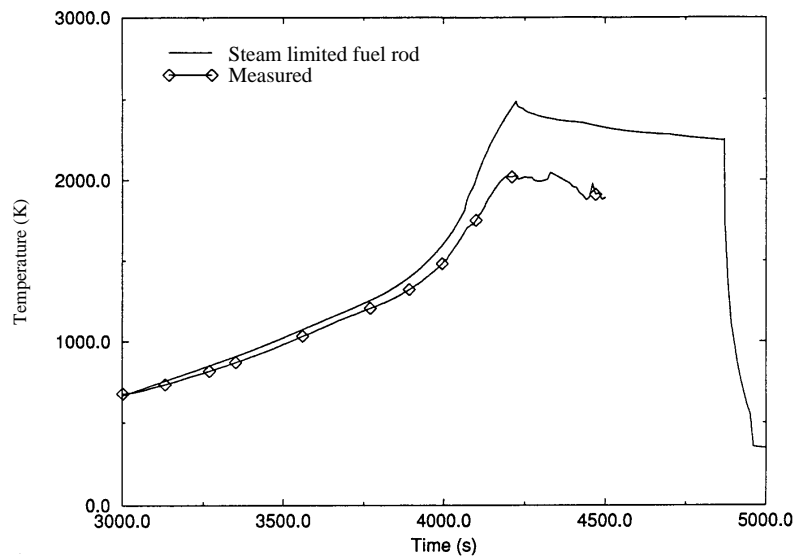


Figure 4-49. CORA-13 calculated and measured temperatures in the bundle at the 950 mm elevation when reflood and hot spots in the bundle are modeled using a failure temperature of 2,450 K.

Table 4-2. Sensitivity Study Comparison for Hydrogen Production

	Grams H produced	% produced after reflood
Data	210	48%
Zr fail 2,250	87	32%
Zr fail 2,450	118	38%

Although it must be confirmed by the experimenters, under prediction of total hydrogen by the code may be explained as follows. The reported hydrogen data in ISP-31 reports^{30,22} appear to have been taken at a distance of approximately 10 m from the core, after the gas had passed through a condenser and into a mixing tank. This could explain some of the time separation between the measured initiation of hydrogen production and that predicted by SCDAP/RELAP5/MOD3.1. More evidence of the effects of this delay is noticed in the temperature information. At 4,000 seconds, the measured temperature indicates the onset of rapid oxidation, especially at the 750 and 950 mm elevations, in agreement with the code prediction. The predicted rise in temperature associated with the onset of rapid oxidation occurs significantly before measurements indicate hydrogen production to occur during the experiment. The under prediction of hydrogen between $t = 4,200$ seconds and $t = 4,800$ seconds is due, in part, to melted material relocating. In the experiment, the relocating materials continued to oxidize in the reflood tank until cooled, but in SCDAP/RELAP5 once relocated into the RELAP5 modeled areas, they are no longer included in the SCDAP oxidation calculation. Another neglected item in the oxidation calculation is the oxidation of the outer surface of the shroud and the upper 0.5 m unheated portion of the bundle. Double-sided oxidation was not initiated for the shroud liner in this calculation. The reflood calculation discussed in this

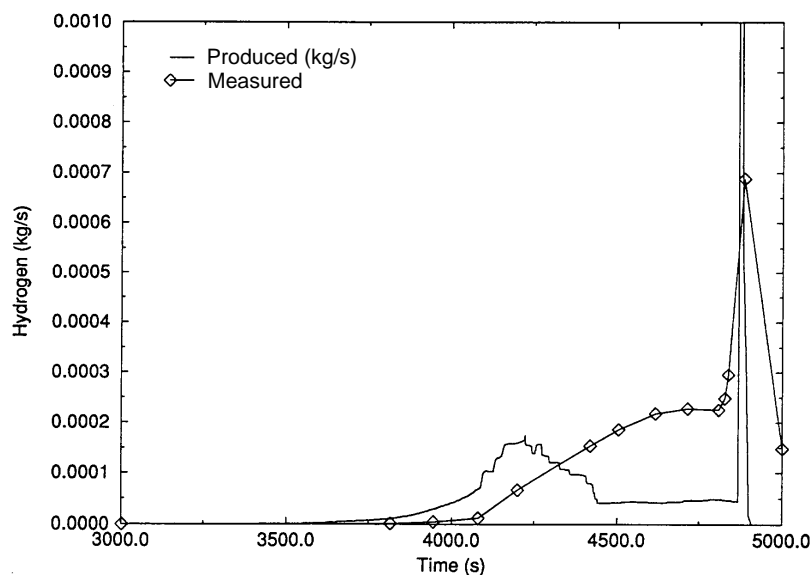


Figure 4-50. CORA-13 calculated and measured hydrogen production rates when reflood and the hot spots in the bundle are modeled using a ZrO_2 failure temperature of 2,450 K

assessment simply feeds water into the lower plenum region at a given mass flow rate with no modeling of the two states, liquid and gaseous, in the volume. The narrowness and height of the reflood hydrogen spike with respect to the data can be explained in two ways: (1) measured data is likely to be dispersed during transport to the measurement location, and, (2) the reflood oxide shattering model in the code instantly shatters the oxide over much of the length of the fuel rod; whereas during the experiment the oxide layer may have shattered over a short time span.

4.2.4 BWR Control Blade Channel Box

The assessment of the ORNL developed control blade/channel box model was performed using the DF-4 experiment and the Browns Ferry nuclear power plant. As discussed in Appendix A the model appears to be accurately predicting the behavior of the control blade and channel box during the early stages of a BWR accident. Code-to-date temperature comparisons of the control blade and channel box regions agree well with measured values. Predicted Browns Ferry control blade behavior also appears to be reasonable.

The DF-4 and Browns Ferry calculations indicate that the blade is behaving as expected. Interactions between the B_4C and stainless steel rodlets begin to occur as temperatures near the input B_4C /stainless steel eutectic temperature. Stainless steel oxidation occurs when expected, and eutectic interactions between the zircaloy channel box and stainless steel agree with the results obtain from separate effects experiments conducted by Hofmann at KfK.¹⁸ Molten blade material is predicted to flow freely down the blade and through the large void regions in the channel box forming a blockage in the cooler regions at the bottom of the bundle. Once a large blockage region has been formed near the bottom of the core, calculations are terminated since complete blockage to flow in the channel box is calculated. In order to

continue the calculations after complete blockage, it is necessary to model flow in what is in effect a “dead-end” control volume. This modeling of flow is difficult to perform.

4.2.5 User Conveniences and Usability Improvements

SCDAP/RELAP5/MOD3.1 is considerably easier to use and is more reliable than previous versions of the code. RELAP5 code changes to reduce numerical instabilities and water property or other state failures have improved the reliability of the code for many types of problems. The addition of time step repetition resulted in substantial reductions in overall run time in problems where the code previously reduced time steps to unacceptable values to insure code stability. Other changes to RELAP5 which improved the reliability of the code and the running time were (1) the treatment of noncondensables on phase appearance and disappearance (2) the time smoothing options for the explicit coupling between radiation heat transfer and hydrodynamic models, and (3) the elimination of discontinuities in thermal-hydraulic constitutive models. These improvements, assessed by RELAP5 developers, resulted in a factor of two decrease in running time for many problems. The number of water property failures decreased considerably from runs performed using earlier versions of the code. Changes made to the input and output of the SCDAP module include (1) the conversion of all input to the RELAP5 free form, numbered card format, (2) the addition of extensive input error checking, (3) the addition of input range checking and best estimate defaults, (4) the addition of options for automatic data compression for restart plot files, and (5) output more descriptive of the degradation phenomena occurring in the reactor core. SCDAP/RELAP5/MOD3.1 with the RELAP5 free formed numbered card input, the extensive error checking, and input range checking, clearly identifies the location, type of error, and unreasonable dimensions or temperatures. As a result of the changes in code input, the time required to set up and qualify an input deck has substantially been reduced since a majority of actual and potential errors can be identified in a single input test run. There are fewer areas where unreasonable or unrealistic variables can be used with SCDAP/RELAP5/MOD3.1 as the code will automatically substitute best estimate default values for selected models, such as the cladding deformation parameters, time smoothing, and debris values and will warn the user if a input variable is out of range. The user can override the default values, which were based on the results of code-to-data comparisons performed as part of earlier code assessment activities, to perform sensitivity calculations to evaluate the influence of modeling uncertainties.

Restart plot files for full plant calculations could become quite large requiring a sizeable allocation of disk space. Most users are presently using workstations for SCDAP/RELAP5 analyses and workstations generally have less disk space than mainframes. The ability to reduce the size of the restart plot file through the use of an internal compression utility is the most notable output improvement in SCDAP/RELAP5/MOD3. The use of the compress option can reduce the size of a restart plot file by a factor of 5. As part of the assessment activities, the compress utility was checked using several test cases based on the experiments and two full size nuclear power plants. The assessment calculations confirmed that the model was working correctly and that plot variables, could be easily stripped from the compression restart file. The code also successfully compressed the restart plot files for a Browns Ferry and Surry full plant analysis, plot data was successfully stripped from the compressed file, and the transient analysis restarted.

5. NODALIZATION STUDY

This section describes a systematic evaluation of axial and radial nodalization effects for Browns Ferry and Surry. The Browns Ferry calculation was a large break loss of coolant transient (LBLOCA) while the Surry transient was a high pressure station blackout transient (TMLB'). To study the effects of axial nodalization of the core region, simplified plant calculations were first performed for each reactor. The number of axial nodes was varied from 5 to 24, and the results compared. Each test deck calculated temperatures high enough to cause severe core damage. Once the optimum axial nodalization was determined, full plant calculations were performed. The number of flow channels used to represent the reactor core for Browns Ferry and Surry was then modified and the calculations rerun to determine the effect of radial detail in modeling the reactor core on predicted core response during a severe accident. Furthermore, the effect of using the nearly implicit hydrodynamic numerical scheme or a time step size smaller than the Courant limit was also investigated. The results of the axial and radial nodalizations, hydrodynamic numerical scheme, and time step size studies are reported in this section. The BWR study is reported in Section 5.1. The study of the axial nodalization of a PWR fuel bundle is presented in Section 5.2.1. The study of the calculated behavior of the Surry PWR during a TMLB' severe accident is described in Section 5.2.2. This section includes a study of the sensitivity of calculated results to nodalization of the reactor core.

5.1 BWR Nodalization

This section will discuss the effects of axial and radial nodalization on SCDAP/RELAP5 predicted results for boiling water reactors (BWRs). To assess the effects of axial detail in the nodalization of the core region, a two-channel model was developed representing a fuel assembly/control blade region of a typical General Electric (GE) boiling water reactor, one flow channel contained four zircaloy-shrouded typical BWR fuel rod assemblies, the other a typical cruciform-shaped control blade. Using the two-channel BWR model, in combination with the new ORNL-developed control blade/channel box model, a series of five calculations were performed with the axial representation of the core region being varied from 5 axial nodes to 24. Results from these calculations up to the point of the formation of a molten pool region in the upper bundle and a region of significant blockage in the channel box, where the ORNL model is no longer applicable, were compared and the optimum core axial representation was determined. Each BWR test deck used in this study calculated temperatures high enough to cause the control blade to fail and cause formation of a blockage region in the channel box. Once the optimum axial nodal representation was determined, full plant calculations of the Browns Ferry Nuclear Power Plant were performed, to study effects of core radial detail on predicted results. For these calculations, the core of the reactor was represented using three, five, and seven flow channels.

5.1.1 Axial Nodalization Study

A model representing four fuel assemblies shrouded in zircaloy and a single control blade region in the Browns Ferry Nuclear Power plant was developed. The model consisted of four zircaloy shrouded 8 x 8 fuel assemblies surrounding a stainless steel clad B₄C control blade. The channel box/control blade model developed by ORNL for SCDAP/RELAP5/MOD3 from experiment specific and/or plant specific models was used for this study. Figure 5-1 shows the RELAP5 nodalization diagram for a core region represented by 10 axial nodes. Two flow channels were used, one representing the flows through the fuel assemblies and the other flows through the channel containing the control blade. For a BWR, a minimum

of two flow channels is required to model the reactor core. The fuel assembly flow channel was full length, 3.6756 m, and consisted of four 8 x 8 fuel assemblies containing 256 fuel rods. Each fuel assembly was surrounded by a zircaloy sheath. The flow channel in which the control blade was situated contained one cruciform control blade containing 88 stainless steel rodlets filled with boron carbide, B_4C . Figure 5-2 shows the SCDAP component nodalization used to model the BWR core region for the two-channel model. The control blade, as with the fuel assemblies, was modeled as full length.

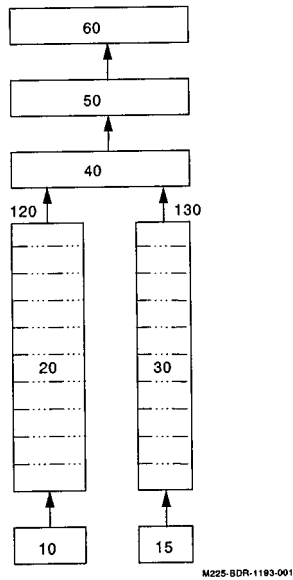


Figure 5-1. RELAP5 nodalization of the core region of the Browns Ferry Nuclear Power Plant.

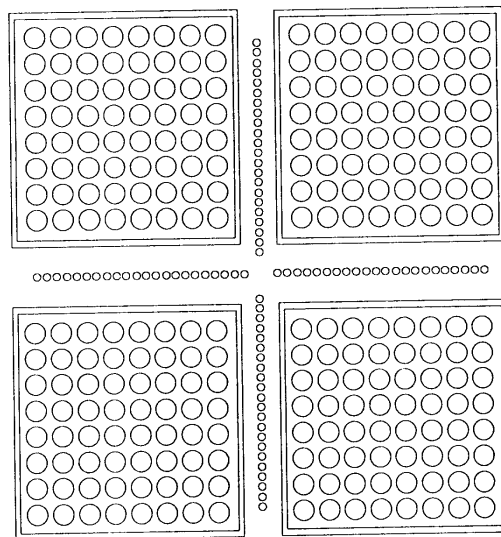


Figure 5-2. SCDAP nodalization used to represent the reactor core for the axial nodalization study.

Boundary conditions were the steady-state initial conditions obtained from previous analyses of the Browns Ferry Nuclear Power Plant and code default values were used as the input options wherever possible.

Since the maximum number of axial nodes is established at compile time, an executable version of SCDAP/RELAP5/MOD3.1 was created that allowed the use of more than 10 axial nodes. The code is normally compiled with a maximum number of 10 axial nodes to represent a component to conserve computer memory. Once this executable was created, the test case using 10 axial nodes with four complete full-size fuel assemblies and one full-size control blade, was rerun to verify that this executable gave results identical to those obtained with the executable used to develop the base input deck for the nodalization study. Results from the two calculations were compared and found to be identical. Figure 5-3, showing the calculated maximum bundle temperature from both calculations, indicates that identical results were obtained from the two executables.

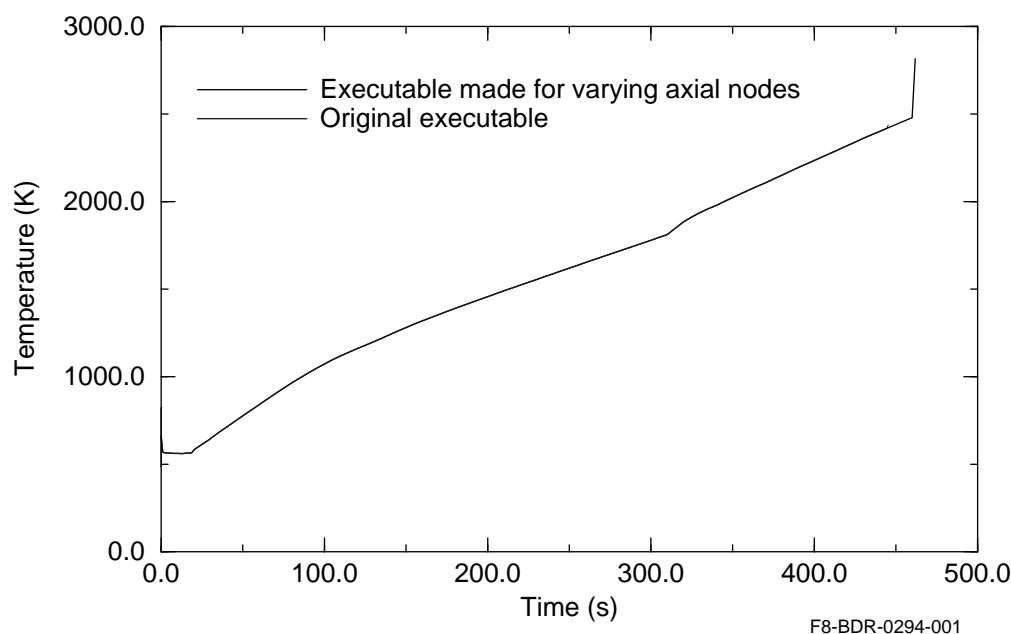


Figure 5-3. Maximum bundle temperature comparison of the original executable which allowed at maximum of 10 nodes in the core and the executable which allowed 30 axial nodes for core modeling.

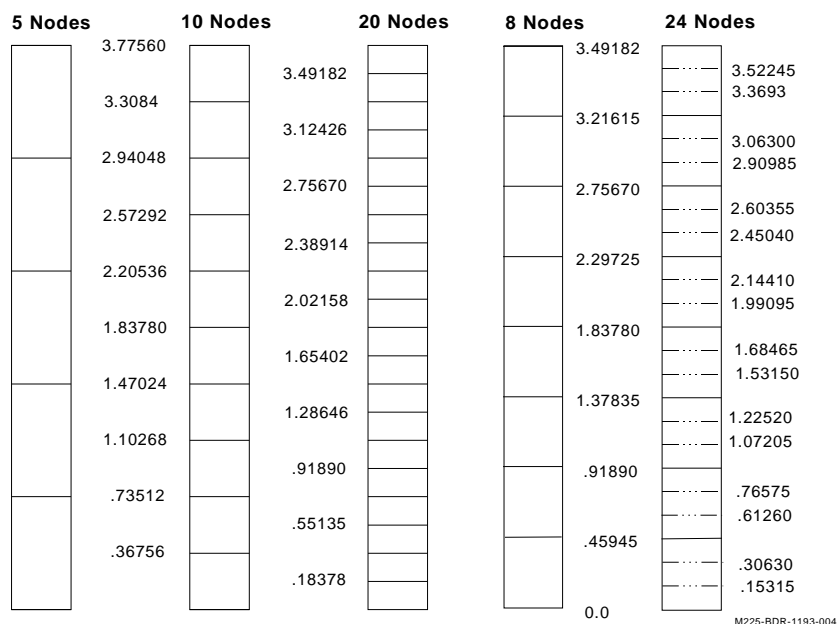
Five separate axial nodalization schemes using the two-channel BWR model were developed to study the effects of the number of axial nodes used to model the core of the reactor on the predicted results. Figure 5-4 shows the axial nodalization schemes used for the analysis and Table 5-1 summarizes the results of the BWR axial nodalization study.

5.1.1.1 Results of the Axial Nodalization Study. Figures 5-5 through 5-8 show the predicted values for the maximum bundle temperature, hydrogen production rate, integral hydrogen production, and CPU time for each case studied. When an extremely course nodalization scheme, five nodes, was used to represent the core, significant differences in the predicted values and computational time were observed: the predicted maximum bundle temperature was 2,234 K (2,816 K for all other axial representa-

Table 5-1. Summary of BWR Nodalization Studies

Case No.	Number of Axial Nodes	CPU Time (s)	Problem Time (s)	BGMCT ^a (K)	Hydrogen Produced (g)
1	5	4068	1,000.0	2,234	2,898
2	8	2,647	460.9	2,816	1,570
3	10	3,159	461.8	2,816	1,516
4	20	7,521	464.1	2,816	1,404
5	24	11,385	469.8	2,816	1,407

a. Peak assembly temperature.

**Figure 5-4.** Axial division of the core for the 5, 8, 10, 20, and 24 node models used in the study.

tions of the bundle), maximum bundle temperature is reached approximately 100 seconds later, once the peak temperature of 2,234 K was attained, bundle temperatures slowly decreased, the rate and quantity of hydrogen produced during the simulated accident was considerably more. All other axial representations of the bundle predicted similar melt progression behavior and temperature response.

The major observed differences between the converged results were CPU time and hydrogen production. Table 5-1 shows the CPU time needed for each calculation to be run to completion or code failure on a DEC 5000 workstation. Looking at the converged cases, 8 to 24 axial nodes, the CPU time increases exponentially as the number of axial nodes used to represent the core region is increased. The quantity and rate of hydrogen appear to be most sensitive to nodalization. A small difference, several seconds, in the deviation of the oxidation process or several degrees K in bundle temperature changes the rate and quantity produced. A ten percent variation is observed between the 8 and 24 node cases, whereas,

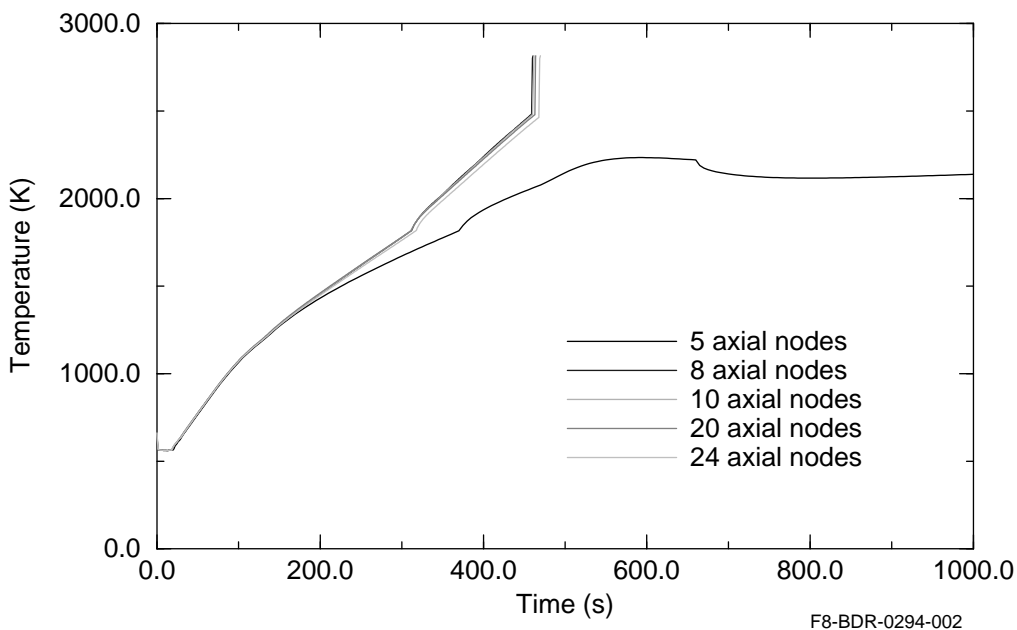


Figure 5-5. Predicted maximum bundle temperatures from the 5, 8, 10, 20, and 24 axial node representation of the bundle.

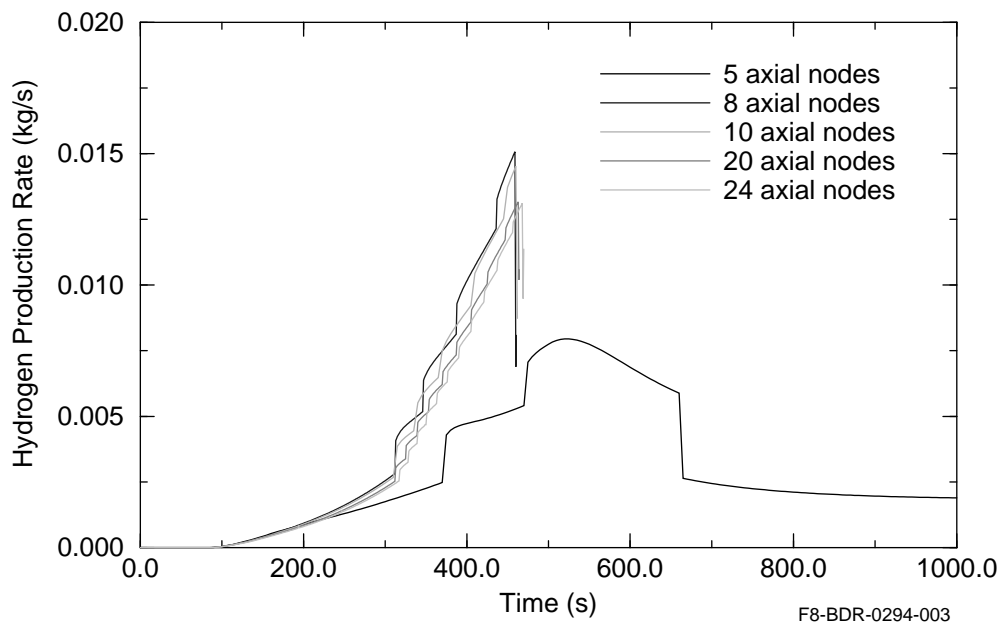


Figure 5-6. Predicted hydrogen generation rate for the 5, 8, 10, 20, and 24 node representations of the bundle.

less than .2% variation is observed between the 20 and 24 node cases. The sensitivity to time or maximum bundle temperature observed for hydrogen production is not seen for any other parameter predicted by the code.

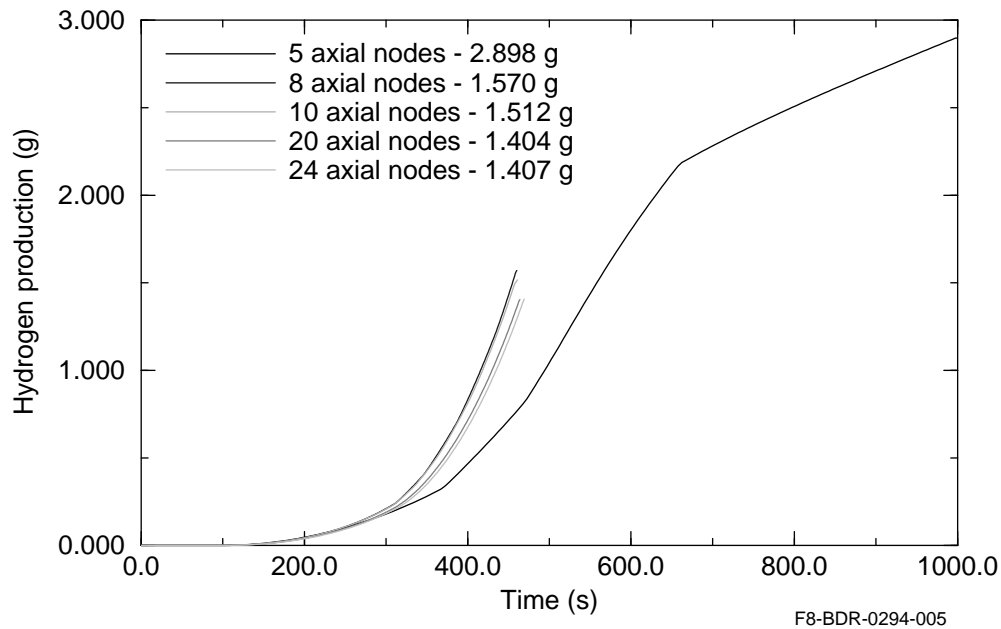


Figure 5-7. Predicted integral hydrogen production for the 5, 8, 10, 20 and 24 node axial representations of the bundle.

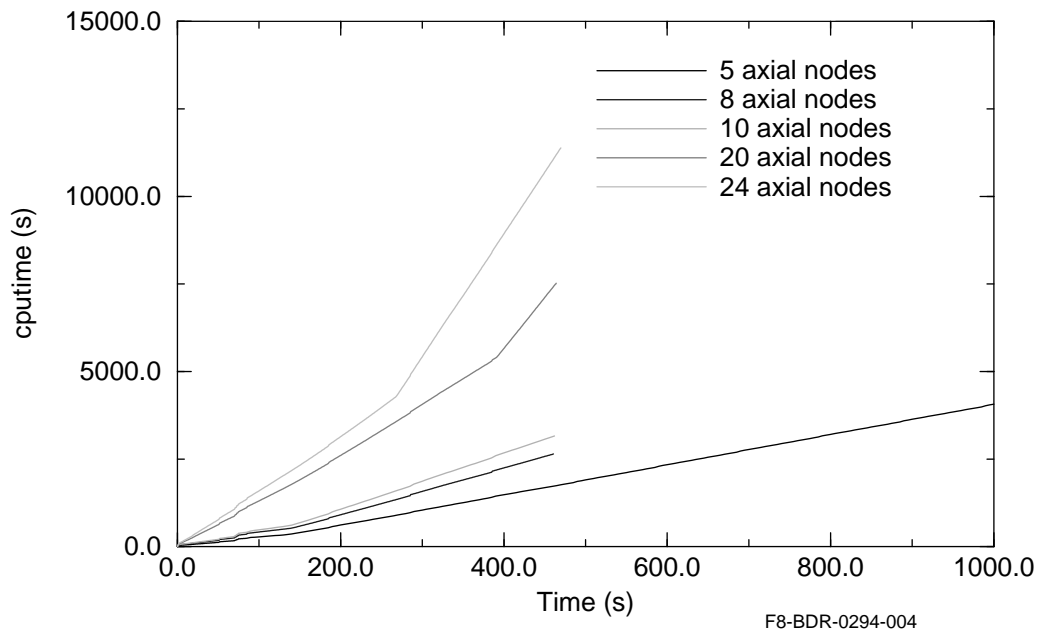


Figure 5-8. CPU time needed to run the 5, 8, 10, 20 and 24 axial node representations of the bundle to completion.

Calculational efficiency can be optimized by using an axial nodalization scheme where the number of represented nodes is a power of two. An odd-even matrix solver is used when the core is represented by 4, 8, or 16 nodes; whereas, the Gauss elimination matrix solver is used for all other axial divisions.

5.1.2 Conclusions

Increasing the number of axial nodes beyond 8 to 10 to represent the reactor core does not significantly improve the predicted results, and the efficiency of the calculation deteriorates as the number of axial nodes used to represent the core is increased. The CPU time needed for the calculation increased dramatically as the number of axial nodes used to represent the core was increased. An 8 to 10 axial node representation of the SCDAP component models give predicted results that are representative of events occurring within the reactor core during a severe accident and at an optimum calculational time. No significant improvement in the predicted results was observed when the number of axial nodes used to represent the components in the core was increased beyond 8 to 10.

5.1.3 Radial Nodalization

An input deck for the Browns Ferry Nuclear Power Plant was developed from the Browns Ferry SCDAP/RELAP5 and Nuclear Plant Analyzer⁸ BWR demonstration deck for use in studying the effects of radial detail in modeling a full-size nuclear power plant. The RELAP5 nodalization used for the Browns Ferry radial nodalization study is shown in Figure 5-9. Initially, the input deck contained no BWR control blade modeling. The blade was not modeled either with the old cylindrical component model or the control blade/channel box model developed by ORNL. The original input deck was modified to reflect the Browns Ferry nuclear core configuration using the ORNL control blade/channel box component model to represent the regions in the reactor core containing a standard General Electric BWR cruciform control blade. The initial input deck was the most detailed using seven flow channels and fifteen SCDAP components to radially model the Browns Ferry reactor core. Less detailed models were developed, one using five flow channels and eleven SCDAP components and the other using three flow channels and seven SCDAP components to radially model the core. Calculations were performed using these less-detailed decks and the results compared with those obtained using the more detailed seven channel core model. A calculation was also performed using the detailed seven-flow-channel-model with the cylindrical control blade component model from SCDAP/RELAP5/MOD3 and earlier released versions of the code. The results of these comparisons are presented in the following section of the report.

5.1.4 Results of the BWR Full Plant Radial Nodalization Study

Figures 5-10 through 5-13 compare the calculated global parameters, nuclear heat generation, maximum bundle temperature, and CPU time from three radial nodalization schemes, three, five, and seven channels, using the ORNL control blade/channel box model and the seven channel model using the earlier cylindrical control blade model for the simulated LBLOCA used for this nodalization study. In Figure 5-10 the predicted core nuclear heat generation for each nodalization scheme drops off, as expected, to 7% steady-state power shortly after initiation of the station blackout. After the initial drop in power, a slow and gradual decay of nuclear heat is predicted to occur throughout the transient. Figure 5-11 shows the predicted maximum bundle temperatures for each radial nodalization scheme. As shown in Figure 5-11, during the early stage of the transient the predicted bundle temperatures are nearly identical for each scheme, including the model using the cylindrical blade model. The three radial nodalization schemes using the ORNL control blade/channel box model are compared in Figure 5-12. As shown in this figure, a small divergence in predicted temperatures is observed, with the three-channel model predicting slightly cooler temperatures throughout the transient. The predicted maximum bundle temperatures from the five- and seven-channel models appear to be converged. As shown in Figure 5-13, CPU time increases as radial

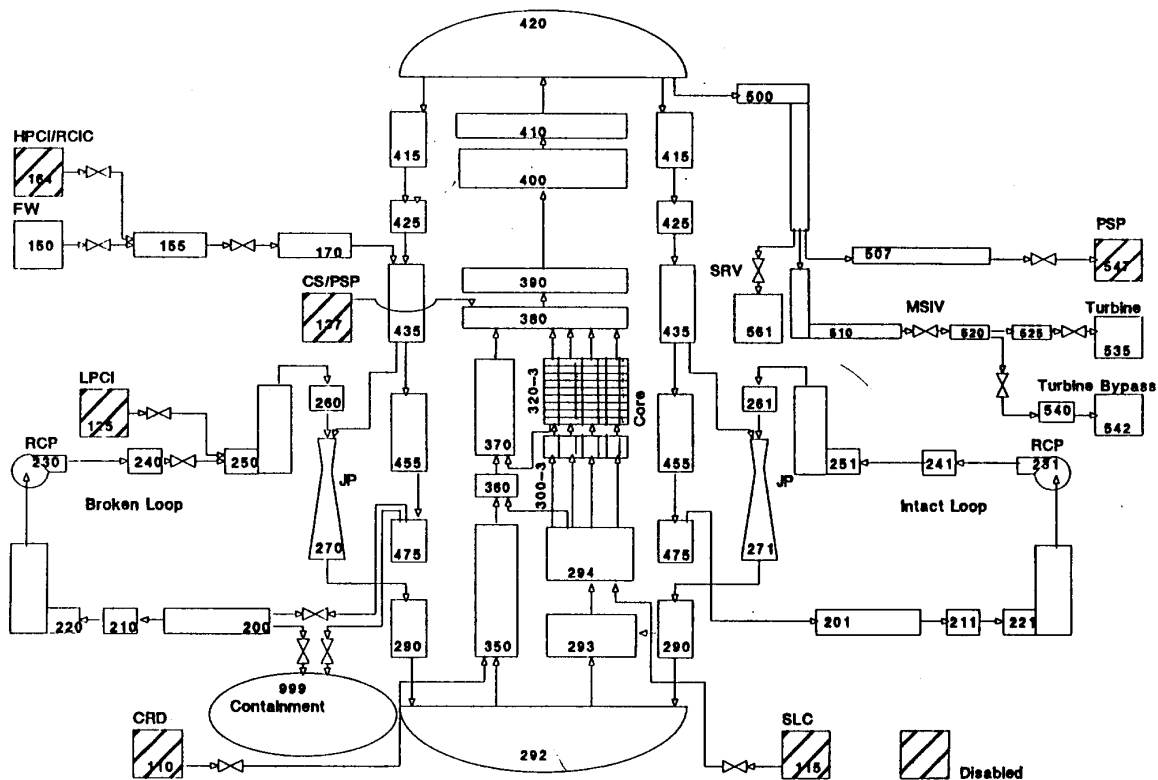


Figure 5-9. RELAP5 nodalization of the Browns Ferry nuclear reactor.

detail increases when the ORNL blade was used to model the core; and when the old cylindrical model was used CPU time increases significantly as the predicted temperature increases and core degradation events begin to occur.

Looking at individual bundle components, shown in Figures 5-14 and 5-15, the temperatures predicted by each nodalization scheme show little variation. Figure 5-14, the predicted control blade temperatures near the axial center of the blade for each nodalization scheme, shows the three-flow-channel model predicting slightly cooler temperatures from that predicted by the five- or seven-channel model or the model using the old blade. Looking at fuel rod temperatures in the axial center of the core for each nodalization scheme (Figure 5-15) again very little difference is observed in the predicted temperatures. Slightly cooler fuel rod temperatures are predicted for the five channel model and the seven channel model using the cylindrical control blade model.

The number of radial channels had little influence on either the hydrogen production rates or integral hydrogen production. However, for this transient the fraction of the core oxidized was very low because of the limited steam supply. Figure 5-16 shows the predicted rate and integral hydrogen production, and Figure 5-17 shows the hydrogen generation rate smoothed out by use of a running average. The smoothing was done so that predicted differences between the hydrogen production rates from each radial representation could be discerned.

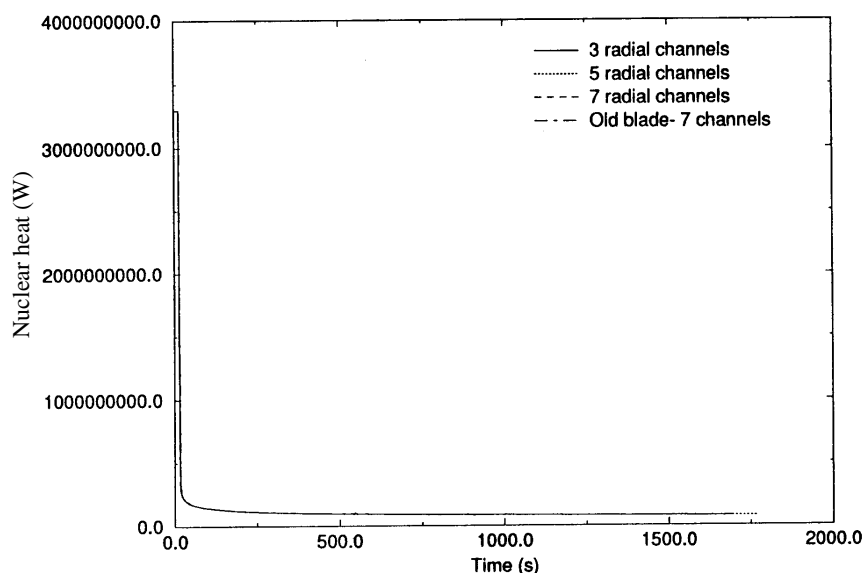


Figure 5-10. Predicted nuclear heat generation for 3, 5, and 7 channel radial representation of the Browns Ferry core using the ORNL blade model and a 7 channel representation using the old model.

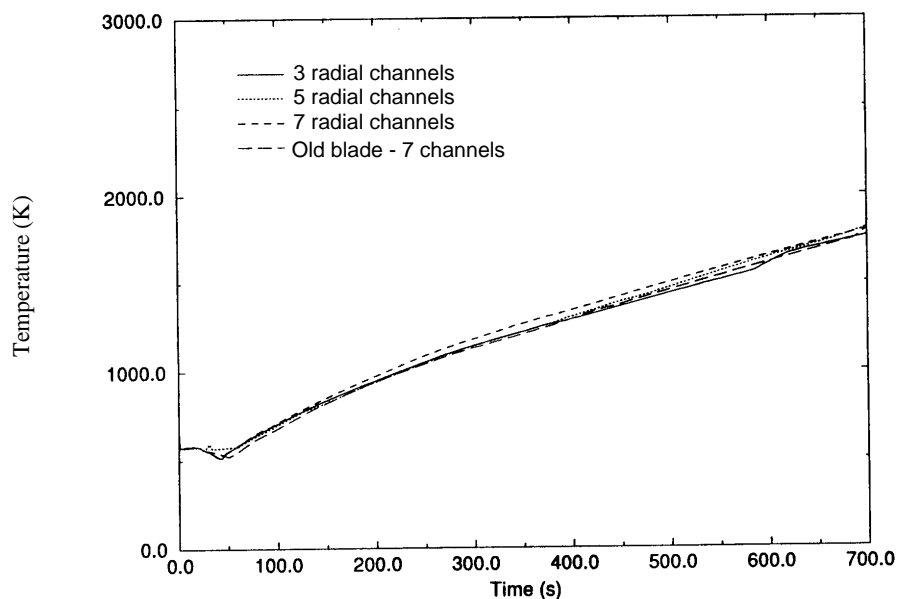


Figure 5-11. Predicted maximum bundle temperatures for the 3, 5, and 7 channel representation of the Browns Ferry core using the ORNL blade model and a 7 channel representation using the old control blade model.

The damage progression predicted by SCDAP/RELAP5/MOD3.1 for each radial representation of the Browns Ferry nuclear core using the ORNL control blade/channel box model and the seven channel representation of the reactor using the old blade model is consistent during the early phase of the accident up to the point of blockage formation. The pattern of fuel rod ballooning shifts using the different number

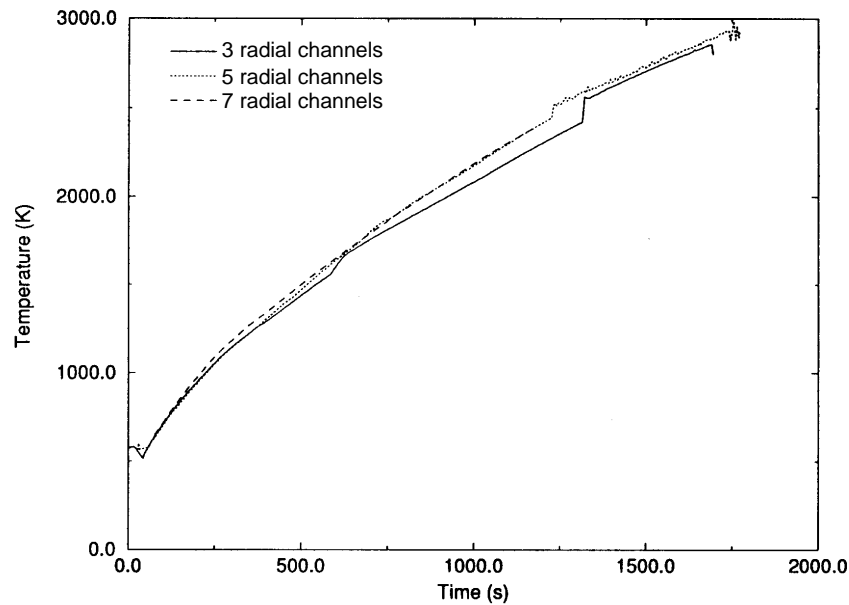


Figure 5-12. Predicted maximum bundle temperatures for the three radial representations of the core using the ORNL control blade/channel box model.

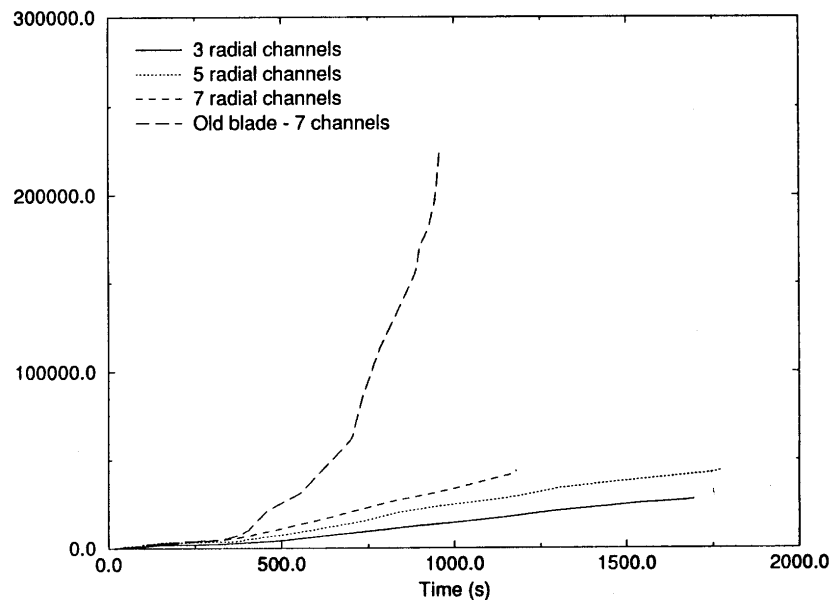


Figure 5-13. Predicted CPU time for the 3, 5, and 7 channel radial representation of the Browns Ferry core and a 7 channel representation using the old control blade model.

of channels but becomes relatively uniform across the core for the seven-channel case. The upper 70-80% of the core, axial nodes 2-7, is completely liquefied, except for small remnants of oxidized cladding, in all three radial representations. The primary differences show up at the bottom of the core. In the three and five channel models no in-core blockages are formed, while in the seven channel model, the control blade model indicates that a local blockage started to form. Since the control blade model is not yet connected to

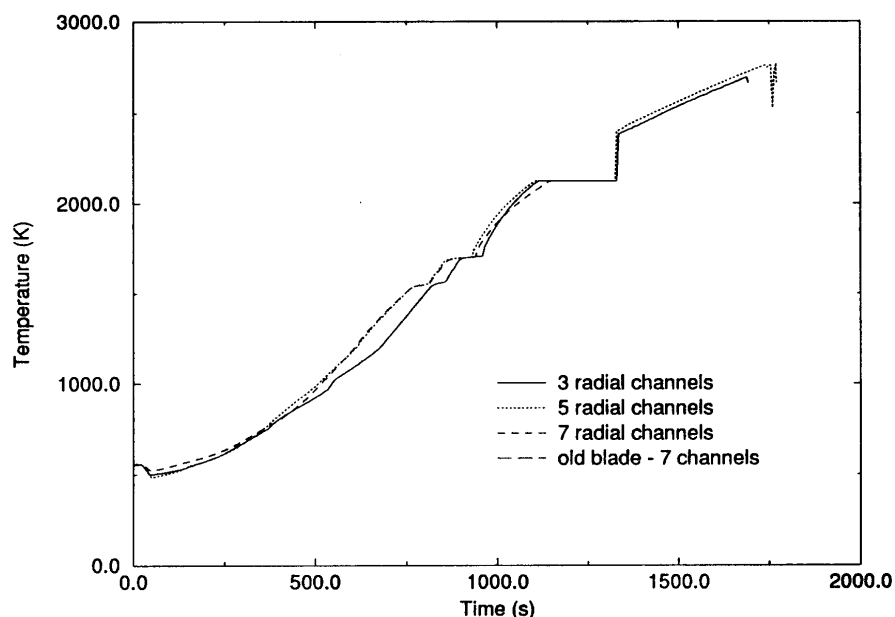


Figure 5-14. Predicted control blade temperatures near the axial center of the bundle for all radial nodalization schemes.

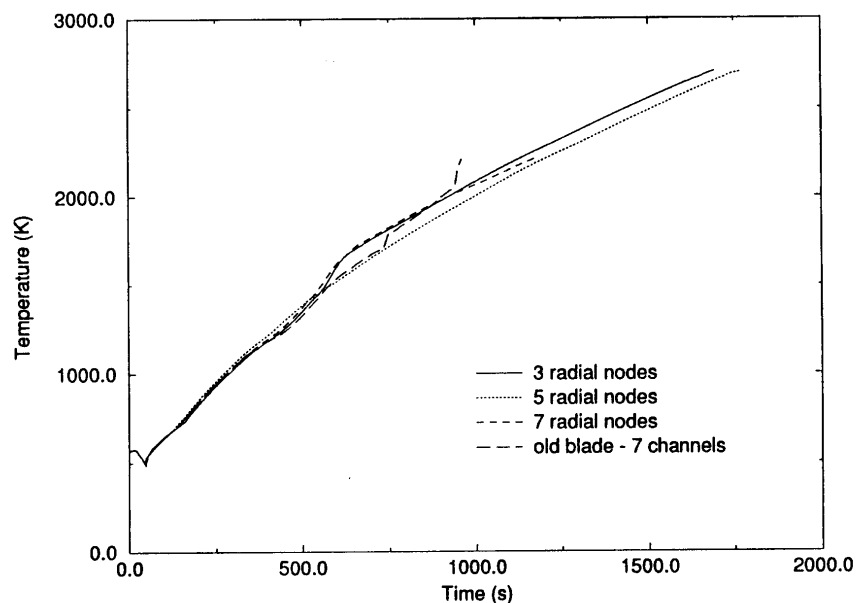


Figure 5-15. Predicted fuel rod temperatures near the axial center of the bundle for all radial nodalization schemes.

either the in-core or lower plenum debris models, it is not possible to determine the influence of different radial channels beyond this stage of the accident.

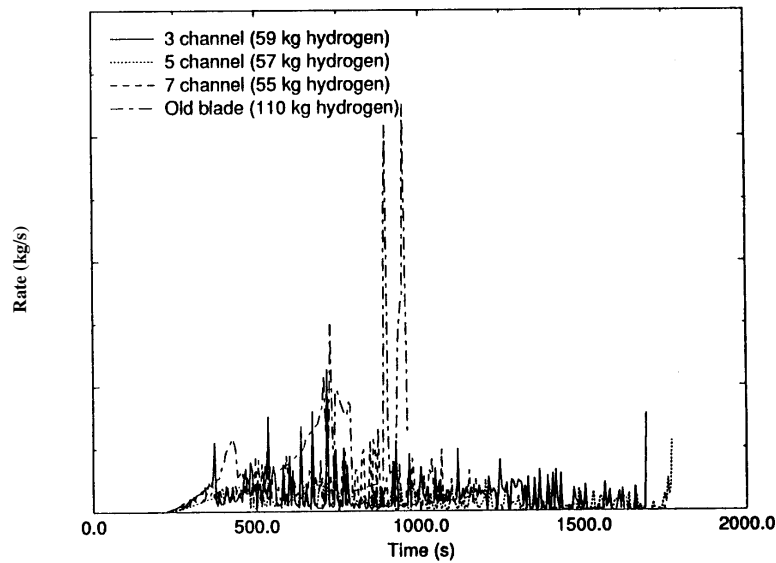


Figure 5-16. Predicted rate and integral hydrogen values for each 3, 5, and 7 radial representations of the Browns Ferry nuclear core.

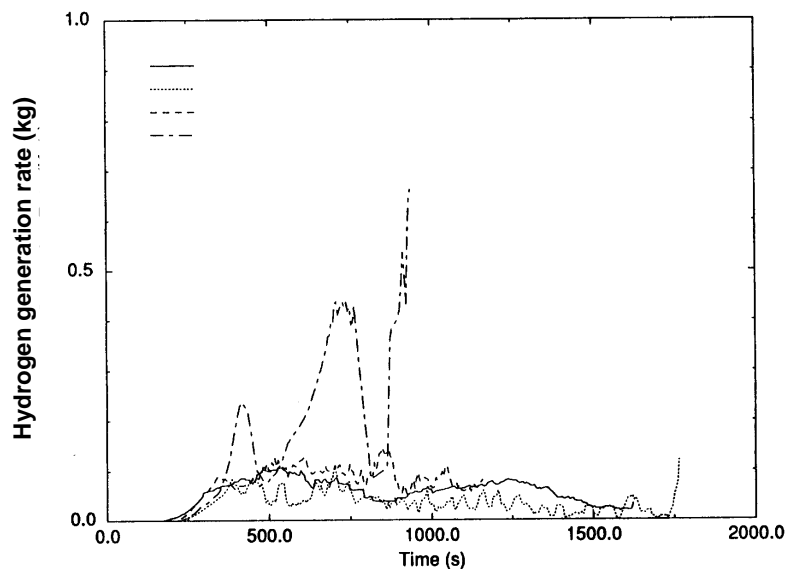


Figure 5-17. Predicted rate of hydrogen produced for the 3, 5, and 7 radial representations of the Browns Ferry nuclear core with smoothing using a running average.

5.1.5 Recommendations and Conclusions

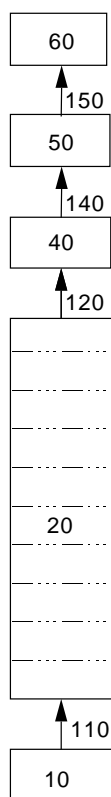
For full BWR plant calculations it is recommended that a minimum of eight to ten axial nodes be used to represent the core containing SCDAP components. For larger problems, selection of a number of volumes that can take advantage of the odd-even matrix solver could result in some reduction in the overall cpu time. For experimental facilities and small test problems, a 10-axial node representation, using the Gauss elimination matrix solver, will also work well. However, if a Gauss elimination matrix solver is used, the time needed to solve the matrix increases with the square of the number of nodes. Whereas, if a

odd-even matrix solver is used, the time needed to solve a matrix increases linearly with the number of nodes. Use of more than 10 axial nodes to represent the core may be counterproductive unless the hydrogen generation is of prime concern. It also is recommended that a minimum of seven radial flow channels be used for full BWR plant calculations. For early phase analysis, the ORNL control blade/channel box component model is also recommended.

5.2 PWR Nodalization

5.2.1 Axial Nodalization

5.2.1.1 Model Development. An input deck to study the effects of the number of axial nodes used to represent the core region of the Surry PWR was developed using a single flow channel containing a fuel assembly consisting of a 15 x 15 array of fuel rods and control rods (204 fuel rods and 21 control rods) identical to the Surry full plant study discussed in the next section. Figure 5-18 shows the nodalization used to represent this single channel model and Figure 5-19 shows the cross-section area of the bundle showing the location of the fuel and control rods in the modeled fuel assembly. Decay power was specified so that a heating rate of approximately 1 K/s was maintained up to the onset of rapid oxidation for a high pressure boil down.



M229-BDR-1293-013

Figure 5-18. Ten axial node RELAP5 nodalization used to study PWR nodalization effects.

5.2.1.2 Description of the Axial Nodalization Study. As for the BWR, the calculations using the base axial nodalization input deck with the transmittal for SCDAP/RELAP5/MOD3.1 and a ver-

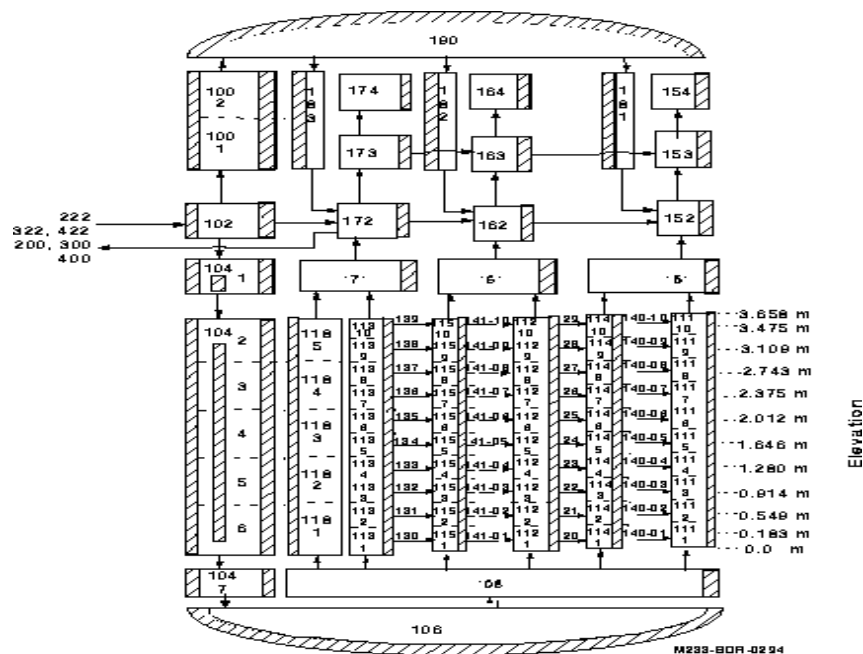


Figure 5-19. Single Surry fuel assembly used for the axial nodalization study.

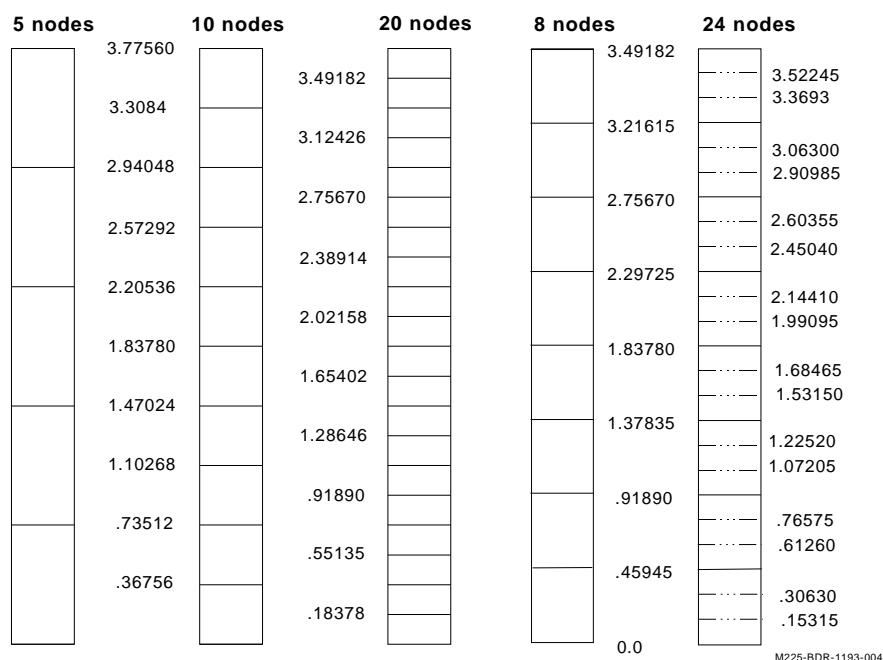
sion created to allow the use of more than 10 axial nodes to model the core region were performed. The results of these calculations were compared and it was confirmed that both executables gave identical results. Calculated values for all plot parameters were compared and determined to be identical.

Seven different axial nodalization schemes were used to determine the optimum axial nodalization needed to accurately represent the core of a pressurized water reactor. An input deck which used default values wherever possible and calculated an initial heating rate of approximately 1K/s when 10 axial nodes were used to model the core axially was considered to be the base deck for this study. A ZrO_2 failure temperature of 2,450 K was used for the PWR axial nodalization study, though one calculation using a ZrO_2 failure temperature of 2,600 K was performed using the base deck to determine the effects of the higher failure temperature on core degradation events. Figure 5-20 shows the axial nodalization schemes used in this study to determine the effect of a finer nodalization on PWR core behavior, and Table 5-2 summarizes the results of varying the number of axial nodes used to model the reactor core in this study. Figures 5-21 to 5-23 show a comparison of the peak bundle temperatures, hydrogen generation rates, and hydrogen production for each of these calculations.

In addition to looking at the effect of the number of axial nodes used to represent the core, the 10 node representation of the core was used to investigate the effect of the location of grid spacers in the nodalization scheme, the nearly implicit numerical scheme, letting the code set the time step size, ZrO_2 failure temperature, and using the nearly implicit at low temperatures and changing to the semi-implicit as temperatures near the onset of rapid oxidation. Table 5-3 is a summary of the studies using the 10 axial node representation of the core described above.

Table 5-2. PWR Axial Nodalization Studies.

Case	Number of nodes	Problem time (s)	CPU time (s)	ZrO ₂ failure temperature (K)	Results
1	5	1,607	3,300	2,450	Gradual rise in temperature core degradation at 1,607 seconds
2	8	751	2,200	2,450	Rapid oxidation at 500 seconds core degradation 751 seconds
3	10	751	2,425	2,450	Rapid oxidation at 500 seconds core degradation 751 seconds
4	20	746	4,150	2,450	Rapid oxidation at 500 seconds core degradation 746 seconds
5	24	745	4,898	2,450	Rapid oxidation at 500 seconds core degradation 745 seconds

**Figure 5-20.** Axial core divisions used to determine the effect of the number of axial divisions on PWR core behavior.

5.2.1.3 Results of the PWR Axial Nodalization Sensitivity Study. The 10 axial node input deck developed to study the effects of axial nodalization on bundle response in a pressurized water reactor (PWR) was also used to determine the optimum conditions for an accurate prediction of bundle damage progression using the least amount of CPU time. The first two cases summarized in Table 5-3 investigated the placement of the grid spacer in the input model. The base input deck had the grid spacers placed at the same elevations as in the Surry Nuclear Power Plant, near or at the upper boundary of an axial node in the model. In one test deck the grid spacers were placed at the lower boundary of the axial node, in the other near the middle of the axial node. Peak bundle temperature, hydrogen production, and damage

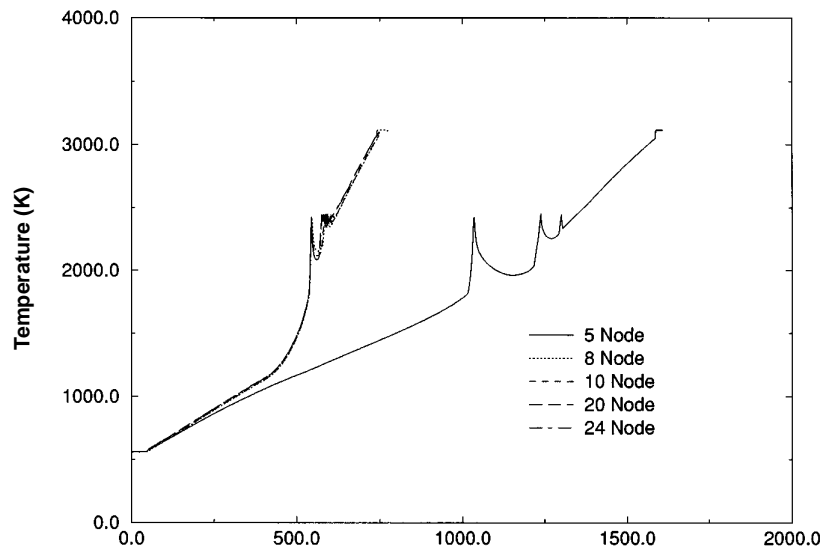


Figure 5-21. Predicted maximum bundle temperatures using 5 different axial divisions of the core.

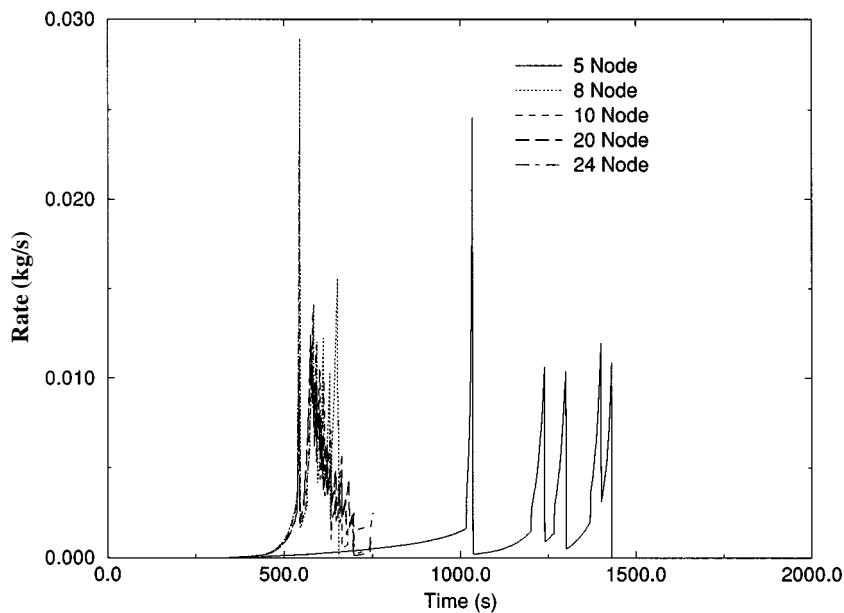


Figure 5-22. Predicted hydrogen generation rates using 5 different axial divisions of the core.

progression were compared from these three calculations. Placement of the grid spacers in the modeled core had little effect on the predicted peak bundle temperature and hydrogen generation rate as shown in Figures 5-24 and 5-25, but significant differences were observed, as shown in Figure 5-26, in channel blockage locations. Results from these studies indicate that, to obtain realistic damage progression predictions, the grid spacers should be placed at the lower boundary of an axial node in the model.

Case 3, summarized in Table 5-3, looked at the effect of increasing the ZrO_2 failure temperature to 2,600 K on predicted results. Temperatures during the early stages of the transient up to the cladding

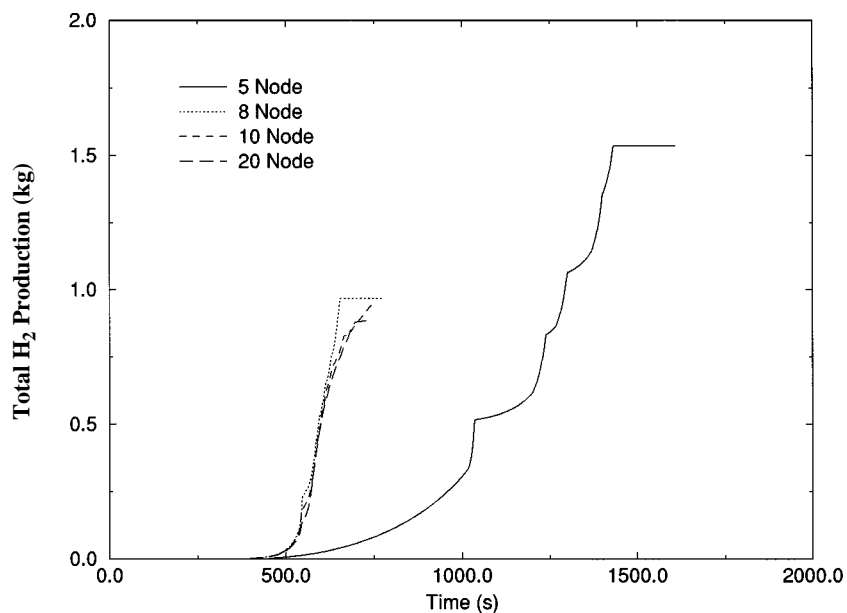


Figure 5-23. Predicted integral hydrogen production using 4 different axial divisions of the core.

Table 5-3. Summary of Sensitivity Studies using 10 Axial Nodes.

Case No.	Description of Case	Results
1	Grid spacers in input deck were input to be at the nodal boundary.	No changes in the calculated results were observed.
2	Grid spacers in input deck were situated in the middle of the axial node.	No changes in temperature response but some changes in damage progression.
3	ZrO ₂ failure temperature set at 2,600 K.	Once rapid oxidation begins, rapid rise in temperature to clad failure and molten pool formation. No damage progression events.
4	Running at the Courant limit.	No changes were observed in the calculated bundle response.
5	Running at a time step size considerably smaller than the courant limit.	No changes were observed in the calculated bundle response. Running time considerably slower.
6	Using the nearly implicit numerical scheme.	Rapid oxidation began slightly earlier slight differences in the rates and quantity of hydrogen produced. Runs 5 times faster than the semi-implicit.
7	Using the nearly implicit at low temperatures and the semi implicit at high temperatures.	No changes were observed in the calculated bundle response from that observed in the base case.

failure are identical. The major observed differences were in the predicted damage progression, peak bundle temperature, and hydrogen generation. When a ZrO₂ failure temperature of 2,600 K was specified,

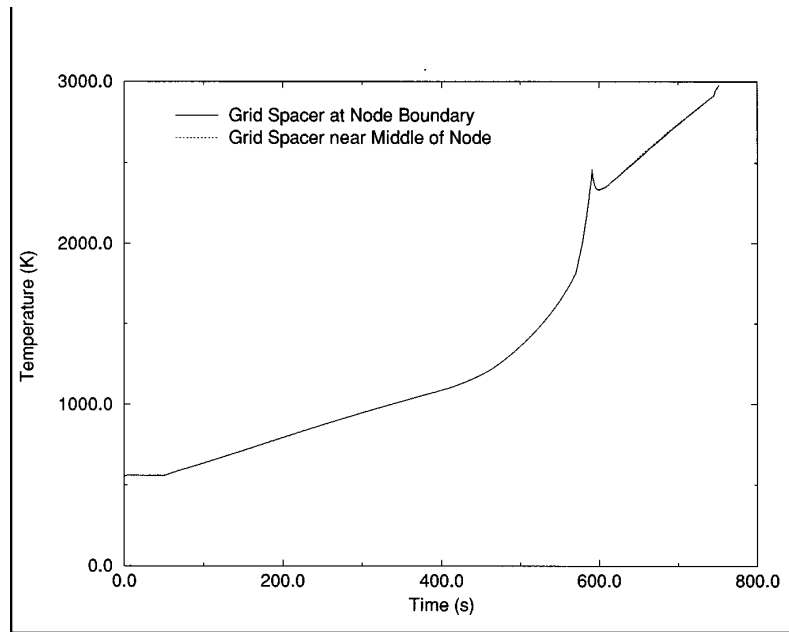


Figure 5-24. Predicted temperatures in the upper bundle.

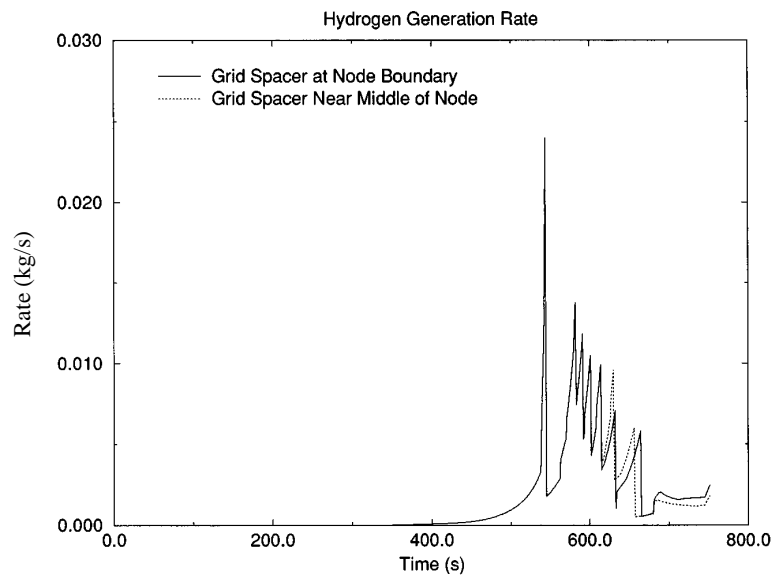


Figure 5-25. Predicted hydrogen generation rates.

oxidation, with continued hydrogen production, continued for a longer period until the specified failure temperature was attained, with no relocation of core materials predicted by the code. The thicker oxide layer formed on the zircaloy cladding, when the higher failure temperature was requested, prevented any clad material from relocating downward.

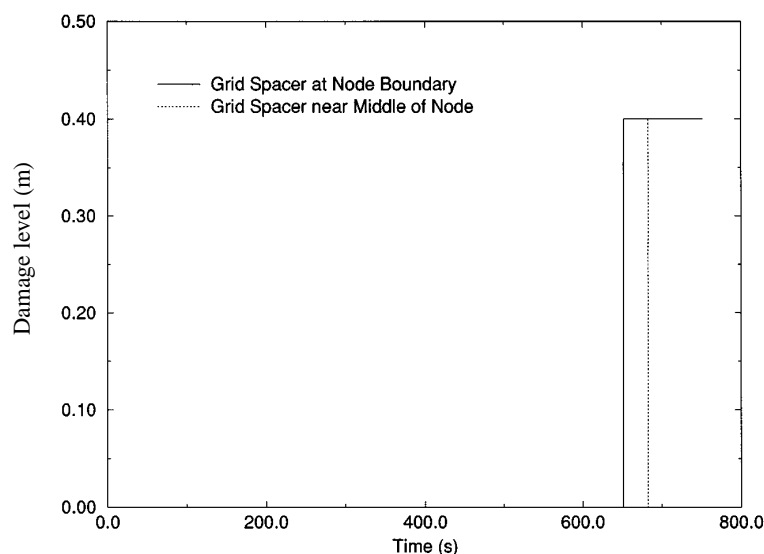


Figure 5-26. Predicted damage level.

Cases 4 and 5 looked at the effect of time step size on predicted results. In Case 4, the code was allowed to run at the Courant limit, whereas in Case 5 the code was forced to take time steps considerably smaller (approximately 10 times) than the Courant limit. Figures 5-27 and 5-28 show the results of this study. The predicted peak bundle temperatures for each calculation are identical (Figure 5-27) but the CPU time varies considerably (Figure 5-28). A further investigation, looking at the core damage progression, indicates that the predicted results for these two cases are identical. Mass error was considerably larger when the nearly implicit, time steps five times larger than the Courant limit, or a relatively small time step, 10 times less than the Courant limit, were used.

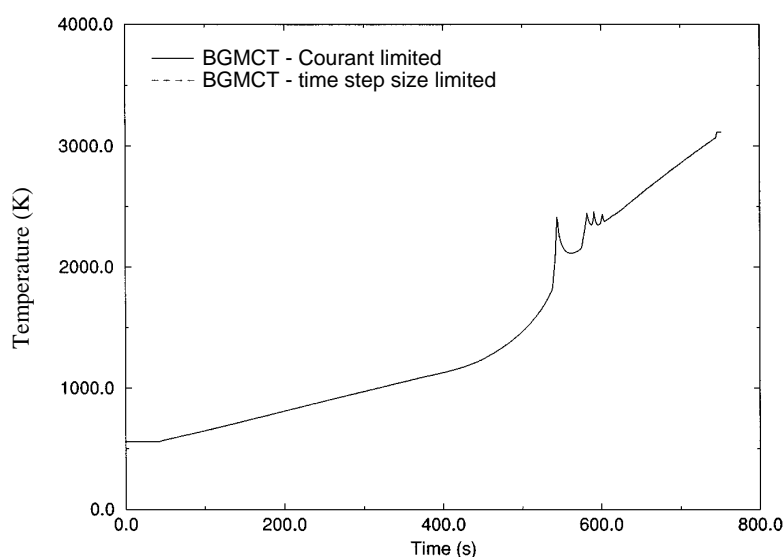


Figure 5-27. Maximum bundle temperatures comparing calculations using Courant limit and forced time step size.

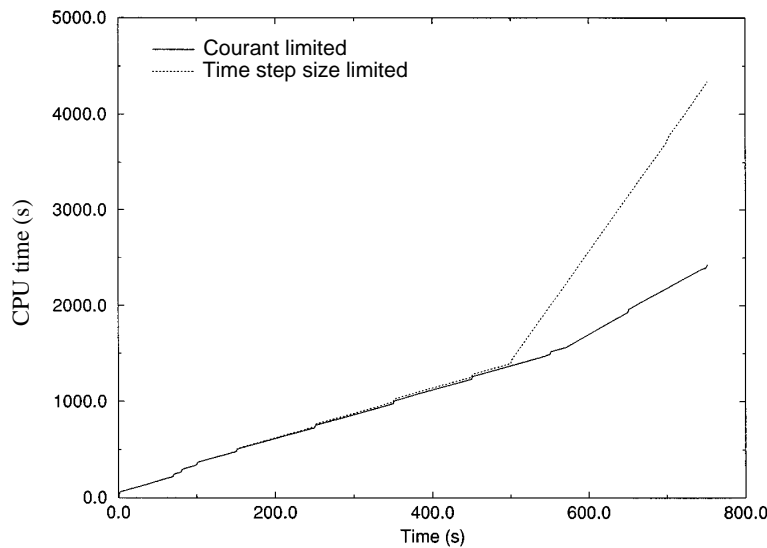


Figure 5-28. CPU time comparing calculations using Courant limit and forced time step size.

Cases 6 and 7 studied the effect of the numerical scheme used, semi-implicit as for the base case, nearly implicit, or nearly implicit at temperatures below 1,400 K and the semi-implicit at temperatures above 1,400 K, on the predicted results and computational speed. Use of the nearly implicit numerical scheme decreased significantly the CPU time needed for the calculation (Figure 5-29), though, as shown in Figure 5-30 predicted the onset of rapid oxidation to occur slightly earlier, approximately 15 seconds. All major damage progression trends and events are predicted to occur approximately 15 seconds early when the nearly implicit numerical scheme is used to calculate predicted behavior. The nearly implicit predicted a heatup rate identical to the semi-implicit when bundle temperatures were less than 1,400 K. Therefore, a calculation was performed using the nearly implicit when bundle temperatures were below 1,400 K and switching to the semi-implicit for the severe accident phase of the transient. Run time decreased dramatically from a full semi-implicit calculation when the nearly implicit numerical scheme was used for the low-temperature portion of the transient and the semi-implicit for the high-temperature portion. Identical results were obtained for both calculations as shown in Figure 5-21, which compares maximum bundle temperature. Other parameters were compared and found to be identical. An evaluation of the results from the cases summarized in Table 5-3 showed that the nearly implicit numerical scheme in SCDAP/RELAP5 could be used for preliminary calculations, where speed is the most important factor, to determine the optimum boundary conditions or for sensitivity studies of uncertainties on bundle response. It is recommended for an accident analysis that a final calculation, using one of the following options, be performed. The first option is the semi-implicit option for the accident transient. The second option is the nearly implicit option during the low-temperature phase of the accident and the semi-implicit option at temperatures above 1,400 K to obtain accurate results using a minimum of CPU time for the calculation.

The base case model which used 10 axial nodes to model the core shows relocation behavior similar to what has been observed during simulated severe accidents in the CORA or PBF experimental facilities. The first core degradation event calculated to occur by the code is the ballooning and rupture of fuel rod cladding followed in succession by the melting and relocation of grid spacer material to a lower elevation in the core, rapid oxidation, the slumping and relocation of oxidized zircaloy fuel rod cladding to a lower elevation, and finally the formation of a molten pool and a cohesive debris region in the hot zone of the

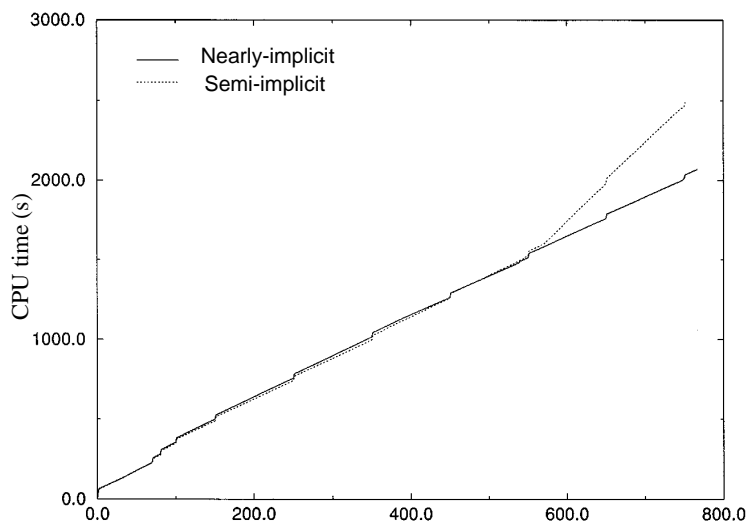


Figure 5-29. Comparison of CPU time using the nearly and semi-implicit numerical schemes.

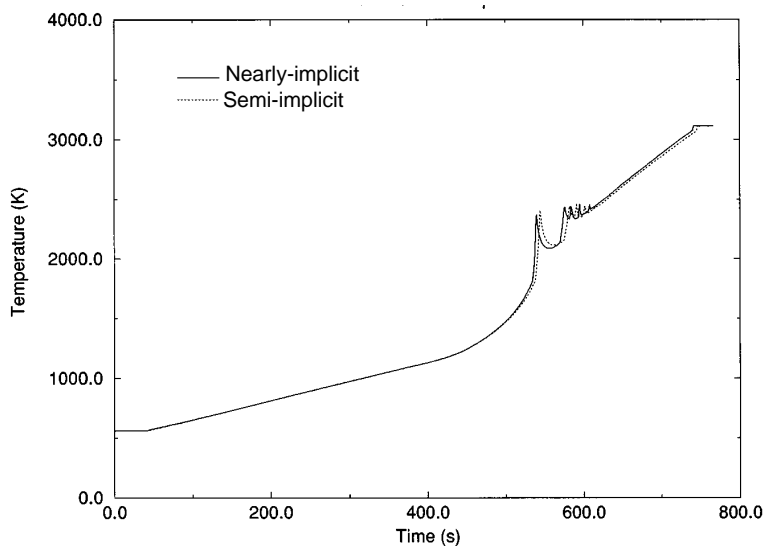


Figure 5-30. Comparison of maximum bundle temperatures using the nearly and semi-implicit numerical schemes.

reactor core. Maximum bundle temperature, component temperatures, CPU time, hydrogen production, and core degradation events were examined for each nodalization scheme and compared to determine the effect of axial detail in modeling the core on predicted behavior. The only changes made to the base case input deck for this study were the number of nodes used to model the nuclear core, nodal heights, and the needed changes to the RELAP5 nuclear core volume to reflect the changes in the number of nodes and nodal volume size.

The five-node case displays an extremely slow and constant heating rate, with the initial oxidation excursion occurring 1,050 seconds into the transient at an initiating temperature that appears to be

significantly higher than those observed in severe core damage experiments or predicted by the code for all other axial nodalization schemes in Figure 5-21, which shows the maximum bundle temperatures for each axial nodalization scheme in this study. For the five-node case, the first core degradation event predicted is the ballooning and rupture of the fuel rod cladding, followed by slumping of the zircaloy cladding, grid spacer relocation, cohesive debris formation, and the formation of a molten pool with total node blockage. Degradation events occurring in the nuclear core are triggered by temperature and occur in each node as an appropriate temperature for that event is reached. Nodal heating rates in the five-node case appear to be considerably slower due to the larger nodal volume over which temperatures, flow rates, and behavioral phenomena are averaged. Therefore, the onset of each degradation event occurs later in time though at a similar temperature.

As shown in Figure 5-21 initial heating rates, the onset of rapid oxidation, and peak bundle temperatures for the 8, 10, 20, and 24 node cases converge. Differences between the predicted heating rates, onset of rapid oxidation and peak bundle temperature for these four cases are extremely small, though the CPU time needed appears to linearly increase with the number of nodes. Examination of the core degradation events predicted to occur and the predicted bundle end state indicate that nearly identical results are obtained for each nodalization scheme. All cases predict the melting and relocation to commence near the top of core and progress downward from the upper axial node melting and relocating over a period of several hundred seconds. Damage progression is calculated to occur until a molten pool with complete blockage of the flow channel is formed at 750 seconds, for each case. Predicted core degradation events for the 8, 10, 20, and 24 axial node cases are nearly identical, though slight differences, a few seconds, in timing is observed between the four cases. In each case as bundle temperatures near 1,000 K cladding balloons and ruptures. Coincident with clad failure a slight decrease in temperature is observed, followed by a gradual rise in heating rate until the onset of rapid oxidation. In PWR experiments, as in the test case, the initial hot spots are in the upper bundle. Cladding begins slumping and relocating from the upper bundle downward. As relocating clad comes in contact with a cooler region near a grid spacer, it slows, begins solidifying and interacting with the grid material results in the failure and relocation of the grid to a lower elevation. During the relocation process a metallic crust forms first and then slumps away at grid spacer locations. Molten material flows downward forming a blocked region in the lower bundle. Temperatures remain hotter and rise faster in the upper bundle. Core damage continues until a molten pool forms near the top. At the end of the simulated accident a debris region, cohesive and rubble has formed near the molten pool. Damage behavior is consistent with what would be expected during a severe accident. The study of changes in the number of axial nodes used to model the nuclear core of a reactor, using a simplified deck representing a typical PWR fuel assembly under severe accident conditions, indicates that once an optimum nodal size has been determined, axial detail has little effect on final predicted results. The least number of nodes giving accurate results appears to be the most efficient.

5.2.2 Nodalization Sensitivity Study of Surry PWR during TMLB' Accident

5.2.2.1 Introduction. This section presents the results of a study of the sensitivity of nodalization of the reactor core on the behavior calculated for the Surry PWR during a TMLB' severe accident. A description is first given of the Surry PWR. Next, two different nodalizations of the reactor core are described. Then, the calculated results for the two nodalizations are described and compared. Finally, guidelines for nodalization of the reactor core are recommended.

5.2.2.2 Plant Description and Nodalization . The Surry nuclear power plant is a Westing-

house-designed pressurized water reactor (PWR) with a rated thermal power of 2,441 MW. The core consists of 157 15 x 15 fuel assemblies with an active fuel height of 3.66 m. Each of the three primary coolant loops contains a U-tube steam generator and a reactor coolant pump. The pressurizer is attached to the hot leg piping of one of the three primary coolant loops. Two power-operated relief valves (PORVs) are located at the top of the pressurizer. The two PORVs have a combined relief capacity of 45.1 kg/s. An accumulator is attached to each of the three cold legs in the primary coolant loop. Each accumulator contains 29,000 kg of borated water pressurized to 4.24 MPa by a nitrogen cover gas.

The coolant loop with the pressurizer connected to its hot leg was nodalized as shown in Figure 5-31. The hot leg is represented by five control volumes, the cold leg by four control volumes, the surge line by three control volumes, and the pressurizer by eight control volumes. The primary side of the steam generator is represented by eight control volumes and the secondary side by twenty control volumes. The loop seal is represented by five coolant volumes. The three coolant loops are represented by a total of 140 control volumes.

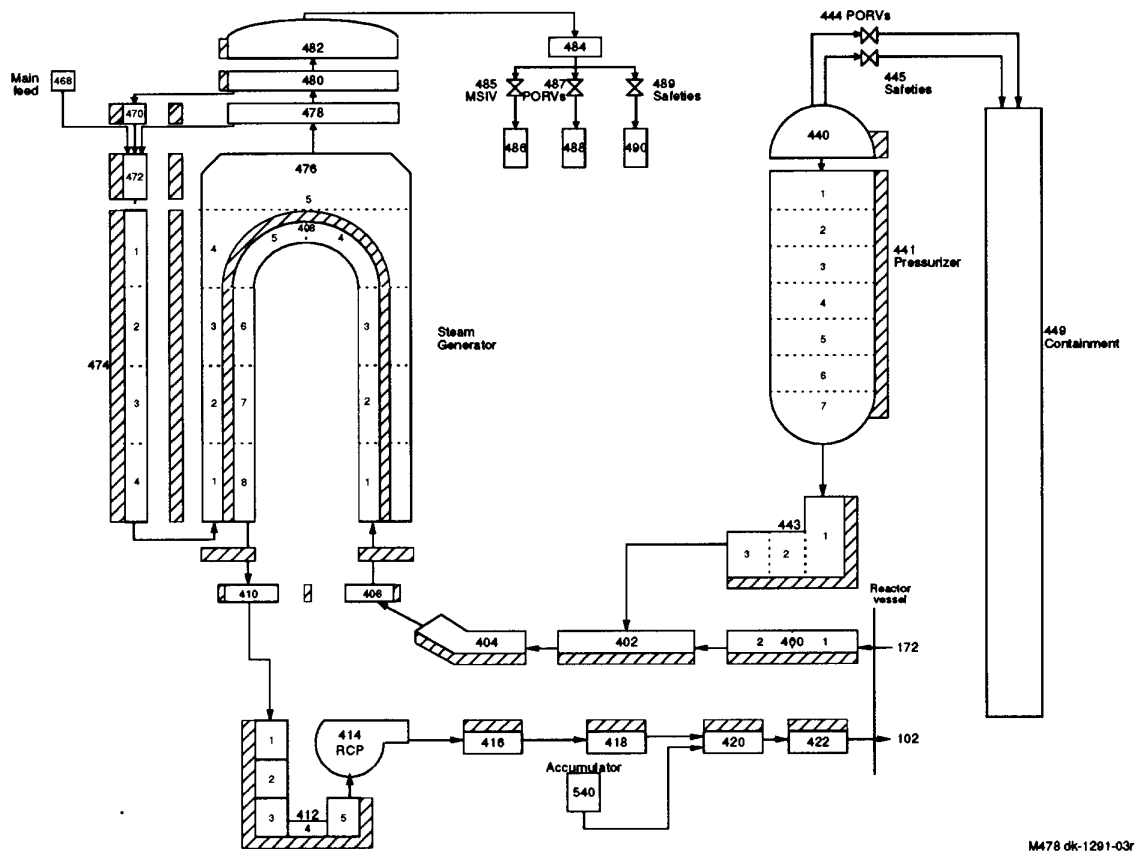


Figure 5-31. Nodalization of primary system loop.

Two nodalizations of the reactor core were performed. The first nodalization divided the reactor core into five radial segments and ten axial nodes. The second nodalization divided the reactor core into five radial segments and twenty axial nodes. The first nodalization is designated as the 5x10 case and the

second as the 5x20 case. An axial cross section of the nodalization of the reactor core is shown in Figure 5-32 and the nodalization of the reactor vessel with the core is shown in Figure 5-33. The fluid conditions in the core region are represented by RELAP5 control volumes 111, 114, 112, 115, and 113, respectively. Each of these control volumes has ten axial segments for the 5x10 case and twenty axial segments for the 5x20 case. The reactor core was also divided into ten axial segments for the 5x10 case and twenty axial segments for the 5x20 case. The five control volumes representing the fluid in the region of the reactor core are connected with each other by cross flow junctions at each axial segment; thus flow in the lateral direction through the core is modeled. The core bypass is represented by control volume number 118 with five subvolumes. The downcomer is represented by control volume number 104 with seven subvolumes. The lower plenum is represented by control volume numbers 106 and 108. A total of seventeen control volumes represent the upper plenum of the reactor vessel.

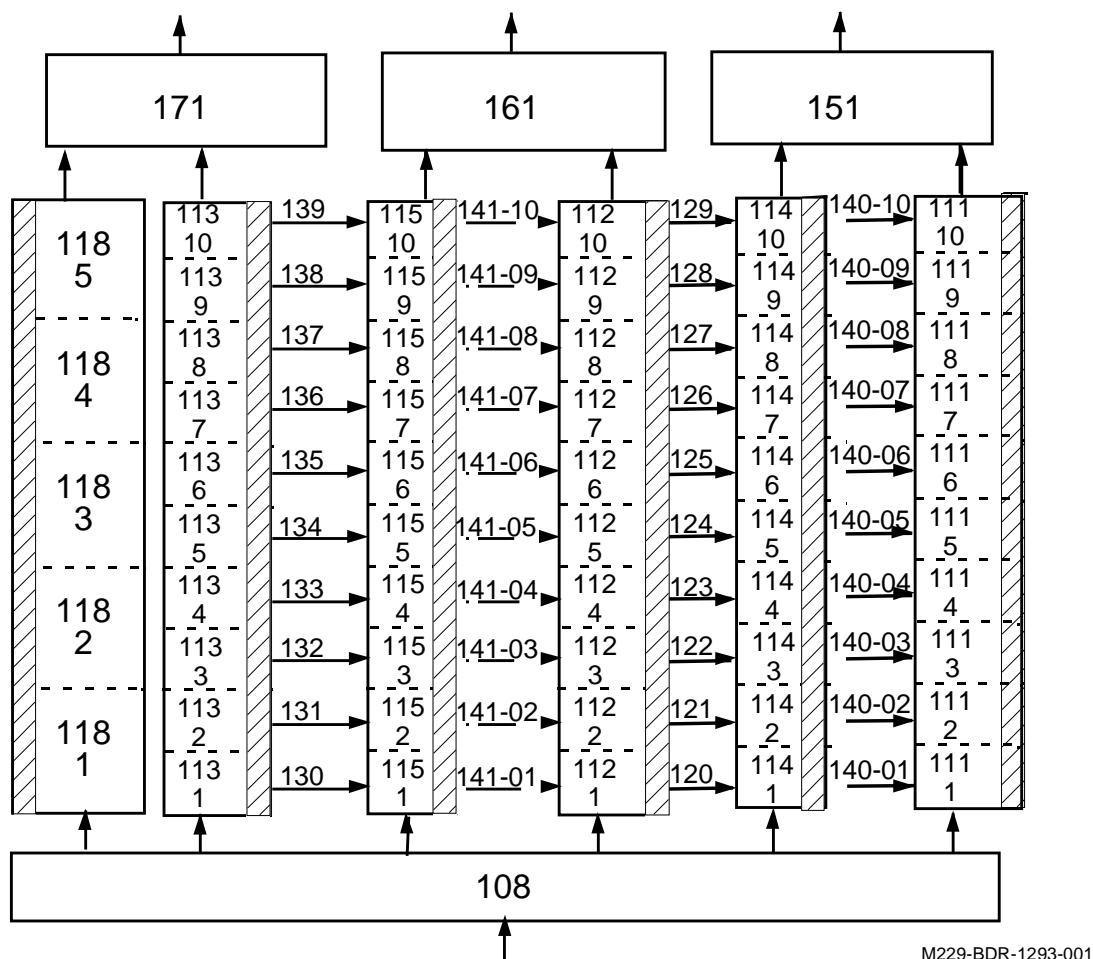


Figure 5-32. Axial cross section of reactor core showing nodalization of core for 5x10 case.

A radial cross section of the nodalization of the reactor core is shown in Figure 5-34. The first radial segment represents the five fuel assemblies at the center of the core. The second radial segment begins at the outer boundary of the first radial segment and extends to the inner boundary of the third segment. It represents twenty fuel assemblies. The third and fourth radial segments represent fuel assemblies radially outward from the second radial segment and the fifth radial segment represents the fuel assemblies at the periphery of the core. The third, fourth, and fifth fuel assemblies represent thirty-six, sixty, and thirty-six fuel assemblies, respectively. The fluid conditions in the first radial segment are represented by RELAP5

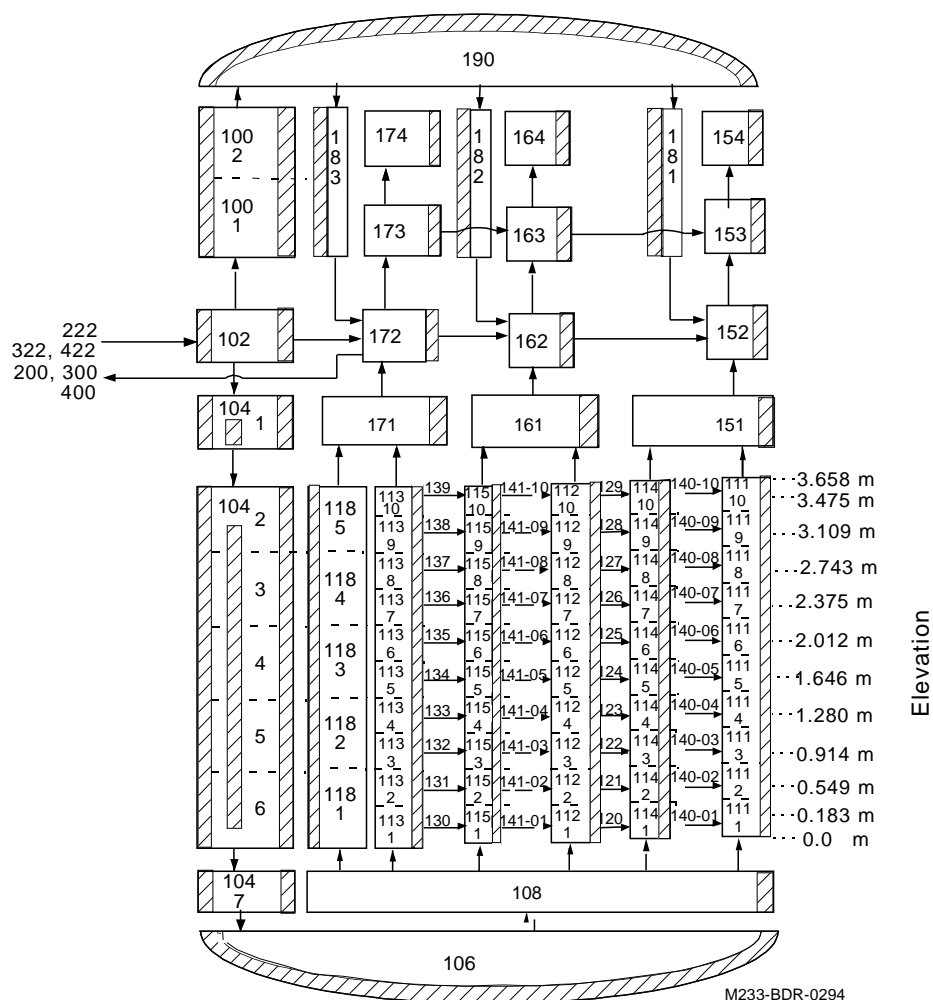


Figure 5-33. Axial cross section of reactor core and vessel for 5x10 case.

control volume number 111. The fluid conditions in the second, third, fourth, and fifth radial segments are represented by the RELAP5 control volumes 114, 112, 115, and 113, respectively. Each radial segment is defined to be a channel. For example, the first radial segment is defined to be Channel 1.

A nodalization sensitivity study for the case of where surge line failure was ignored showed that a five channel nodalization of the core calculates a somewhat different rate of heatup of the reactor core than a three channel nodalization. This study is described in Appendix B. In this study, ceramic melting was calculated to occur significantly earlier for the three channel nodalization than for the five channel nodalization. For analyses in which surge line rupture is not modeled, the calculated difference in rate of heatup of the core is not significant. But for analyses in which surge line rupture is modeled, the timing of the core heatup is more important and thus a five channel model of the core is considered better than a three channel model.

The variation in rod power in the radial direction for the five channel cases is shown in Table 5-5. The power is almost uniform within the two inner most channels and within the next two flow channels

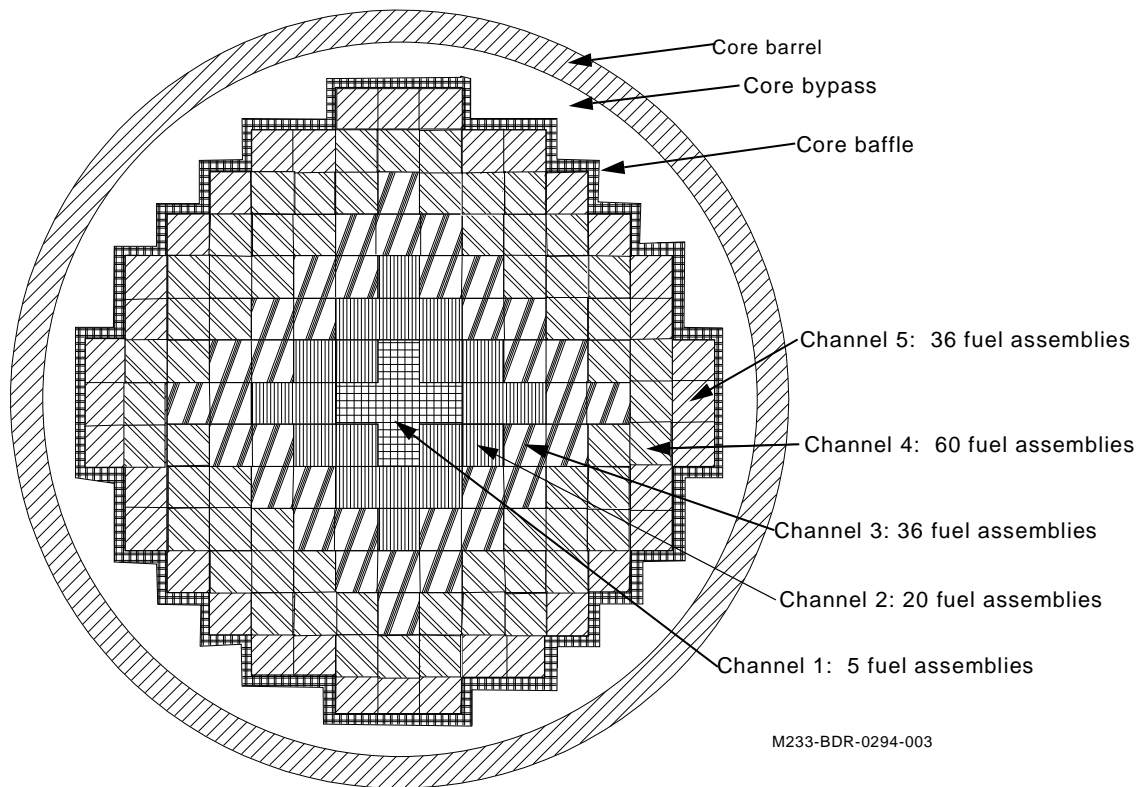


Figure 5-34. Radial cross section of reactor vessel showing nodalization of core.

outside of the two inner most channels. The power in the outer flow channel is significantly less than that in the other flow channels. The power is maximum in the center channel, which has a linear power that is 1.169 times the average core linear power. The average linear power of fuel rods in the center channel is 24.35 kW/m. The variation in power in the axial direction is the same for all of the flow channels.

Table 5-4. Radial power distribution

Channel No.	Average fuel rod power at start of transient (kW/m)	Ratio of power to average core power
1	24.35	1.169
2	24.32	1.167
3	21.85	1.048
4	21.84	1.048
5	15.81	0.759

The fuel rods in each fuel assembly were represented by a SCDAP fuel rod component and the control rods were represented by a SCDAP PWR control rod component. Each fuel assembly was represented as having 204 fuel rods and 21 control rods. Each fuel rod and control rod was divided into ten axial nodes for the 5x10 case and twenty axial nodes for the 5x20 case. The fuel rods and control rods were located in the fuel assembly as shown in Figure 5-35. The water rods were represented by control rods. The fuel rods have a fuel pellet stack that is 3.6576 m in length. The fuel pellets are 4.634 mm in radius. The cladding has an outer radius of 5.359 mm and a thickness of 0.617 mm. The reactor core was represented by a total of ten SCDAP components, namely a fuel rod and control rod component for each of the five channels. Each fuel bundle has six Inconel spacer grids, at elevations above the bottom of the reactor core of 0.0 m, 0.73 m, 1.46 m, 1.83 m, 2.19 m, and 2.93m, respectively. These spacer grids were represented by the SCDAP spacer grid model.

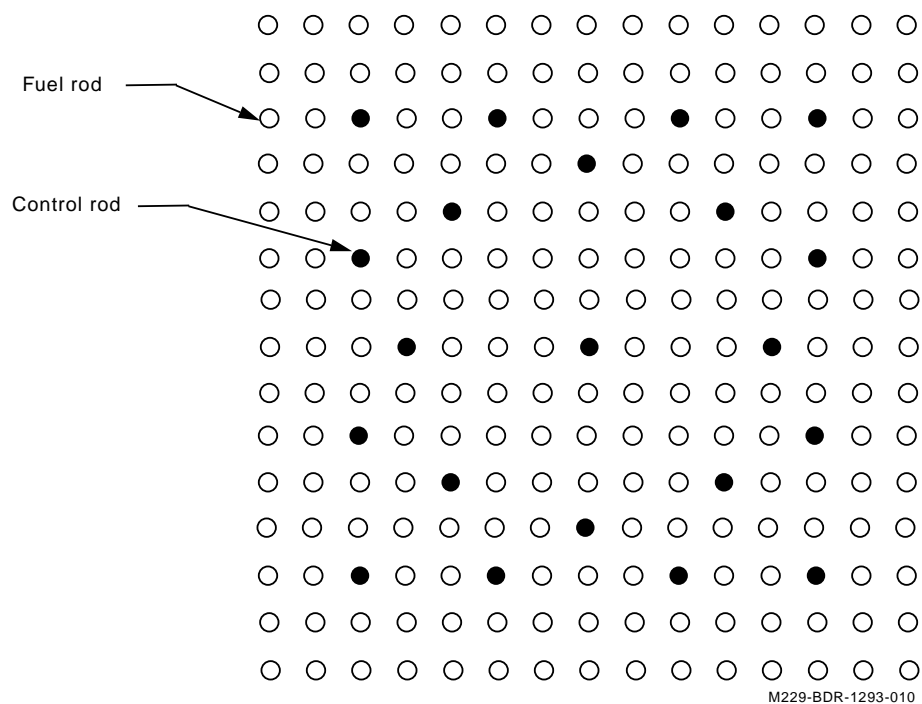


Figure 5-35. Layout of fuel rods and control rods in fuel assembly.

The lower head of the reactor vessel was represented by the COUPLE debris model. This representation was performed in order to calculate the heatup of the lower head in response to slumping molten material from the core region and in order to calculate the time of rupture of the lower head. The lower head was represented with a 3x16 mesh. Nodes were located at the inner and outer surfaces and the midplane of the lower head. Thus the lower head is divided into three nodes through its wall and is divided into sixteen single nodes in the meridional direction.

5.2.2.3 Boundary Conditions and Modeling Options. The severe accident analyzed was a station blackout without operator actions. This accident is designated as a TMLB' sequence. The accident is initiated by loss of offsite power. Onsite ac power is also unavailable because the diesel generators fail to

start or fail to supply power. Decay heat removal through the steam generators cannot be maintained in the long term because there is no ac power for the electrical pumps, and the steam driven auxiliary feedwater pumps also fail to supply water.

The severe accident evolves as follows. The loss of offsite power causes reactor scram to occur. Next, the pressure on the secondary side of the steam generators exceeds the set point pressure, resulting in opening of the relief valves. The inventory of water on the secondary sides of the steam generator then gradually boils away. After water on the secondary side of the steam generators is depleted, then boiling begins to occur in the reactor core. After a period of time, the pressure in the primary coolant loop exceeds the set point pressure and the PORVs open to relieve the pressure. The inventory of coolant in the reactor core is then gradually depleted over a period of time. Damage to the reactor core begins after the inventory of reactor vessel water has depleted to the point that the reactor core is uncovered. The flow of hot steam through the PORV eventually results in heatup and creep rupture of the surge line. This rupture is assumed to cause a 0.146 m (5.7 inches) diameter hole in the surge line. This hole causes the primary system to rapidly depressurize, with the result that accumulator injection occurs. Decay heat eventually boils off all of the water from the accumulator injection and the reactor core heats up to the point of molten pool formation. The progression of damage is calculated to the point of slumping of molten reactor core material to the lower head of the reactor vessel and then rupture of the lower head. This scenario without rupture of the surge line was analyzed in an assessment of the potential for high pressure melt ejection in the event of a station blackout.²⁵

The boundary conditions applied to the reactor system and the behavior of the reactor system were simplified in three areas and damage progression parameters were defined in four areas. First, the Reactor Coolant Pumps seals were assumed to remain intact and thus prevent leakage of water. Second, the rupture of the surge line was assumed to result in a hole with an area that was 33% of the flow area of the surge line. Third, countercurrent natural circulation in the hot legs and surge line was assumed to not occur. Fourth, the modeling option was selected that results in a molten pool slumping to the lower head as soon as it had spread to the periphery of the core. Fifth, the modeling option was selected that results in a stream of slumping molten material staying intact instead of breaking up. Sixth, the temperature at which embrittled fuel rods fragment during quenching was defined to be 100 K hotter than the saturation temperature of water. Seventh, the gap heat transfer coefficient at the interface between debris and the lower head was defined to be 10,000 W/m²K, which is the upper bound value.

5.2.2.4 Summary of Calculated Behavior. The behavior of the Surry reactor was calculated from initiation of the accident through rupture of the lower head. The sequence of major events in the reactor is shown in Table 5-5. For the 5x10 case, core uncover was calculated to begin 9,180 seconds after the loss of offsite power and the beginning of the accident. All values of time refer to time since the beginning of the accident. The core uncover time for the 5x20 case was 9,220 seconds. The fuel rods were calculated to begin to rupture at times of 11,880 seconds and 11,680 seconds for the 5x10 and 5x20 cases, respectively. This event is the beginning of core damage. The rupture of the fuel rods was calculated to begin in Channel 1, occur next in Channel 2, then in Channel 4, and next in Channel 3. The fuel rods ruptured at an elevation near the midplane of the reactor core and at a temperature near 1250 K. Since the fuel rods were partially oxidized, the maximum cladding hoop strains were less than 2%. Double-sided oxidation of the cladding was calculated to not occur due to the small value of the rupture strain. The fuel rods in Channel 5 failed due to eutectic reaction with spacer grids rather than by ballooning and rupture. A rapid increase in temperature due to oxidation begins at 12,000 seconds. The spacer grids were calculated to

begin to slump due to liquefaction at a time of 12,130 seconds for the 5x10 case and 12,040 seconds for the 5x20 case. The fuel rod cladding is calculated to begin to melt at 12,450 seconds for the 5x10 case and 12,360 seconds for the 5x20 case. The surge line is calculated to rupture at 13,040 seconds for the 5x10 case and at 13,160 seconds for the 5x20 case. A hole in the surge line with an area equal to 33% of the cross-sectional area of the surge line is assumed to result from rupture of the surge line. The surge line has a diameter of 0.2641 m (10.4 inches). The melting of the first 20,000 kg of UO_2 , which is approximately the mass of core material that slumped to the lower head of the TMI-2 reactor during its accident, occurred at times of 18,050 seconds and 18,420 seconds for the 5x10 and 5x20 cases, respectively. The molten pool is calculated to have spread across the entire reactor core at 19,450 seconds for the 5x10 case and at 20,890 seconds for the 5x20 case. Since the modeling option was selected that assumed a structurally unstable supporting crust exists when the pool has spread to the periphery of the core, the molten pool was calculated to slump to the lower head at the time that it reached the core periphery. When slumping occurred, all the melt material in the molten pool was assumed to slump. This is equivalent to assuming the melt causes erosion of the initial crust failure point to a sufficient depth to allow all molten material to slump. The slumping of the molten pool resulted in a transfer of more than half of the reactor core from the core region to the lower head of the reactor vessel for both the 5x10 and 5x20 cases. A total of 53,500 kg of UO_2 (65% of total mass of UO_2 in core) and 12,900 kg of ZrO_2 was calculated to slump to the lower head for the 5x10 case. A total of 53,200 kg of UO_2 and 12,900 kg of ZrO_2 was calculated to slump to the lower head for the 5x20 case. The slumping of the molten pool resulted in formation of a debris bed in the lower head with a depth of 1.33 m for the 5x10 case and 1.26 m for the 5x20 case. The depth of the debris bed is somewhat less for the 5x20 case because it calculated a less amount of material to slump to the lower head before the time of molten pool slumping. The lower head is calculated to fail due to creep rupture at 21,770 seconds for the 5x10 case and at 23,140 seconds for the 5x20 case. The oxidation of the reactor core was calculated to produce a total of 377 kg of hydrogen for the 5x10 case and 320 kg of hydrogen for the 5x20 case. For both cases, the cladding in the upper 60% of the reactor core was calculated to completely oxidize in place. The computer CPU time for the 5x20 case was a factor of 1.7 greater than that for the 5x10 case.

Table 5-5. Comparison of timing of damage progression for 5x10 and 5x20 cases.

Event or threshold in damage progression	5x10	5x20
	time (s)	time (s)
beginning of core uncover	9,180	9,220
beginning of rupture of fuel rods	11,890	11,680
beginning of slumping of spacer grids	12,130	12,040
beginning of melting of fuel rod cladding (temperature greater than 2,200 K)	12,450	12,360
rupture of surge line	13,040	13,160
beginning of accumulator injection	13,140	13,270
beginning of second core heatup	13,660	13,560

Table 5-5. Comparison of timing of damage progression for 5x10 and 5x20 cases. (Continued)

Event or threshold in damage progression	5x10	5x20
	time (s)	time (s)
beginning of ceramic melting (beginning of molten pool)	17,650	17,922
ceramic melting of 20,000 kg of UO ₂	18,050	18,420
ceramic melting spread to periphery of core	19,450	20,890
massive slumping of molten pool to lower head	19,450	20,890
rupture of lower head	21,770	23,140

The calculated transient behavior of the reactor is next described. First, the reactor power history is shown. Second, the transient inventory of water in the reactor vessel is described. Third, the transient pressure of the primary coolant system is presented. Fourth, the history of the maximum temperature in the reactor core is shown. Fifth, the cumulative hydrogen production is described. Last, the transient heatup of the lower head is shown.

The transient reactor power was calculated by the reactor kinetics model in SCDAP/RELAP5. The calculated reactor power for the first 100 seconds of the accident is shown in Figure 5-36 and the calculated power for the first 10,000 seconds is shown in Figure 5-37. Within 10 seconds of reactor scram the power has decreased to a few percent of the steady state power of 2,441 MW. At 10,000 seconds after the start of the transient, the reactor power is 1% of the steady state power. The transient reactor power is identical for the 5x10 and 5x20 cases.

The inventory of water in the reactor vessel is indicated by the collapsed liquid level in the reactor vessel. The histories of the collapsed liquid level for the 5x10 and 5x20 cases are shown in Figure 5-38. The elevations of the top and bottom of the fuel rods relative to the bottom of the reactor vessel are 6.7 m and 3.0 m, respectively. The collapsed liquid level histories are almost identical for the 5x10 and 5x20 cases. The calculated times for beginning of core uncover for the 5x10 and 5x20 cases are 9,180 seconds and 9,220 seconds, respectively. The rupture of the surge line causes a sharp decrease in the liquid level and accumulator injection causes a sharp increase in liquid level. The collapsed liquid level is calculated to rise to the top of the fuel rods for the 5x10 case and to within 1.4 m of the top of the rods for the 5x20 case. After accumulator injection, both the 5x10 and 5x20 cases calculate a similar rate of boiloff of the accumulator water that reflooded the core.

The calculated pressure history in the cold leg of the primary coolant system is shown in Figure 5-39 for the 5x10 and 5x20 cases. The pressure decreases following reactor scram due to the steam generators removing more energy than that produced in the reactor core by decay heat. The steam generators are calculated to dryout at 3,580 seconds for both the 5x10 and 5x20 cases. The oscillations in pressure before the dryout of the steam generators are due to the action of steam generator secondary relief valves. The oscillations following the dryout of the steam generators are due to the action of the PORV, which causes the pressure to cycle between the opening and closing set points of the PORV. The rupture of the surge line causes the system pressure to decrease from 15.9 MPa to 1 MPa in 530 seconds. Accumulator injection

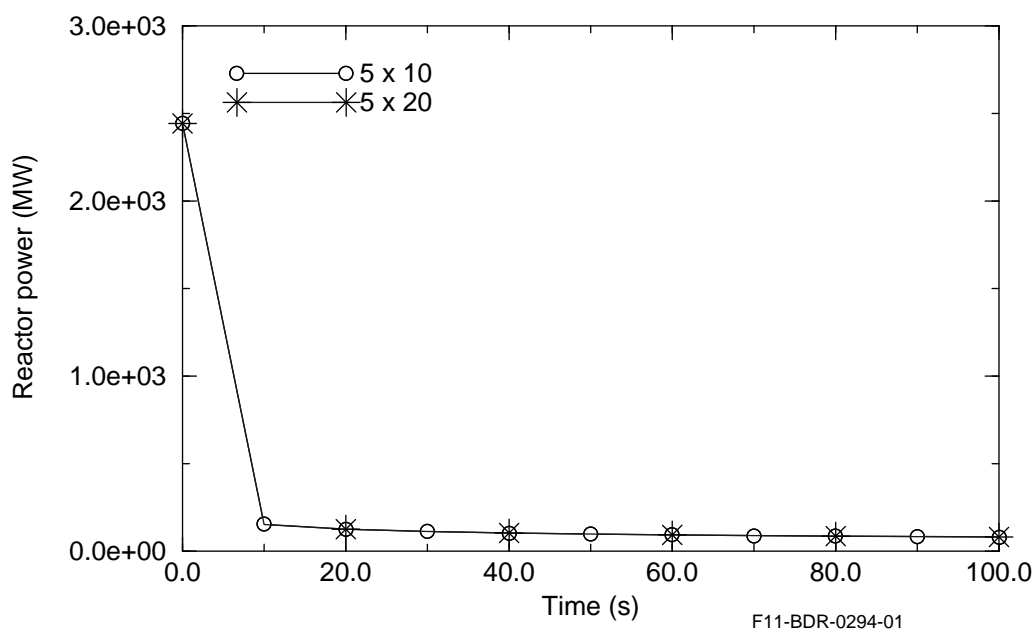


Figure 5-36. Reactor power history from 0.0 to 100 seconds.

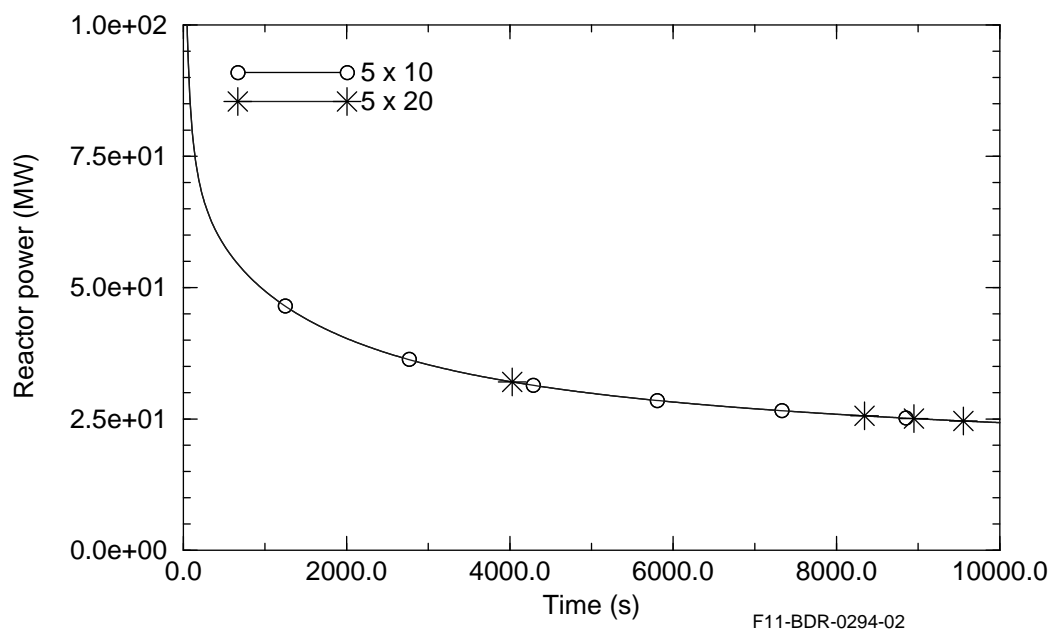


Figure 5-37. Reactor power history from 0.0 to 10,000 seconds.

causes the system pressure to increase to a maximum value 2 MPa. At 15,000 seconds the system pressure has decreased to 0.13 MPa. The slumping of a large pool of molten core material to the lower head caused

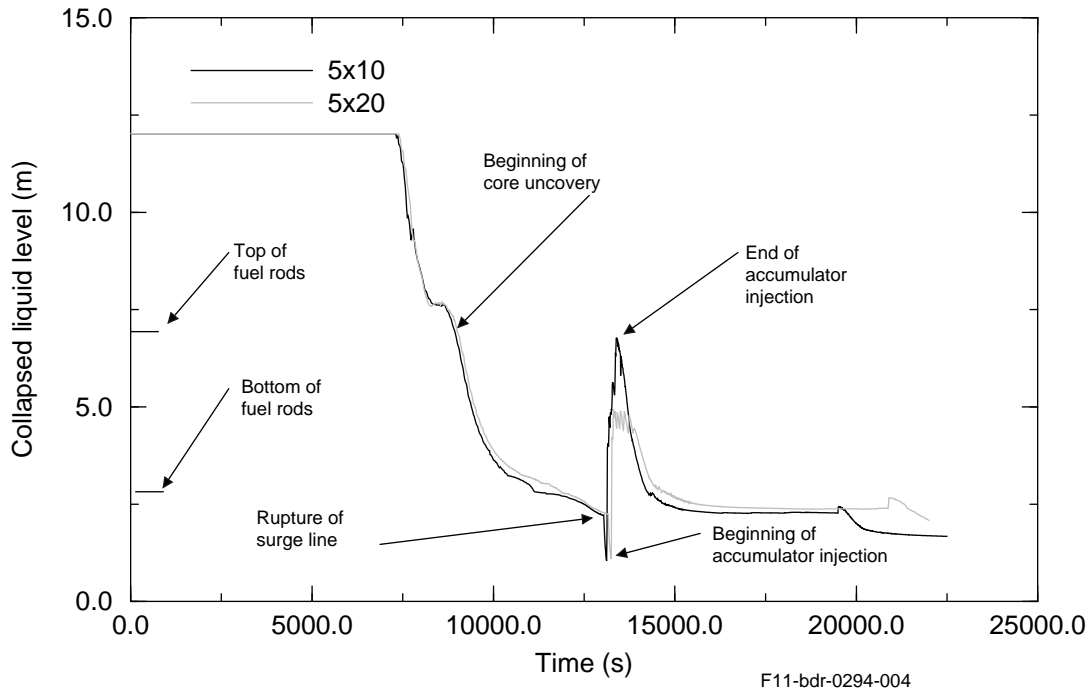


Figure 5-38. Collapsed liquid level in reactor vessel.

the system pressure to increase from 0.13 MPa to a maximum value of 0.4 MPa. The calculated pressure histories for the 5x10 and 5x20 cases are similar.

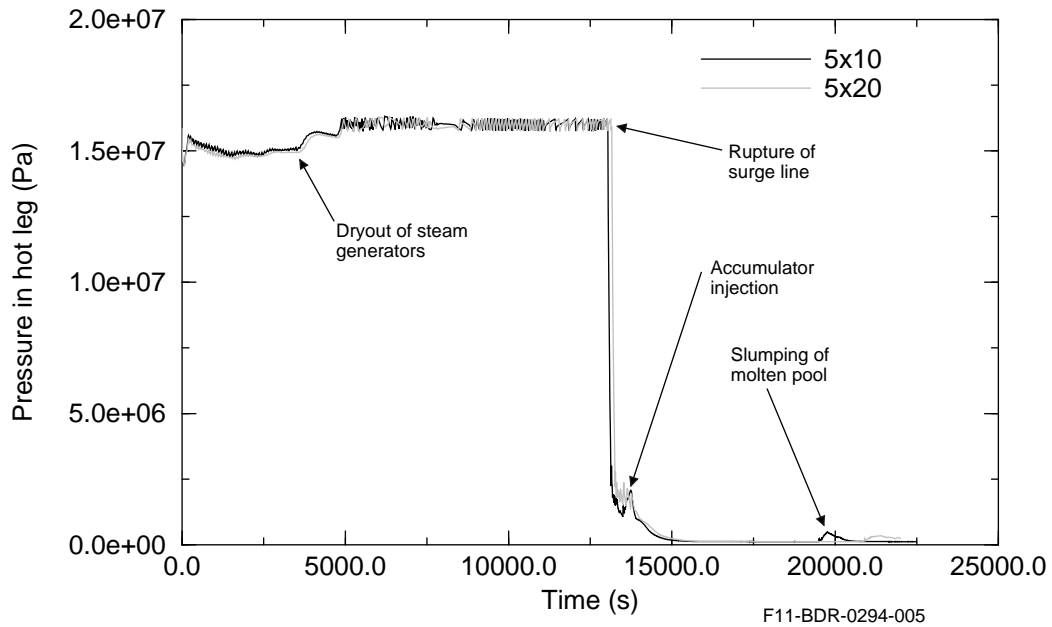


Figure 5-39. Pressure history of primary coolant system.

The calculated maximum core temperature histories are the similar for the 5x10 and 5x20 cases. The calculated maximum core temperature histories for the two cases are shown in Figure 5-40. The reactor core begins to heatup following the beginning of core uncovering at 9,200 seconds. The heatup becomes much more rapid beginning at 12,000 seconds due to oxidation of the reactor core. The maximum core temperature during the temperature excursion driven by cladding oxidation is 2,600 K for the 5x10 case and 2,680 K for the 5x20 case. These maximum temperatures are less than the temperature at which ceramic melting and molten pool formation occurs, which is 2,830 K. The reflood of the reactor core following accumulator injection caused the reactor core to quench. The accumulator injection was triggered by rupture of the surge line. The accumulator injection cooled the reactor core to 450 K for the 5x10 case and 600 K for the 5x20 case. Boiloff of the water injected by the accumulators caused the reactor core to dryout and heatup a second time. During the second heatup, the reactor core is calculated to heatup to the point of molten pool formation. For the 5x10 case, the molten pool is calculated to slump to the lower head 1,800 seconds after the beginning of molten pool formation.

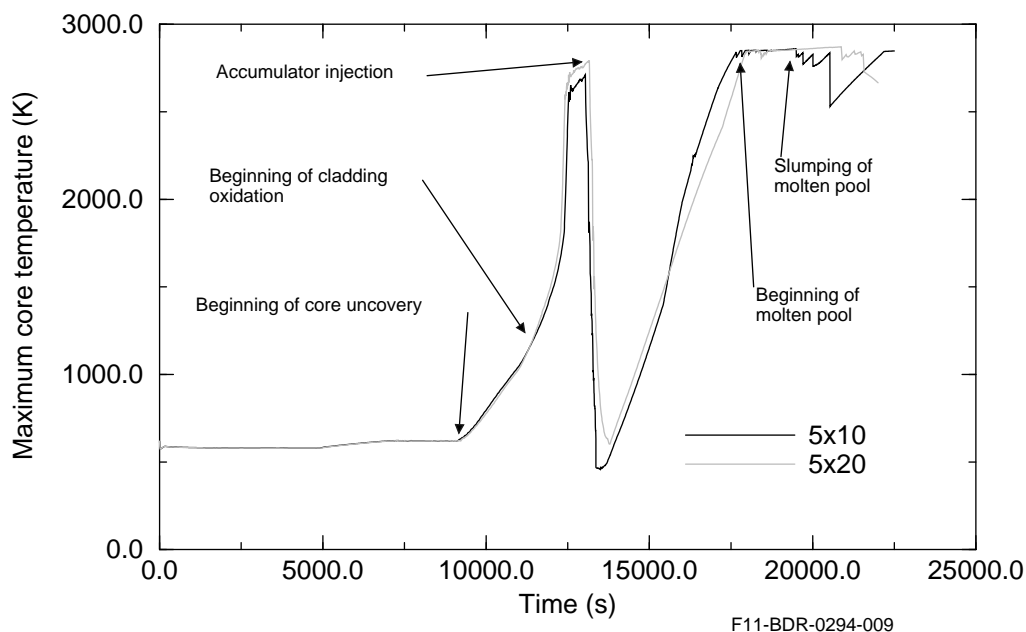
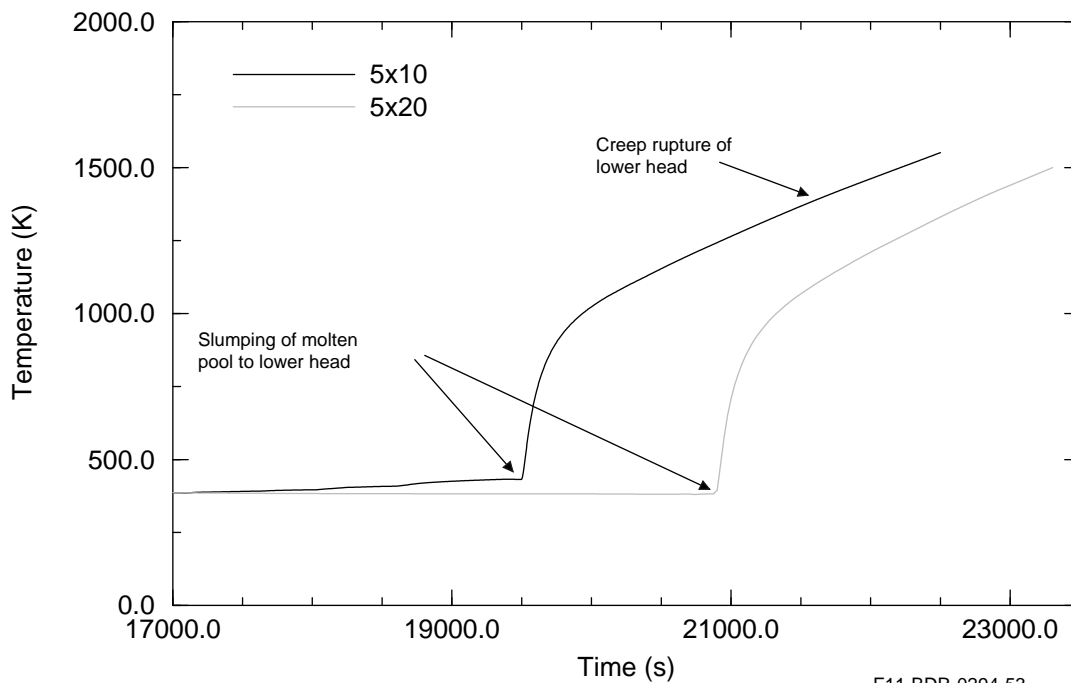


Figure 5-40. History of maximum core temperature.

The history of the maximum temperature of the midplane of the lower head of the reactor vessel is shown in Figure 5-41 for the 5x10 and 5x20 cases. The maximum temperature at the midplane was less than 500 K until slumping of the molten pool. Then, the temperature increased to 1,000 K within 470 seconds. The lower head is calculated to fail due to creep rupture at 21,770 seconds for the 5x10 case and at 23,140 seconds for the 5x20 case. The maximum midplane temperature at the time of failure was 1,390 K and the internal pressure in the vessel was 0.125 MPa. The internal pressure when the maximum midplane temperature first exceeded 1,000 K was 0.37 MPa.

Most of the hydrogen produced by oxidation of the reactor core was calculated to occur before rupture of the surge line. The accumulated hydrogen production for the 5x10 and 5x20 cases is shown in Figure 5-42. The total hydrogen production calculation for the 5x10 case was calculated to be 377 kg for the 5x10 case and 320 kg for the 5x20 case. This difference in hydrogen production is due to the 5x10 case



F11-BDR-0294-53

Figure 5-41. History of maximum temperature at midplane of lower head of reactor vessel.

calculating that the oxidation excursion propagated to a lower elevation in the core than the 5x20 case. This point is discussed further in the next section.

5.2.2.5 Description of Heatup of Reactor Core Before Surge Line Failure. This section describes in more detail the calculated heatup of the reactor core before failure of the surge line. The timing and spatial distribution in the heatup and oxidation of the reactor core are described.

The oxidation of the reactor core began in the top and center region of the core and then spread downward and outward. The 5x10 and 5x20 cases calculated a similar propagation of core oxidation. The rate of heatup before the oxidation excursion was 0.23 K/s and the maximum rate of heatup during the oxidation excursion was 8 K/s. The heatup of fuel rods in the center channel of the reactor core at several different elevations is shown in Figure 5-43 for the 5x10 case and in Figure 5-44 for the 5x20 case. The oxidation excursion propagated from the 3.5 m elevation to the 2.0 m elevation in 120 seconds. The heatup of fuel rods at the 2.7 m elevation in each of the five channels is shown in Figure 5-45 for the 5x10 case. The oxidation excursion propagated from the center of the core to the periphery of the core in 160 seconds.

The heatup of the fuel rods during the temperature excursion is limited by the amount of cladding available for oxidation. This point is shown in Figure 5-46, which shows, at two different locations in the reactor core, the temperature and oxide thickness of the fuel rods. The first location is that of fuel rods in the center flow channel at the 2.7 m elevation. The second location is that at the 2.7 m elevation at the outer part of the core. An oxide thickness of 9.1 mm corresponds with complete oxidation of the cladding. At both locations the heatup was sharply reduced by complete oxidation of the cladding at that location. The plots are taken from calculations for the 5x10 case. The 5x20 case has similar results. For both cases, the cladding in the fuel rods was calculated to be 100% oxidized in the upper half of the reactor core.

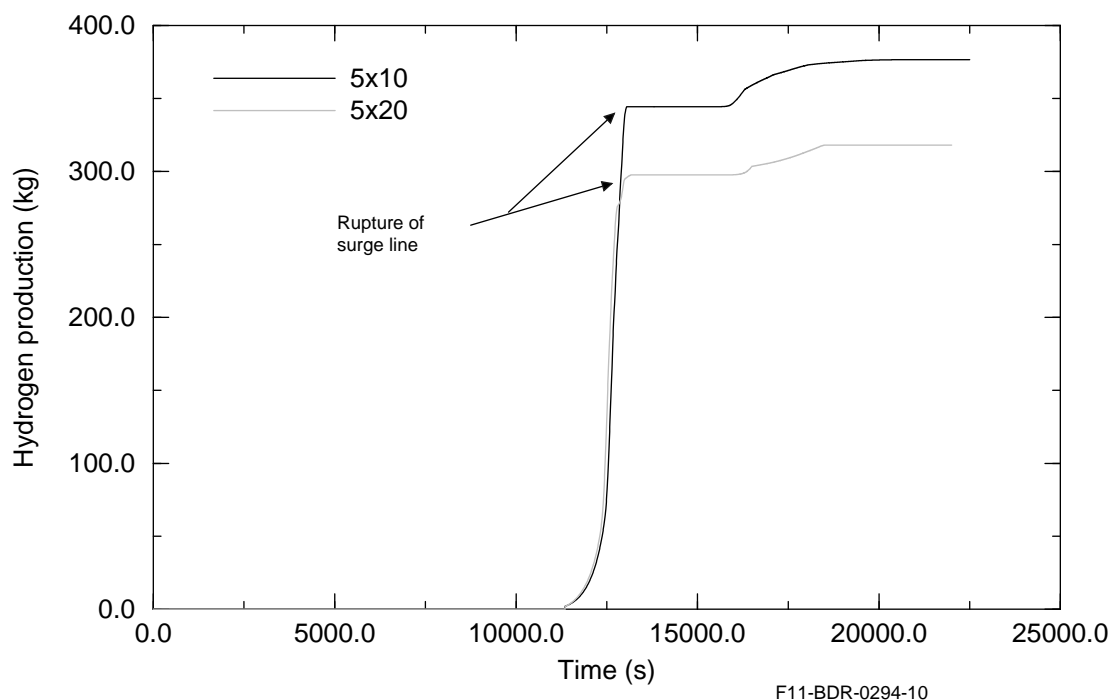


Figure 5-42. Accumulated production of hydrogen.

The oxidation excursion was calculated to propagate 0.4 m farther toward the bottom of the core for the 5x10 case than the 5x20 case. The fuel rod temperature histories at several elevations in the bottom half of the center fuel channel are shown in Figures 5-47 for the 5x10 case and in for the 5x20 case. These figures show that a temperature excursion was calculated to occur at the 1.3 m elevation for the 5x10 case but not for the 5x20 case. This difference in calculated propagation of reactor core oxidation resulted in a higher amount of hydrogen production being calculated for the 5x10 case than for the 5x20 case.

During the period of intense oxidation, the total heat generation from oxidation is about four times greater than the total heat generation from decay heat. Figure 5-49 shows the core heat generation from oxidation and that from decay heat for the 5x10 case. The peak rate of heat generation from oxidation is a little larger than 100 MW. The heat generation from decay heat during this period is about 25 MW. The local rate of heat generation due to oxidation during the oxidation excursion was calculated to be up to a factor of 25 greater than the local nuclear heat generation rate.

The calculated rate of hydrogen production during the period of intense oxidation for the two cases is shown in Figure 5-50. The oxidation excursion was calculated to begin about 100 seconds earlier for the 5x20 case than for the 5x10 case. Both cases calculate a maximum rate of hydrogen production of about 1 kg/s.

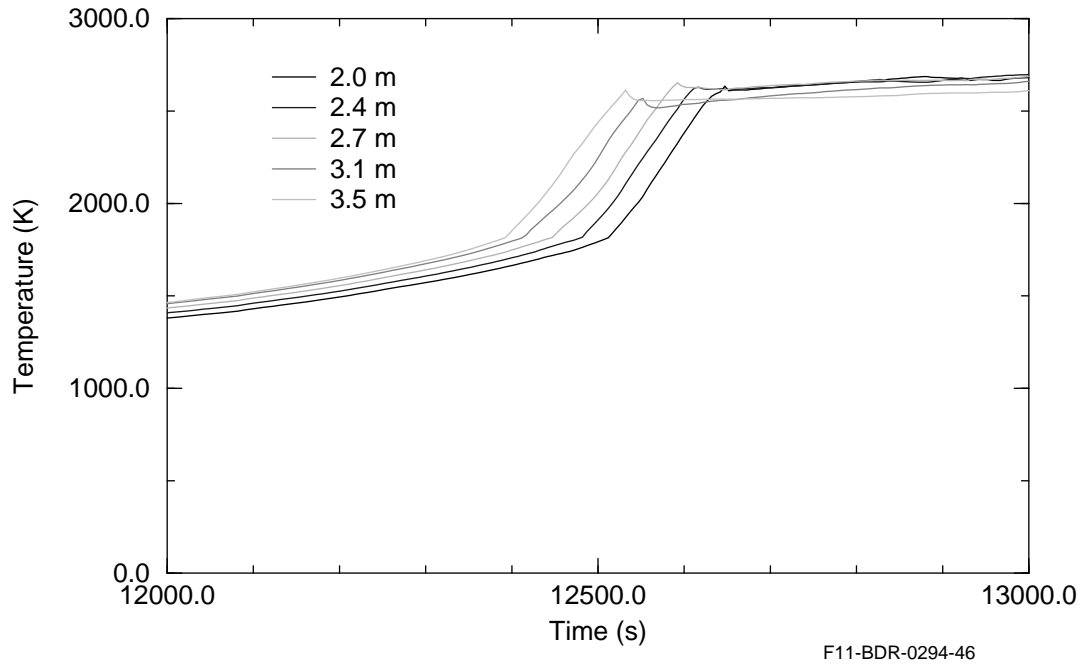


Figure 5-43. Temperature history of fuel rods at several elevations in the center channel for 5x10 case.

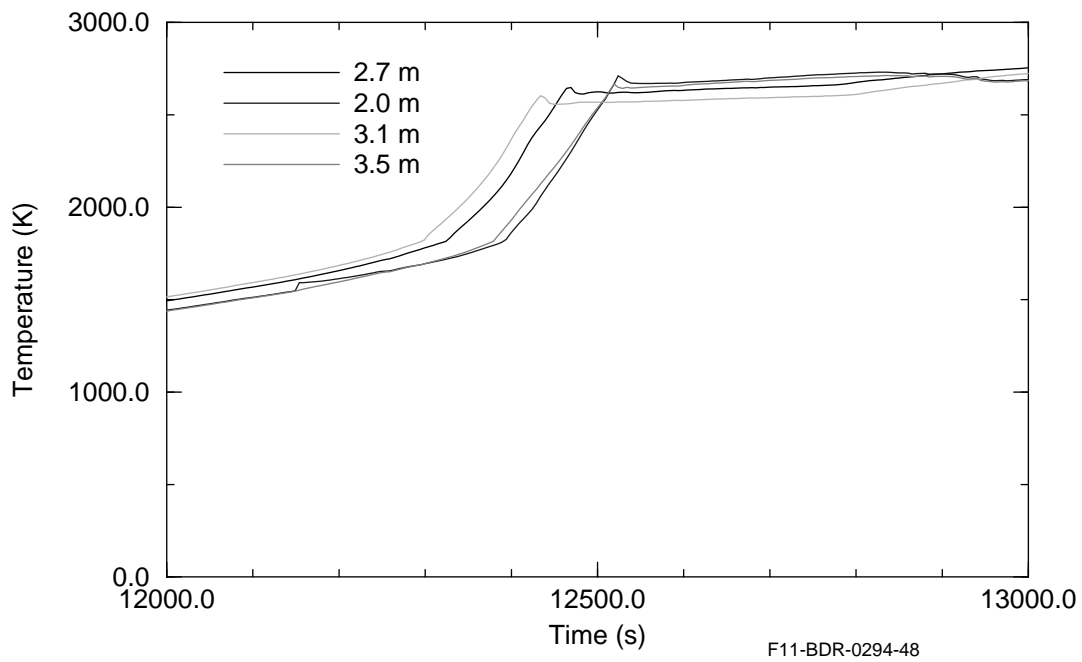


Figure 5-44. Temperature history of fuel rods at several elevations in the center channel for 5x20 case.

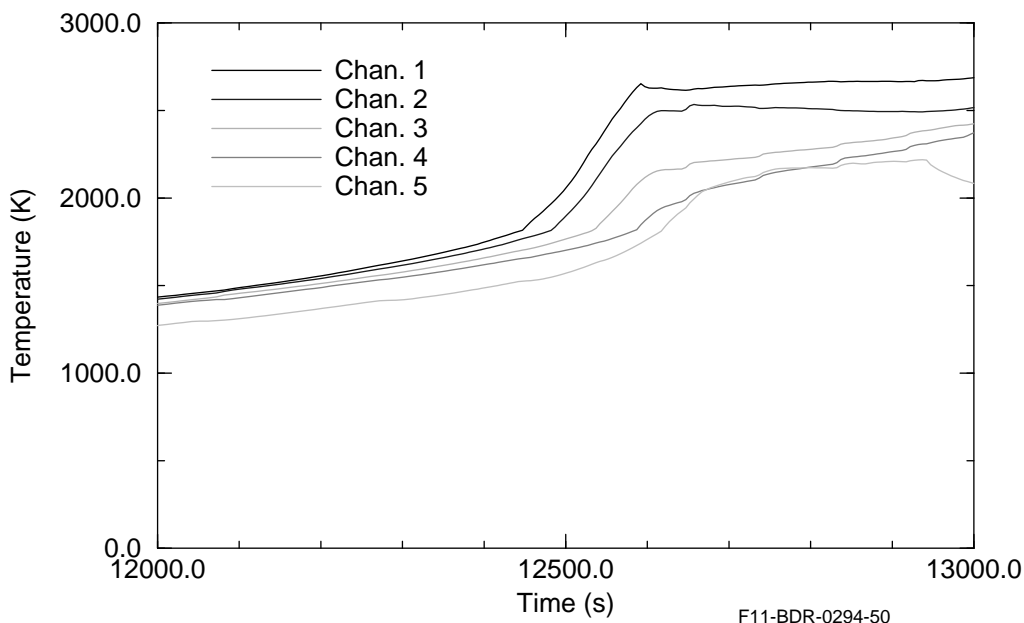


Figure 5-45. Temperature history of fuel rods at 2.7 m elevation for each channel for 5x10 case.

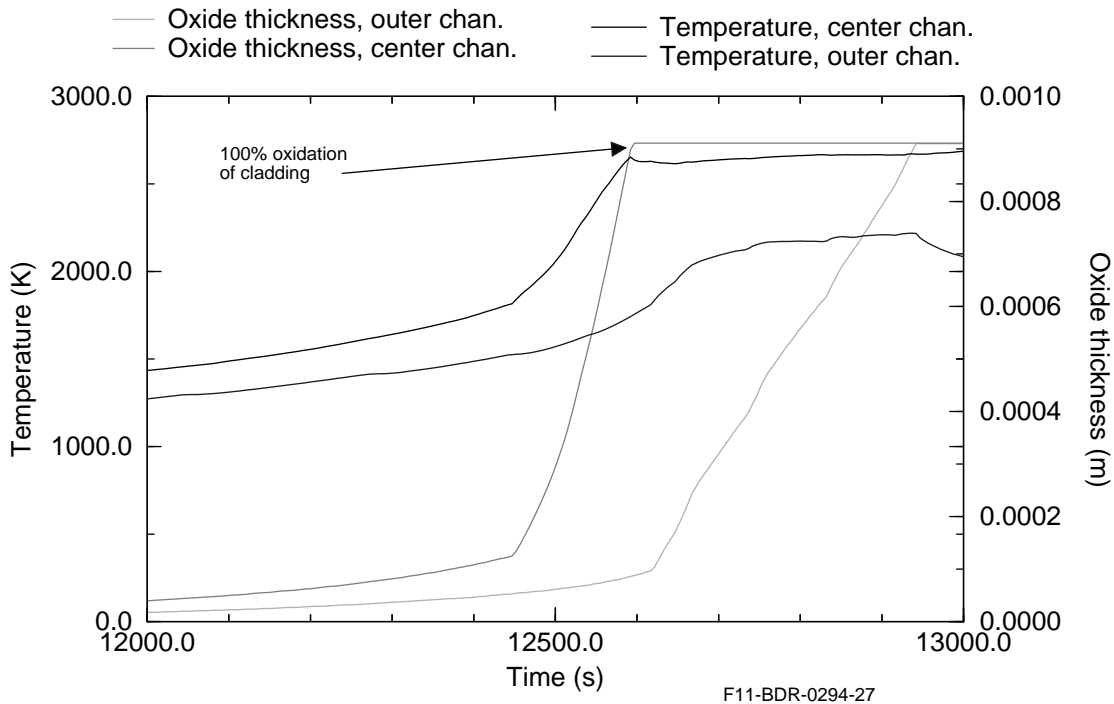


Figure 5-46. Temperature and oxide thickness histories at 2.7 m elevations for center and periphery outer flow channels for 5x10 case.

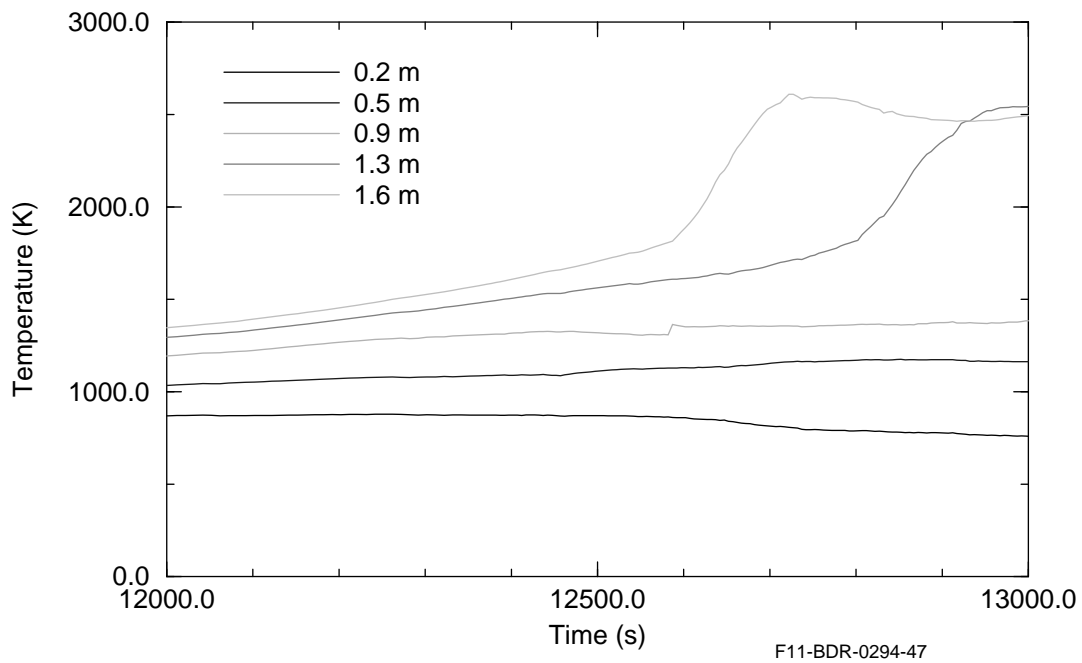


Figure 5-47. Temperature history of fuel rods in bottom half of center fuel channel for 5x10 case.

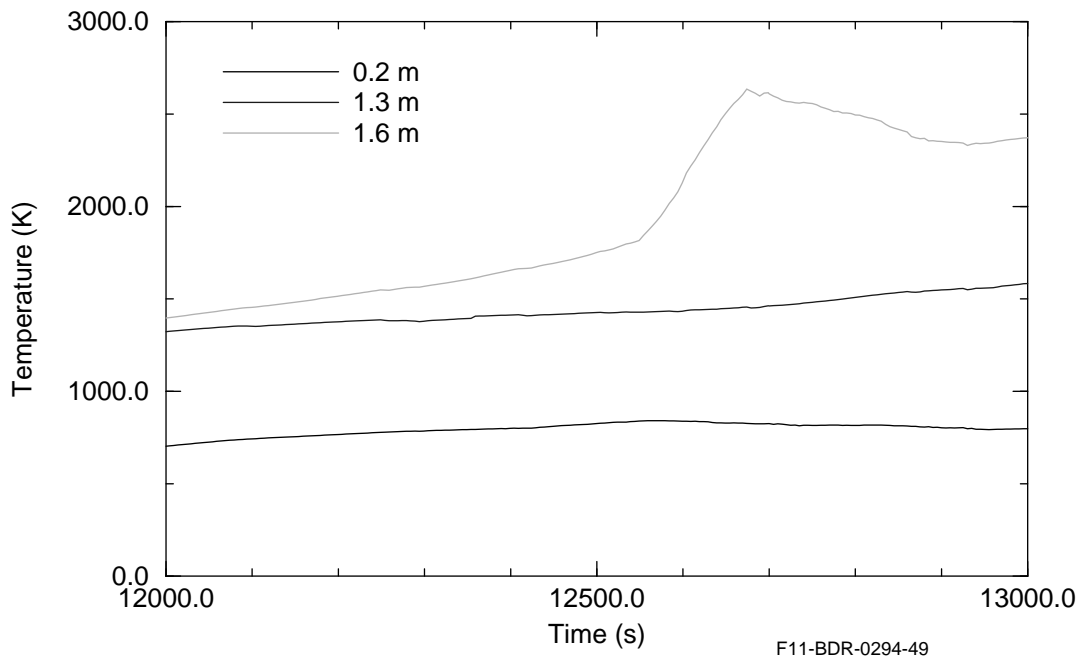


Figure 5-48. Temperature history of fuel rods in bottom half of center fuel channel for 5x20 case.

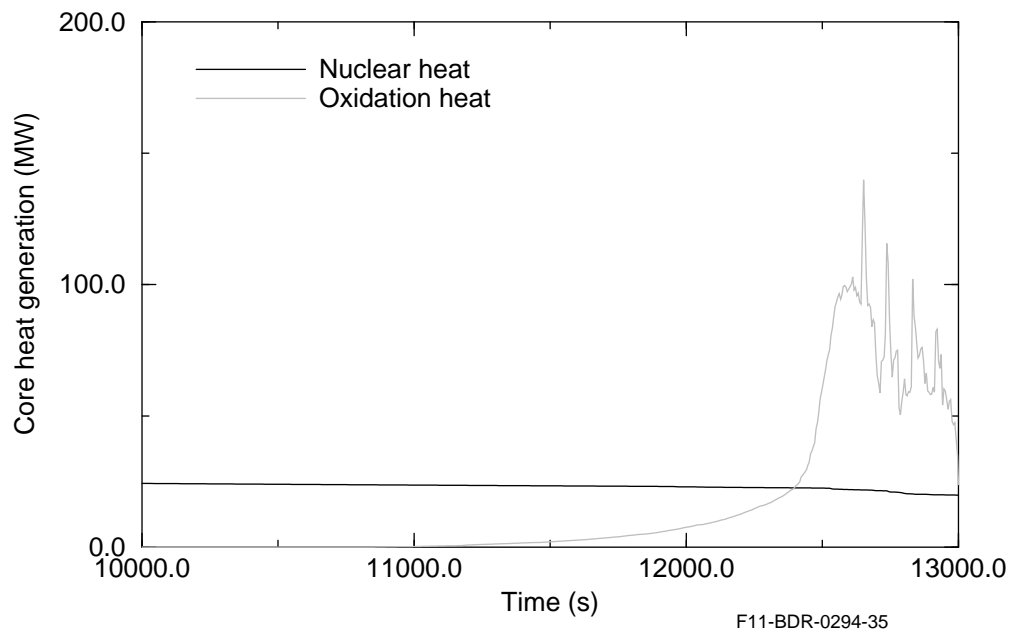


Figure 5-49. Heat generation in reactor core from oxidation and decay heat.

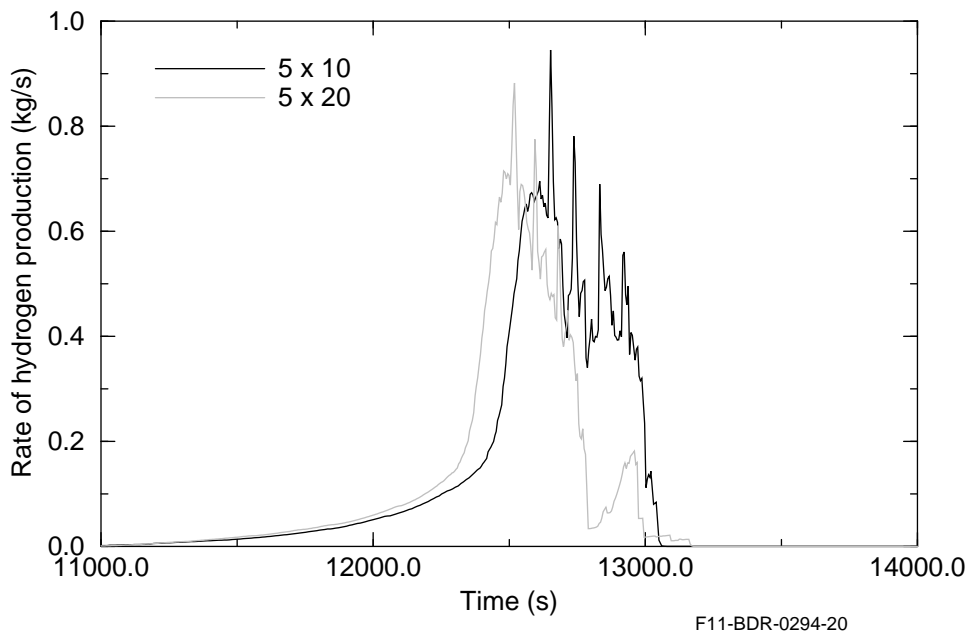


Figure 5-50. Rate of hydrogen production.

5.2.2.6 Late Phase Damage Progression. This section describes the damage progression in the reactor core from the time of fragmentation of the reactor core to slumping of the molten pool to the

lower head of the reactor vessel.

The 5x10 and 5x20 cases calculate a similar thermal response of the reactor core during the reflood of the core and during the period of late phase damage progression. In both cases, the reflood of the reactor core due to accumulator injection was calculated to temporarily quench the entire reactor core. In both cases, the reactor core was calculated to heatup to the point of molten pool formation following boiloff of the reflood water. The temperature of the fuel rods at two elevations in the center fuel channel are shown in Figure 5-51 for both the 5x10 and 5x20 cases. The reflood caused the core temperatures to decrease from 2,700 K to less than 650 K. The core was calculated to be quenched in about 400 seconds. The 5x10 case calculated a little more cooling of the reactor core than the 5x20 case. The reactor core was then calculated to heatup again due to boiloff of the reflood water. The heatup begins at the top of the reactor core and propagates downward. The heatup at the 1.3 m elevation begins 600 seconds later than the heatup at the 2.7 m elevation for the 5x10 case. The initial rate of heatup is about 0.5 K/s. The heatup is due to decay heat and oxidation in fuel rods in the lower one-third of the core. Ceramic melting is calculated to begin 4,500 seconds after the beginning of accumulator injection. After ceramic melting has begun, the heatup is calculated to occur at a much slower rate due to material phase change.

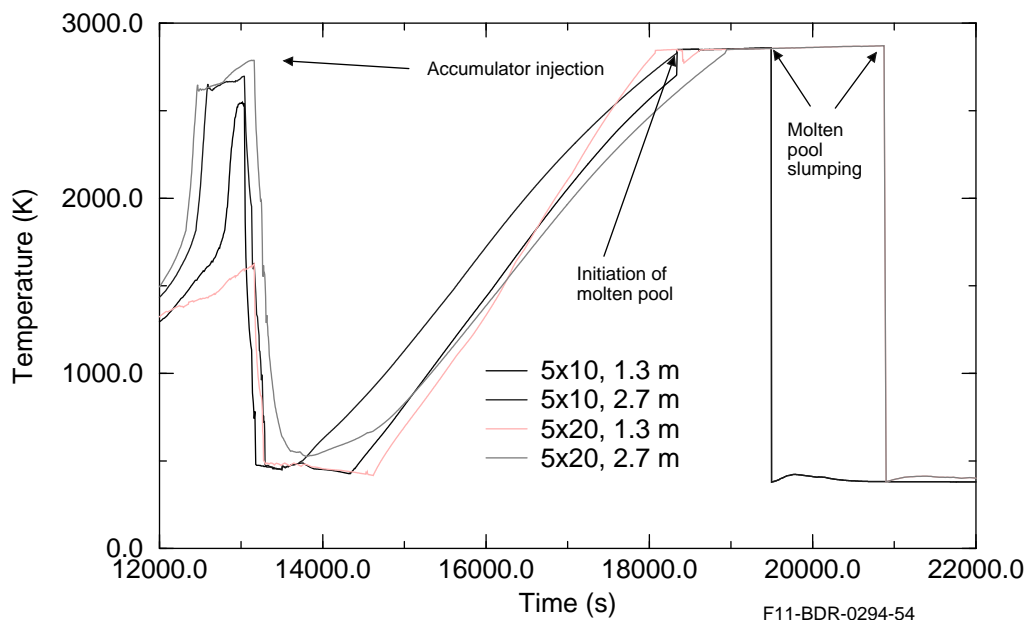


Figure 5-51. Thermal response of reactor core during reflood and late phase damage progression.

The temperature variations in the radial direction in the reactor core are also similar for the 5x10 and 5x20 cases. Figure 5-52 shows the temperature histories of fuel rods at the 2.0 m elevation for the inner and outer flow channels in the reactor core. The temperature histories are shown for both the 5x10 and 5x20 cases. In both cases the fuel rods in the inner and outer channels are calculated to quench at the same rate. The fuel rods in the inner and outer channels also begin to heatup at the same time due to dryout of the reactor core. The heatup of the fuel rods in the outer channel is less than that of those in the inner channel. Heatup to the point of ceramic melting is calculated to occur 1,800 seconds later in the outer channel than the inner channel for the 5x10 case and 3,000 seconds later in the outer channel than the inner channel for the 5x20 case.

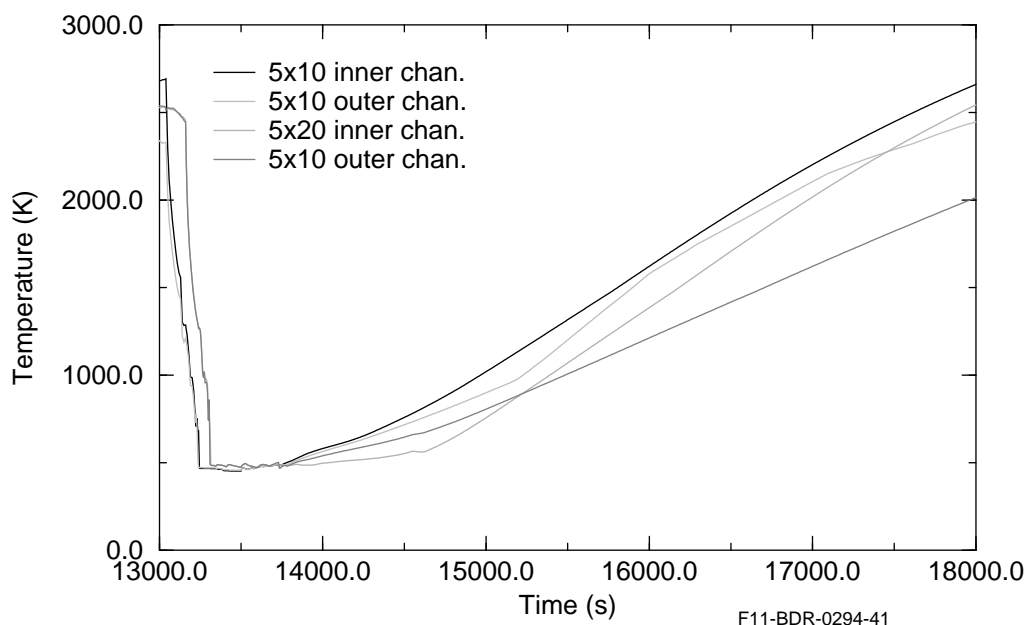


Figure 5-52. Radial distribution in temperature of reactor core during reflood and late phase damage progression.

The upper half of the reactor core was calculated to disintegrate into porous debris following reflood of the reactor core due to accumulator injection. The disintegration into porous debris was due to the quenching of embrittled fuel rods. The upper half of the reactor core was calculated to be completely oxidized and thus embrittled. The core degradation following reflood of the core is shown for the 5x10 case in Figure 5-53 and for the 5x20 case in Figure 5-54. The 5x20 case calculated somewhat less disintegration of the top center of the reactor core than the 5x10 case. This smaller disintegration was due to the 5x20 case calculating somewhat less cooling of the reactor core than the 5x10 case. The fragmentation temperature was defined to be 100 K hotter than the saturation temperature of water. This definition of the fragmentation temperature resulted in it having a value of 600 K at the time of core reflood. For the 5x10 case the entire reactor core was calculated to be cooled to less than 600 K. For the 5x20 case, the top center of the reactor core was calculated to always remain a little hotter than 600 K. The fragmentation temperature is not well defined. An upper bound value of the fragmentation temperature is estimated to be the temperature at which the transition from the film boiling mode of heat transfer to the nucleate boiling mode of heat transfer begins during the process of quenching hot fuel rods. This temperature may be several hundred degrees K higher than saturation temperature. If the upper bound value of the fragmentation temperature had been selected, then the 5x20 case would have also calculated fragmentation of the entire upper half of the core and the subsequent damage progression for the two cases would have been in closer agreement. Thus these differences in calculated core degradation between the 5x10 and 5x20 cases are considered to not be significant.

The progression of ceramic melting was calculated to be similar for the 5x10 and 5x20 cases. Figure 5-55 shows the calculated effective radius of the molten pool for the 5x10 and 5x20 cases. The effective radius is the radius of a hemisphere with a volume equal to the volume of molten material in the reactor core. Ceramic melting is calculated to begin at 17,650 seconds for the 5x10 case and at 17,920 seconds for

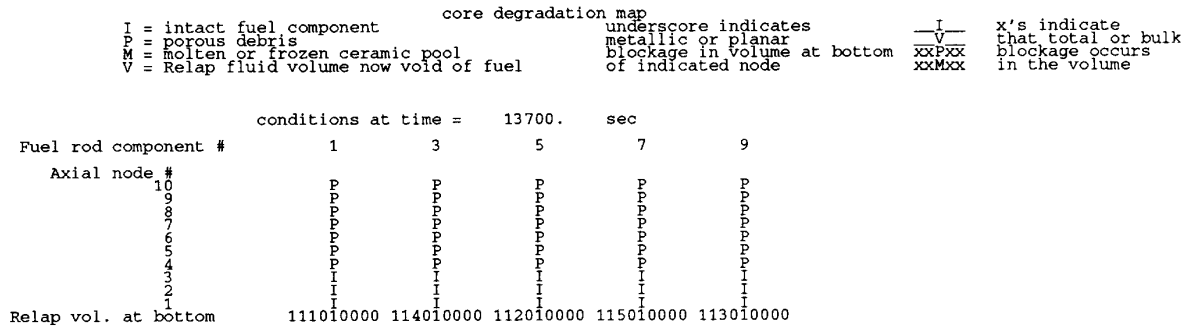


Figure 5-53. Core degradation map after reflood for 5x10 case.

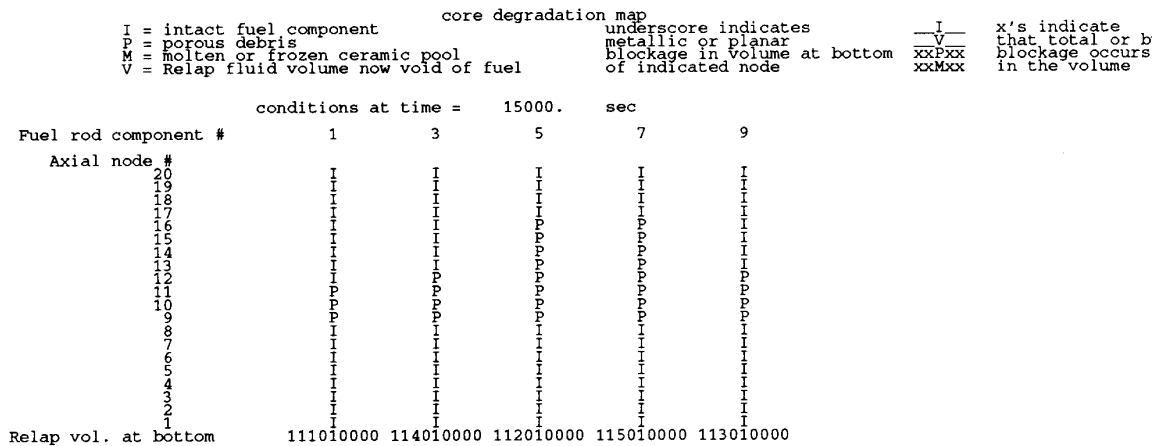


Figure 5-54. Core degradation map after reflood for the 5x20 case.

the 5x20 case. Both cases calculate that the effective radius increases from 0.0 m to 1.0 m within a 500 seconds period of time. The rate of increase in size of the molten pool decreases after this initial period of rapid increase in size. The effective radius is calculated to increase to a maximum value of 1.5 m due to melting of about 65% of the fuel in the reactor core. The molten pool is calculated to slump to the lower

head at 19,450 seconds for the 5x10 case and at 20,890 seconds for the 5x20 case. This difference in slumping time of 1,440 seconds is partly due to differences in core degradation during the reflood of the reactor core. These differences in core degradation were due to selecting as a user option the lowest possible bound on fragmentation temperature of embrittled fuel rods that are quenched. If a slightly larger fragmentation temperature had been selected, then about the same extent of core degradation during reflood would have been calculated for the two cases and the time of molten pool slumping for the two cases would probably be in closer agreement.

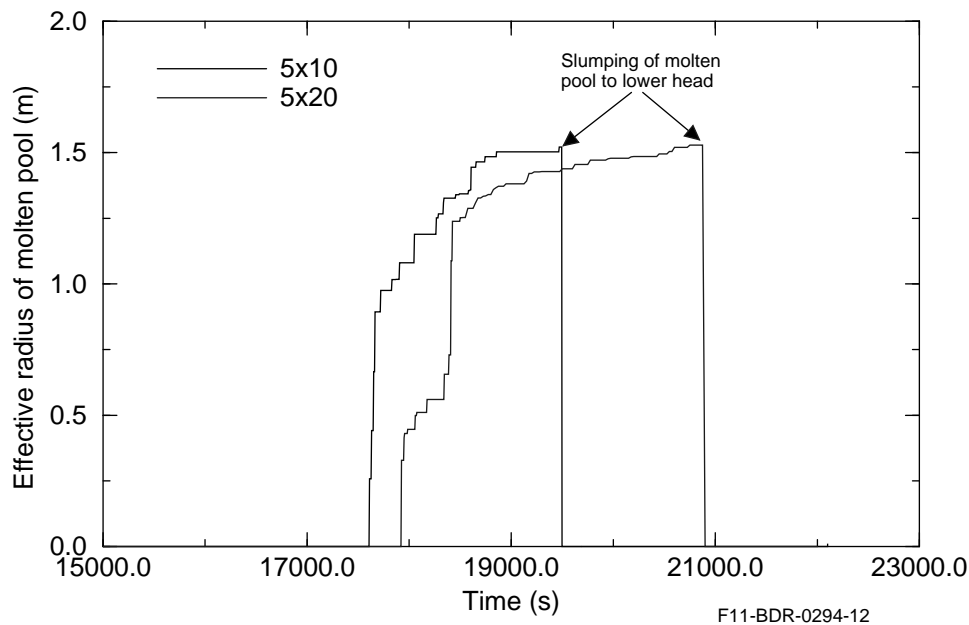
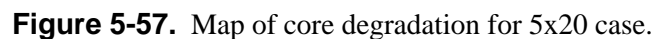


Figure 5-55. Effective radius of molten pool for 5x10 and 5x20 cases.

The calculated evolution in molten pool formation is next described. Figure 5-56 shows the core degradation calculated for the 5x10 case. The molten pool formation began at the 0.6m elevation in the four inner flow channels. The molten pool formation began at this relatively low elevation due to oxidation of fuel rods at this elevation. The molten pool formation then occurred in the middle of the fourth channel, then in the middle of the inner two channels and then in the third channel. At 19,000 seconds, all but the lower and upper parts of the middle four channels were molten. No molten material existed in the outer channel at this time. Figure 5-57 shows the location of the molten pool for the 5x20 case at 18,500 seconds. For this case, the molten pool formation began in the inner two channels at the 1.0 m elevation. Molten pool formation began in the third and fourth channels at the 1.2 m elevation at a time 500 seconds later than the beginning of molten pool formation in the inner two channels. Molten pool formation in the outer channel began 3,000 seconds later than molten pool formation in the inner two channels. The molten pool was calculated to slump to the lower head at 19,450 seconds for the 5x10 case and at 20,890 seconds for the 5x20 case.

The heatup of the lower head in response to slumping of the molten pool was similar for the 5x10 and 5x20 cases. The calculated temperature response of the midplane of the lower head at two different elevations is shown in Figure 5-58 for the 5x10 and 5x20 cases. For the 5x10 case, the bottom center location of the lower head was calculated to be heated to a temperature of 800 K by control rod material

Figure 5-56. Map of core degradation for 5x10 case.



that slumped to the lower head before molten pool slumping. The 5x20 case did not calculate as much slumping of control rod material as the 5x10 case. The slumping of the molten pool caused an almost equal heatup of the lower head from an elevation of 0.31 m above the bottom center location of the lower head to an elevation of 1.16 m above the bottom center location. The core material in the lower head extended upward to a height of 1.3 m following slumping of the molten pool. The control rod material at the bottom of the lower head acted as a buffer that partially shield the bottom center location of the lower head from the molten pool material that slumped to the lower head. The maximum temperature of the midplane of the lower head at the time of rupture of the lower head was 1390 K. The maximum temperature in the debris in the lower head is shown in Figure 5-59 for the 5x10 and 5x20 cases. Before slumping of the molten pool, the maximum temperature was 1,000 K. After slumping of the molten pool, the maximum temperature increased almost instantaneously from 1,000 K to 2,500 K and then gradually increased from 2,500 K to 3,000 K during a 2,000 seconds period of time.

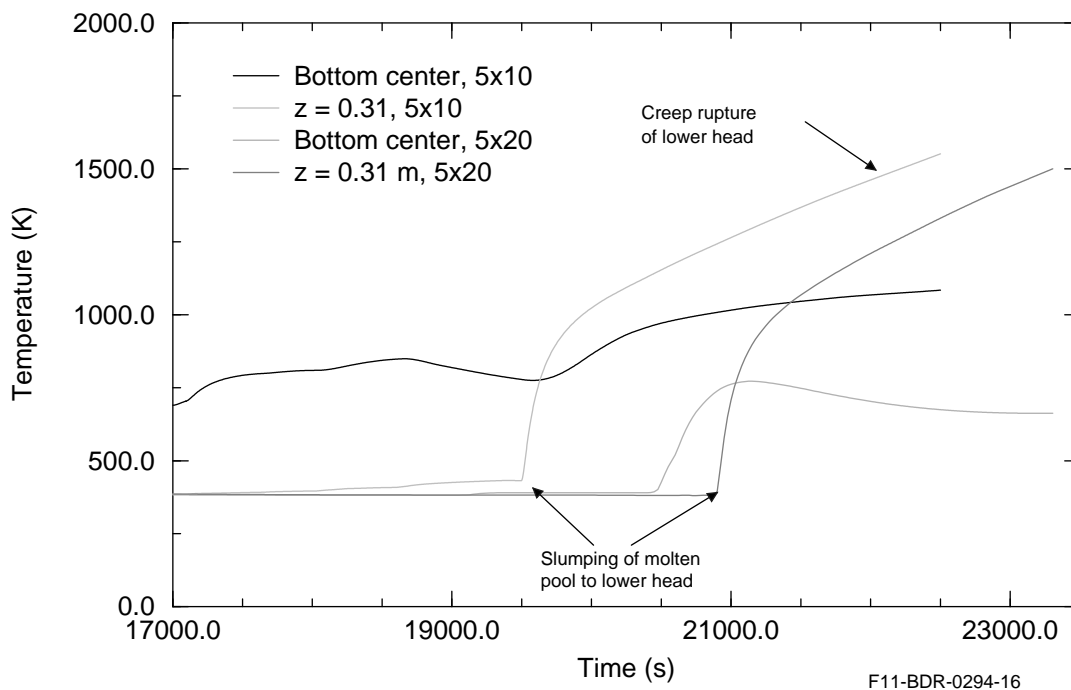


Figure 5-58. History of maximum temperature at midplane of lower head of reactor vessel.

5.2.2.7 Thermal Hydraulic Behavior and Heatup of Components in Reactor System.

This section describes the thermal hydraulic behavior in the region of the reactor core and the heatup of the surge line and structures in the lower plenum.

Natural circulation of the steam was calculated to occur in the core region after the beginning of core uncover and before rupture of the surge line. The calculated velocity of steam at the top of the core for three radial locations is shown in Figure 5-60 for the 5x10 case and in Figure 5-61 for the 5x20 case. Both cases calculate a similar variation in velocity of the steam. During the period of core uncover before surge line rupture, the steam in the center channel flows upward at a velocity of about 0.35 m/s and the steam in the outer channel flows downward at a rate of about 0.6 m/s. Following rupture of the surge line and during the reflood of the core, the steam throughout the core flows upward at a rate of about 3 m/s. The velocity gradually decreases during the period of boiloff of the reflood water.

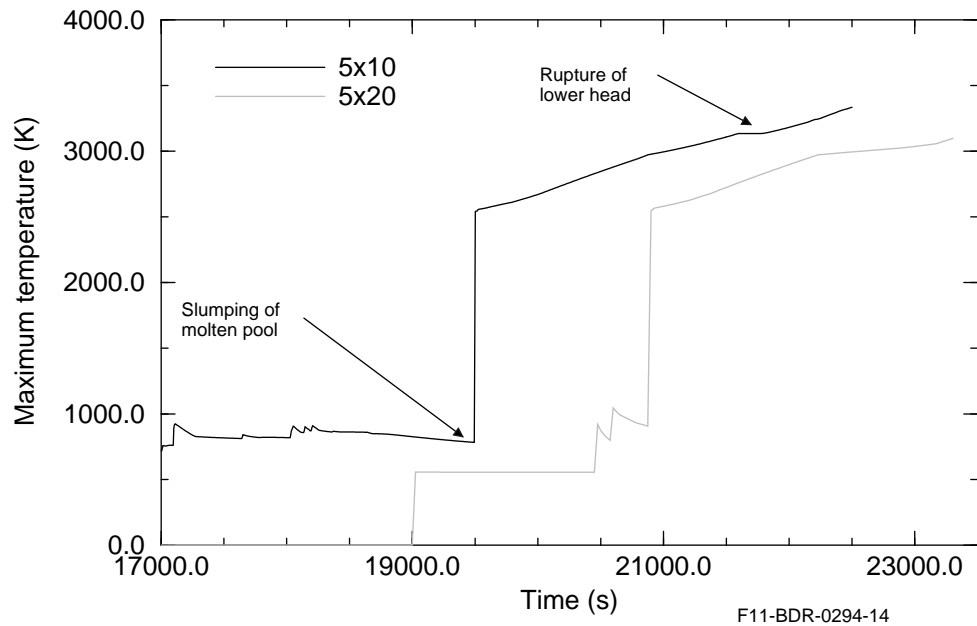


Figure 5-59. History of maximum temperature of debris in lower head of reactor vessel.

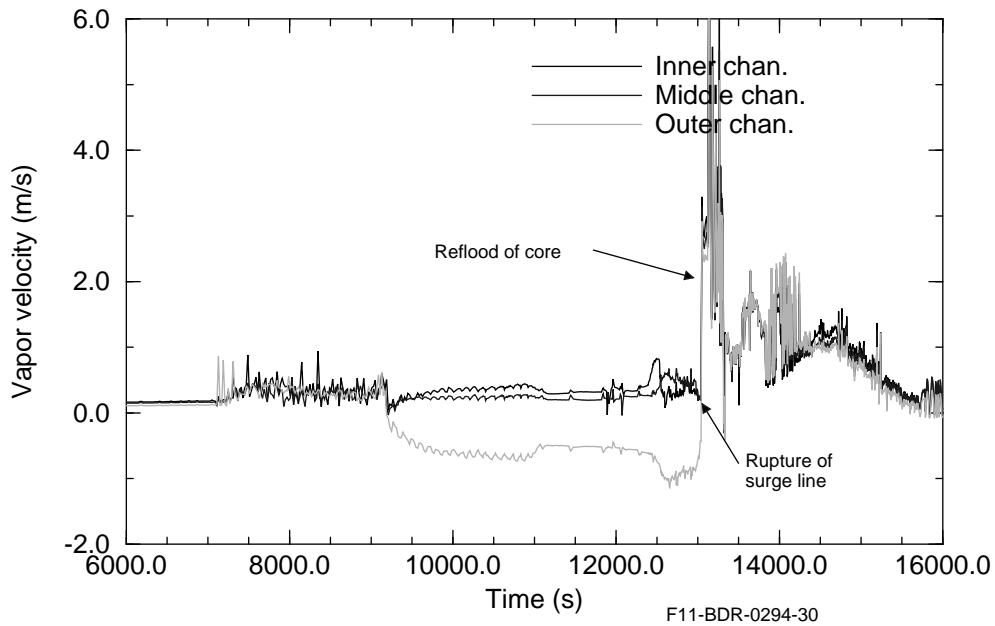


Figure 5-60. Variation in radial direction of velocity of steam at top of core for 5x10 case.

The volume fraction of liquid at the midplane level of the reactor core is shown in Figure 5-62. The volume fraction increases from 0.0 to about 0.8 following reflood of the core. The midplane of the center channel is calculated to dryout about 600 seconds sooner for the 5x10 case than the 5x20 case.

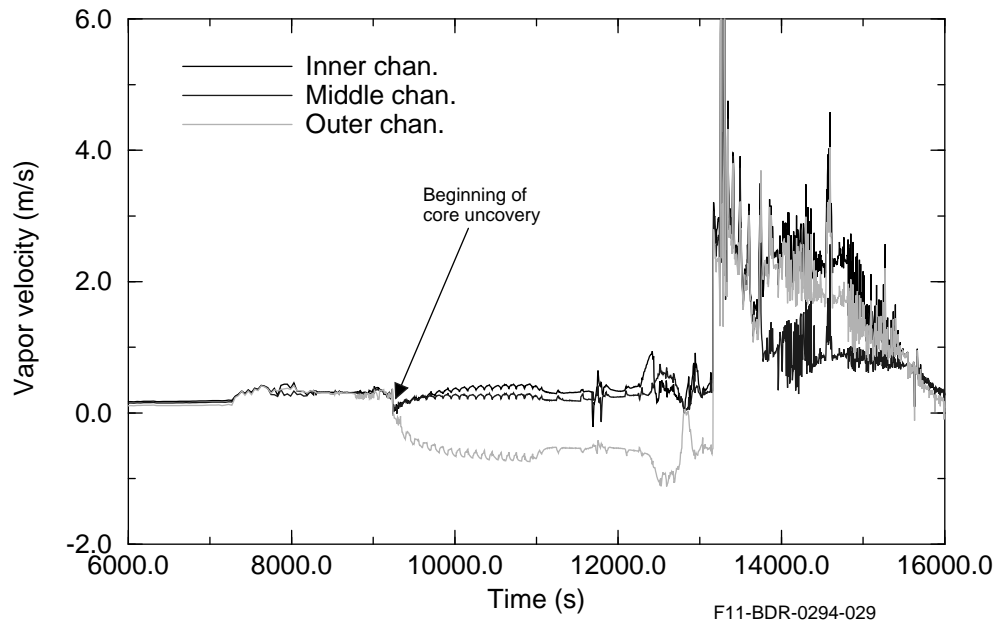


Figure 5-61. Variation in radial direction of velocity of steam at top of core for 5x20 case.

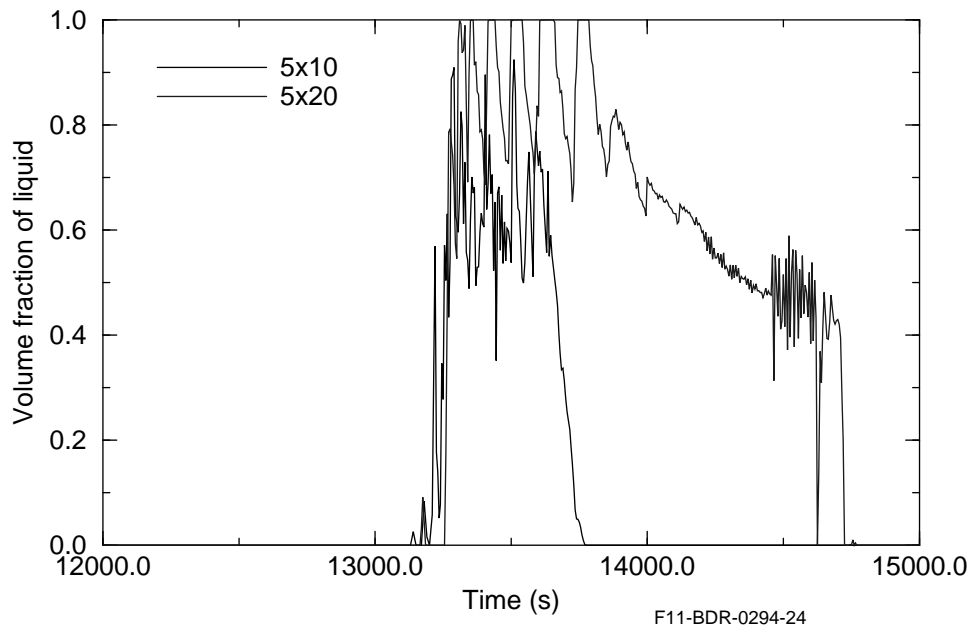


Figure 5-62. Volume fraction of liquid at midplane of center channel of reactor core.

The history of the temperature of the steam at the top of the core at three different radial locations for the 5x20 case is shown in Figure 5-63. The temperature of the steam in the outer channel is significantly less than that in the center channel due to natural circulation in the core and upper plenum region of the reactor vessel. The temperatures at the three locations are similar following rupture of the surge line and

reflood of the reactor core. The reflood of the core results in a cooling of the structures in the upper plenum region of the reactor vessel due to the much cooler steam that is transported to this region after reflood.

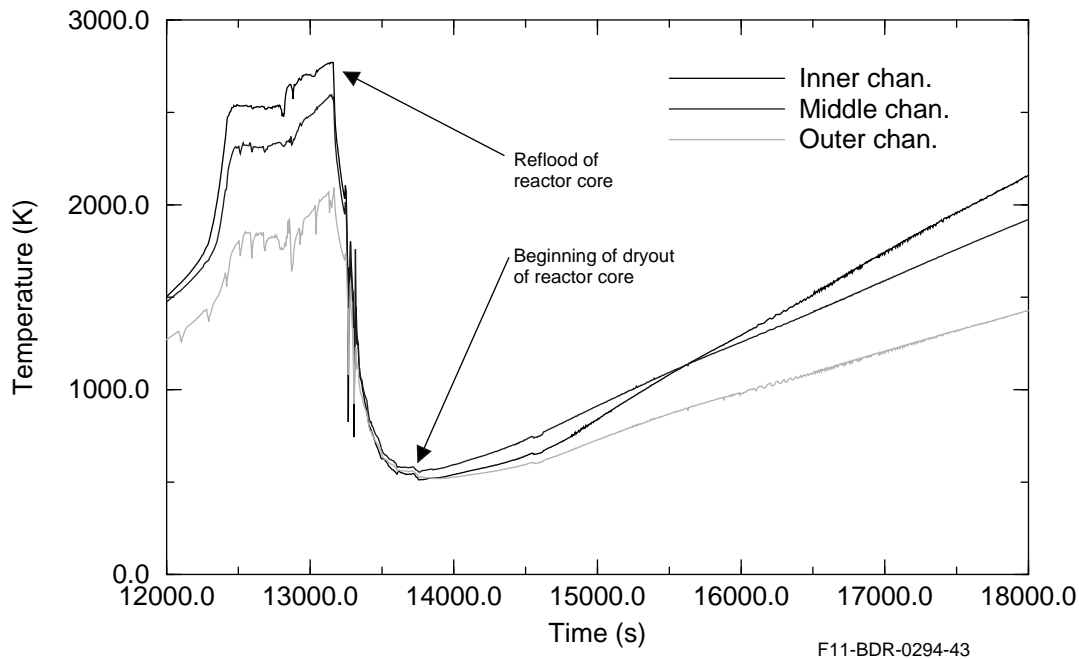


Figure 5-63. Temperature of steam at top of core at three radial locations for 5x20 case.

The calculated temperature of structures in the lower part of the upper plenum of the reactor vessel is shown in Figure 5-64. The rate of heatup of the structures is the same for the 5x10 and 5x20 cases. The maximum temperature for these structures is 1,550 K for the 5x10 case and is 1,700 K for the 5x20 case. The melting temperature of these structures is about 1,700 K. The temperature of these structures is calculated to decrease following rupture of the surge line. The 5x20 case calculates a greater maximum temperature of these structures because it calculates a later rupture of the surge line.

The history of the temperature of the hottest section of the surge line is shown in Figure 5-65. The calculated rate of heatup is similar for the 5x10 and 5x20 cases. The temperature of the surge line at rupture for the 5x10 case is 1,200 K. The calculated temperature of the surge line decreases following rupture.

The history of the rate of flow of steam through the break in the surge line is shown in Figure 5-66 for the 5x10 and 5x20 cases. A similar rate of flow through the break is calculated. The maximum rate of flow was calculated to be about 300 kg/s. The accumulated flow of steam through the surge line is shown in Figure 5-67. A total of 64,000 kg of steam is calculated to flow through the break before slumping of the molten pool. An additional 6,000 kg of steam is calculated to flow through the break during the increase in primary system pressure caused by slumping of the molten pool.

5.2.2.8 Conclusions. A comparison of the calculated behavior of a PWR during a TMLB' accident using two different nodalizations of the reactor core has defined the differences in results due to nodalization. In one case the reactor core was divided into five radial segments each with ten axial nodes and in the other case the core was divided into five radial segments each with twenty axial nodes. The

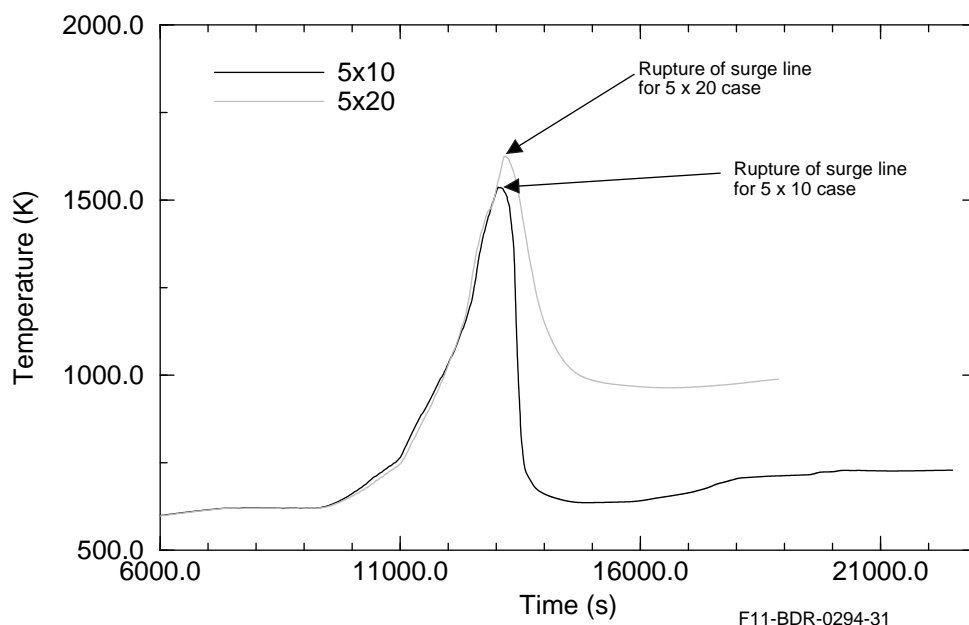


Figure 5-64. Temperature history of structures in lower part of upper plenum region of reactor vessel.

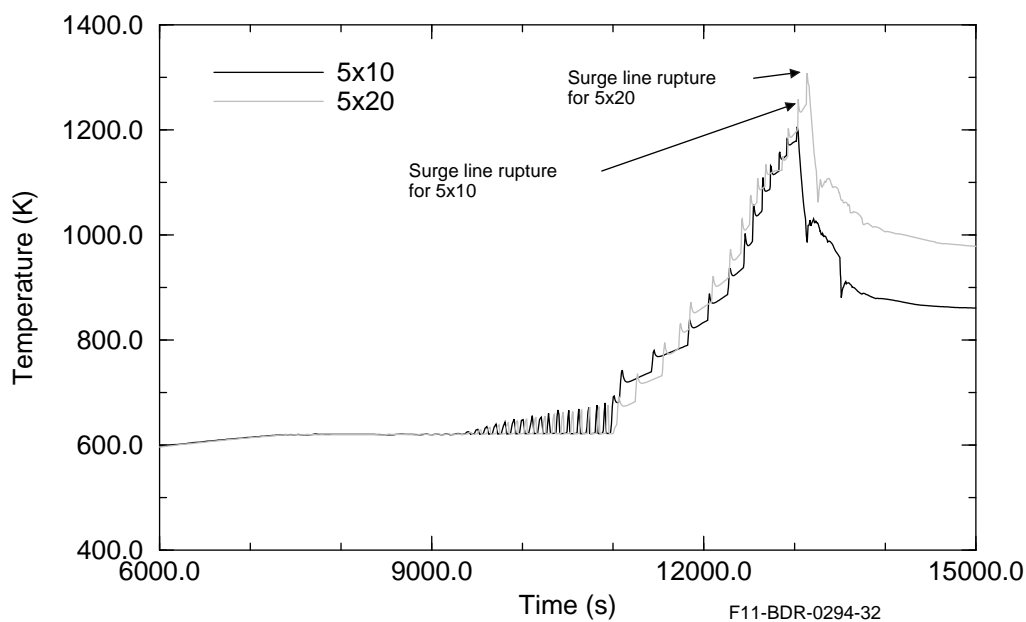


Figure 5-65. Temperature history of surge line.

major parameters in this accident are: 1. time of rupture of the surge line, 2. time of beginning of ceramic melting in the reactor core, 3. amount of molten core material that slumps to the lower head, 4. time of slumping of molten core material to the lower head, 5. time of creep rupture of the lower head, and 6. amount of hydrogen produced by oxidation of the reactor core. The 5x10 and 5x20 nodalizations result in

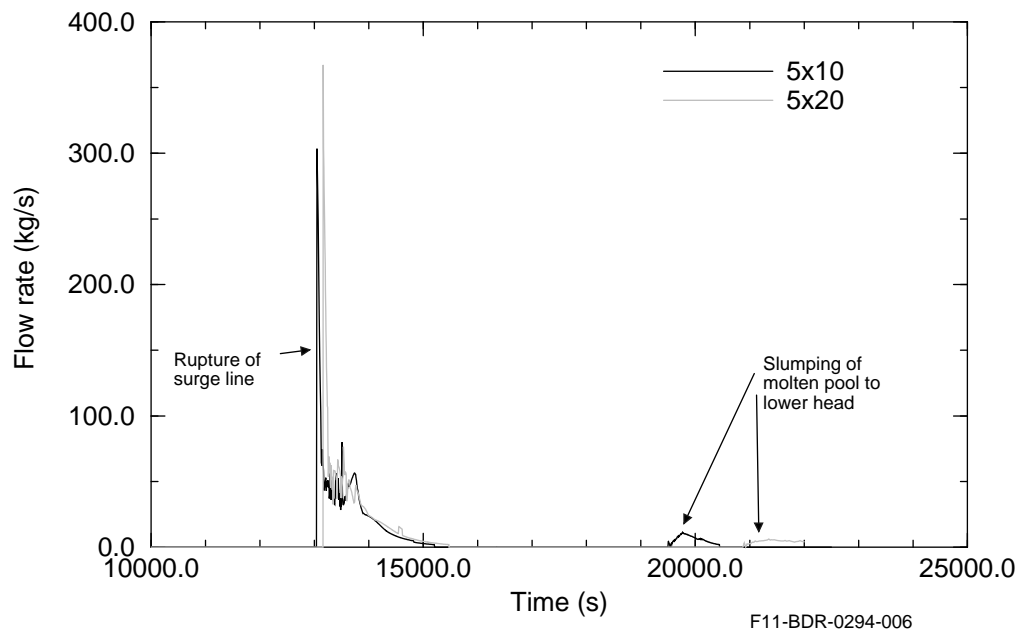


Figure 5-66. History of rate of flow of steam through break in surge line.

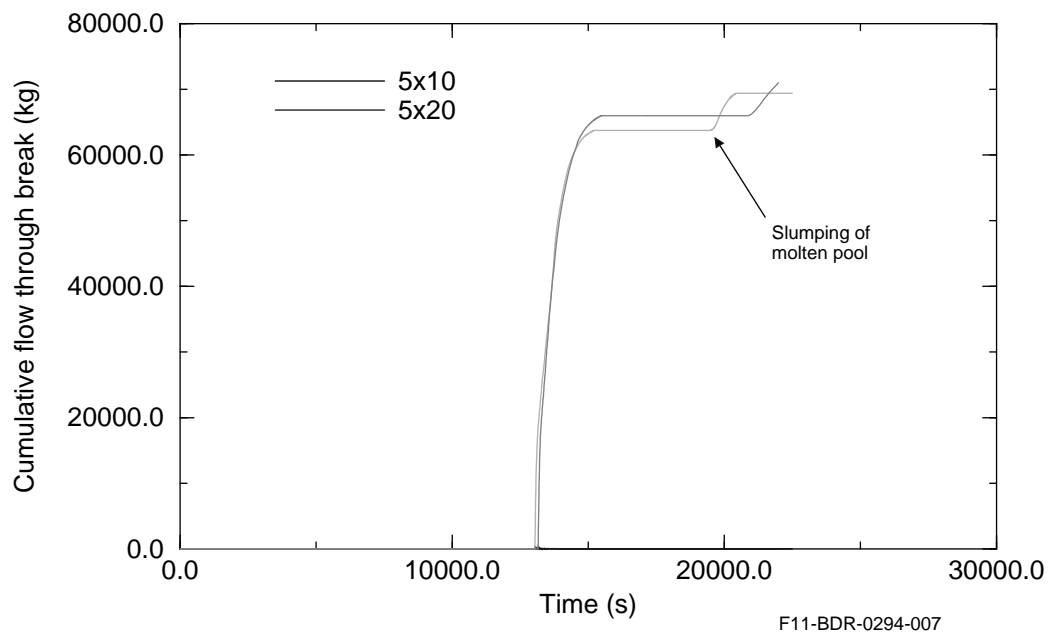


Figure 5-67. Accumulated flow of steam through break in surge line.

almost identical values for the first three parameters. The 5x10 case results in a 18% greater amount of hydrogen production than the 5x20 case. This difference in hydrogen production is similar to the differences in hydrogen production between the ten and twenty axial node cases for the analyses of BWR and

PWR fuel assemblies as reported in Sections 5.1.1.1 and 5.2.1.3. The calculated time of slumping of a large pool of molten material and the creep rupture of the lower head is 7% earlier for the 5x10 case than the 5x20 case. The CPU time for the analysis of the 5x20 case was a factor of 1.7 larger than that for the 5x10 case. The analysis of a severe accident requires in its planning stage an evaluation of whether these differences in results of 7% to 18% justify a factor of 1.7 increase in computational effort.

The representation of a reactor core with three or less radial segments may result in an inaccurate calculation of the evolution of melt progression. In the analysis of the Surry TMLB' performed with the 3x10 nodalization, the initial location of the molten pool was calculated to be in the middle radial segment. In the analyses performed with five radial segments, the initial formation of the molten pool was calculated to occur in the center radial segment. These differences in the location of initial molten pool formation were due to the center radial segment having a higher power for the five radial segment case than for the three radial segment case. The higher power was sufficient to cause the initial location of the molten pool to occur in the center radial segment, which is the location at which the initial formation of the molten pool is expected to occur. Another difference between the three and five radial segment cases was the distribution in flow velocities in the core region after blockage due to molten pool formation. For the three radial segment case, the large flow area of the middle radial segment relative to the center radial segment resulted in a large diversion of steam flow to the center radial segment after blockage was calculated for the middle radial segment. The large diversion of steam to the center radial segment caused an unrealistic cooling of the center radial segment. This cooling was an artifact of the large differences in flow area of the center and middle radial segments and thus was an artifact of the coarse radial nodalization of the reactor core.

An important pair of parameters for a severe accident analysis are the extent of oxidation of fuel rod cladding and its peak temperature during the period of its temperature excursion due to oxidation. In the analyses of the behavior of the Surry PWR during a TMLB', the cladding was calculated to be completely oxidized just before the fuel rods would have been heated to the point of ceramic melting and molten pool formation. After oxidation is complete, a sharp reduction in heat generation occurs. If the fuel rod cladding had been a little thicker, the fuel rods would have heated up to the point of molten pool formation during the oxidation excursion period of the accident. Thus the time to beginning of ceramic melting and the formation of a molten pool is sensitive to the thickness of the cladding of the fuel rods. For oxidation excursions at low pressure the possibility is less likely of the cladding being completely oxidized before heatup to the temperature of ceramic melting due to the less heat capacity and thus less cooling for low pressure steam relative to high pressure steam.

The analyses of the Surry PWR showed that natural circulation within the reactor vessel can result in the transfer of a significant amount of the heat generation in a reactor core to structures in the upper plenum region. This transfer of heat from the core region to other structures is indicated by the hot temperature calculated for structures in the upper plenum. During the period in which the reactor core is oxidizing, the heat transferred by natural circulation from the core region to the structures in the upper plenum may cause enough cooling of the oxidizing parts of the reactor core that these parts are not heated above the ceramic melting temperature.

6. CONCLUSIONS

The comparisons between SCDAP/RELAP5/MOD3.1, earlier versions of the code, and data from early phase experiments indicate that the modeling improvements and error corrections incorporated into SCDAP/RELAP5/MOD3.1 have resulted in noticeable improvements in the code. The addition of models for (a) renewed oxidation during reflood and associated vapor diffusion limits, (b) grid spacer effects, and (c) the melting of BWR control blades and channel boxes have had the most obvious impact on the early phases of the accident. Changes in the axial and radial spreading, and corrections to the molten pool crust failure models to account for recent results obtained from the ACRR MP tests, have had the most impact for the later stages. In the latter case, as discussed below, the molten pool crust failure modifications may have a significant impact on how the code predicts the slumping of core material from the core region.

The improvements in the code to enhance the usability and reliability of the code through changes in the input style and code numerics were very significant in the overall assessment because they made it possible to set up and run the large number of calculations over a relatively short period of time. Not only did the code-to-data comparisons run smoothly but the Surry and Browns Ferry full plant calculations ran well, Surry up to the point of lower head failure. This is particularly encouraging in light of the numerous code failures experienced by the users of previous versions of the code when calculating the later stages of a severe accident. The results from the limited time step studies indicate that not only is the code much more stable than previous versions but that it can take advantage of Courant violating time steps in many cases without significant impact on the results.

The assessment of the code against a relatively wide sample of early phase data indicated that the code can typically predict the response of representative fuel assemblies, and in the case of the LOFT LP-FP-2, a representative reactor coolant system with an accuracy comparable to the uncertainties in the experiments themselves. The variation between calculated and observed behavior is less than 20% for thermal response, fuel rod ballooning and rupture, zircaloy oxidation and hydrogen production, and the liquefaction and relocation of the different structures in the core with some variations substantially less. The most obvious improvements were for the (a) early relocation of core materials associated with Inconel spacer grid-fuel rod cladding and BWR control blade-channel box material interactions and (b) accelerated heating, melting, and hydrogen production during reflood. Although there is still a systematic underprediction of about 50% in the hydrogen production during reflood, previous versions of the code were incapable of predicting any of the important effects observed during the reflooding of damaged bundles.

The assessment using early phase data also indicated that there are several areas where additional model development or a refinement of the experimental analysis may be required to reduce the variation between calculated and measured data. Modeling deficiencies identified included those in the (a) fuel rod ballooning models associated with oxide strengthening of the cladding, (b) fuel dissolution models where the fuel is maintained near the cladding melting temperature for an extended period of time, (c) oxidation models where the oxidation may be overpredicted during the accelerated heatup prior to cladding melting and melt relocation and underpredicted during melt relocation and reflood. Areas where the variation between calculated and observed behavior was relatively large were due to either inadequate modeling of the experimental facility or modeling deficiencies. Modeling deficiencies that may be a major factor in these variations include (a) reflux cooling in the upper bundle for DF-4 and SFD 1-1, (b) upper test train

heating and oxidation for the CORA tests, and (c) axial heat conduction and lower plenum heating for SFD 1-3.

It must be noted, however, that the experiments used in the assessment were limited to an average initial heating rate varying from 0.5 to 1 K/s, with the exception of the PBF SFD-ST experiment. As a result, relatively distinct regions of melting occurred starting with Inconel spacer and control material relocation between 1,500 to 1,700 K, fuel rod cladding melting, and associated fuel dissolution, starting at 2,150 K, and then ceramic fuel and oxidized cladding melting starting at 2,870 K. These distinctive melting zones are a direct result of the limited amount of material oxidation that can take place at this heating rate. However, as discussed in more detail below, none of the calculations for Browns Ferry or Surry, resulted in initial heating rates within this range. The heating rates for Browns Ferry were in the range of 1 to 2 K/s under totally steam starved conditions, while the maximum heating rates for Surry before oxidation were 0.3 K/s with nearly complete cladding oxidation at a temperature below 2,150 K.

Other limitations in the assessment which may or may not have a significant impact on the estimated modeling uncertainty bounds include:

1. The assessment primarily focused upon PWR experiments using fresh fuel. The limited assessment of BWR assembly behavior using DF-4 indicated that the new BWR control blade model performed very well. However, since material interactions dominate the control blade meltdown process, changes in heating rates and oxidation prior to control blade liquefaction may result in substantially different trends. The assessment of the SFD 1-3 and SFD 1-4 tests indicated no significant differences between calculated and observed behavior that could be attributed to the irradiated fuel used in these tests. However, comparisons with other experiments, conducted in a more reducing environment or a lower pressures where fuel foaming may be important, may exhibit different trends.
2. The assessment used the full range of tests in the PBF SFD series but only included a small percentage or no tests from other major experimental programs. A limited number of the CORA, ACRR, and Phebus tests and none of the tests in the Fuel Length High Temperature test series were used for the assessment.
3. The quantitative assessment of uncertainties in important early phase models was based upon three representative experiments and no quantitative assessment was performed for the late phase models. In the latter case, because of the limited availability of experimental results, other techniques will have to be established to quantify modeling uncertainties.

The plant calculations that were performed, a LBLOCA in Browns Ferry and a station blackout in Surry, also were important contributors to the overall assessment. In addition to confirming that the new control blade model was performing as expected, the Browns Ferry calculations indicated that, in the LBLOCA transient, the upper 80-90% of the core heated up relatively quickly resulting in rapid melt relocation to the bottom of the core. As a result, the penetration of the melt through the core plate, and behavior of the core plate in retaining molten control and fuel rod materials, will be the dominant uncertainty in the subsequent behavior. The continuation of BWR plant calculations into the later stages of an accident beyond that used in this assessment will require a series of calculations modeling the core plate and lower plenum in more detail using the COUPLE model in conjunction with user defined bounding studies on melt penetration. Extensions of the new control blade model and the addition of specific core

plate models will be required before the code can automatically continue. The Surry calculations indicated that not only were the late-phase modeling changes working properly but a relatively minor change in the molten pool crust failure criteria to reflect recent experimental results had a dramatic impact on the slumping of material into the lower plenum. Now the ceramic crust that forms as the result of the axial and radial spreading of the molten pool will maintain the molten pool indefinitely if there is adequate cooling on the exterior to remove decay heat and prevent further spreading. However, although this model has not been compared to TMI-2, it seems likely that the behavior of the crust supporting a molten pool that was calculated for Surry is inconsistent with the crust behavior determined to have occurred in TMI-2. As a result, it is expected that additional model development will be required for the crust failure model to represent both the small scale crust failure experiments and the global TMI-2 response.

Also the Browns Ferry nodalization studies indicated that for a LBLOCA transient with a relatively uniform heating rate of 1 to 2 K/s in the upper 80-90% of the core, that there were no significant time and spatially dependent nodalization problems with the code up to the point of blockage formation at the bottom of the core. In the BWR nodalization studies, the following was concluded:

1. Increasing the number of axial nodes above 8 to represent the reactor core does not significantly improve the predicted results although the total oxidation and hydrogen production results show an asymptotic decrease of 15% in increasing the axial nodalization from 8 to 24.
2. Axial nodalization of 5 is inadequate and the results are significantly altered.
3. Increasing the number of radial flow channels from 3 to 7 channels (one representative assembly to 3 representative assemblies) does not have any significant influence on the core temperatures and hydrogen production. The temperatures and total hydrogen production for the 5 and 7 channel models converge. The pattern of damage progression is influenced by the increasing number of channels, the ballooning pattern changes, as does the formation of blockage regions associated with control blade melting. In all cases much of the core is completely liquefied prior to the formation of any blockages at the bottom of the core. Since the ORNL control blade model is not linked to any core blockage or lower plenum heatup models, it is not possible to determine what effect the different number of radial channels will have upon the later stages of the accident although it appears that 3 and 5 channel representations may not be adequate for BWR plant calculations once blockages start to form.

The nodalization studies for a single fuel assembly in the Surry mPWR also indicated that no significant nodalization effects are present. The following was concluded:

1. Increasing the number of axial nodes above 10 did not improve the results although the oxidation and hydrogen production decreased asymptotically by 15% in increasing from 8 to 20 nodes.
2. A variation of time step by a factor of five below and above the Courant limit had relatively little effect on the overall results. The reduction in time step below the Courant limit increased the run time substantially and resulted in an increase in the coolant mass error. The use of the nearly-implicit time step option, that allowed time steps a factor of five greater than the Courant limit, significantly reduced the run time with minimal impact on the results up until accelerated heat-

ing due to cladding oxidation. As a result, it was concluded for problems of this type, that a combination of the nearly-implicit and semi-implicit, which limits the time step to the Courant limit, time step options be used with the nearly-implicit option being used for the initial core uncover until temperatures reach 1,400 K and the semi-implicit option used after that point.

The nodalization studies performed with a representation of the full Surry plant indicates that an adequate nodalization of the reactor core is achieved with five radial channels and ten to twenty axial nodes. Analyses with ten and twenty axial nodes produce almost identical calculated values for time of surge line failure, time of beginning of ceramic melting of the reactor core, and amount of molten core material that slumps to the lower head. The ten axial node case calculated 18% more hydrogen production than that calculated by the twenty axial node case and a 7% earlier time of slumping of a large molten pool than that calculated by the twenty axial node case. The CPU time for the twenty axial node case was a factor of 1.7 times larger than that for the ten axial node case. These factors require evaluation in the planning stages of a severe accident analysis to determine the required extent of nodalization of the reactor core.

7. REFERENCES

1. T. Heames et al., *VICTORIA: A Mechanistic Model of Radionuclide Behavior in the Reactor Coolant System Under Severe Accident Conditions*, NUREG/CR-5545, SAND90-0756, Rev. 1, December 1992.
2. C. M. Allison, C. S. Miller, and N. L. Wade (eds.) *RELAP5/MOD3 Code Manual*, Volumes I through IV, NUREG/CR-5535, EGG-2596, June 1990.
3. C. M. Allison and G. H. Beers, "Comparisons of the SCDAP Computer Code with Bundle Data Under Severe Accident Conditions," *Seventh International SMIRT Conference*, Chicago, IL, August 22-26, 1983.
4. E. C. Lemmon, *COUPLE/FLUID: A Two-Dimensional Finite Element Thermal Conduction and Advection Code*, EGG-ISD-SCD-80-1, February 1980.
5. J. Rest and S. A. Zawadzki, "FASTGRASS-VFP/PARAGRASS-VFP Version 50531, Users Guide," *Argonne National Laboratory Quarterly Report, January-March 1983*, Volume I, NUREG/CR-3689, ANL-83-85, Volume I, June 1983.
6. *PATRAN Plus User's Manual*, Release 2.4, PDA Engineering, Costa Mesa, CA, 1987.
7. *ABAQUS User's Manual*, Version 4.6, Hibbitt, Karlsson & Sorensen, Inc., Providence, RI, 1987.
8. D. M. Snider, K. L. Wagner, and W. Grush, *Nuclear Plant Analyzer (NPA) Reference Manual Mod1*, EGG-EAST-9096, April 1990.
9. K. D. Bergeron et al., *User's Manual for CONTAIN 1.0, A Computer Code for Severe Nuclear Reactor Accident Containment Analysis*, NUREG/CR-4085, SAND84-1204, May 1985.
10. L. T. Ritchie et al., *CRAC2 Model Description*, NUREG/CR-2552, SAND82-0342, March 1984.
11. D. I. Chanin et al., *MELCOR Accident Consequence Code System (MACCS Version 1.5)*, NUREG/CR-4691, SAND86-1562, July 1988, DRAFT
12. C. M. Allison, J. K. Hohorst, C. H. Heath, and K. L. Davis, *SCDAP/RELAP5/MOD3 Assessment; Assessment of Early Phase Damage Progression Models*, EGG-SSRE-10098, February, 1992.
13. C. Slater et al., Development and Assessment of RELAP5/MOD3, 1993 RELAP5 *International Users Seminar*, Boston, MA, July 6 - 10, 1993.
14. C. M. Allison and E. C. Johnson (eds.), *SCDAP/RELAP5/MOD3 Code Manual, Volumes 1-4*, (DRAFT), NUREG/CR-5273, September 1990.
15. P. Hofmann and M. Markiewicz, "Chemical Behavior of (Ag-In-Cd) in Severe LWR Accidents," KfK-4670, 1991.
16. P. Hofmann, E. A. Garcia, and M. Markiewicz, "Results of Separate - Effects Test, Influence of Cladding Oxidation on Chemical Interactions with Other Bundle Components," *International CORA Workshop 1990*, Karlsruhe, Germany, October 1- 4, 1990.
17. E. A. Garcia, P. Hofmann, and A. Denis, "Chemical Interaction Between Inconel Spacer Grids and Zircaloy Cladding, Formation of Liquid Phases Due to Chemical Interaction and Its Modeling, KfK-4921, Karlsruhe, Germany, to be published.
18. P. Hofmann, M. Markiewicz, and J. Spino, "Reasons for the Low-Temperature Failure of BWR Absorber Elements," *Severe Accident Research Program Partners Review Meeting, Idaho Falls, ID, April 10-14, 1989*.

References

19. P. Hofmann, S. Hagen, G. Schanz, and L. Sepold, "Material Behavior in the Large PWR Bundle Experiment CORA-7," *International CORA 1991 Workshop*, Karlsruhe, Germany, September 23-26, 1991
20. J. K. Hohorst, D. T. Hagerman, and C. M. Allison, *Appendix A., Recent SCDAP/RELAP5/MOD3 Analytical Results for International Standard Problem 31 - COR-13*, Appendix to EGG-SSRE-10174, August, 1993.
21. R. W. Wright (presenter), J. K. Hohorst (author), "Analysis of the OECD-CSNI International Standard Problem 31 Using SCDAP/RELAP5," *ISP-31 International Standard Problem 31 Workshop*, Karlsruhe, Germany, October 1992.
22. S. Hagen, P. Hofmann, V. Noack, G. Schanz, G. Schumacher, and L. Sepold, "*Results of SFD Experiment CORA-13 (OECD International Standard Problem 31,*" KfK 5054, February 1993.
23. R. O. Gauntt, R. D. Gasser, and L. J. Ott, "*The DF-4 Fuel Damage Experiment in ACRR with a BWR Control Blade and Channel Box,*" NUREG/CR-4671, SAND86-1443, November 1989.
24. J. K. Hohorst and C. M. Allison, *DF-4 Analysis Using SCDAP/RELAP5*, *Nuclear Technology*, Vol. 98, May 1992, pp. 149-159.
25. D. L. Knudson and C. A. Dobbe, "*Assessment of the Potential for High Pressure Melt Ejection Resulting from a Surry Station Blackout,*" NUREG/CR5949, EGG-2689, May 1993.
26. Z. R. Martinson, et al, "*PBF Severe Fuel Damage Test 1-3 Test Results Report,*" NUREG/CR-5354, EGG-2565, October 1989.
27. D. A. Petti, et al, "*Power Burst Facility (PBF) Severe Fuel Damage Test 1-4 Test Results Report,*" NUREG/CR-5163, EGG-2542.
28. J. K. Hohorst, C. M. Allison, T. J. Haste, R. P. Hiles, and S. Hagen, "*Assessment of SCDAP/RELAP5 Using Data from the CORA Core Melt Progression Experiments*", NURETH-5, Salt Lake City, UT, September, 1992
29. P. Parsons, E. Hindle and C. Mann, "*The Deformation, Oxidation and Embrittlement of PWR Fuel Rod Cladding in a Loss-of-Coolant Accident*", ND-R-1351(S), CSNI State-of-the Art Report, September, 1989.
30. M. Firnhaber, K. Trambauer, S. Hagen, and P. Hofmann, "*International Standard Problem No. 31, CORA-13 Experiment of Severe Fuel Damage,*" OECD-CSNI Preliminary Comparison Report (DRAFT), August 1992.

Appendix A

Summary of Assessment Calculations Using SCDAP/RELAP5/MOD3.1

Appendix A

Summary of Assessment Calculations Using SCDAP/RELAP5/MOD3.1

Both experimental test and full-plant calculations were run on SCDAP/RELAP5/MOD3.1 of the code as part of the assessment process. The full-plant models included Surry, TMI-2, and Browns Ferry. The Surry plant model had been used to support depressurization studies.^{A-1} The TMI-2 plant model is being used to support an ongoing analysis of natural circulation during the early phases of the accident.^{A-2} The boiling water reactor (BWR) plant deck is a more detailed version of a Browns Ferry deck developed for large-break loss-of-coolant accident (LBLOCA) analysis.^{A-3} The experimental analysis test problems included CORA-13, CORA-7, ACRR DF-4, PBF SFD 1-4, PBF SFD 1-3, PBF SFD 1-1, PBF SFD ST, PHEBUS B9+, and LOFT LP-FP-2. The majority of these experimental test decks were developed previously to support a systematic code-to-data assessment of previous versions of SCDAP/RELAP5/MOD3. All of the decks were modified to reflect the new input requirements for SCDAP/RELAP5/MOD3.1.

A.1. KfK EXPERIMENT CORA-13

The CORA-13 experiment was selected for the code assessment effort for two important reasons. First, the experiment is the subject of an OECD-CSNI international standard problem exercise. As a result, the experiment has exceptionally well characterized and documented thermal-hydraulic boundary conditions, on-line measurements, and post-test metallurgical examination results.

Specific calculational results included in this appendix are those requested by OECD-CSNI in the specifications for the International Standard Problem ISP-31.^{A-4} These results include bundle and test train temperatures, hydrogen production, onset of rapid oxidation due to the exothermal zircaloy-steam interaction, blockage formation, and the liquefaction and relocation of bundle materials.

A.1.1 Cora Facility And Test Conditions

The CORA facility test section and bundle, illustrated in Figure A-1, incorporates a representative 2 m high fuel rod bundle with a 1 m electrically heated region that simulates decay power. The CORA-13 test bundle, configured to represent a PWR, consists of the equivalent of a 7x7 array of fuel and absorber rods with the corners removed. The test bundle is surrounded by an insulating shroud consisting of a 1.2 mm thick Zircaloy-4 liner and fibrous ZrO_2 insulating material, 19 mm thick. Windows, 30x40 mm, were cut into the insulating shroud at three elevations, 390, 590, and 790 mm, to allow viewing and video recording of bundle damage progression during the experiment. All structures in the facility above the 1,471 mm level and below the -220 mm level in the bundle were cooled to near room temperature by water.

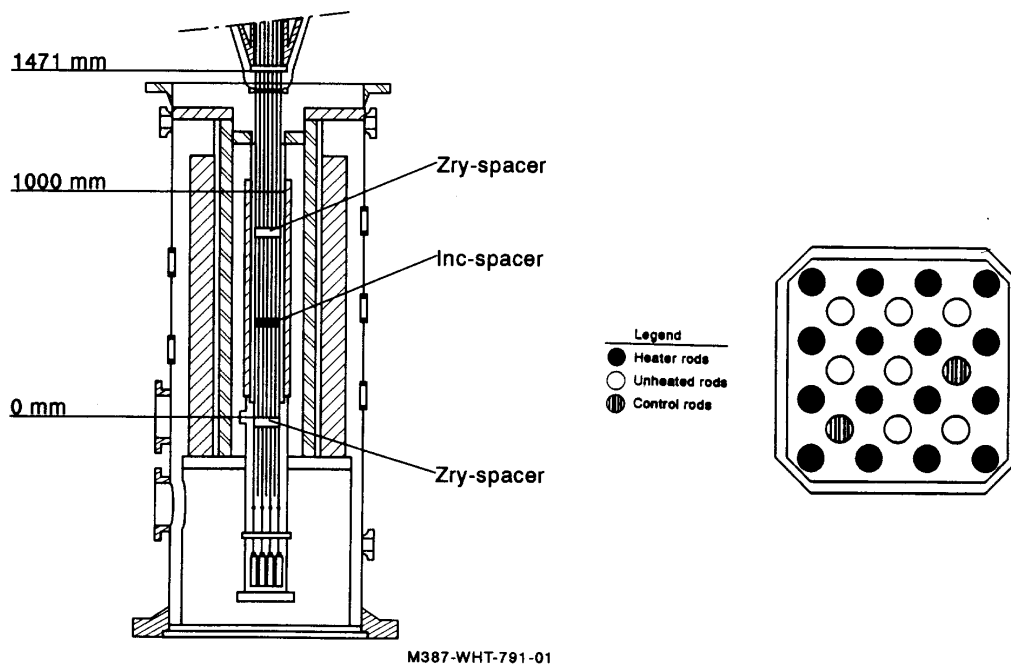


Figure A-1. Schematic of the CORA facility test section and the test bundle.

The CORA-13 bundle consisted of 16 electrically heated simulator rods of typical PWR size. These simulator rods consisted of a central 6 mm in diameter tungsten heater element surrounded by annular UO_2 pellets clad with zircaloy. Intermixed with the heater rods were 7 unheated fuel rods and 2 absorber rods. The unheated rods, of typical PWR size, consisted of solid UO_2 pellets surrounded by Zircaloy-4 cladding; the absorber rods, typical of those used in a PWR, consisted of Ag (80%), In (15%), Cd (5%) absorber material sheathed in stainless steel inserted into a Zircaloy-4 guide tube.

Three spacer grids were used in the bundle to maintain the positioning of the rods during the experiment. The spacer grids at the 880 and -5 mm elevations were made of Zircaloy-4, whereas the spacer grid at the 495 mm elevation was made of Inconel 718.

A.1.1.1 Test Conditions

The CORA-13 test was divided into three distinct phases clearly specified by the experiment organizers, (a) the gas preheat phase, (b) the transient phase, and (c) the cooling phase. During the gas preheat phase a low constant power of 0.65 kW was input to the heater rods while 8 g/s of preheated argon flowed through the bundle.^{A-4} During this phase, the bundle insulation was equilibrated at temperatures sufficiently high to prevent steam condensation during the test. System pressure was maintained at the desired test pressure of 0.22 MPa. During the transient phase, bundle heatup was accomplished by a rise in total bundle electrical power from 6 to 27 kW over a period of 1,750 seconds. Power to the heater rods was increased linearly with time to develop a heatup rate equal to 1 K/s up to the onset of rapid oxidation. Power to the heater rods was maintained at maximum for several hundred seconds. Throughout the test, argon flow through the bundle was maintained at 8 g/s. Steam flow at a rate of 6 g/s was introduced into the bundle 300 seconds after the initiation of power to the heater rods. Superheated steam flowed through the bundle for 1,600 seconds until the termination of power at 4,900 seconds to the simulator rods. The argon or argon/steam mixture heated to 1,000 K in a superheater, cooled as it flowed through the 40 foot connecting pipe to the bundle inlet. The bundle inlet temperature remained near 800 K during the early phase of the transient, increasing by approximately 200 K, 500 seconds after the initiation of power to the heater rods. Figure A-2 shows the argon and steam flow rates used for the experiment, along with the input bundle electric power. The cooling phase of the experiment was initiated by the rise of the quench cylinder starting at 4,870 seconds and the termination of electric power to the heater rods 30 seconds later. The water filled quench tank was raised at a rate of 1 cm/s over the hot bundle.

Throughout the test, bundle temperatures and conditions were monitored by a data acquisition system consisting of numerous thermocouples, pyrometers, boroscopes, mass spectrometers, electrical current and voltage monitors, and computers. Damage progression of the bundle core was viewed and recorded using video monitors. Upon completion of the test, the bundle was sliced into small sections and a metallurgical examination performed.

A.1.2 Changes to the Input Model

Changes were made to the input model to better represent the conditions in the test facility during the test. The original model used for the analysis was developed from models developed for earlier CORA tests and did not represent lower bundle and plenum conditions during reflood, heater rod electrodes, or individual fuel rods adequately. The changes made to the input, using only provided or published material property data, temperature and pressure histories provided by the experimenters, bounding sensitivity

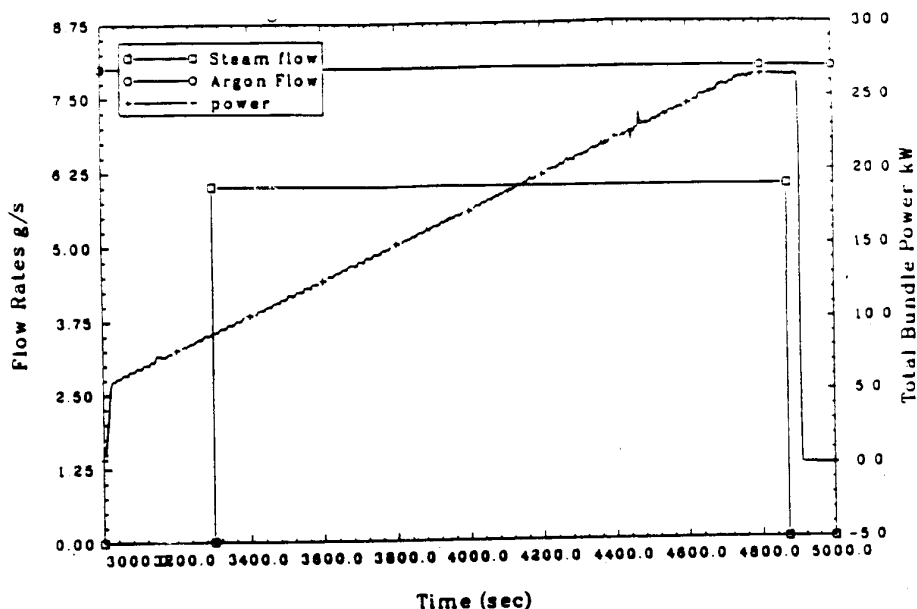


Figure A-2. Argon and steam flow rates used during the CORA-13 experiment.

studies of uncertainties in the test conditions, and the default variables in the code are summarized in this section.

A.1.2.1 Lower Bundle Modeling Prior to and During Reflood

In earlier input models of the CORA test facility the lower region of the test bundle was modeled using four RELAP5 volumes, one for the inlet steam mixing chamber, one for the first lower plenum region, one for the second lower plenum region and one for the reflood tank. All volumes except the reflood tank were assumed to contain steam at 2.2 Bar pressure. Between the reflood volume and the second lower plenum volume a time dependent junction was used to simulate the rising of the reflood tank over the bundle. Heat structures, representing the heated and unheated fuel rods, were placed in all lower plenum volumes except the volume representing the reflood tank. Power was input to the heated rod to simulate decay heat in the core. As a result temperatures in the lower quarter of the bundle were overpredicted since the lower 200 mm of the fuel rods that were submerged in water were not correctly represented in the input model.

To eliminate this problem changes were made in the input deck to simulate the volume sizes to match the physical structure of the experimental facility better and provide closer agreement with the provided initial conditions. The second lower plenum region is now nearly filled with water at the onset of the problem. Another correction applied to the model was to change the materials used in the lower portion of the heated fuel rods to match the actual materials used during the experiment. The previous input deck considered the upper and lower portions of the heated rod to be tungsten surrounded by annular UO_2 rather than the molybdenum and copper used in these sections of the fuel rod during the experiment. The revised input deck models the upper and lower portions of the heated rods, above and below the 1 m heated zone, as molybdenum and copper, the same size as used in the experiment. When the upper and lower regions of

the heated fuel rod were considered to be tungsten surrounded by UO_2 , the thermal conductivity for the portion of the fuel rod submerged in water and used in the calculation was considerably lower than the thermal conductivity would be if actual values for molybdenum and copper were used in their respective regions of the bundle. By changing the materials in the lower regions of the bundle and using the correct material properties for these material, better temperature comparisons are achieved.

A.1.2.2 Heater Rod Electrode

Earlier versions of the code contained an error in the power calculation for the heater rod model, which caused the power to the heater rod to be inaccurately calculated by the code. The error effected a number of calculations that have been reported using earlier versions of the code. In addition to the correction in power, the input deck used for this analysis more accurately represented the simulator rod used to heat the CORA bundle. For previous analyses using the code only the tungsten portion of the rod was represented. For the analysis reported in this appendix exact modeling of the molybdenum and copper portions of the heating element as well as the heating attributed to these sections of the heater were included. Only data furnished in the problem specifications report or published material properties for these elements were used in the model.

A.1.2.3 Localized Hot Spots in Bundle

In previous CORA calculations four components were used to model the PWR test bundle. One component was used to represent the seven unheated fuel rods, a second component the simulator rods, a third the control rods, and a fourth to represent the insulated shroud. Using this representation, each component represented the average behavior of that component in the bundle. However in this experiment conditions surrounding each fuel rod or section of the shroud are not identical. Some areas in the test bundle can experience localized hot spots due to local inhomogeneities in power generation, heat transfer or flow conditions, during the bundle heating, melting and reflood. To simulate the effect of these hot spots in the test, an additional SCDAP fuel rod component, component 5, with steam starvation limits, rather than vapor diffusion limits, was added to the input deck.

A.1.3 Results of the Calculations

A.1.3.1 Influence of the Material Interaction Model

Results of calculations performed with SCDAP/RELAP5/MOD3 indicated that the inclusion of the grid spacer/material interaction model impacted the calculated core damage progression in the following manner: (a) initial fuel rod clad failure occurred near the Inconel grid spacer at a temperature substantially lower than calculated in earlier versions of the code; (b) cladding began to liquefy at temperatures near 1,500 K due to eutectics being formed between Inconel from the grid spacer and the zircaloy fuel rod clad; (c) a blockage region consisting of accumulated melted debris formed near the location of the grid spacer. Figure A-3 compares the calculated unheated fuel rod temperature from the earlier calculation^{A-5} using SCDAP/RELAP5/MOD3 and SCDAP/RELAP5/MOD3.1 with the measured data at the 750 mm elevation. The figure shows that the calculated temperature response of the bundle components was not adversely effected by the addition of the grid spacer model. The most notable improvement in the calculated results was the formation of a large blockage region near the Inconel grid spacer. Figure A-4, a Severe Accident Nuclear Plant Analyzer (SANPA) snapshot of the bundle end-state shows the blockage

formed at 450 mm elevation agreeing with the published data from the destructive bundle examination.^{A-6} Figure A-5 shows an artist conception of the calculated and measured end-state of the bundle.

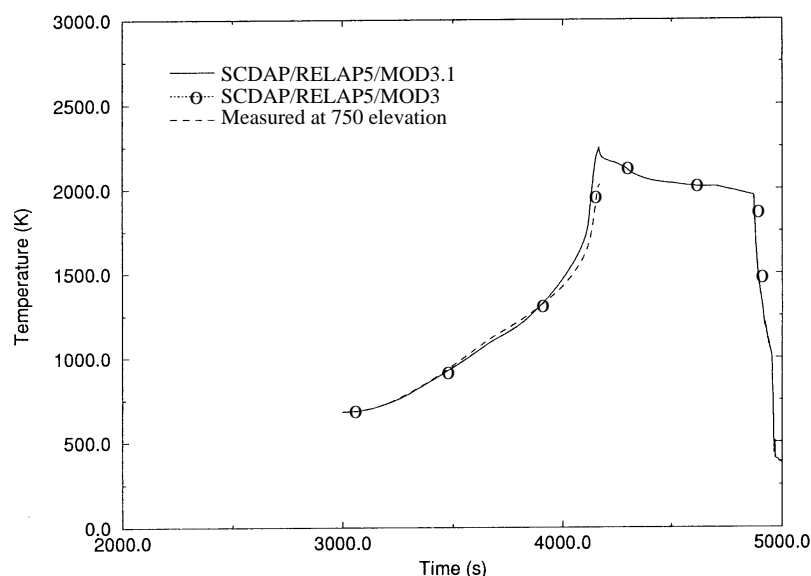


Figure A-3. Comparison of calculated fuel rod temperatures from SCDAP/RELAP5/MOD3 and SCDAP/RELAP5/MOD3.1 with measured at 750 mm elevation.

A.1.3.2 Vapor Limited Diffusion of Steam in Zircaloy

Early versions of the code prior to SCDAP/RELAP5/MOD3.1 limited the oxidation of the fuel rod cladding by steam starvation which did not accurately model the interactions between the zircaloy and gases flowing through the bundle. When the heat/mass transfer analogy based on vapor limited diffusion of steam to the zircaloy surface was implemented in the code, heating rates in the bundle slowed considerably and the onset of hydrogen production was delayed several hundred seconds and occurred over a longer period of time than observed when steam starvation limits were imposed. Figures A-6 to A-8 compare the results of these calculations with the measured data in the upper, middle and lower regions of the bundle and Figure A-9 shows the rate of hydrogen production from both calculations. The predicted bundle heating when vapor diffusion limits on oxidation are used exclusively tend to be delayed considerably from the data in the upper bundle, whereas when steam starvation is used to limit oxidation, temperatures in the upper bundle agree well with the measured data, but lower bundle temperatures are overpredicted. All calculations were performed using a ZrO_2 failure temperature of 2,250 K.

Although representative fuel rods are intended to describe the average behavior of fuel rods in an experimental bundle, in reality, local hot spots may exist due to local inhomogeneities in power generation, heat transfer or flow. Although these hot spots may not influence the overall behavior of the bundle or core, the local heat generation due to oxidation is strongly effected due to the exponential dependency of oxidation rates upon temperature. Consequently a more representative fuel bundle was tried which used one SCDAP fuel rod component to represent the local hot spots in the bundle, and another to represent the average rods in a region. Oxidation in the rod representing the hot spots was limited by steam starvation, and in the average rods by vapor diffusion. The predicted temperature response in the bundle using this

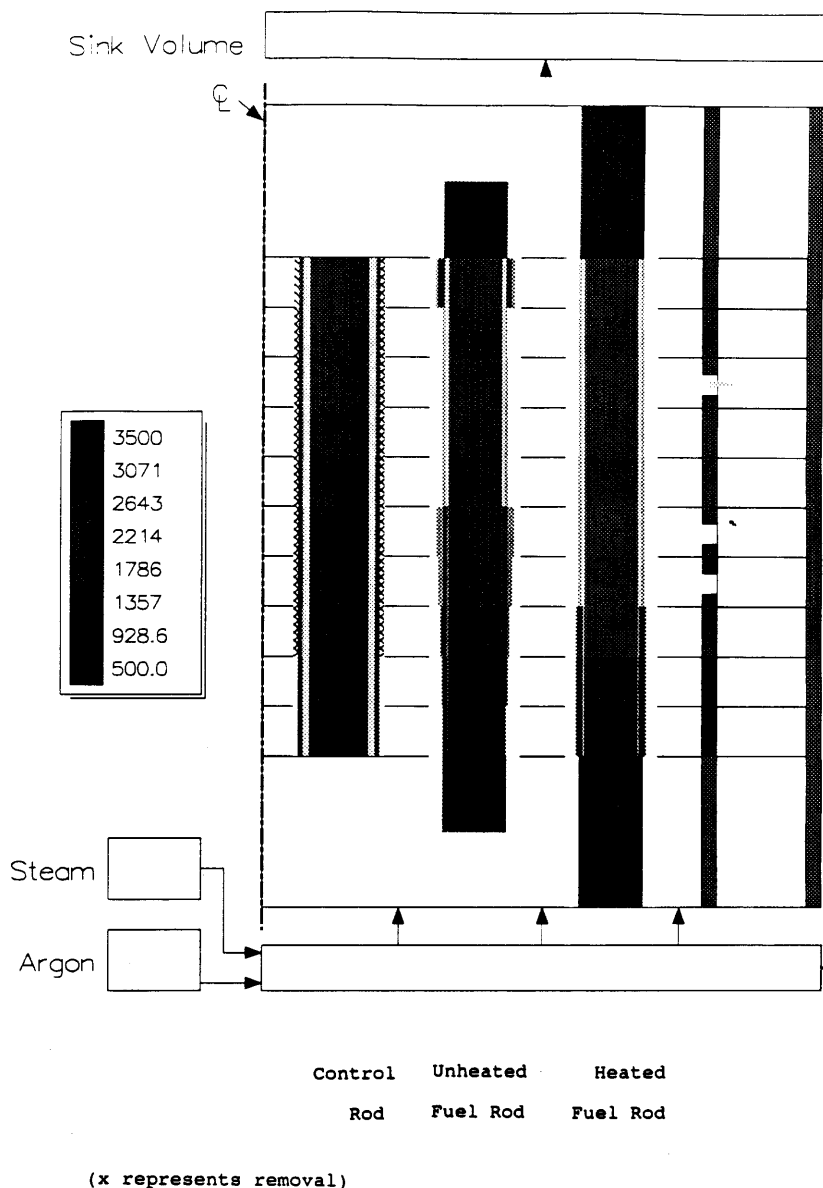


Figure A-4. Severe Accident Nuclear Plant Analyzer representation of the bundle end-state with grid spacer model in code.

approach, the reflood model activated, and a ZrO_2 failure temperature of 2,250 K agreed well with the measured data. The predicted rate of hydrogen production during the transient reflected the measured rate during the early stages of the experiment as well as the increased hydrogen production during reflood, though the total quantity produced was still underpredicted. Code to data comparisons of unheated fuel rod temperatures at various elevations in the bundle are shown in Figures A-10 to A-12 and a comparison of predicted hydrogen production with the measured is shown in Figure A-14.

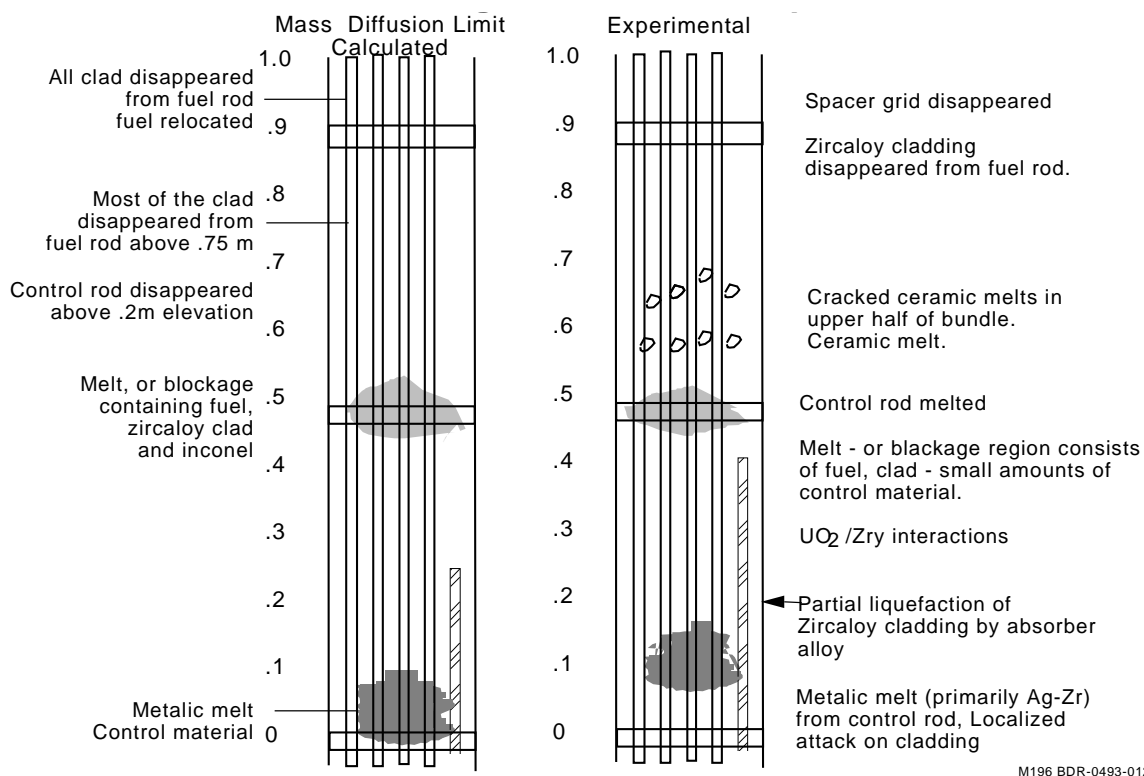


Figure A-5. Artist rendition of the bundle showing the calculated and measured end-state.

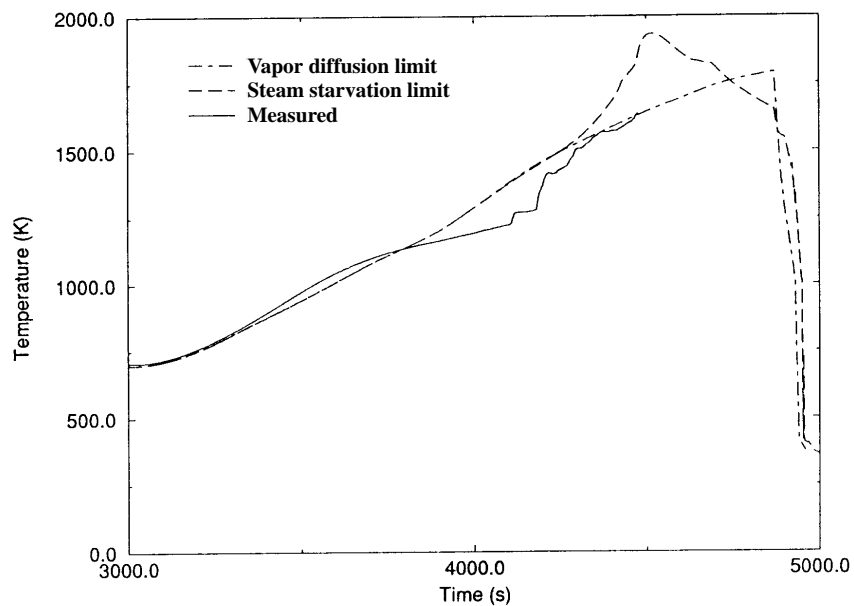


Figure A-6. Calculated and measured temperatures at the 350 mm elevation - vapor diffusion and steamed starved limitations.

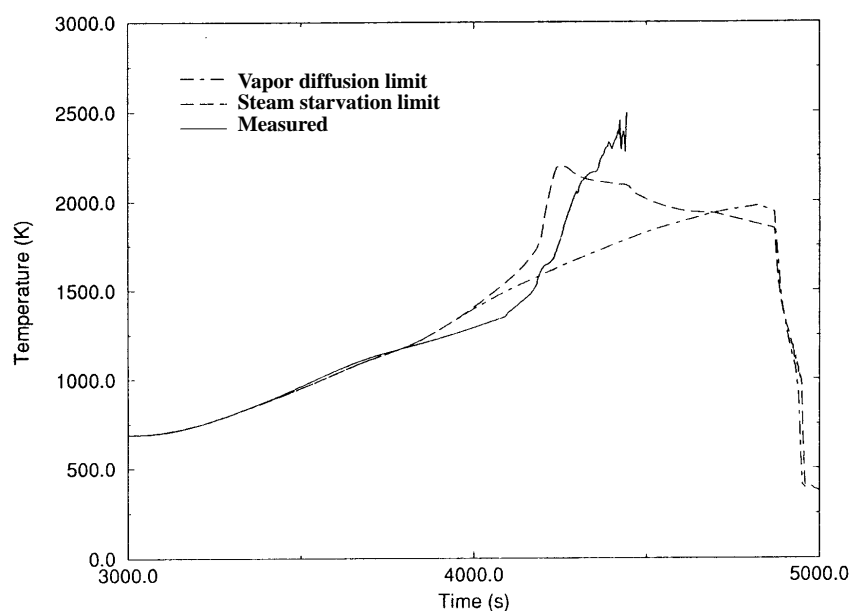


Figure A-7. Calculated and measured temperatures at the 550 mm elevation - vapor diffusion and steamed starved limitations.

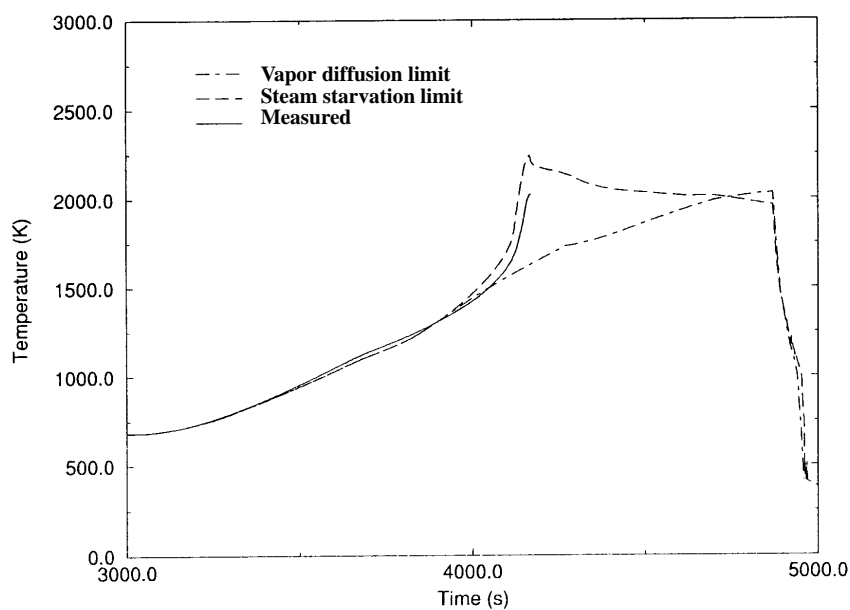


Figure A-8. Calculated and measured temperatures at the 750 mm elevation - vapor diffusion and steamed starved limitations.

A.1.3.3 Effects of the Reflood Model

Changes to the input deck were made to accurately represent the lower plenum volumes and the reflood tank and to activate the reflood and oxide shattering model. Modeling changes were made to

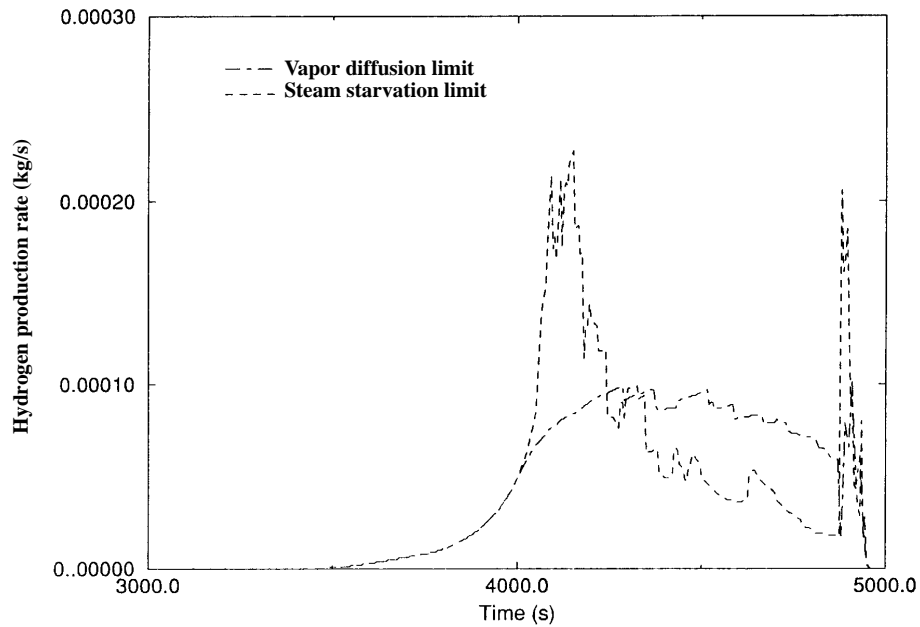


Figure A-9. Hydrogen production rates from the steamed starved and vapor diffusion limited cases.

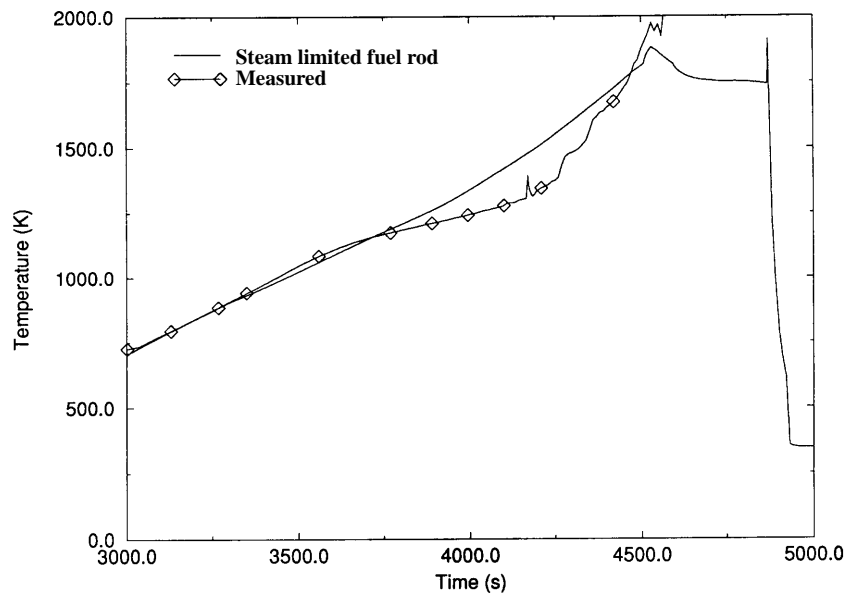


Figure A-10. Calculated and measured temperatures at the 350 mm elevation when reflood and hot spots in the bundle are modeled using a ZrO_2 failure temperature of 2,250 K.

decrease the power in the lower plenum so that the lower heating rates attributable to the molybdenum and copper were reasonable, position the simulator and unheated fuel rods correctly in the lower plenum

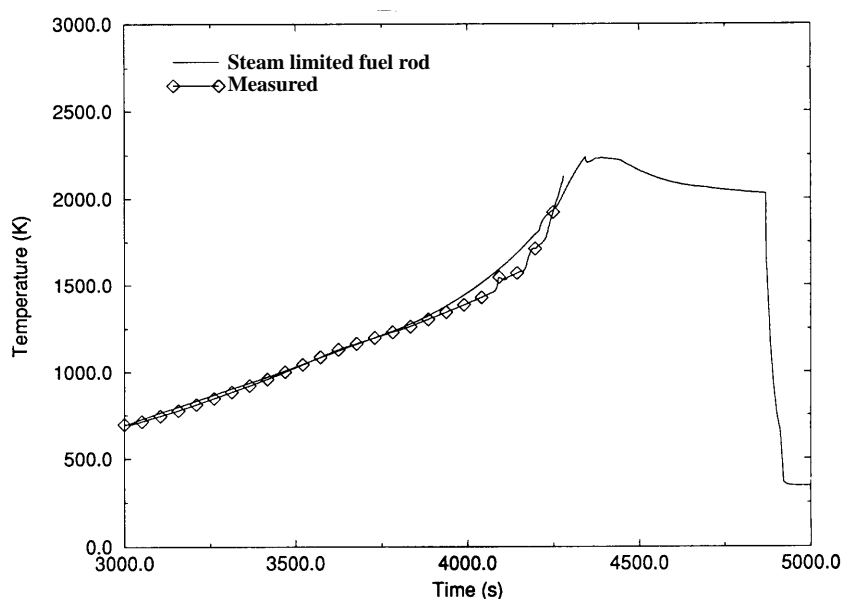


Figure A-11. Calculated and measured temperatures at the 550 mm elevation when reflood hot spots in the bundle are modeled using a ZrO_2 failure temperature of 2,250 K.

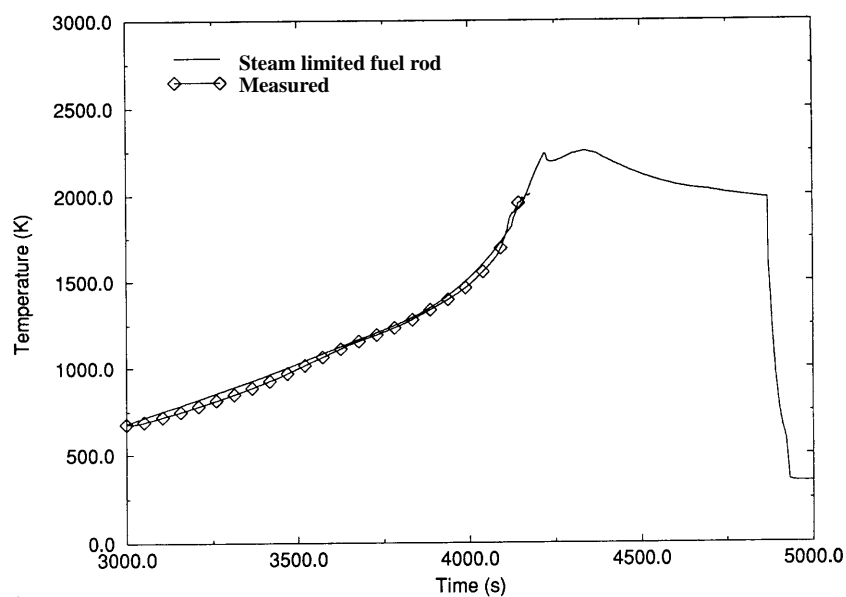


Figure A-12. Calculated and measured temperatures at the 750 mm elevation when reflood and hot spots in the bundle are modeled using a ZrO_2 failure temperature of 2,250 K.

region, and allow RELAP5 to calculate the evaporation rate from the quench tank prior to the quenching phase of the experiment. Using these input changes and a ZrO_2 failure temperature of 2,450 K, the calculated temperature response in all areas of the bundle agrees well with the measured data. Figures A-15 to A-18 show the calculated temperatures at four elevations in the bundle compared to the measured

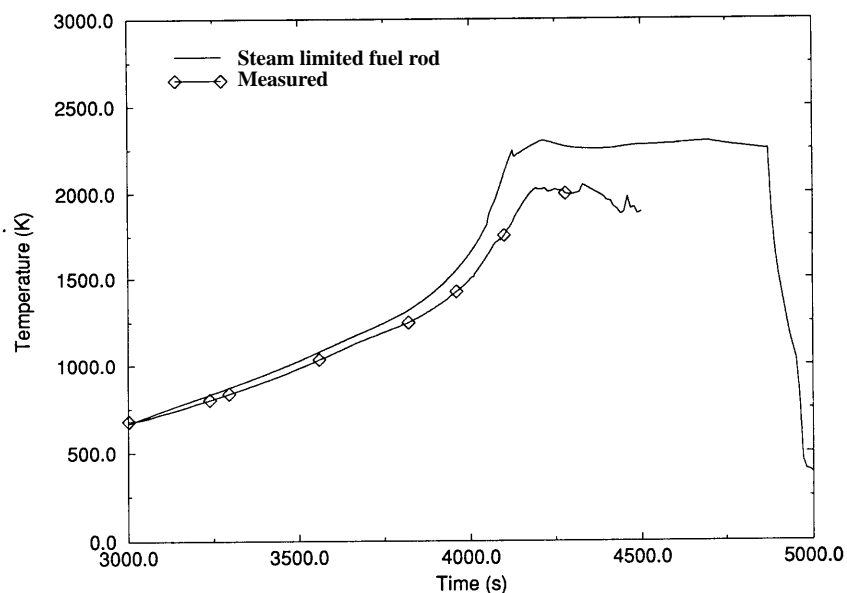


Figure A-13. Calculated and measured temperatures at the 950 mm elevation when reflood and hot spots in the bundle are modeled using a ZrO_2 failure temperature of 2,250 K.

values at the same elevations when the above described modeling changes were used and the reflood model activated.

As shown in the figures the predicted results showed good agreement with the data. The temperature in the lower quarter of the bundle is overpredicted but is improved over previous results. Further improvements will require more detailed modeling of the lower plenum and quench tank. The figures show the predicted temperatures in the upper three-quarters of the bundle agreeing well with the data.

A.1.3.3.1 Hydrogen Production. Figure A-19 shows the predicted hydrogen production rate compared to the measured rate when the reflood model in the code has been activated, hot spots modeled, and the ZrO_2 failure temperature set to 2,450 K. The code is now accurately predicting the hydrogen spike at reflood and the percent of the total predicted hydrogen produced during reflood, although the total calculated amount produced during the experiment is still underpredicted. Table A-1 shows the results of several sensitivity studies performed using the reflood model.

Although it must be confirmed by the experimenters underprediction of total hydrogen by the code may be explained as follows. The reported hydrogen data in ISP-31 reports^{A-4,A-6} appears to have been taken at a distance of approximately 10 m from the core, after the gas had passed through a condenser and into a mixing tank. This could explain some of the time separation between the measured initiation of hydrogen production and that predicted by SCDAP/RELAP5/MOD3.1. More evidence of the effects of

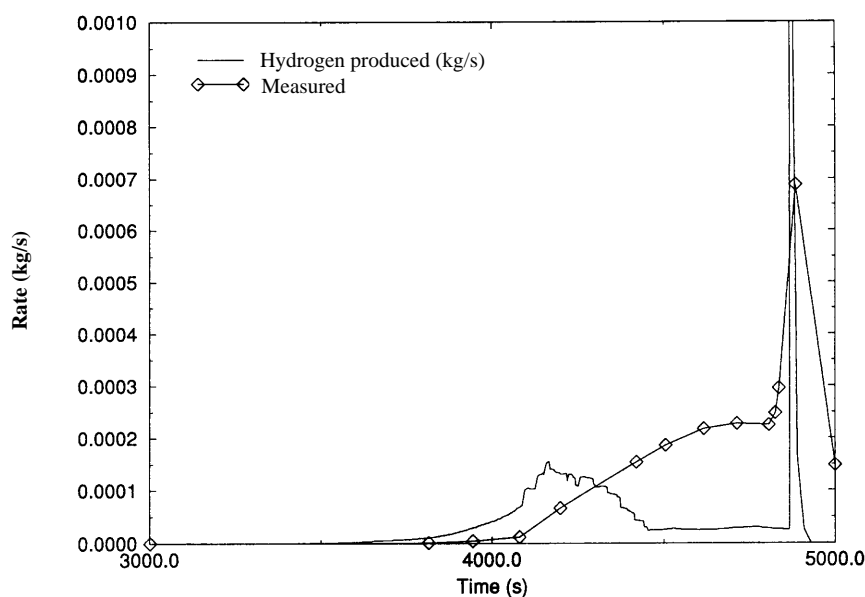


Figure A-14. Hydrogen production with reflood and the hot spots in the bundle are modeled using a ZrO_2 failure temperature of 2,250 K.

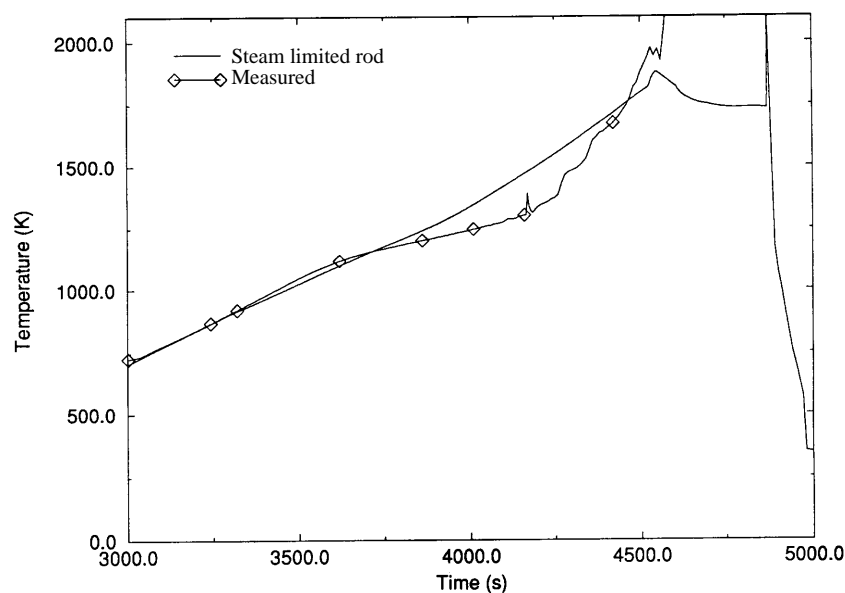


Figure A-15. Calculated and measured temperatures at the 350 mm elevation when reflood and the hot spots in the bundle are modeled using a ZrO_2 failure temperature of 2,450 K.

this delay is noticed in the temperature information. At 4,000 seconds, the measured temperature indicates the onset of rapid oxidation, especially at the 750 and 950 mm elevations, in agreement with the code prediction. The measured rise in temperature associated with the onset of rapid oxidation occurs significantly before measurements indicate hydrogen production to occur during the experiment. The

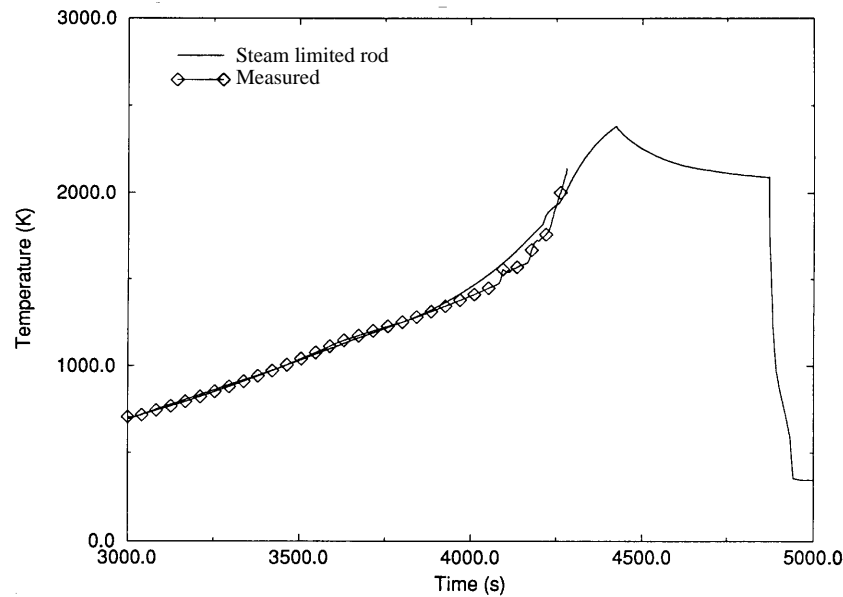


Figure A-16. Calculated and measured temperatures at the 550 mm elevation when reflood and the hot spots in the bundle are modeled using a ZrO_2 failure temperature of 2,450 K.

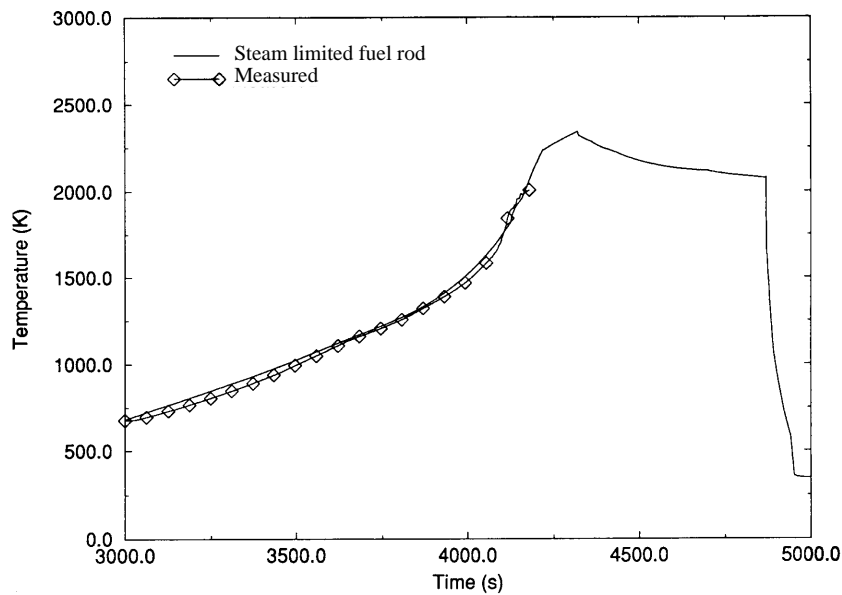


Figure A-17. Calculated and measured temperatures at the 750 mm elevation when reflood and the hot spots in the bundle are modeled using a ZrO_2 failure temperature of 2,450 K.

underprediction of hydrogen between $t = 4,200$ seconds and $t = 4,800$ seconds is due, in part, to melted material relocating. In the experiment the relocating materials continued to oxidize in the reflood tank until cooled, but in SCDAP/RELAP5 once relocated into the RELAP5 modeled areas they are no longer included in the SCDAP oxidation calculation. Another neglected item in the oxidation calculation is the oxidation of the outer surface of the shroud and the upper 0.5 m unheated portion of the bundle. Double

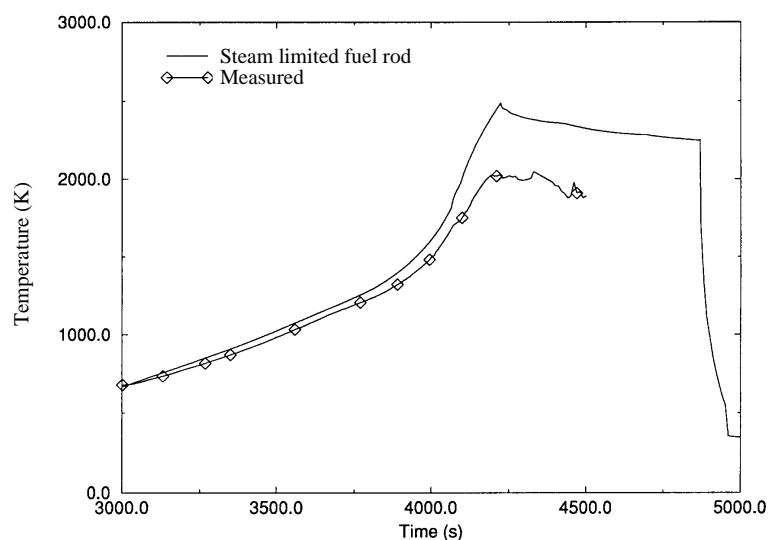


Figure A-18. Calculated and measured temperatures in the bundle at the 950 mm elevation when reflood and hot spots in the bundle are modeled using a failure temperature of 2,450 K.

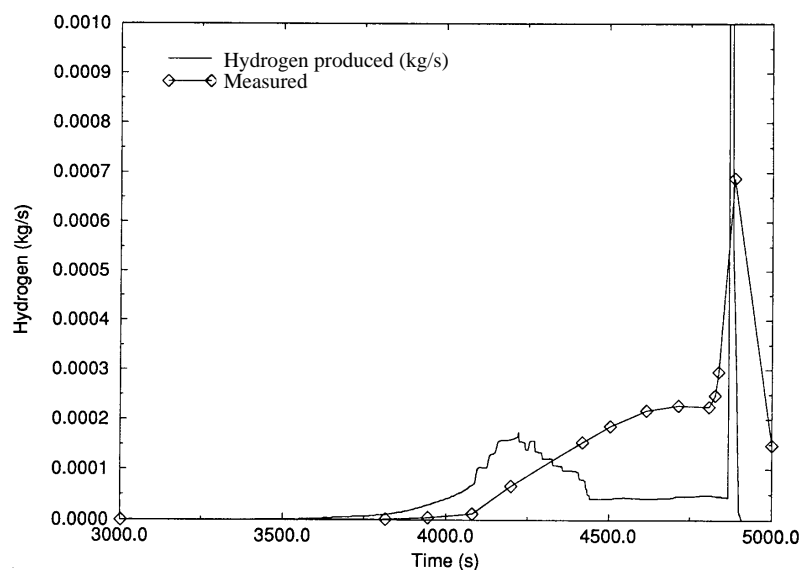


Figure A-19. Calculated and measured hydrogen production rates when reflood and the hot spots in the bundle are modeled using a ZrO_2 failure temperature of 2,450 K.

sided oxidation was not initiated for the shroud liner in this calculation. The reflood calculation discussed in this appendix simply feeds water into the lower plenum region at a given mass flow rate with no modeling of the two state regions. The narrowness and height of the reflood hydrogen spike with respect to the data can be explained in two ways; 1) measured data is likely to be dispersed during the transport to the

Table A-1. Sensitivity Study Comparison for Hydrogen Production.

	Hydrogen produced (g)	Percent produced after reflood
Data	210	48%
Zr fail 2,250 K	87	32%
Zr fail 2,450 K	118	38%
Steam limited	79	12%
Diffusion limited	83	1%

measurement location and 2) the reflood oxide shattering model instantly shatters the oxide over much of the length of the fuel rod whereas during the experiment the oxide layer may have shattered over a short time span.

A.1.3.3.2 End-state of the Bundle. The end-state of the core as calculated by SCDAP/RELAP5/MOD3.1 and the final state of the core from the experiment are in good agreement. The end-state of the bundle determined from the metallurgical examination of the damaged bundle, showed the control rod missing above the 400 mm elevation and significant damage in the 300 to 400 mm range. SCDAP predicted control rod to completely disappear above the 200 mm elevation. The code and the metallurgical examination of the bundle show flow blockages at the second, Inconel, grid spacer location and relocated metallic melt at the bottom of the core.

A.1.3.4 Impact of the New Style Input

The RELAP5 card number style input was used for all calculations using SCDAP/RELAP5/MOD3.1. Replacing the free form input used in SCDAP/RELAP5/MOD3 with the newer RELAP5 style cards caused no noticeable effects on the code predictions but does significantly decrease the time needed to prepare an input deck. The input checking routines clearly describe the errors detected and their location in the input deck. Card number style input increases the reusability of components by allowing the user to apply a cut and paste approach to deck design and since card order is no longer significant the major problems encountered during deck preparation have been eliminated. With the free form style of input used in SCDAP/RELAP5/MOD3, cards and numbers had to be in a required order and form and errors in input were not identified therefore a considerable amount of time could be required to develop and debug the deck.

A.1.4 Conclusions

The code improvements, error correction, and changes to the input model to better describe the test facility and conditions significantly improved the code's ability to predict the test. When the test bundle and heated fuel rods are modeled to accurately describe their physical characteristics prior to the start of the test, the models and default values in the code do an excellent job of predicting the test with the exception of the total hydrogen production, which was underpredicted. Additional refinement of the input model to include the outer oxidation of the shroud liner and upper 0.5 m unheated portion of the bundle may be necessary to improve the prediction of hydrogen production. The use of a separate component to

model areas in the core where hot spots could develop due to localized changes in flow rates, heat transfer or power generation and the activation of the reflood model improve the test results considerably with the measured and calculated values agreeing well.

A.2. KfK EXPERIMENT CORA-7

The CORA series of heatup and meltdown experiments, conducted at Kernforschungszentrum, Karlsruhe (KfK), West Germany, examined core damage progression behavior under severe accident conditions. These steam-fed, out-of-pile tests used a combination of electrically heated and unheated bundle components to simulate decay heating in the core. Due to the ease in configuring a bundle and systematically controlling the test conditions, key severe accident phenomena, such as fuel rod ballooning, bundle meltdown, and quench-induced fragmentation for both PWR- and BWR-configured bundles, were studied.

The CORA-7^{A-7} experiment was chosen primarily to assess modeling improvements in liquefied absorber drainage, nested shroud radiation, and the grid spacer model. Additional improvements assessed implicitly include code reliability and usability improvements related to time smoothing, restart, input, and output.

A.2.1 Experiment Transient Model

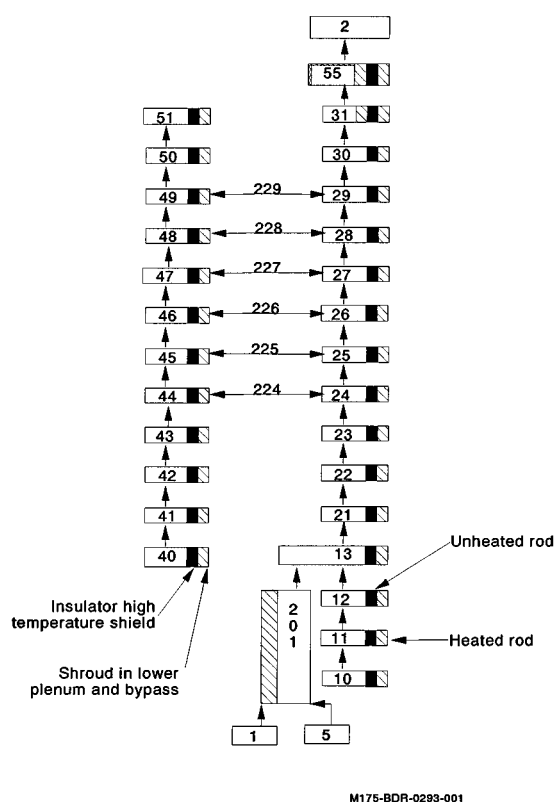
The CORA facility test section incorporated a representative 2 m high fuel rod bundle with a 1 m electrically heated region simulating reactor heatup. The test bundle for the CORA-7 experiment, which simulated a large bundle PWR, consisted of 32 simulator heater rods, 28 unheated fuel rods, and 5 Ag-In-Cd control rods, surrounded by an insulated shroud (a zircaloy liner surrounded by a porous zirconia insulation containing small viewing windows). The electrically heated simulator rods consisted of a central tungsten heater element surrounded by annular uranium dioxide pellets clad with zircaloy. The unheated rods consisted of solid depleted UO₂ pellets clad with zircaloy. The absorber rods used in the CORA-7 PWR experiment were stainless steel tubes containing Ag-In-Cd absorber material inserted into zircaloy guide tubes.

The test procedure used for the CORA-7 experiment was as follows. Hot argon (~1,000 K) was allowed to flow through the bundle for at least 12 hours to bring the bundle and gas to thermal equilibrium. The transient was initiated by applying electrical power to the heater rods with continued argon flow. Approximately 6 minutes into the transient, superheated steam was mixed with the hot argon and allowed to flow through the bundle as the power was linearly increased. After steam flow was terminated, the bundle was allowed to continue heating until the desired peak temperature (2,100 K) was attained. At this time, power to the heater rods was terminated and the system was allowed to cool gradually. Throughout the test, bundle temperatures were monitored by thermocouples attached to all the bundle components and the bundle damage progression was viewed on video displays. Significant events during the CORA-7 experiment are listed in Table A-2.

The SCDAP/RELAP5/MOD3 nodalization for the CORA-7 experiment is shown in Figure A-20. The original CORA-7 deck contained four SCDAP components: a fuel component, which modeled the unheated fuel rods; a simulator component, which modeled the heated rods; an Ag-In-Cd control rod component; and a shroud component. Each component was divided into 10 equal-length axial nodes. The fuel and simulator rods, control rods, and shroud were modeled with 6, 5, and 17 radial nodes, respectively. This CORA-7 deck was converted to the new-style SCDAP input and used as the base case input deck.

Table A-2. Event table for the CORA-7 experiment.

Event	Peak Temperature Experiment (K)	Peak Temperature Base Case (K)	Time (s)
Transient initiated by applying increasing power to the heater rod with continuous argon flow	-	-	3,000
Superheated steam introduced into bundle	-	916.2	3,300
Peak temperature reached	-	2,247.0	4,021
Steam flow and power terminated	2,300.0	-	4,200

**Figure A-20.** Nodalization for the CORA-7 experiment.

In order to assess the nested shroud radiation modeling capability, the original CORA-7 deck was further modified as follows. A second SCDAP shroud component, representing the high-temperature shield surrounding the test bundle, was added, replacing the RELAP5 heat structures previously used to model the high-temperature shield. Also, the radiation input was revised to represent two bundles--one containing the test bundle and the other containing both shroud components. (This input had been implemented previously in a CORA-5 deck used for radiation model development.) This revised CORA-7 deck was also converted to the new-style SCDAP input.

A.2.2 Results

The results obtained using the latest version of SCDAP/RELAP5/MOD3 have been examined for accuracy of code predictions and compared with results obtained both from experimental analysis and previous code versions. Significant findings are reported below.

A.2.2.1 Base Case.

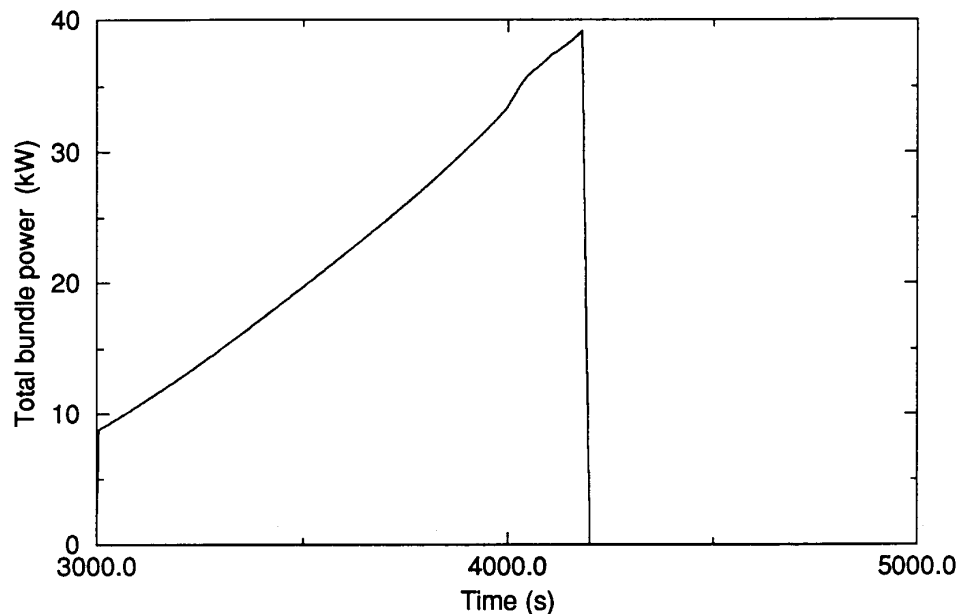


Figure A-21. Total core power for the CORA-7 experiment.

Figure A-21 depicts the total bundle power calculated during the CORA-7 experiment, which closely follows the actual input power curve of the experiment.

The surface temperatures for all four SCDAP components are shown in Figures A-22 through A-29. All of the temperature curves closely follow the progression of the experiment, and most of them agree very well with experimental data. Although the code over predicts fuel rod surface temperature at the 0.35 m axial elevation, the calculated results are in closer agreement with experimental data than previous versions.^{A-8}

Total hydrogen production is shown in Figure A-30. For the CORA-7 experiment, the calculated total amount of hydrogen produced (~105 g) is very close to that measured during the experiment (114 g). Previous SCDAP/RELAP5 calculations overpredicted the amount of hydrogen generated by 66 g.^{A-8}

A.2.2.2 Nested Shroud Case.

The surface temperatures for all four SCDAP components are shown in Figures A-31 through A-35. In this case, the temperature curves exhibit a much slower heatup rate, resulting in lower peak temperatures than are shown in Figures A-22 through A-29. Total hydrogen production is also lower (~75 g). This result

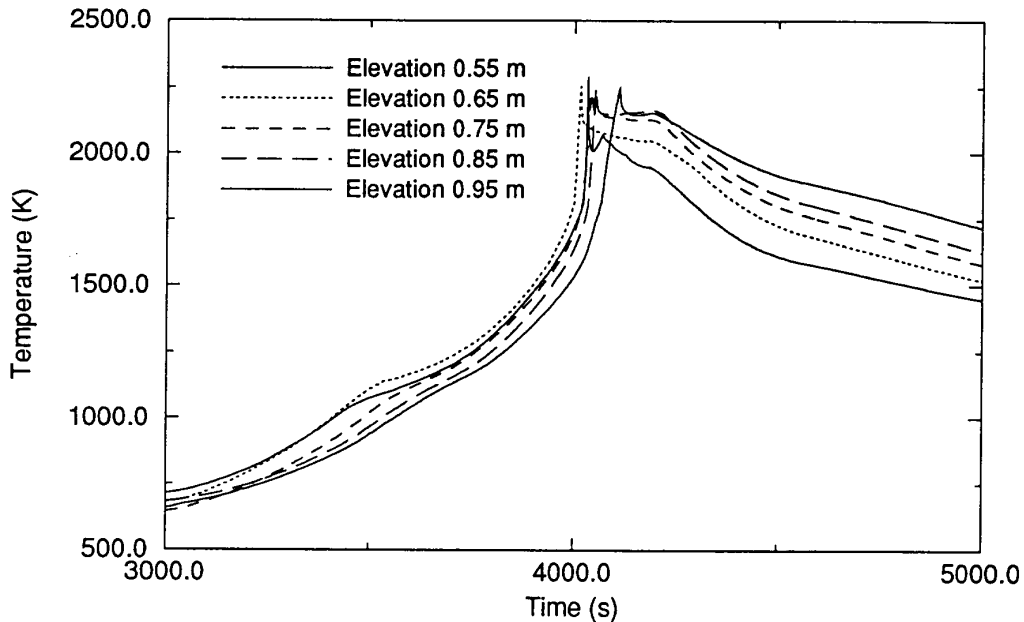


Figure A-22. Surface temperature for the top half of the fuel rod component for the CORA-7 experiment.

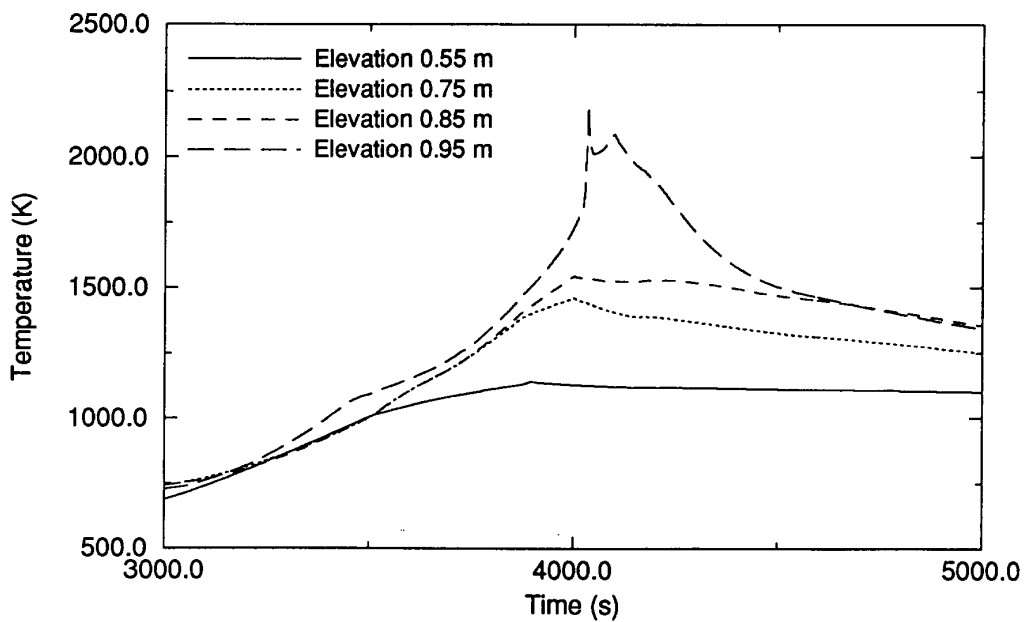


Figure A-23. Surface temperature for the bottom half of the fuel rod component for the CORA-7 experiment.

may be due to an over prediction of the heat capacity of the high-temperature shield, which would cause

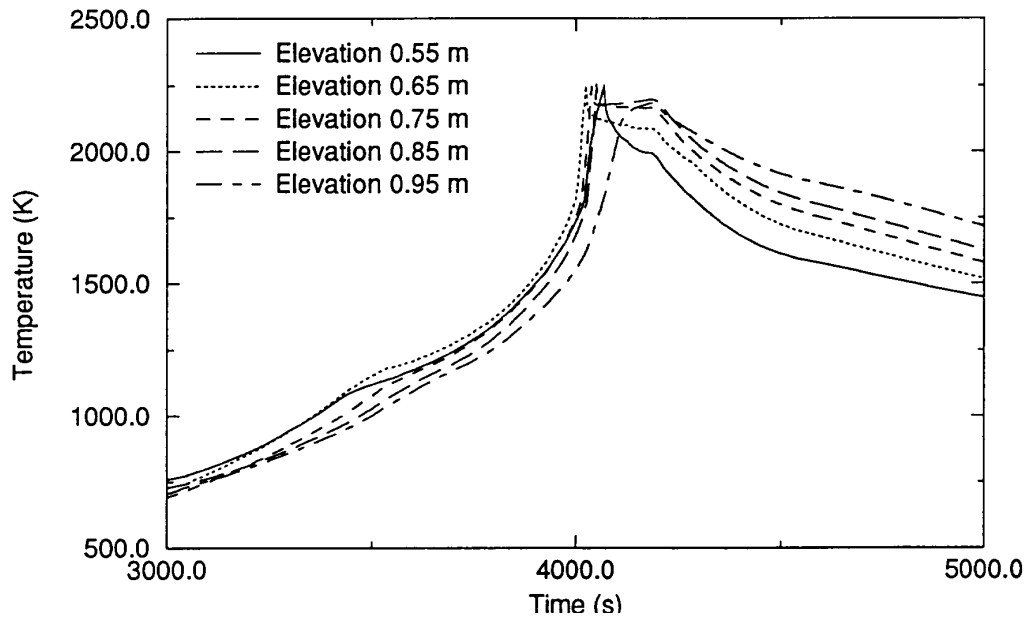


Figure A-24. Surface temperature for the top half of the simulator rod component for the CORA-7 experiment.

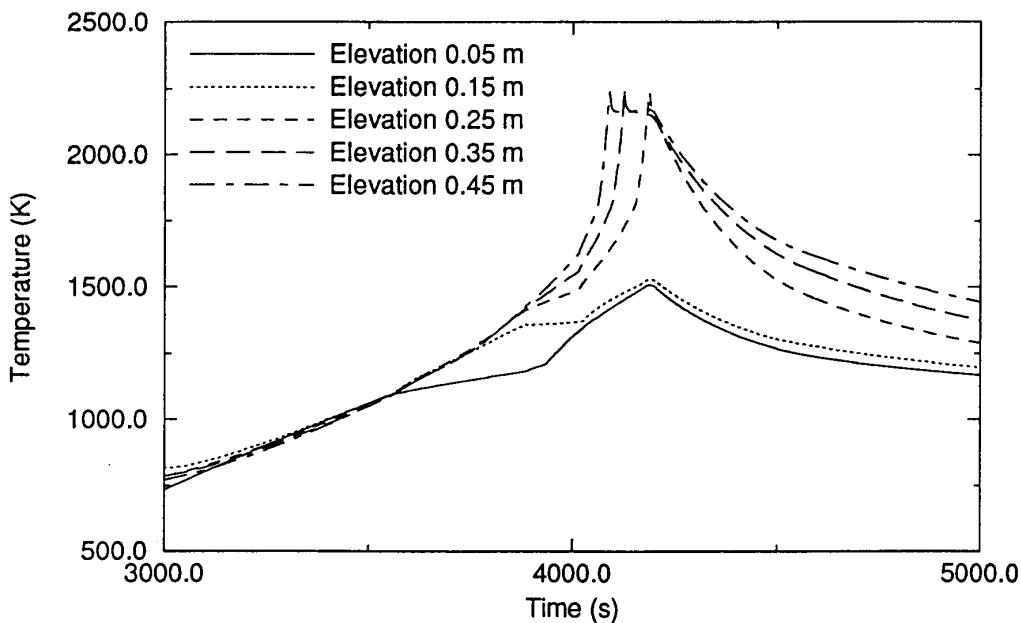


Figure A-25. Surface temperature for the bottom half of the simulator rod component for the CORA-7 experiment.

excessive heat removal from the test bundle.

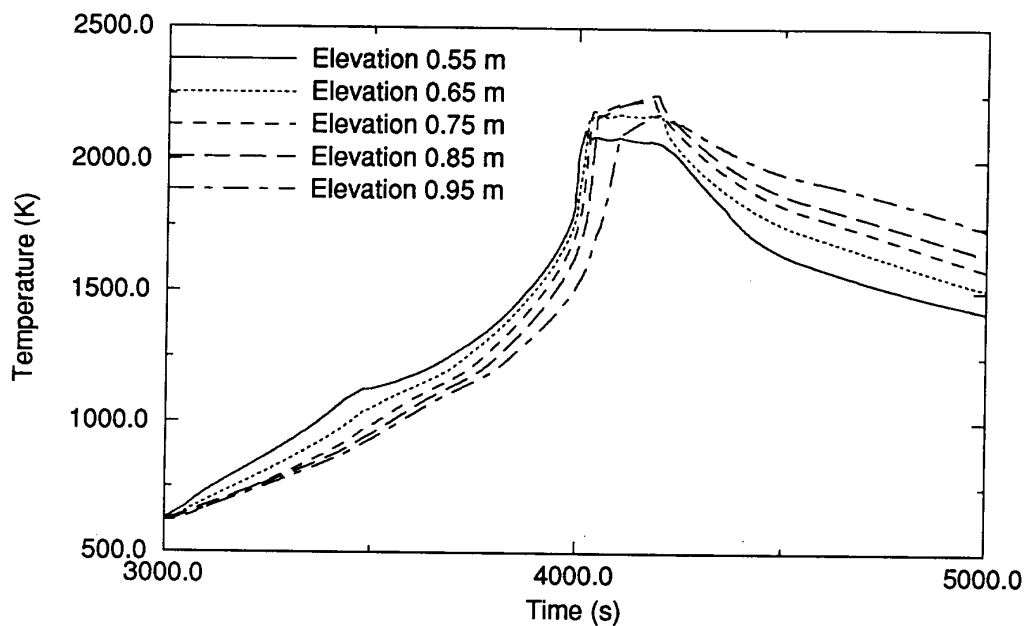


Figure A-26. Surface temperature for the top half of the shroud component for the CORA-7 experiment.

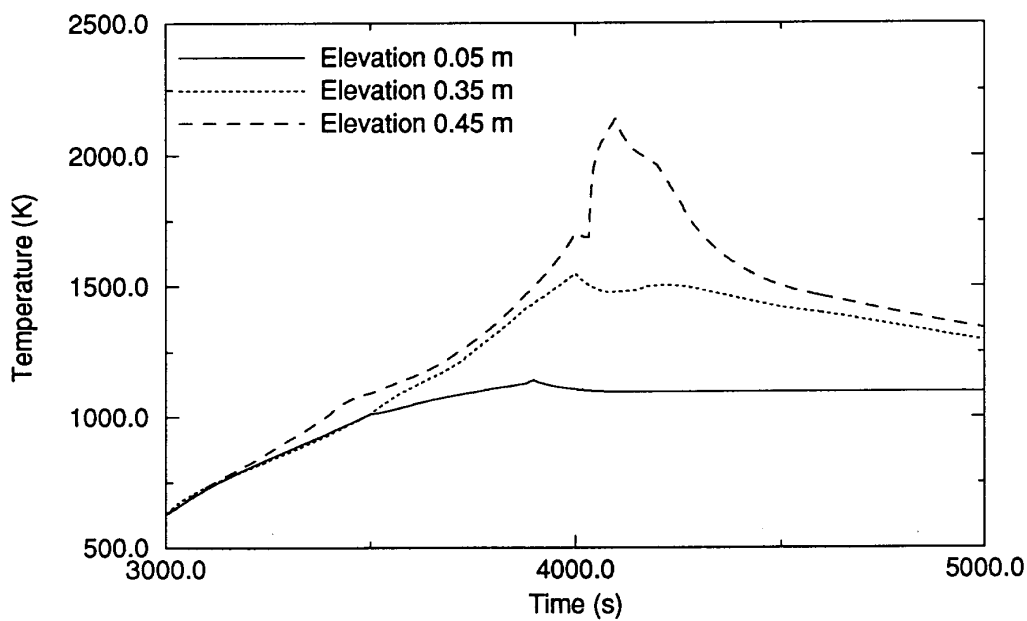


Figure A-27. Surface temperature for the bottom half of the shroud component for the CORA-7 experiment.

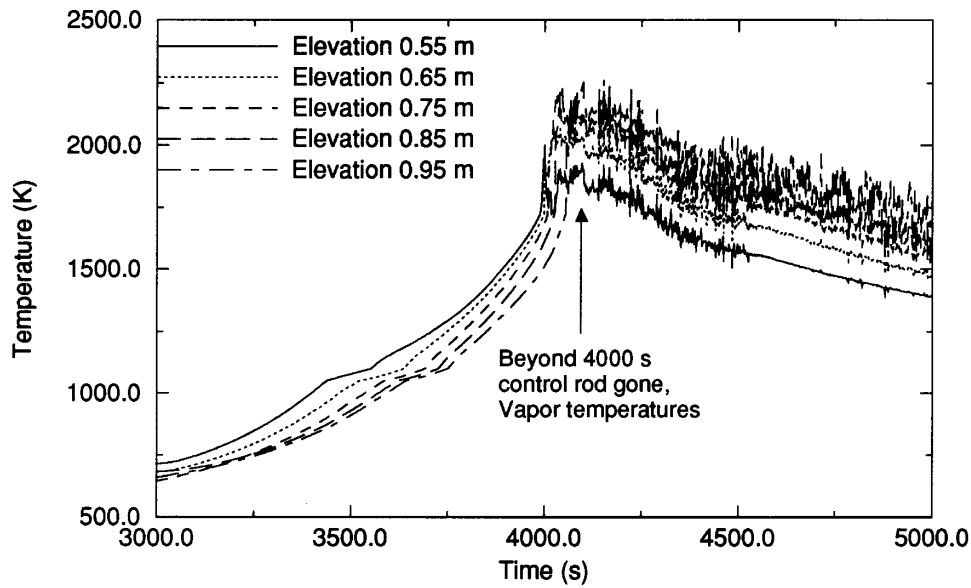


Figure A-28. Surface temperature for the top half of the control rod component for the CORA-7 experiment.

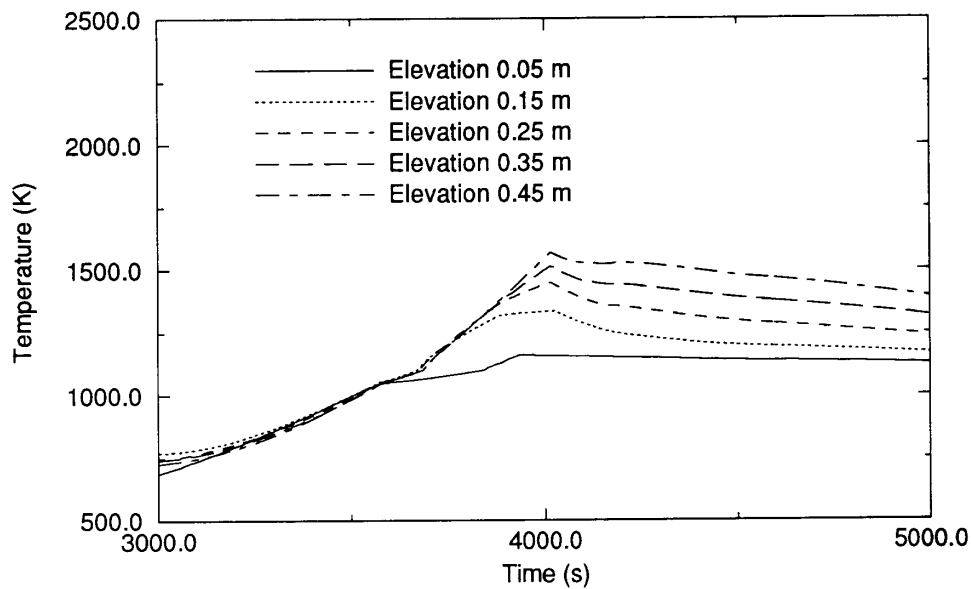


Figure A-29. Surface temperature for the bottom half of the control rod component for the CORA-7 experiment.

A.2.3 Code Performance

In general, SCDAP/RELAP5/MOD3 performed well for the CORA-7 experiment. Figure A-36 depicts the CPU time for CORA-7, which is comparable with previous runs.

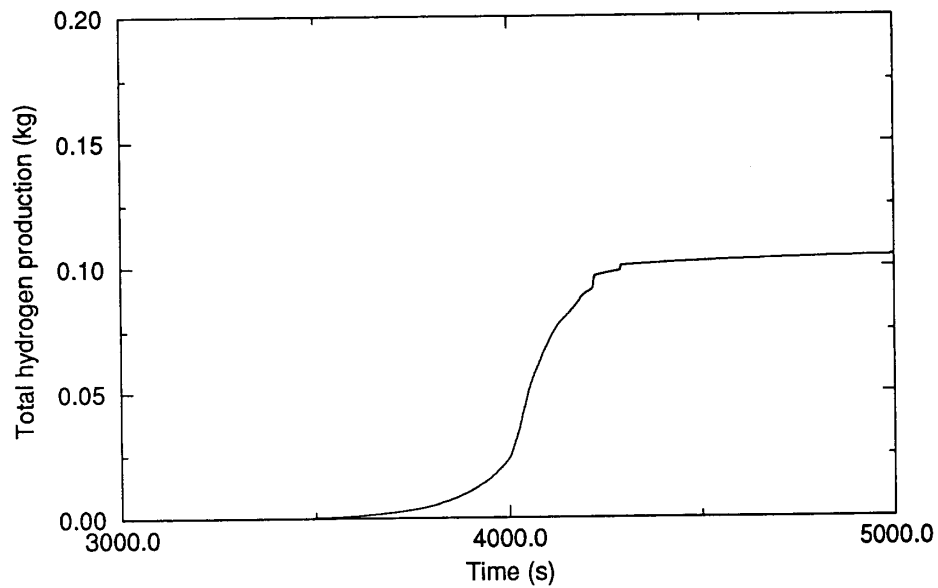


Figure A-30. Total hydrogen production for the CORA-7 experiment.

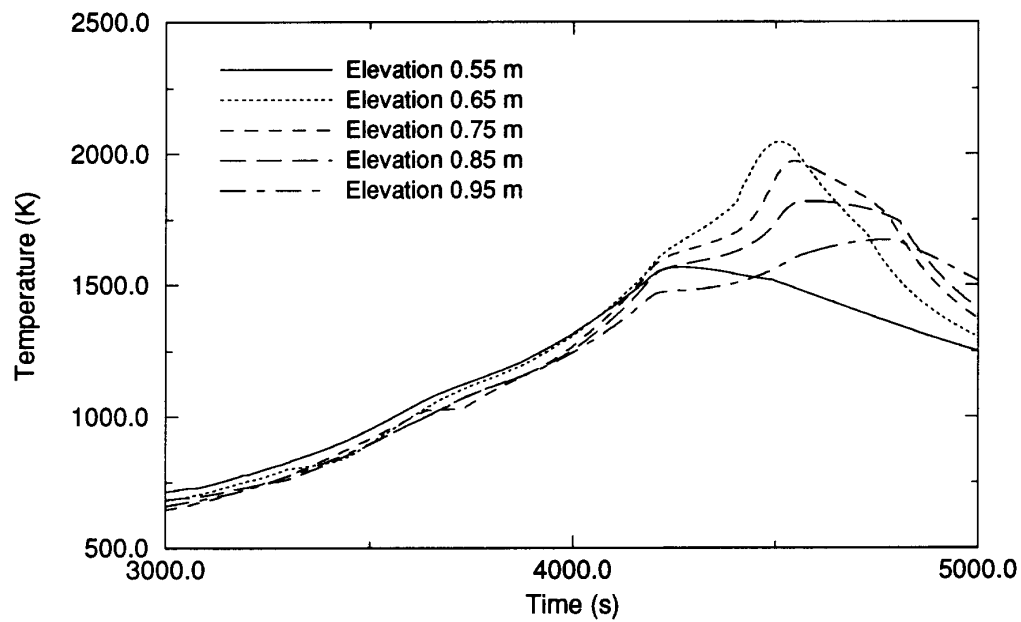


Figure A-31. Surface temperature for the top half of the fuel rod component for the nested shroud model of the CORA-7 experiment.

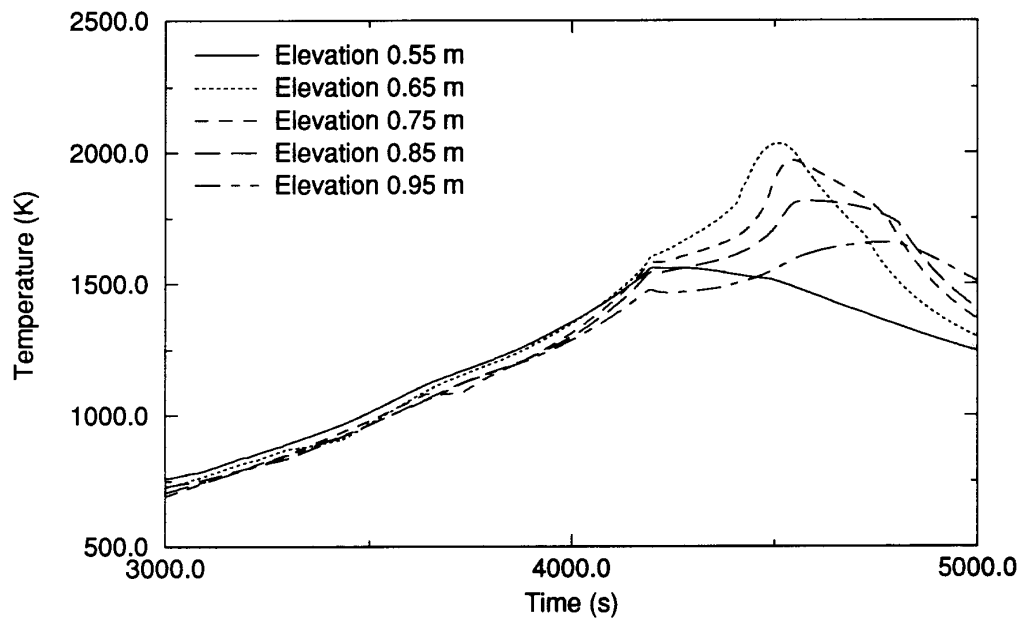


Figure A-32. Surface temperature for the top half of the simulator rod component for the nested shroud model of the CORA-7 experiment.

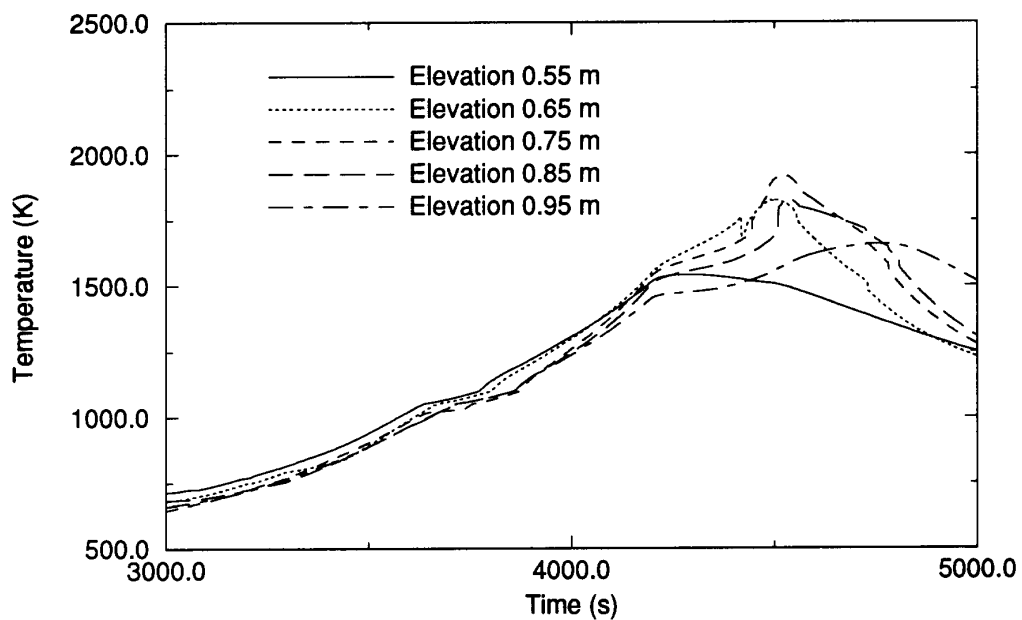


Figure A-33. Surface temperature for the top half of the control rod component for the nested shroud model of the CORA-7 experiment.

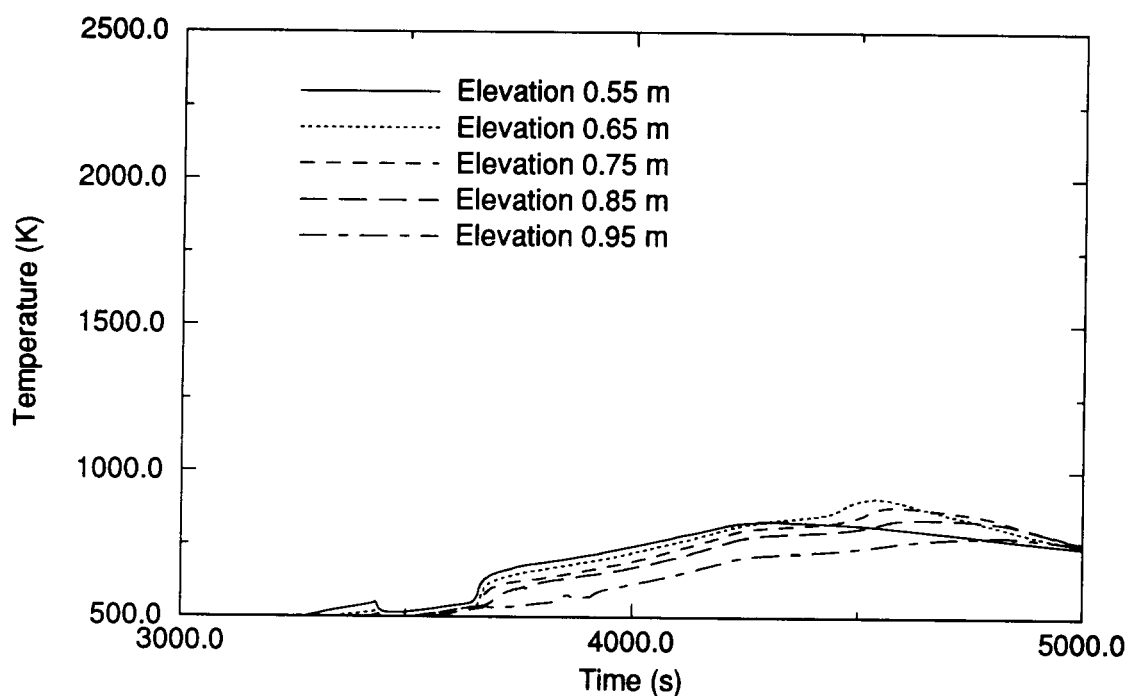


Figure A-34. Surface temperature for the top half of the inner shroud component for the nested shroud model of the CORA-7 experiment.

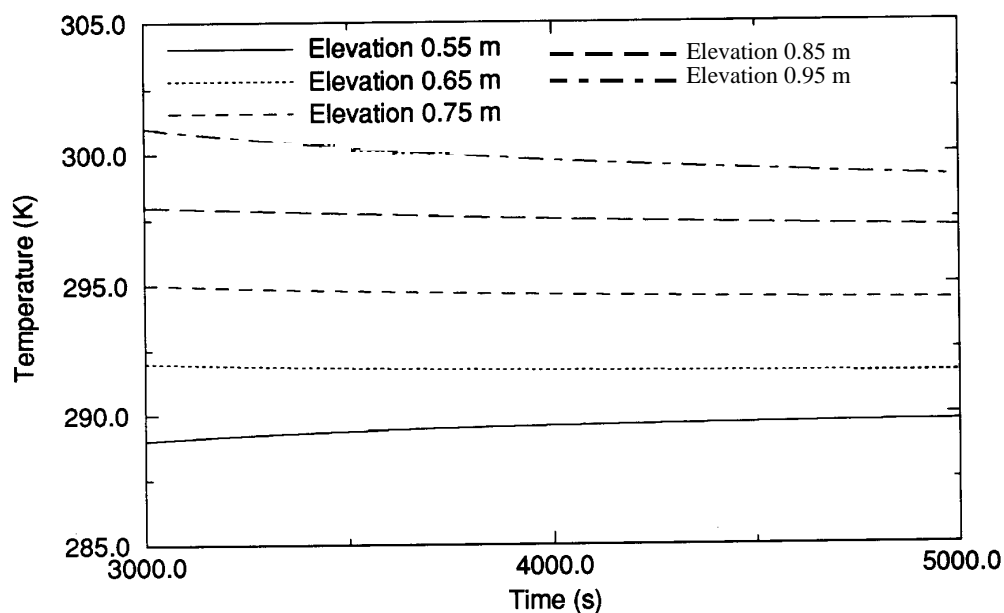


Figure A-35. Surface temperature for the top half of the high-temperature shield shroud component for the nested shroud model of the CORA-7 experiment.

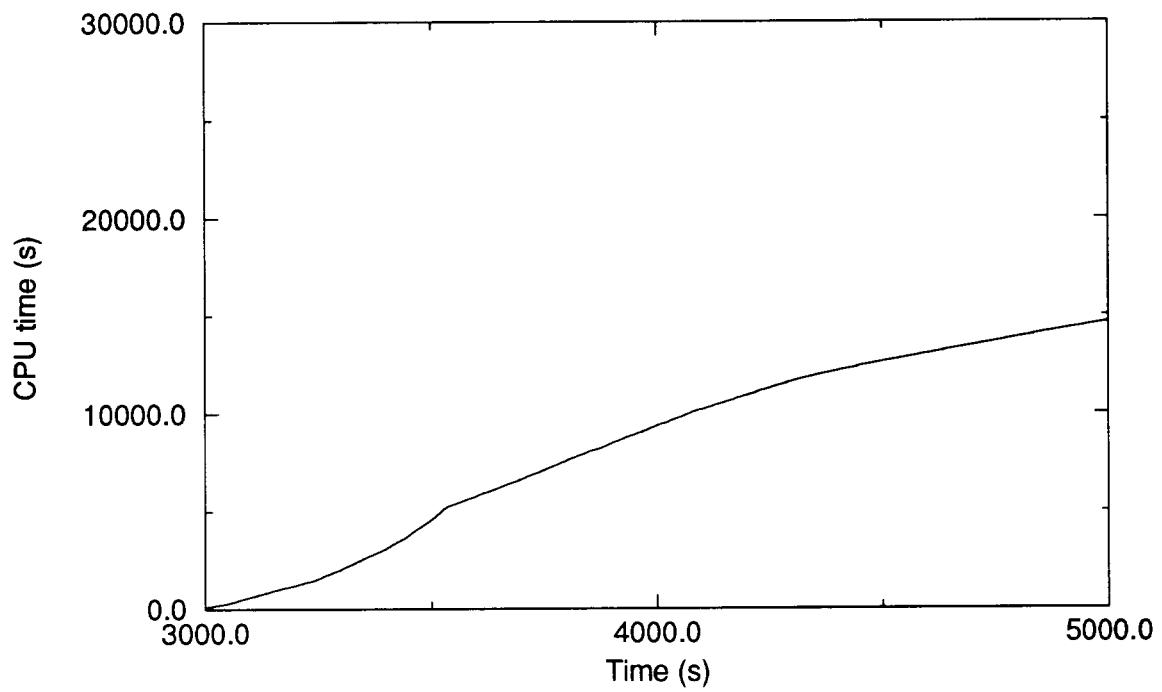


Figure A-36. CPU time for the CORA-7 experiment.

A.3. ACRR EXPERIMENT DF-4

The Annular Core Research Reactor (ACRR) at Sandia National Laboratory (SNL) featured an annular core located at the bottom of a 10 m deep water-filled tank. The experimental fuel bundle and shroud were placed in a dry capsule in the central flux trap region of the driver core. The experimental bundle was heated by fission power. Steam from a superheater was injected into the test section of the capsule. During the nuclear phase of the experiment, the test bundle and fission-product-carrying effluents were contained within the capsule. Hydrogen produced by oxidation of the fuel rod cladding was removed by CuO recombiner beds.

ACRR Experiment DF-4^{A-9} was chosen primarily to assess the performance of the BWR control blade model developed at Oak Ridge National Laboratory (ORNL).^{A-10} Additional improvements assessed implicitly include code reliability and usability improvements related to time smoothing, input, and output.

A.3.1 Experiment Transient Model

The ACRR Debris Formation - 4 (DF-4) experiment was the first in-pile experiment that used BWR structures and control components. Its primary purpose was to examine the phenomena associated with failures of and interactions between the control blade, fuel canister, and fuel rods in the BWR core. The test bundle consisted of a zircaloy-lined ZrO₂ thermal shroud, 14 0.508 m PWR-type fuel rods enriched to 10 wt% ²³⁵U, and a zircaloy channel box containing a B₄C control blade. The control blade consisted of five stainless steel tubes containing B₄C powder surrounded by a stainless steel sheath. PWR fuel rods were chosen because of their ready availability.

The DF-4 experiment consisted of five distinct phases. During the preheat (or start-up) phase, the system was stabilized and pre-transient boundary conditions were established. During the initial nuclear heatup phase, steam flows were reestablished and initial nuclear heating took place. During the test bundle equilibration phase, bundle temperatures were slowly raised to achieve equilibrium among the bundle components. During the pre-transient phase, the test bundle heatup rate was raised to ~1.2 K/s, resulting in control blade failure and the beginning of the oxidation transient phase. This phase continued until both inlet steam and ACRR power were terminated (~8,100 seconds). Throughout the test, bundle temperatures were monitored by thermocouples attached to all the bundle components and the bundle damage progression was viewed on video displays. Significant events during the DF-4 experiment are listed in Table A-3.

The SCDAP/RELAP5 nodalization of the ACRR test train used in the analysis of the DF-4 experiment is shown in Figure A-37. For the RELAP5 portion of the analysis, two parallel channels were used to model the hydraulic conditions inside the 0.5 m test section. The first channel (component 20) represents the region bounded by the outer wall of the channel box on the inside and the stainless steel pressure boundary on the outside; it also contains the zircaloy-clad fuel rods and the porous and ceramic ZrO₂ insulation. The second channel (component 30) represents the thermal-hydraulic conditions inside the channel box and surrounding the stainless steel B₄C control blade. The pressure boundaries at the inlet and outlet of the test section were modeled by two time-dependent volumes (10 and 60). The steam flow split into the test section (80% to the fuel rod channel and 20% to the control blade channel) was modeled by two time-dependent junctions (111 and 112).

Table A-3. Event table for the DF-4 experiment.

Event	Peak Temperature Experiment (K)	Peak Temperature Base Case (K)	Peak Temperature Blade Case (K)	Time (s)
Preheat phase	473	-	-	0 - 5000
Initial nuclear heating phase				
Fuel	500 - 1,175	495 - 1,218	500 - 1,216	5,000 - 6,500
Blade	500 - 600	500 - 729	500 - 530	
Test bundle equilibration phase				
Fuel	1,175 - 1,375	1,218 - 1,622	1,216 - 1,714	6,500 - 7,200
Blade	600 - 1,300	729 - 1,322	514 - 1,257	
Pretransient phase				
Fuel	1,375 - 1,675	1,622 - 2,620	1,714 - 2,579	7,200 - 7,550
Blade	1,300 - 2,000+	1,322 - 2,657	1,257 - 1,506	
Blade failure:				7,440
Blade	1,550	2,082	1,506	
Blade sheath			1,661	
Channel box			2,124	
Oxidation transient phase	1,675 - 2,400+	2,620 - 2,933	2,563 - 3,094	7,550 - 8,100
Fuel rod failure	1,975	2,633	2,563	7,550
Cooldown		-	-	8,100 - 9,000

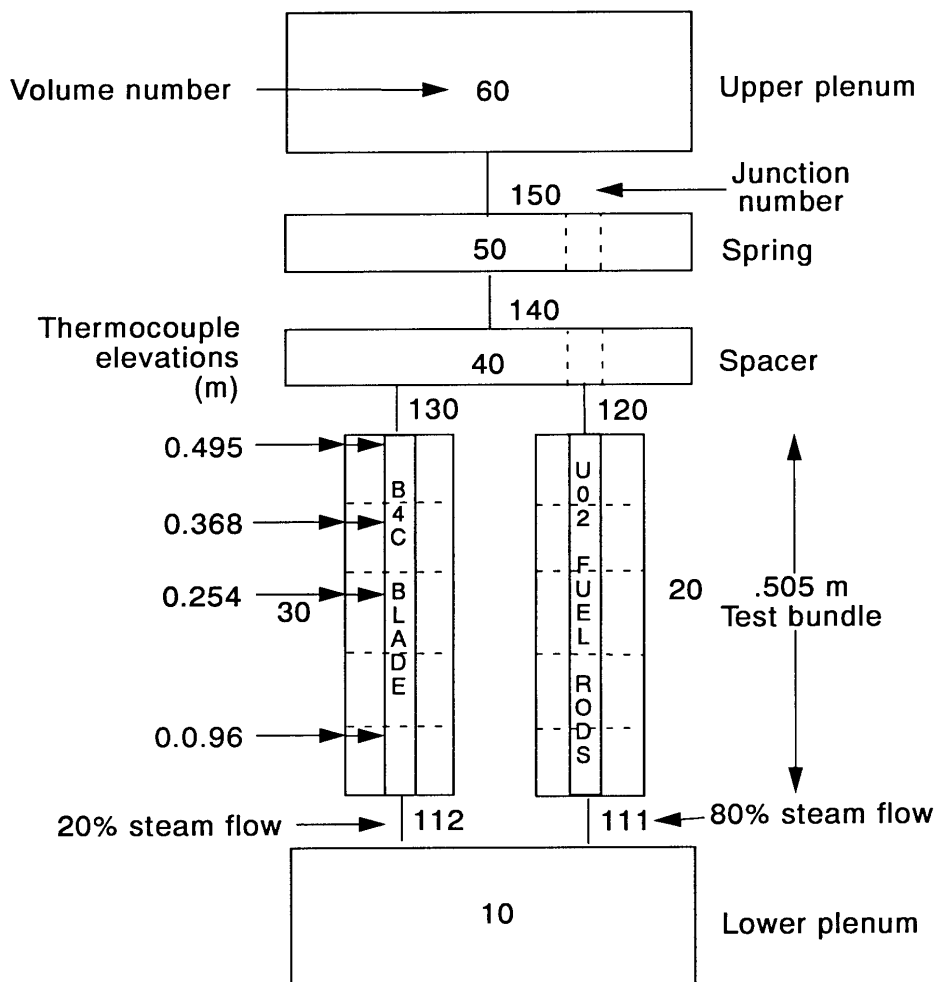
For the initial analysis, four representative SCDAP structural components were used to model the DF-4 test bundle. The first component (fuel) models the 10% enriched UO_2 fuel rods. The second component (shroud) models the shroud inner liner, ZrO_2 insulation, and stainless steel pressure tube. The third component (shroud) models the zircaloy channel box, and the fourth component (BWR control rod) models the stainless steel-clad B_4C control blade. Each component was divided into five equal-length axial nodes. The fuel rod was modeled using five radial nodes; the insulation was modeled using nine radial nodes; and the channel box was modeled using four radial nodes. For a subsequent analysis, the third and fourth components were replaced with the BWR control blade model developed at Oak Ridge National Laboratory (ORNL).^{A-10}

A.3.2 Results

The results obtained using the latest version of SCDAP/RELAP5/MOD3 have been examined for accuracy of code predictions and compared with results obtained both from experimental analysis and previous code versions.^{A-11} Significant findings are reported below.

A.3.2.1 DF-4 Base Case.

The DF-4 base case used the original SCDAP modeling (see Section 3.3.1) for the BWR control blade. The DF-4 base case was run successfully to the end of the oxidation transient phase (~8,100 seconds).



M175-BDR-0293-002

Figure A-37. Test train nodalization for the DF-4 experiment.

Figure A-38 depicts the total bundle power calculated during the DF-4 experiment, which closely follows the actual input power curve of the experiment.

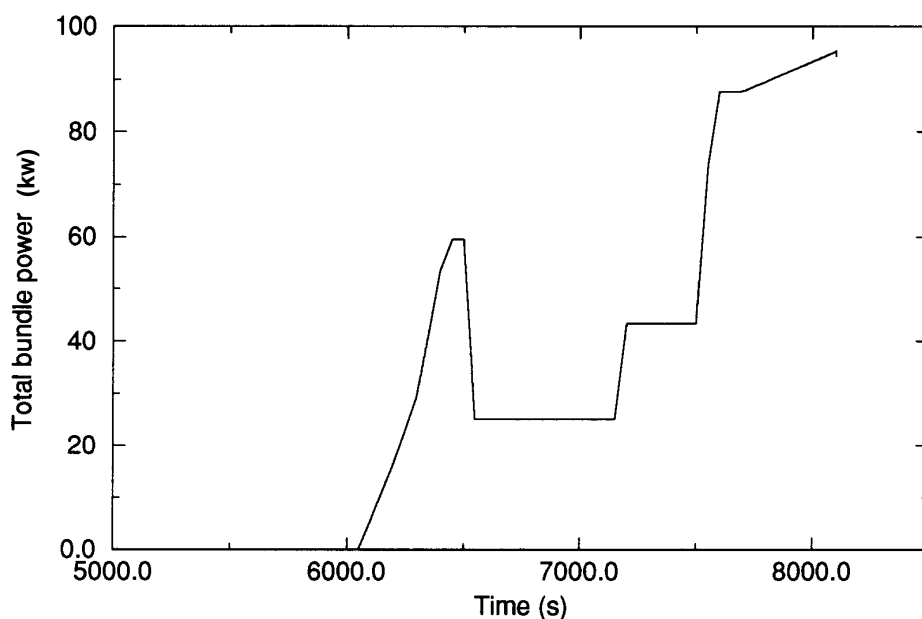


Figure A-38. Total core power for the DF-4 experiment.

The surface temperatures for all four SCDAP components are shown in Figures A-39 through A-41. The distinct phases of the experiment can be seen in the temperature curves, and the calculated temperatures closely follow those determined experimentally for the initial phases of the experiment. However, once the heatup and oxidation transient phases are reached, fuel rod temperatures are considerably higher than experimental values, and subsequent fuel rod failure occurs ~230 seconds earlier in the transient. These results are consistent with results previously reported.^{A-11}

Total hydrogen production is shown in Figure A-42. For the DF-4 base case, the calculated total amount of hydrogen produced (~70 g) is considerably higher than the ~37 g determined experimentally, which is consistent with the more severe damage calculated.

A.3.2.2 DF-4 Blade Case.

For the DF-4 blade case, the original input deck was modified to incorporate the ORNL control blade/channel box interaction and melt relocation model.^{A-10} This model, designated SCDAP Component 3, replaced SCDAP components 3 and 4 (shroud and BWR control rod) of the base case deck. The DF-4 blade case was run successfully to 8,020 seconds.

Figure A-43 depicts the calculated total bundle power, which is very similar to the power curve calculated in the DF-4 base case.

The surface temperatures for the two original SCDAP components and selected temperatures from the ORNL blade model are shown in Figures A-44 through A-48. The temperature curves for the fuel rod

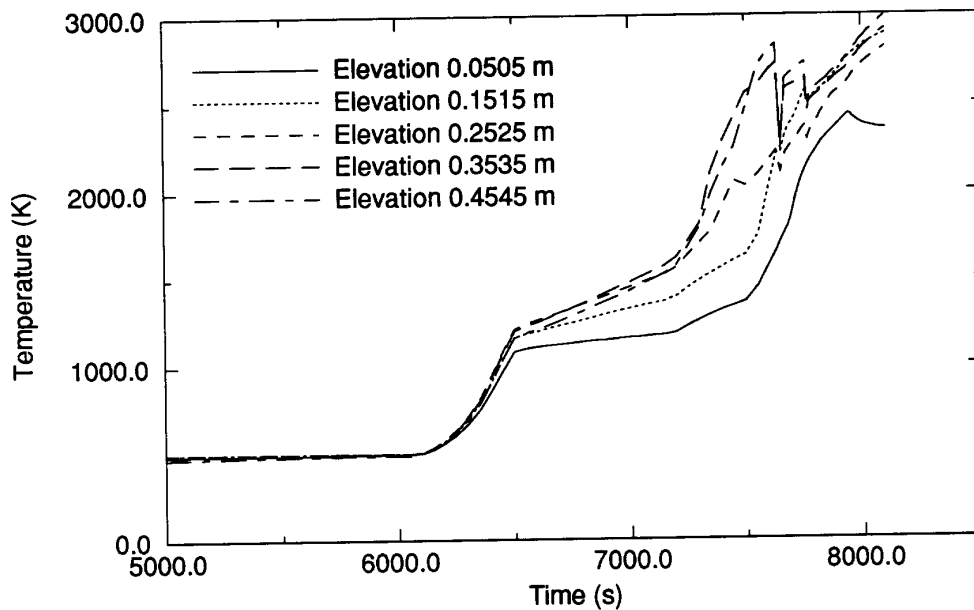


Figure A-39. Surface temperature for the fuel rod component for the DF-4 experiment.

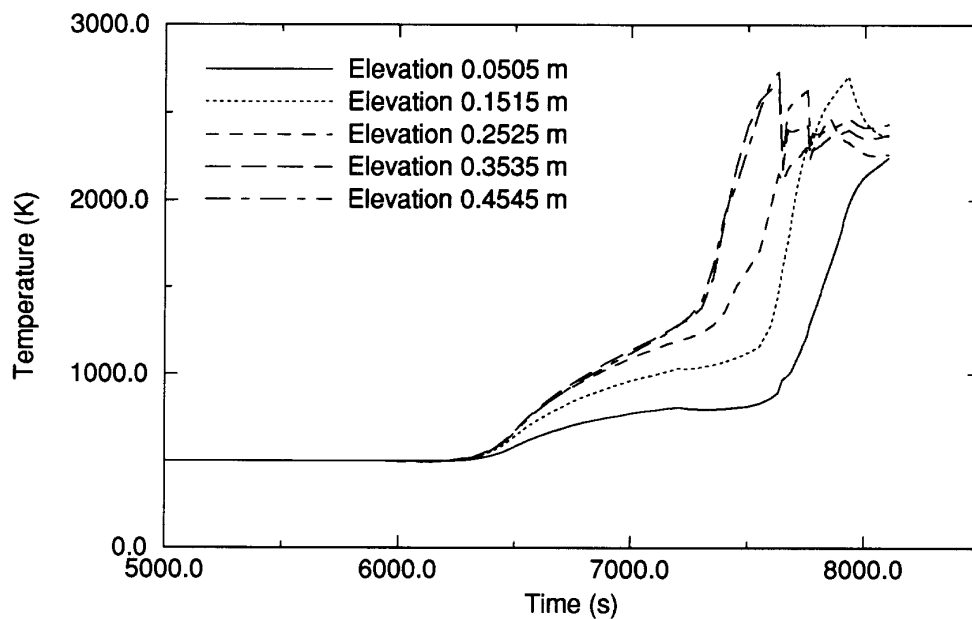


Figure A-40. Surface temperature for the shroud component representing the ZrO_2 insulation for the DF-4 experiment.

and outer shroud (Figures A-44 and A-45) are similar to those calculated in the base case. The temperature

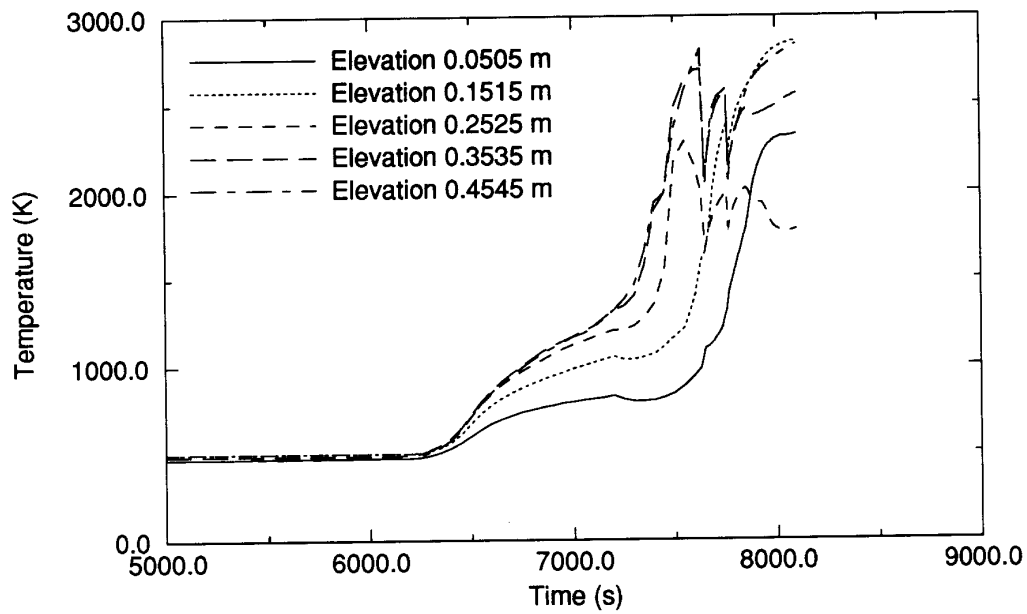


Figure A-41. Surface temperature for the BWR control rod component for the DF-4 experiment.

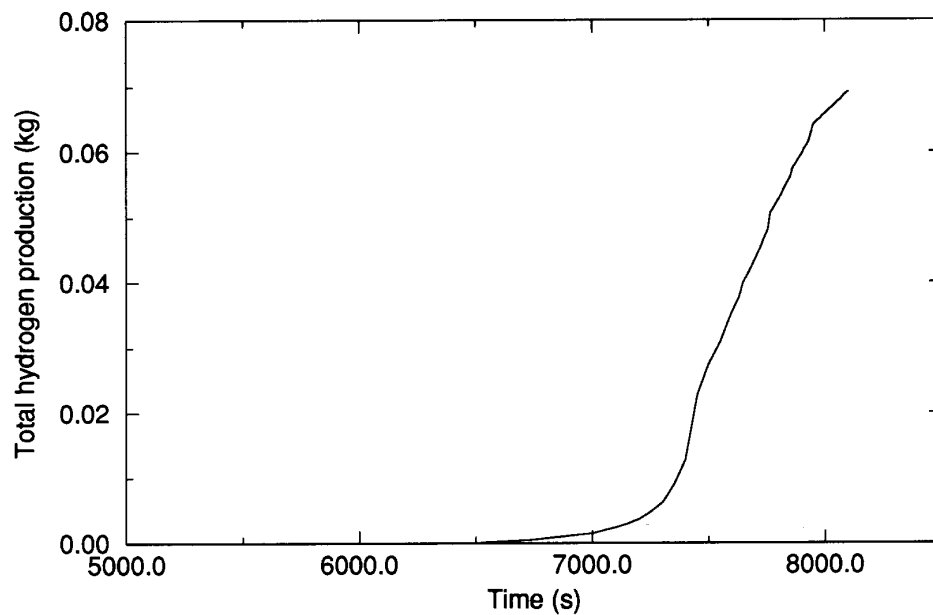


Figure A-42. Total hydrogen production for the DF-4 experiment.

curves for the control blade and channel box more closely follow experimental results until the time of

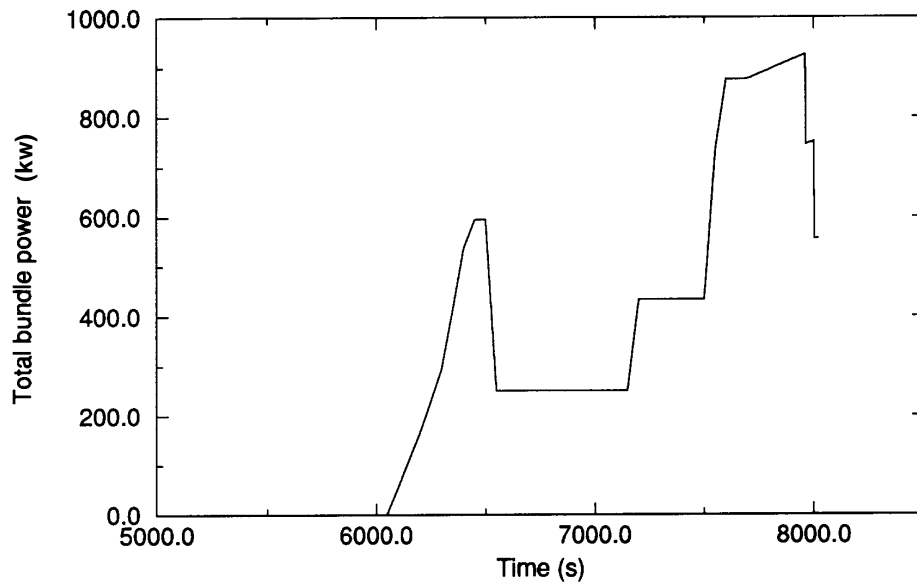


Figure A-43. Total core power for the DF-4 experiment using the ORNL blade model.

blade failure (7,440 seconds), where they are set to a constant value.

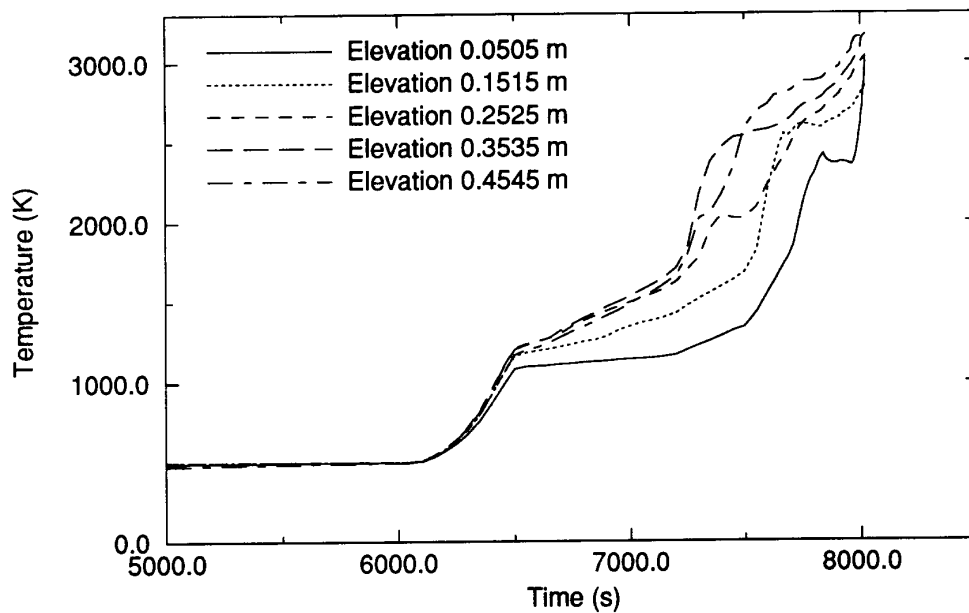


Figure A-44. Surface temperature for the fuel rod component for the DF-4 experiment using the ORNL blade model.

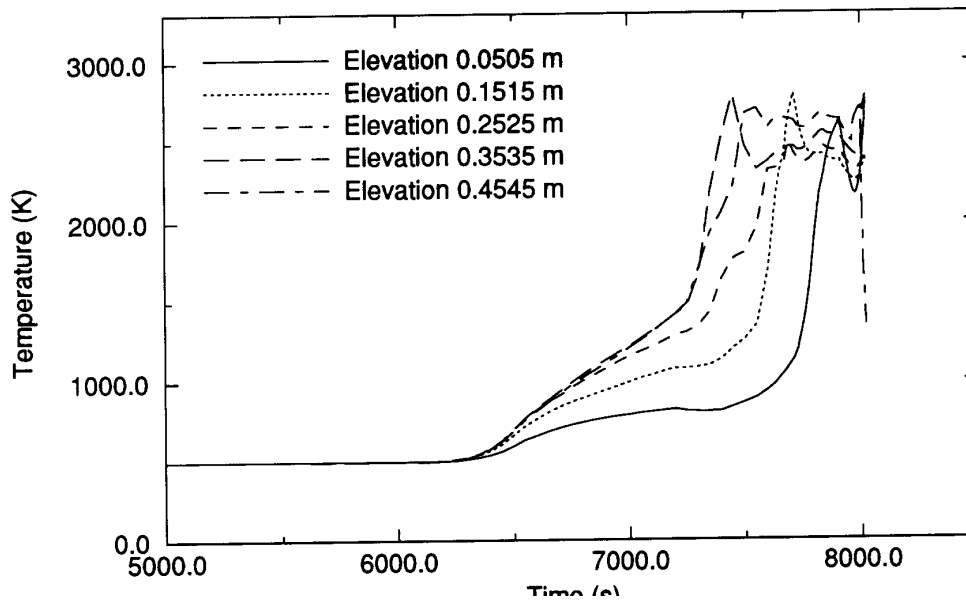


Figure A-45. Surface temperature for the shroud component representing the ZrO_2 insulation for the DF-4 experiment using the ORNL blade model.

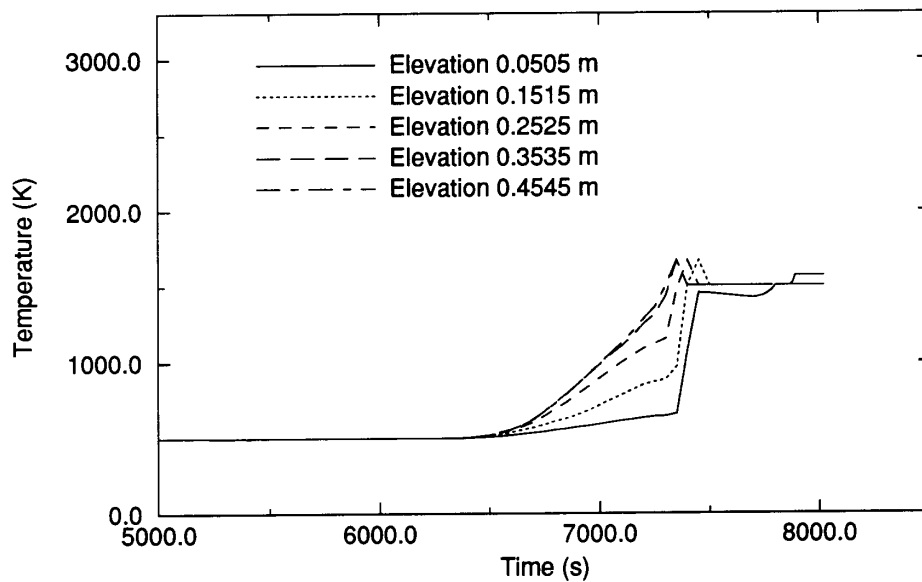


Figure A-46. Surface temperature for the control blade for the DF-4 experiment using the ORNL blade model.

Total hydrogen production is shown in Figure A-49. For the DF-4 blade case, the calculated total amount of hydrogen produced (~42 g) is much closer to that determined experimentally (37 g).

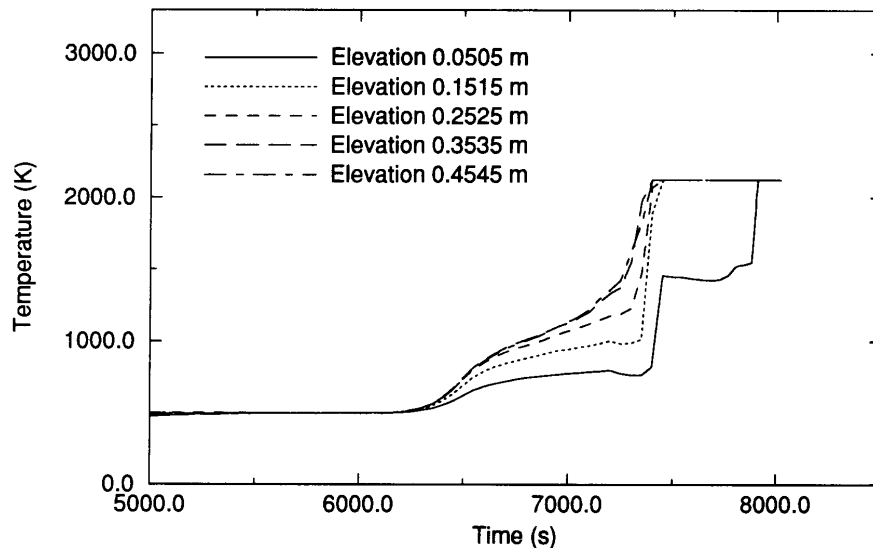


Figure A-47. Surface temperature for channel box segment 1 for the DF-4 experiment using the ORNL blade model.

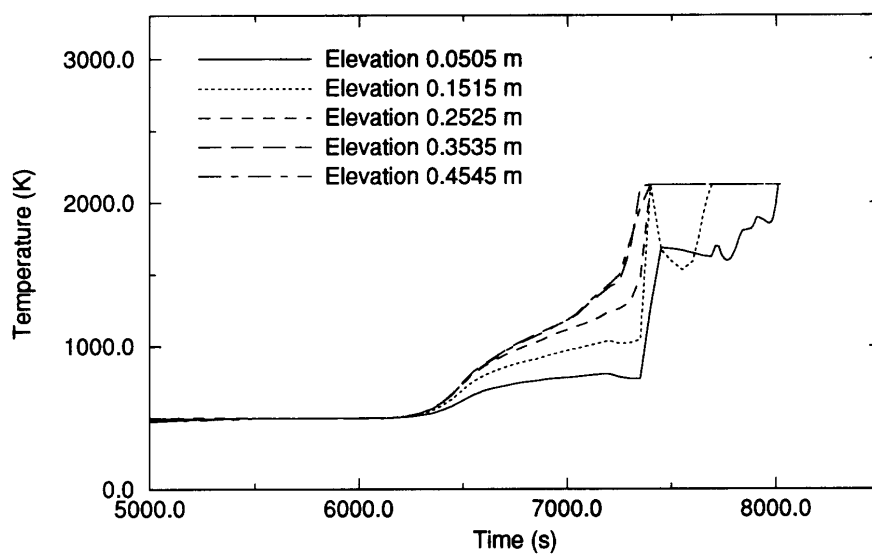


Figure A-48. Surface temperature for channel box segment 2 for the DF-4 experiment using the ORNL blade model.

A.3.3 Code Performance

In general, SCDAP/RELAP5/MOD3 performed adequately for both DF-4 cases. Figure A-50 depicts the CPU time for the DF-4 base case. As expected, CPU time increased during the oxidation transient

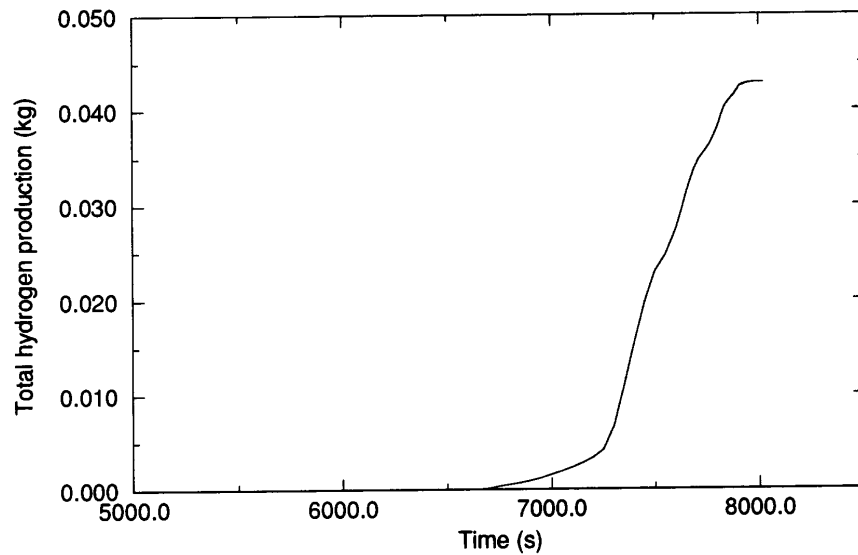


Figure A-49. Total hydrogen production for the DF-4 experiment using the ORNL blade model.

phase, since it was necessary to reduce the time step to avoid water property failures. The same time step reduction scheme was used to run the DF-4 blade case, with a corresponding increase in CPU time.

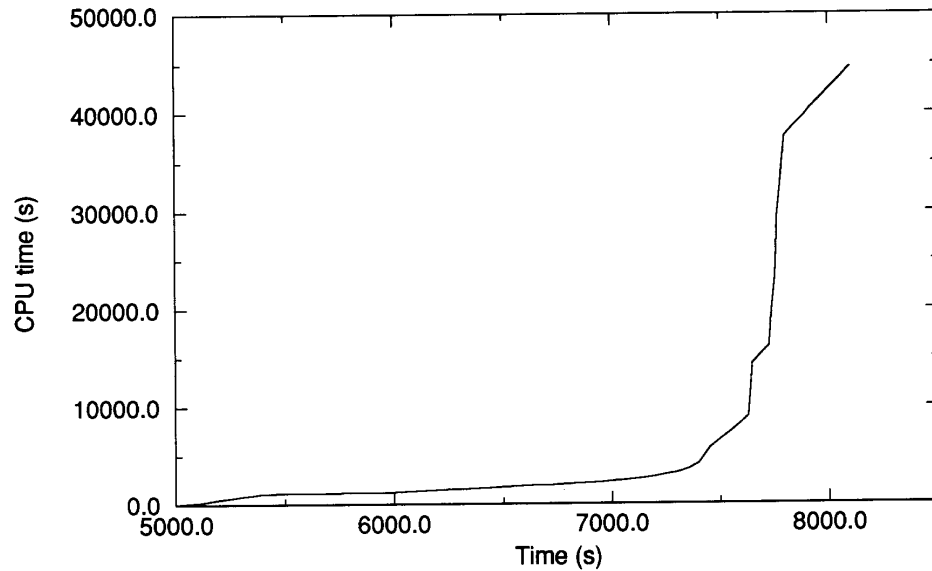


Figure A-50. CPU time for the DF-4 experiment.

The ORNL control blade model provided good results in most areas when compared both to experimental and calculated data. It was not possible to test the ORNL control blade model using the new-style SCDAP input, since the coding for this model had not been completed, at the time of these calculations.

A.4. PBF SFD 1-4 EXPERIMENT

The Severe Fuel Damage (SFD) research program was initiated by the U. S. Nuclear Regulatory Commission (NRC) to develop a data base and models to predict (a) the overall response of the core and associated structures, (b) the rate of release of fission products, their chemical forms, and characteristics of their transport and deposition in the primary system, (c) the rate of hydrogen generation from the interaction of coolant with the fuel, cladding, and reactor structure, and (d) the coolability of the damaged fuel following reflood.

The fourth in a series of severe fuel damage experiments, SFD 1-4,^{A-12} was conducted in the Power Burst Facility (PBF) at the Idaho National Engineering Laboratory (INEL) on February 7, 1985. Test SFD 1-4 has provided data that have significantly improved the understanding of early phase pressurized water reactor (PWR) melt progression. The experimental results from the PBF SFD 1-4 test and those of other integral and separate effects tests were used in assessing damage progression models introduced in the SCDAP/RELAP5 code.

A.4.1 Description of the SCDAP/RELAP5 Model

The SFD 1-4 test train incorporated a fuel bundle containing 26 pre-irradiated fuel rods with an average burnup of 36 GWd/MtU, two fresh instrumented fuel rods and four silver-indium-cadmium control rods. One of the four control rods was instrumented. The absorber material was an alloy consisting of 80% Ag, 15% In, and 5% Cd by weight. The spacing between fuel rods and control rod tubes in the test assembly was maintained by three Inconel spacer grids ~40 mm in height located at 0.09, 0.49, and 0.94 m elevations. The active length for the fresh and the irradiated fuel rods was 1 m.

The fuel bundle was housed in an insulated shroud to minimize radial heat losses. The shroud was composed by a zircaloy inner liner, an insulated shroud (porous zirconia), an inner and outer zircaloy shroud wall, a zircaloy flow tube, and finally the in-pile tube. The insulated region was pressurized with argon, and the gap between the inner and outer shroud walls was pressurized with helium.

A.4.1.1 Nodalization

The entire experimental structure was modeled using the SCDAP/RELAP5 code. As shown in Figure A-51, the test bundle was represented by seven SCDAP components, (1) the three irradiated fuel rods of the inner ring, (2) the fresh fuel rod of the inner ring, (3) the fresh fuel rod of the middle ring, (4) the seven irradiated fuel rods of the middle ring, (5) the four control rods of the middle ring, (6) the 16 irradiated fuel rods of the outer ring, and (7) the shroud.

The fuel components were modeled using four radial nodes; the control rods were modeled using five radial nodes; and the shroud was modeled using 19 radial nodes.

As shown in Figure A-52, all the components were modeled using 10 axial nodes, each node being 0.1 m tall and communicating with the 10 corresponding RELAP5 hydrodynamic control volumes. The external surface of the shroud was connected to a single RELAP5 hydrodynamic control volume representing the bypass.

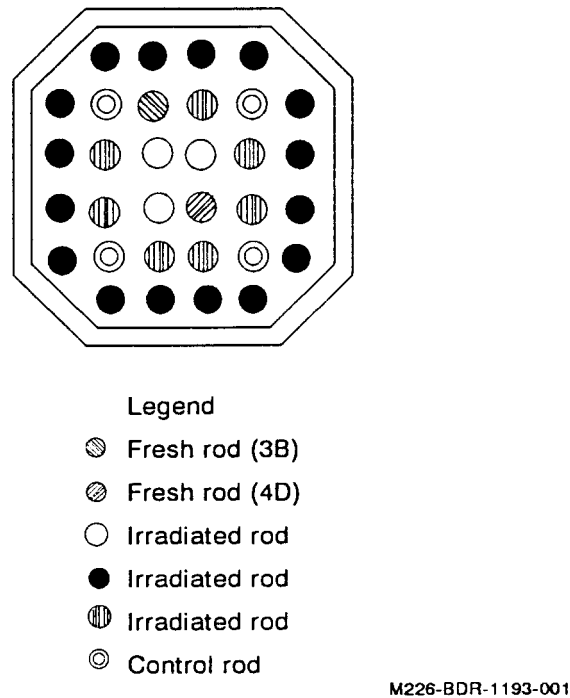


Figure A-51. Core representation for the SFD 1-4 experiment.

A.4.1.1.1 Initial Conditions. All the fuel rods were pressurized with helium to 2 MPa at room temperature, except the fresh fuel rod (4D), which was pressurized to 3.8 MPa. The SCDAP/RELAP5 calculation transient was started after the boildown phase at 1000 seconds when the two-phase level in the bundle was ~0.20 m. The mean temperature of the fuel rods was initialized at 810 K with an internal pressure of ~5.4 MPa (~10.3 MPa for the fuel rod 4D).

The initial fission product inventory was calculated by the FASTGRASS model of the SCDAP/RELAP5 code using a realistic power history prior to the test.

A.4.1.2 Boundary Conditions

The estimation of the total nuclear power generated in the bundle as well as the uncertainty envelope ($\pm 20\%$) were obtained from reactor power measurements and reactor physics calculations (Figure A-53).

The axial power profiles were represented in the calculations using three discrete curves. The calculations were started using the profile corresponding to an intact bundle partially filled with water, then shifted to a profile representing an intact bundle filled with steam (1,020 seconds) and finally to a profile representing a damaged bundle with relocated control rod materials and filled with steam (2,050 seconds).

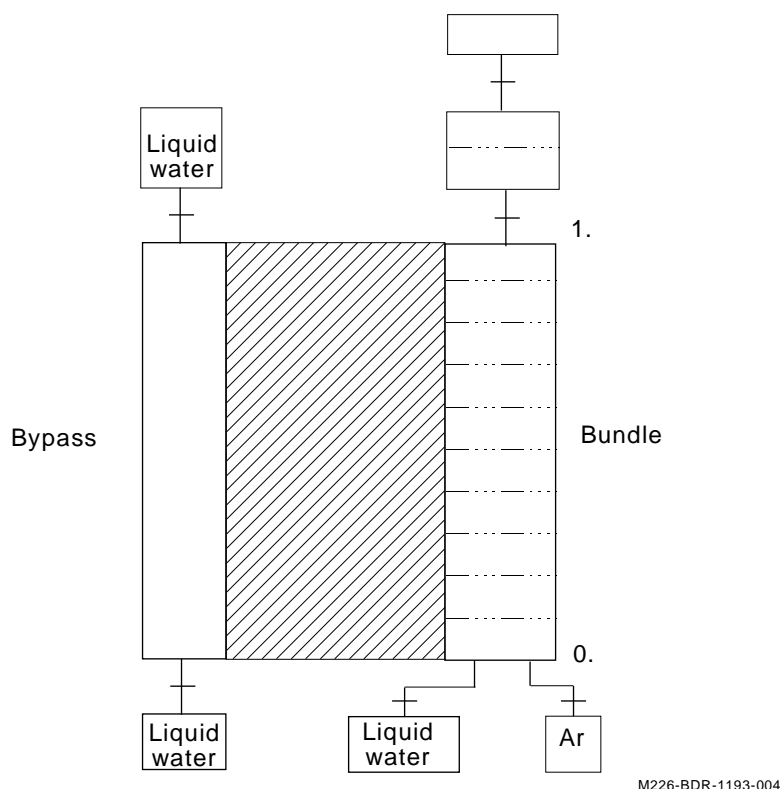


Figure A-52. Nodalization of test train for the SFD 1-4 experiment.

A constant water inlet flow rate of 0.6 g/s with a temperature of 532 K and a pressure of 6.95 MPa was used over the transient. An argon flow rate 0.26 g/s was injected at the bottom of the bundle for the first 1,965 seconds of the transient then increased to 0.58 g/s until 3,280 seconds and finally maintained at 1.88 g/s until the end of the transient.

A.4.2 Results

Calculations presented in this section were performed using SCDAP/RELAP5/MOD3.1 with options such as semi-implicit hydrodynamic scheme and time smoothing of the radiative heat transfer.

A.4.2.1 Thermal Behavior

The preliminary calculation (PC) performed using the best estimate (BE) nuclear power underpredicted the cladding temperatures (~ 100 K) for the first 1,600 seconds in the transient (Figure A-54). This result indicated that the net power gained by the bundle was underpredicted. A better estimation of the cladding temperatures could be obtained by increasing the total nuclear power or by decreasing the radial heat losses through the shroud.

Calculated temperatures in better agreement with the experimental data (Figure A-54) were obtained in a base calculation (BC) using the upper bound of the nuclear power (nominal power + 20%). In this calculation, cladding rupture by internal overpressure was only predicted for the fresh fuel rod 4D at 1,280

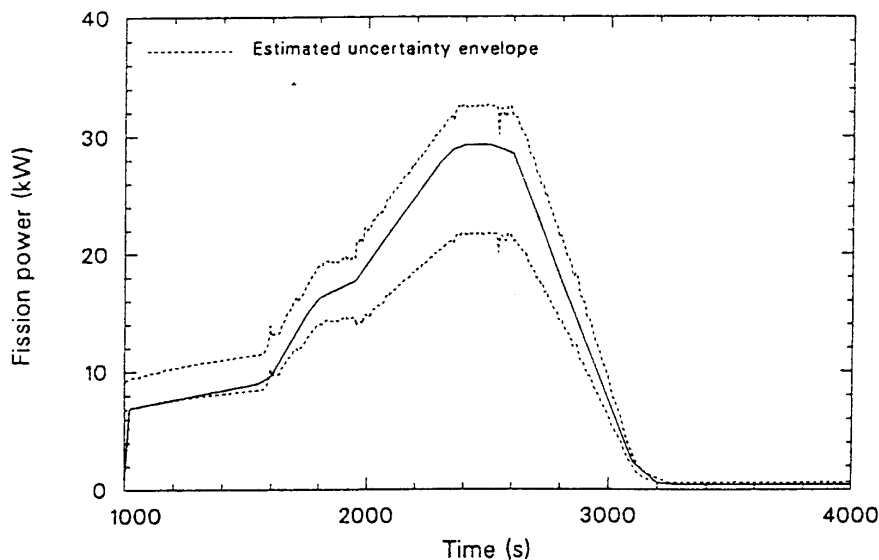


Figure A-53. Total core power for the SFD 1-4 experiment.

seconds. For all the other fuel rods, the chemical interaction between Inconel from the spacer grids and zircaloy started at mid-bundle at about 1,600 seconds ($\sim 1,250$ K) and ended at 1,870 seconds with complete cladding dissolution over an axial length of 66 mm. The total zircaloy dissolution by Inconel allowed steam to fill the internal gap between the fuel and the cladding and to produce a double-sided oxidation over a length of ~ 0.2 m. However, the high heatup rate observed in the test just before 1,900 seconds (~ 3.5 K/s) was not correctly calculated by the code.

Additional sensitivity calculations were carried out to explain the increase of the cladding heatup rate observed in the test just before 1,900 seconds. The BE calculation was obtained by forcing all of the fuel rods to transition from single-sided to double-sided oxidation at 1,750 seconds over a length of ~ 0.9 m. This transition in oxidation behavior was imposed in the code by decreasing the rupture strain (2%). The resulting time of the cladding ruptures was consistent with that observed in the test. Under these conditions, the calculated cladding temperature responses were in correct agreement with the test until thermocouple failures just before 2,000 seconds (Figures A-55 and A-56). However, the temperature of the shroud inner liner at mid-bundle was underpredicted. The calculated maximum fuel temperature ($\sim 2,780$ K) was obtained at 2,460 seconds at the 0.75 m elevation.

The collapsed liquid level, as well as steaming flow rate and steam temperatures in the bundle, agreed with those measured during the test. Local steam-starved conditions in the upper part of the bundle were calculated to occur shortly before 2,000 seconds. The analyses of the test scenario showed that the bundle experienced steam-starved conditions from $\sim 2,100$ to $\sim 3,200$ seconds. The calculation indicated that the steam-starved front started to move upward at 2,300 seconds. However, no additional zircaloy oxidation and hydrogen generation were calculated in the upper part of the bundle due to an early material

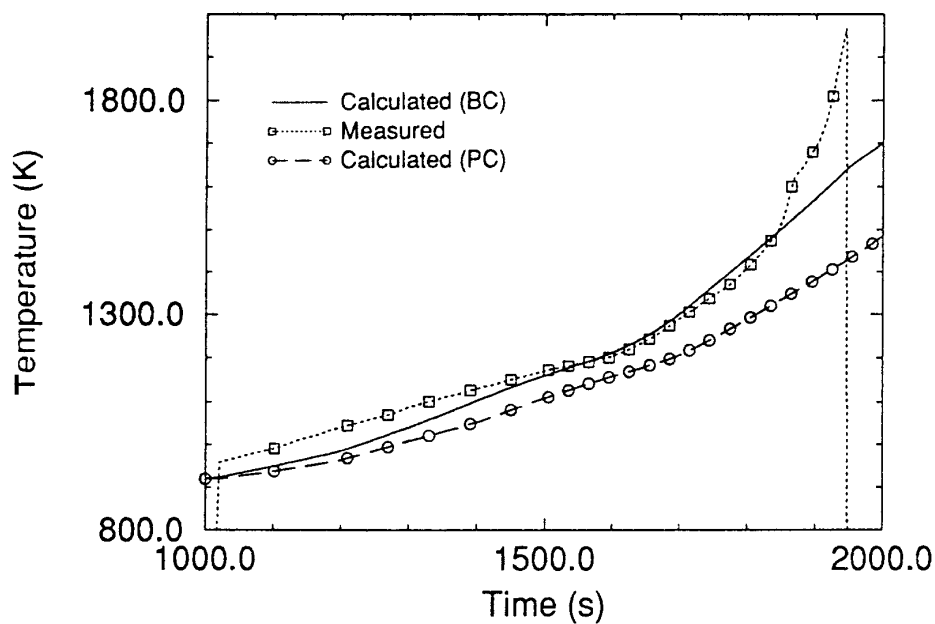


Figure A-54. Cladding temperatures at 0.55 m elevation. PC: Calculation using BE nuclear power. BC: Calculation using BE nuclear power + 20%.

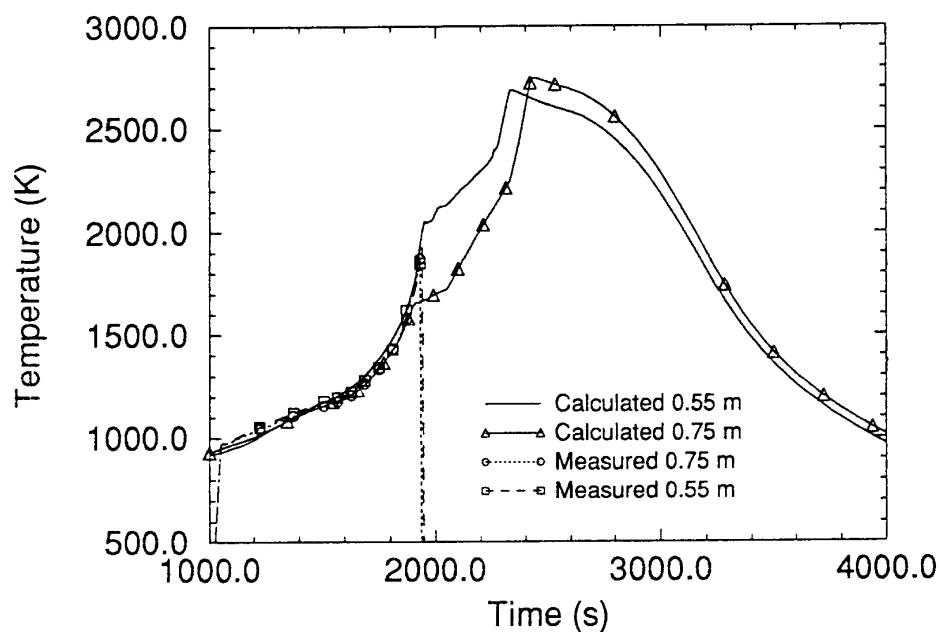


Figure A-55. Cladding temperatures for the top half of the fuel rods for the SFD 1-4 experiment (BE calculation using BE nuclear power + 20%).

relocation from 1,995 seconds. At ~2,500 seconds, the bundle was calculated to be filled with a steam-rich

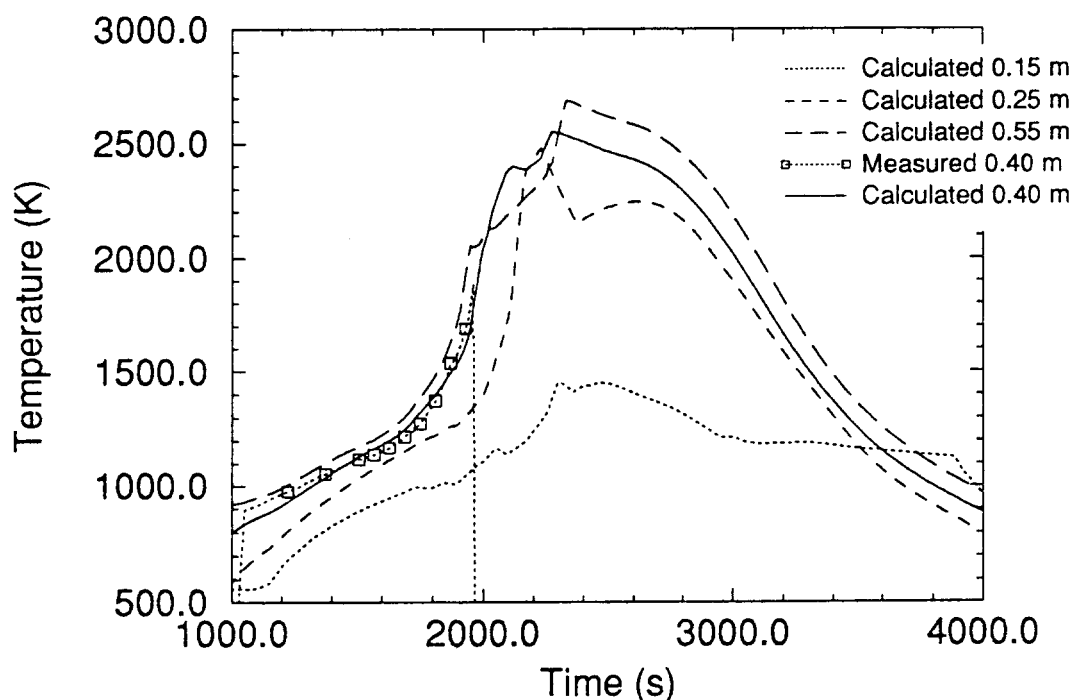


Figure A-56. Cladding temperatures for the bottom half of the fuel rod components for the SFD 1-4 experiment (BE calculation using BE nuclear power + 20%).

atmosphere.

A.4.2.2 Hydrogen Production

The BE calculation assumed the relocation of molten zircaloy occurring from 2,400 K for a cladding oxidation less than 60%. The calculated total hydrogen production (~60 g) was underpredicted by the code (86 ± 12 g in the test).

However, comparison between the calculated and the measured hydrogen generation rate showed an under prediction of the hydrogen released at the end of the calculation (from ~2,600 seconds). The under prediction of the hydrogen generation rate at the end of the transient was mainly due to the lack of the molten material oxidation model in the current version of the code.

Cladding material relocations were calculated to occur mainly during the period of steam-starved conditions. Consequently, material relocation criteria were found to have a weak effect on the total hydrogen mass generated. Sensitivity calculations performed using a relocation temperature criterion of 2,300 K showed a total hydrogen production of 58 g. The slight decrease of the total hydrogen generation (~2 g) in this calculation was due to an early onset of material relocation (~25 seconds earlier compared to the BE calculation). Conversely, a relocation temperature criterion of 2,500 K delayed material relocation by ~100 seconds but increased the total hydrogen generation by only ~5%. However, unrealistic fuel temperatures were obtained at the end of this calculation (>3,000 K at 2,400 seconds).

Cladding oxidation in the BE calculation was less than ~45% in the lower part of the bundle and ~30% in the upper elevations. The under prediction of cladding oxidation in the lower part of the bundle (~100% measured in the PIE) was mainly attributed to an early decladding of the fuel rods from this region. Extension of the interaction time between steam and zircaloy cladding was obtained in a sensitivity calculation using a relocation temperature criterion of 2,500 K. Under these conditions, the cladding was calculated to be ~100% oxidized at the 0.25m elevation. The over prediction of cladding oxidation in the upper elevation (a few percent measured in the PIE) was probably due to an immediate cladding relocation as the cladding experienced temperatures exceeding the zircaloy melting point (~2,050 K).

A.4.2.3 Metallic Material Relocation

The main events predicted to occur during the BE calculation are reported in Table A-4. The control rods failed at ~1,950 seconds at the melting temperature of the stainless steel (~1,730 K). The absorber material above the failure elevation (~0.45 m) was totally molten and the liquefied material immediately drained outside the control rod through the breach and refroze in the lower part of the bundle. At the end of the calculation, all components of the control rod above ~0.2 m elevation relocated, and 94% of the liquefied absorber material refroze below the test bundle.

Table A-4. Simulated sequence of events for SFD 1-4 experiment.

Event	Calculation (BE Calculation)		Experiment	
	Cladding Temperature (K)	Time (s)	Cladding Temperature (K)	Time (s)
Cladding dissolution by Inconel	1,385	1,750 ^a	~1,380	1,700 - 1,800 (cladding rupture)
Onset of fission product (FP) release	1,385	1,750 ^b	~1,380	1,700
	1,550	1,830 ^c		
	2,150	1,970 ^d		
Control rod failure	1,730 ^e	1,950	~1,730	1,928 - 1,978
Shroud inner liner failure	1,770 ^f	1,946 ^g	~1,700 ^f	1,946
Onset of fuel dissolution	2,150	1,970		
Fuel rod relocation	2,400	1,995 - 2,435		2,300 - 2,600
Maximum fuel temperature	2,780	2,460	~2,800	

a. The time of complete cladding dissolution by Inconel was predicted at 1,870 seconds in the base calculation. This time was shifted 120 seconds forward in the BE calculation. The resulting time (~1,750 seconds) was consistent with the cladding ruptures observed in the test.

b. Due to cladding ruptures and gap release

c. Increase of FP releases due to temperature effect

d. Increase of FP releases due to fuel dissolution

e. Control rod temperatures at 0.50 m elevation

f. Shroud temperature at 0.50 m elevation

g. Imposed in the code

The metallic (U-Zr-O) material relocation was predicted to occur between 1,995 and 2,435 seconds in the BE calculation. The onset of material relocation was calculated earlier than that observed in the experiment (~2,300 seconds in the test). The beginning of the relocation of liquefied fuel and cladding materials occurred between 0.45 and 0.55 m elevations. At the end of the calculation, the axial extent of the degradation region was 0.8 m (from 0.2 to 1 m elevations). Relocated materials formed a cohesive debris ~0.20 m thick in the lower part of the bundle.

The onset of fuel dissolution by molten zircaloy was predicted to occur at 1970 seconds at the 0.45 m elevation for all the fuel rods. The calculated total fuel dissolution (~13.3%) was slightly underpredicted compared to the experiment (~18%). Sensitivity study performed with a cladding relocation criteria of 2,300 K showed an underestimation of fuel dissolution (~4%). Conversely, a cladding relocation criteria of 2,500 K led to a large overestimation of fuel dissolution (>35%).

Analyses of the PIE indicated a very low fuel dissolution in the upper part of the bundle. It is believed that as the cladding in the upper elevations experienced temperatures exceeding the zircaloy melting point, it immediately relocated to the middle portion of the bundle limiting local fuel dissolution. Better agreement with the experimental data was obtained by reducing the interaction time between fuel and cladding. Local fuel dissolution in the upper elevations was only ~3% in a calculation using a cladding relocation criterion of 2,300 K.

A.4.2.4 Fission Product Releases

The total releases of the noble gases (21.8%) and volatile fission products (FPs) (23.5%) obtained in the BE calculation were in correct agreement with the releases observed during the test (noble gases ~23% to ~52%; volatile FPs ~24% to ~51%).

Fission product releases due to cladding ruptures were predicted to occur at ~1,750 seconds. At 1,830 seconds, the total cumulated release from the gaps of the irradiated fuel rods was ~1% of the total initial inventory.

The calculated rate of FPs releases was very low for 80 seconds after the cladding failures. At 1,830 seconds, the FPs releases again increased as the maximum fuel temperature exceeded 1,550 K. About 2.5% of the total fission products were calculated to be released due to the temperature effect after cladding ruptures and before fuel dissolution.

The calculation indicated a large increase of the FPs releases caused by fuel dissolution by molten zircaloy at 1,970 seconds as the cladding temperature reached 2,150 K. About 18.5% of the total fission products were calculated to be released after the onset of fuel dissolution.

The total FPs releases were due to cladding ruptures, temperature effect, and fuel dissolution but were mainly produced from the irradiated fuel rods. In particular, no fission product release from the fresh rods was calculated by the code prior to fuel dissolution.

A.4.2.5 Code Performance

Long central processing unit (CPU) times (~39 hours for a simulated transient of 4,000 seconds) were obtained when modeling the bypass region using 10 axial RELAP5 hydrodynamic control volumes. The CPU time was reduced by a factor of four using a bypass region modeled by a single hydrodynamic volume. Under these conditions, the total CPU time for a simulated transient of 4,000 seconds was 9.75 hours on an IBMRisc Workstation. However, the CPU time increased as the conditions became more severe in the calculation. The ratio (CPU time/simulated time) was only 1.21 at 2,000 seconds prior to any material relocation; but during the period of material relocation, this ratio increased and reached 8.78 at the end of the calculation.

A.5. PBF SFD 1-3 EXPERIMENT

The Severe Fuel Damage (SFD) research program was initiated by the U.S Nuclear Regulatory Commission (NRC) to develop a data base and models to predict (a) the overall response of the core and associated structures, (b) the rate of release of fission products, their chemical forms, and characteristics of their transport and deposition in the primary system, (c) the rate of hydrogen generation from the interaction of coolant with the fuel, cladding, and reactor structure, and (d) the coolability of the damaged fuel following reflood.

The third in a series of four severe fuel damage experiments, SFD 1-3,^{A-13} was conducted in the Power Burst Facility (PBF) at the Idaho National Engineering Laboratory (INEL) on August 3, 1984. Test SFD 1-3 has provided data that have significantly improved the understanding of early phase pressurized water reactor (PWR) melt progression. The experimental results from the PBF SFD 1-3 test and those of other integral and separate effects tests were used in assessing damage progression models introduced in the SCDAP/RELAP5 code.

A.5.1 Description of the SCDAP/RELAP5 Model

The SFD 1-3 test train incorporated a fuel bundle containing 26 pre-irradiated fuel rods with an average burnup of 38 GWd/MtU, two fresh instrumented fuel rods and four empty zircaloy control rod guide tubes. Spacing between fuel rods and control rods tubes in the test assembly was maintained by three Inconel spacer grids ~40 mm in height located at 0.09, 0.49, and 0.94 m elevations. The active length for the fresh and irradiated fuel rods was 1 m.

The fuel bundle was housed in an insulated shroud to minimize the radial heat losses. The shroud was composed by a zircaloy inner liner, an insulated shroud (porous zirconia), an inner and outer zircaloy shroud wall, a zircaloy flow tube, and finally the in-pile tube. The insulated region was pressurized with argon, and the gap between the inner and outer shroud walls was pressurized with helium.

A.5.1.1 Nodalization

The entire experimental structure was modeled using SCDAP/RELAP5 code. As shown in Figure A-57, the test train was represented by seven SCDAP components, (1) the three irradiated fuel rods of the inner ring, (2) the fresh fuel rod of the inner ring, (3) the fresh fuel rod of the middle ring, (4) the seven irradiated fuel rods of the middle ring, (5) the four empty control rods, (6) the 16 irradiated fuel rods of the outer ring, and (7) the shroud.

The fuel components were modeled using four radial nodes; the control rods were modeled using five radial nodes; and the shroud was modeled using 19 radial nodes.

As shown in Figure A-58, all the components were modeled using 10 axial nodes each node being 0.1 m tall and communicating with the 10 corresponding RELAP5 hydrodynamic control volumes. The external surface of the shroud was connected to a single RELAP5 hydrodynamic control volume representing the bypass. An additional external volume and a valve connected to the bundle control volumes at 0.35 m elevation were represented to model the depressurization observed in the test at 1,733 seconds.

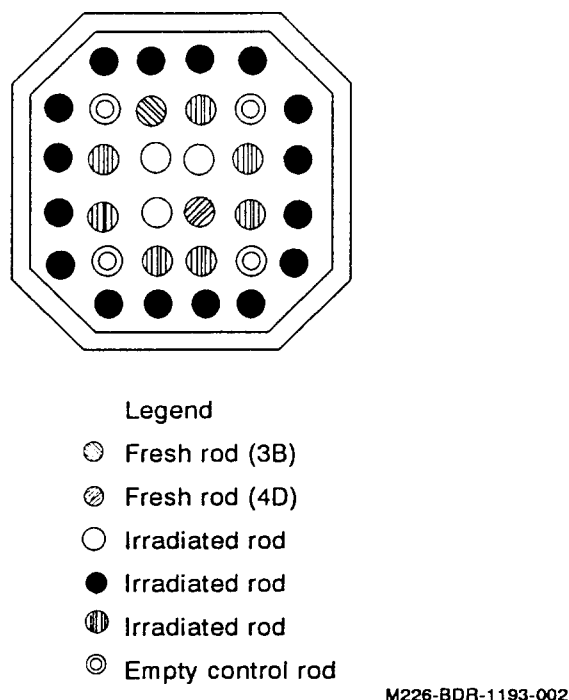


Figure A-57. Core representation for the SFD 1-3 experiment.

A.5.1.2 Initial Conditions

All the fuel rods were pressurized with helium to 2 MPa at room temperature, except the fresh fuel rod (4D), which was pressurized to 3 MPa. The SCDAP/RELAP5 calculation transient was started after the boildown phase when the two-phase level in the bundle was ~0.20 m. The mean temperature of the fuel rods was initialized at 585 K with an internal pressure of ~3.9 MPa (~5.9 MPa for the fuel rod 4D).

The initial fission product inventory was calculated by the FASTGRASS model of the SCDAP/RELAP5 code using a realistic power history prior to the test.

A.5.1.3 Boundary Conditions

The estimation of the total nuclear power generated in the bundle as well as the uncertainty envelope ($\pm 15\%$) were obtained from reactor power measurements and reactor physics calculations (Figure A-59).

The axial power profiles were represented in the calculations using three discrete curves. The calculations were started using a profile identified as 20% water-filled conditions, then shifted to a profile representing the 10% water-filled conditions (700 seconds) and then finally to a profile representing the steam-filled bundle at times after 1,600 seconds.

A constant water inlet flow rate of 0.6 g/s with a temperature of 530 K and a pressure of 6.9 MPa was used for the first 1,733 seconds in the transient. Analyses of the experimental scenario indicated that the

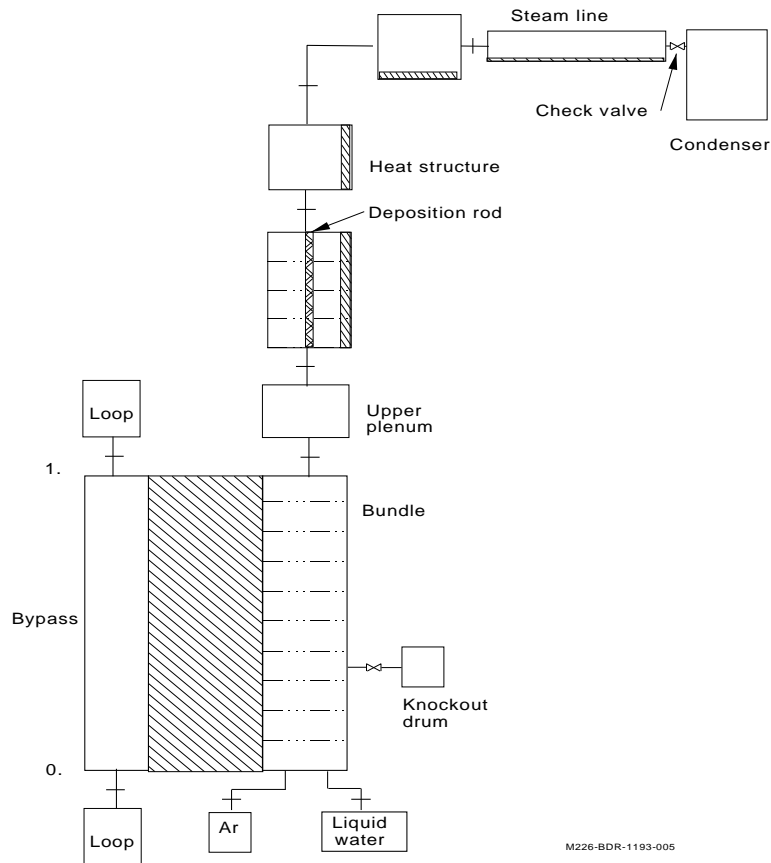


Figure A-58. Nodalization of test train for the SFD 1-3 experiment.

two-phase level was below the bottom of the fuel rods after the bundle depressurization observed at 1,733 seconds. In the SCDAP/RELAP5 calculations, the steam inlet flow rate and the temperature delivered to the bundle after 1,733 seconds were deduced from the experimental history of the two-phase level in the lower plenum.

An argon flow rate 1.35 g/s was injected at the bottom of the bundle at 2,880 seconds and was maintained constant until the end of the transient.

A.5.2 Results

The calculations presented in this section were performed using SCDAP/RELAP5/MOD3.1 with options such as semi-implicit hydrodynamic scheme and time smoothing of the radiative heat transfer.

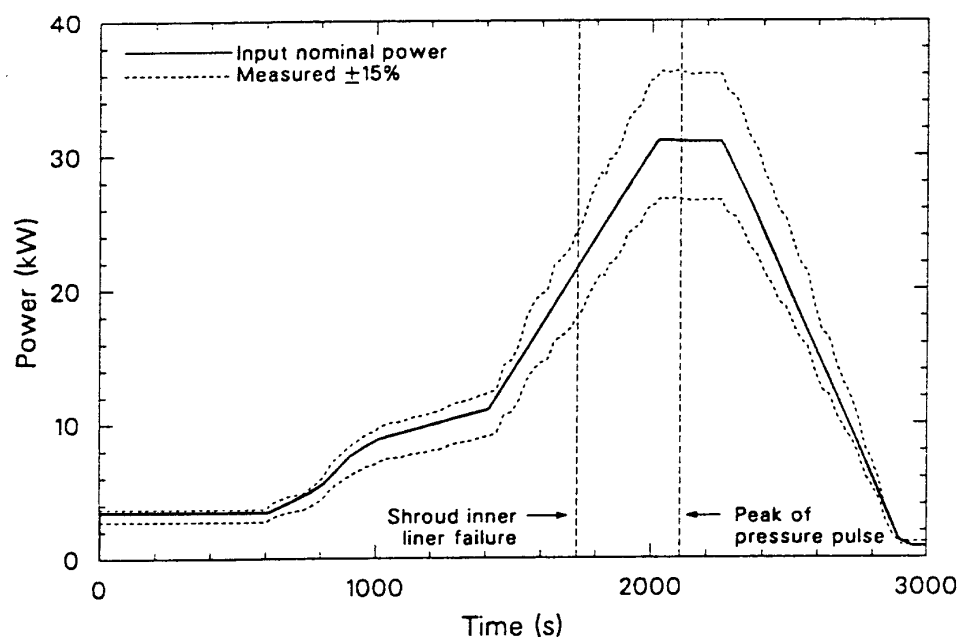


Figure A-59. Total core power for the SFD 1-3 experiment.

A.5.2.1 Thermal Behavior

The preliminary calculation (PC) performed using the best estimate (BE) nuclear power generated in the bundle showed an under prediction of the cladding heatup rate after 1,500 seconds in the transient (Figure A-60).

Calculated temperatures in better agreement with the experimental data were obtained in a base calculation (BC) using the upper bound of the nuclear power (nominal power + 15%) from 1,000 seconds (Figure A-60). In this calculation, cladding rupture by internal overpressure was only predicted for the fresh fuel rod 4D at 1,540 seconds. For all the other fuel rods, the chemical interaction between Inconel from the spacer grids and zircaloy started at mid-bundle at about 1,500 seconds (~1,250 K) and ended at 1,700 seconds with complete cladding dissolution over an axial length of ~58 mm. The total zircaloy dissolution by Inconel allowed steam to fill the internal gap between the fuel and the cladding and to produce a double-sided oxidation over a length of ~0.2 m. However, the high heatup rate observed in the test after 1,500 seconds (~2.3 K/s at 0.40 m elevation) was not correctly calculated by the code.

Additional sensitivity calculations were carried out to explain the increase of the cladding heatup rate observed in the test after 1,500 seconds. The BE calculation was obtained forcing all of the fuel rods to transition from single-sided to double-sided oxidation at 1,550 seconds over a length of ~0.9 m. This transition in oxidation behavior was imposed in the code by increasing the initial internal pressure in the fuel rods. The resulting time of the cladding rupture was consistent with that observed in the test. Under these conditions, the calculated cladding temperature responses were in correct agreement with the

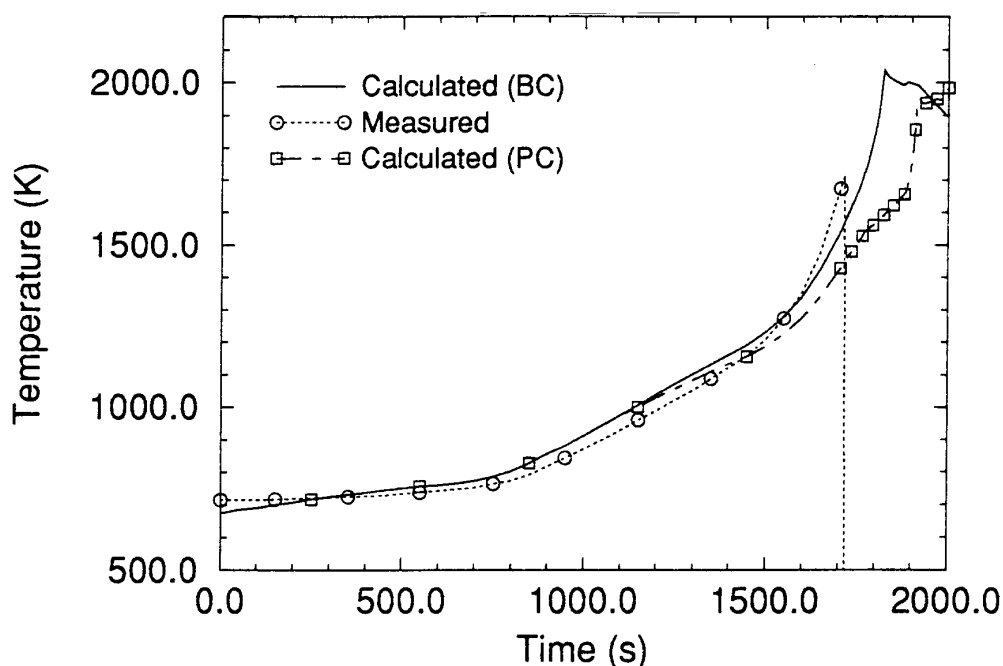


Figure A-60. Cladding temperatures at 0.40 m elevation. PC: Calculation using BE nuclear power. BC: Calculation using BE nuclear power + 15%.

experimental data until thermocouple failures just before 2,000 seconds (Figures A-61 & A-62). The calculated maximum fuel temperature (~2,625 K) was obtained at 1,880 seconds at 0.65 m elevation.

The collapsed liquid level as well as steaming flow rate and steam temperatures in the bundle agreed with those measured during the test. Analyses of the test scenario indicated that the bundle experienced steam-starved conditions between ~1,730 and ~3,000 seconds. Steam-starved conditions in the upper part of the bundle were calculated to occur shortly before the depressurization at 1,733 seconds. However, just after the depressurization, a steam-rich atmosphere was calculated in the bundle. Two main reasons were identified to explain the discrepancy between the experiment and the calculation. First, a relatively pure steam flow coming from the exit line and filling the bundle was calculated due to the depressurization after 1,000 seconds. Second, steam-rich atmosphere was predicted partially because of the absence of the oxidation model of molten materials in the current version of the code.

A.5.2.2 Hydrogen Production

The BE calculation assumed the relocation of molten zircaloy occurring from 2,400 K for a cladding oxidation less than 60%. The calculated total hydrogen production (~82 g) was overpredicted by the code (59 ± 7 g in the test). The discrepancy between the SCDAP/RELAP5 results and the experimental data was attributed to the absence of a steam-starved period in the calculation.

Sensitivity calculations performed using a relocation temperature criterion of 2,300 K showed a total hydrogen production of 75 g. The ~8% decrease of the calculated total hydrogen generation was due to an early onset of material relocation (~23 seconds earlier). Conversely, a relocation criterion of 30% imposed

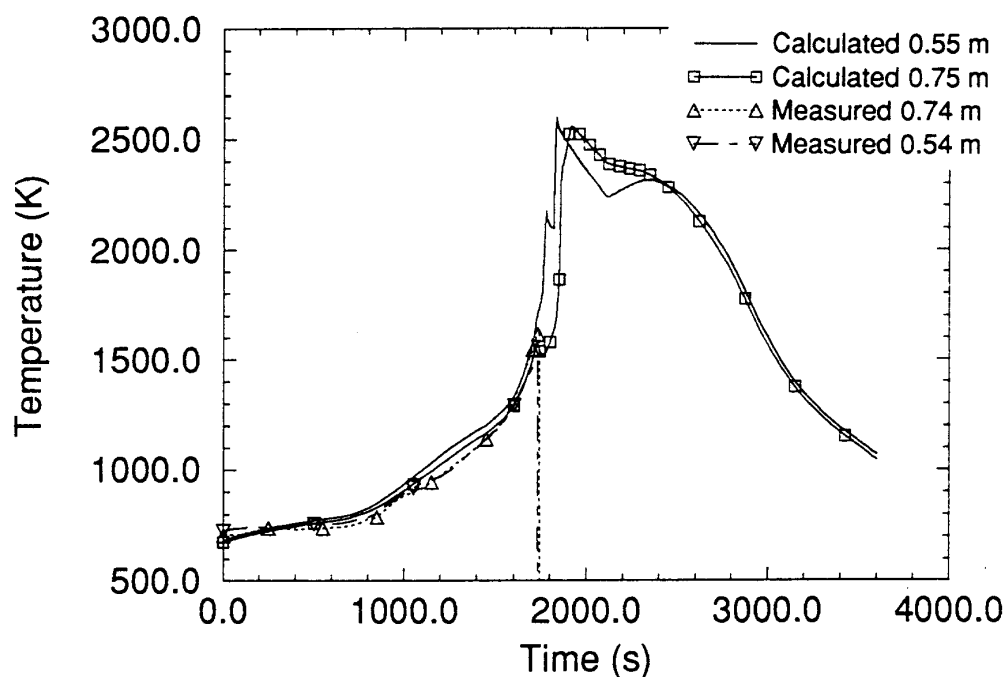


Figure A-61. Cladding temperatures for the top half of the fuel rods for the SFD 1-3 experiment (BE calculation using BE nuclear power + 15% after 1000 seconds).

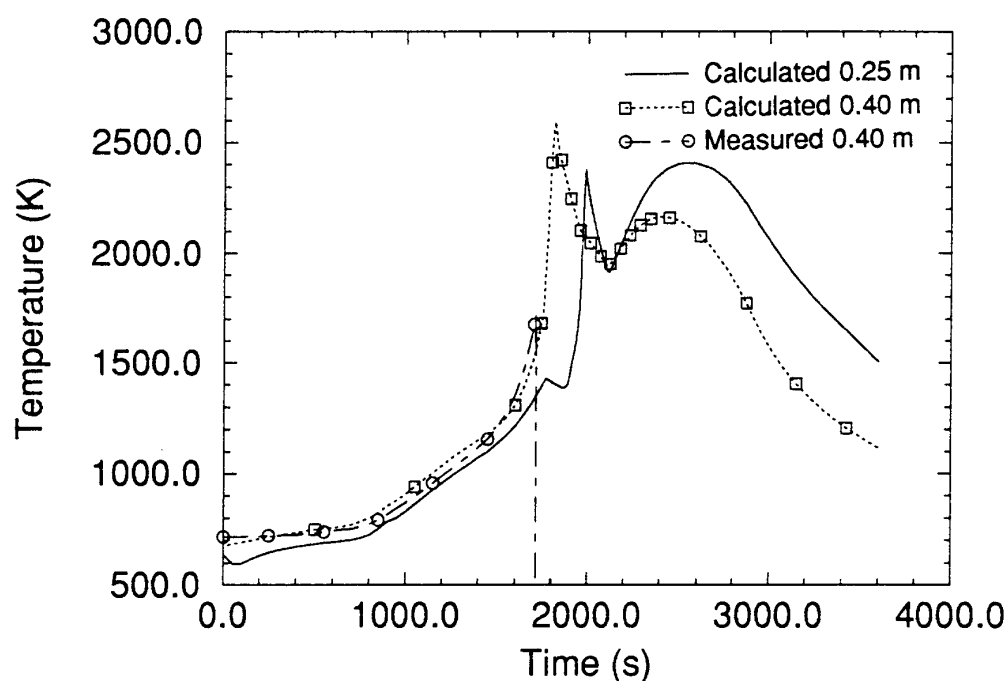


Figure A-62. Cladding temperatures for the bottom half of the fuel rod components for the SFD 1-3 experiment (BE calculation using BE nuclear power + 15% after 1,000 seconds).

on the cladding oxidation showed an increase of the total hydrogen generation by ~8%; but unrealistic fuel temperatures were obtained at the end of this calculation (>3,000 K at 1,952 seconds).

Comparison between the axial profiles of cladding oxidation obtained in the BE calculation and the experiment showed an over prediction of cladding oxidation in the upper part of the bundle. The cladding was calculated to be ~100% oxidized between 0.35 and 0.65 m elevations, whereas complete oxidation was only measured at ~0.1 m elevation from the PIE. Above 0.65 m elevation, the code predicted a cladding oxidation of ~30% (~5% estimated from the PIE). The over prediction of the cladding oxidation in the upper elevation was mainly attributed to the absence of steam-starved conditions in the calculation after the bundle depressurization at 1,733 seconds.

A.5.2.3 Metallic Material Relocation

The main events predicted to occur during the BE calculation are reported in Table A-5.

The metallic (U-Zr-O) material relocation was predicted to occur between 1,800 and 2,000 seconds in the BE calculation. Material relocations based on the analyses of the test scenario were estimated between ~1,850–2,150 seconds. The onset of the relocation of liquefied fuel and cladding materials were calculated to occur between the 0.30 and 0.40 m elevations on the outer fuel rods. At the end of the calculation, the degradation region extended axially from the 0.5 m to the 1 m elevations. Relocated materials formed a cohesive debris ~0.10 m thick in the lower part of the bundle.

Table A-5. Simulated sequence of events for SFD 1-3 experiment.

Event	Calculation (BE Calculation)		Experiment	
	Cladding Temperature (K)	Time (s)	Cladding Temperature (K)	Time (s)
Cladding dissolution by Inconel	1,385	1,550 - 1,600 ^a	~1,380	1,500 - 1,550 (cladding rupture)
Onset of FP release	1,385	1,550 - 1,600 ^b	~1,380	1,500
	1,550	1,700 ^c		
	2,150	1,770 ^d		
Shroud inner liner failure	1,590 ^e	1,733 ^f	~1,350 ^f	1,733
Onset of fuel dissolution	2,150	1,770		
Fuel rod relocation	2,400	1,800 - 2,000		1,850 - 2,150
Maximum fuel temperature	2,625	1,880	~2,800	

a. The time of complete cladding dissolution by Inconel was predicted at 1,700 seconds in the base calculation. This time was shifted 150 seconds forward in the BE calculation. The resulting time (~1,550 seconds) was consistent with the cladding ruptures observed in the test.

b. Due to cladding ruptures and gap release

c. Increase of FP releases due to temperature effect

d. Increase of FP releases due to fuel dissolution

e. Shroud temperature

f. Imposed in the code

The onset of fuel dissolution by molten zircaloy was predicted to start at 1,770 seconds at the 0.45 m elevation for all the fuel rods as the maximum cladding temperature exceeded ~2,150 K. The calculated total fuel dissolution (14.2%) was slightly underpredicted compared to the experiment (~18%).

Sensitivity studies performed with a cladding relocation criterion of 2,300 K showed an underestimation of fuel dissolution (~4%). Additional calculations using a relocation criterion of 30% for the cladding oxidation indicated a large over prediction of total fuel dissolution (>40%).

Very low fuel dissolution was measured in the upper part of the bundle in spite of a local high fuel temperature deduced from the PIE (~2,200 K). It is believed that the fuel/clad interaction existed for a relatively short time in a steam-starved environment for developing significant dissolution. Calculated local fuel dissolution in the upper part of the bundle (~13%) was overpredicted using a cladding relocation criterion of 2,400 K. Better agreement with the experimental data was obtained using a cladding relocation criterion of 2,300 K. In this calculation, local fuel dissolution in the upper elevation was only ~2.5%.

A.5.2.4 Fission Product Releases

The total releases of the noble gases (21.6%) and volatile fission products (FPs) (23.2%) obtained in the BE calculation were correctly predicted compared with the releases observed in the test (noble gases-⁸⁵Kr- ~10% to ~30%; volatile FPs ~8% to ~26%).

Fission product releases due to cladding ruptures were predicted to occur between 1,550 and 1,600 seconds. The total cumulated release from the gaps of the irradiated fuel rods was ~1% at 1,600 seconds.

After the cladding failure, the calculated rate of FPs releases was very low for 100 seconds. At 1,700 seconds, the FPs releases again increased as the maximum fuel temperature exceeded 1,550 K. About 2.5% of the total fission products were calculated to be released due to the temperature effect after cladding ruptures and before fuel dissolution.

The calculation indicated a large increase of the FPs releases caused by fuel dissolution by molten zircaloy at 1,770 seconds as the cladding temperature reached 2,150 K. About 18.5% of the total fission products were calculated to be released after the onset of fuel dissolution.

The total FPs releases were due to cladding ruptures, temperature effect, and fuel dissolution but were mainly produced from the irradiated fuel rods. In particular, no fission product release from the fresh rods was calculated by the code prior to fuel dissolution.

A.5.2.5 Code Performance

The total central processing unit (CPU) time for a simulated transient of 3,600 seconds was 7.9 hours on an IBM RISC Workstation. However, the CPU time increased as the conditions became more severe in the calculation. The ratio (CPU time/simulated time) was only 1.4 at 1,780 seconds prior to any material relocation; but, during the period of material relocation, this ratio increased and reached 7.9 at 3,600 seconds.

A.6. PBF SFD 1-1 EXPERIMENT

The Severe Fuel Damage (SFD) research program was initiated by the U. S. Nuclear Regulatory Commission (NRC) to develop a data base and models to predict (a) the overall response of the core and associated structures, (b) the rate of release of fission products, their chemical forms, and characteristics of their transport and deposition in the primary system, (c) the rate of hydrogen generation from the interaction of coolant with the fuel, cladding, and reactor structure, and (d) the coolability of the damaged fuel following reflood.

The second in a series of four severe fuel damage experiments, SFD 1-1,^{A-14} was conducted in the Power Burst Facility (PBF) at the Idaho National Engineering Laboratory (INEL) on September 8, 1983. Test SFD 1-1 has provided data that have significantly improved the understanding of early phase pressurized water reactor (PWR) melt progression. The experimental results from the PBF SFD 1-1 test and those of other integral and separate effects tests were used in assessing the damage progression models introduced in the SCDAP/RELAP5 code.

A.6.1 Description of the SCDAP/RELAP5 Model

The SFD 1-1 test train incorporated a fuel bundle containing 32 trace-irradiated fuel rods with an average burnup of 79 MWd/MtU. The fuel rods and the shroud were instrumented by thermocouples and a pressure sensor. The spacing between fuel rods in the test assembly was maintained by three Inconel spacer grids ~40 mm in height located at 0.05, 0.45, and 0.86 m elevations. The active length for the fuel rods was 1 m.

The fuel bundle was housed in an insulated shroud to minimize radial heat losses. The shroud consisted of a zircaloy inner liner, an insulated shroud (porous zirconia), an inner and outer zircaloy shroud wall, a zircaloy flow tube, and finally the in-pile tube. The insulated region was pressurized with argon, and the gap between the inner and outer shroud walls was pressurized with helium.

A.6.1.1 Nodalization

The entire experimental structure was modeled using SCDAP/RELAP5 code. As shown in Figure A-63, the test bundle was represented by four SCDAP components, including (1) the 4 fuel rods of the inner ring, (2) the 12 fuel rods of the middle ring, (3) the 16 fuel rods of the outer ring, and (4) the shroud. The fuel components were modeled using four radial nodes, and the shroud was modeled using 19 radial nodes.

As shown in Figure A-64, all the components were modeled using 10 axial nodes each node being 0.1 m tall and communicating with the 10 corresponding RELAP5 hydrodynamic control volumes. The external surface of the shroud was connected to a single RELAP5 hydrodynamic control volume representing the bypass.

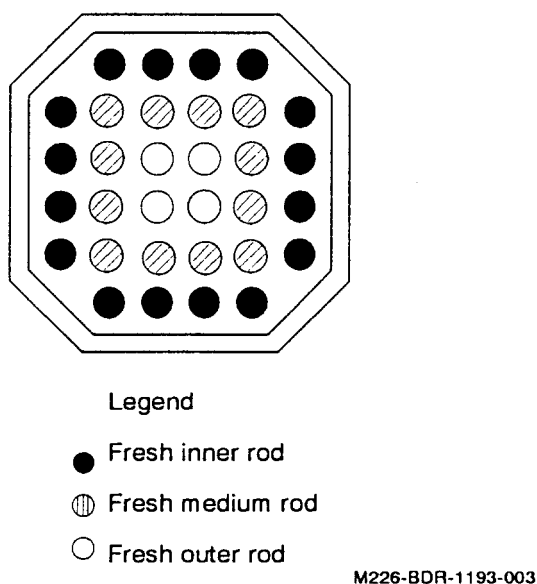


Figure A-63. Core representation for the SFD 1-1 experiment.

A.6.1.2 Initial Conditions

All the fuel rods were pressurized with helium to 3.8 MPa at room temperature. The SCDAP/RELAP5 calculation transient was started after the boildown phase when the two-phase level was ~0.1 m elevation. The mean temperature of the rods was initialized at 715 K with an internal pressure of ~9 MPa.

The initial fission product inventory was calculated by the FASTGRASS model of the SCDAP/RELAP5 code using a realistic power history prior to the test.

A.6.1.3 Boundary Conditions

The estimation of the total nuclear power generated in the bundle as well as the uncertainty envelope (+7% and -15%) was obtained from reactor power measurements and reactor physics calculations.

The axial power profile was represented in the calculations using a single discrete curve provided by fission chambers located on the shroud outer wall and reactor physics calculations.

A mean water inlet flow rate of 0.64 g/s, with a temperature of 531 K and a pressure of 6.8 MPa, was used over the transient. An argon flow rate 1.3 g/s was injected at the bottom of the bundle from 3,200 seconds and was maintained until the end of the transient.

The reflood phase after 3,500 seconds was not considered in these calculations.

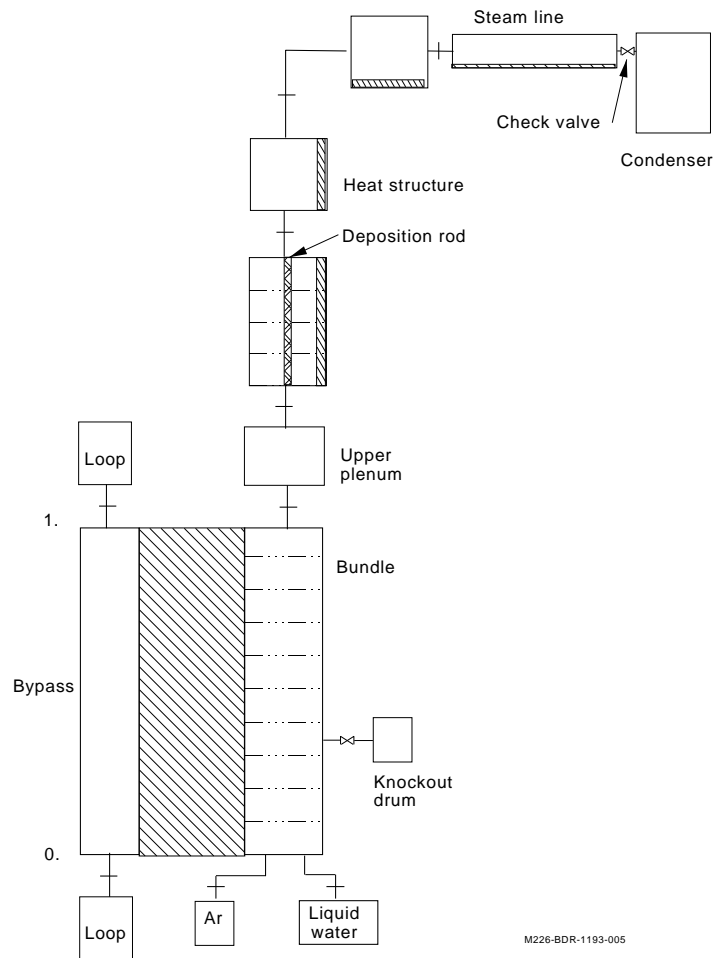


Figure A-64. Nodalization of test train for the SFD 1-1 experiment.

A.6.2 Results

The calculations presented in this section were performed using SCDAP/RELAP5/MOD3.1 with options such as semi-implicit hydrodynamic scheme and time smoothing of the radiative heat transfer.

A.6.2.1 Thermal Behavior

The preliminary calculation (PC) performed using the best estimate (BE) boundary conditions (nuclear power, water flow rate and temperature) showed a large over prediction of both the cladding temperatures and the collapsed liquid level in the bundle.

Analyses of the experimental scenario indicated evidences of steam condensation in the fallback barrier located just above the fuel rods. The nodalization used in these calculations (Figure A-64) did not represent in detail the structures in the upper part of the test bundle and therefore could not account for steam condensation effects. Previous analysis performed using RELAP5 stand-alone code showed that

steam exiting the bundle condensed on the upper structures and drained back into the bundle. This reflux coolant had to be re-vaporized resulting in less power available for heating up the bundle components. The RELAP5 estimation of the net effective power (EP) gained by the bundle is reported in Figure A-65. In addition, the reflux of saturated water downward to the lower part of the fuel rods increased the temperature of the subcooled water injected at the bottom of the bundle. However, this phenomenon was not considered in the base calculations.

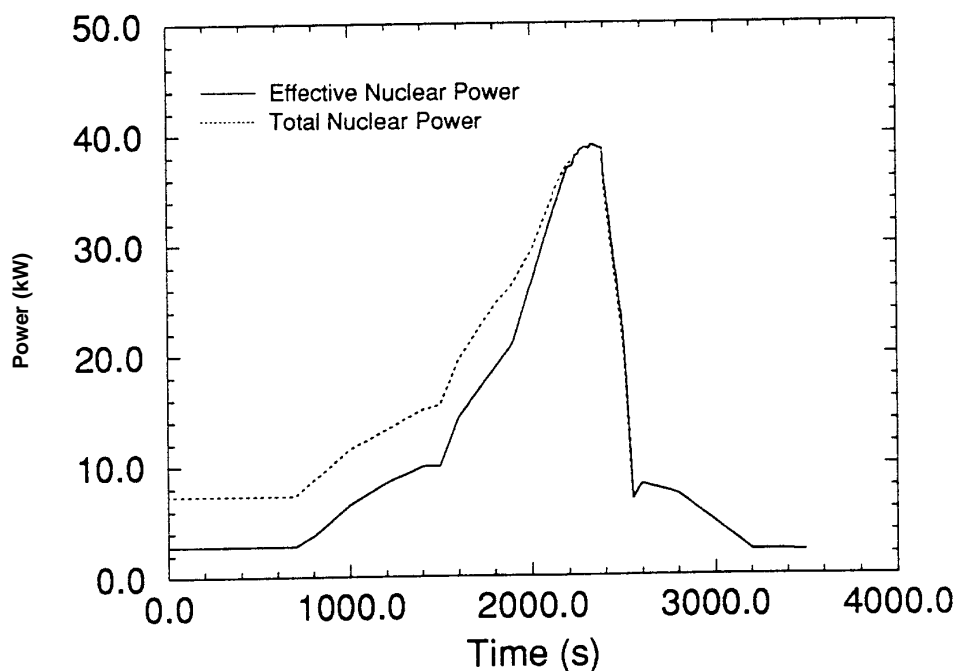


Figure A-65. Total core power for the SFD 1-1 experiment.

Calculated cladding temperatures in better agreement with the experimental data were obtained using the effective power generated in the bundle. This BE calculation showed a correct agreement of the calculated cladding temperatures compared with the experimental data, until the thermocouple failures around 2,000 seconds (Figures A-66 and A-67). The cladding ruptures due to cladding internal overpressure were predicted to occur between 1,464 and 1,492 seconds, with a double-sided oxidation extending over ~0.4 m. This result was consistent with the cladding ruptures and the onset of FPs release observed in the test (~1,538–1,632 seconds).

The calculated collapsed liquid level was overpredicted for the first 2,200 seconds in the transient, leading the steam generated in the bundle to be underpredicted. Local steam-starved conditions in the upper part of the bundle were calculated to occur shortly after 1,800 seconds. The analyses of the test scenario showed that the oxidation of the relocated molten materials combined with the shroud inner liner failure (~1,920 seconds) caused nearly complete flow blockage in the lower part of the bundle and a hydrogen-rich gas mixture to flow around the melt. The time of complete steam consumption deduced from the test scenario was ~2,400 seconds (~600 seconds later than calculated).

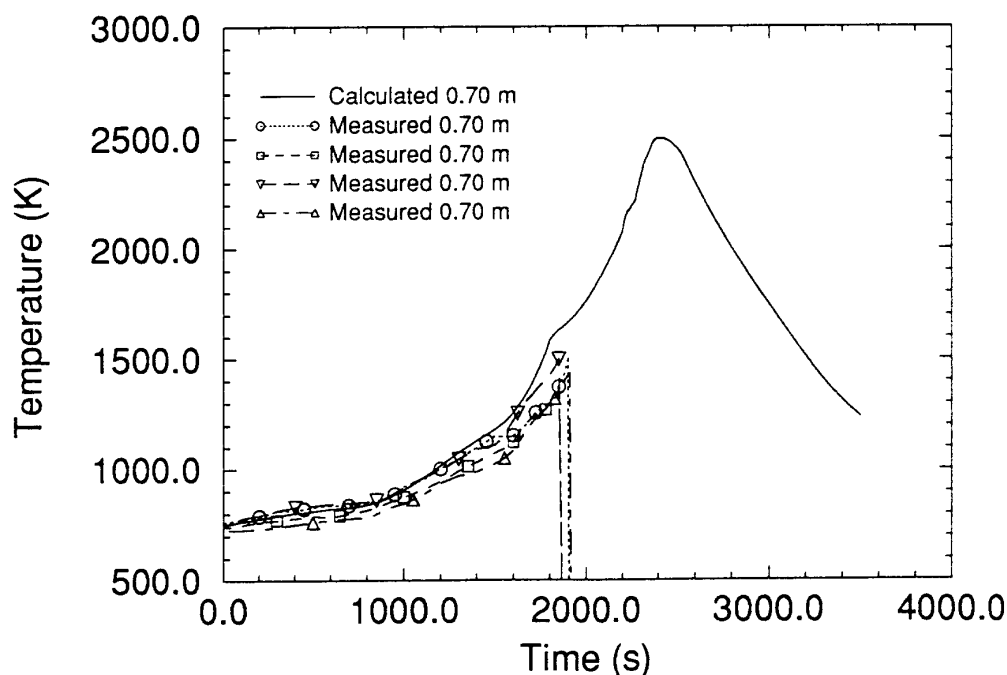


Figure A-66. Cladding temperatures for the top half of the fuel rods for the SFD 1-1 experiment (BE calculation).

As explained above, the temperature of the water delivered to the bundle could be higher than that measured in the test because of the reflux coolant from condensation effects. The collapsed liquid level and the steam generated in the bundle were correctly predicted in a sensitivity calculation using saturation conditions of the water injected at the bottom of the fuel rods (68 MPa, 558 K). This calculation indicated an increase of the steam generated in the bundle by 25% during the first 2,000 seconds. However, no significant effect was found at the onset of steam-starved conditions because of a large hydrogen flow rate generated at 1,800 seconds. The hydrogen generation rate started to increase dramatically at 1,500 seconds and rapidly reached the steam-starved limit at 1,800 seconds.

The end of steam-starved conditions deduced from the test scenario was estimated at ~2,600 seconds. The BE calculation indicated that the onset of material relocation (~2,240 seconds) led to the prediction of the steam-rich atmosphere in the upper part of the bundle because of the absence of the oxidation model of molten materials in the current version of the code. Therefore, the end of steam-starved conditions was calculated to occur at ~2,240 seconds (~360 seconds earlier than that deduced from the test).

The axial profile of the calculated maximum fuel temperatures in the BE calculation along with that deduced from the PIE are reported in Figure A-68. This figure shows an over prediction of the temperature in the upper part of the bundle and an under prediction in the lower part.

The calculated maximum fuel temperature (~2,600 K) was obtained at mid-bundle at 2,425 seconds, approximately 185 seconds after the prediction of the onset of cladding material relocation and the end of steam-starved conditions in the upper part of the bundle. The steam-rich environment predicted by the code between 2,240–2,425 seconds and the resulting power generated from zircaloy oxidation could

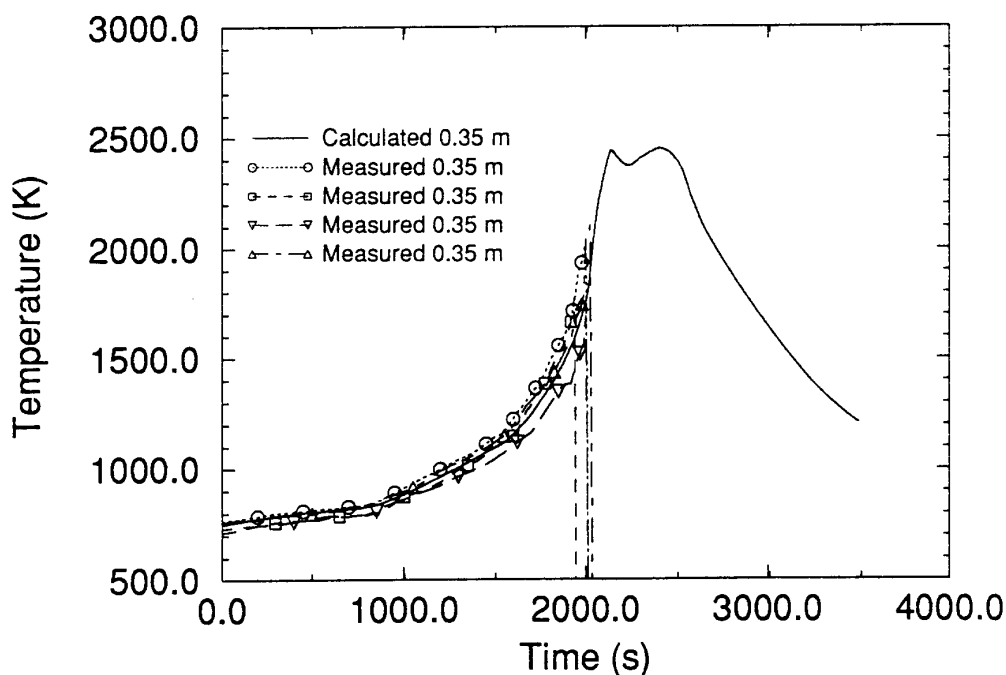


Figure A-67. Cladding temperatures for the bottom half of the fuel rod components for the SFD 1-1 experiment (BE calculation).

explain the over prediction of the fuel temperature in the upper part of the bundle. Moreover, the under prediction of the maximum fuel temperatures obtained at 0.15 m elevation was partially attributed to the absence of molten material oxidation in the calculation.

A.6.2.2 Hydrogen Production

The BE calculation assumed the relocation of molten zircaloy occurring from 2,300 K for a cladding oxidation less than 60%. The calculated total hydrogen production (~ 94 g) was overpredicted (64 ± 7 g in the test). This discrepancy is most likely due to the overprediction of the cladding temperature in the upper half of the bundle.

A sensitivity study performed using a relocation temperature criterion of 2,400 K showed a total hydrogen production of 110 g, but no cladding relocation was predicted in this calculation. The same tendency was observed in a calculation using a cladding temperature criterion of 2,300 K and a cladding oxidation of 30% (the calculated hydrogen production was 104 g).

Complete cladding oxidation was predicted at mid-bundle in the BE calculation. Cladding oxidation in the lower and upper parts of the bundle was about 30%. However, large uncertainties with PIE measurements prevent quantitative comparisons with the calculation of oxidized material distribution. But, calculated cladding oxidation in the upper elevations was probably overestimated.

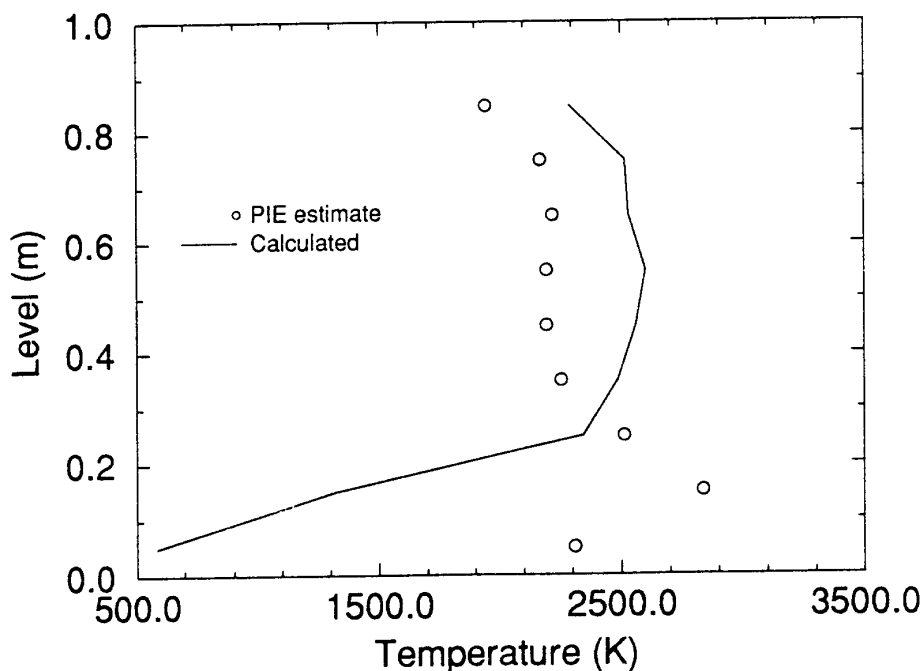


Figure A-68. Axial profile of maximum fuel temperature (BE calculation).

A.6.2.3 Metallic Material Relocation

The main events observed in the BE calculation are reported in Table A-6. The first events occurring during the calculation were the cladding ruptures (1,464-1,492 seconds) caused by internal overpressure. The slumping of the grid spacer located at mid-bundle was calculated at 1780 seconds as the cladding temperature reached 1,615 K. At 0.55 m elevation, all the fuel rod cladding was predicted to be completely dissolved by the grid spacer over an axial length of 60 mm.

The metallic (U-Zr-O) material relocation was predicted to occur between 2,240 and 2,592 seconds in the BE calculation. The onset of the relocation of liquefied fuel and cladding materials occurred at 0.65 m elevation. At the end of the calculation, the degradation region axially extended from 0.5 to 1 m elevations. Relocated materials formed a cohesive debris ~0.12 m in height in the lower part of the bundle.

The onset of fuel dissolution by molten zircaloy was calculated at 2,055 seconds at 0.35 m elevation for all the fuel rods as the cladding temperatures exceeded ~2,150 K. The calculated total fuel dissolution (~6.1%) was underpredicted compared to the experiment (~16%). Two main reasons could explain the discrepancy between the calculation and the experimental data (a) the fuel dissolution profile deduced from the PIE showed large fuel dissolution at ~0.15 m elevation due to material relocation and high local temperatures. As explained in the previous section, the code underpredicted the temperatures in the lower

Table A-6. Simulated sequence of events for SFD 1-1 experiment.

Calculation (BE Calculation)			Experiment	
Event	Cladding Temperature (K)	Time (s)	Cladding Temperature (K)	Time (s)
Cladding dissolution by Inconel	1,190	1,464 - 1,492	1,067 - 1,139	1,538 - 1,632
Onset of FP release	2,150	2,055 ^a	~1,050 >2,030	~1,400 ^b ~2,000 ^a
Shroud inner liner failure	1,650 ^c	1,920 ^d		1,920
Onset of fuel dissolution	2,150	2,055	>2,030	>2,000
Fuel rod relocation	2,300	2,240 - 2,592	>2,030	>2,000
Maximum fuel temperature	2,600	2,425	2,870	~2,400 - 2,470

a. Due to fuel dissolution

b. Due to cladding rupture

c. Inner liner temperature

d. Imposed in the code

part of the bundle and consequently could have underpredicted local fuel dissolution and (b) the analyses of the PIE suggested that fuel relocation as solid material occurred from the upper part of the fuel rods and liquefied in the lower part of the bundle increasing total fuel dissolution. This effect was not considered in the current version of the code. Very low fuel dissolution was measured in the upper part of the bundle in spite of a local high fuel temperature deduced from the PIE (~2,200 K). It is believed that the clad/fuel interaction existed for a relatively short time in a steam-starved environment for developing significant dissolution. Calculated local fuel dissolution in the upper part of the bundle (~5%) was overpredicted using a cladding relocation criterion of 2,300 K. Better agreement with the experimental data was obtained using a cladding relocation criterion of 2,200 K. In this calculation, local fuel dissolution in the upper elevation was only ~1%.

A.6.2.4 Fission Product Releases

In spite of an under prediction of fuel dissolution by a factor of 2.5, the calculated total noble gas FPs releases (7.2% and 7.6%, respectively) were in correct agreement with the releases observed in the test (noble gases ~2.6% to ~9.3%; volatile FPs ~9% to ~12%).

Releases of the noble gases and volatile fission products were predicted to start at 2,055 seconds in the BE calculation. The FPs releases from the fresh fuel rods calculated by the code were driven by fuel dissolution by molten zircaloy. No fission product emission was calculated prior to the onset of fuel dissolution at 2,055 seconds.

A.6.2.5 Code Performances

The total central processing unit (CPU) time for a simulated transient of 3,500 seconds was 1.76 hours on an IBM RISC Workstation. However, the CPU time increased as the conditions became more severe in the calculation. The ratio (CPU time/simulated time) was only 1.02 at 2,150 seconds prior to any material relocation; but, during the material relocation, this ratio increased and reached 1.81 at the end of the transient.

A.7. PBF SCOPING TEST EXPERIMENT

The severe fuel damage (SFD) research program was initiated by the U.S Nuclear Regulatory Commission (NRC) to develop a data base and models to predict (a) the overall response of the core and associated structures, (b) the rate of release of fission products, their chemical forms, and characteristics of their transport and deposition in the primary system, (c) the rate of hydrogen generation from the interaction of coolant with the fuel, cladding, and reactor structure, and (d) the coolability of the damaged fuel following reflood.

Scoping Test SFD-ST,^{A-15} the first in a series of severe fuel damage experiments, was conducted in the Power Burst Facility (PBF) at the Idaho National Engineering Laboratory (INEL) on October 28, 1982. A major objective of SFD-ST was to gain experience in performing such tests. However, SFD-ST has provided data that have significantly improved the understanding of early phase pressurized water reactor (PWR) melt progression. The experimental results from the SFD-ST and those of other integral and separate effects tests were used in assessing the damage progression models introduced in the SCDAP/RELAP5 code.

A.7.1 Description of the SCDAP/RELAP5 Model

The SFD-ST test train incorporated a fuel bundle containing 32 trace-irradiated fuel rods with an average burnup of 91 MWd/MtU. The fuel rods and the shroud were instrumented by thermocouples and pressure sensors. The spacing between fuel rods in the test assembly was maintained by three Inconel spacer grids ~40 mm in height located at 0.05, 0.45, and 0.86 m elevations. The active length for the fresh fuel rods was ~0.92 m.

The fuel bundle was housed in an insulated shroud to minimize radial heat losses. The shroud was composed of a zircaloy inner liner, an insulated shroud (porous zirconia), an inner and outer zircaloy shroud wall, a zircaloy flow tube, and finally the in-pile tube. The insulated region was pressurized with argon, and the gap between the inner and outer shroud walls was pressurized with helium.

A.7.1.1 Nodalization

The entire experimental structure was modeled using SCDAP/RELAP5 code. As shown in Figure A-69, the test bundle was represented by four SCDAP components, including (1) the 4 fuel rods of the inner ring, (2) the 12 fuel rods of the middle ring, (3) the 16 fuel rods of the outer ring, and (4) the shroud.

The fuel components were modeled using four radial nodes, and the shroud was modeled using 19 radial nodes.

As shown in Figure A-69, all the components were modeled using 10 axial nodes, each node being 0.1 m tall and communicating with the 10 corresponding RELAP5 hydrodynamic control volumes. The external surface of the shroud was connected to a single RELAP5 hydrodynamic control volume representing the bypass.

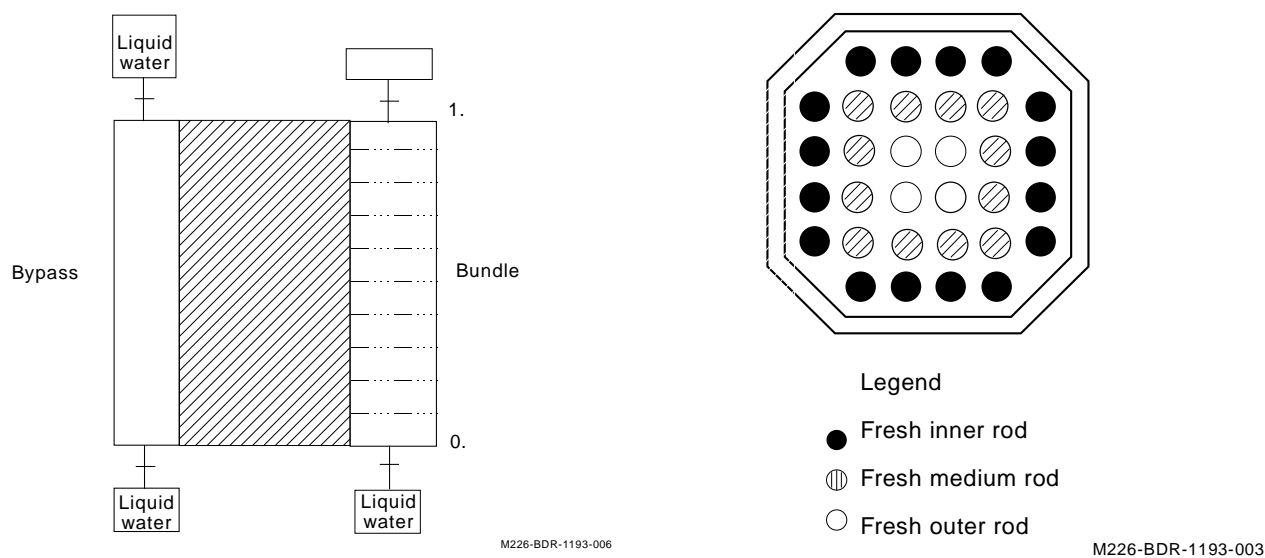


Figure A-69. Nodalization and core representation of the test train for the SFD-ST experiment.

A.7.1.2 Initial Conditions

All the fuel rods were pressurized to 3.8 MPa with helium at room temperature. The SCDAP/RELAP5 calculation transient was started after the boildown phase when the two-phase level was at the ~0.4 m elevation. The mean temperature of the rods was initialized at ~610 K with an internal pressure of ~7.7 MPa.

The initial fission product inventory was calculated by the FASTGRASS model of the SCDAP/RELAP5 code using a realistic power history prior to the test.

A.7.1.3 Boundary Conditions

The estimation of the total nuclear power generated in the bundle was obtained from reactor power measurements and reactor physics calculations (Figure A-70). The uncertainty envelope for the measured total nuclear power was $\pm 15\%$.

The axial power profile was represented in the calculations using three discrete curves. The calculations were started using a profile identified as partial water-filled conditions, then was shifted to a profile representing the 10% water-filled conditions (11,690 seconds) and then finally to a profile representing the steam-filled bundle at time after 12,183 seconds.

A high water inlet flow rate of ~16 g/s, with a temperature of ~525 K and a pressure of 6.65 MPa, was delivered to the bundle over the transient. The experiment was terminated at ~13,348 seconds by manually scrambling the reactor and by reflooding the test bundle.

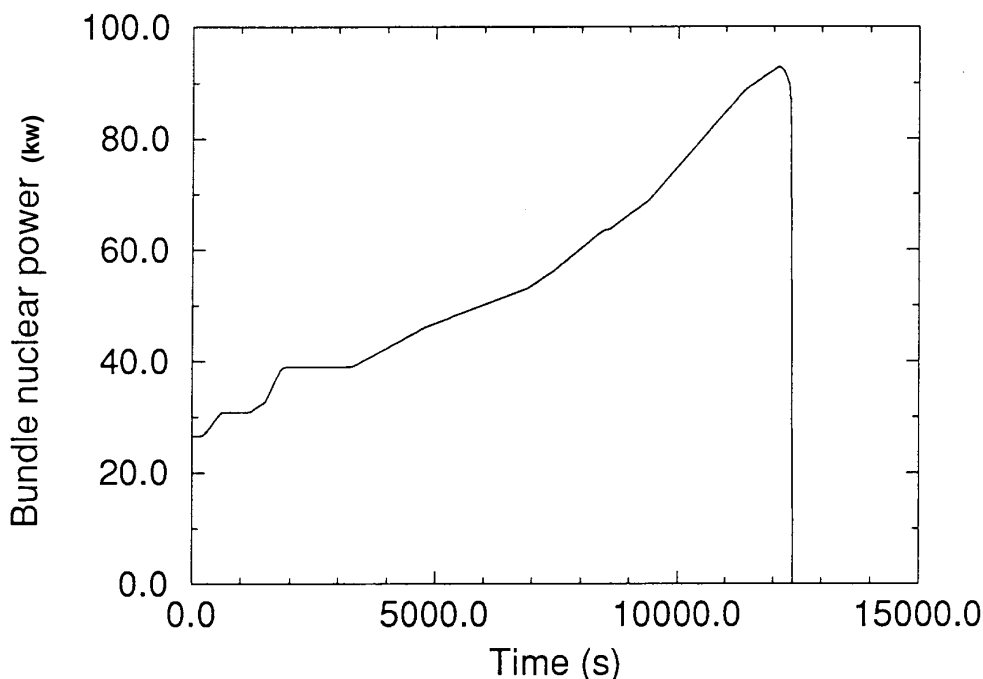


Figure A-70. Total bundle power for the SFD-ST experiment.

A.7.1.4 Shroud Thermal Conductivity

The thermal conductivity of the shroud insulator was measured prior to the test but analysis of the experimental scenario showed evidence of shroud thermal conductivity variations during the transient. However, the measured thermal conductivity of the shroud insulator was used over the entire SCDAP/RELAP5/MOD3 calculations.

A.7.2 Results

The calculations, presented in this section, were performed using SCDAP/RELAP5/MOD3.1 with options such as semi-implicit hydrodynamic scheme and time smoothing of the radiative heat transfer. In the calculations, the shattering of all the partially oxidized cladding was assumed to be instantaneous and was imposed in the code shortly before the reflooding period (~12,324 seconds).

A.7.2.1 Thermal Behavior

The preliminary calculation (PC) performed using the best estimate boundary conditions (nuclear power, water inlet flow rate and temperature) showed an under prediction of the cladding temperatures in the upper part of the bundle (Figure A-71). This results indicated that the net power gain by the bundle was underpredicted. The inlet water flow rate, the thermal conductivity of the shroud insulator as well as the nuclear power generated in the bundle were recognized to be the major uncertainty factors in the SFD-ST analysis. Better estimations of the cladding temperatures could be obtained by tuning one of these parameters inside the experimental uncertainty range.

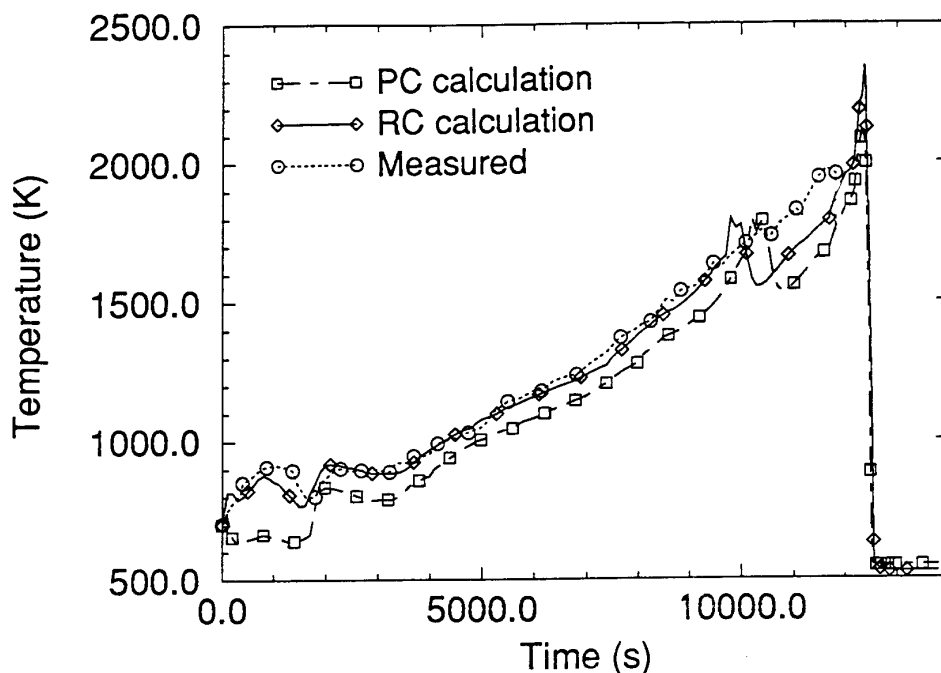


Figure A-71. Cladding temperatures for the top half of the fuel rods for the SFD-ST experiment. PC: preliminary calculation. RC: reference calculation.

Calculated temperatures in better agreement with the experimental data were obtained in a reference calculation (RC) using an adjustment of the nuclear power generated in the bundle. The best estimate nuclear power deduced from the test was increased by 15% until ~1,511 seconds and then increased by 7% until the end of the calculation. Under these conditions the cladding temperatures in the upper elevations were correctly calculated for the first 9,600 seconds into the transient (Figure A-71). In the SFD-ST test scenario, the water inlet flow rate delivered to the bundle was much higher than those used in the other PBF SFD tests. Consequently, the calculated maximum cladding temperatures were obtained in the upper part of the fuel rods between 0.75 and 0.85 m elevations.

In the RC calculation, the cladding ruptures by internal overpressure were predicted to occur at ~4,500 seconds at the 0.85 m elevation as the local cladding temperatures exceeded ~1,070 K. Cladding rupture allowed steam to fill the internal gap between the fuel and the cladding and to produce a double-sided oxidation from 0.5 to 1 m elevations. The cladding ruptures were calculated to occur at a lower temperature and earlier than those observed in the experiment (~1,100-1,200 K and ~5,000-6,200 seconds in the test).

At ~9,750 seconds, the code predicted oxidation runaway at the 0.75 m elevation as the local cladding temperature exceeded 1,850 K. At this elevation, the temperature escalation was calculated to continue for about ~100 seconds, until complete cladding oxidation. However, no temperature escalation was observed in the test probably because of a complete consumption of the zircaloy cladding as the temperatures exceeded ~1,850 K.

In the RC calculation, the interaction between cladding zircaloy and Inconel of the upper spacer grid was predicted to start at ~7,000 seconds and to end at ~8,450 seconds (~1,550 K) with the slumping of the eutectic materials onto the middle spacer grid located at 0.55 m elevation. The code predicted no effect of the relocation of the upper spacer grid on the cladding temperatures. Shortly before ~10,000 seconds, the middle spacer grid was calculated to slump and to relocate at the 0.15 m elevation below the liquid level.

The relocation of the two upper spacer grids caused a fast cool down of the fuel rods. Two main reasons could explain the rapid decrease of the fuel rod temperatures. First, the reduction of the oxidation power due to zircaloy relocation after the interaction with the middle spacer grid. Second, the relocation of the spacer grid below the liquid level resulted in a ~0.1 m upward displacement of the corresponding water volume and caused a partial quenching of the fuel rods (Figure A-72).

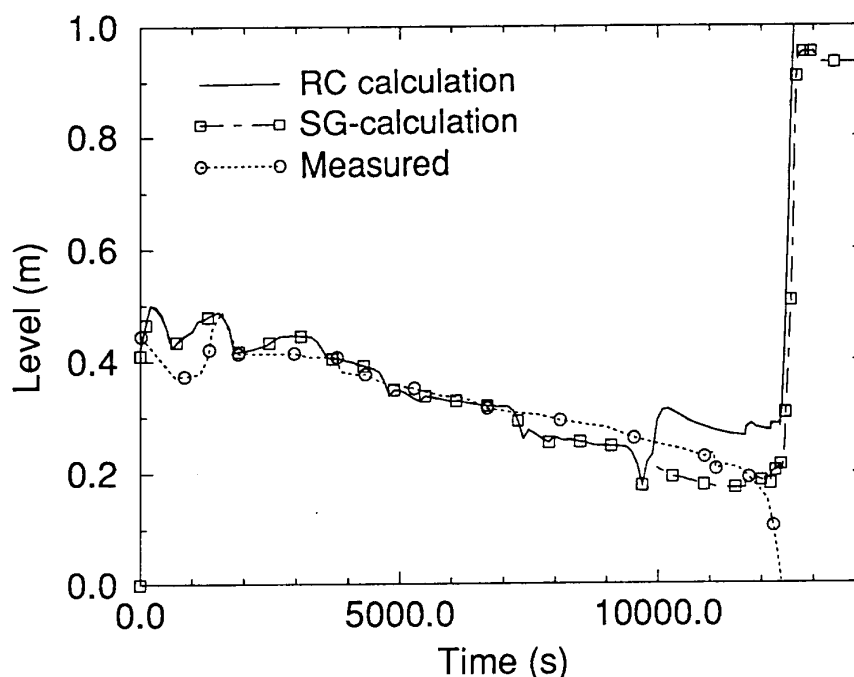


Figure A-72. Collapsed liquid level in the bundle for the SFD-ST experiment. RC: reference calculation. SG-: calculation without spacer grid.

However, no significant temperature reduction was observed in the test at ~10,000 seconds and the measured collapsed liquid level showed a continuous decrease until the reflooding phase. This results could indicate that the spacer grid model used in the current version of the code overpredicted the zircaloy mass dissolved by Inconel.

Complete dryout of the bundle was not obtained in the RC calculation as observed in the test at ~12,390 seconds. The minimum collapsed liquid level (~0.1 m) was predicted at ~9,650 seconds.

Analysis of the SFD-ST test scenario indicated that the reactor scrambling and the reduction of the nuclear power generated in the bundle at 12,348 seconds resulted in a reflooding of the fuel rods. During this period, the quenching and the shattering of the partially oxidized cladding increased the zircaloy oxidation reaction in the bundle.

This phase was simulated in the SFD-ST analyses using the SCDAP/RELAP5/MOD3 code. A maximum cladding temperature of $\sim 3,120$ K was obtained in the RC calculation at the 0.45 m elevation during the reflooding period. This result was consistent with the maximum temperature deduced from the PIE. The maximum cladding temperatures calculated in the upper part of the bundle was only 2,400 K (2,670-2,960 K estimated from the PIE). The bundle was calculated to be completely filled with water ~ 300 seconds after the reactor scrambling (this phase lasted ~ 480 seconds in the experiment)

A sensitivity calculation (SG) was performed without the spacer grids to study the effect of these components. The cladding temperatures and the collapsed liquid level obtained in this calculation were in better agreement with the experimental results. The rapid cool down of the fuel rods due to the relocation of the spacer grids was not predicted in this sensitivity study (Figure A-73). However, the code did not predict complete dryout of the bundle (Figure A-72).

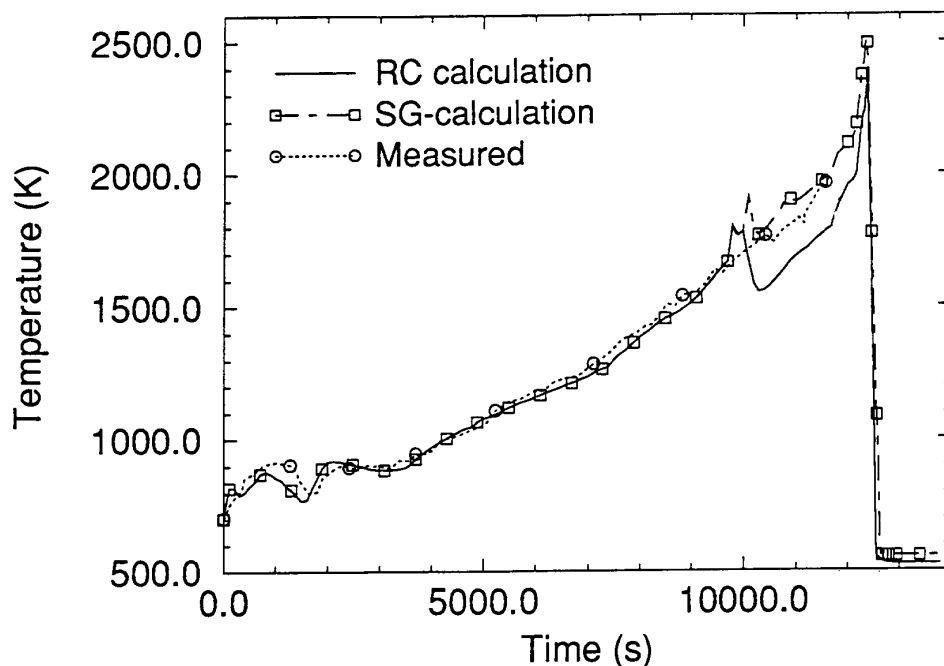


Figure A-73. Cladding temperatures for the top half of the fuel rods for the SFD-ST experiment. RC: reference calculation. SG-: calculation without spacer grid.

A.7.3 Cladding Oxidation and Hydrogen Production

The onset of hydrogen generation was calculated to start at $\sim 5,000$ seconds as the maximum cladding temperature in the upper elevations exceeded $\sim 1,100$ K (Figure A-74). At $\sim 10,000$ seconds the predicted hydrogen mass rate decreased due to a complete cladding oxidation in the upper part of the bundle.

The total hydrogen mass generated during the RC calculation (~ 105 g) was slightly underpredicted compared to that deduced from the PIE ($\sim 150 \pm 35$ g). The predicted total hydrogen mass generated was ~ 85 g before the reactor scrambling. About ~ 20 g of the hydrogen mass was calculated to be released from the bundle during the reflooding period.

This discrepancy was mainly attributed to the over prediction of the collapsed liquid level just before the reflooding period resulting in a low percent of cladding oxidation to be calculated in the lower part of the bundle. Before the reflooding phase, the calculated percent of cladding oxidation were less than ~1% below the 0.30 m elevation, less than ~20% between 0.30 and 0.50 m elevations and 100% above the 0.50 m elevation. At the end of the calculation the percent cladding oxidation were less than ~1%, ~80% and 100%, respectively. The PIE indicated a complete cladding oxidation at the 0.27 m elevation.

The increase of the hydrogen rate released from the bundle due to the quenching and the shattering of the cladding was measured in the test with a large uncertainty. However, comparison with the calculated hydrogen rate showed a correct prediction of the magnitude of the hydrogen peak during the reflooding phase (~1 g/s). A large increase of the hydrogen mass released was predicted shortly after cladding shattering and proceed for about ~40 seconds. The analyses of the test scenario suggested that the hydrogen peak observed during the reflooding period was more spread over the time (probably between 300 and 600 seconds).

This discrepancy was attributed to the instantaneous shattering of the cladding assumed in the calculation. During the test, the cladding shattering and the resulting increase of the hydrogen mass generated was probably more progressive as the liquid level rose in the bundle.

In the RC calculation, the hydrogen peak was mainly due to the shattering of the partially oxidized cladding below the 0.50 m elevation. Shortly before the reactor scrambling, the calculated hydrogen flux generated from the cladding outer surface at the 0.45 m elevation was ~2.5 mg/cm²/s. The local hydrogen flux dramatically increased to ~1,150 mg/cm²/s just after cladding shattering at the beginning of the reflooding period.

The total hydrogen mass generated calculated in the SG- calculation (without spacer grid) was ~140 g and ~25 g was released during the reflooding phase (Figure A-74). The increase of the hydrogen mass generated compared to that obtained in the RC calculation was mainly due to the extent of the cladding oxidation downward the lower part of the bundle (the cladding oxidation was ~85% between 0.20 m and 0.50 m elevations in the SG calculation).

A.7.3.1 Metallic and Ceramic Material Relocation

The main events observed in the RC calculation are reported in Table A-7. The first event occurring during the calculation was the cladding ruptures (~4,500 seconds) caused by internal overpressure.

The onset of local cladding dissolution by Inconel of the upper spacer grid located at 0.95 m was calculated to start at ~7,000 seconds as the local temperature exceeded ~1,250 K. This interaction was predicted to end at ~8,450 seconds (~1,550 K) with complete cladding dissolution over an axial length of

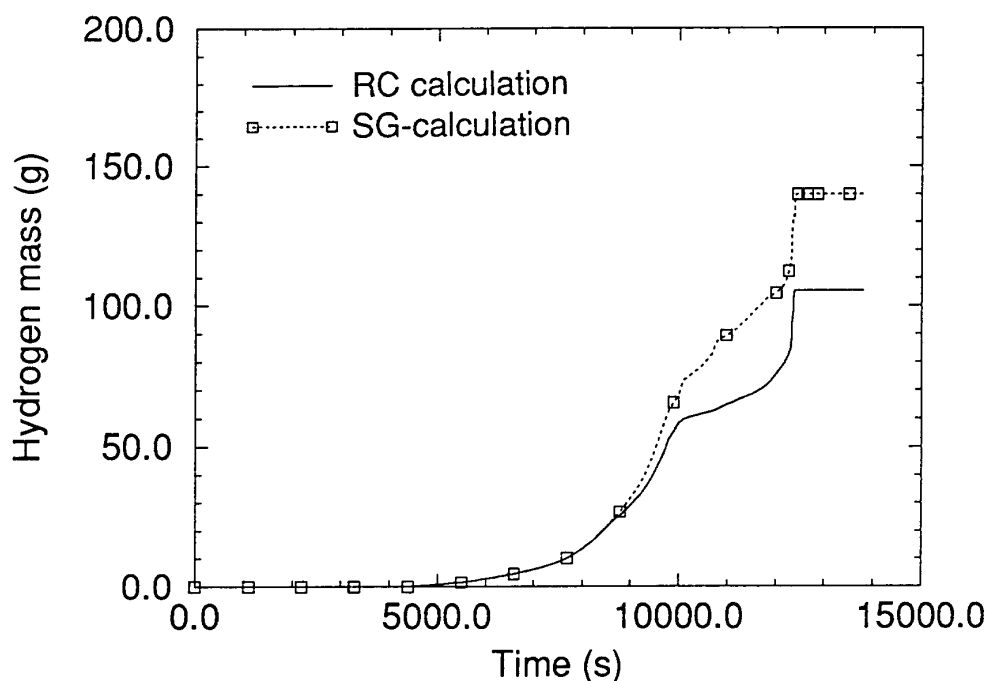


Figure A-74. Total hydrogen generation mass for the SFD-ST experiment. RC: reference calculation. SG-: calculation without spacer grid.

~85 mm and the slumping of the liquefied eutectic. About ~275 g of metallic zircaloy was calculated to be dissolved and to slump onto the middle spacer grid located at ~0.55 m.

Local cladding dissolution by Inconel of the middle spacer grid was calculated to start at ~8,150 seconds (~1,250 K). Shortly before ~10,000 seconds, the middle spacer grid was calculated to slump and relocated as the local cladding temperature exceeded ~1,550 K. At the 0.50 m elevation, all the fuel rod cladding was predicted to be completely dissolved by the spacer grid over an axial length of ~60 mm. The relocated materials were calculated to refreeze at the 0.15 m elevation below the liquid level producing a cohesive debris ~95 mm height.

The onset of fuel dissolution by molten zircaloy was calculated to occur at ~12,320 seconds at the 0.45 m elevation as the local cladding temperature exceeded ~2,150 K. The total fuel dissolution (~10%) was slightly underpredicted compared to that measured in the PIE (~15%). However the axial extent of fuel dissolution was calculated to be limited from 0.30 m to 0.50 m elevations.

At ~12,330 seconds in the RC calculation, the cladding temperature at the 0.45 m elevation (~3,120 K) was predicted to exceed the melting point of the oxide shell and a breach occurred in the oxidized fuel rods. At this elevation the relocated materials consisted mainly of zircaloy oxide.

The RC calculation assumed the relocation of the liquefied fuel and the molten zircaloy occurring from 2,680 K for a percent of cladding oxidation less than 60%. Cladding material relocations due to this criterion were calculated to occur at ~12,360 seconds at the 0.35 m elevation. The relocated materials

Table A-7. Simulated sequence of events for SFD-ST experiment.

Event	Calculation (BE Calculation)		Experiment	
	Cladding Temperature (K)	Time (s)	Cladding Temperature (K)	Time (s)
Cladding rupture	1,070	~4,500	~1,100 - 1,200	~5,000 - 6,200
Cladding dissolution by Inconel (upper grid spacer)	~1,250 ~1,550	~7,000 ^a ~8,450 ^b		
Cladding dissolution by Inconel (middle grid spacer)	~1,250 ~1,550	8,150 ^a 10,000 ^b		
Shroud inner liner failure	1,580 ^c	11,040 ^d		~11,040
Onset of FP release	2,150	12,320 ^e	~1,100-1,200 ~2,100	~5,500 ^f ~12,000
Onset of fuel dissolution	2,150	12,320	~2,100	~12,000
Fuel rod relocation	3,120 2,680	~12,330 ^g ~12,360 ^h		
Maximum cladding temperature	3,120	~12,330	~2,670 - 3,000	~12,348 - 12,828

a. Beginning of zircaloy/Inconel interaction

b. End of zircaloy/Inconel interaction

c. Shroud temperature

d. Imposed in the code

e. Due to fuel dissolution

f. Due to cladding rupture

g. Melting of the oxide shell

h. Cladding failure due to the relocation criteria (Cladding temperature > 2,680 K - Percent of cladding oxidation < 60%)

(~170 g of metallic zircaloy) were calculated to refreeze at the 0.15 m elevation, producing a cohesive debris ~140 mm height.

A.7.3.2 Fission Product Releases

The calculated total noble gas and volatile fission product (FPs) releases (~17.3%) were underpredicted compared to the releases observed in the test (noble gases ~50%; volatile FPs ~32% to ~51%). Analysis of the test scenario suggested that more than 50% of the fission products was released during the reflooding period. However, the code does not consider the increase of FPs emissions due to fuel shattering and consequently underpredicted the total FPs releases.

Releases of the noble gases and volatile fission products were predicted to start at 12,320 seconds in the RC calculation. The FPs releases from the fresh fuel rods calculated by the code were driven by fuel dissolution by molten zircaloy. No fission product emission was calculated prior to the onset of fuel dissolution at ~12,320 seconds.

A.7.3.3 Code Performances

The total central processing unit (CPU) time for a simulated transient of 12,800 seconds was ~11 hours on an IBM RISC Workstation. The CPU time increased as the conditions became more severe in the calculation. The ratio (CPU time/simulated time) was only 1.7 at 8,200 seconds prior to any material relocation; but during the material relocation and the reflooding period, this ratio increased and reached 2.8 at the end of the transient.

A.8. PHEBUS B9+ EXPERIMENT

The PHEBUS severe fuel damage (SFD) research program was conducted in France by the Commissariat à l'Energie Atomique (CEA) to investigate the main phenomena occurring during core degradation of a pressurized water reactor (PWR).

PHEBUS B9+,^{A-16} the fifth in a series of six severe fuel damage experiments, was conducted in the PHEBUS facility at Cadarache Nuclear Center in January 1989. The objectives of the PHEBUS B9+ test were to develop a data base and models to predict: (a) zircaloy cladding oxidation, (b) mechanical behavior of the external oxide shell, (c) fuel and oxide dissolution by molten zircaloy, and (d) relocation of the melt.

Different hydrodynamic aspects such as blowdown or core boildown were not reproduced in the PHEBUS B9+ test. Consequently, this test provided a unique opportunity to assess the basic material interaction phenomena occurring during a severe accident. In 1990, the PHEBUS B9+ test was chosen by the OECD/CSNI for the International Standard Problem ISP28.

The PHEBUS B9+ test has provided data that have significantly improved understanding of the early phase of PWR melt progression. Experimental results from the B9+ test and those of other integral and separate effects tests were used to assess damage progression models introduced in several computer codes including SCDAP/RELAP5/MOD3.1.

A.8.1 Description of the Test Train

The PHEBUS B9+ test train incorporated a fuel bundle containing 21 fresh fuel rods in a 12.6 mm square pitch matrix. The spacing between fuel rods in the test assembly was maintained by two Inconel spacer grids ~38 mm in height located at 0.138 and 0.661 m elevations. The top of the fuel rods was fitted with a fusible seal having a low melting temperature (~1,100 K) to avoid cladding deformations. Total lengths of the zircaloy cladding and the fuel pellet stack were ~1.04 and 0.8 m, respectively.

The fuel bundle was housed in an octagonal insulated shroud to minimize radial heat losses. The shroud consisted of a zircaloy inner liner (0.6 mm thick), an insulated shroud of porous zirconia (~21.25 mm thick), a thin layer of high density zirconia (1 mm thick), and a stainless steel tube (8 mm thick).

A constant low helium flow rate (~0.05 g/s) at a pressure of 1.9 MPa was delivered to the insulated region during the test to limit variations in shroud thermal conductivity caused by steam or hydrogen entering from the fluid channel.

A.8.2 Description of the Test Scenario

The PHEBUS B9+ test scenario was divided into: (a) an oxidation phase for ~140 minutes, (b) a heatup phase in pure helium for ~93 minutes, and (c) a slow cooldown phase.

A calibrated flow rate of pure superheated steam was delivered to the bundle in the first period of the test. The steam phase was pursued until complete oxidation of the cladding at mid-bundle.

The aim of the second period was to produce a significant fuel dissolution by molten zircaloy in complete steam-starved conditions. This phase was initiated by switching the flow rate from steam to helium at 8,370 seconds. The nuclear power generated in the bundle was increased by step from 8,370 to ~13,770 seconds to obtain a maximum fuel temperature of ~2,750 K.

The final slow cooldown period was performed in helium by reducing gradually the nuclear power to preserve the bundle geometry obtained in the previous phase.

A.8.3 Description of the SCDAP/RELAP5 Model

A.8.3.1 Nodalization

The entire experimental bundle structure was modeled using the SCDAP/RELAP5 code, including the two Inconel spacer grids, the shroud, and the bypass loop. As shown in Figure A-75, the test bundle was represented by four SCDAP components, including (a) one central fuel rod, (b) the 8 fuel rods of the middle ring, (c) the 12 fuel rods of the outer ring, and (d) the shroud.

The fuel rod components were modeled using 6 radial nodes, and the shroud was nodalized using 16 radial nodes.

As shown in Figure A-75, all the components were modeled using 10 axial nodes, each node being 0.08 m tall and communicating with the 10 corresponding RELAP5 hydrodynamic control volumes. The external surface of the shroud was connected to a single RELAP5 hydrodynamic control volume representing the bypass.

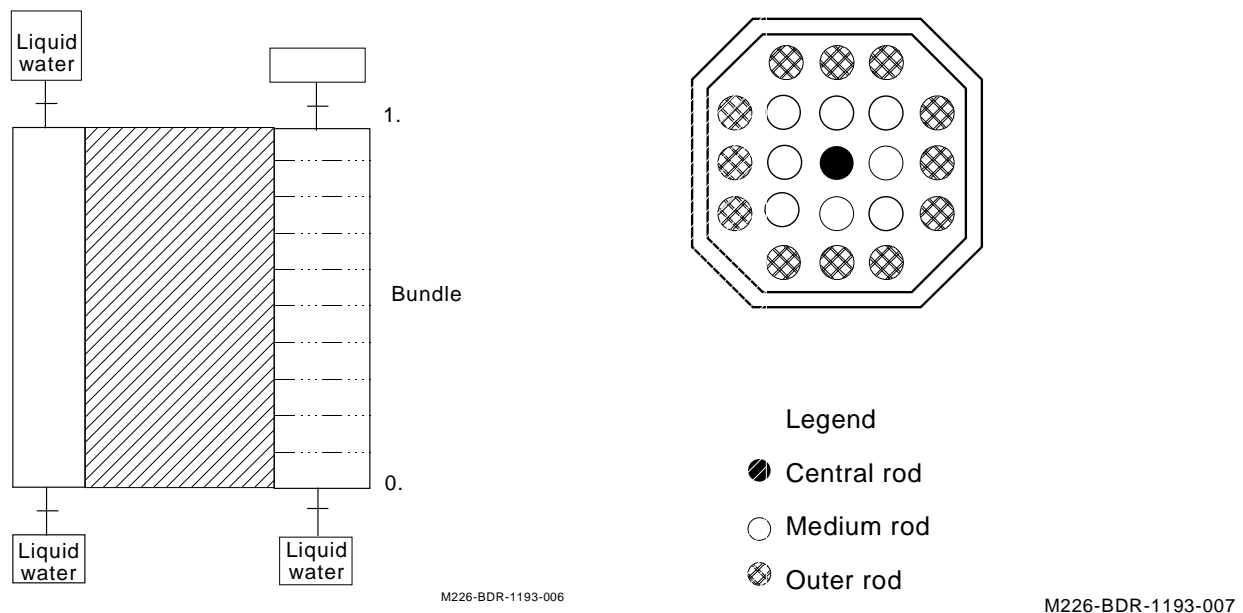


Figure A-75. Nodalization and core representation of the test train for the PHEBUS B9+ experiment.

A.8.3.2 Initial Conditions

All the fuel rods were pressurized with helium to 0.7 MPa at room temperature. The temperature of the fuel rods and the shroud structures was initialized at 528 K with a pressure of ~1.2 MPa.

A.8.3.3 Boundary Conditions

The estimation of the total nuclear power generated in the bundle as well as the uncertainty envelope ($\pm 2.5\%$) was obtained from reactor power measurements and reactor physics calculations (Figure A- 76).

The axial power profiles were represented in the calculations using three discrete curves corresponding to successive positions of the control rods in the driver core. During the test, the local nuclear power around the mid-plane of the fuel rods was nearly constant and increased in the upper part of the bundle as the operators raised the control rods.

A constant ~2 g/s inlet flow rate of superheated steam (528 K, 1.9 MPa) was used over the first phase of the transient. A helium flow rate of ~0.5 g/s (528 K, 1.9 MPa) was injected at the bottom of the bundle at 8,370 seconds and was maintained until the end of the experiment.

The thermal conductivity of the porous zirconia fed with helium was measured in the laboratory prior to the test but with a large uncertainty due to pressure conditions used in the measurements (0.1 MPa instead of 1.9 MPa in the B9+ test). Nevertheless, thermal conductivity of the porous zirconia deduced from the laboratory measurements was provided in the ISP-28 specifications.

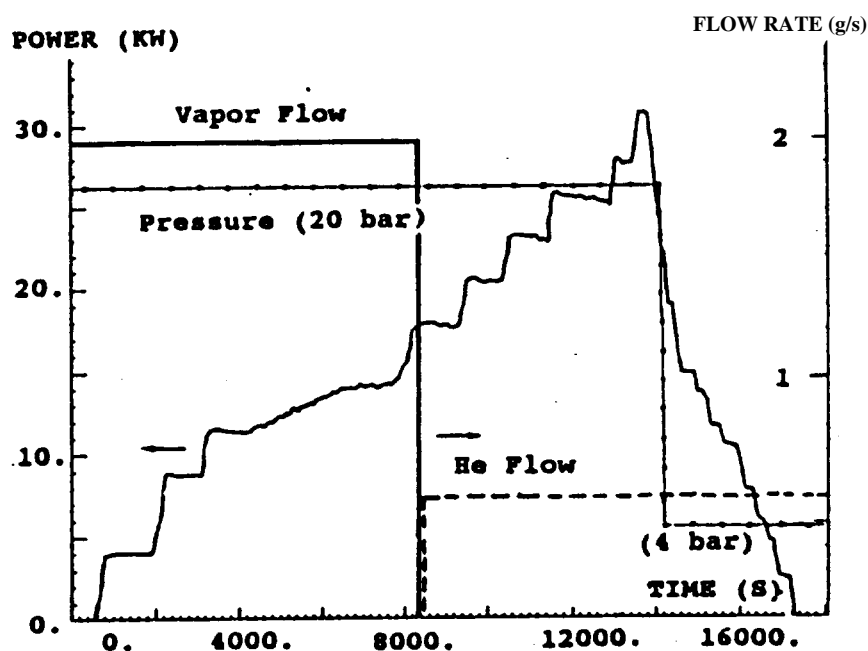


Figure A-76. Total core power for the PHEBUS B9+ experiment.

A.8.4 Results

Calculations presented in this section were performed using SCDAP/RELAP5/MOD3.1 with options such as semi-implicit hydrodynamic scheme, steam diffusion limit through hydrogen and time smoothing of the radiative heat transfer.

A.8.4.1 Thermal Behavior

A preliminary calculation performed using the thermal conductivity of the porous zirconia of the shroud recommended in the ISP-28 specifications showed a large over prediction of the cladding temperatures from the first seconds in the transient. Analysis of the power balance in the bundle indicated that the temperature response was mainly driven by radial heat losses through the shroud. Consequently, the main parameter controlling the bundle thermal behavior was the thermal conductivity of the porous zirconia. This finding was recognized to be the major uncertainty in the analyses of the PHEBUS B9+ test.

A.8.4.1.1 Thermal Behavior in the Steam Phase. Calculated temperatures that were in good agreement with the experimental data (Figures A-77 and A-78) were obtained by using best estimate (BE) calculation by increasing the thermal conductivity of the porous zirconia recommended in the ISP-28 specifications by a factor of ~3.2. Under these conditions, the calculated cladding temperatures were correctly calculated between 0.30 and 0.60 m elevations until thermocouple failures. However, the calculated fuel rod temperatures were overpredicted (~50 K) at the bottom of the bundle (0.20 m elevation) and underpredicted (~100 K) in the upper part (0.70 m elevation).

Typical oxidation runaway and temperature escalation (at the 0.60 m elevation) observed in the test as the cladding temperature exceeded 1,850 K were well predicted by the code. Steam starve conditions were not calculated during the oxidation runaway.

Many thermocouples used in the test correctly operated until the oxidation runaway occurred at ~8,370 seconds. The temperature measurements during the entire steam phase provided the opportunity to evaluate the radial thermal gradients in the bundle. The calculated temperature differences at mid-bundle between the central and the outer rods and between the outer rods and the liner were respectively ~50 and ~190 K at ~8,000 seconds. These temperature differences were estimated at ~90 and ~190 K, respectively. The underprediction of the radial temperature gradient in the bundle was attributed to an assumption that the radiative heat transfers in the bundle were homogenous (anisotropic factors set to zero) and to the fact that the SCDAP/RELAP5 modeling used a single thermal hydraulic channel.

The liner temperatures at different locations agreed with those measured during the steam phase. The gas temperature was well calculated at the bundle outlet, but slightly overpredicted in the lower part of the fuel rods.

A.8.4.1.2 Thermal Behavior in the Helium Phase. At 8,370 seconds in the experiment, the steam/helium switch of the flow rate delivered to the bundle stopped the oxidation runaway observed at the 0.60 m elevation. At this elevation, the first consequence of helium injection was a rapid cooldown of the fuel rods due to the sudden decrease of the oxidation power generated in the cladding. After ~1,000 seconds, the fuel rod temperature rose again due to an increase in nuclear power. This thermal behavior was

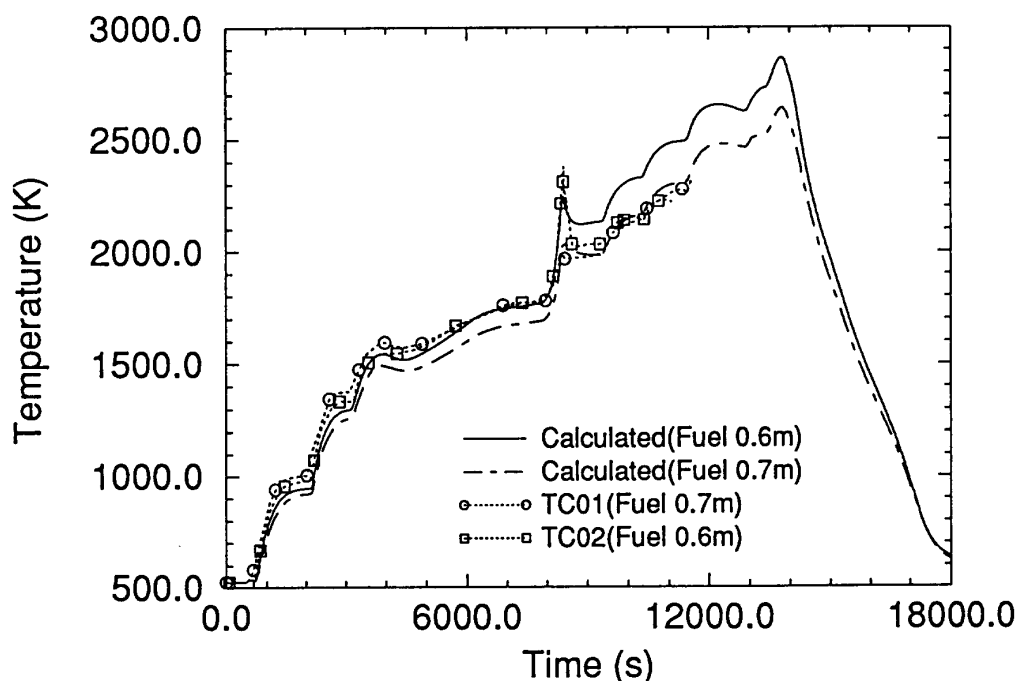


Figure A-77. PHEBUS B9+ test cladding temperatures in the upper part of the bundle.

well predicted by the code.

The calculated maximum fuel temperature (~2,800 K) was obtained at ~13,770 seconds in the transient and agreed with the maximum temperature deduced from the PIE (~2,750 K).

A.8.4.2 Cladding Oxidation and Hydrogen Production

The BE calculation assumed the relocation of molten zircaloy occurring from 2,300 K for a cladding oxidation less than 50%. The calculated total hydrogen production (33 g) was correctly predicted by the code (39 ± 8 g in the test).

However, two main reasons could limit the total hydrogen generation calculated by the code. First, the actual length of the zircaloy cladding was ~1.04 m, but the current version of the code considered the cladding and the fissile lengths to be identical (0.8 m). The initial mass of zircaloy was underestimated by ~160 g in the upper part of the bundle (the conversion of 160 g of zircaloy can produce ~7 g of hydrogen). Second, the upper Inconel spacer grid was calculated to slump after interaction with the zircaloy cladding at ~3,700 seconds. About 140 g of zircaloy were predicted to be liquefied in the eutectic reaction. The current version of the code did not consider oxidation of the liquefied materials and therefore limited the calculated total hydrogen generation (the conversion of 140 g of zircaloy can produce ~6 g of hydrogen).

A sensitivity calculation was performed increasing the thermal conductivity of the porous zirconia of the shroud by 5%. The calculated cladding temperature at the 0.60 m elevation decreased by 35 K at 7,500

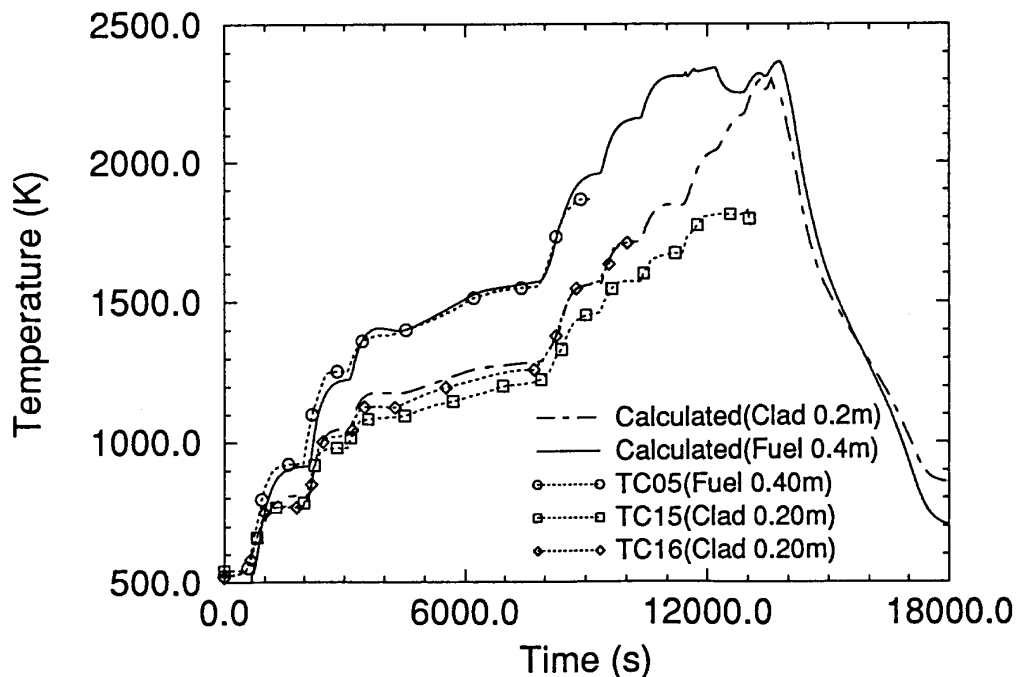


Figure A-78. PHEBUS B9+ test cladding temperatures in the lower part of the bundle.

seconds compared with the BE calculation. The resulting total hydrogen generation was 29 g (33 g in the BE calculation).

The cladding oxidation profile predicted in the BE calculation at the end of the steam phase is compared with the measurements in Figure A-79. The oxidation profile was correctly calculated from 0.3 to 0.60 m elevations, but local cladding oxidation was overpredicted in the lower part of the bundle and underpredicted in the upper part. The differences between the code predictions and the experimental data were the results of the temperature discrepancies between the calculation and the test (See Section ‘Thermal Behavior in the Steam Phase’). The calculated local cladding oxidation at 0.64 m was not reported in Figure A-79 because the code predicted a zircaloy/Inconel interaction at this elevation and an early slumping of the cladding at ~3700 seconds.

A.8.4.3 Metallic Material Relocation

The main events observed in the BE calculation are reported in Table A-8.

The onset of the interaction between zircaloy cladding and the upper Inconel spacer grid was calculated to occur at ~2,600 seconds as the local cladding temperature exceeded ~1,250 K. The zircaloy/Inconel interaction ended at ~3,700 seconds (~1,550 K) as the liquefied eutectic slumped in the lower part of the bundle. At the 0.66 m elevation, the cladding was calculated to be completely dissolved over an axial length of ~74 mm. However, the PIE indicated that the interaction zone was probably lower than those calculated by the code. Double-sided cladding oxidation was not considered in the calculation

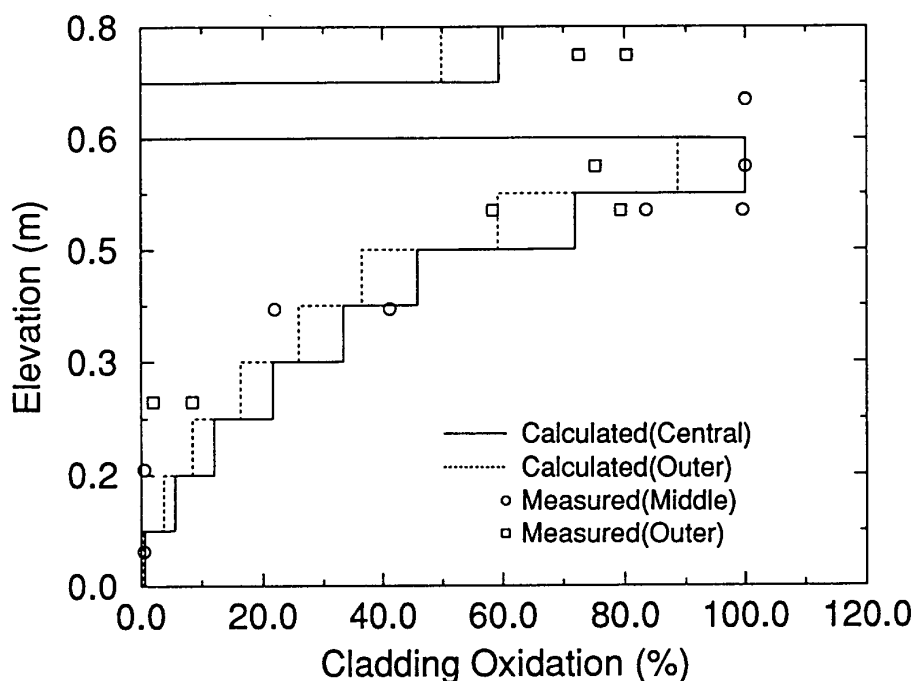


Figure A-79. PHEBUS B9+ test cladding oxidation profile in the bundle.

because of a low cladding deformation (<5% at 0.60 m) predicted by the code as the fusible seals melted at ~2,750 seconds.

The onset of the interaction between zircaloy cladding and the lower Inconel spacer grid was calculated to occur at ~8,000 seconds (~1,250 K) and ended at ~9,700 seconds (~1,520 K) with the slumping of the liquefied eutectic. At the 0.138 m elevation, the cladding was calculated as completely dissolved over an axial length of ~90 mm. However, the PIE indicated a very low zircaloy dissolution by Inconel at the 0.138 m elevation. The large interaction zone obtained in the calculation could be partially due to the over prediction of the temperature in the lower part of the bundle.

The onset of fuel dissolution was predicted to occur at ~9,600 seconds at the 0.60 m elevation in the BE calculation as the cladding temperature exceeded 2,250 K. The total fuel dissolution of ~37% obtained at the end of the calculation was overpredicted compared to the experiment (<10% in the test). The over prediction of fuel dissolution by molten zircaloy was mainly attributed to the lack of oxide dissolution modeling by molten zircaloy in the current version of the code. The fuel dissolution profile is compared to the experimental results in Figure A-80.

Cladding relocations were calculated to occur between ~11,400 and 13,770 seconds in the BE calculation. The beginning of the relocation of liquefied fuel and cladding materials was calculated at the 0.44 m elevation. At the end of the calculation, the degradation zone on the fuel rods extended from 0.08 to 0.48 m elevations. A comparison with the PIE indicated that the extent of the degradation zone in the lower

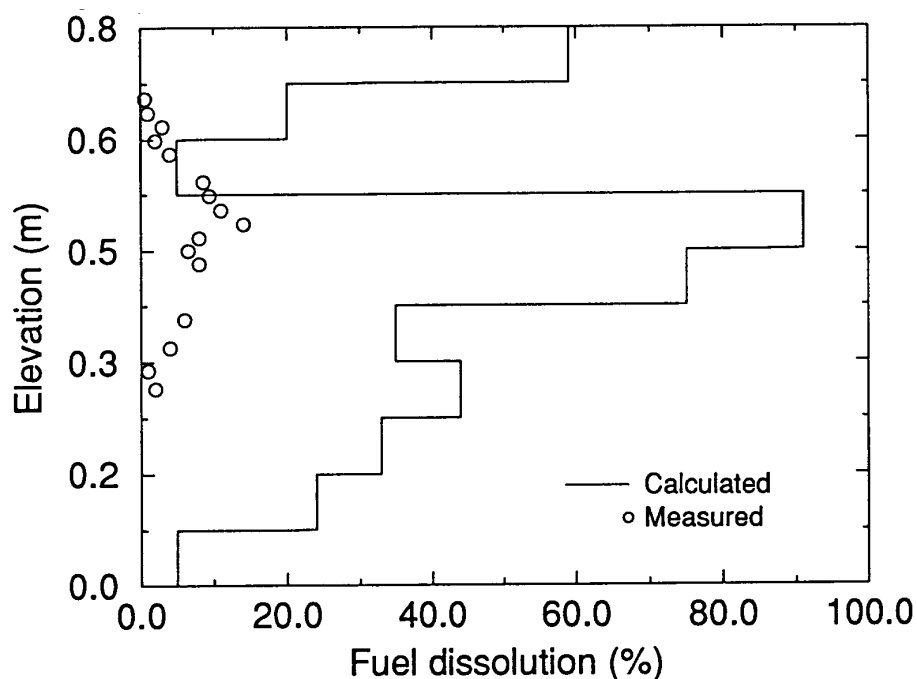


Figure A-80. PHEBUS B9+ test total fuel dissolution in the bundle.

part of the bundle was overpredicted by the code. The large cladding relocation in the lower part of the bundle obtained in the calculation was mainly attributed to the over prediction of the local temperatures.

Table A-8. Simulated sequence of events for PHEBUS B9+ experiment.

Calculation (BE Calculation)		
Event	Cladding Temperature (K)	Time (s)
Cladding dissolution by Inconel (upper grid spacer)	~1,250	2,600 ^a
	~1,550	3,700 ^b
Cladding dissolution by Inconel (lower grid spacer)	~1,250	8,000 ^a
	~1,520	9,700 ^b
Onset of fuel dissolution	~2,250	~9,600
Onset of fuel rod degradation	2,300	~11,400
Maximum fuel temperature	2,800	~13,770

a. Beginning of zircaloy/Inconel interaction.

b. End of zircaloy/Inconel interaction.

A.8.4.4 Bundle Blockage

The PIE indicated the formation of two partial bundle blockages. The larger one was located between 0.20 and 0.28 m elevations, well above the lower spacer grid. The reduction of the flow area at the 0.26 m elevation was estimated at ~21%. The second partial bundle blockage was located at the ~0.05 m elevation and was mainly the result of both the zircaloy/Inconel interaction and spacer grid melting. The reduction of the flow area was ~10% at this elevation.

The material relocation was mainly calculated to occur below the bottom of the fuel rods. No reduction of the flow area was calculated between 0.20 and 0.28 m elevations. The code only predicted a partial bundle blockage of ~37% at the 0.04 m elevation. The relocated materials at this elevation consisted of ~70% UO₂ (in weight). The discrepancy between the code and the experiment of the location of the refrozen materials was probably due to the over prediction of the cladding temperatures in the lower part of the bundle.

A.8.4.5 Code Performances

The total central processing unit (CPU) time for a simulated transient of 18,000 seconds was ~26 hours on an IBMRisc Workstation. However, the CPU time increased as the conditions become more severe in the calculation. The ratio (CPU time/simulated time) was only ~3 at the end of the steam phase (8,370 seconds) prior to any material relocation; but, during the material relocation (the helium phase), this ratio increased and reached ~5.3 at the end of the calculation.

A.9. OECD LOFT LP-FP-2

This section describes an analysis of the OECD LOFT LP-FP-2 experiment using the SCDAP/RELAP5 computer code. This experiment was uniquely appropriate for assessment of early phase core damage progression models because the transient resulted in oxidation in a steam-rich environment, and because the transient was allowed to progress well into early phase core damage.

The SCDAP/RELAP5 analysis is presented in three sections. First, a discussion of the input model is presented, followed by the results from the transient analysis, and finally the assessment of the SCDAP/RELAP5 early phase core damage models is summarized.

A.9.1 Input Model

There is a long history of analysis of the OECD LOFT LP-FP-2 experiment with SCDAP/RELAP5. Several analysts with multiple input models have used many versions of the code to analyze the experiment.^{A-17,A-18,A-19} In the course of performing these calculations, a number of modifications have been made to the original LP-FP-2 model. These revisions were made to permit the code to handle the transient more smoothly and to better represent a particular aspect of the facility. For the analysis described here, the author has endeavored to make the best use possible of the previous analyses. This has consisted of reviewing the analyses and utilizing the best of the model revisions.

A.9.1.1 Primary Coolant System Model

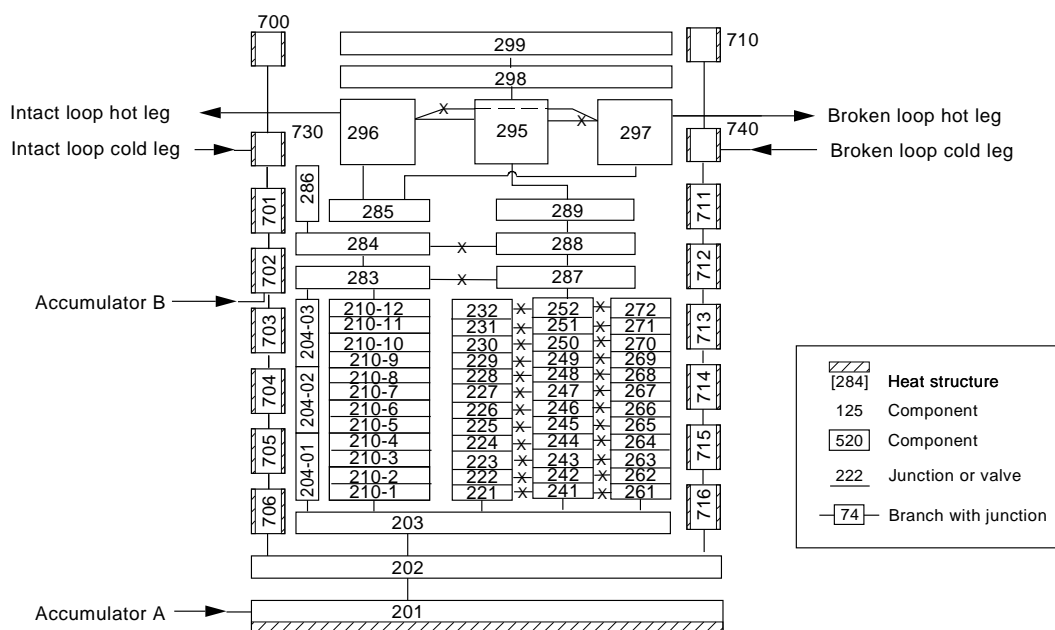
The primary system model for the current analysis is similar to LOFT facility models that have been developed in the past, with several revisions intended to establish a best-estimate thermal-hydraulic model. The most significant of these modifications are:

- The downcomer model was changed to a split (two-channel) downcomer model and was renodalized to allow volume boundaries to have the same elevation as core volume boundaries. Analysts have oscillated between the use of single channel and split down-comer models. Advocates of the single-channel downcomer claim calculational simplicity with minimal impact on hydraulic response during a large break. However, the reactor vessel mass inventory is sufficiently critical during the small- break portion of this calculation that the split downcomer model has been reinstituted. The downcomer elevations were renodalized because previous calculations have shown that when the downcomer and core have different elevations, oscillations in liquid level can occur.
- The upper plenum structure surface areas were modified to reflect detailed surface area calculations.^{A-20} Also the upper plenum thickness was modified to reflect estimates of the upper plenum structural mass. This modification was introduced to better simulate the fission product transport phenomena observed during the transient.
- RELAP5 heat structures representing the center fuel module (CFM) high-, medium-, and low-power fuel rods, control rods, guide tubes, and thermal shroud were all replaced with SCDAP components. Also, the RELAP5 single- channel model of the CFM was replaced with a three-channel model. This allows signifi-

cantly better simulation of core blockage and relocation and their impact on coolant flow diversion.

- RELAP5 heat structures representing peripheral module fuel rods were replaced with SCDAP components representing high- and average-power fuel rods.

The SCDAP/RELAP5 model of the LOFT reactor vessel is shown in Figure A-81, while the ex-vessel PCS is shown in Figure A-82. This nodalization, representative of a Westinghouse 4-loop plant, models all components in the PCS, such as the intact and broken loops, steam generator and secondary system, and reactor vessel.



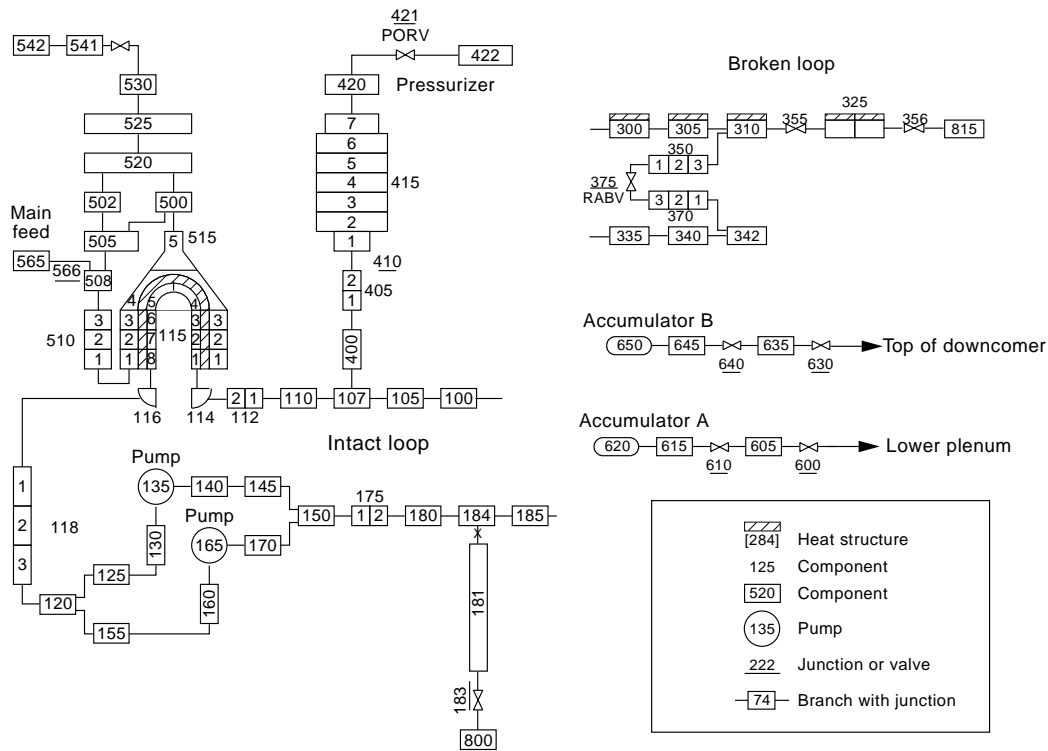
M165-BDR-1292-01r

Figure A-81. SCDAP/RELAP5 nodalization diagram of LP-FP-2 reactor vessel.

A.9.1.2 Core Model

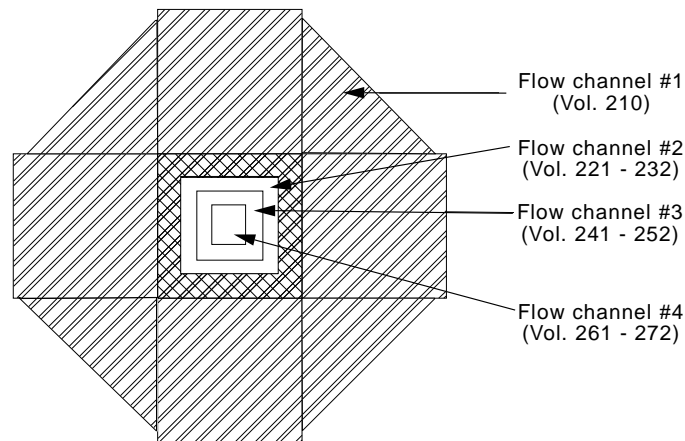
The reactor core was modeled as four separate channels, one representing the peripheral fuel bundles and three representing the CFM, as shown in Figure A-83. The center fuel module (CFM) was modeled using nine SCDAP components, as shown in Figure A-84.

The center fuel module fuel rods were modeled with six components. These six components were divided into three pairs of rods, each pair representing a bank of fuel rods different only in power. This was necessary because these rods were enriched to 10%, causing significant thermal neutron depletion, and therefore a depression in the radial power profile of approximately 13%. A pair of identical fuel rod components were used to model each bank, because it has become a standard practice to bound the oxidation response with a pair of components, the first modeling oxidation limited only by steam availability, and the second modeling oxidation limited by the diffusion of steam through a hydrogen boundary layer. Although modeling these bounding phenomena had little impact on the analysis of the transient phase of LP-FP-2, it can impact the results if significant quantities of hydrogen are being



M165-BDR-1292-002

Figure A-82. SCDAP/RELAP5 nodalization diagram of LP-FP-2 primary system.



M101-BDR-0492-005r

Figure A-83. Radial core hydrodynamic nodalization.

generated by the oxidation process. Three additional components were used to model the Ag-In-Cd control rods, the guide tubes, and the zircaloy-lined insulating shroud surrounding the CFM. Figure A-84 illustrates the CFM nodalization, showing the three banks of fuel rods, as well as the locations of the guide

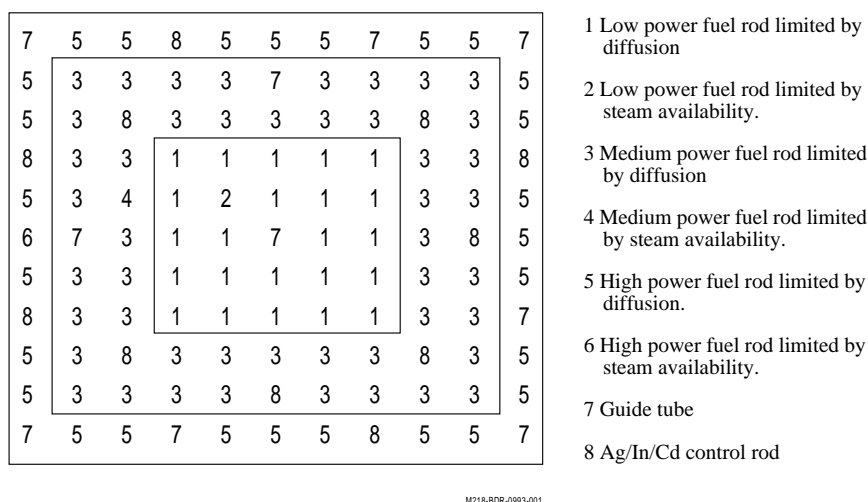


Figure A-84. SCDAP center fuel module nodalization.

tubes and Ag/In/Cd control rods. The thermal shroud surrounding the CFM was modeled as a separate component.

As discussed earlier, the CFM was divided into three parallel flow channels, each surrounding a single group of fuel rods. In the past, the thermal-hydraulic representation of the LOFT core used a hot-channel approach.^{A-18} This approach consisted of using one hydraulic channel to model flow conditions for the average flow channel and a second hydraulic channel to model flow conditions in the hottest channel. This hot-channel approach had been used successfully in the past to model large- and small-break experiments. Unfortunately, because of the implied assumption that all fuel rods within the same flow channel behave independently of one another, this approach has been shown to be inaccurate during any transient where fuel rod geometry changes.^{A-21} Basically, as the flow through the unit cell around a fuel rod is disrupted, additional coolant flow is diverted into adjacent channels, making them less likely to undergo geometry change. This violates the assumption that each fuel rod within the hydraulic channel is independent. For this reason, the CFM was divided into three parallel flow channels. Since the peripheral modules experienced no deformation, the assumption of independence remains valid; and the hydraulic model was left unchanged, with one channel representing all modules.

A.9.1.3 Initial Conditions

Reactor conditions at the start of the transient were established in the usual manner used with RELAP5 in that the initial core power was defined and a set of steady-state controllers were applied to the primary coolant pumps, pressurizer spray and heaters, feed system, and secondary system. Several hundred seconds of null transient were then performed with the model to allow the steady-state controllers to bring the system to an equilibrium condition.

After reaching equilibrium, the thermal and hydraulic conditions (mass flow, internal energy, pressure, and so on) and initial temperature distributions for heat structures and SCDAP components were

transferred into a second input deck, through the use of PYGMALION. Table A-9 compares the initial measured and calculated hydraulic conditions for several significant parameters.

Table A-9. Comparison of calculated and measured initial conditions.

Parameter	Measured value	Calculated value
Primary coolant system		
Core delta T (K)	11.7 ± 1.4	11.35
Primary system pressure (MPa)	14.98 ± 0.1	15.08
Hot leg temperature	571.6 ± 0.8	570.5
Cold leg temperature (K)	559.9 ± 1.1	559.9
Loop mass flow (kg/s)	475 ± 2.5	475.01
Reactor vessel		
Power level (MW)	26.8 ± 1.4	26.8
Decay heat at 200 s (kW)	684.8	695.19
Maximum linear heat generation (kW/m)	42.6 ± 3.6	43.0
Secondary system		
Secondary pressure (MPa)	6.38 ± 0.08	6.09
Pressurizer		
Liquid volume (m ³)	0.57 ± 0.03	0.57
Steam volume (m ³)	0.37 ± 0.03	0.37
Water temperature (K)	616.9 ± 2.1	605.9
Pressure (MPa)	15.1 ± 0.1	15.05
Liquid level (m)	1.06 ± 0.06	1.06
Boron suppression tank		
Pressure (kPa)	95 ± 3	100

A.9.1.4 Boundary Conditions

Boundary conditions for experiments in the LOFT facility were usually very well defined, because experiments in this facility were routinely used for thermal-hydraulic code development or assessment. The boundary condition with the greatest uncertainty in experimental facilities is nearly always environmental heat losses. LOFT environmental heat losses, however, have been parametrically defined over a series of 26 experiments, covering a wide range of break sizes and is therefore well-characterized. The heat losses during the LP-FP-2 transient were modeled as three separate quantities, from the reactor vessel, the steam generator, and the intact loop piping.

The remaining boundary conditions for the OECD LOFT LP-FP-2 experiment were, unfortunately, not as well defined as previous LOFT experiments. Because the objectives of this experiment were directed exclusively towards early phase severe core damage phenomena and fission product transport, definition of thermal-hydraulic boundary conditions was sacrificed to provide added confidence in meeting the core damage objectives. The primary analytical difficulty is that the intermediate size break on the intact loop cold leg, through which 80% of the system coolant inventory was expelled, was merely a non-instrumented, non-orificed pipe. Although maximizing early coolant depletion, as intended, the lack of an orifice at this break has forced all subsequent analyses to rely on secondary indications, such as time of core uncover, to characterize the PCS mass balance.

Radial and axial power profiles were measured with traversing in-core probes (TIP's), and decay heat has been well defined by detailed reactor physics calculations. Pressure in the BST, the simulated containment, was modeled as a constant. Although pressure in an effluent tank 13 times as large as the PCS will increase marginally as the system experiences blowdown, it has no significant effect on primary system response.

The remaining boundary conditions, specifically the specification of significant thermal-hydraulic events such as valve and pump operation, were modeled using a RELAP5 control system based primarily on the measured timing of each operation. The specification of these events to the facility control room were based upon system pressure, and attempts were made early in the analysis of this experiment to specify operator action based upon pressure. However, in a transient such as the interfacing systems LOCA which this experiment simulated, when the system pressure decreases slowly, it was determined that a small discrepancy in pressure could significantly impact the timing of valve operation. Wherever possible, then, the effects of operator actions were simulated based upon the experiment time.

A.9.2 Transient Analysis

SCDAP/RELAP5 has been used to analyze the LP-FP-2 experiment as early as the experiment's planning stages. However, in the seven years since the experiment, a number of significant improvements have been made to SCDAP/RELAP5. For this reason, an analysis of the experiment was performed with the objective of assessing the state of the code against experimental and identifying parameters which are key to the analysis.

A.9.2.1 System Thermal Hydraulic Behavior

In most severe accident analyses, the uncertainty in the thermal-hydraulic behavior of the PCS dominates the uncertainty of the analyses. This is emphasized in the analysis of the LP-FP-2 experiment because the experiment focused exclusively on early phase severe accident phenomena prior to corium relocation into the lower vessel.

As was mentioned in the discussion of boundary conditions, the primary difficulty in analyzing the LP-FP-2 experiment has always been the evaluation of the primary system mass balance. The best-estimate analysis presented here has been no exception. It has not been difficult in the past to tune the loss coefficients on both the intact loop cold leg break and the simulated LPIS line such that the PCS pressure is matched exactly. Unfortunately, for all system models used to date, this causes the system to retain too much fluid in the reactor vessel, thereby delaying the start of core uncover by as much as 500 seconds. Two hypotheses have been advanced to explain the inability of the model to predict both system pressure and time of core uncover: first, that the mass balance has been correctly tracked but has been distributed incorrectly about the system; or, secondly, that the distribution is roughly correct but that the input model does not correctly characterize the reactor vessel internals and has therefore caused the energy deposition to the coolant to be too low. Although it should be possible to modify the input model to examine these two hypotheses, the additional resources required would not significantly benefit the assessment of severe accident code models, which remains the primary goal of this analysis. In order to evaluate the severe accident models, more emphasis was placed on correctly predicting the time of core uncover than on duplicating system pressure. Figure A-85 compares the calculated and measured system pressure during the transient phase of the experiment.

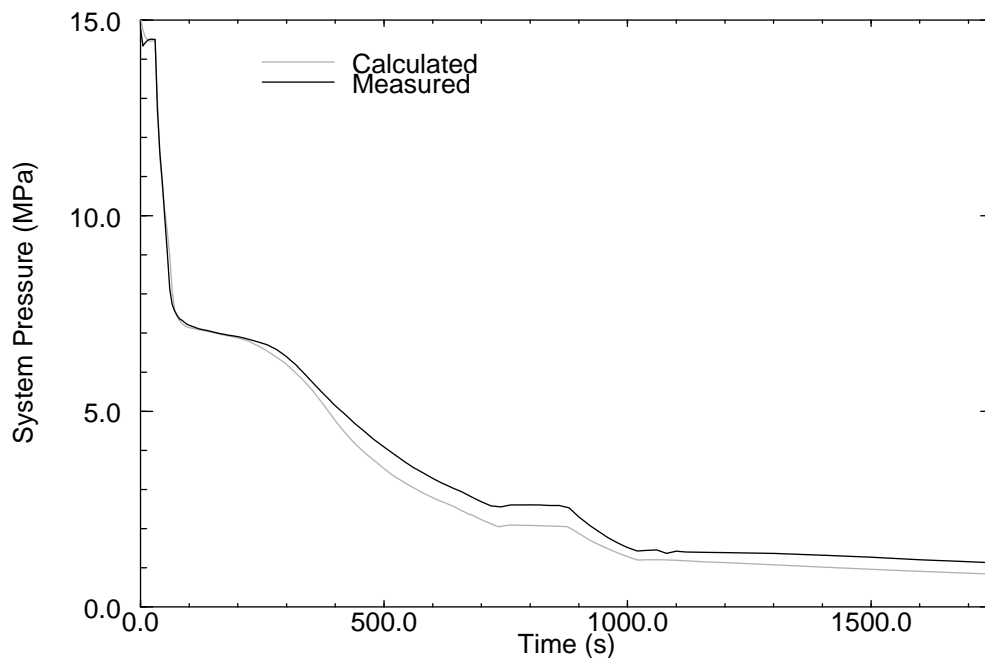


Figure A-85. Comparison of measured and calculated system pressure.

Figure A-86 shows the core dryout time as a function of elevation above the bottom of the active core. This figure illustrates that SCDAP/RELAP5 predicts that the top of the core is low enough in power that it is initially cooled by steam/entrained liquid until the liquid level drops to an elevation of 0.9 m. The code tracks core dryout very well until valve cycling causes perturbations in the liquid level. The code predicts core dryout in the bottom-most portion of the core later than measured.

One of the locations where estimates of coolant system mass flow is available is in the simulated LPIS line. This mass flow has been estimated from pressure, temperature, and differential pressure data associated with the LPIS venturi.^{A-18} The result of this estimate is compared to the mass flow calculated for the simulated LPIS line by SCDAP/RELAP5 in Figure A-87. As seen in this figure, the predicted flow rate during the later phase of the experiment is less than the expected value. Since the driving force for this flow is the pressure differential between the reactor vessel and the simulated containment, such an under prediction is consistent with the under prediction of system pressure.

One of the key parameters in an assessment of the ability of SCDAP/RELAP5 to predict core damage phenomena is the core temperature history. Figure A-88 compares the calculated cladding response with that measured at the 10 inch elevation. As seen in this figure, the time of core uncover at the bottom of the core is late and the core heatup rate is too fast. This difference in thermal response is caused by the discrepancy in the vessel liquid inventory just discussed. Figure A-89 compares the calculated cladding temperature at the 27 inch elevation (the peak power zone) with that measured during the experiment. This figure shows that the time of core uncover at the center of the core is predicted very well. The cladding heatup rate is also predicted very well until 877 seconds, when the operators began a series of valve operations to lower the system pressure to prevent fission product instrumentation damage. This valve operation (reopening of the intact loop cold leg break and PORV) caused some cooling of the thermocouples. Whether this measured cooling was representative of what occurred throughout the core or

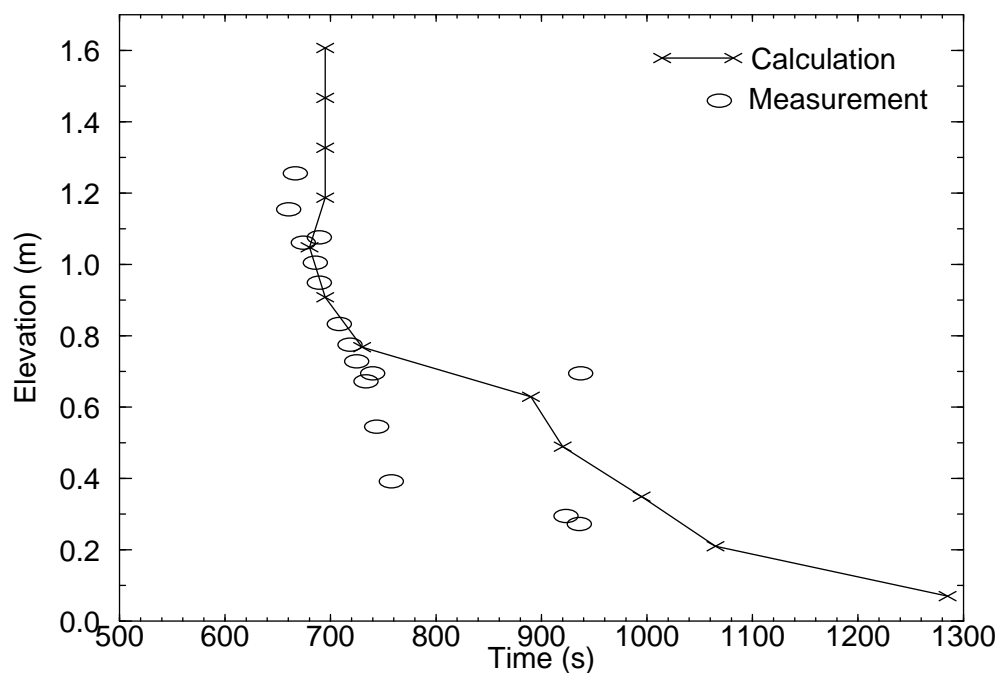


Figure A-86. Comparison of calculated and measured core dryout time.

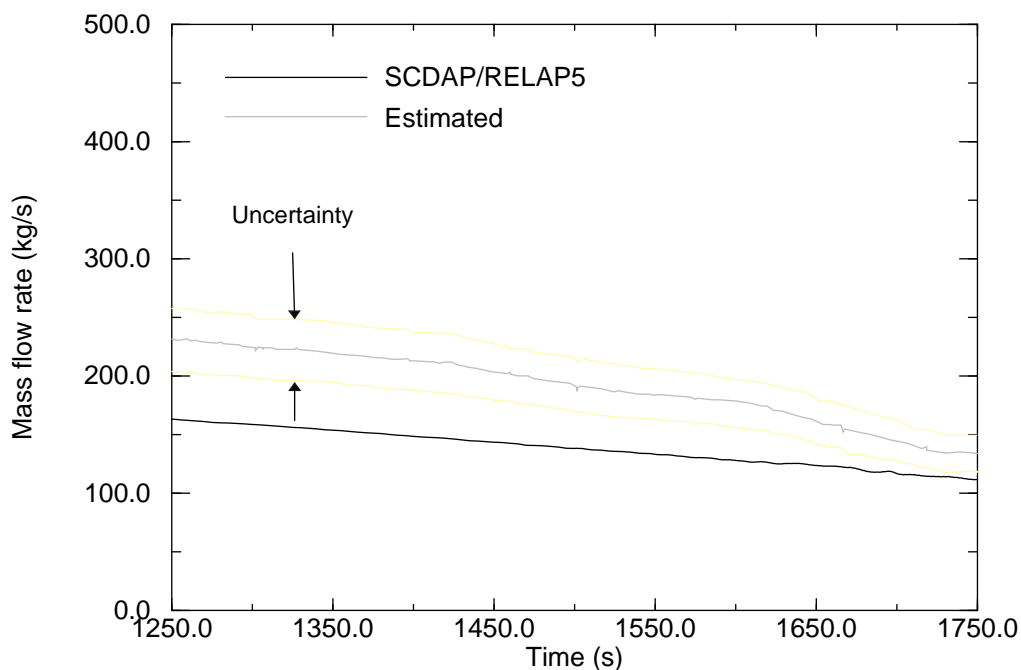


Figure A-87. Calculated and estimated LPIS mass flow rate.

only on the instrumented rods is unknown, but the current combination of input model and code was unable to model it. Figure A-90 compares the calculated cladding temperature with that measured at the 42 inch elevation. Although the instrumentation in this part of the core did not survive to experience the early

severe accident phase of the experiment, early indications show that the calculated cladding behavior is within the uncertainty of the measurement. It should be noted on all comparisons to experimental data that as the thermocouple indicates rapid oxidation rates and temperatures in excess of 1,800 K, the instrument is probably no longer tracking local cladding response.

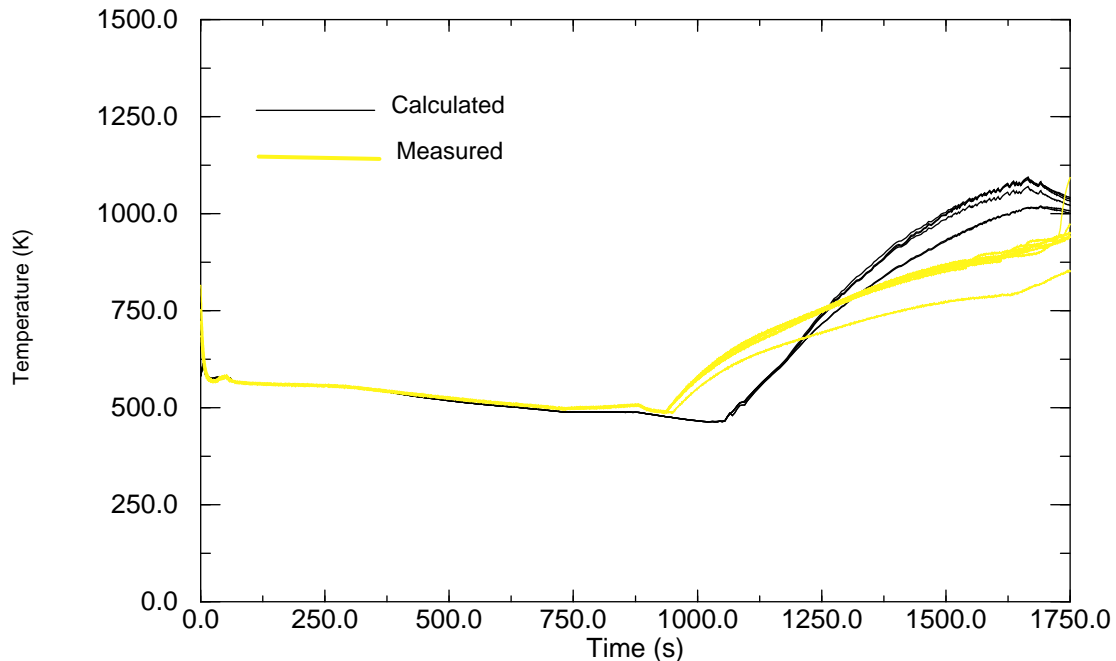


Figure A-88. Calculated and measured cladding temperature at the 10 inch elevation.

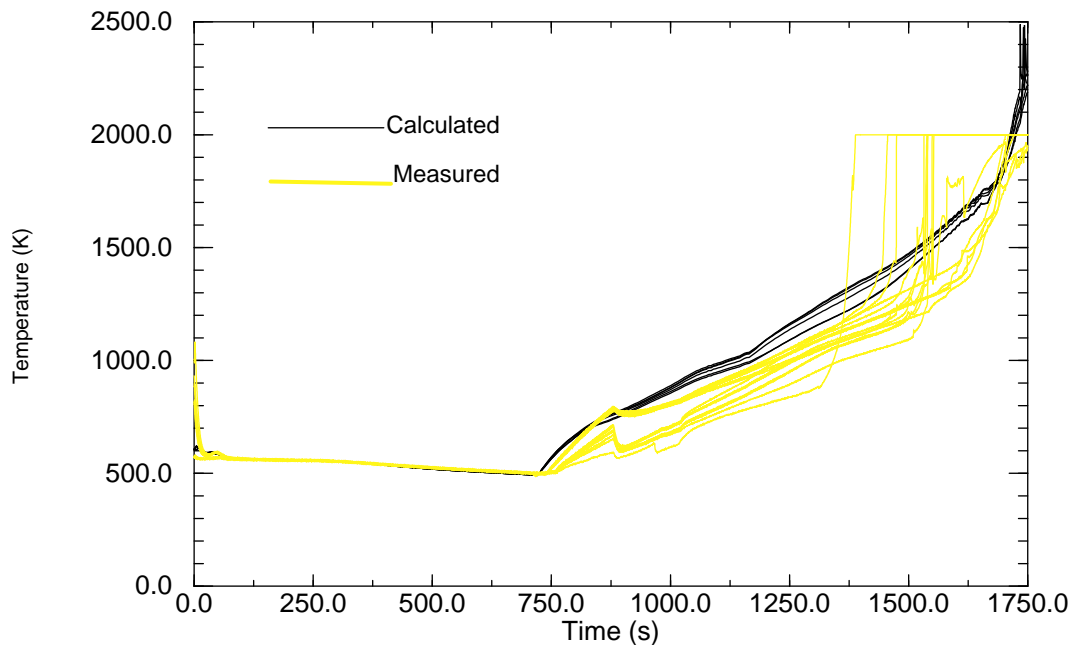


Figure A-89. Calculated and measured cladding temperature at the 27 inch elevation.

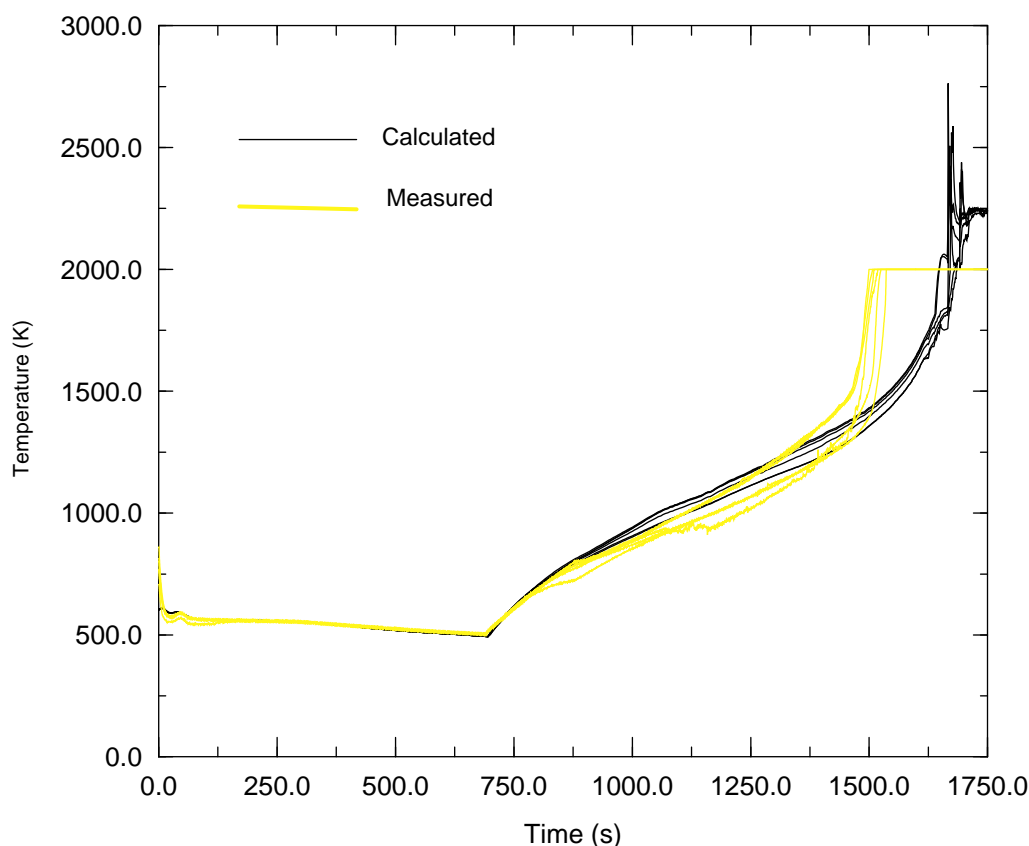


Figure A-90. Calculated and measured cladding temperature at the 42 inch elevation.

Figure A-91 illustrates the radial temperature across the center fuel module at the 42 inch elevation. This node is the highest temperature node, and is the node at which cladding rupture is predicted. The response at this elevation is just as expected, with the core heatup beginning universally across the module at the same point in time, the response remaining very similar until radiation heat transfer and fuel rod geometry changes begin to cause distinctions across the module. At approximately 1,150 seconds the fuel rod in the center channel is predicted to rupture. This matches the first measurement of fission product gap release of 1,200 seconds. After fuel rod rupture at this elevation, SCDAP/RELAP5 models double-sided oxidation at the failure elevation. After 1,500 seconds, core damage and blockage due to material relocation cause the middle channel to heatup less rapidly than the channels on either side of it. At approximately 1,550 seconds, the cladding in the average channel is completely oxidized at this location and the lack of oxidation heat generation causes the component to cool to the coolant temperature. At approximately 1,665 seconds the Ag-In-Cd control rods are predicted to fail. This is only slightly later than the estimated failure of 1,520 seconds, indicated by relocation of molten material to the lower portions of the core.

Figure A-92 shows a comparison between the calculated and measured response on the outer surface of the flow shroud at the high core temperature elevation (42 inch). This comparison indicates that the heat conduction through the flow shroud is underpredicted. This under prediction is probably caused by the uncertainty in the time-of failure of the shroud liner and the consequent uncertainty in the time-dependent thermal conductivity of the ZrO_2 insulation as coolant penetrated the insulation. The same under prediction

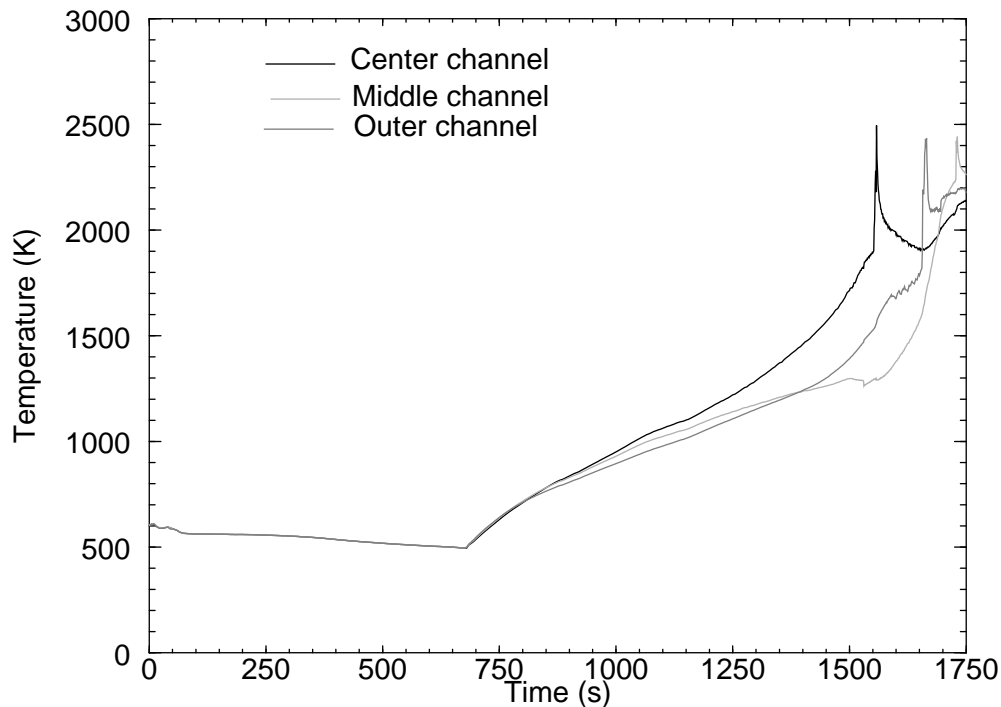


Figure A-91. Radial temperature profile across the center fuel module at 42 inch elevation.

of CFM heat loss through the thermal shroud is shown on all elevations of the shroud. An under prediction of heat loss was expected at the top and bottom of the core, due to the fact that SCDAP/RELAP5 can only model a single thermal conductivity for all elevations of the shroud, when in reality the designers specified different density ZrO_2 at the top and bottom of the shroud.

In summary, SCDAP/RELAP5 is modeling the thermal and hydraulic response of the core reasonably well. Even though dryout at the bottom-most portion of the center fuel module is being predicted slightly late, it has little effect on the transient analysis, and the boundary conditions to the core damage models are accurately tracked.

A.9.2.2 Key Transient Parameters

One of the objectives of this analysis was to identify modeling parameters which had an impact on the calculated response during the transient phase of the LP-FP-2 experiment. Two parameters were identified during this portion of the analysis (1) the threshold for double-sided oxidation, and (2) the oxidation limiting model.

It is interesting to note that early calculations of the LP-FP-2 transient allowed double-sided oxidation to occur over too great a length of the fuel rod. This model uses a threshold local hoop strain to determine whether or not double-sided oxidation is occurring. Early calculations used a threshold hoop strain of 2%, resulting in too rapid a heatup below the peak temperature node and delayed the heatup at higher elevations due to steam starvation. It also caused a significant over-prediction of the transient hydrogen generation. The current calculation uses a threshold local hoop strain equal to the rupture strain, thereby allowing double-sided oxidation only at the ruptured node. This increase in the threshold for

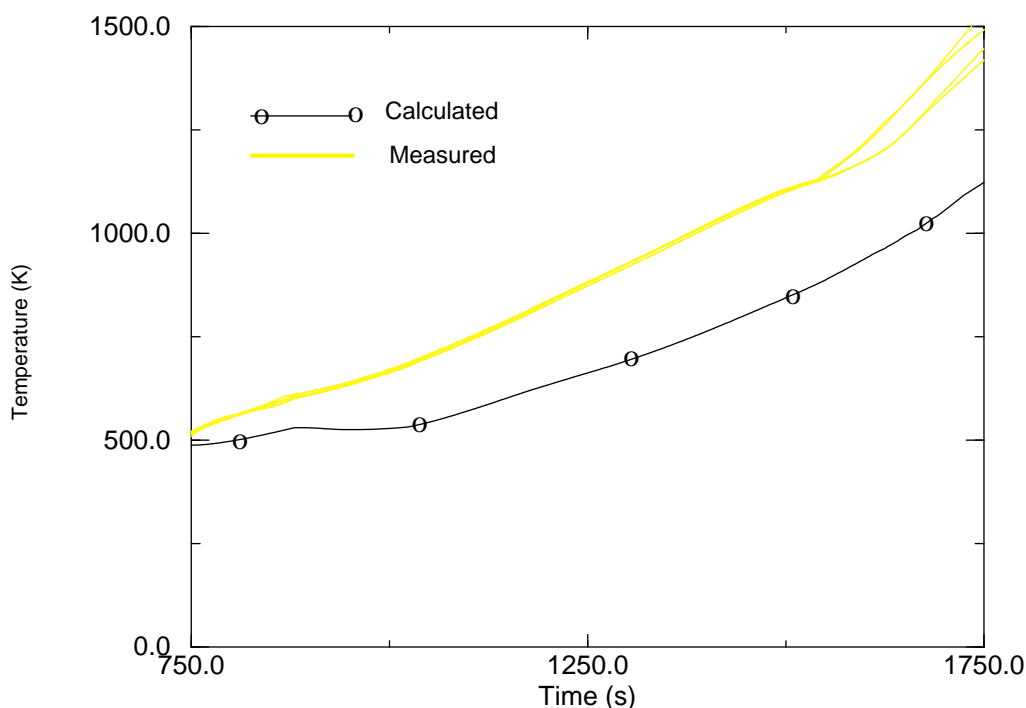


Figure A-92. Calculated and measured outer shroud temperatures at the 42 inch elevation

double-sided oxidation may be an artifact of either the low burnup fuel, or the non-prototypical fuel rod pre-pressurization. However, this analysis suggests that the default threshold for double-sided oxidation be increased to the rupture strain.

One of the parameters which was identified as potentially impacting the calculated transient response was the type of oxidation limit imposed on the fuel rods. SCDAP/RELAP5 has traditionally allowed the zircaloy cladding to oxidize at a rate limited only by the availability of steam. A recent extension has added the capability of limiting the oxidation rate by the limit of steam diffusion through a hydrogen boundary layer. The analysis described here modeled the fuel rods in each coolant channel with a pair of fuel rod components which were identical except for the oxidation rate limit imposed. The results of this bounding analysis are shown in Figure A-93. As could be expected the difference in the oxidation limiting models does not become apparent until rapid oxidation begins, and even then the LOFT core is sufficiently steam rich that the diffusion limit does not lag significantly behind the steam availability limit.

A.9.2.3 Transient Damage Progression.

The ability of SCDAP/RELAP5 to predict core damage during the transient phase of LP-FP-2 has been and will continue to be of keen interest to the code developers. A facility which provided experimental evidence of core damage during the early phases of a severe accident is invaluable to the code development and assessment process.

One of the more interesting parameters to characterize the integral response of a damaged core is the hydrogen production rate, both because of its significance to the risk evaluation process and because it represents an integral measurement of core response. Figure A-94 shows the hydrogen production

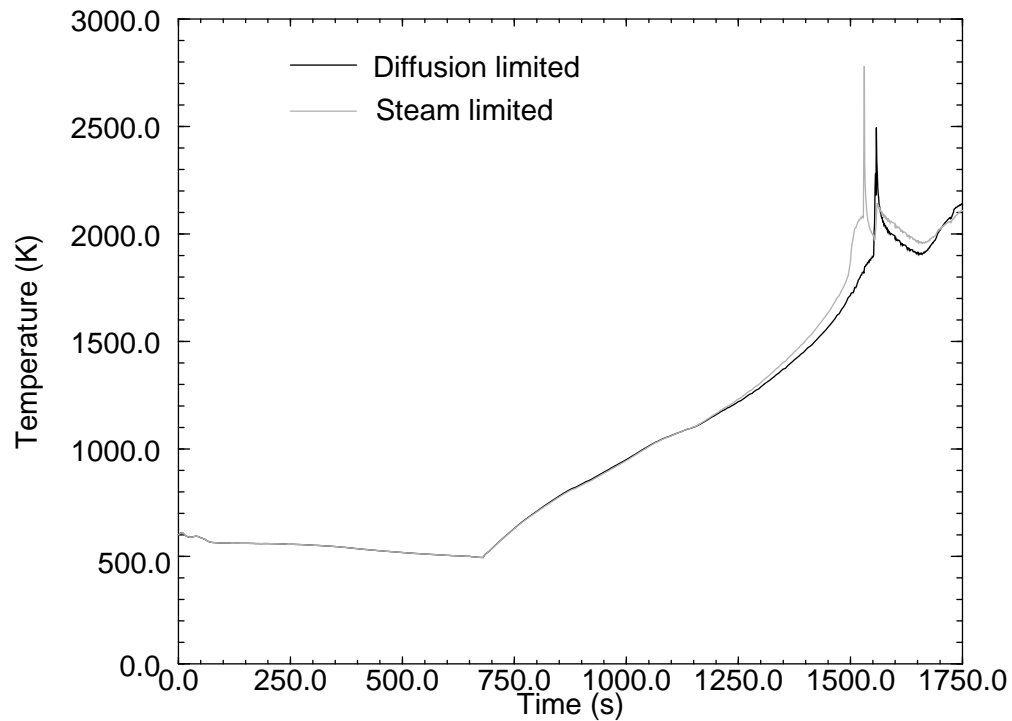


Figure A-93. Effect of oxidation rate limit on identical fuel rod components.

calculated by SCDAP/RELAP5 for the transient portion of the experiment. The cumulative hydrogen production during the transient portion is predicted to be approximately 270 g. This compares very well with the estimated transient production of 205 ± 11 g.

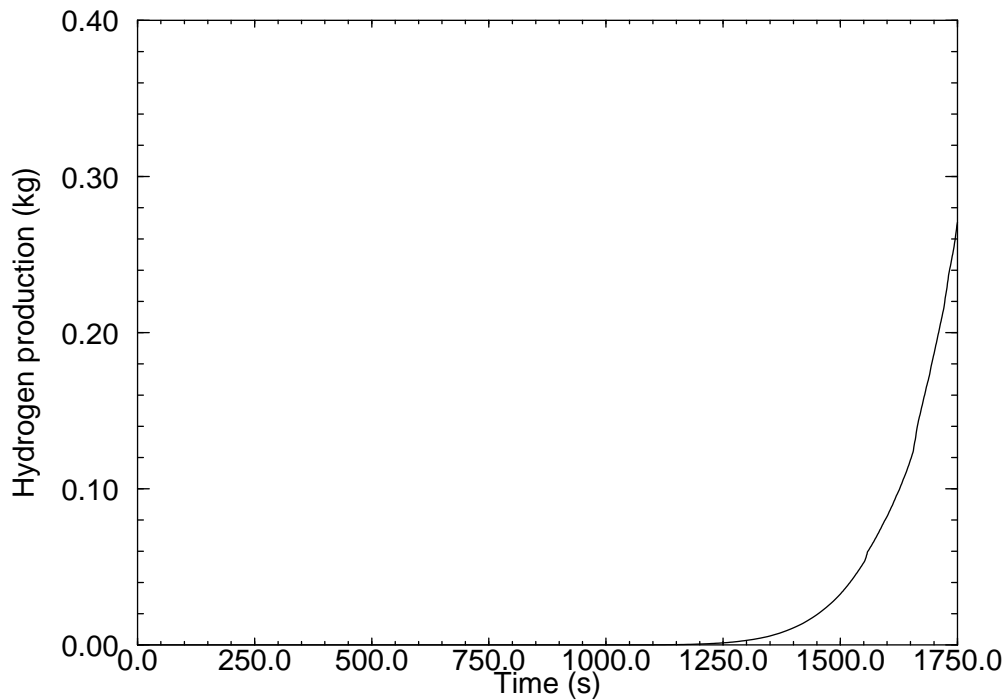


Figure A-94. Calculated hydrogen production.

Figure A-95 illustrates the overall condition of the LOFT CFM just prior to the initiation of reflood. This figure illustrates the condition of the three primary fuel rod groups, as well as the Ag-In-Cd control rods. As seen in this figure, all three fuel rod groups have ballooned and failed at axial node eight, which represents the hottest portion of the CFM. This corresponds with measurements of the temperature at the 42 inch elevation. As is typical in damage progression in the LOFT core, this elevation is just above the peak power zone. It can be observed that the cladding ballooning is as localized as the axial nodalization will allow, and that there has been no significant fuel rod damage other than localized deformation and cladding failure. No significant ceramic fuel rod melting has been predicted to occur. This core condition coincides quite well with posttest examination of the bundle, although it does not adequately describe the eutectic formation which is believed to have occurred when molten absorber material was sprayed onto adjacent fuel rods.

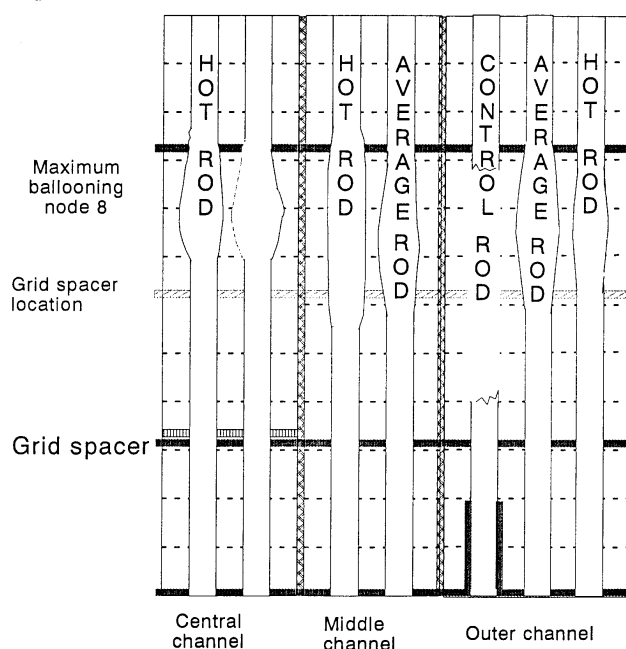


Figure A-95. Calculated core end state prior to reflood.

Figure A-95 also illustrates the predicted control rod damage. As shown, all of the Ag-In-Cd absorber material has melted and voided axial zones five through nine. All experimental data support the theory that the central region of the Ag-In-Cd control rods melted and generated sufficient internal pressure to breach the stainless steel sheath as well as the zircaloy guide tube. The molten absorber material was then sprayed onto adjacent hot fuel rod cladding, causing fuel rod metallic melting by eutectic formation as well as providing a cloud of vaporized absorber material for fission product transport. A significant portion of the absorber material was observed to relocate to the bottom of the fuel module, where it resolidified approximately 0.15 to 0.3 m above the coolant level. Since SCDAP/RELAP5 does not have the capability of modeling the phenomena of absorber material spraying onto adjacent fuel rods, the code predicted that the relocating absorber material would flow down the outside of the guide tube to the bottom of the fuel module and solidify in the volume just above the coolant level. Since RELAP5 predicted the coolant level to be slightly lower than measured, the calculated solidification occurred slightly lower than measured.

The ability of the code to predict fuel rod ballooning and rupture is illustrated in Figure A-96, which shows the fuel rod cladding outer radius predicted for each of the three fuel rod groups, each of which were within a separate flow channel in the CFM. Previous analysis^{A-21} has shown that the capability added to SCDAP/RELAP5 to model multiple flow channels within a single enclosure can impact the phenomena observed during the early phases of a severe accident. If the CFM is modeled as a single hot channel, as has been done in the past, flow diverted by the deforming fuel rods is channeled into the peripheral module, thereby imposing coplanar blockage and overestimating the CFM flow blockage. Now that the radiation enclosure representing the CFM can enclose multiple flow channels, flow diverted by deforming fuel rods in one channel is directed into an adjacent flow channel within the CFM, thereby causing additional cooling in that channel and reducing or delaying the deformation in that channel. This capability also allows the code to model cold wall effects, due to the presence of the cold walls of the shroud. Although no measurements were made of fuel rod cladding deformation, an indirect measure of channel blockage can be inferred by the fact that sufficient coolant flow was maintained through the CFM to maintain zircaloy oxidation.

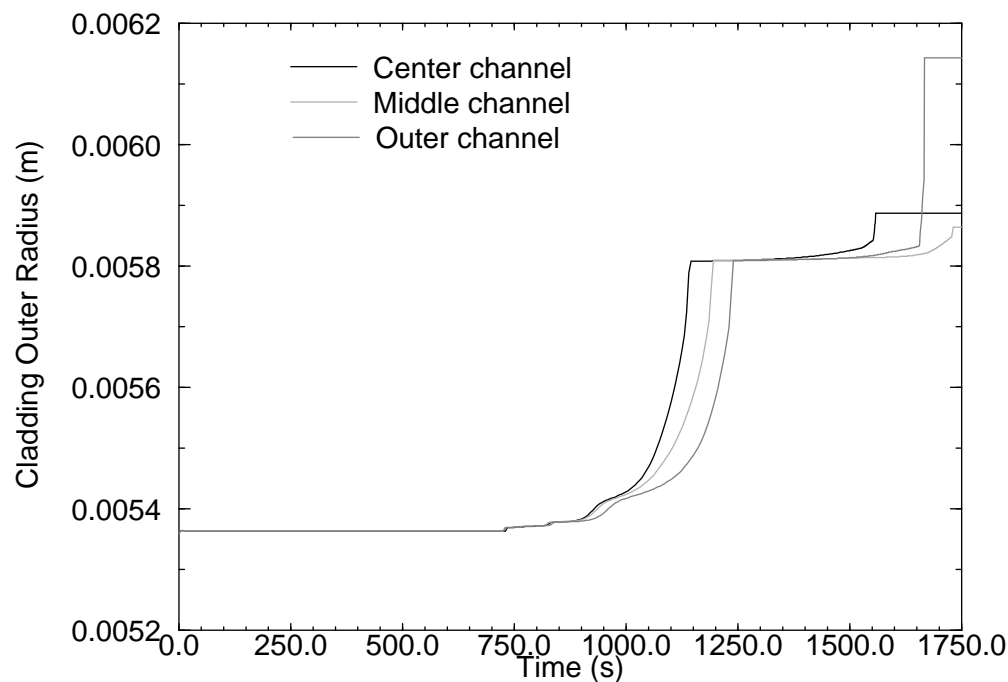


Figure A-96. Cladding outer radii.

A.9.3 Assessment Summary

The analyses of severe accident transients continues to be dominated by uncertainties in the thermal-hydraulic conditions. The ability of SCDAP/RELAP5/MOD3 to predict core temperatures is stable and reliable, provided the thermal-hydraulic boundary conditions are realistic. The mechanics of heat conduction and oxidation are handled in a manner that produces results within the uncertainties encountered during the LP-FP-2 experiment. Each core damage phenomena observed during the transient portion of the experiment was triggered within the correct temperature range with the possible exception of the onset of rapid oxidation. The codes late prediction of this onset may be an artifact of the LOFT thermocouple effect, which would not be applicable to commercial fuel rods. The thermal results tracked observed phenomena quite well, with the exception of phenomena related to the eutectic interaction between control rod absorb-

er material and zircaloy. The lack of a model to simulate the interaction between Ag and zircaloy has not significantly impacted the prediction of temperatures but would significantly impact any fission product transport analysis. The impact on fission product transport is significant because a cloud of vaporized control rod material would be created at the same time and location as massive cladding disruption, causing significant interaction between iodine and the vaporized absorber material.

The ability of SCDAP/RELAP5/MOD3 to model hydrogen production and transport has improved since SCDAP/RELAP5/MOD2.5, although this phenomenon is highly dependent on the reliability of the hydraulic prediction. It should be noted however, that difficulties are still encountered when non-condensable quality approaches unity. SCDAP/RELAP5/MOD3 has accurately predicted core damage progression within the limits of the hydraulic calculation for this analysis.

In conclusion, if reasonably realistic boundary conditions can be provided, the severe accident models within SCDAP/RELAP5 are capable of yielding best-estimate results. Resorting to the use of user-specified input parameters outside the range of defensible choices is not needed. The uncertainty in the LP-FP-2 transient analysis is dominated by uncertainties in the thermal-hydraulic response of the primary coolant system (PCS). The greatest uncertainty remains the experimental uncertainties, such as the break flow. A lack of instrumentation on the most significant break flow path, the intact loop cold leg break line, has led to the necessity for parametric studies of break flow resistance.

A.10. SURRY PLANT TRANSIENT RESULTS

The Surry plant transient calculations were performed for the purpose of identifying and correcting residual code errors in SCDAP/RELAP5/MOD3.1 and to verify that modeling and reliability improvements made to the code were operational. A detailed assessment of each model improvement was not the intent of this work. Improvements were made in the areas of code reliability, early phase modeling and late phase modeling. The following code reliability improvements were exercised: time smoothing, auto time-step repetition, radiation time step control, globally convergent Newton's method, restart, new style input, output improvements, and data compression. The following early phase modeling improvements were exercised: decay power, and liquefied absorber drainage.

The key to a successful process of identifying and correcting residual code errors is run time. Since a typical Surry plant calculation may take as long as two weeks to run, accelerated Surry plant calculations were performed to both aid in correcting code errors and to address reliability and modeling improvements. A Surry verification TMLB^a calculation was also performed for demonstrational purposes and to help test coding improvement made to SCDAP/RELAP5/MOD3.1.

A.10.1 Plant Transient Model

The Surry nuclear power plant is a Westinghouse-designed pressurized water reactor (PWR) with a rated thermal power of 2441 MW. The core consists of 156 15x15 assemblies with an active fuel height of 3.66 m. There are three primary coolant loops. Each loop contains a U-tube steam generator, a reactor coolant pump, and associated piping. A single pressurizer is attached to the hot leg piping on one of the three loops. Two power-operated relief valves (PORVs) are located at the top of the pressurizer. One accumulator, with 29,100 kg of 322 K borated water pressurized to 4.24 MPa by a nitrogen cover gas, is attached to each cold leg.

Two types of calculations were performed as part of this work, accelerated transients and a repetition of an earlier TMLB' calculation. Several accelerated decks were built to assist in the debugging effort, but only one deck was constructed for the TMLB' calculation. The accelerated verification decks were adapted from the Surry base deck used in a study of intentional depressurization,^{A-1} which evaluated a TMLB' sequence with the late intentional depressurization strategy employed. The late depressurization strategy consisted of latching the PORVs open when the core exit temperature of 922 K was reached.

For the accelerated decks, two modifications were made to accelerate the calculation. Changes were made to the total reactor power, and to the PORV and safety relief valve (SRV) flow areas. A high reactor power was used during the transient in order to accelerate the calculated core damage. With the increased reactor power, it was necessary to increase both the PORV and SRV flow areas by a factor of ten to avoid pressures near the critical point.

The deck used to perform an unaccelerated TMLB' calculation was also adapted from the Surry base deck used in a study of intentional depressurization.^{A-1} The calculation is a repetition of Case 2 from an earlier calculation.^b

a. A TMLB' sequence is a loss of both onsite and offsite AC power, with immediate failure of the steam-driven auxiliary feedwater pump.

For all decks, a total of six SCDAP components distributed in three RELAP5 flow channels were used to model the reactor core. Table A-10 shows the location of each SCDAP component with the number of representative rods being modeled and the corresponding RELAP5 flow channel. A typical 15x15 fuel assembly used in the Surry nuclear power plant consists of fuel rods, control rods, control rod guide tubes, and an instrument tube. However, for this and previous Surry calculations, only SCDAP fuel rod and control rod components were used in modeling the core. The modeling of the empty control rod guide tubes and instrument tubes were lumped into the control rod. The method used in lumping the mass of the empty control rod guide tubes and instrument tubes into the control rod component is described in the footnote.

Table A-10. SCDAP component placement and the number of representative rods for Surry NPP.

Flow channel	SCDAP component number/ Number of fuel rods	SCDAP component number/ Number of control rods
Inner flow channel (core pipe volume 111)	1 / 5,100	2 / 525
Middle flow channel (core pipe volume 112)	3 / 19,584	4 / 2,016
Outer flow channel (core pipe volume 113)	5 / 7,344	6 / 756

Several RELAP5 components were used to simulate the thermal-hydraulics. These components modeled the reactor vessel, the piping in all three primary coolant loops, the pressurizer and associated surge line, all three steam generators with associated relief valves, and selected parts of the secondary system. Additionally, a single valve component was used to represent both PORVs, and a single valve component was used to represent all three SRVs. To accommodate the elevated transient heat load for this accelerated calculation, the cross-sectional flow area of both valves was increased by a factor of ten. The reactor vessel nodalization, as developed by Bayless,^{A-22} is shown in Figure A-97. As indicated, three parallel flow channels extend from the lower plenum through the core to the upper reactor vessel head. Heat structures, which are shown as shaded areas, represent the structural mass of the reactor vessel walls, the core barrel and baffle, the thermal shield, the upper and lower core support plates, and structures in the upper and lower plena. External surfaces of all heat structures were assumed to be adiabatic. The nodalization of the primary coolant loop containing the pressurizer is shown in Figure A-98.

b. D. L. Knudson and C. A. Dobbe, *Assessment of the Potential for High Pressure Melt Ejection Resulting From a Surry Station Blackout Transient (DRAFT)*, NUREG/CR-5949, EGG-2689, DRAFT.

The lower reactor vessel head was modeled with a single COUPLE mesh, shown in Figure A-99. The axisymmetric mesh includes a total of 320 nodes with 285 elements. Convection and radiation heat transfer were modeled at all interfaces between the coolant and debris. In addition, convection and radiation heat transfer were modeled along the vessel wall at all nodes that are not submerged by debris (those nodes exposed to primary coolant/steam). The external surface of the lower head was assumed to be adiabatic.

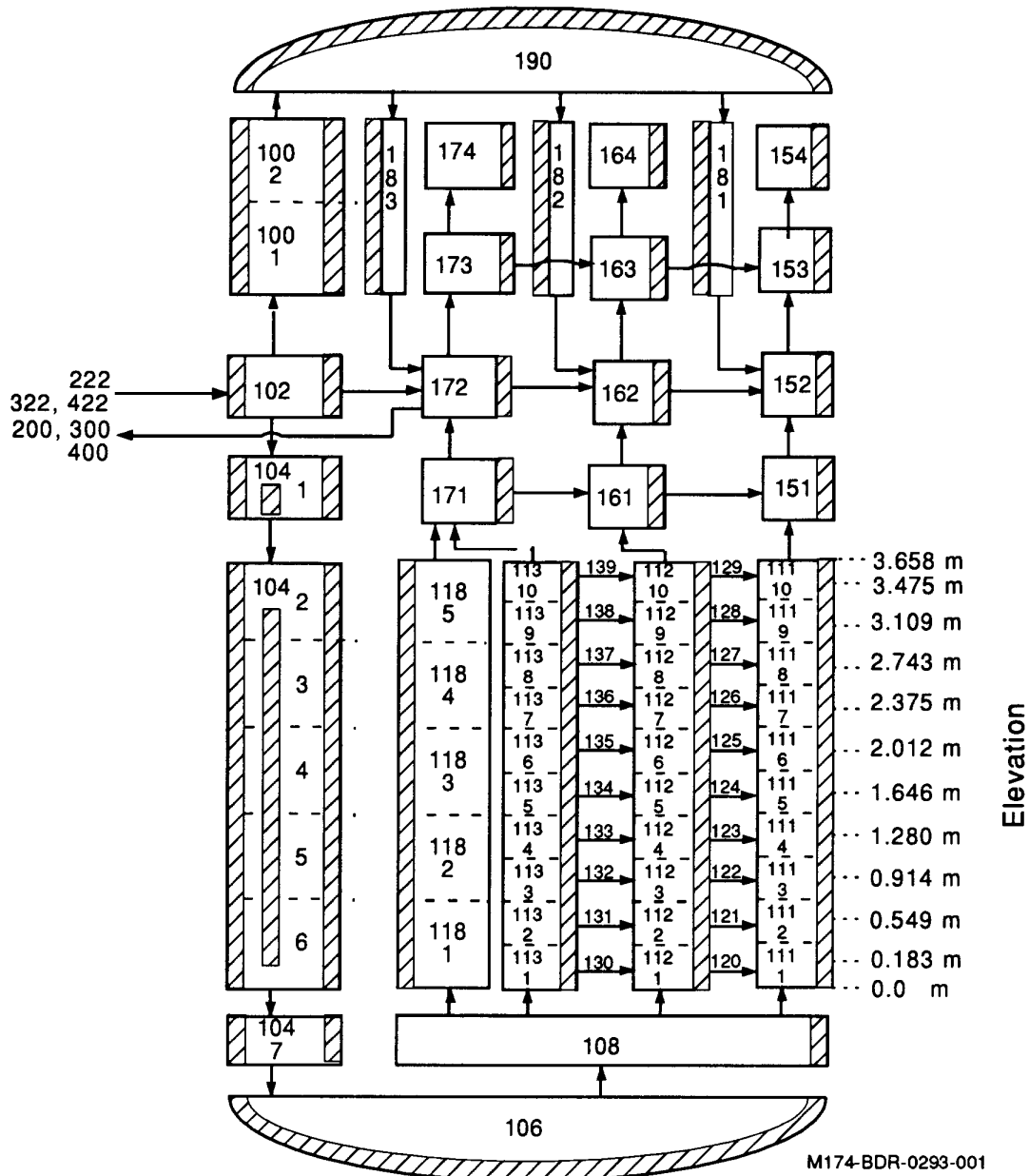


Figure A-97. Vessel nodalization for the Surry plant transient.

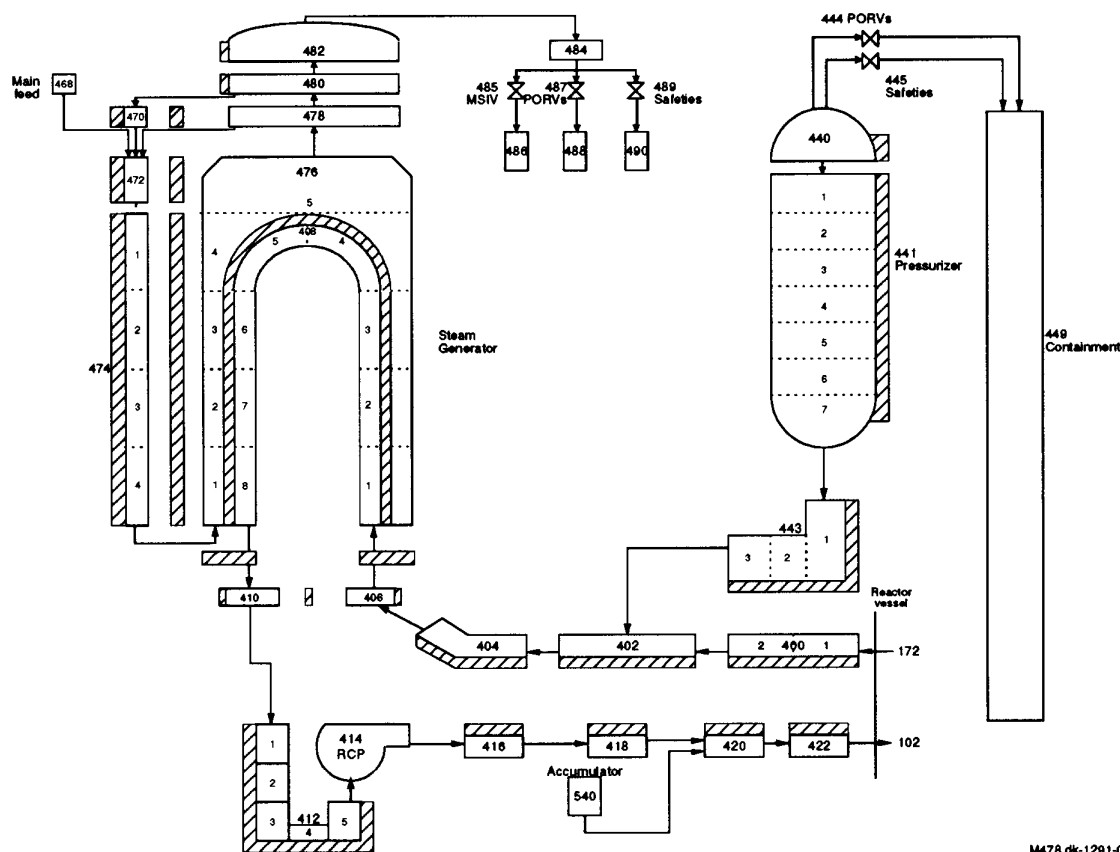


Figure A-98. Pressurizer coolant loop for the Surry plant transient.

A.10.2 General Results for Surry TMLB' Calculation

Upon initiation of the TMLB' transient, the reactor coolant pumps (RCPs) were tripped off and the reactor was scrammed. During the ensuing RCP coastdown, the coolant was transported from the vessel to the steam generators. Full loop circulation of the coolant continued even after the RCPs completely coasted down because the heat sink of the steam generator secondary side water volume set up a natural circulation flow path for heat removal from the core. However, because there was no feedwater supplying water to the steam generators, full loop natural circulation continued only until the steam generator secondary side water volume became depleted at 4,910 seconds. At this point, the RCS rapidly pressurized until the PORV set point pressure was reached at 4,880 seconds, the beginning of PORV cycling. Because the RCS coolant inventory was continually being removed by the PORVs cycling, the core eventually began to uncover at 9,240 seconds. Onset of oxidation occurred at 10,880 seconds, and the first fuel rod failure was caused by grid spacer interaction at 12,260 seconds. At 12,320 seconds, a rubble bed was formed in the inner flow channel at the 2.375 m elevation. Surge line creep rupture failure occurred at 13,375 seconds, and creep rupture failure in the hot leg was calculated at 14,260 seconds. (Although a rupture would cause a change in the boundary conditions, the calculation was allowed to continue on without modeling the ruptures in the pressure boundaries.) Massive slumping to the lower head first

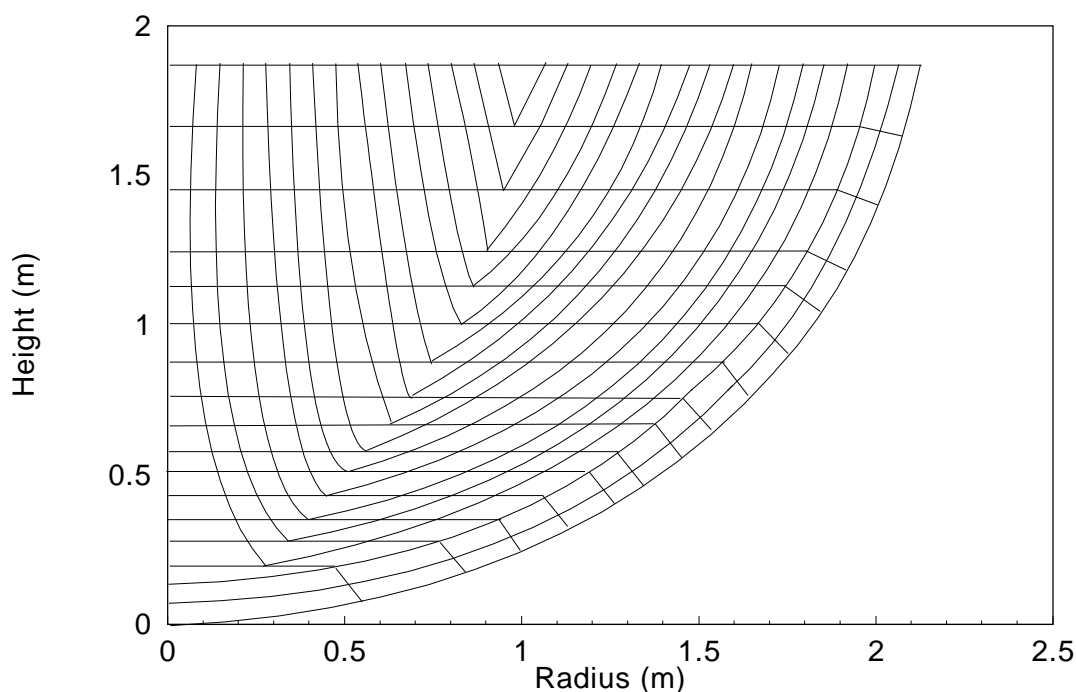


Figure A-99. COUPLE mesh representing the lower reactor vessel head for the Surry plant transient.

occurred at 14,470 seconds, and lower head failure occurred at 14,910 seconds. Table A-12 summarizes event sequence and timing with the associated peak core surface temperatures.

A.10.2.1 Power Generation.

The space-independent reactor kinetics power option was used to calculate the total reactor power. As noted in the opening paragraph, modeling improvements were made to the decay power model. A deficiency in the decay heat model had previously caused the calculated decay heat to be significantly less than the actual decay heat at locations where a large fraction of the fuel had been dissolved by chemical reaction with the fuel rod cladding. This deficiency is easily identified by a step change in the decay heat. Figure A-100 shows a time history plot of the total reactor power. As evident by the plot, no unusual step changes occurred, indicating that this deficiency has been resolved.

A.10.2.2 Thermal-Hydraulic Response.

The RCS pressure response is shown in Figure A-101. The initial drop in pressure was a result of the steam generators removing more energy than was being generated in the core. The oscillations in the pressure prior to steam generator dryout at 4,910 seconds reflect the cycling of the steam generator secondary relief valves. Following steam generator dryout, the pressure increased to the PORV opening pressure. The pressure then cycled between the opening and closing set point (16.2 and 15.7 MPa) for the remainder of the transient. Initially, superheated steam was vented through the PORVs. The change in the

Table A-11. Event sequence and timing for Surry TMLB^a.

Event	Peak Core Surface Temperature (K)	Time (s)
Transient initiation	620	0
RCPs coast down	590	150
Beginning of PORVs cycling	580	4,880
Steam generator dryout	580	4,910
Start of core uncover	630	9,240
Onset of fuel rod oxidation	1,000	10,890
Core completely uncovered	1,150	11,400
Fuel rod cladding failure due to grid spacer interaction (Fuel rod in inner flow channel at 3.109m elevation)	1,550	12,260
Initial fuel rod melt relocation (Fuel rod inner flow channel, material slumped to 2.375m elevation)	1,550	12,260
Initial rubble bed formation (Fuel rod in outer flow channel at 0.549 m elevation)	1,590	12,320
Surge line creep rupture failure	2,700	13,375
First slumping of control rod material to lower head	2,980	14,200
Hot leg creep rupture failure (loop containing pressurizer)	2,990	14,260
Initial molten pool formation	3,031	14,470
Failure of lower crust: massive slumping to lower head	3,031	14,470
Creep rupture failure of lower head ^a	2,960	14,910

a. Based upon 1,200 K vessel wall mid-plane temperature.

pressure response at 7,820 seconds resulted from saturated vapor and liquid steam being vented through the PORVs. By 8,930 seconds, superheated steam was again vented through the PORVs.

RCS blowdown was not modeled in response to any pressure boundary failures. As a result, there was no RCS pressure reduction associated with the failures listed in Table A-12.

Cladding surface temperatures are shown in Figures A-102 through A-113 for all SCDAP components. The heatup progressed from the top down and radially outward as the liquid boiled out of the core. The upper portions of the core began oxidizing at 10,890 seconds when the cladding temperature exceeded 1,000 K. When the temperatures reached 1,850 K, the oxidation kinetics changed; and the heatup became more rapid. Shortly after 12,500 seconds, temperatures in the upper portions of the core began to roll over. The temperature rollover was due to excessive amounts of hydrogen being generated in the lower

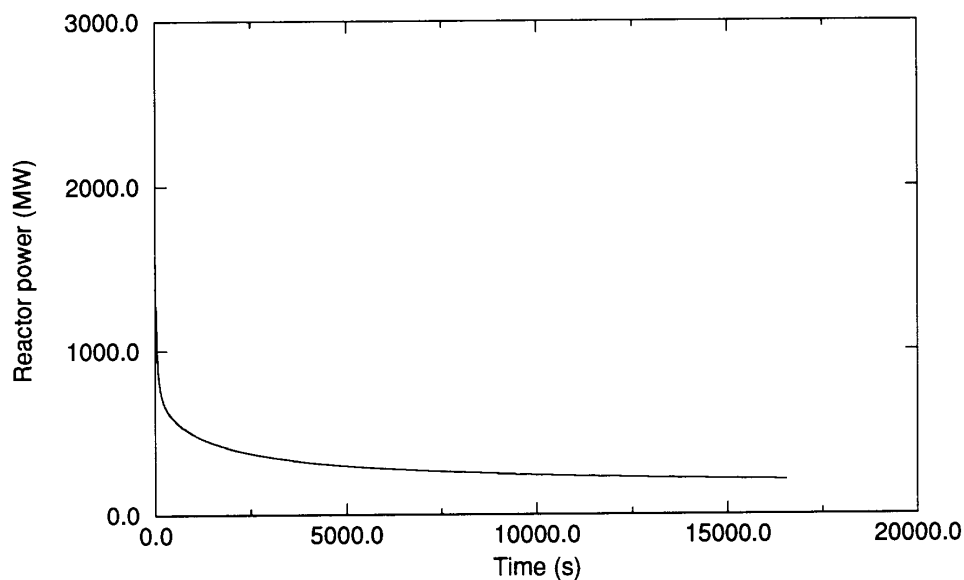


Figure A-100. Total core power for the Surry plant transient.

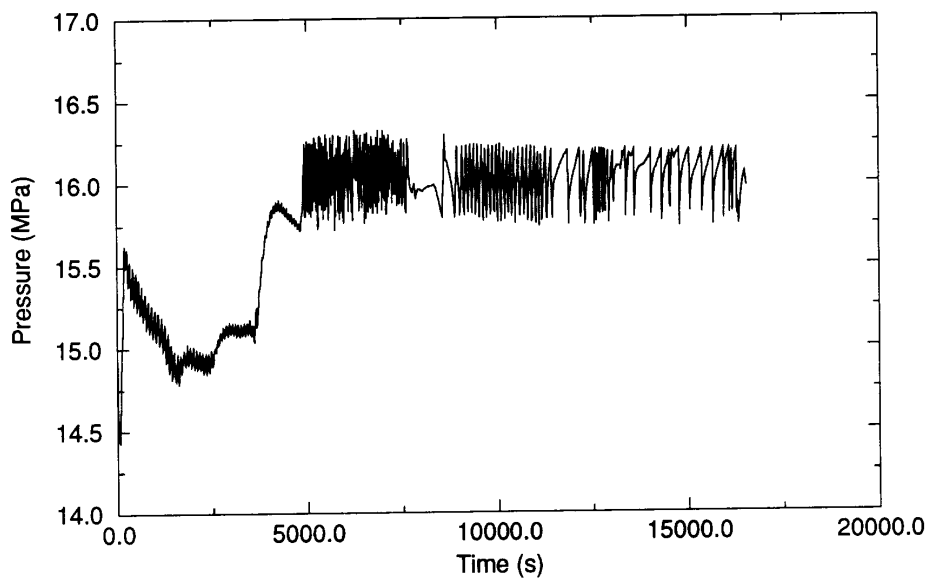


Figure A-101. System pressure for the Surry plant transient.

portions of the core, which steam-limited the oxidation process in the upper portions of the core. At 14,470 seconds, a molten pool was formed in the inner flow channel at the 2.012 m elevation. The substrate supporting the molten pool at the time of molten pool formation was 0.025 m. The specified crust failure thickness was 0.03m, the recommended default value. Because the substrate supporting the molten pool was less than the specified crust failure thickness, crust failure was predicted at the time of molten pool

formation. Once a molten pool relocates to the lower head, the SCDAP component temperatures at that elevation are reset to the saturation temperature for the RELAP5 volume that they occupy. The step change in temperature for both at the 2.012 m elevation in the inner flow channel reflects the crust failure and molten material relocation to the lower head.

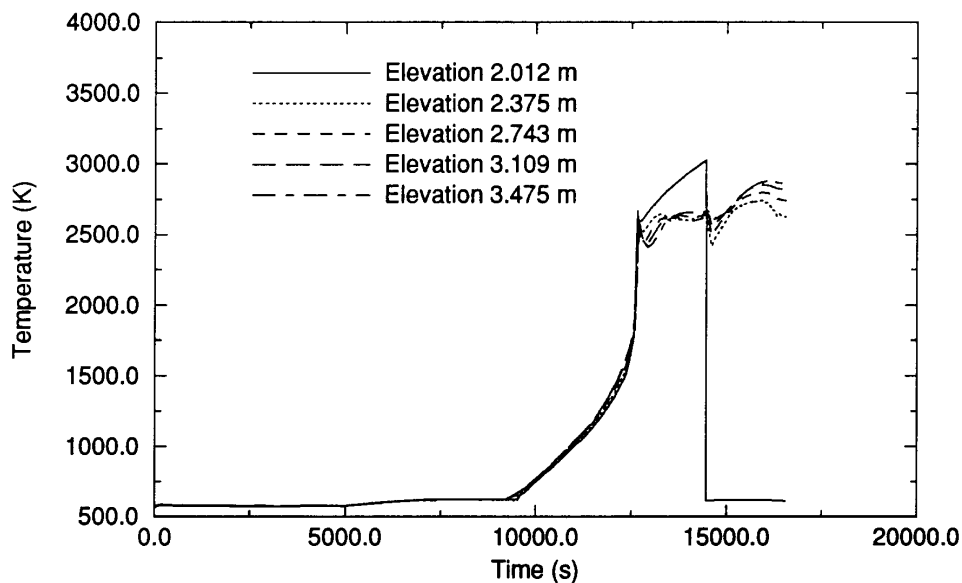


Figure A-102. Surface temperature for the top half of the inner channel fuel rod component for the Surry plant transient.

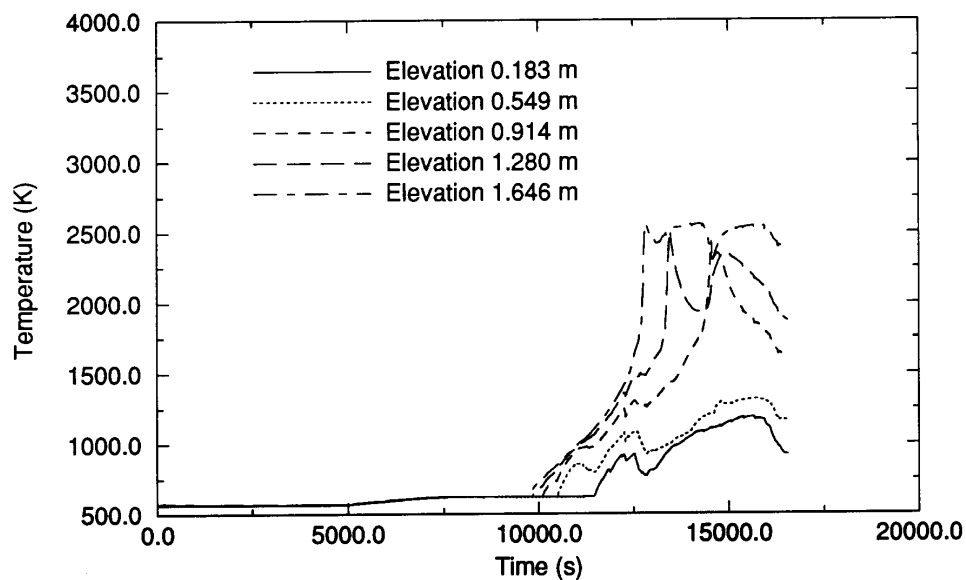


Figure A-103. Surface temperature for the bottom half of the inner channel fuel rod component for the Surry plant transient.

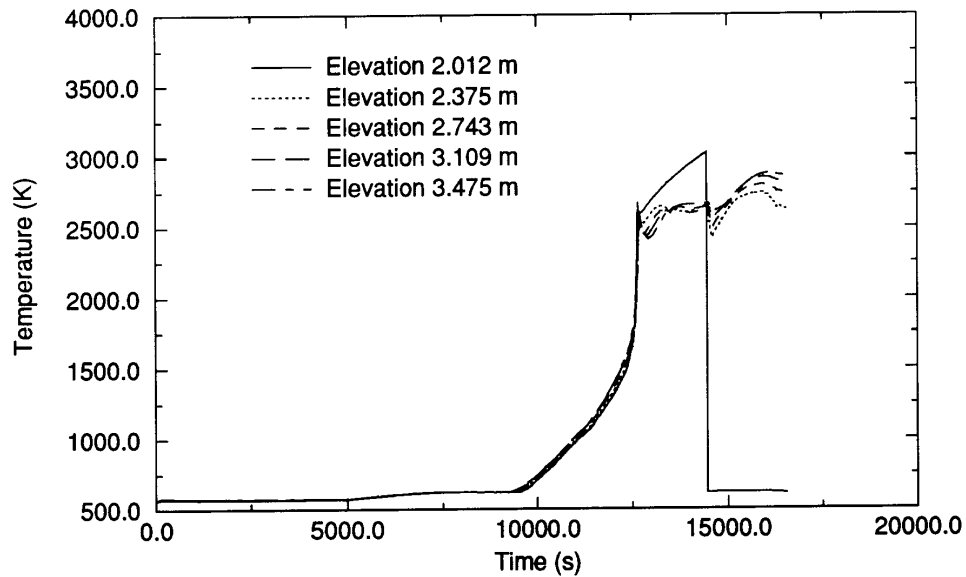


Figure A-104. Surface temperature for the top half of the inner channel control rod component for the Surry plant transient.

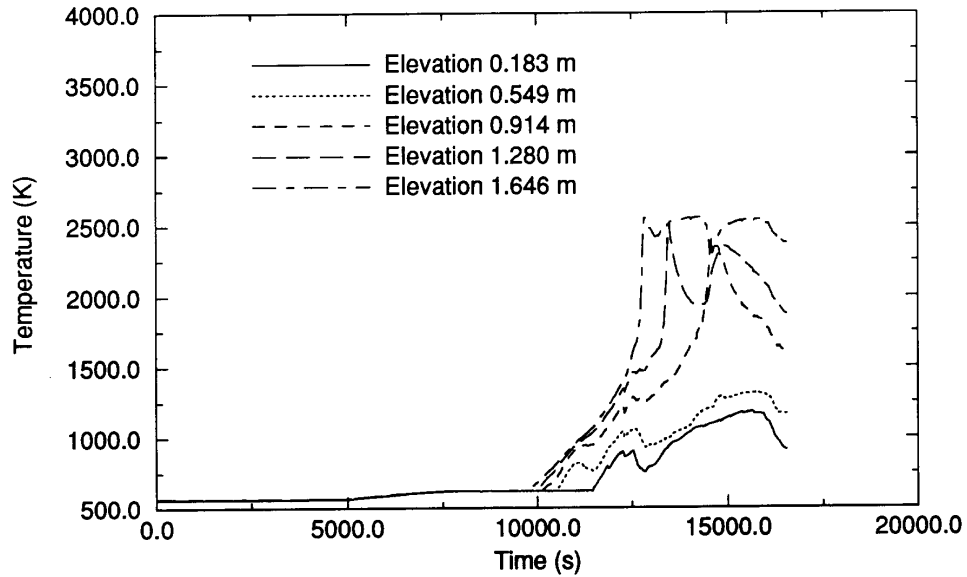


Figure A-105. Surface temperature for the bottom half of the inner channel control rod component for the Surry plant transient.

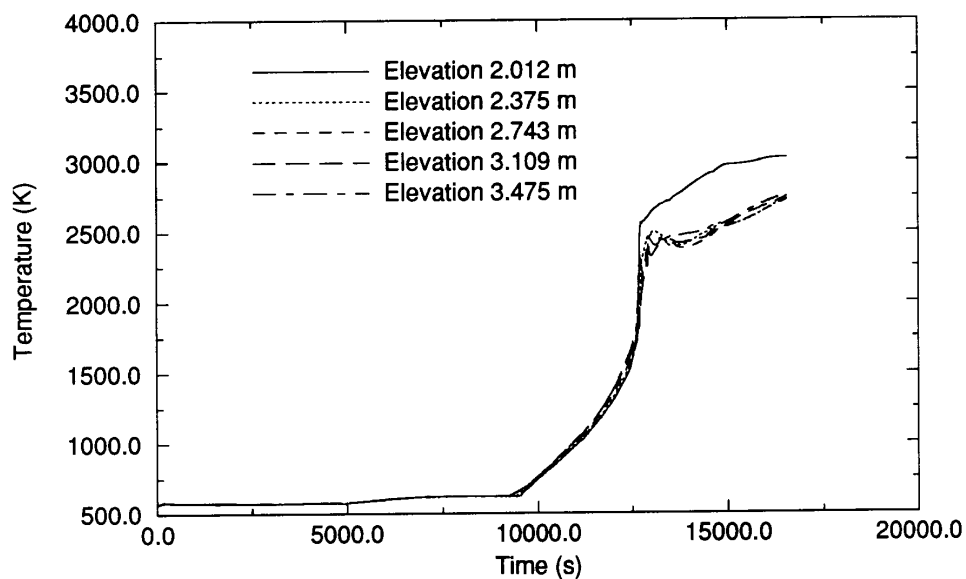


Figure A-106. Surface temperature for the top half of the middle channel fuel rod component for the Surry plant transient.

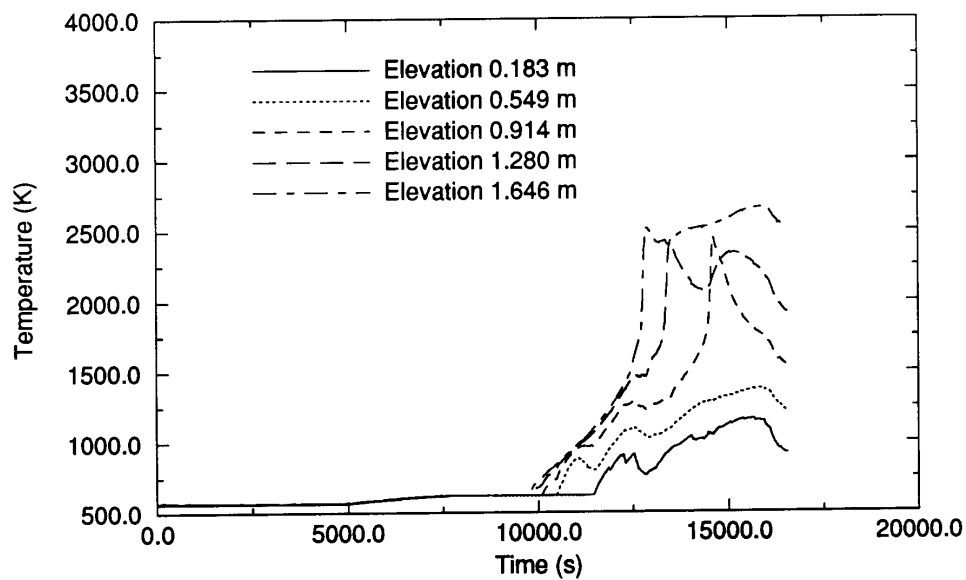


Figure A-107. Surface temperature for the bottom half of the middle channel fuel rod component for the Surry plant transient.

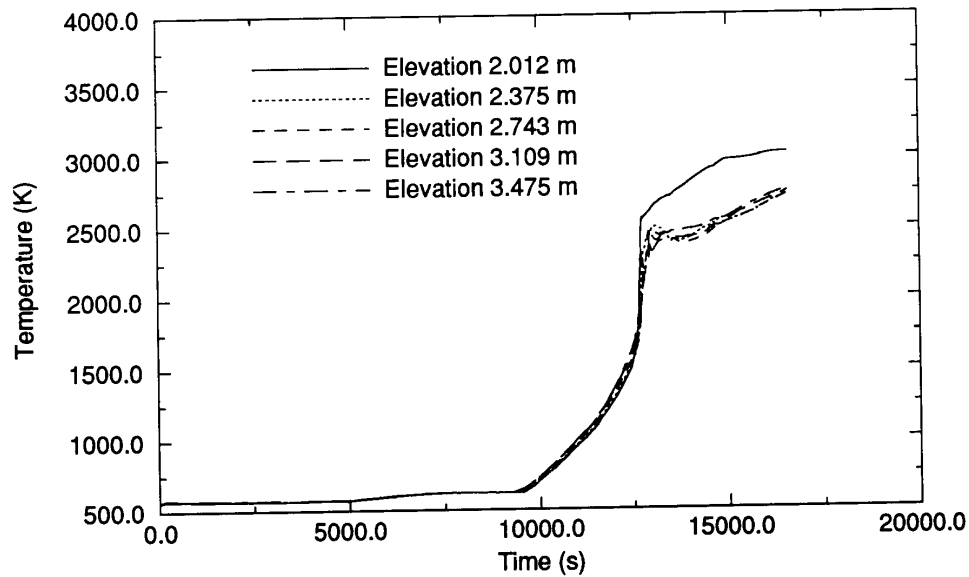


Figure A-108. Surface temperature for the top half of the middle channel control rod component for the Surry plant transient.

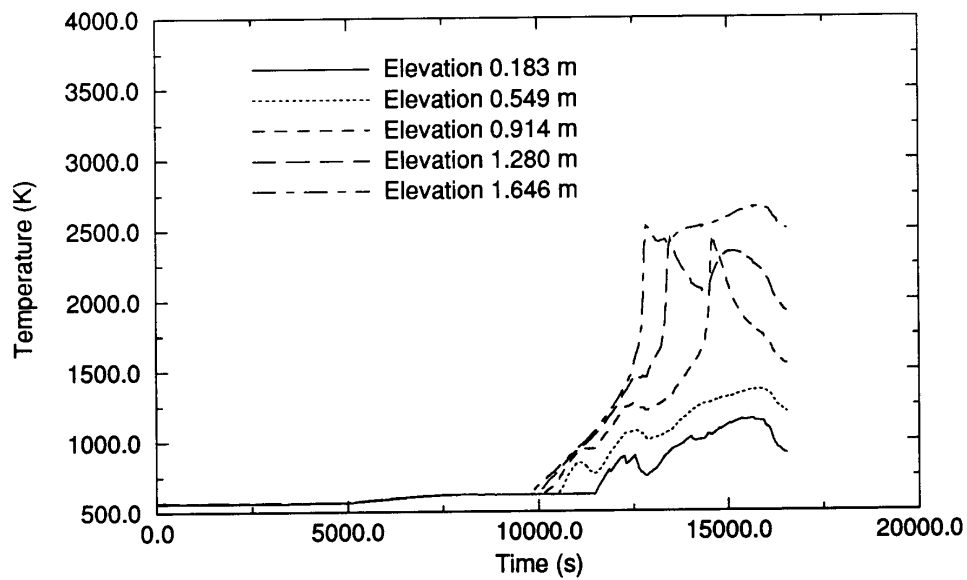


Figure A-109. Surface temperature for the bottom half of the middle channel control rod component for the Surry plant transient.

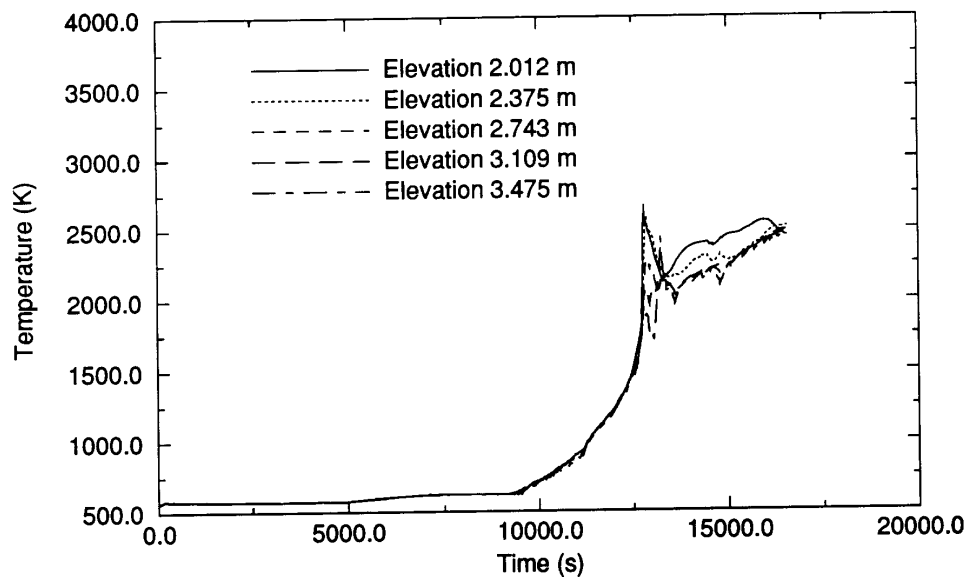


Figure A-110. Surface temperature for the top half of the outer channel fuel rod component for the Surry plant transient.

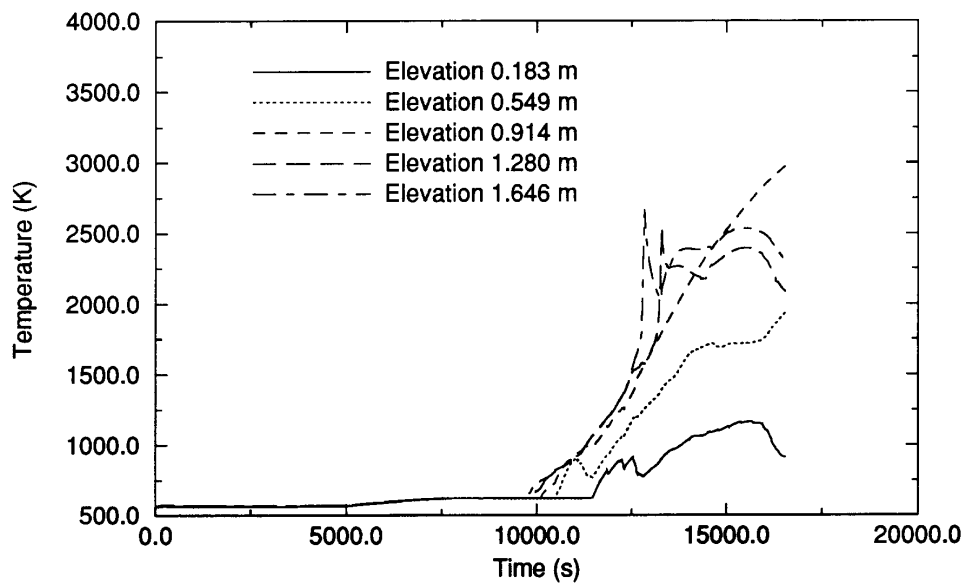


Figure A-111. Surface temperature for the bottom half of the outer channel fuel rod component for the Surry plant transient.

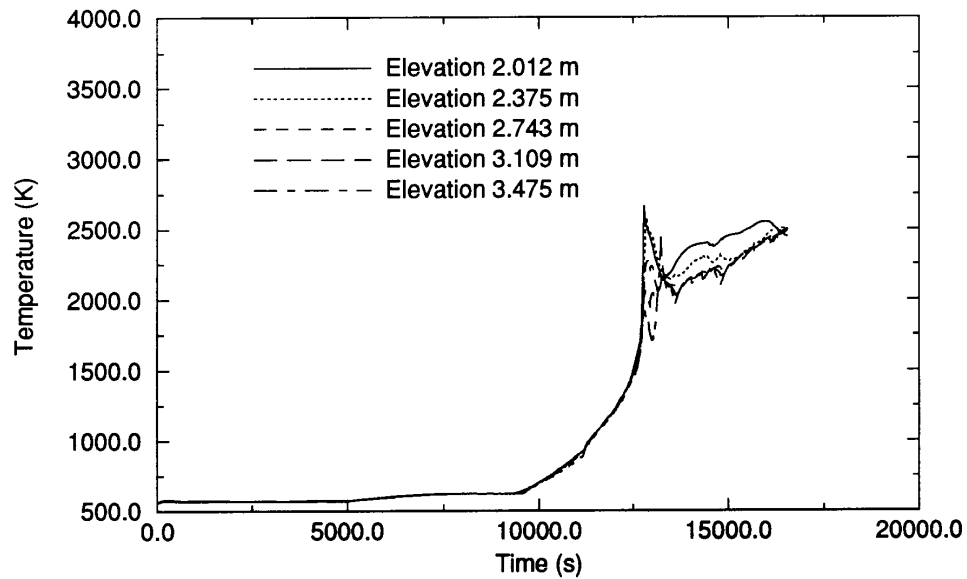


Figure A-112. Surface temperature for the top half of the outer channel control rod component for the Surry plant transient.

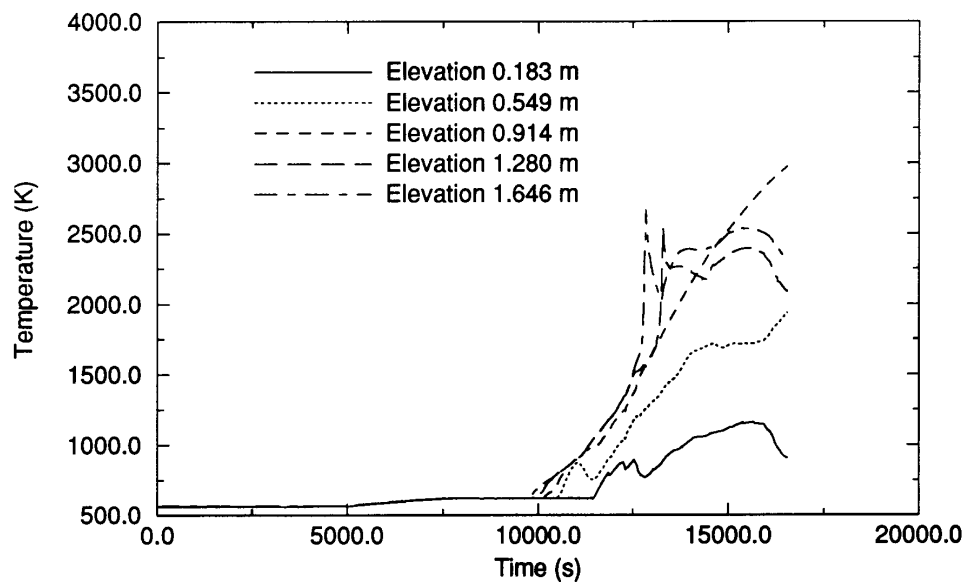


Figure A-113. Surface temperature for the bottom half of the outer channel control rod component for the Surry plant transient.

Table A-12. Event sequence and timing for Surry TMLB’.

Event	Peak Core Surface Temperature (K)	Time (s)
Transient initiation	620	0
RCPs coast down	590	150
Beginning of PORVs cycling	580	4,880
Steam generator dryout	580	4,910
Start of core uncover	630	9,240
Onset of fuel rod oxidation	1,000	10,890
Core completely uncovered	1,150	11,400
Fuel rod cladding failure due to grid spacer interaction (Fuel rod in inner flow channel at 3.109m elevation)	1,550	12,260
Initial fuel rod melt relocation (Fuel rod inner flow channel, material slumped to 2.375m elevation)	1,550	12,260
Initial rubble bed formation (Fuel rod in outer flow channel at 0.549 m elevation)	1,590	12,320
Surge line creep rupture failure	2,700	13,375
First slumping of control rod material to lower head	2,980	14,200
Hot leg creep rupture failure (loop containing pressurizer)	2,990	14,260
Initial molten pool formation	3,031	14,470
Failure of lower crust: massive slumping to lower head	3,031	14,470
Creep rupture failure of lower head ^a	2,960	14,910

a. Based upon 1,200 K vessel wall mid-plane temperature.

A.10.2.3 Hydrogen Production

Figure A-114 shows the total hydrogen production. Oxidation began when the fuel rod cladding temperatures exceeded 1,000 K. The calculation was allowed to run 2,080 seconds past lower head failure. At this time, 390 kg of hydrogen were produced. Based on the information given in Reference A-1, this represents approximately 58% oxidation of all fuel rod cladding.

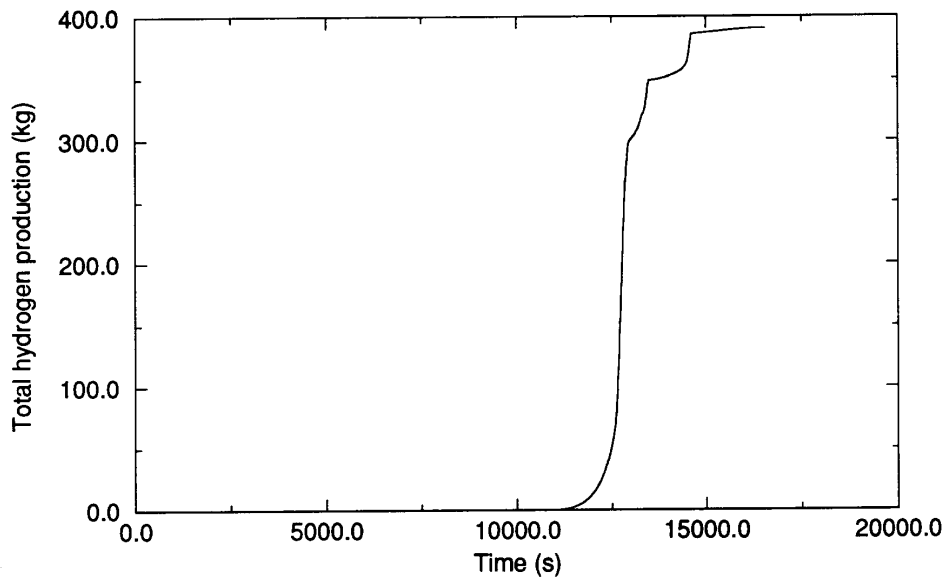


Figure A-114. Total hydrogen production for the Surry plant transient.

A.10.2.4 Damage Progression Response

As part of the code reliability improvements, output improvements were made. Core degradation maps are now printed with every major edit. Figure A-115 shows core degradation maps at the beginning and end of the calculation. The map at time 269 seconds shows the SCDAP fuel rod components and their respective RELAP5 volumes. It also shows the damage state of the core (intact.) The map at the end of the calculation shows a voided volume at axial node 6 (2.012 m elevation) in the inner flow channel. The voided region resulted when the molten pool at that elevation relocated to the lower head. The map also shows porous debris at axial nodes 2 and 3 in the outer flow channel. Further examinations showed that the porous debris (identified in the code as rubble debris) resulted from a quench and fragmentation of embrittled cladding at 12,320 seconds, due to a small reduction in the temperatures associated with enhanced steam cooling. At the time of quench and fragmentation, a small amount of liquid entered the core at the 0.183 m elevation, resulting in the cooling of the 0.549 m elevation. The temperature at the time of quench and fragmentation was 1,066 K. The maximum surface temperature prior to fragmentation was 1,080 K, and the alpha layer had grown to the inner cladding radius, resulting in a beta thickness of identically zero.

A.10.2.5 Lower Plenum Response.

One of the late-phase modeling improvements that the TMLB' calculation was intended to evaluate was that which addressed the drainage of the absorber material (Ag-In-Cd) in PWR control rods. Previously, a code error caused control rod material that had slumped and solidified to be calculated to stay in place after it liquefied a second time. The lower plenum response lends supporting evidence that this code deficiency has been resolved. Figure A-116, showing the peak lower plenum debris bed temperature, indicates an increase in temperature at 14,200 seconds. This temperature increase is in response to molten

```

OAJOR EDIT !!!time= 269.000 sec
.....^B.....
                                core degradation map
I = intact fuel component      underscore indicates      I      x's indicate
P = porous debris              metallic or planar          V      that total or bulk
M = molten or frozen ceramic pool blockage in volume at bottom  XXPXX blockage occurs
V = Relap fluid volume now void of fuel of indicated node    xxMxx in the volume

Fuel rod component #          1          3          5
Axial node #
10          I          I          I
9           I          I          I
8           I          I          I
7           I          I          I
6           I          I          I
5           I          I          I
4           I          I          I
3           I          I          I
2           I          I          I
1           I          I          I
Relap vol. at bottom      111010000 112010000 113010000
.....^B.....

OAJOR EDIT !!!time= 16271.0 sec
.....^B.....
1 conditions of in-core molten pool at time = 16271. sec
effective radius of pool      = 0.0000E+00 (m)      total heat generated in pool = 0.0000E+00 (W)
volume of molten pool         = 0.0000E+00 (m*3)      total rate of heat removal   = 0.0000E+00 (W)

                                core degradation map
I = intact fuel component      underscore indicates      I      x's indicate
P = porous debris              metallic or planar          V      that total or bulk
M = molten or frozen ceramic pool blockage in volume at bottom  XXPXX blockage occurs
V = Relap fluid volume now void of fuel of indicated node    xxMxx in the volume

Fuel rod component #          1          3          5
Axial node #
10          I          I          I
9           I          I          I
8           I          I          I
7           I          I          I
6           V          I          I
5           I          I          I
4           I          I          I
3           I          I          P
2           I          I          P
1           I          I          I
Relap vol. at bottom      111010000 112010000 113010000
.....^B.....

```

Figure A-115. Damage progression map from SCDAP output for Surry plant transient.

PWR control rod material draining to the lower head, and it was found that this relocation came from a stratified cohesive debris. Before this deficiency was resolved, control rod material would not have been able to relocate independently from a stratified cohesive debris. At 14,470 seconds, massive slumping to the lower head began; and the lower plenum debris bed temperature peaked at 2,150 K.

Figure A-117 shows the debris bed height in the lower plenum. Again, the lower head began to fill at 14,200 seconds when molten PWR control rod material began draining to the lower head. After massive slumping at 14,470 seconds, the debris height was calculated to be 0.24 m.

Figures A-118 through A-120 show the lower plenum temperature history plots for the 0.2-, 0.5-, and 1.0- m elevations measured with respect to the bottom of the vessel. Outer vessel wall, inner vessel wall, and debris temperatures are compared at each elevation. Up to the point of molten material entering the lower head, the vessel wall temperatures were responding to the fluid boundary conditions supplied by the RELAP5 volume modeling the lower head. The code sets the debris temperature to the initial condition temperature until relocating debris fills the COUPLE mesh modeling the debris in the lower head. The maximum debris height was 0.24 m; thus, the 0.2 m elevation plot was the only one showing the thermal response of the vessel wall in contact with the relocated debris. The calculated temperatures look reasonable.

A.10.3 Code Performance

Code performance was evaluated in several areas. Subsections will discuss code reliability improvements, CPU usage, and give a benchmark comparison to a TMLB' calculation run on an earlier version of SCDAP/RELAP5.

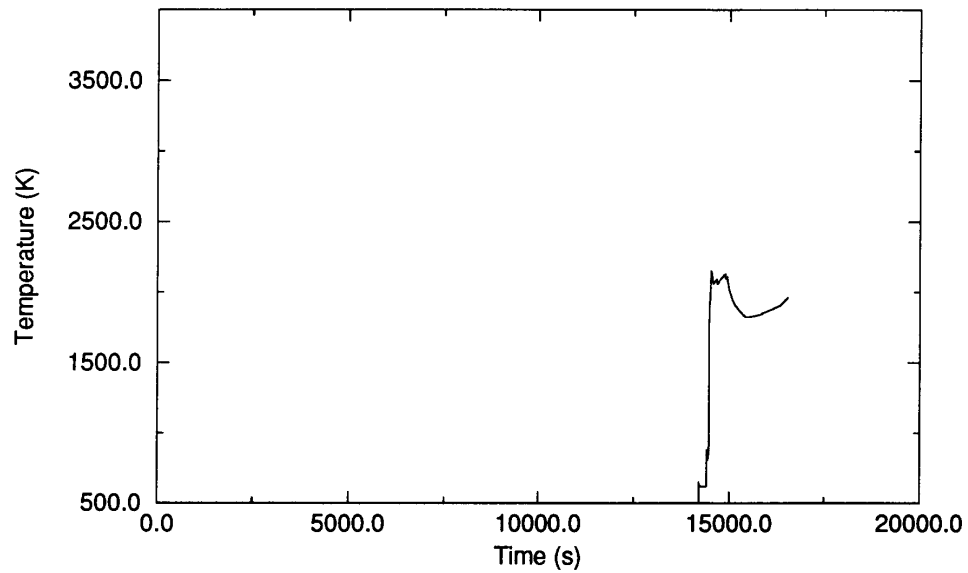


Figure A-116. Peak lower plenum debris bed temperature for the Surry plant transient.

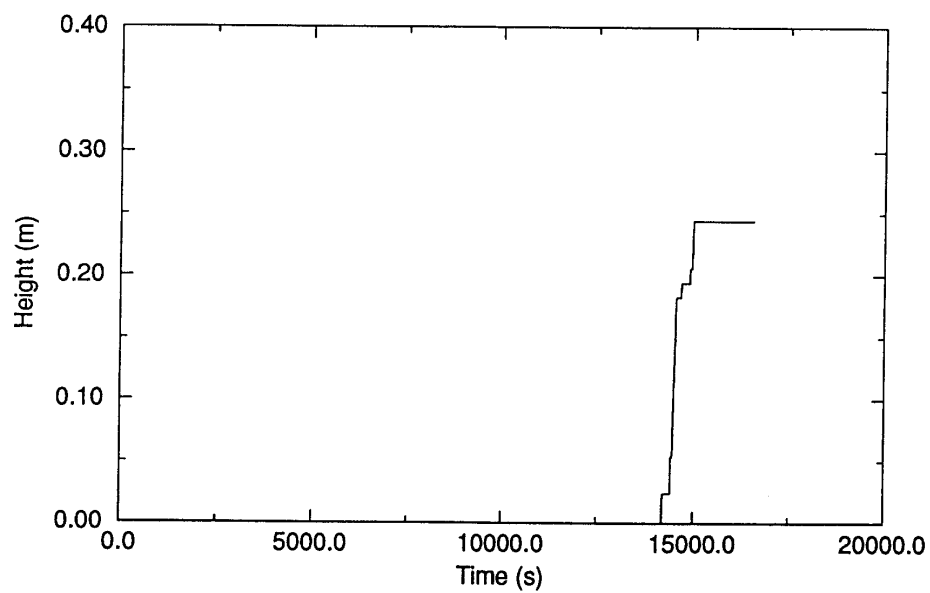


Figure A-117. Lower plenum debris height for the Surry plant transient.

A.10.3.1 Code Reliability Improvements

Several of the new code reliability improvements were exercised during the course of completing this work. The improvements include time smoothing, time step repetition, radiation time step control, globally

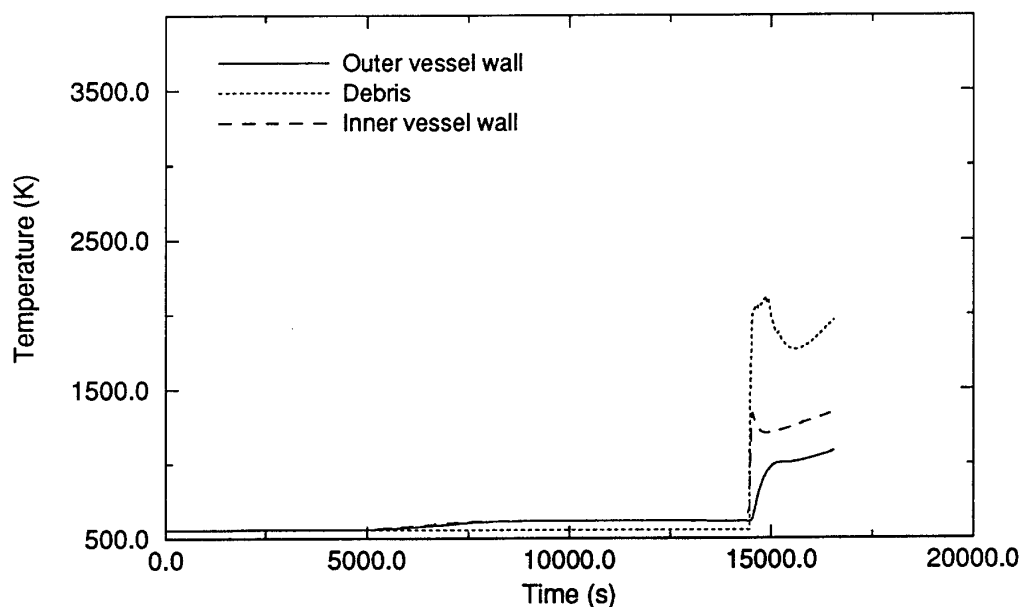


Figure A-118. Lower plenum debris and head axial temperature distribution for the 0.2 m elevation for the Surry plant transient.

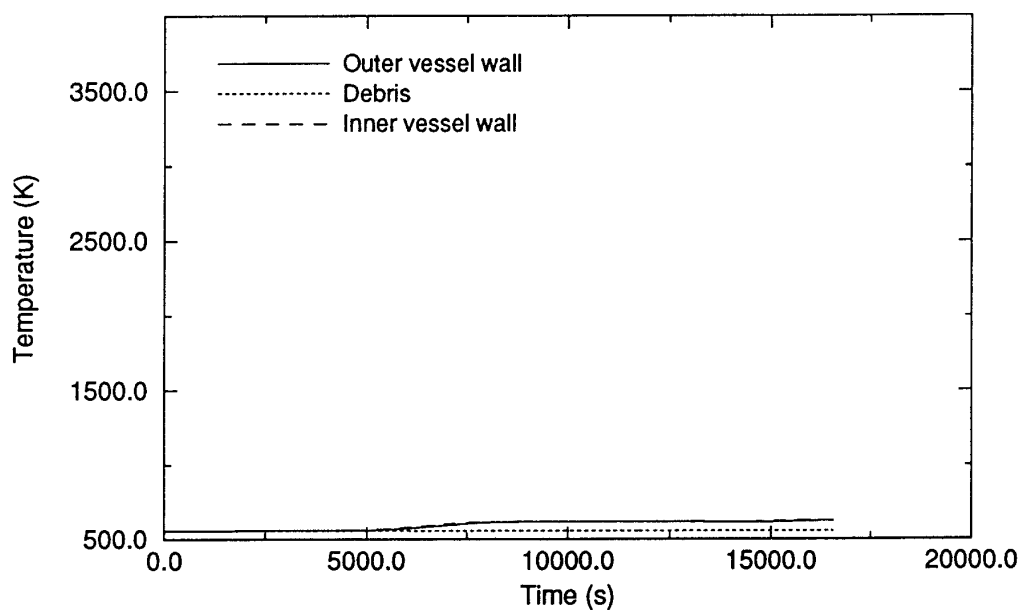


Figure A-119. Lower plenum debris and head axial temperature distribution for the 0.5 m elevation for the Surry plant transient.

convergent Newton's method for noncondensable state equations, restart, new style input, and data compression.

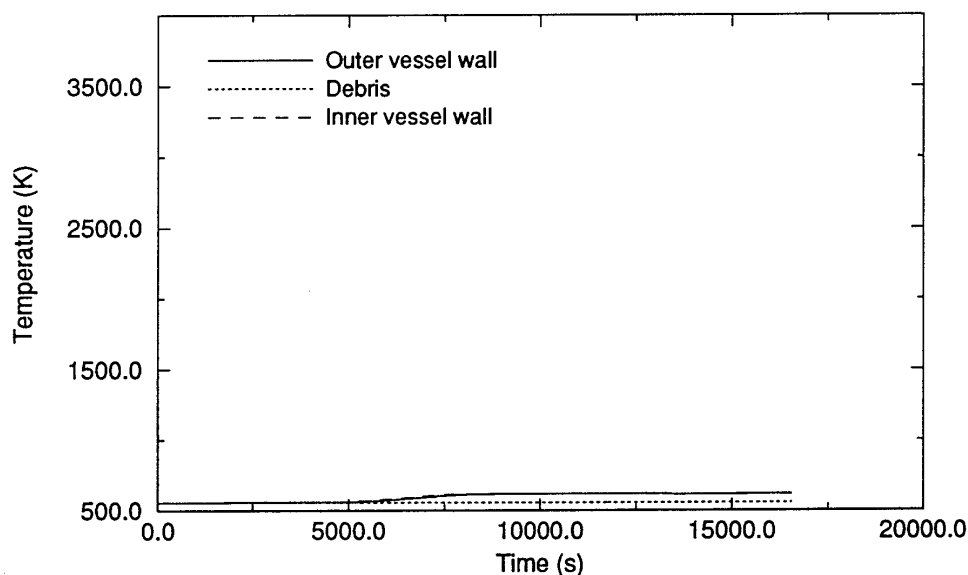


Figure A-120. Lower plenum debris and head axial temperature distribution for the 1.0 m elevation for the Surry plant transient.

For the TMLB' calculation, time smoothing, time step repetition, radiation time step control, and the globally convergent Newton's method were used to complete the calculation. Attempts were made to run without the last three options turned on, which ended in water property failures and non-condensable non-convergence problems shortly after the onset of oxidation. With the aforementioned options turned on, the calculation was run from start to finish on a single restart requesting 0.5-second time steps. Furthermore, no oscillatory temperature excursions were observed, which can normally be expected when taking large time steps. Overall, these options seem to function very well together.

Data dependence on restart frequency had been previously identified and corrected. To verify the general nature of the correction, several restarts were performed that varied the restart frequency while performing accelerated Surry calculations, and no restart dependence was observed.

Two identical accelerated Surry calculations were performed--one with data compression turned on and the other with data compression turned off (default.) The calculations were performed out to a maximum core temperature of 3,000 K, and a comparison of the two calculations show identical results. For the data compression case, the restart plot size was 30,024,785 bytes, and for the case run without data compression the restart plot size was 53,578,248 bytes. This represents a 56% reduction in file size.

A.10.3.2 New Style Input.

Two accelerated decks were run to verify the new style input. The decks were identical except for the style of SCDAP input and the units used. For the old-style deck, the SCDAP input was in SI units and the RELAP5 input was in British units. For the new-style input deck British units were used throughout.

The new style of input has many advantages. The RELAP5 card style made assembling the accelerated input deck simple. Input error trapping also caught input errors before runs were made, which resulted in a great time savings. For example, the initial new style input deck was built before all of the unit conversions were available in the code, thus the deck had both British and Metric input. Once all of the unit conversions became operational in the code and the initial new style input deck was run, the error trapping in the code identified inconsistent input due to the mixed unit input. The problem, which could have resulted in several hours of lost time, was quickly corrected in a matter of minutes.

A.10.3.3 CPU Usage.

Figure A-121 shows the CPU time required to perform the TMLB' calculation. A total of 46.6 CPU hours was used.

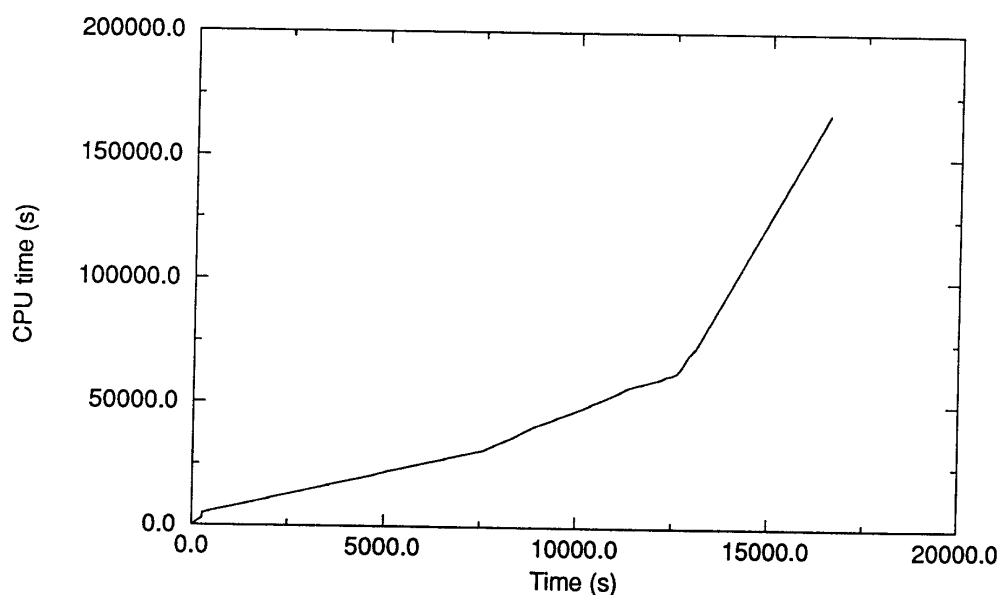


Figure A-121. CPU time for the Surry plant transient.

A.10.3.4 SCDAP/RELAP5/MOD3 and SCDAP/RELAP5/MOD3.1 Comparison

Two Surry calculations were performed using different code versions. The first calculation was run on SCDAP/RELAP5/MOD3 and the second calculation was run on SCDAP/RELAP5/MOD3.1. The SCDAP/RELAP5/MOD3.1 calculation used nodalization with initial and boundary conditions identical to a previous study^a which was performed using SCDAP/RELAP5/MOD3. The SCDAP/RELAP5/MOD3.1 calculation differed from the SCDAP/RELAP5/MOD3 calculation only in the code version used and in the code option used to model total reactor power. The SCDAP/RELAP5/MOD3.1 calculation used the space-independent reactor kinetics power option to model power, while the SCDAP/RELAP5/MOD3 calculation used SCDAP power tables. Table A-13 shows the comparison for the two calculations. As indicated, the

a. Case 2 of D. L. Knudson and C. A. Dobbe, *Assessment of the Potential for High Pressure Melt Ejection Resulting From a Surry Station Blackout Transient (DRAFT)*, NUREG/CR-5949, EGG-2689, DRAFT.

event timing for the SCDAP/RELAP5/MOD3.1 calculation lagged the SCDAP/RELAP5/MOD3 calculation up to the point where the liquid level in the core dropped below the fuel rods. Fuel rod cladding failure came earlier and at a lower temperature for the SCDAP/RELAP5/MOD3.1 case, due to the new grid spacer fuel rod interaction model not available on the SCDAP/RELAP5/MOD3 calculation. Predicted lower head failure for the SCDAP/RELAP5/MOD3.1 calculation came 690 seconds earlier than the SCDAP/RELAP5/MOD3 calculation. Considering the uncertainty in the user-specified crust failure thickness of 0.03 m, which controls molten pool relocation time, this result looks reasonable.

Table A-13. Version comparison for the SCDAP/RELAP5/MOD3 and SCDAP/RELAP5/MOD3.1 calculations.

Event	SCDAP/RELAP5/ MOD3 Calculation	SCDAP/RELAP5/ MOD3.1 Calculation
Transient initiation	0	0
Onset of fuel rod oxidation	10,620	10,890
Reactor vessel liquid level drops below bottom of fuel rods	10,640	11,400
Fuel rod cladding failure	12,360	12,260
Surge line creep rupture failure	12,930	13,380
Hot leg creep rupture failure (loop containing pressurizer)	14,060	14,260
Initial molten pool formation	15,180	14,470
Failure of lower crust: massive slumping to lower head	15,470	14,470
Creep rupture failure of lower head	15,600	14,910

A.11. TMI-2

The Three Mile Island Unit 2, (TMI-2) accident input deck was chosen as a mechanism to verify the models used in SCDAP/RELAP5/MOD3 for a pressurized water reactor (PWR) under severe accident conditions. This accident was considered a good mechanism to evaluate the affect of the addition of new user conveniences, models, and error corrections on calculated results, since a large quantity of TMI-2 data and calculated results using earlier versions of SCDAP/RELAP5 exist. This verification effort looked at the effects of changing the input style from free format to RELAP5-style card numbers, the addition of a radiation time smoothing option, restart improvements, natural circulation modeling, and the implementation of the grid spacer material interaction model in the code. For the verification testing, the deck was not accelerated. All important events modeled in the input deck are controlled by occurrence time. By modeling the time each important event occurred rather than by using an initiating temperature, pressure or flow rate the accident scenario could be accurately represented in the input deck.

Calculated results using SCDAP/RELAP5/MOD3.1 were compared with TMI-2 data and with results from an analysis of the TMI-2 accident using an earlier version as part of a natural circulation study performed at the Idaho National Engineering Laboratory. This analysis calculated nuclear core temperatures in the middle channel of the model agreeing with published TMI-2 data.

A.11.1 Plant Transient Model

The input deck used was previously developed to closely represent the TMI-2 accident scenario for the natural circulation study. Changes necessary for the SCDAP/RELAP5/MOD3.1 version and new style of input were made for these calculations. The modeled accident was initiated by cessation of secondary feedwater flow to the steam generator and a turbine trip. In response to the cessation of feedwater flow to the steam generator, the reactor coolant system responded in a normal manner--reactor coolant system pressure increased; the electromatic relief valve started to operate; the reactor shut down due to a high pressure trip signal; heat generation from the reactor dropped to the decay heat level; and the system pressure dropped to the normal operating set point.

Forty seconds into the modeled accident, the water level in the steam generator dropped to a level that opened the emergency feedwater valves. At this time, the valves between the control valves and the steam generators failed to open, preventing delivery of the emergency feedwater to the steam generator. These valves were opened manually at eight minutes. Fifteen minutes into the accident, when system pressure reached the normal operating pressure, the electromagnetic relief valve failed to close. A safety valve on the reactor coolant drain tank was opened 3 minutes into the transient, since water flowing through the opened electromagnetic relief valve flowed into the coolant drain tank. At 74 minutes, the coolant pumps in the B loop of the reactor were turned off; and at 100 minutes, the A-loop pumps were tripped. At 142 minutes, a block valve (PORV), in series with the electromagnetic relief valve, was closed, stopping the flow of water to the reactor coolant drainage tank. At 174 minutes, the 2B coolant pump was turned on. The period of significant flow through the B-loop hot leg was less than 15 seconds. At 200 minutes, the high pressure injection system (HPIS) was activated for approximately 17 minutes. All major events that occurred during the early stages of the accident--valves opening, closing, sticking open, pump transients, and cooling--were modeled to start at the times they occurred during the course of the TMI-2 accident.

The development of the original input deck proceeded by combining two Oconee-1 NPP input decks previously used for the analysis of station blackout depressurization and LOCA pin failure timing and modifying the resulting input deck to represent the TMI-2 accident scenario. The Oconee-1 plant is a sister plant to TMI-2 with nearly identical mechanical design features and steady-state operating specifications; therefore, the quality-controlled model for the Oconee-1 plant was used to simulate the plant conditions at the time the accident was initiated and to specify appropriate boundary conditions at the beginning of the accident simulation. The RELAP5 module in the code was used to simulate the plant thermal-hydraulics and heat transfer affecting the structural mass in the reactor, and the SCDAP module was used to simulate the degradation, melting, and relocation behavior of the core components--fuel rods, control rods, and guide tubes--during the course of the TMI-2 accident.

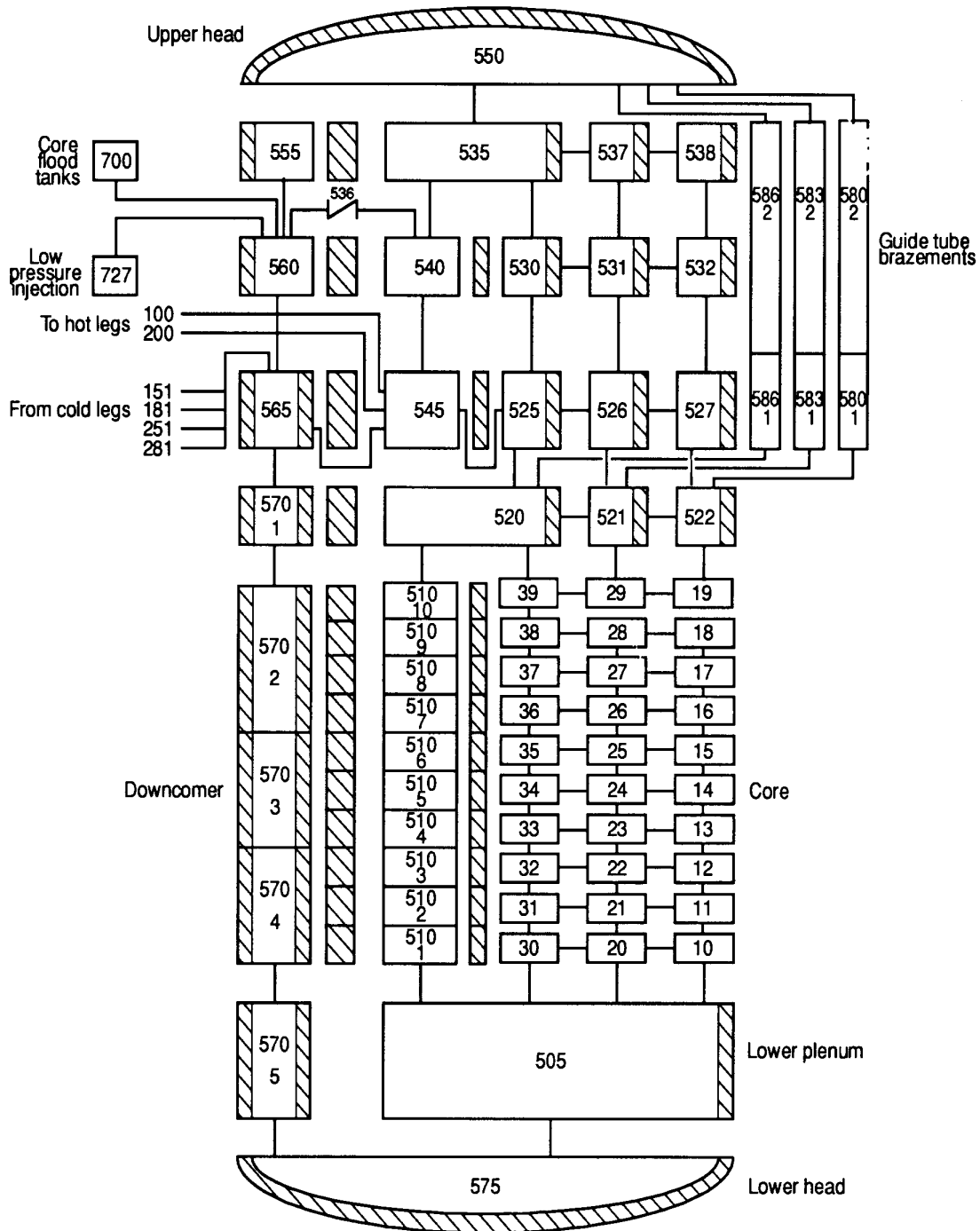
The RELAP5 module simulated thermal-hydraulic conditions in the reactor vessel, the piping in all primary coolant loops, the pressurizer, steam generators, and parts of the steam generator secondary system. Figure A-122 shows the RELAP5 thermal-hydraulic nodalization used to represent the reactor vessel. This model represents all major components in the vessel, including an inlet annulus, downcomer, lower head, lower plenum, core, core bypass, and control rod guide tube brazements. The primary flow path through the system is represented, as are the flow paths, though of lesser importance, through the core bypass, the downcomer, around the hot leg nozzle in the upper plenum, and through the guide tubes. As shown in Figure A-122, three parallel flow channels extended from the lower plenum through the core to the support plate between the upper plenum and the upper head. The RELAP5 heat structures, designated as shaded areas in the nodalization diagram, represent the structural mass of the reactor vessel walls, the core barrel and baffle, the thermal shield, the upper and lower core support plates, and the structures in the upper and lower plenum.

Nodalizations for the coolant loops in the reactor are shown in Figures A-123 and A-124. The nodalization used for the coolant loops allowed full loop natural circulation of superheated steam during the transient. Figures A-125 and A-126 give a detailed nodalization of the TMI-2 pressurizer and steam generator. RELAP5 heat structures are used to represent the structural mass in the steam generator.

The fuel rods, control rods, and guide tubes in the core of the reactor are represented using SCDAP component models. Using this scheme of modeling to represent three distinct regions in the reactor vessel, the central channel contains fuel rods and control rods, the middle channel contains fuel rods and control rods, and the outer and cooler channel contains fuel rods and empty control rod guide tubes.

The TMI-2 accident input deck was not accelerated, since the modeled important events taking place during the course of the accident were initiated at the time they occurred in the accident, rather than by an occurrence of pressure, temperature or flow rates.

The analysis of the TMI-2 accident is driven by boundary conditions; therefore, to obtain initial boundary conditions consistent with those in the plant at the time of the initiation of the accident, boundary conditions for the Oconee-1 NPP were used to develop the input deck. Since the steady-state operating specifications for Oconee-1 and TMI-2 were similar, steady-state operating conditions for Oconee-1 were taken as the operating conditions in TMI-2 before and at the start of the accident. The initial pressure of the reactor system was set to 2,200 psig, and the pressure of the containment building was set to 100 psig, close to the normal steady-state operating pressures. The mass flow rates through the core and the remainder of the reactor system were those recommended for the TMI-2 standard problem



M028 RBN 1191 03

Figure A-122. Nodalization of the TMI-2 reactor pressure vessel.

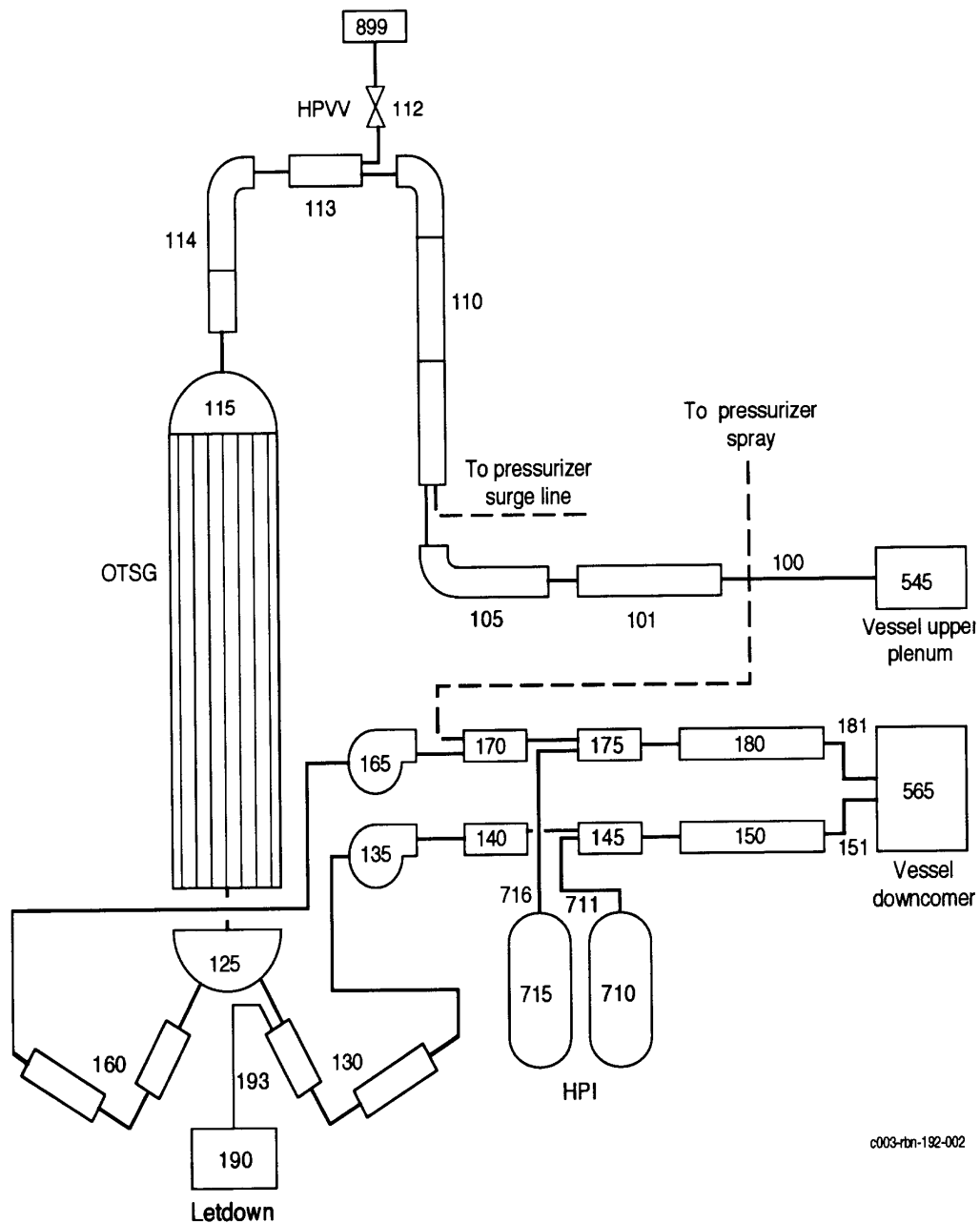


Figure A-123. Nodalization of the TMI-2 coolant loop A.

exercise^{A-23,A-24} and were controlled through the use of control variables to simulate the actual flow rates through the system before and during the accident. Power input into the reactor during the accident was a best-estimate of the fission product decay heat using the ANS standard plus a contribution from the actinides present in the system during the initial 200 seconds of the accident. After the first 200 seconds, the decay heat numbers for the TMI-2 accident published by Los Alamos National Laboratory were used. Steady-state operating temperatures were as specified, and the initial temperatures at the start of the

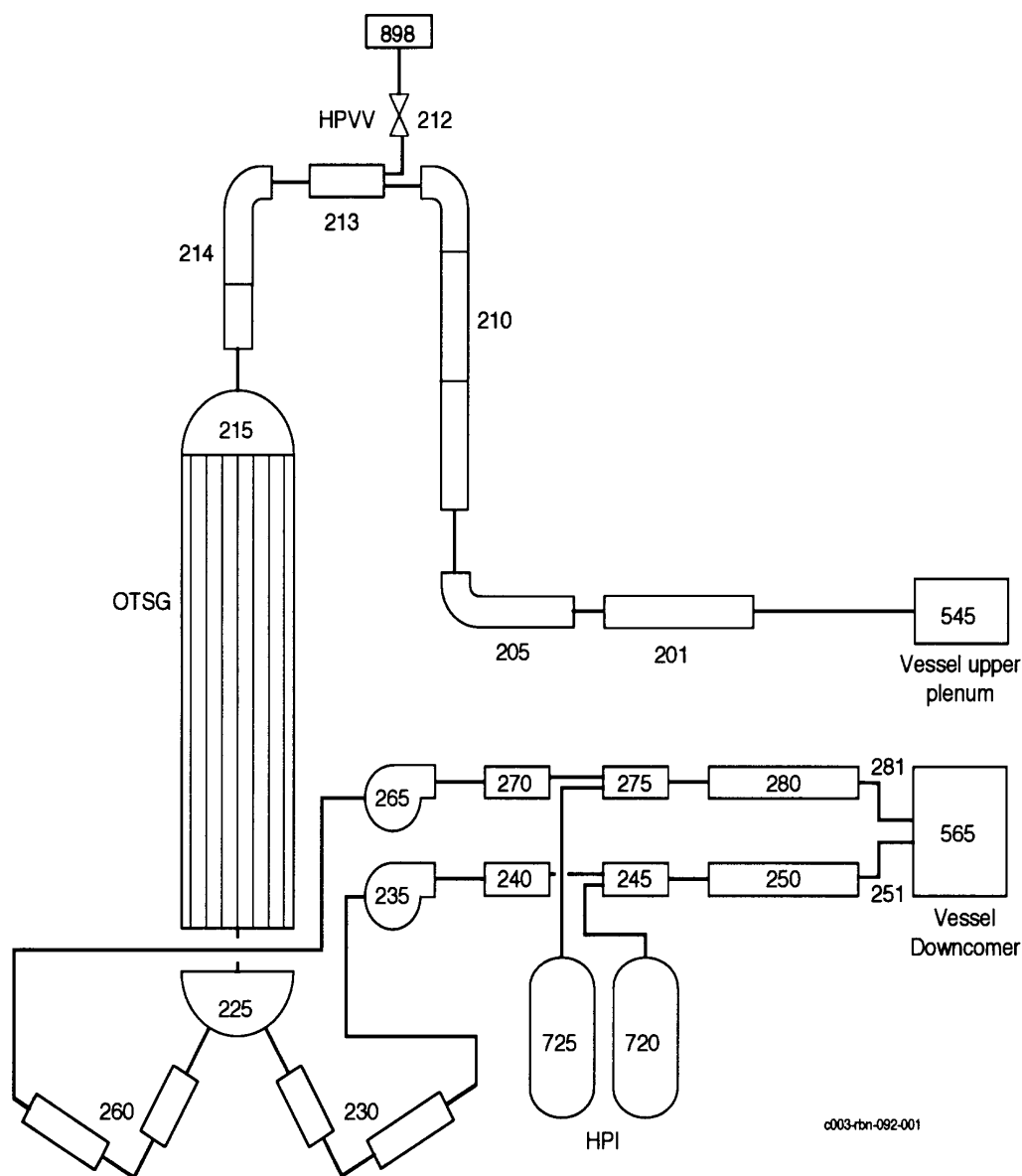


Figure A-124. Nodalization of the TMI-2 coolant loop B.

transient were as measured. The pressure (100 psig) and temperature in the containment building were as measured. The remaining important boundary conditions not explicitly modeled--emergency feedwater mass flow rates, letdown mass flow rate, HPI/makeup mass flow rate, auxiliary feedwater mass flow rate, steam generator secondary side pressure, and core decay power--were inferred from TMI data and engineering analysis. The emergency feedwater water mass flow rate was determined by using steam generator liquid levels, which were based on a measurement of the differential pressure within the steam generator. The critical flow through the PORV, modeled using a single velocity (homogenous) model, matched the measured values in the TMI data base. A control system was used to calculate the EFW mass

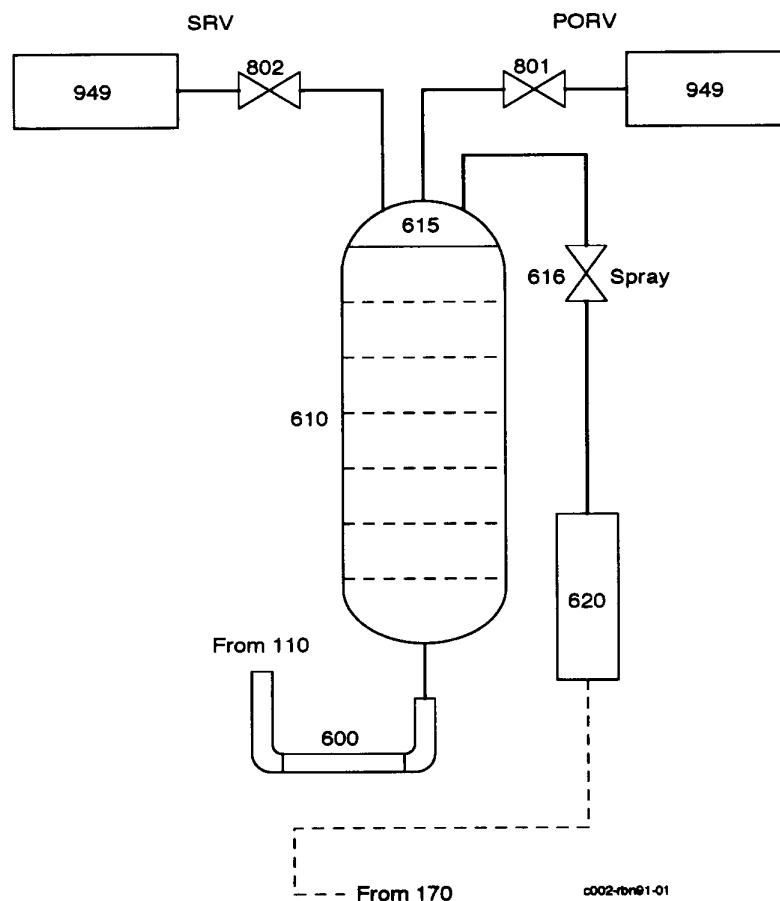


Figure A-125. Nodalization of the TMI-2 pressurizer.

flow rate, which matched the measured liquid level in the steam generator. The letdown mass flow rate was estimated from an energy balance on the letdown coolers.

Figure A-127 shows the letdown mass flow rate used in the analysis of the TMI-2 accident compared to the measured. The flow rates for the HPI/makeup were estimated by Anderson^{A-25} by assuming a constant HPI/makeup rate between two known states, the time of core uncover, and the minimum water level at 174 minutes. Mass flow rates for these boundary conditions were input as tables for use during the analysis.

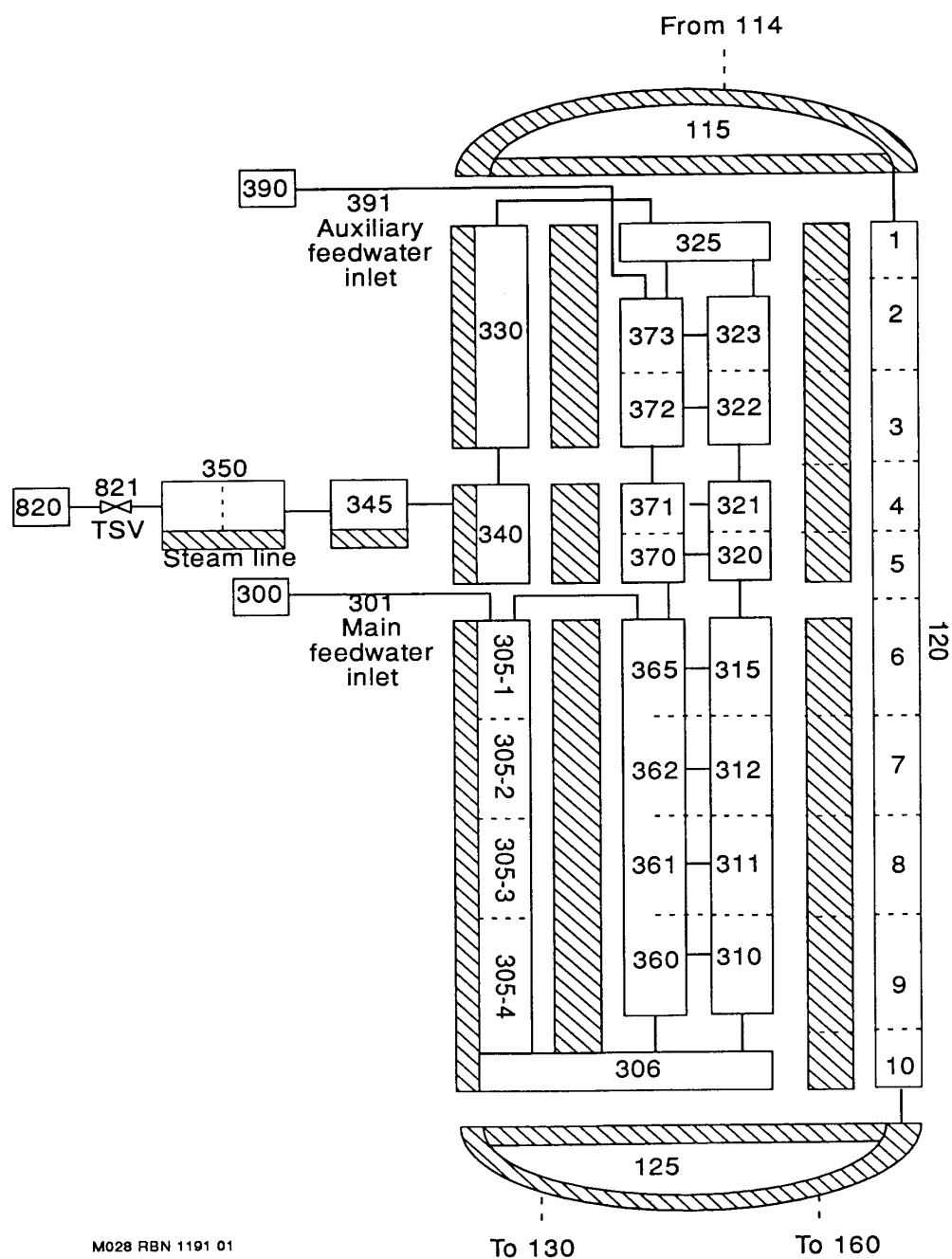


Figure A-126. Nodalization of the TMI-2 coolant loop A steam generator.

A.11.2 Results

Table A-14 summarizes the TMI accident and includes all important events during the course of the

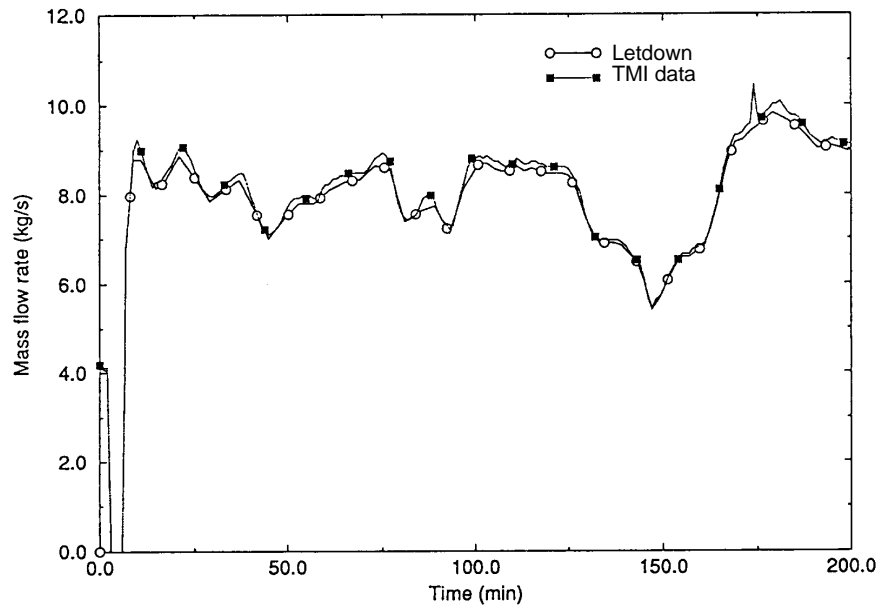


Figure A-127. Letdown mass flow rate used in the TMI-2 accident analysis.

accident.

Table A-14. Key events occurring during the TMI-2 accident.

Event	Peak Temperature (F)	Time (s)
Turbine tripped	619	0
Emergency feedwater pumps started	619	0
Electromagnetic relief valve opened	619	0.3
Reactor scrammed	619	0.08
PORV stuck open	615	15.0
Emergency feedwater valves opened	613	40.0
Safety valve to coolant drainage tank opened	612	180.0
Valves opened manually	610	480.0

Table A-14. Key events occurring during the TMI-2 accident. (Continued)

Event	Peak Temperature (F)	Time (s)
Rupture disk on coolant tank burst	610	900
B-loop pumps turned off	570	4,380
A-loop pumps turned off	561	6,000
Core uncovered	554	6,600
Cladding ballooning begun (upper half of rod)	750	7,500
Cladding failure began ^a		8,100
Block valve to coolant drainage tank closed (pressurizer dumps coolant into core)	860	8,520
Initial core melting ^a		
B-loop pump turned on ^a		10,440
B-loop pump transient ended ^a		10,455

a. Calculated temperatures not hot enough for these events to occur.

A.11.3 Power Generation.

The steady-state power profile for the Oconee-1 NPP was used for the reactor during the transient. Once the reactor scrammed, power to the reactor core came from decay heat. Figure A-128 shows the reactor power generated during the course of the accident.

Thermal-Hydraulic Response. Predicted behavior for TMI-2 was compared with measured data as part of the code verification process. Figure A-129 shows the calculated maximum bundle temperature during the accident. The temperature follows what would be expected until PORV block valve closure. A period of rapid core heatup began 124 minutes into the accident and continued until the PORV block valve was closed at 139 minutes. At the time of PORV closure, the temperature in the core was calculated to be near 900 K. At this time, the calculated pressure in the RCS was less than the pressure in the pressurizer steam dome; and liquid was calculated to drain from the pressurizer into the reactor vessel. (The pressurizer did not drain during the TMI-2 accident or in the previous SCDAP/RELAP5 calculation). Figure A-130 shows the calculated and measured pressurizer liquid level, and Figure A-131 showed the calculated liquid level in the reactor vessel. The calculated pressurizer liquid level matched the measured well until the PORV closure. At this time the code calculated the pressurizer to drain, while the measured liquid level in the pressurizer remained relatively constant.

The effect of the pressurizer draining into the reactor vessel is also shown in Figure A-131, which shows the collapsed liquid level in the reactor vessel. After the calculated drainage of pressurizer liquid, the reactor vessel remained half full of water for a relatively long period of time rather than continuing to boil dry as happened during the accident. Since there are known uncertainties in boundary conditions

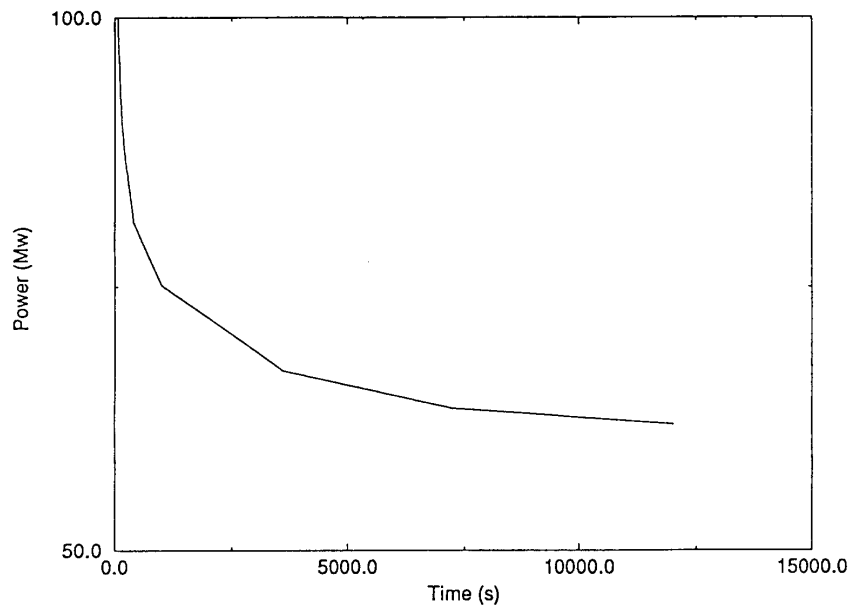


Figure A-128. Total core power for the TMI-2 plant transient.

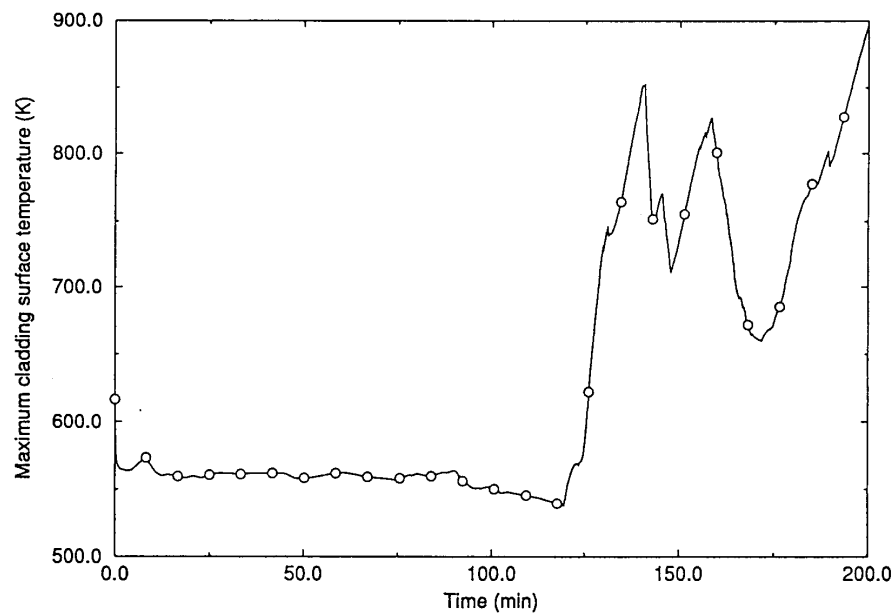


Figure A-129. Calculated maximum fuel bundle temperature for the TMI-2 plant transient.

during this period of the accident, a slight variation in the steam dome pressure calculated by RELAP5 could cause the variation in pressurizer behavior observed between code versions.

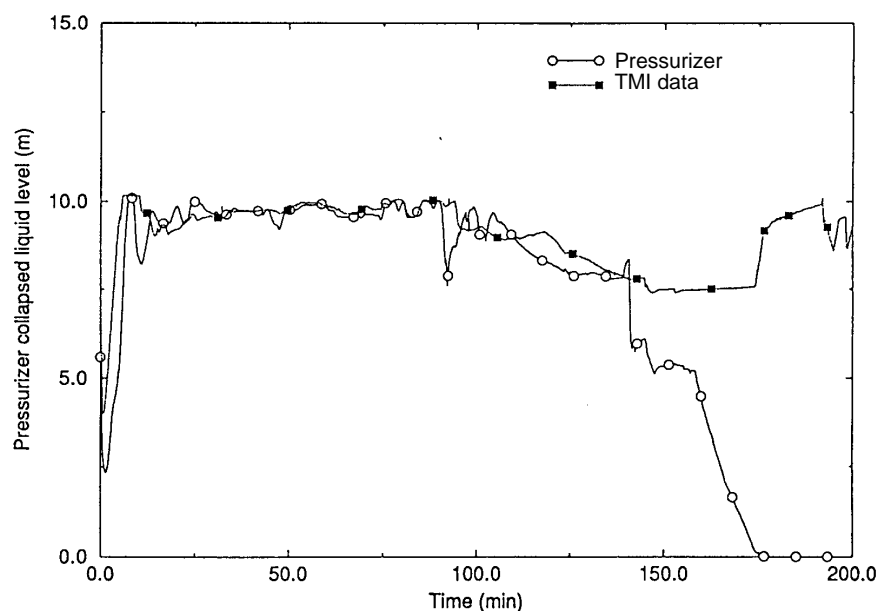


Figure A-130. Calculated and measured pressurizer liquid level for the TMI-2 plant transient.

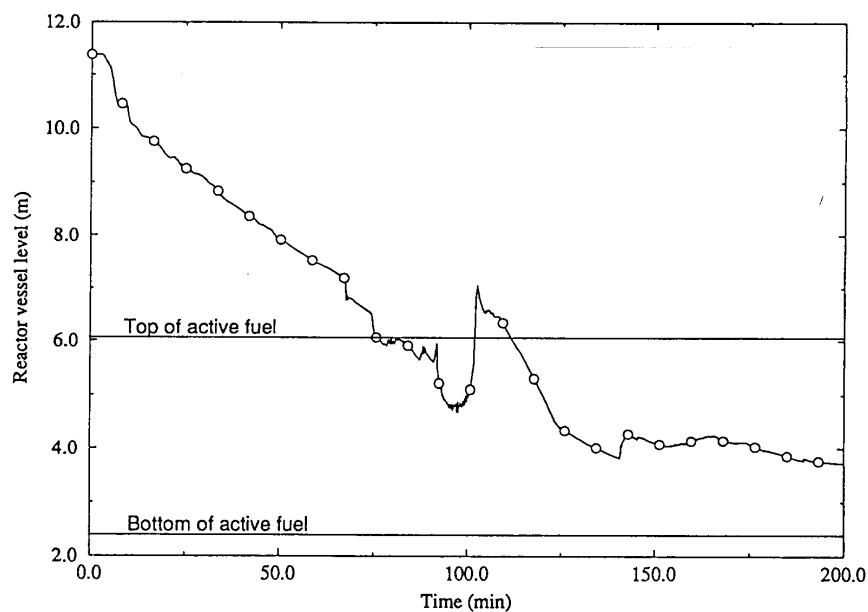


Figure A-131. Collapsed liquid level in the reactor vessel for the TMI-2 plant transient.

Figure A-132 shows the calculated and measured pressures in the RCS, steam generator A, and steam generator B. This figure shows the code calculating the pressures in the two steam generators accurately--the control variable modeling the B-pump transient was not included in the input deck at this time. The code also calculated the pressure in the RCS accurately until PORV block valve closure. At this time, both the calculated and measured RCS pressure began rising, with the calculated leveling off for

about 30 minutes at 7.5 MPa before beginning a gradual rise, while the measured rose rapidly to near 15 MPa before leveling off at 13 MPa near 200 minutes.

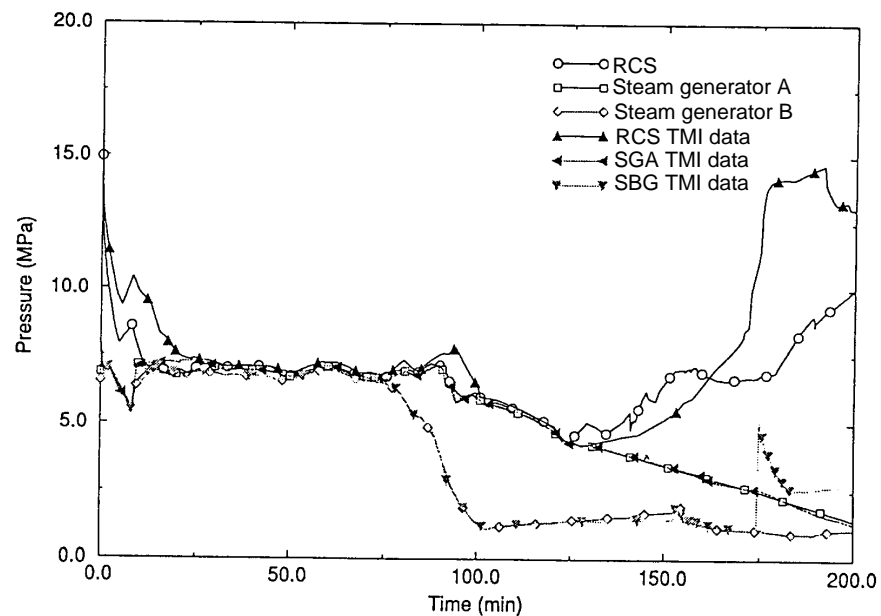


Figure A-132. Calculated and measured pressures in the RCS, steam generator A, and steam generator B.

Figure A-133 shows mass flow rates in the Loop A and B hot leg, and Figure A-134 shows the flow rates through the RCS PORV. Both agree well with the measured data during the calculation. The calculated flow rates in kg/s through the A and B hot legs are slightly less than the measured, but the trend agrees well with the data, while the flow rates through the RCS PORV match data quite well.

A.11.4 Code Performance

Table A-15 lists the models and code capabilities evaluated using the TMI-2 full plant deck for verification of SCDAP/RELAP5/MOD3.

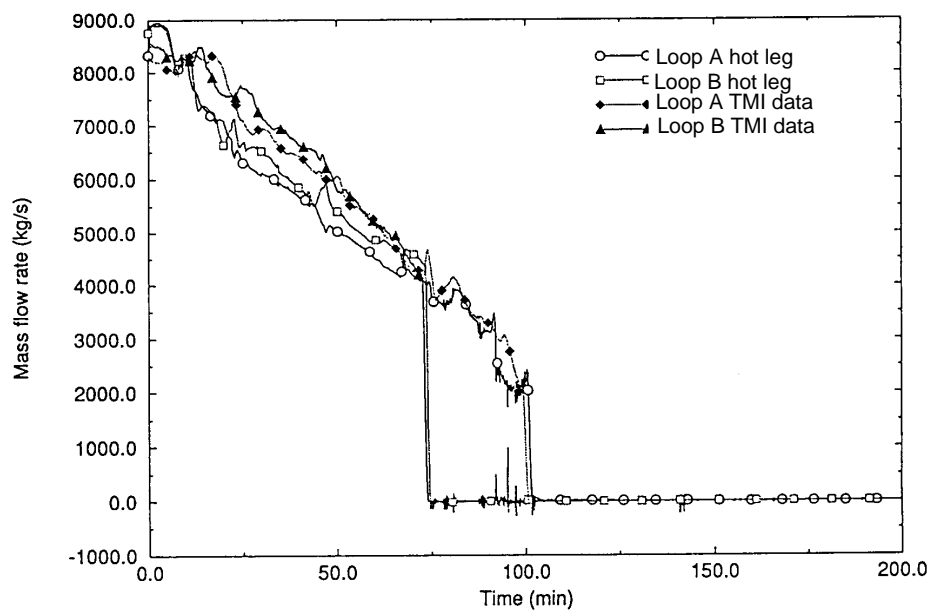


Figure A-133. Mass flow rates in the Loop A and B hot leg for the TMI-2 plant transient.

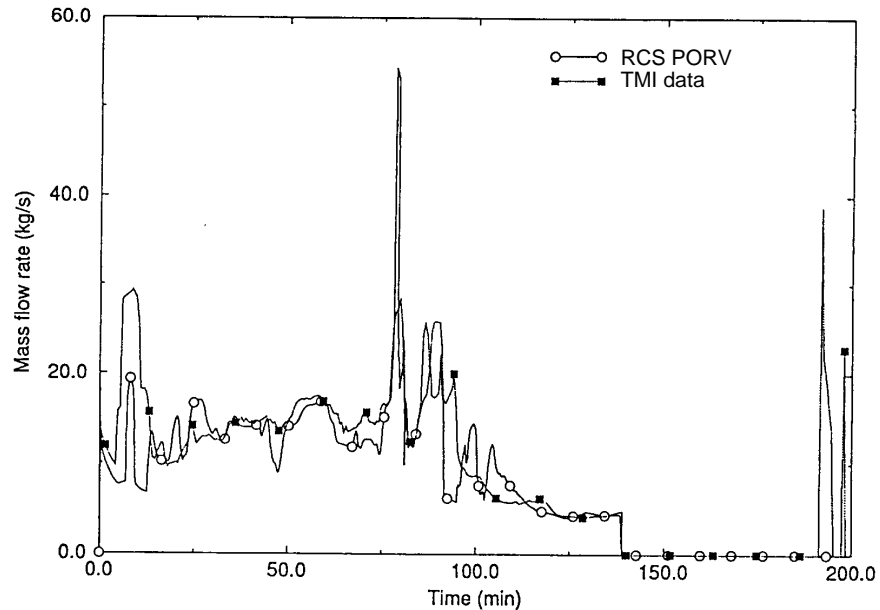


Figure A-134. Mass flow rates in the RCS PORV for the TMI-2 plant transient.

Table A-15. Models and capabilities verified by TMI-2 calculation.

Model	Results ^a
Time smoothing	Time smoothing was turned on, with no oscillations in the vapor temperatures.
Restart improvements	Restart worked without problems.
Input improvements	RELAP5 card number style input works well; changes can be made on restart; easy to change old-style input to new.
Output improvements	A better picture of the reactor core during a severe accident is presented; easy to read and understand. ^a
Data compression	Data take up less storage space on the disk; restart from the compressed data works well.
Natural circulation modeling	The TMI-2 deck used for the verification problem was the same as the one used for a natural circulation study. Results were different after PORV block valve closure.

a. The TMI-2 calculation, due to a dump of water in the pressurizer, did not reach high enough temperatures for significant ballooning or more severe core damage to occur.

A.12. Browns Ferry

The Browns Ferry NPP was chosen as a mechanism to verify models, input and output improvements, new capabilities, and error corrections implemented in the pre-release version of SCDAP/RELAP5/MOD3 when a boiling water reactor (BWR) under severe accident conditions is being analyzed. The BWR accident chosen to be used for code verification was a LOCA with no emergency core cooling (ECC). To simulate this accident, the ECCS was disabled, so no emergency cooling water entered the Browns Ferry core after initiation of the accident.

To evaluate the effect of new models and capabilities such as time smoothing, material interactions at grid spacer locations, and fuel rod ballooning in the code, the calculated core heatup, damage progression in the core, mass flow rates, and gas velocities were plotted to verify that the new models were calculating damage phenomena occurring during a severe accident correctly with no obvious numerical instabilities. The ease of converting the free-form input used in the presently released version of the code to card numbers, similar to the input style used for RELAP5, has also been evaluated, as were the calculated results.

A.12.1 Plant Transient Model

The verification deck modeled a large-break LOCA that could occur in the Browns Ferry BWR NPP. In the simulated accident, the modeled break occurred at 12 seconds and the reactor was scrammed 0.5 seconds later. Immediately after the initiation of the accident, the following events occurred. The water level in the annulus surrounding the reactor core dropped from approximately 45 to 12.5 feet within a short period of time; fuel temperatures in the core dropped rapidly; and the pressure in the upper plenum of the reactor dropped from 7 MPa at the start of the accident to 0.40 MPa 100 seconds later. Immediately after reactor scram, the main steam isolation valve (MSIV) opened and a recirculation pump tripped on. The voiding of the cooling water and the lowering of pressure in the reactor vessel triggered core uncover. In the modeled accident, the core uncovered within a period of 17 seconds. Once a region of the core uncovered, temperatures in the fuel assemblies in that region began to rise. Temperatures in uncovered regions of the core continued to rise rapidly until the fuel rods ruptured and/or severe damage occurred.

The containment for the Browns Ferry NPP modeled in the verification problems was filled with saturated air at a constant pressure of 15 psia (0.1 MPa). Before the start of the accident, pressure in the reactor vessel was 7.03 MPa; the initial system temperature was 546 F (558.7 K); and the power was 3,300 MW. The accelerated transient used a power of 1,500 MW. The initial inlet flow to the hot region in the reactor core was 2,900 kg/s.

A previously developed SCDAP/RELAP5 input deck was used to develop the Browns Ferry verification deck, using RELAP5-style card numbers for the SCDAP input module. The reactor core was modeled using eight flow channels, representing core regions with different characteristics and flow rates and a bypass region. Four channels were used to represent the flow areas in regions of the core containing fuel assemblies, and three flow channels were used to represent the channel boxes containing control blades. One modeled flow channel contained all fuel assemblies not in contact with a control blade, whereas, the other six flow channels, three pairs of fuel assembly-channel box flow channels, represented core regions of different gas mass flow rates and power histories. Each channel box flow channel contained a standard cruciform BWR control blade, modeled using the old BWR control blade component

model since the BWR control blade model developed by Oak Ridge National Laboratory (ORNL)^{A-10} was not implemented at the time of this calculation. In the modeled core regions containing a BWR control blade, each cruciform blade was modeled to be in contact with four fuel assemblies. A zircaloy shroud surrounded each 8 by 8 fuel rod assembly in the reactor core. The zircaloy shroud surrounding each fuel assembly also represented the outside walls of the channel box containing the control blade.

The fuel rods (62) and water rods (2) in each 8 x 8 assembly were modeled using the SCDAP fuel rod component model. (The fuel rod component model with an extremely small fuel pellet radius was used to model the water rod). Channel 1 comprised 24 assemblies containing 1,488 fuel rods and 48 water rods; Channel 2, 192 assemblies containing 11,904 fuel rods and 384 water rods; Channel 3, 332 assemblies containing 20,584 fuel rods and 664 water rods; and channel 4, 216 assemblies containing 13,392 fuel rods and 432 water rods. Channel 5 contained the control blades in contact with the fuel assemblies in Channel 2; Channel 6 contained the control blades in contact with the fuel assemblies in Channel 3; and Channel 7 contained the control blades in contact with the fuel assemblies in Channel 4. Each stainless steel-sheathed cruciform control blade contained 88 rodlets filled with boron carbide (B_4C); therefore the 48 blades in Channel 5 contained 4,224 rodlets; the 83 blades in Channel 6 contained 7,304 rodlets; and the 54 blades in Channel 7 contained 4,752 rodlets.

To expedite the creation of the BWR verification deck, the only modifications made to the Browns Ferry input deck, that previously was used to demonstrate the code's ability to calculate a BWR accident for the SCDAP/RELAP5/MOD3 peer review,^{A-3} were to the reactor core region. Since the demonstration deck did not model the core regions containing the control blades, the input models for these flow paths in the core and the B_4C control blades were added to the verification deck. This procedure allowed an input deck to be developed without any major changes to the RELAP5 thermal-hydraulic component models and gave a fairly accurate representation of a generic BWR plant, similar in design to the Browns Ferry NPP.

The zircaloy surrounding each fuel assembly, which also represented an outside wall of the channel box containing a control blade, was represented using a SCDAP shroud model. The option where the code calculates the view factors used to calculate rod-to-rod and control-blade-to-channel box radiation heat transfer was used for this calculation. RELAP5 component models, heat structures, and control variables were used to model the remainder of the plant, including the steam generators, emergency core cooling system, pumps, and the thermal-hydraulic conditions of the reactor.

Figure A-135 shows the RELAP5 nodalization diagram used to model the Browns Ferry NPP. The reactor was represented in the input model using 116 volumes and 130 junctions, and each flow channel in the core of the reactor was represented using the RELAP5 pipe component divided into 8 axial volumes. The seven-channel reactor core containing SCDAP component models was powered by reactor kinetics.

A.12.2 Results

The initiation of the accident, the events that occurred during the accident, the time and temperature at which they occurred, and the consequences of these events are presented in Table A-16, an event table depicting the history of the postulated Browns Ferry accident scenario.

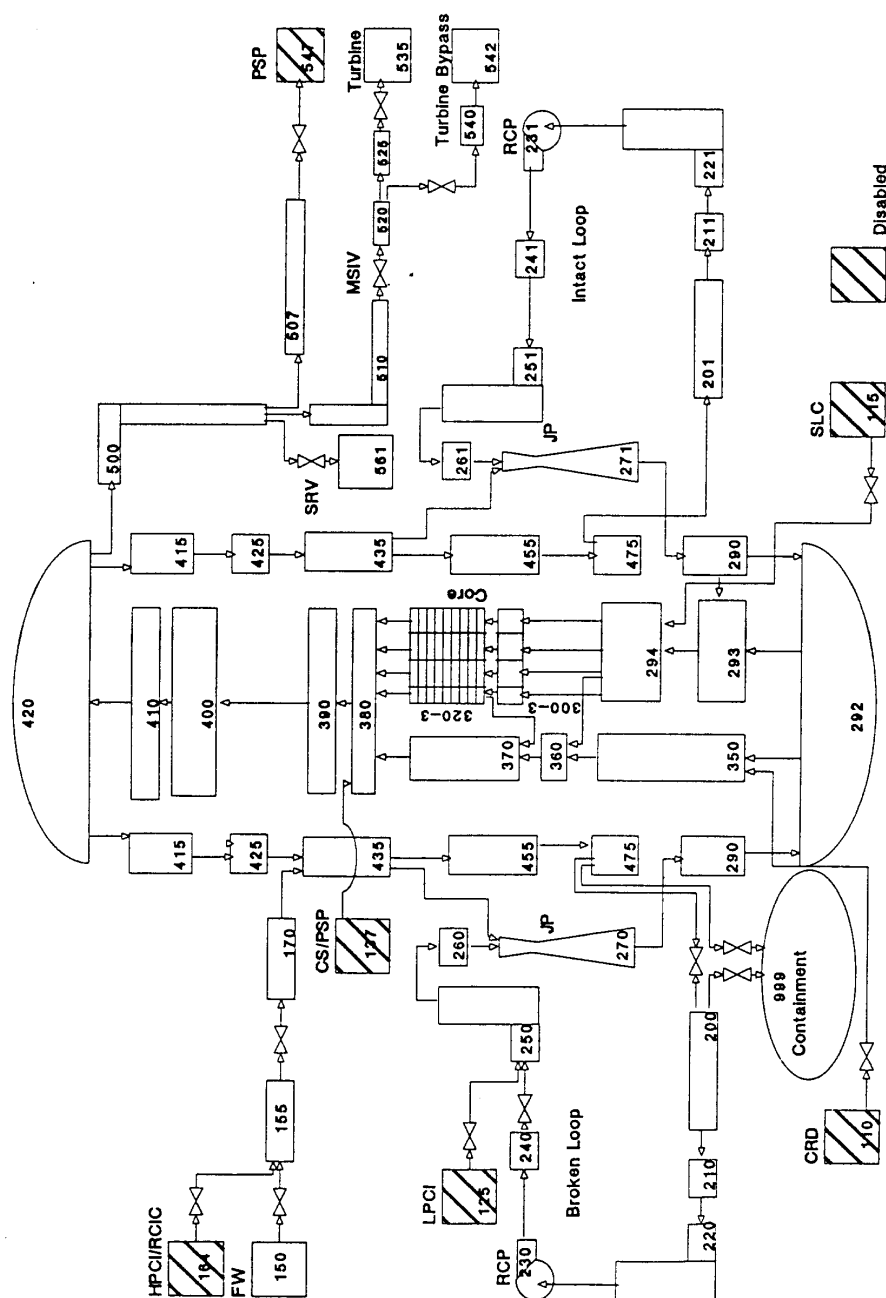


Figure A-135. Nodalization for the Browns Ferry plant transient.

A.12.2.1 Power Generation.

Figure A-136 shows power input to the reactor core during the course of the severe accident modeled by this fast-running verification deck. Power to the reactor core was set at 1,500 MW during the initial stages of the accident. Immediately after the accident initiation, the water surrounding the reactor vessel

Table A-16. Key events in the Browns Ferry accelerated calculation.

Event	Peak Temperature (F)	Time (s)
Steady state	546	0 - 10
Accident initiated (break opened)	546	10 - 12
Reactor scrammed	546	12.5
MSIV closed	546	13.0
Recirculation pump tripped	546	13.0
Core uncover began	650	43.0
Core uncover ended	1,250	60.0
Initial fuel rod ballooning		
Channel 1	800	
Channel 2	800	
Channel 3	800	
Channel 4	800	
Initial fuel rod rupture		
Channel 1	1,400	92.0
Channel 2	1,500	75.0
Channel 3	1,250	75.0
Channel 4	1,500	75.0
Initial control blade melt relocation		
Channel 2	1,250	108.0
Channel 3	1,250	75.0
Channel 4	1,250	100.0
Fuel rod rupture in the hottest region of the core (occurred in Channel 2, upper half of the fuel rod)		
Initial rubble bed formation --none		
End of calculation		109.5

began flowing out of the system and the reactor was scrammed. To facilitate rapid heating of the core, Figure A-136 shows the reactor power, which remained constant during the course of the severe accident.

Thermal-Hydraulic Response. The calculated thermal-hydraulic response of the system pressure when the accelerated transient input deck was used for the analysis is shown in Figure A-137. Immediately after scram (12.5 seconds into the transient), the system began to depressurize and continued to depressurize, slowly, until the recirculation pumps were tripped. Coincident with the tripping of the recirculation pumps at 18 seconds, an increase in pressure to near the initial set point was observed. At 25

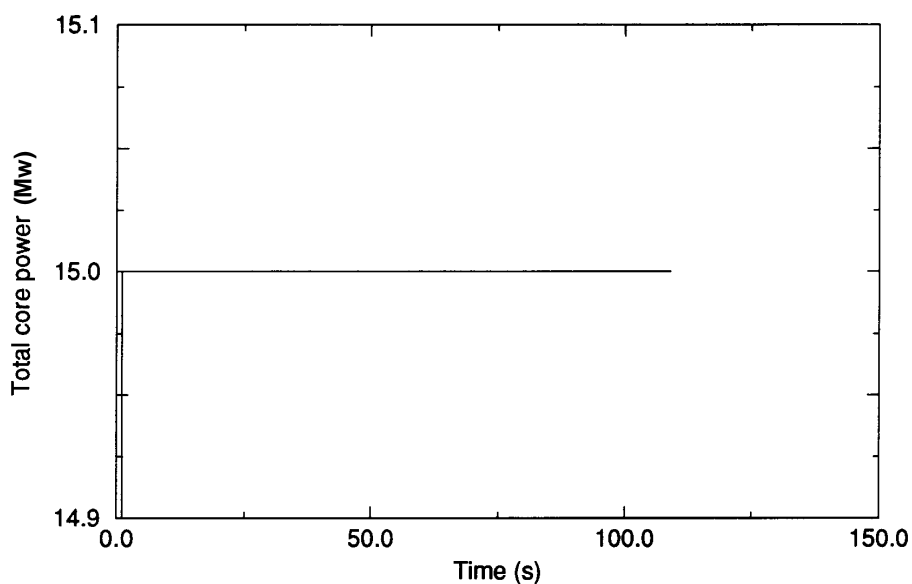


Figure A-136. Total core power for the Browns Ferry plant transient.

seconds, a steady depressurization of the system, coinciding with the core uncover phase, from ~7 to ~1.0 MPa at 60 seconds was calculated to occur. Once the system pressure reached 1.0 MPa, the rate of depressurization slowed, dropping from 1.0 to ~0.4 MPa at 100 seconds transient time. Core uncover was calculated to occur for a period of 35 seconds. Once the core completely uncovered, depressurization slowed significantly, as all elevations in the core entered a period of rapid heating. System pressure continued to drop during the core uncover phase and through the early stages of the heatup phase of the accident, when only the elevations voided of water in the reactor core were heating. Once the core dried out completely and rapid zircaloy oxidation began, depressurization slowed significantly and the system pressure began to stabilize near 0.40 MPa.

Figures A-138 to A-167 show the predicted temperature response of the core components during the postulated accident. The fuel rods, water rods, and the channel boxes in Channel 1, an outer region in the core containing no control blades, began heating at the middle axial elevations of the fuel assemblies later in the postulated accelerated accident and attained temperatures considerably less, approximately 800 K, than fuel assemblies in channels containing control blades. Plots of the fuel rod surface, water rod, shroud, and control blade temperature response in channels adjacent to control material show temperature escalation starting at a hot spot near the middle axial elevation of the fuel assembly and progressing downward for several seconds transient time before an upward movement of the oxidation front is calculated to occur. Channel 2, modeled to represent approximately 20% of the core and to receive a slightly larger fraction of the reactor power, was the hot channel, attaining a maximum temperature in excess of 2,500 K. The onset of heating of each component at a specific elevation in Channel 2 occurred first, followed closely by the same modeled core component in Channels 3 and 4, respectively. Calculated cladding surface temperatures in core regions modeled to contain control blades show a slight leveling of the calculated temperature response near 1,500 K immediately before the onset of rapid oxidation. The

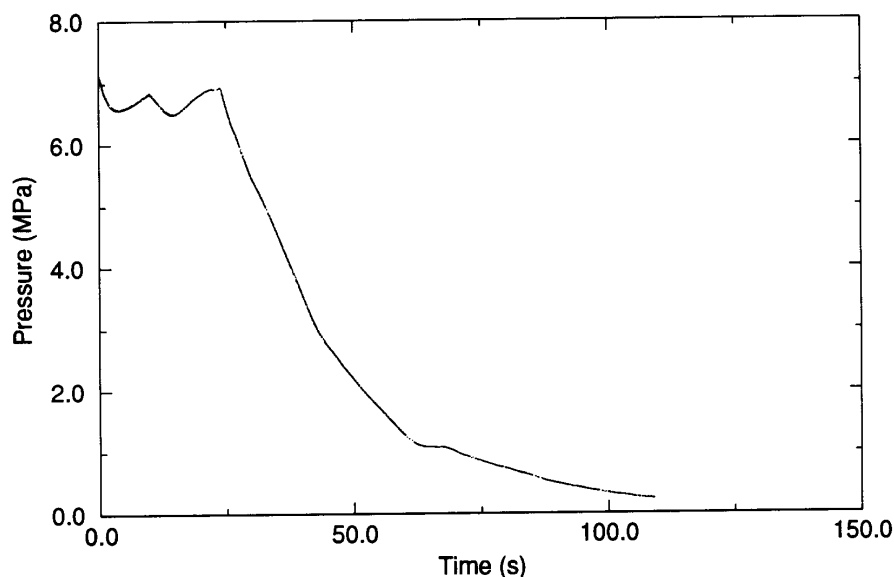


Figure A-137. System pressure for the Browns Ferry plant transient.

figures showing the temperature response of the control blades in each modeled channel indicate that the code is calculating heatup of the control blade to begin 15 seconds later and the temperature at the end of the transient to be several hundred degrees cooler than that calculated for the fuel rod cladding in the same modeled channel. The results of these calculations using a deck in which heating of the core region has been accelerated appear to be reasonable.

The figures show that the observed temperature response in the core of the reactor is similar to what was observed in the DF-4^{A-26} and CORA-18 BWR^{A-27} experiments. The initial hot spot for each modeled component in a represented flow channel occurred near the axial mid-point of the modeled component. Oxidation of exposed zircaloy in each flow channel began at an axial node near the middle of the reactor core, between 1.7 and 2.1 m, then progressed downward for several seconds before progressing upward toward the top of the core. As can be seen in the figures, the upper- and lower-most elevations of the core components modeled in each channel are the coldest, and the middle elevations are the hottest.

Figures A-138 to A-167 show that calculated temperatures at each axial node of modeled control blades, except the lower-most axial node, begin an extremely slow temperature rise, coinciding with the onset of the calculated temperature escalation for the fuel rod cladding surface temperatures in each modeled channel. The figures show the control blade temperatures to begin escalating rapidly coinciding with the onset of zircaloy oxidation in the channel. Temperatures at the lower-most axial node are calculated to drop steadily from the onset of the slow heating of the fuel rods, through the period of rapid oxidation, to the termination of the severe accident calculation. The calculated control blade and channel box temperatures did not reach temperatures hot enough to form stainless steel-B₄C eutectic melts during the simulated accident.

Temperatures in the channel boxes in each core region followed trends similar to those observed in the modeled channel boxes for the DF-4 and CORA-18 experiments. The upper and lowermost elevations are the coldest, and the middle elevations the hottest.

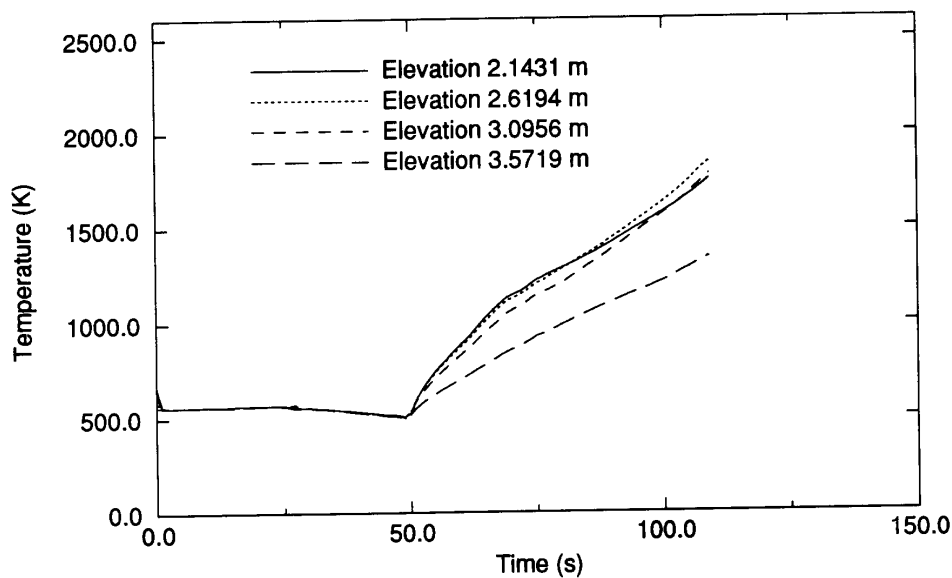


Figure A-138. Surface temperatures for the top half of the Channel 1 fuel rod component for the Browns Ferry plant transient.

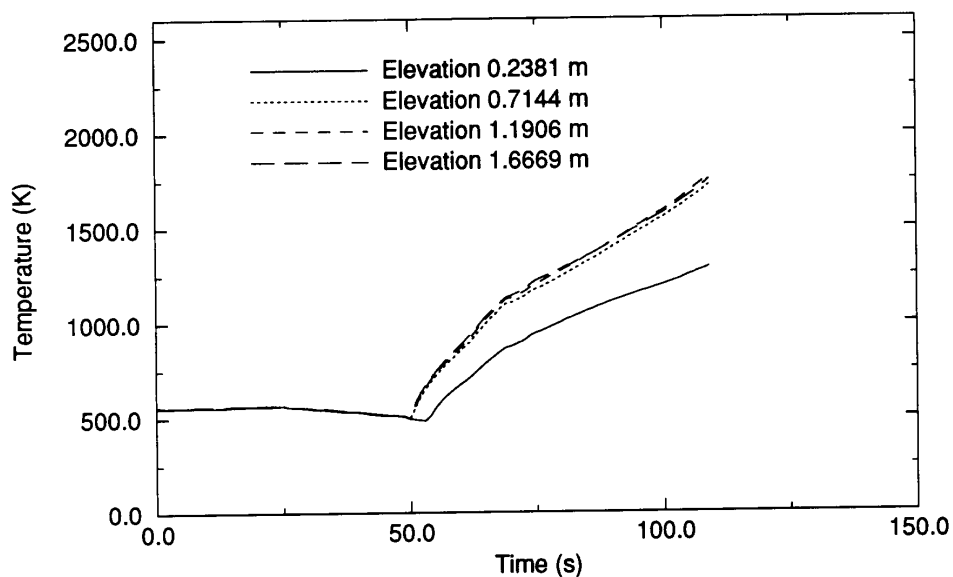


Figure A-139. Surface temperatures for the bottom half of the Channel 1 fuel rod component for the Browns Ferry plant transient.

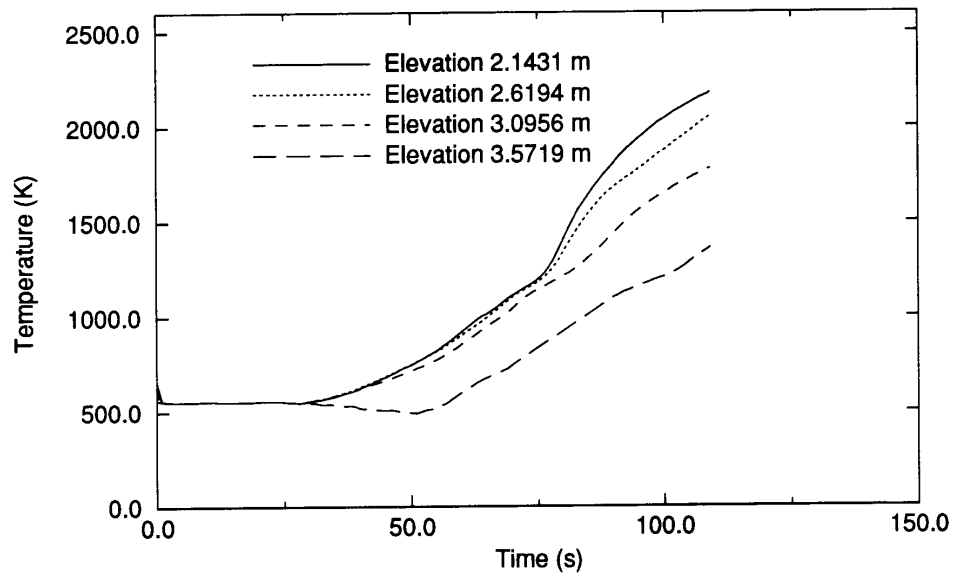


Figure A-140. Surface temperatures for the top half of the Channel 1 water rod component for the Browns Ferry plant transient.

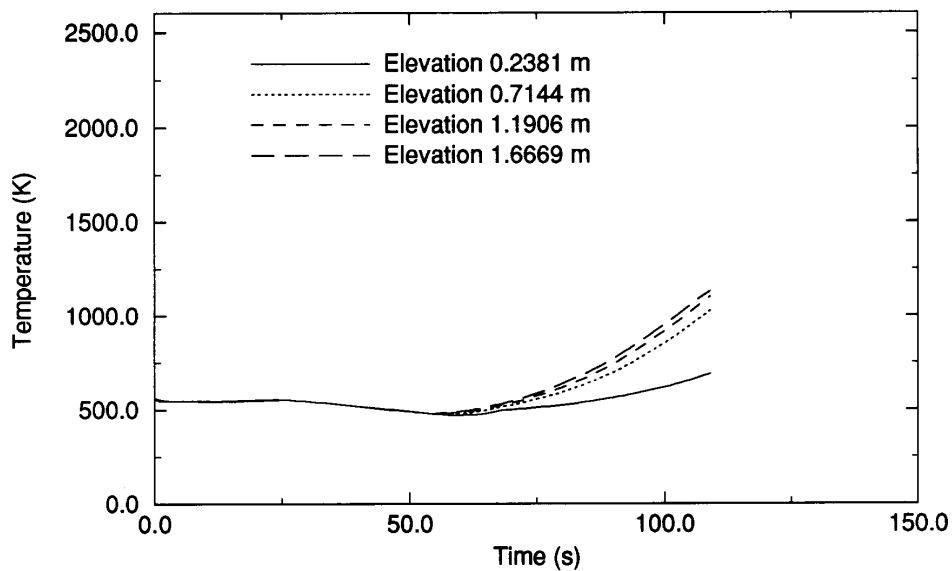


Figure A-141. Surface temperatures for the bottom half of the Channel 1 water rod component for the Browns Ferry plant transient.

Figure A-168 shows the calculated heat transfer in the four channels containing fuel assemblies. During the initial stages of the accident, while the core is uncovering and the pressure decreasing, the code

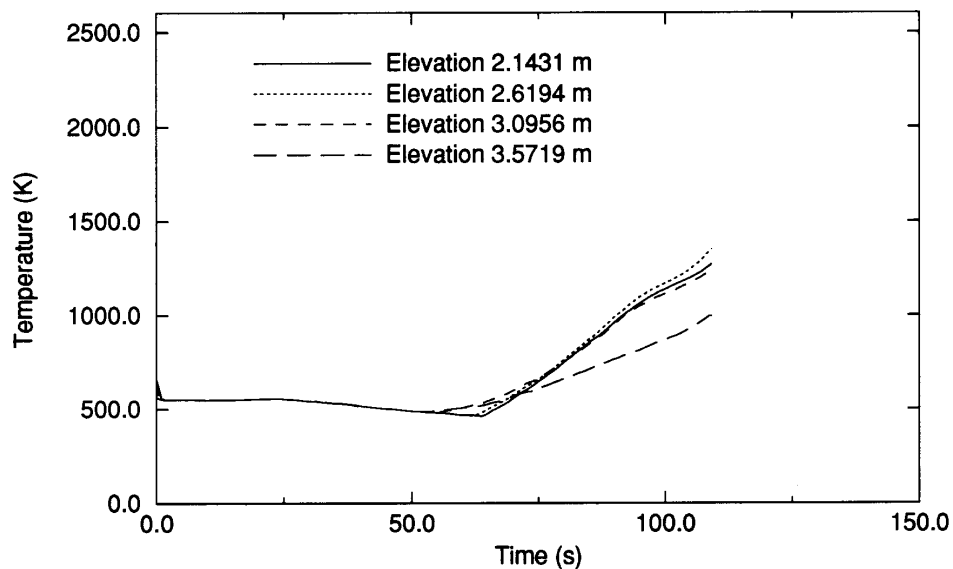


Figure A-142. Surface temperatures for the top half of the Channel 1 shroud component for the Browns Ferry plant transient.

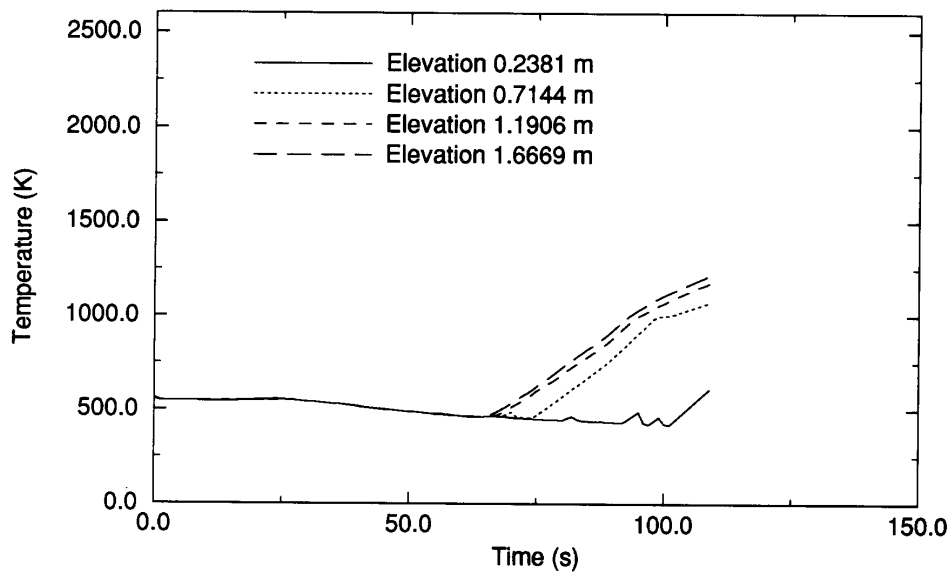


Figure A-143. Surface temperatures for the bottom half of the Channel 1 shroud component for the Browns Ferry plant transient.

calculated a larger heat transfer coefficient during the early stages of the accident indicating that the heat transfer is more efficient when the components are cool.

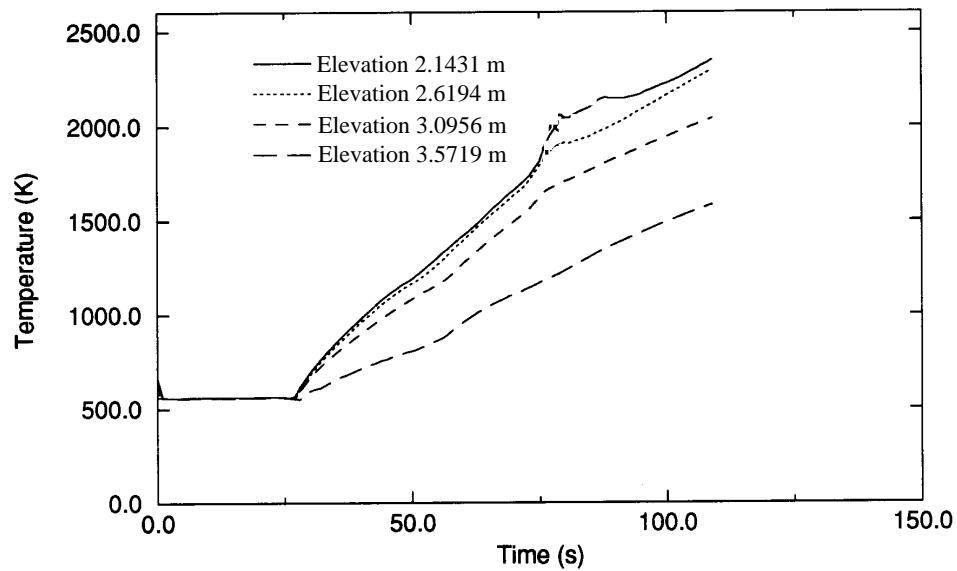


Figure A-144. Surface temperatures for the top half of the Channel 2 fuel rod component for the Browns Ferry plant transient.

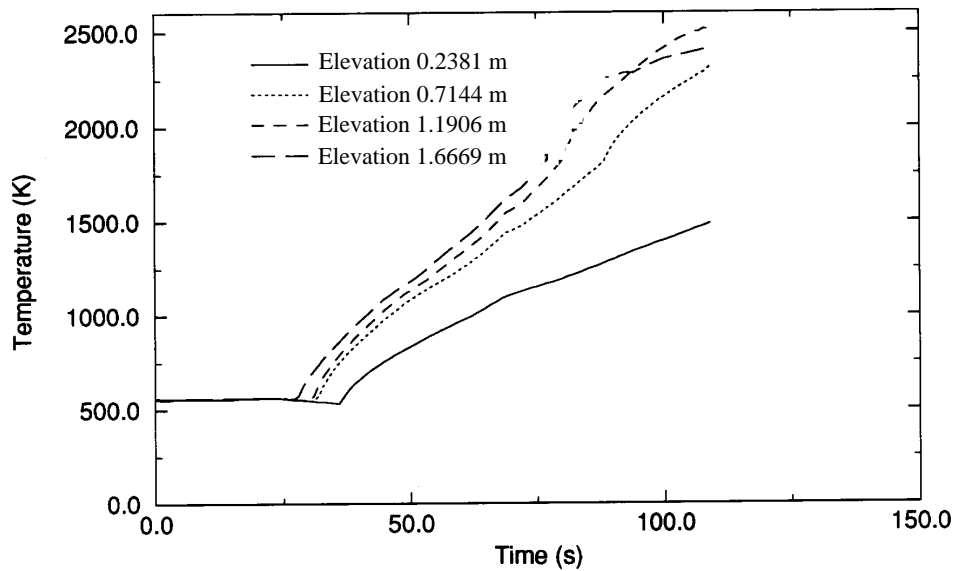


Figure A-145. Surface temperatures for the bottom half of the Channel 2 fuel rod component for the Browns Ferry plant transient.

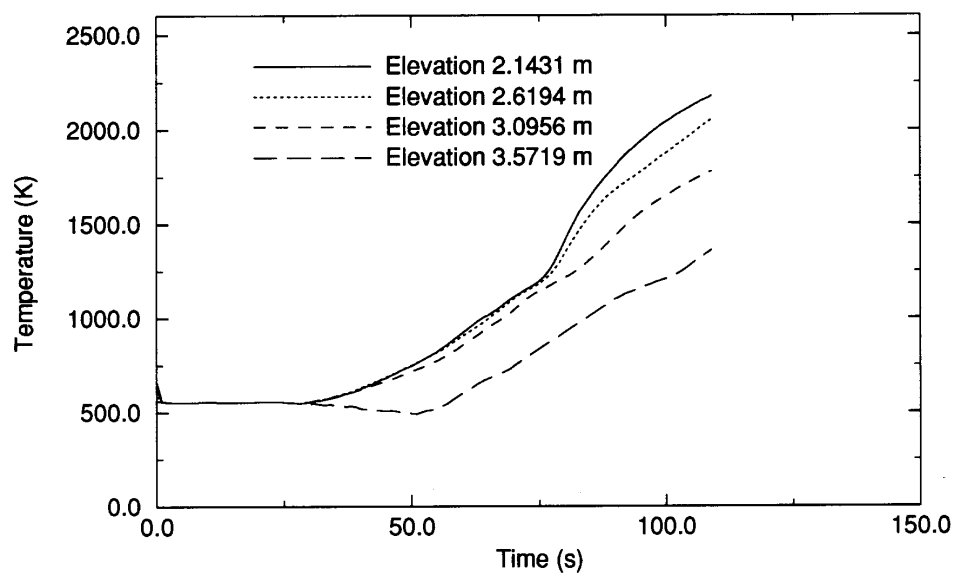


Figure A-146. Surface temperatures for the top half of the Channel 2 water rod component for the Browns Ferry plant transient.

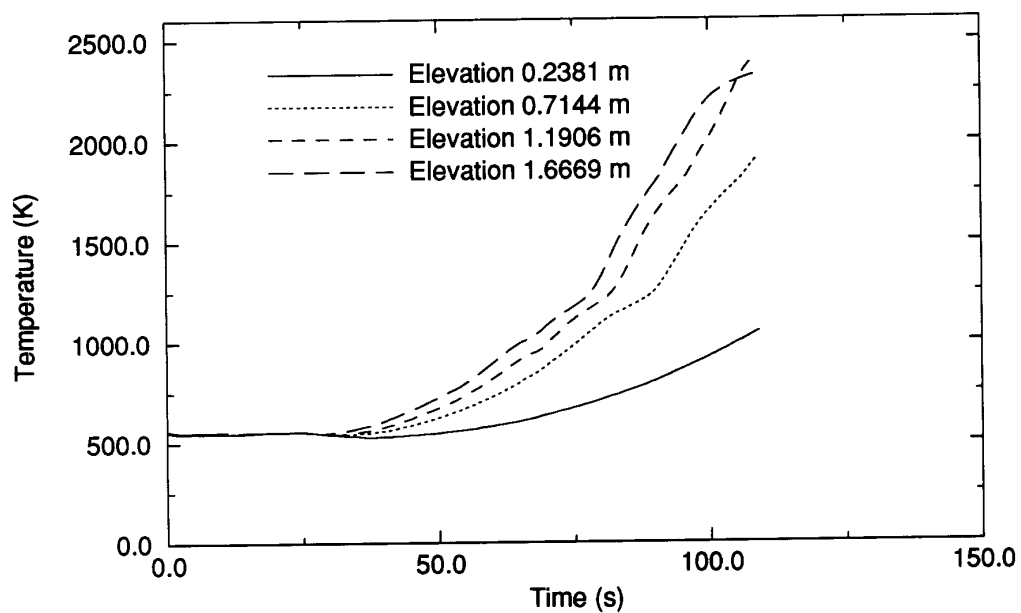


Figure A-147. Surface temperatures for the bottom half of the Channel 2 water rod component for the Browns Ferry plant transient.

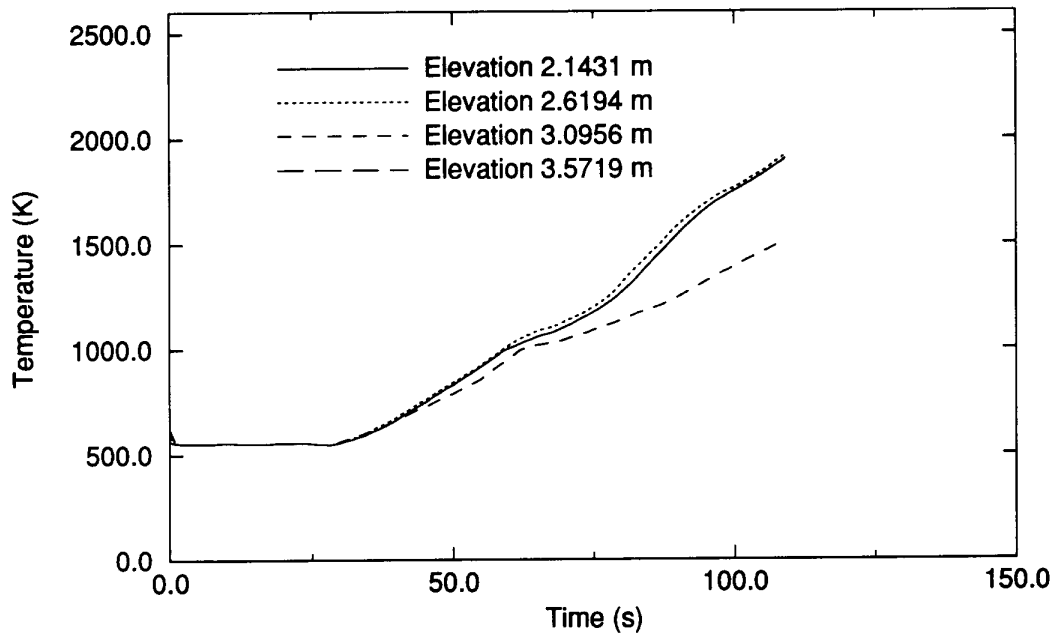


Figure A-148. Surface temperatures for the top half of the Channel 2 shroud component for the Browns Ferry plant transient.

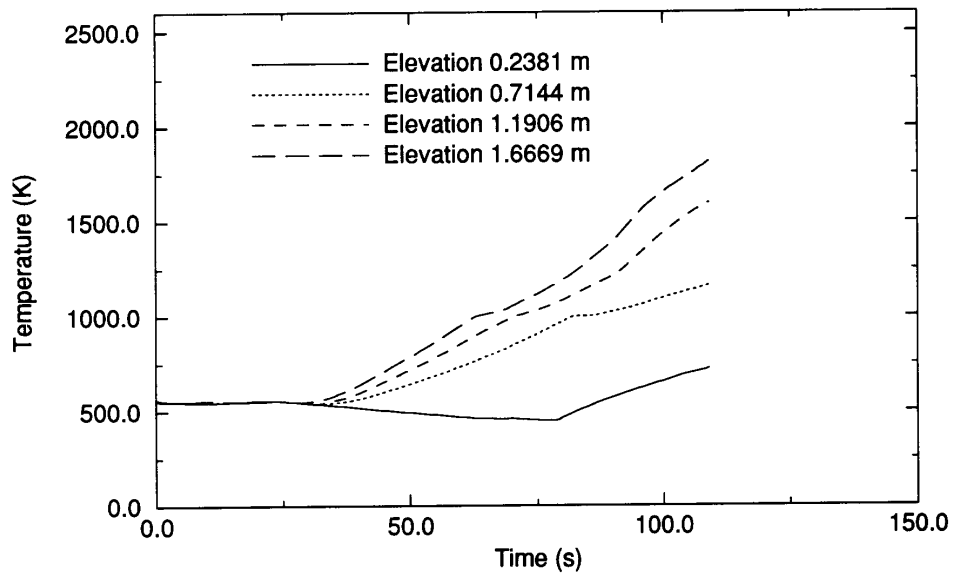


Figure A-149. Surface temperature for the bottom half of the Channel 2 shroud component for the Browns Ferry plant transient.

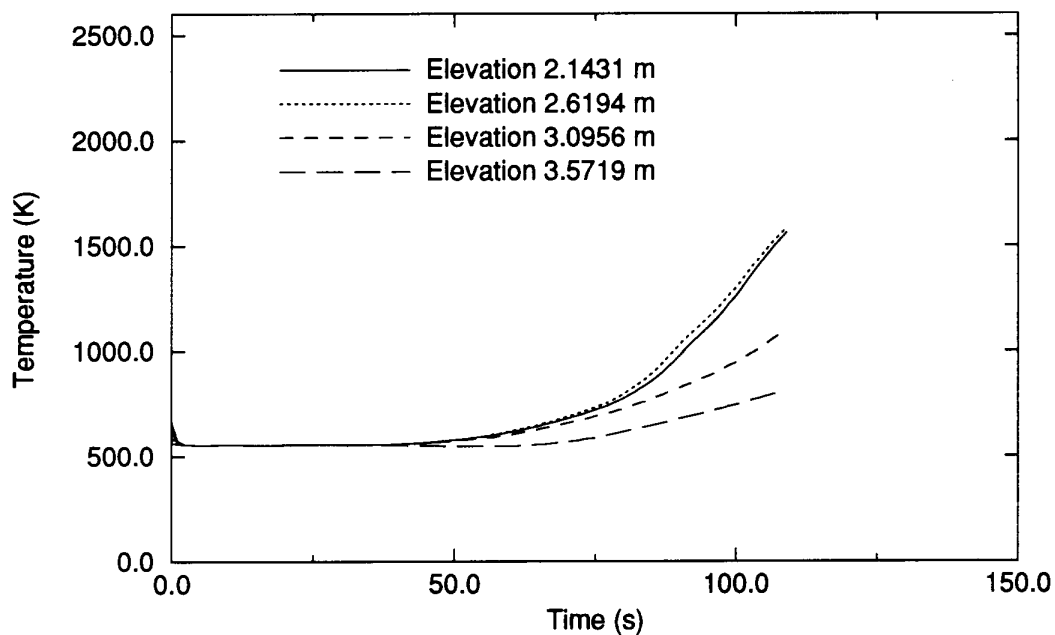


Figure A-150. Surface temperatures for the top half of the Channel 2 control rod component for the Browns Ferry plant transient.

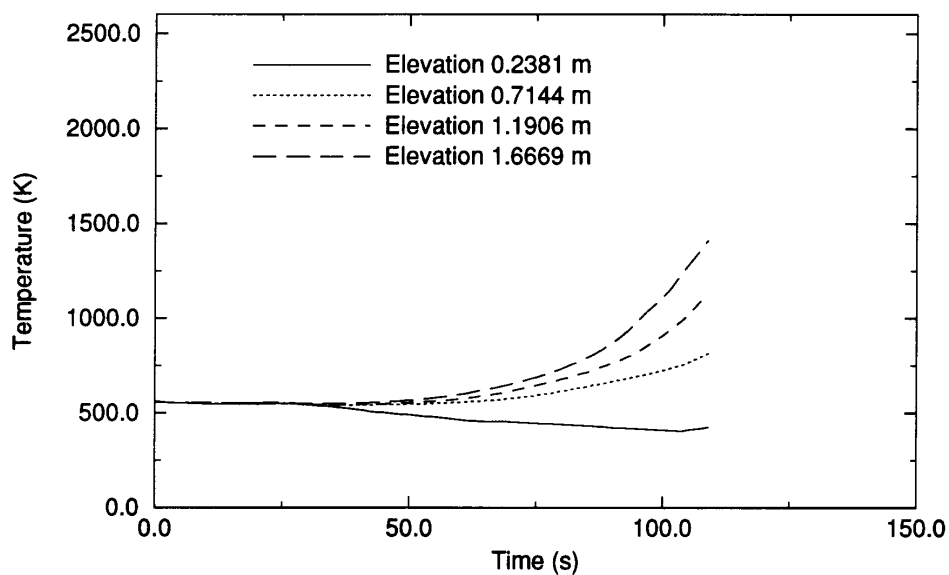


Figure A-151. Surface temperatures for the bottom half of the Channel 2 control rod component for the Browns Ferry plant transient.

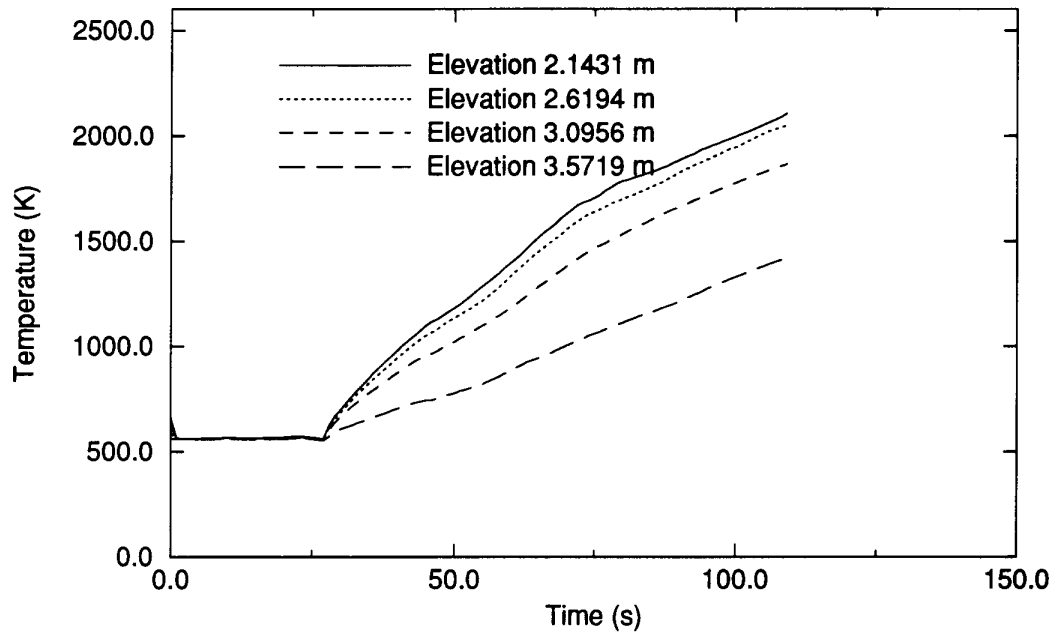


Figure A-152. Surface temperatures for the top half of the Channel 3 fuel rod component for the Browns Ferry plant transient.

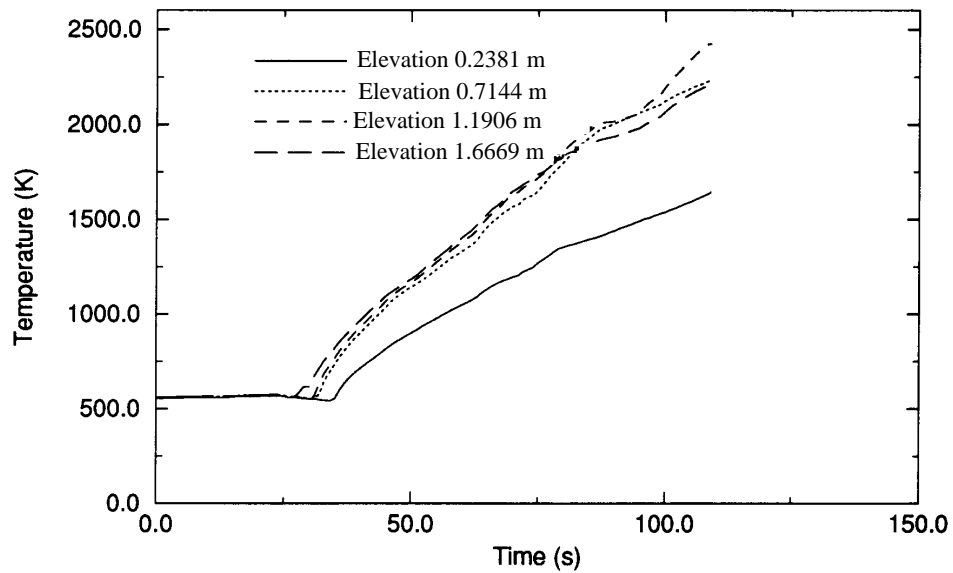


Figure A-153. Surface temperatures for the bottom half of the Channel 3 fuel rod component for the Browns Ferry plant transient.

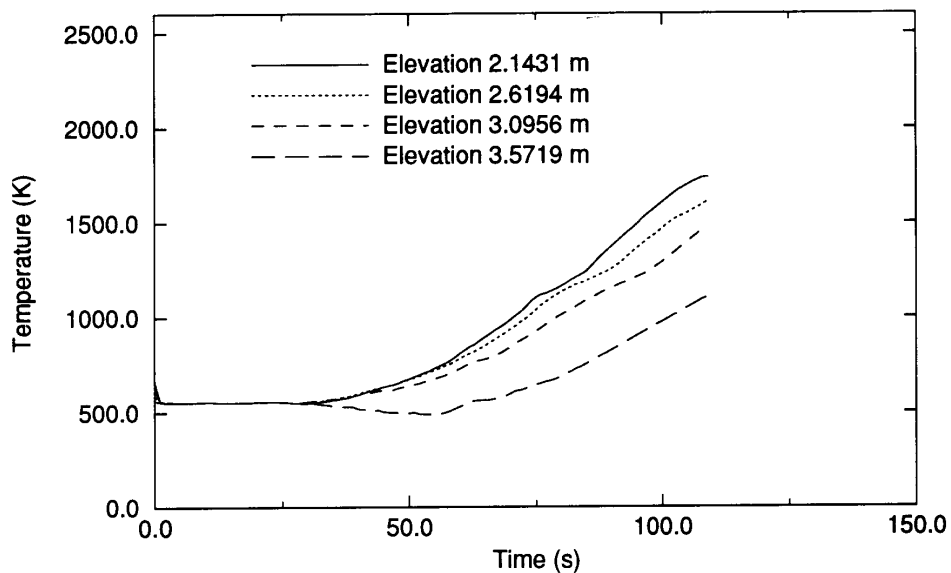


Figure A-154. Surface temperatures for the top half of the Channel 3 water rod component for the Browns Ferry plant transient.

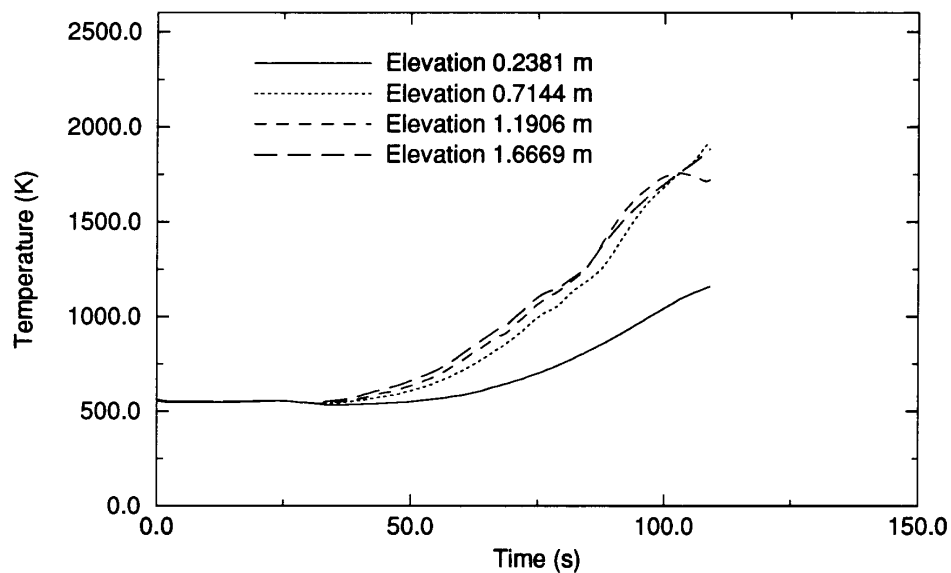


Figure A-155. Surface temperatures for the bottom half of the Channel 3 water rod component for the Browns Ferry plant transient.

A.12.2.2 Hydrogen Production.

The calculated hydrogen production for the Browns Ferry accelerated severe accident transient

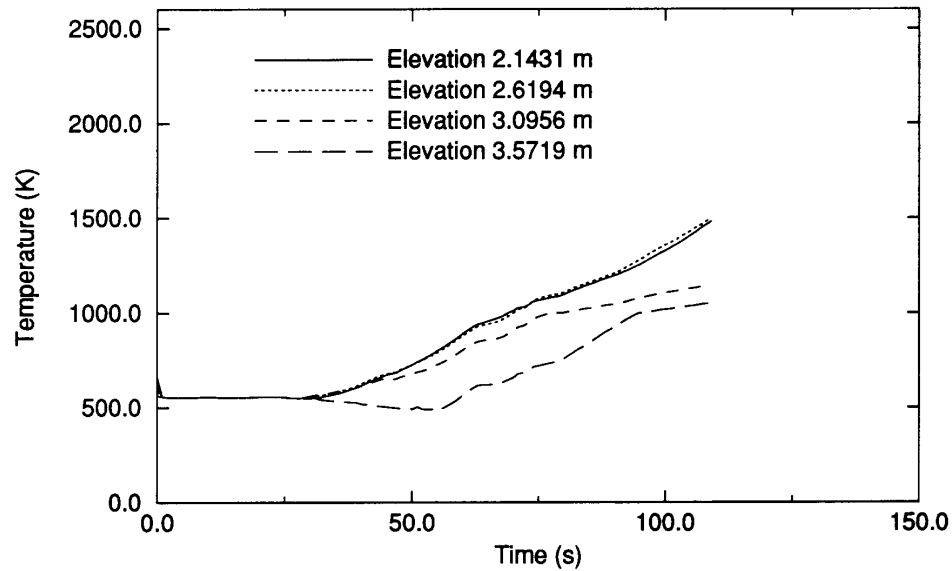


Figure A-156. Surface temperatures for the top half of the Channel 3 shroud component for the Browns Ferry plant transient.

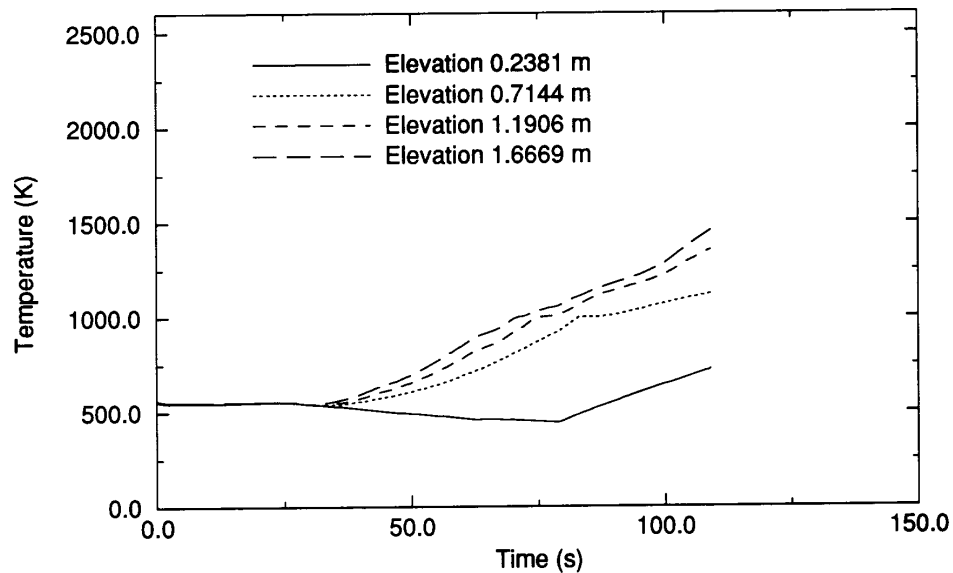


Figure A-157. Surface temperatures for the bottom half of the Channel 3 shroud component for the Browns Ferry plant transient.

appears to be as expected. Figure A-169 shows the total hydrogen produced during the accident. Maximum hydrogen production during the experiment occurs during the period of rapid oxidation. Approximately 200 kg of hydrogen were calculated to be produced during the course of the accident.

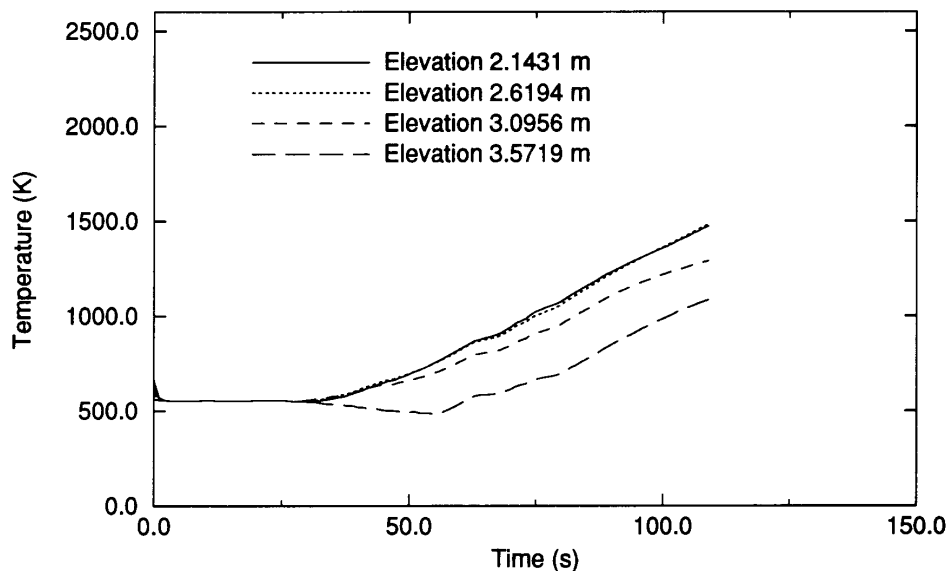


Figure A-158. Surface temperatures for the top half of the Channel 3 control rod component for the Browns Ferry plant transient.

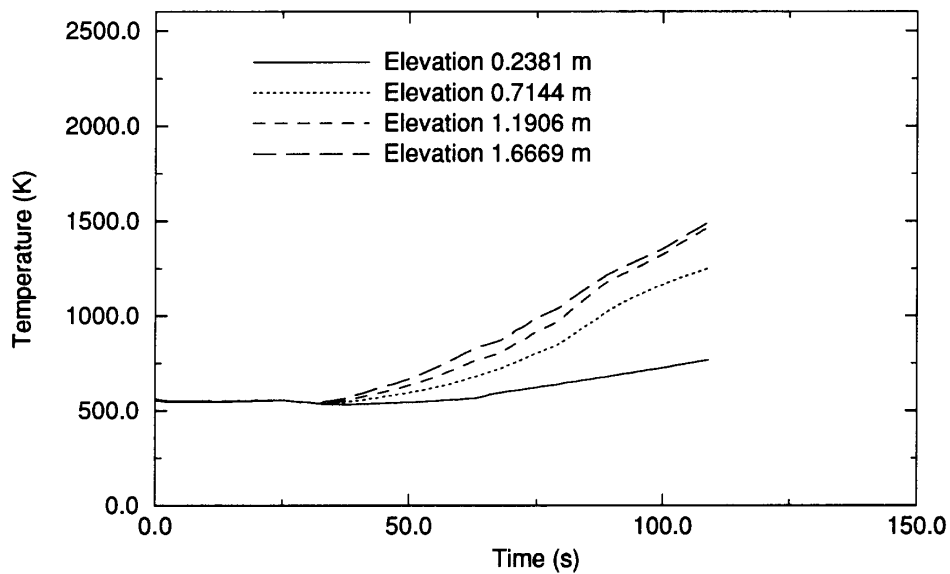


Figure A-159. Surface temperatures for the bottom half of the Channel 3 control rod component for the Browns Ferry plant transient.

A.12.3 Code Performance

The Browns Ferry accelerated transient calculated temperatures in excess of 2,500 K in about 8 hours

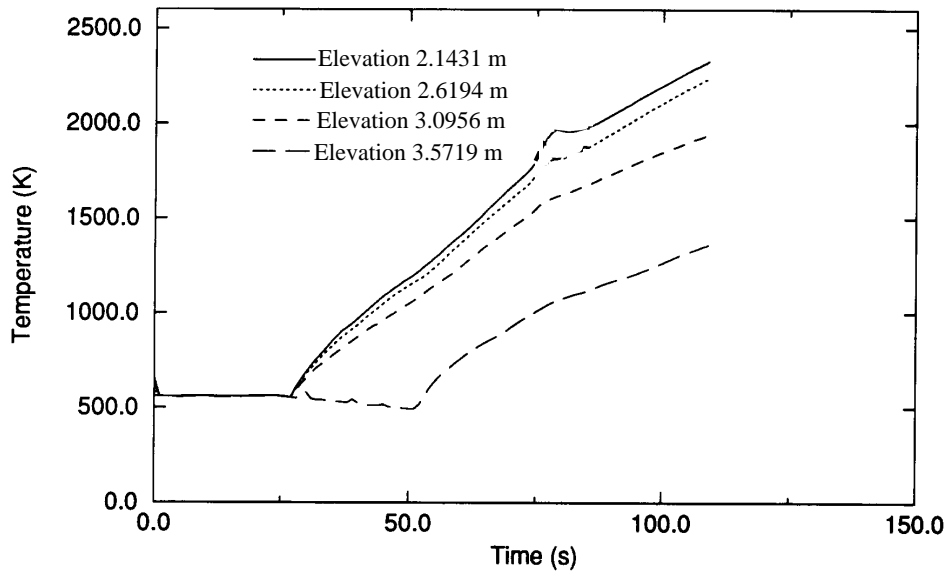


Figure A-160. Surface temperatures for the top half of the Channel 4 fuel rod component for the Browns Ferry plant transient.

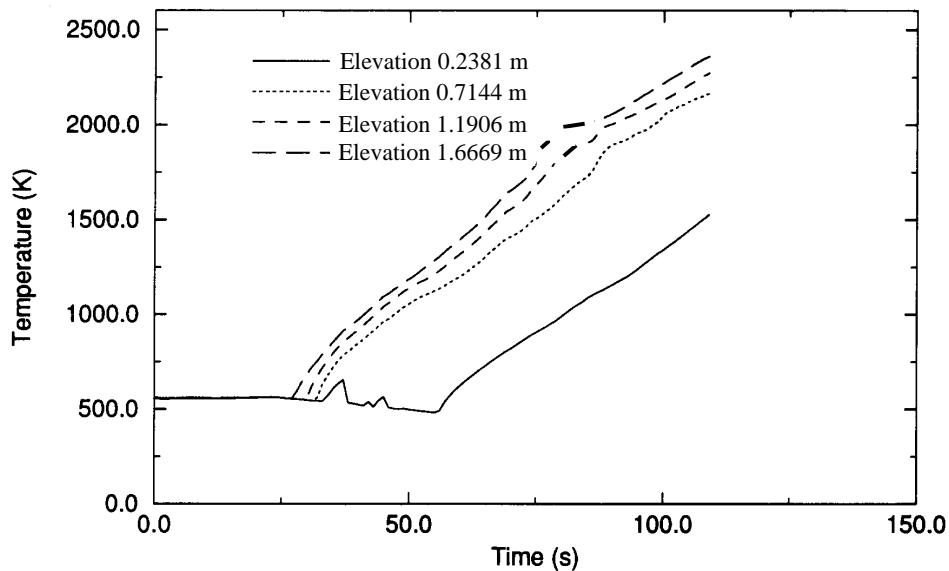


Figure A-161. Surface temperatures for the bottom half of the Channel 4 fuel rod component for the Browns Ferry plant transient.

CPU time, allowing the models used during a plant transient to be exercised in a short period of time, rather than the week required to perform a full-plant calculation. Figure A-170 shows the CPU time used for each second of transient. During the early stages of the accident, when the core was uncovering and

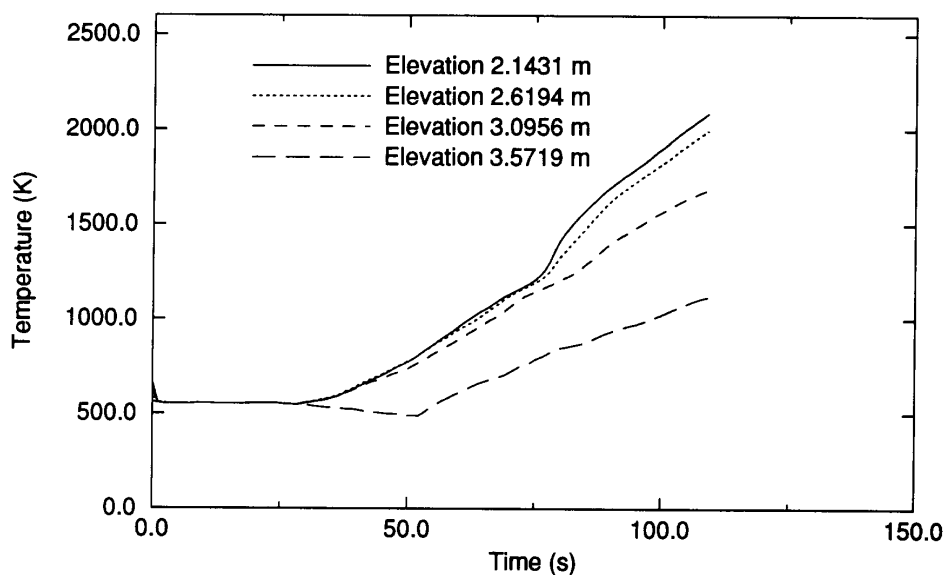


Figure A-162. Surface temperatures for the top half of the Channel 4 water rod component for the Browns Ferry plant transient.

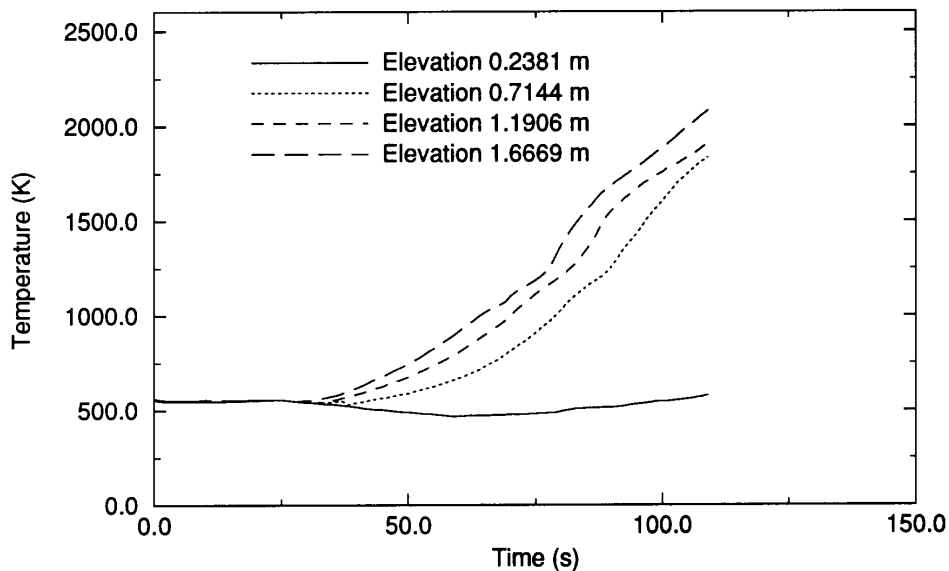


Figure A-163. Surface temperatures for the bottom half of the Channel 4 water rod component for the Browns Ferry plant transient.

depressurizing, the ratio of CPU time to problem time was good. The calculation progressed smoothly using 0.02-second time steps, running at or near the Courant limit. As the accident progressed into the severe damage states and the damage events occurring in the core became more complex, the ratio of CPU time to problem time increased dramatically. At this time, for the accelerated transient the time step size

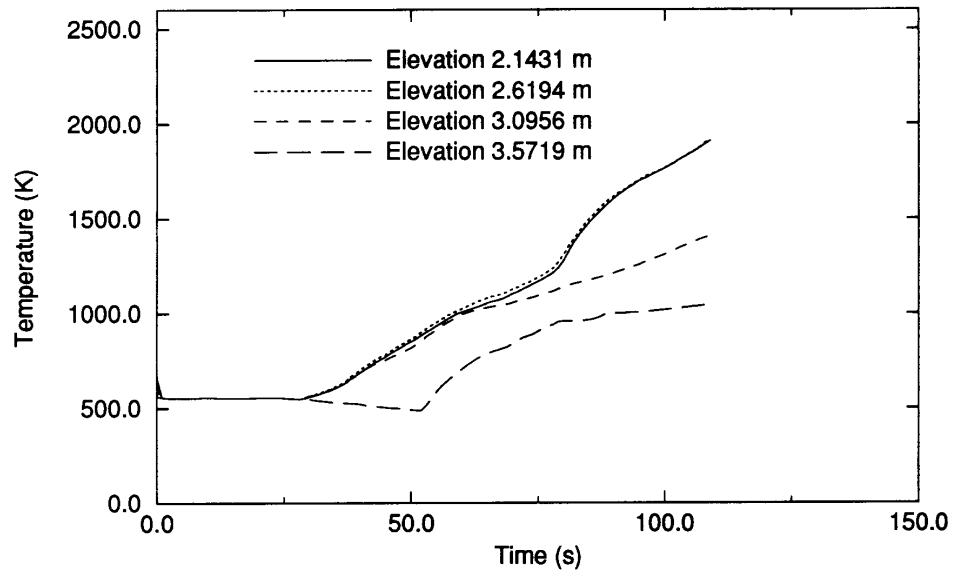


Figure A-164. Surface temperatures for the top half of the Channel 4 shroud component for the Browns Ferry plant transient.

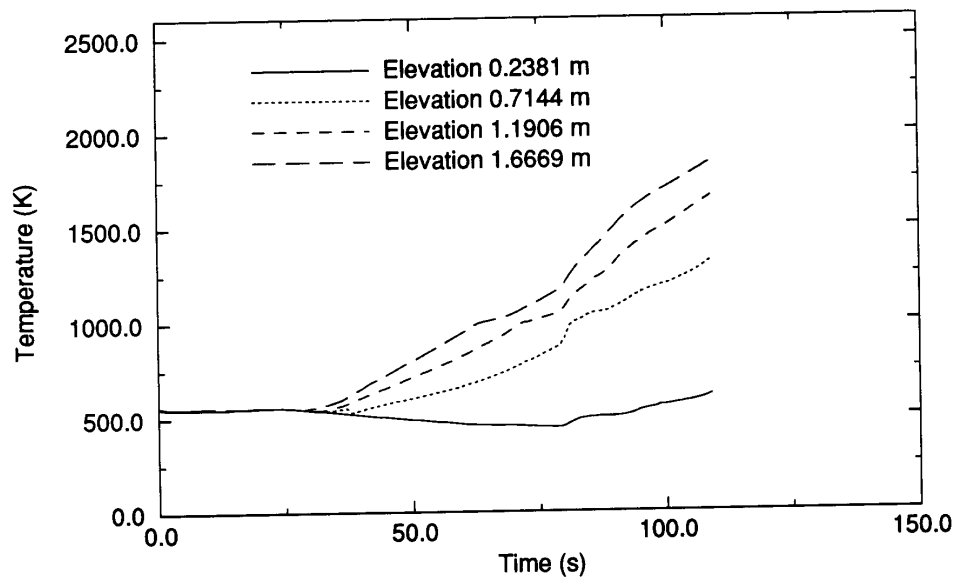


Figure A-165. Surface temperatures for the bottom half of the Channel 4 shroud component for the Browns Ferry plant transient.

was decreased to between 1 and 2 milliseconds. The heatup trends calculated by the accelerated deck agreed with the calculated and measured analytical results for the BWR experiments, DF-4 and CORA-18,

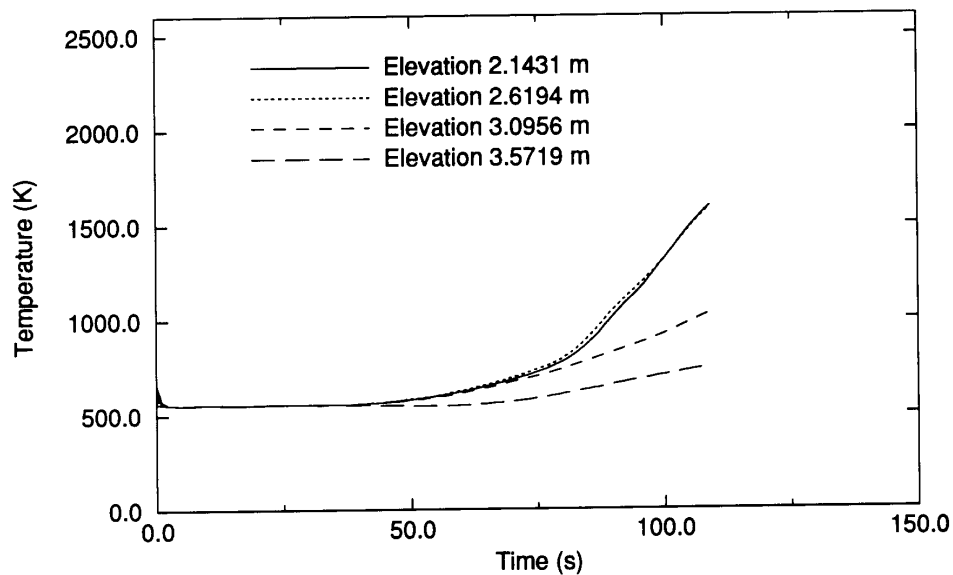


Figure A-166. Surface temperatures for the top half of the Channel 4 control rod component for the Browns Ferry plant transient.

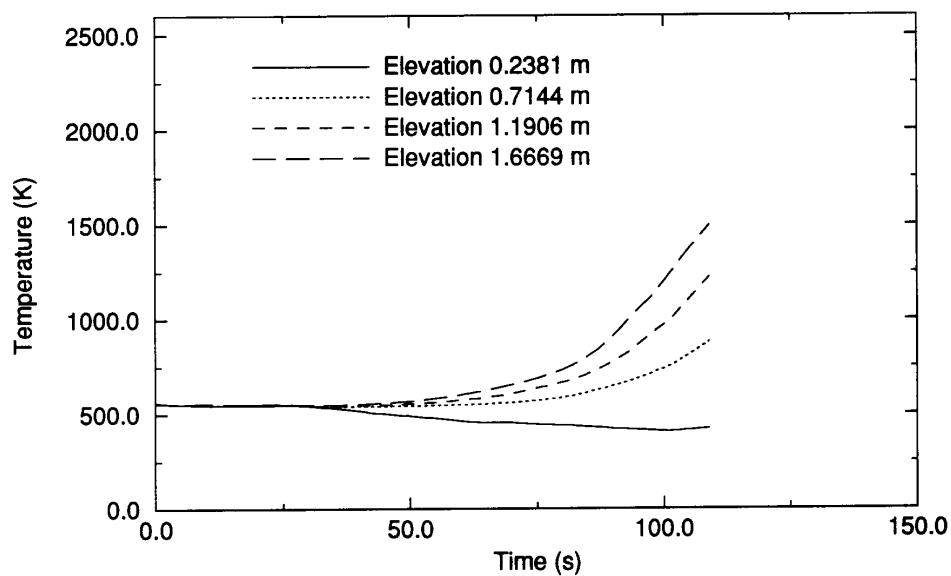


Figure A-167. Surface temperatures for the bottom half of the Channel 4 control rod component for the Browns Ferry plant transient.

indicating that the code is correctly exercising the BWR-specific as well as the thermal-hydraulic models in the code.

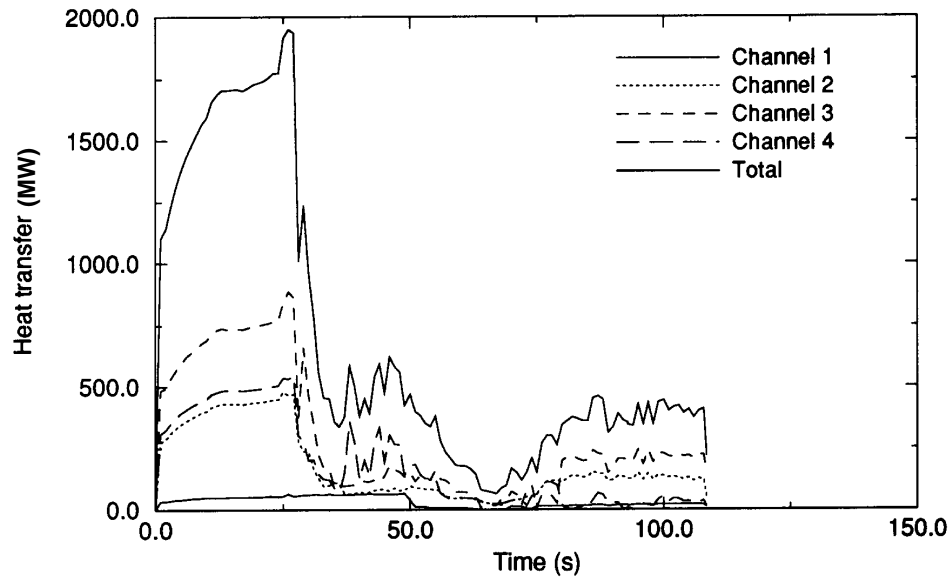


Figure A-168. Total heat transfer in the four fuel assembly channels for the Browns Ferry plant transient.

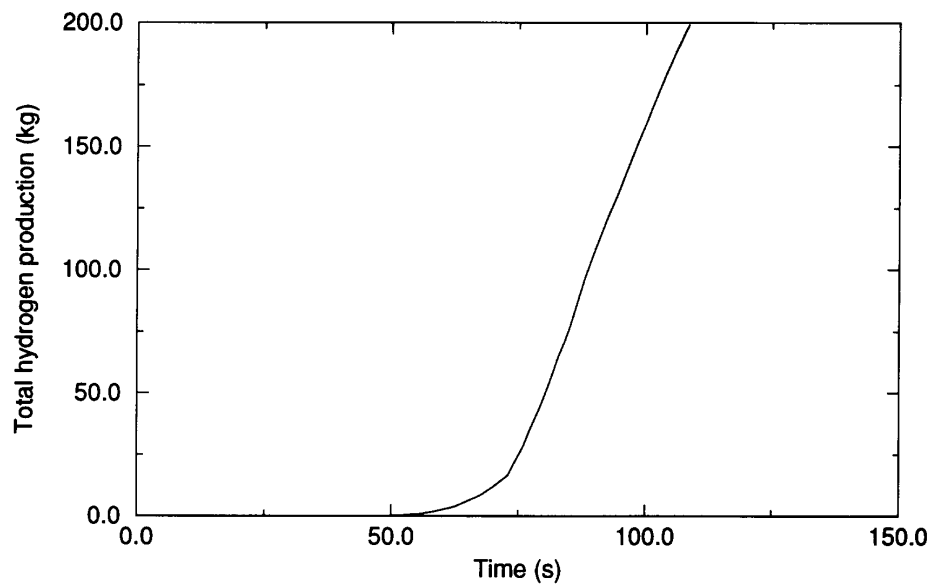


Figure A-169. Total hydrogen production for the Browns Ferry plant transient.

The development of an input deck using the RELAP5-style card numbers from a previously used input deck using free format was quite simple. Conversion from a Brown's Ferry input deck using free format SCDAP component input to an input deck using RELAP5-style card number input was accomplished in a day. Debugging of the deck took several hours. The error messages printed to the output

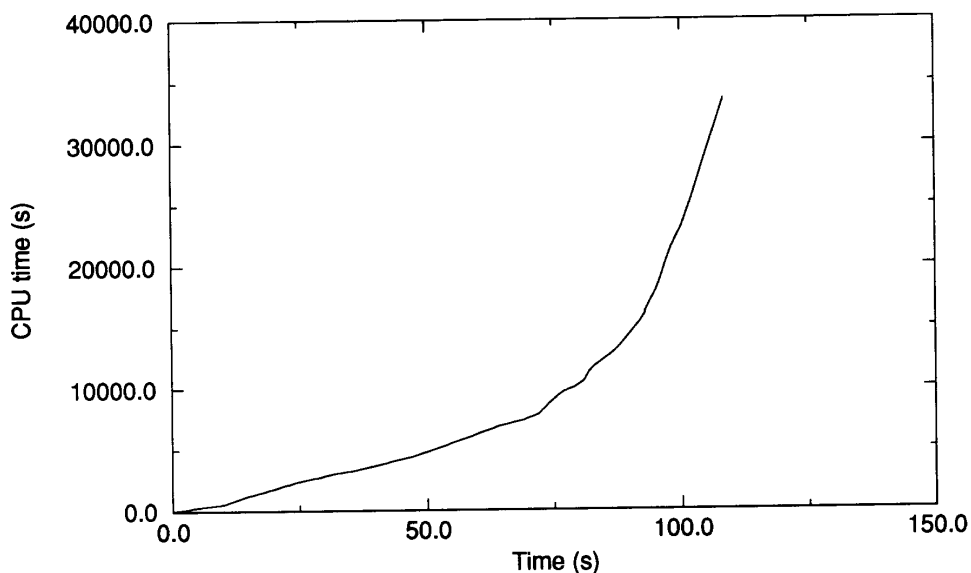


Figure A-170. CPU time for the Browns Ferry plant transient.

file made debugging the input deck relatively easy. The printed error messages also warn the user of component dimensions and user-supplied input quantities that are out of range of accepted values. These messages are helpful in verifying the model built for the analysis of a reactor or experimental facility.

Table A-17 lists the new models, new capabilities and improvements exercised during the verification testing using the accelerated Brown's Ferry input deck. The table lists all new models and capabilities that were to be verified, whether or not these models or capabilities were exercised by the Browns Ferry verification deck, and comments relating to the performance and/or ease of using the new model or capability where applicable.

Table A-17. Models and capabilities verified by Browns Ferry calculation.

Model	Results
Time smoothing	No oscillations were noted in results.
Implicit steam starvation	No oscillations were noted in results.
Restart improvements	The calculations were restarted, and the calculated results were identical to those calculated by the code in that area before the restart.
Input improvements	RELAP5 card number style input works well; changes can be made on restart; easy to change old-style input to new.
Output improvements	Error diagnostics and calculated results are easier to understand. The error diagnostics during input checking significantly decreased the time needed to debug an input deck.
Decay power	The kinetics model in RELAP5 was used to calculate reactor power during the accident.
Nested shroud radiation	The channel containing the control blade was nested between channels containing fuel assemblies. This model appears to work well.

A.13. REFERENCES

- A-1. D. A. Brownson et al., *Intentional Depressurization Accident Management Strategy for Pressurized Water Reactors*, NUREG/CR-5937, EGG-2688, February 1993.
- A-2. C. A. Dobbe, Preliminary SCDAP/RELAP5/MOD3 Results of the TMI-2 Accident Calculation, presented by D. J. Hanson at a Program Review Meeting, April 13, 1993.
- A-3. *SCDAP/RELAP5 Independent Peer Review*, LA-12481, January, 1993
- A-4. M. Firnhaber, K. Trambauer, S. Hagen, and P. Hofmann, *Specification of the International Standard Problem ISP-31: CORA 13 Experiment on Severe Fuel Damage*, August 1991, Revision 1, October 1991.
- A-5. R. W. Wright for J. K. Hohorst, "Analysis of the OECD-CSNI International Standard Problem 31 using SCDAP/RELAP5", *ISP-31 International Standard Problem Workshop, Karlsruhe, Germany*, October 1992.
- A-6. S. Hagen, P. Hofmann, V. Noack, G. Schanz, G. Schumacher, and L. Sepold, *Results of SFD Experiment CORA-13 (OECD International Standard Problem 31)*, KfK 5054, February 1993.
- A-7. S. Hagen, et al., "CORA Experiments on the Materials Behavior of LWR Fuel Rod Bundles at High Temperatures," *Proceedings of the 19th Water Reactor Safety Meeting*, NUREG/CP-0119, April 1992.
- A-8. J. K. Hohorst and C. M. Allison, *Analysis of CORA-7 and CORA-18 Large PWR and BWR Bundle Heating and Melting Experiments Using SCDAP/RELAP5/MOD3*, EGG-SSRE-10208, May 1992.
- A-9. R. Gauntt, et al., *The DF-4 Fuel Damage Experiment in ACRR with a BWR Control Blade and Channel Box*, NUREG/CR-4671, November 1989.
- A-10. F. P. Griffin, *BWR Control Blade/Channel Box Interaction and Melt Relocation Models for SCDAP*, ORNL/NRC/LTR-92/12, June 15, 1992.
- A-11. J. K. Hohorst, *Debris Formation Experiment Analysis Using SCDAP/RELAP5/MOD2*, EGG-EAST-8586, June 1989.
- A-12. D. A. Petti, et al., *PBF Severe Fuel Damage Test 1-4 Test Results Reports*, NUREG/CR-5163, April 1989.
- A-13. Z. R. Martinson, et al., *PBF Severe Fuel Damage Test 1-3 Test Results Report*, NUREG/CR-5354, October 1989.
- A-14. Z. R. Martinson, et al., *PBF Severe Fuel Damage Test 1-1 Test Results Report*, Vol. 1, NUREG/CR-2682, October 1986.
- A-15. A. D. Knipe, et al., *PBF Severe Fuel Damage Scoping Test -- Test Results Report*, NUREG/CR-4683, August 1986.
- A-16. B. Adroguer, et al., *Comparison Report of the OECD/CSNI International Standard Problem 28*, OECD NEA CSNI Report No. 28, December 1992.
- A-17. J. P. Adams et al., *Quick-Look Report on OECD LOFT Experiment LP-FP-2*, OECD LOFT-T-3804, September 1984.
- A-18. M. L. Carboneau, V. T. Berta, and S. M. Modro, *Experiment Analysis and Summary Report for OECD LOFT Project Fission Product Experiment LP-FP-2*, OECD LOFT-T-3806, June 1989.
- A-19. S. Guntay et al., *A Post Test Analysis of the OECD LOFT Experiment LP-FP-2 Using the Computer Programs SCDAP/RELAP5, TRAP-MELT2.2, and PULSE*, PSI-Bericht Nr. 95, April 1991.

- A-20. M. L. Carboneau et al., *OECD LOFT Fission Product Experiment LP-FP-2 Data Report*, OECD LOFT-T-3805, May 1987.
- A-21. E. W. Coryell and K. R. Katsma, *Design Report: Modifications to Examine the Influence of Cold Wall Effects on Core Damage Progression*, EGG-SSRE-10221, April 1992.
- A-22. P. D. Bayless, *Analyses of Natural Circulation During a Surry Station Blackout Using SCDAP/RELAP5*, NUREG/CR-5214, EGG-2547, October 1988.
- A-23. D. Giessing, "The TMI Analysis Exercise," *Trans. Am. Nucl. Soc.*, 57, 1988, p. 434.
- A-24. D. W. Golden et.al., "Summary of the Three Mile Island Unit 2 Analysis Exercise," *Nuclear Technology*, 87, 1989, pp. 326-333.
- A-25. J. Anderson, *Analysis of TMI-2 Pressurizer Level Indications*, EGG-TMI-7100, January 1986
- A-26. J. K. Hohorst and C. M. Allison, "DF-4 Analysis Using SCDAP/RELAP5," *Nuclear Technology*, 98, May 1992, pp. 149-159.
- A-27. J. K. Hohorst and C. M. Allison, *Analysis of CORA-7 and CORA-18 Large PWR and BWR Bundle Heating and Melting Experiments using SCDAP/RELAP5*, EGG-SSRE-10208, May 1992.

Appendix B

Calculated Behavior of Surry PWR During TMLB' Accident With No Rupture of Surge Line

B.1. INTRODUCTION

This section presents the results of analyses performed for a severe accident in the Surry PWR in which the surge line is assumed to never rupture. First, the nodalization for the base case calculation is described. In this base case calculation, the reactor core was divided into three flow channel and each flow channel was divided into ten axial segments. The calculated behavior of the Surry PWR during a TMLB' accident is then described in detail. Next, a description of two other nodalizations of the reactor core are described. In one of these cases the reactor core was divided into five flow channels with ten axial segments, and, in the other case the reactor core was divided into five flow channels with twenty axial segments. Finally, comparisons are made of the behavior calculated for each nodalization case. Similarities and differences in the calculated behavior are noted and explanations are noted for differences in calculated behavior.

The nodalization of the reactor core and vessel is shown in Figures B-1 and B-2. A cross-section in the axial direction of the reactor vessel is shown in Figure B-1. The center flow channel is represented by control volume number 111, the middle channel by control volume number 112, and the outer channel by control volume number 113. The three channels are connected with each other by crossflow junctions; thus flow in the lateral direction through the core is modeled. The core bypass is represented by control volume number 118. The downcomer is represented by control volume number 104 with seven subvolumes. The lower plenum is represented by control volume numbers 106 and 108. A total of seventeen control volumes represent the upper plenum of the reactor vessel. A radial cross-section of the reactor core is shown in Figure B-2. The center flow channel represents 25 fuel assemblies, the middle flow channel represents 96 fuel assemblies, and the outer flow channel represents 36 fuel assemblies.

The power in the fuel rods varied with flow channel. The variation in average rod power in the radial direction for the three channel case is shown in Table B-1. The power variation in the axial direction was the same for all three flow channels. The peak power in the axial direction occurs at an elevation of 0.82 m, where the power is 1.15 times the average power in the axial direction. From 0.82 m to 3.02 m elevations, the axial power factor decreases in an approximately linear manner from a value of 1.15 to a value of 1.03. The axial power factor decreases rapidly as the elevation increases above 3.0 m and as the elevation decreases below 0.6 m.

The fuel rods in each fuel assembly were represented by one SCDAP fuel rod component and the control rods were represented by one SCDAP control rod component. Each fuel assembly was represented as having 204 fuel rods and 21 control rods. The fuel rods and control rods were located in the fuel assembly as shown in Figure B-3. The water rods were represented by control rods. The fuel rods have a fuel pellet stack that is 3.6576 m in length. The fuel pellets are 4.634 mm in radius. The cladding has an outer radius of 5.359 mm and a thickness of 0.617 mm. The reactor core was represented by a total of six SCDAP components, namely a fuel rod and control rod component for each of the three flow channels. Each fuel bundle has six Inconel spacer grids, at elevations above the bottom of the reactor core of 0.0 m, 0.73 m, 1.46 m, 1.83 m, 2.19 m, and 2.93m, respectively. These spacer grids were represented by the SCDAP spacer grid model.

The lower head of the reactor vessel was represented by the COUPLE debris model. This representation was performed in order to calculate the heatup of the lower head in response to slumping molten material from the core region and in order to calculate the time of rupture of the lower head. The

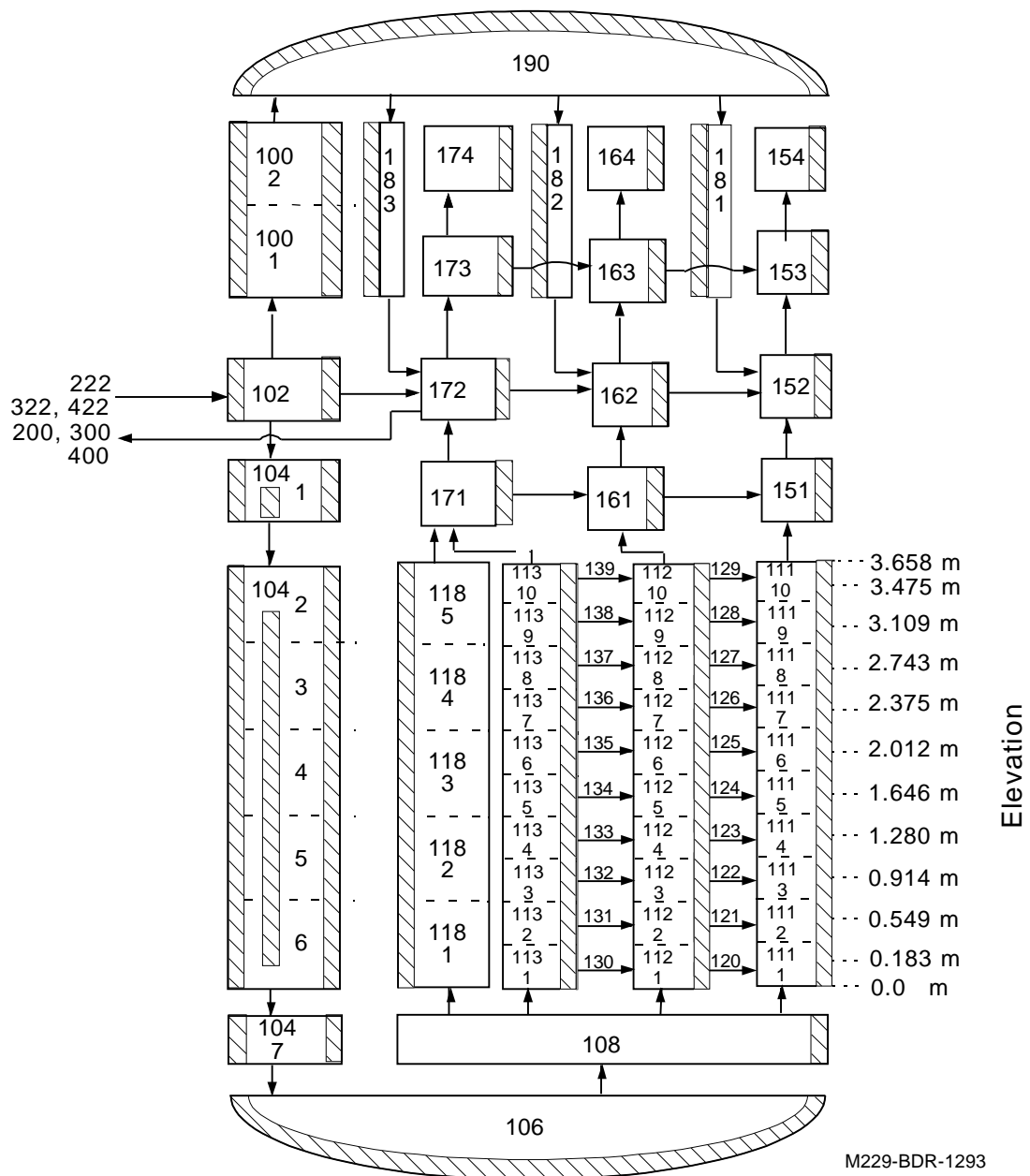


Figure B-1. Axial cross-section showing nodalization of reactor vessel and reactor core.

lower head was represented with a 3x16 mesh. Nodes were located at the inner and outer surfaces and the midplane of the lower head. The lower head is divided into sixteen axial nodes in the meridional direction.

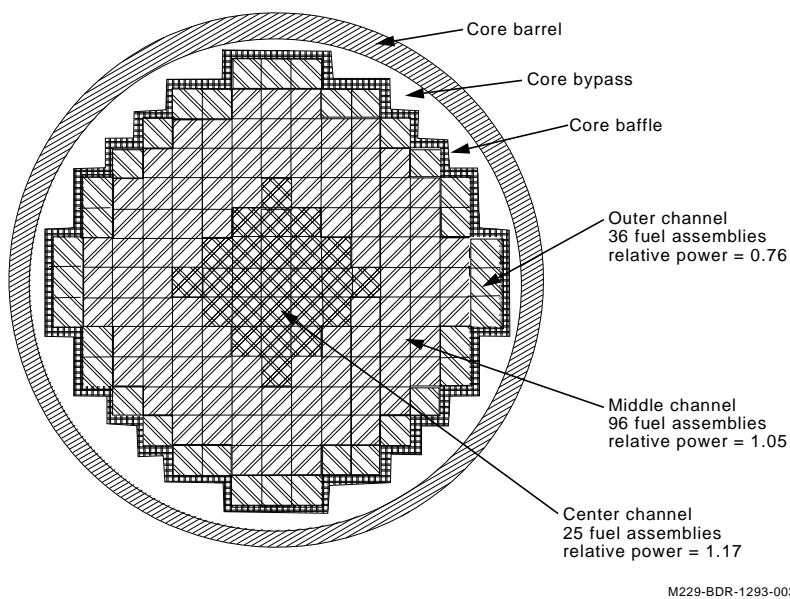


Figure B-2. Radial cross-section showing nodalization of reactor core.

Table B-1. Radial power distribution in reactor core.

Flow channel	Fuel rod power at start of transient (kW/m)	Ratio of power to average core power
Center	24.33	1.17
Middle	21.84	1.05
Outer	15.81	0.76



B.2. CALCULATED BEHAVIOR FOR BASE CASE ANALYSIS

The severe accident analyzed was a station blackout without operator actions. This accident is designated as a TMLB' sequence. The accident is initiated by loss of offsite power. Onsite ac power is also unavailable because the diesel generators fail to start or fail to supply power. Decay heat removal through the steam generators cannot be maintained in the long term because there is no ac power for the electrical pumps, and the steam driven auxiliary feedwater pumps also fail to supply water. The surge line is considered to never rupture.

The severe accident evolves as follows. The loss of offsite power causes reactor scram to occur. Next, the pressure on the secondary side of the steam generators exceeds the set point pressure, resulting in opening of the relief valves. The inventory of water on the secondary sides of the steam generator then gradually boils away. After water on the secondary side of the steam generators is depleted, then boiling begins to occur in the reactor core. After a period of time, the pressure in the primary coolant loop exceeds the set point pressure and the PORVs open to relieve the pressure. The inventory of coolant in the reactor core is then gradually depleted over a period of time. Damage to the reactor core begins after the inventory of reactor vessel water has depleted to the point that the reactor core is uncovered. The progression of damage is calculated to the point of slumping of molten reactor core material to the lower head of the reactor vessel and then rupture of the lower head.

A scenario is calculated that is designed to determine the time of failure of the lower head of the reactor vessel in the event that ruptures do not occur ex-vessel and that no leakage of water occurs through the reactor coolant pump. This scenario was analyzed in an assessment of the potential for high pressure melt ejection in the event of a station blackout.^a This scenario results in the pressure in the primary coolant system remaining high much longer than in a best estimate calculations. The primary system pressure also remains high for hours after the surge line has been calculated to rupture. As a result of the system pressure remaining high, a considerable amount of heat is removed from the reactor core due to natural convection in the reactor vessel. The heat removed from the reactor core is transferred to structures in the upper plenum of the reactor vessel and to other structures. The structures in the lower part of the upper plenum are calculated to melt but the melting of these structures is not represented in the analysis. There is also the possibility that countercurrent natural circulation may occur in the hot legs. This natural circulation in the hot legs was not modeled.

The behavior of the Surry reactor was calculated from initiation of the accident through rupture of the lower head. The sequence of major events in the reactor is shown in Table B-2. Core uncover was calculated to begin 9,000 seconds after the loss of offsite power and the beginning of the accident. All values of time refer to time since the beginning of the accident. A rapid increase in temperature due to oxidation begins at 10,000 seconds. The fuel rods were calculated to begin to rupture at a time of 11,950 seconds. This event is the beginning of core damage. The spacer grids were calculated to begin to slump due to liquefaction at a time of 12,196 seconds. The fuel rod cladding is calculated to begin to melt at 12,560 seconds. The surge line is calculated to rupture at 13,035 seconds. The hot leg with the pressurizer is calculated to rupture at 13,990 seconds. The rupture of the surge line and hot leg and the flow of steam through the resulting breach, however, is not modeled. The beginning of ceramic melting and thus the

a. D. L. Knudson and C. A. Dobbe, "Assessment of the Potential for High Pressure Melt Ejection Resulting from a Surry Station Blackout," NUREG/CR5949, EGG-2689, May 1993.

beginning of formation of a molten pool occurs at a time of 12,860 seconds. The melting of the first 20,000 kg of UO_2 , which is approximately the mass of core material that slumped to the lower head of the TMI-2 reactor during its accident, occurred at a time of 17,100 seconds. At 28,770 seconds the molten pool is calculated to have spread across the entire reactor core. The lower head is calculated to fail due to creep rupture at 36,275 seconds and with an average temperature of 1,017 K. The failure was calculated to occur before slumping of the molten pool in the core region. The lower head was heated to the point of creep rupture by hot steam flowing by natural circulation from the upper plenum region of the vessel to the lower plenum region. A creep rupture calculation was not performed on the upper head, but it is expected that a calculation would predict it to fail due to creep rupture before the lower head for the case of its temperature always being greater than that of the lower head. This was the case for this analysis. The upper head was calculated to be heated to the temperature at which the lower head failed at the time of 19,000 seconds. A total of 420 kg of hydrogen is calculated to be produced by oxidation of the components in the reactor core. Only a small fraction of the fuel rods in the reactor core (1.6%) are calculated to experience metallic meltdown. The meltdown that did occur was located in the 2.6 m to 2.9 m interval of elevation in the center flow channel. Most of the cladding in the upper 70% of the reactor core was calculated to completely oxidize in place.

Table B-2. Calculated progression of damage in Surry reactor during TMLB'

Event or threshold in damage progression	Time of occurrence (s)
Beginning of rupture of fuel rods	11,950
Beginning of slumping of spacer grids	12,196
Beginning of melting of cladding (temperature > 2,200 K)	12,560
Beginning of ceramic melting (molten pool starts to form)	12,860
Ceramic melting of 20,000 kg of UO_2	17,100
Ceramic melting spread across entire core	28,770
Rupture of lower head	36,275
Amount of hydrogen produced due to oxidation of reactor core	420 kg
Percentage of fuel rod cladding with metallic meltdown	1.6%

The calculated power history of the reactor core is shown in Figures B-4 and B-5. The power history was calculated by the reactor kinetics package in RELAP5. Figure B-4 shows the power history for the first 100 seconds of the accident. The reactor power decreases rapidly to a few percent of steady-state power in response to scram. The steady-state power was 2,441 MW. Figure B-5 shows the reactor power out to 30,000 seconds. During this period of time the power is due to the decay of fission products and actinides.

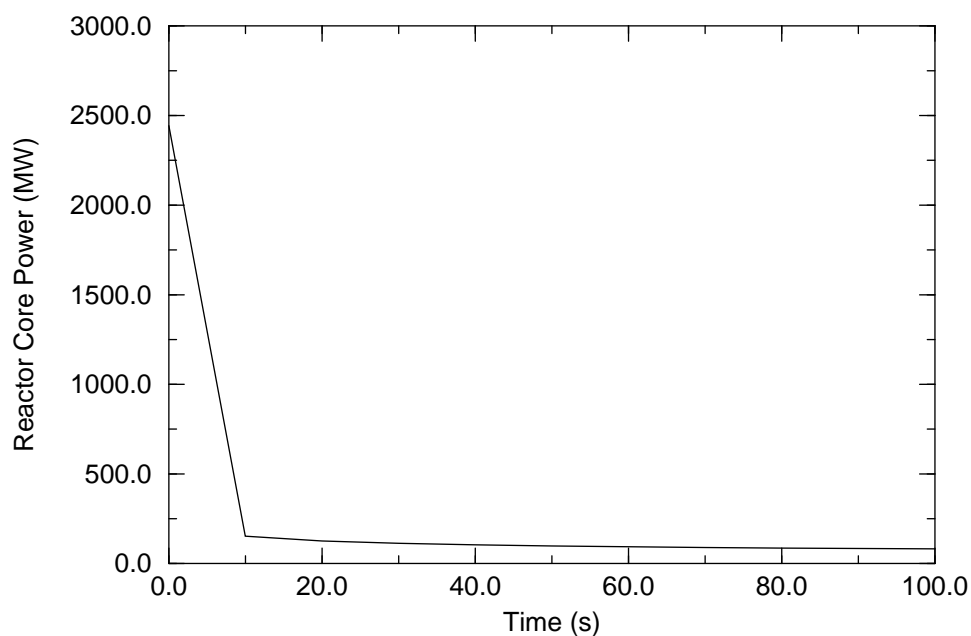


Figure B-4. Reactor power history from 0.0 to 100 seconds.

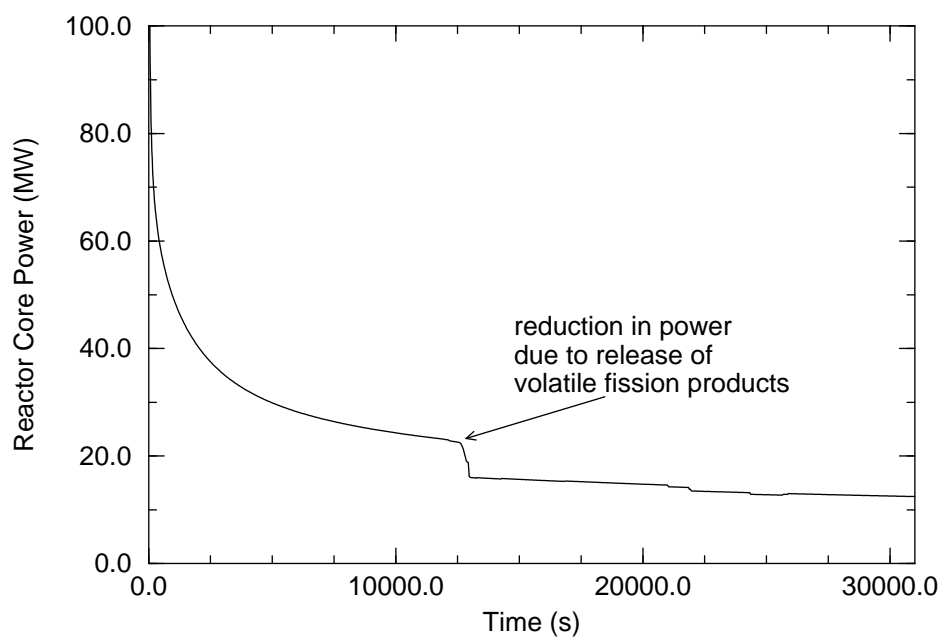
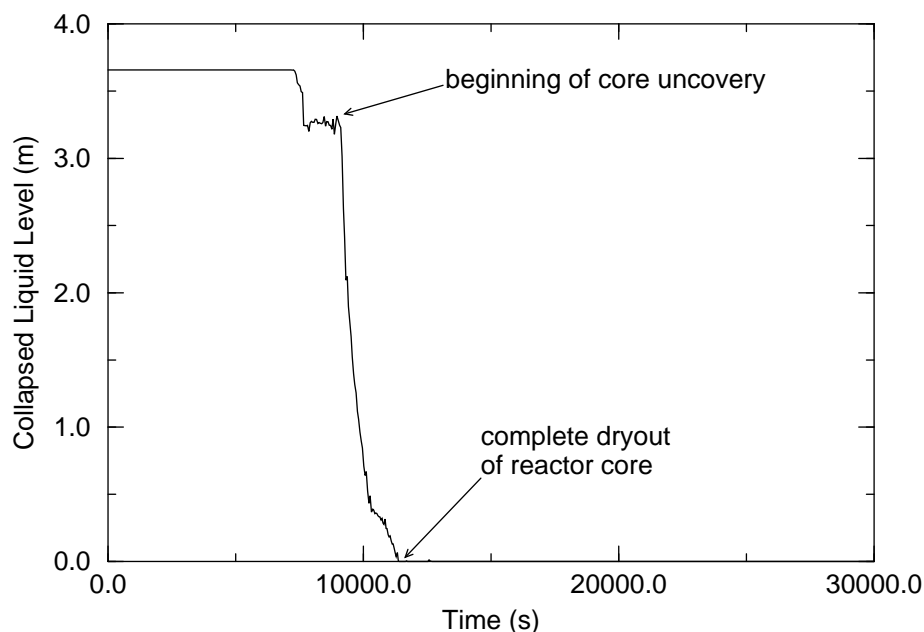


Figure B-5. Reactor power history from 0.0 to 30,000 seconds.

The calculated history of the collapsed liquid level in the reactor core is shown in Figure . The reactor core was calculated to begin to uncover at 8,500 seconds. The rate of uncover decreases as the water level drops to the bottom of the core. By 11,200 seconds, the core is calculated to be completely uncovered.



Collapsed liquid level in reactor vessel.

The calculated pressure history in the cold leg of the primary coolant system is shown in Figure B-6. The pressure decreases following reactor scram due to the steam generators removing more energy than that produced in the reactor core by decay heat. Oscillations occur during the period in which the steam generators dry out due to steam generator secondary relief valves. Following steam generator dryout the pressure in the primary coolant system increased to the PORV opening pressure. For the remainder of the accident the pressure cycled between the PORV opening and closing setpoints.

The calculated maximum temperature of the reactor core during the accident is shown in Figure B-7. The reactor core begins to heatup following the beginning of core uncover at 9,000 seconds. The rate of heat increases when oxidation begins for the parts of the core with a temperature greater than 1,000 K. During the most intense part of oxidation the rate of heatup is about 2.2 K/s. The oxidation of 100% of the cladding results in a slower rate of heatup of the cladding. In a few locations in the reactor core the oxidation stopped due to meltdown of the metallic part of the fuel rod cladding. After the oxidation driven heatup of the reactor core has been completed, the rate of heatup is reduced to about 0.2 K/s in response to decay heat. Ceramic melting of the reactor core is calculated to begin at a time of 12,860 seconds and at a temperature of 2,870 K, which is the eutectic melting temperature of a mixture of UO_2 and ZrO_2 . The temperature then increases to 3,130 K at 20,000 seconds and then remains constant for a long period of time. The temperature remains constant because of a phase change in the UO_2 . The occasional small, temporary decreases in maximum temperature are due to material at a temperature less than the melting temperature of UO_2 becoming a part of the molten pool.

Subsequent calculations should be performed with a correction to the temperature range in which the heat of fusions of ZrO_2 and UO_2 are taken into account.^a As the mixture heats up above its solidus

a. Personal communication, Don Hagman, EG&G Idaho, Inc., November. 5, 1993.

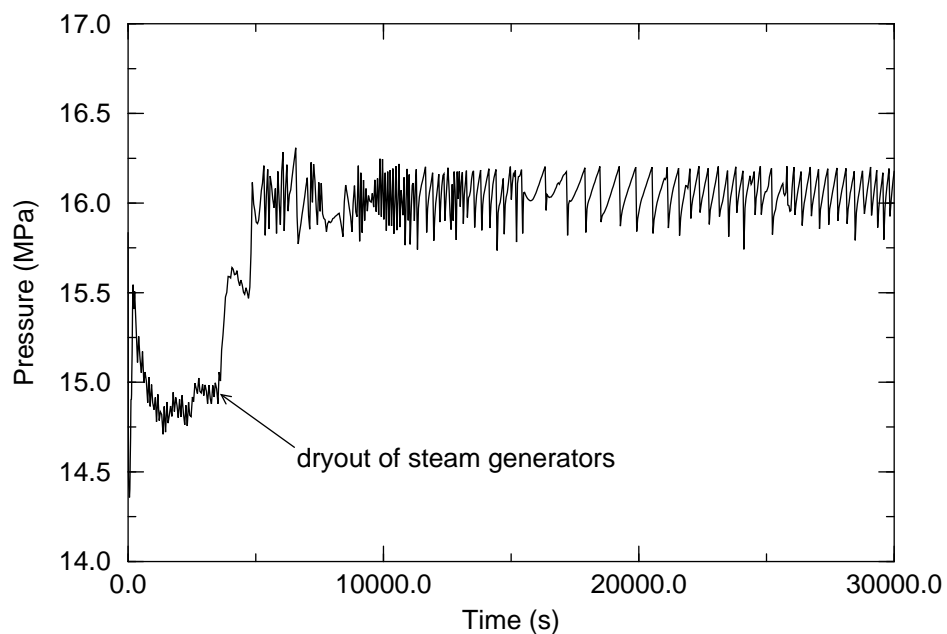


Figure B-6. Pressure history of primary coolant system.

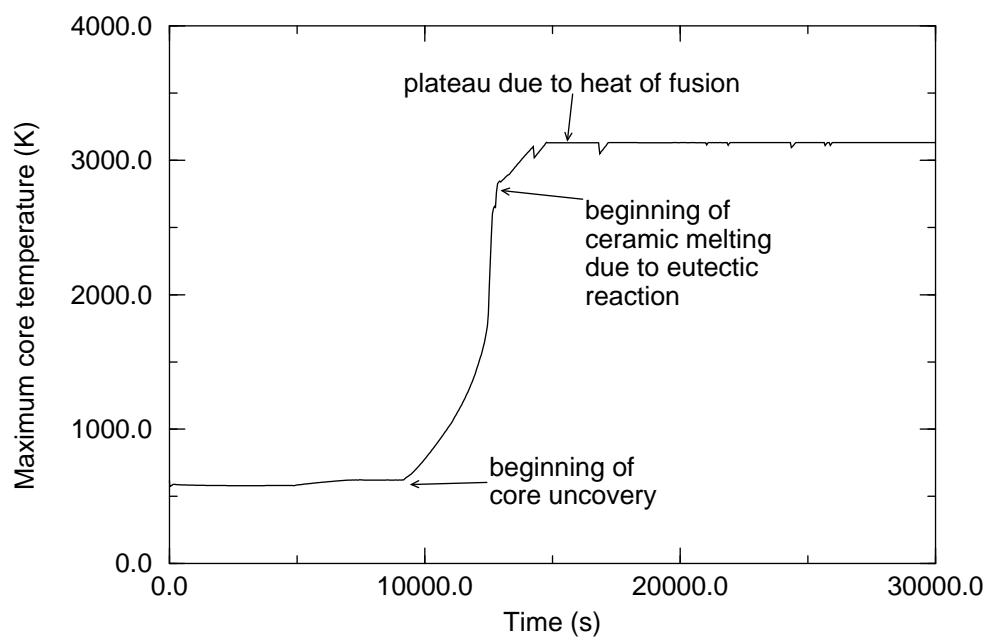


Figure B-7. History of maximum core temperature.

temperature, the heat of fusion should be applied uniformly from its solidus temperature to its liquidus temperature. The solidus temperature is less than 2,850 K and the liquidus temperature is less than 2,900 K for a mixture of UO_2 and ZrO_2 as was calculated to exist in the Surry TMLB'. As a result the heat of fusion

in the UO_2 increases the heat capacity of a mixture of UO_2 and ZrO_2 in the temperature range of about 2,850 K to 2,900 K instead of at a temperature of 3,130 K as is shown in Figure B-7.

The calculated temperature at the 2.7 m elevation of the fuel rods in the three flow channels is shown in Figure B-8. The elevation of 2.7 m is selected because it is the elevation at which intense oxidation begins. The heatup of the fuel rods in the middle flow channel lags that of the center flow channel by about 100 seconds. The heatup of fuel rods in the outer flow channel lags that of the center flow channel by about 300 seconds. The rate of heatup increases significantly due to oxidation when the temperature exceeds 1,850 K and the intensity of the oxidation increases due to the phase change of the cladding oxide. For the fuel rods in the center flow channel, the rate of heatup as this temperature is exceeded changes from 0.5 K/s to 5 K/s. The diversion of flow due to blockage occurring in the center fuel channel at the time of 12,860 seconds causes the rate of heatup of fuel rods in the middle flow channel to decrease at 12,860 seconds. Similarly, the diversion of flow to due blockage occurring in the middle flow channel at 13,050 seconds causes a temporary cooling of the fuel rods in the outer flow channel. The cooling is amplified by the relative size of the outer flow channel to the middle flow channel; the middle flow channel is significantly larger than the outer flow channel.

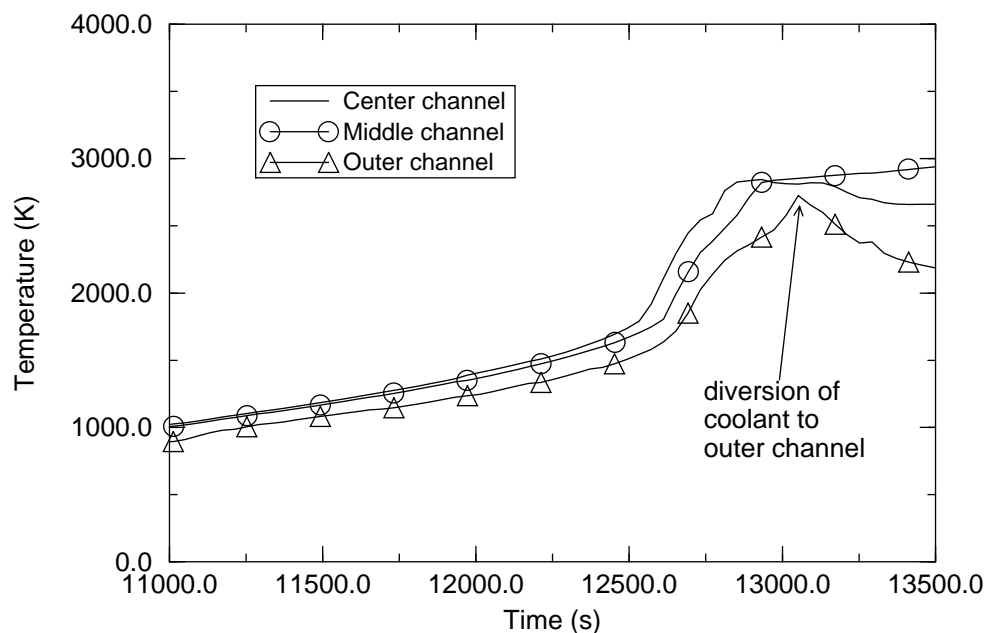


Figure B-8. Temperature histories of fuel rods in each flow channel at 2.7 m elevation.

The temperature histories in the inner and outer flow channels at the midplane of the reactor core are significantly effected by the blockage that is calculated to occur in the middle flow channel. The elevation of 2.0 m is slightly above the midplane of the core. The calculated temperature histories at the 2.0 m elevation for the fuel rods in the three flow channels are shown in Figure B-9. The fuel rods in the middle flow channel heatup a little faster than those in the inner channel. This more rapid heatup occurs due to the natural circulation pattern that has developed in the reactor vessel. The steam is calculated to flow up the center and middle channels of the reactor core and down the outer channel. In the 10,000 to 12,500 seconds period of time the steam velocity in the center channel is about twice that in the middle flow channel. Since the steam has a large amount of heat capacity due to the high pressure in the reactor vessel, this difference

in steam velocities causes a little slower rate of heatup of the fuel rods in the center flow channel relative to that in the middle flow channel. As a result, the fuel rods in the middle flow channel are calculated to begin ceramic melting before fuel rods in the center channel. The onset of ceramic melting in the middle flow channel results in a diversion of coolant to the center flow channel and a significant cooling of fuel rods in the center flow channel. The calculated extent of cooling is amplified by the large cross-section area of the middle flow channel relative to the inner flow channel. The inner flow channel is calculated to be blocked first due to ceramic melting at the elevation of 2.7 m at 22,000 seconds. This blockage, however, is not coplanar with that in the middle flow channel. As a result, the fuel rods in the center channel at the 2.0 m elevation stay in the temperature range of 2,000 K to 2,100 K until 25,000 seconds. After this time, the flow in the center flow channel is reduced to the point that heatup of the fuel rods resumes.

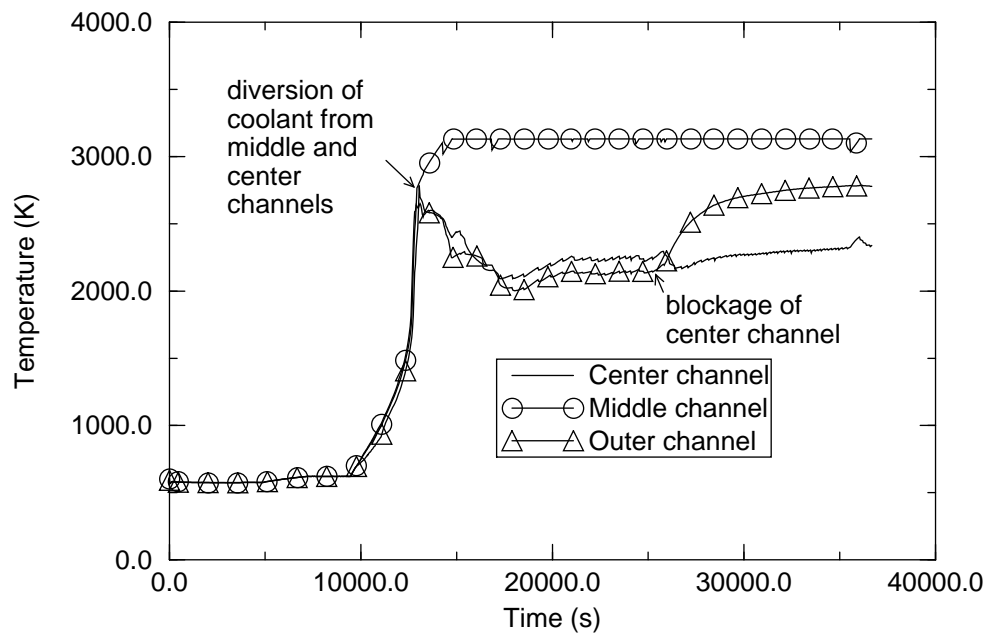


Figure B-9. Temperature histories of fuel rods in each flow channel at 2.0 m elevation.

The accumulated production of hydrogen is shown in Figure B-10. The total amount of hydrogen produced in the reactor core is calculated to be 420 kg. The calculated rate of hydrogen production in the reactor core is shown in Figure B-11. Most of the hydrogen production is calculated to take place between 10,000 and 15,000 seconds. The peak rate of hydrogen production is 0.7 kg/s.

The calculated local extent of oxidation of the fuel rod cladding for three different locations in the reactor core are shown in Figure B-12. This figure shows the thickness of the oxide shell in the fuel rod cladding as a function of time. The thicknesses are shown for fuel rods in each of the three flow channels at an elevation of 2.7 m. The elevation of 2.7 m is selected because it is the elevation at which intense oxidation begins. For the fuel rods in the center flow channel, the figure shows that the oxidation is calculated to occur at an approximately constant rate for 200 seconds from 12,600 to 12,800 seconds. The cladding is completely oxidized at 12,800 seconds at the 2.7 m elevation for the fuel rods in the center flow channel. The oxidation of the fuel rods in the middle flow channel occurs about 100 seconds later than that in the center channel. Oxidation of the fuel rods in the outer flow channel occurs about 250 seconds later than that in the center flow channel.

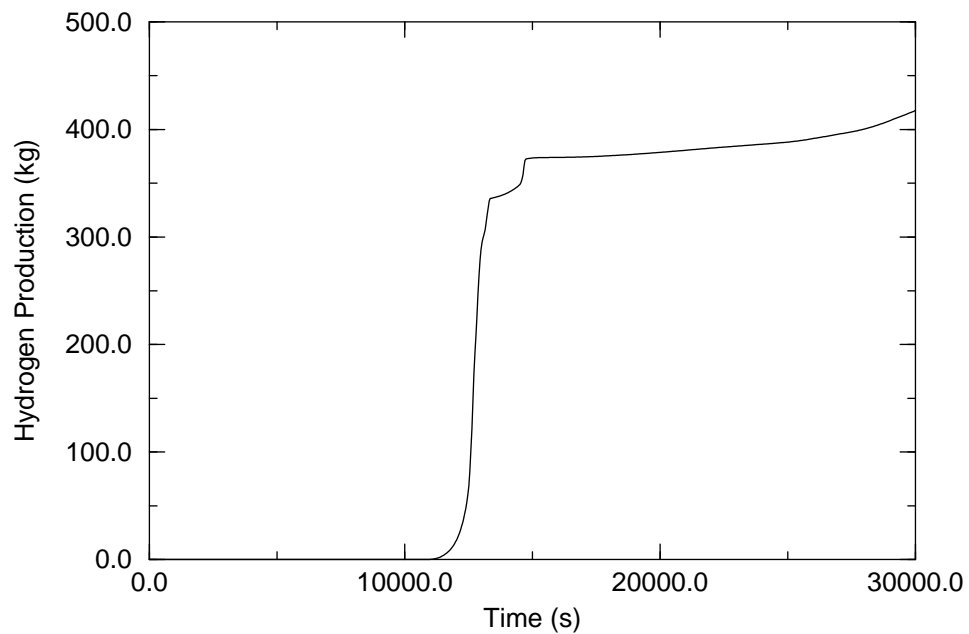


Figure B-10. Accumulated production of hydrogen.

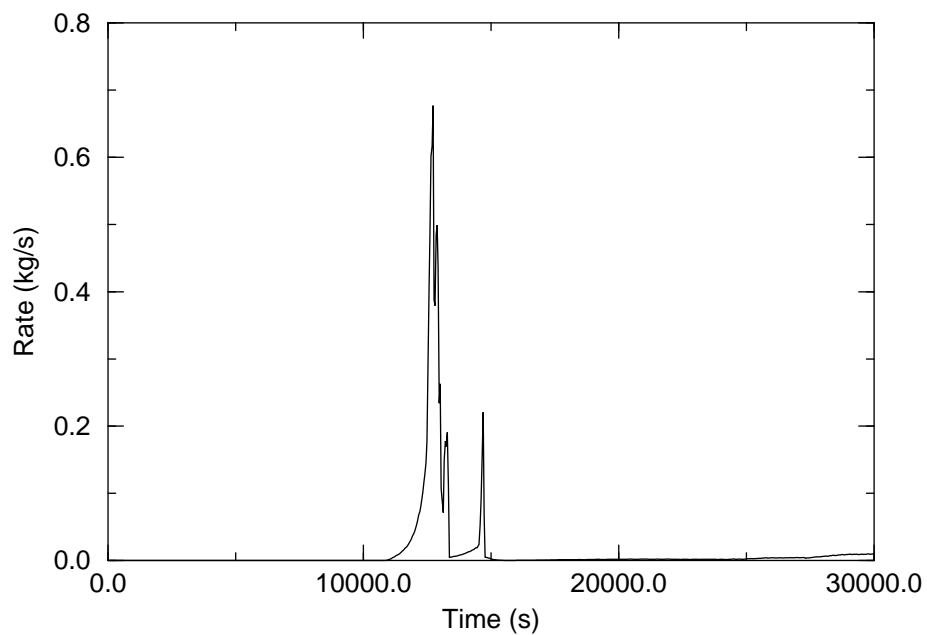


Figure B-11. Rate of hydrogen production due to oxidation of reactor core.

The natural circulation flow pattern in the reactor core is shown in Figure B-13 of the velocity of the steam at the top of the core for the three flow channels. After 9,000 seconds the reactor core has uncovered. After core uncover, the steam velocity is upward in the center and middle flow channels and downward in the outer channel. From 10,000 to 12,400 seconds the steam velocity in the center flow channel is upward

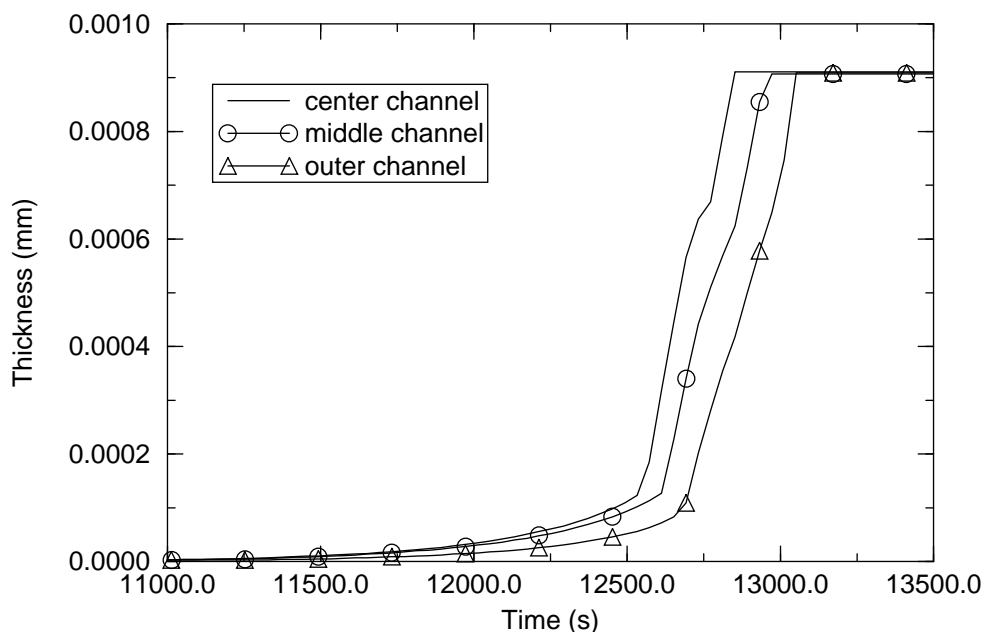


Figure B-12. Extent of oxidation of fuel rods in each flow channel at elevation of 2.7 m.

with an approximate velocity of 0.3 m/s and is downward with an approximate velocity of 0.6 m/s in the outer flow channel. The velocity in the middle channel is upward with a velocity about half that of the center channel. The natural circulation pattern is maintained even after blockage of the core due to ceramic melting extending radially across the entire core. This blockage spread across the entire core occurs at 28,770 seconds.

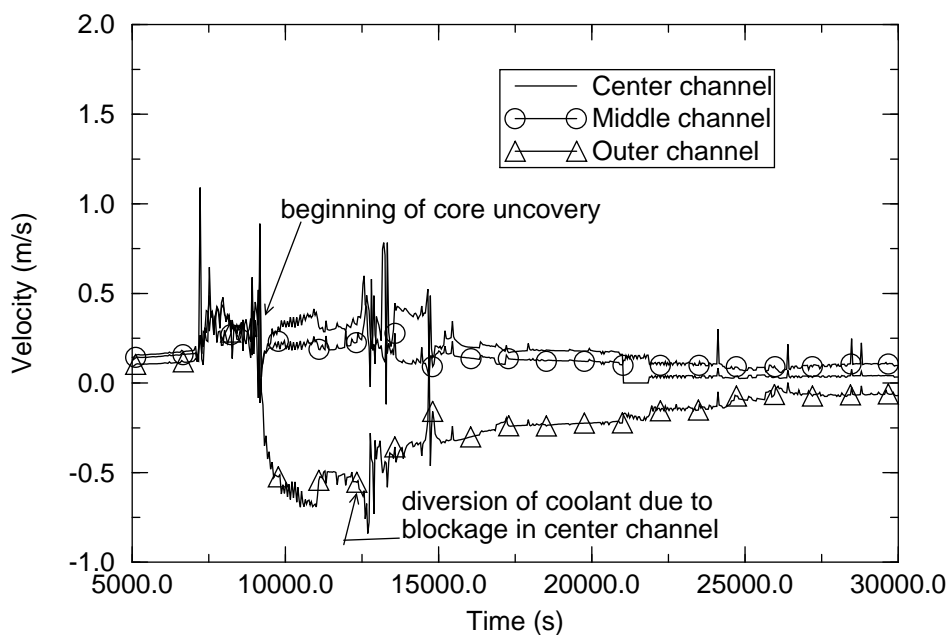


Figure B-13. Velocities of steam in each flow channel at top of reactor core.

The steam going from the core region to the upper plenum is hot enough to melt the stainless steel structures in the upper plenum. The temperature histories of the steam at the top of the core are shown in Figure B-14. The steam temperature for the center channel has a maximum value of 2,700 K at 12,800 seconds. This is the time the oxidation of the reactor core is the most intense and is just before blockage in the middle channel due to ceramic melting. After this time, the steam temperature for the center channel decreases to 2,500 K at 15,000 seconds and then gradually increases to 2,700 K at 20,000 seconds. The temperature of the steam in the middle channel is almost as hot as that in the center channel. The steam temperatures are well above the 1,700 K melting temperature of the stainless steel structures in the upper plenum. The temperature of the steam for the outer channel is about 300 K cooler than that for the center and middle channels. The temperature is cooler at this location because the steam is coming from the upper plenum region where it has been cooled by the structures in the upper plenum. The steam for the center and middle channels is coming from the core region.

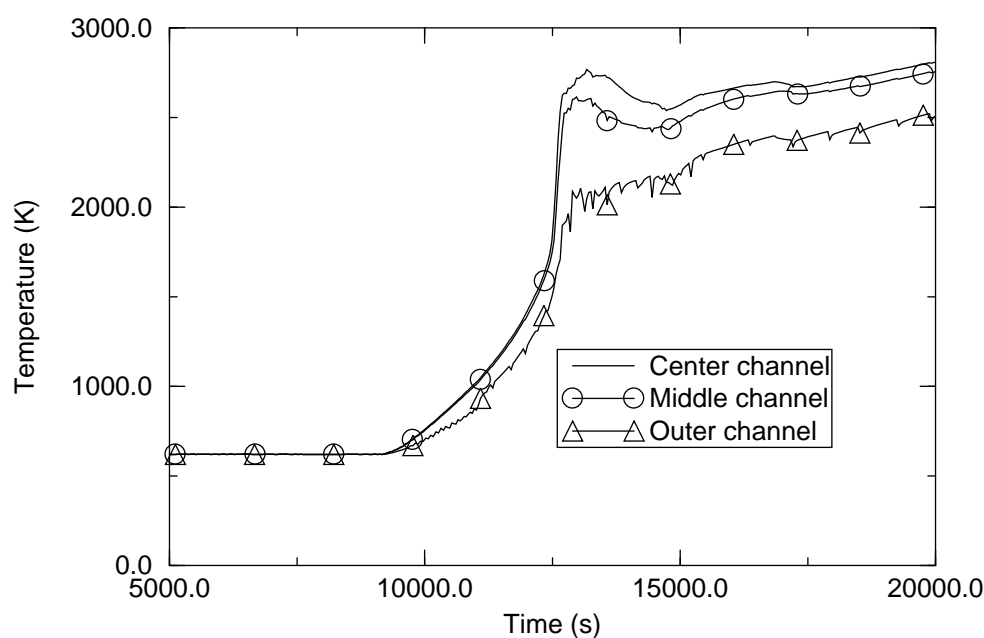


Figure B-14. Steam temperatures in each flow channel at top of reactor core.

The structures in the lower part of the upper plenum were calculated to be heated to temperatures above their melting temperature. The calculated temperature histories for the structures in the lower and upper parts of the upper plenum are shown in Figure B-15. These structures are made of stainless steel and have a melting temperature of about 1,700 K. The structures in the lower part of the upper plenum are heated to their melting temperature at a time 13,000 seconds. The melting and ablation of these structures was not modeled. The structures in the upper part of the upper plenum were heated to a maximum temperature of 1,370 K at 30,000 seconds. If the ablation of the structures in the lower part of the plenum had been modeled, the calculated temperature of the structures in the upper part of the plenum would have been higher.

The piping in the surge line was calculated to be rapidly heated after intense oxidation began in the reactor core. The calculated temperature history of the surge line is shown in Figure B-16. The temperature

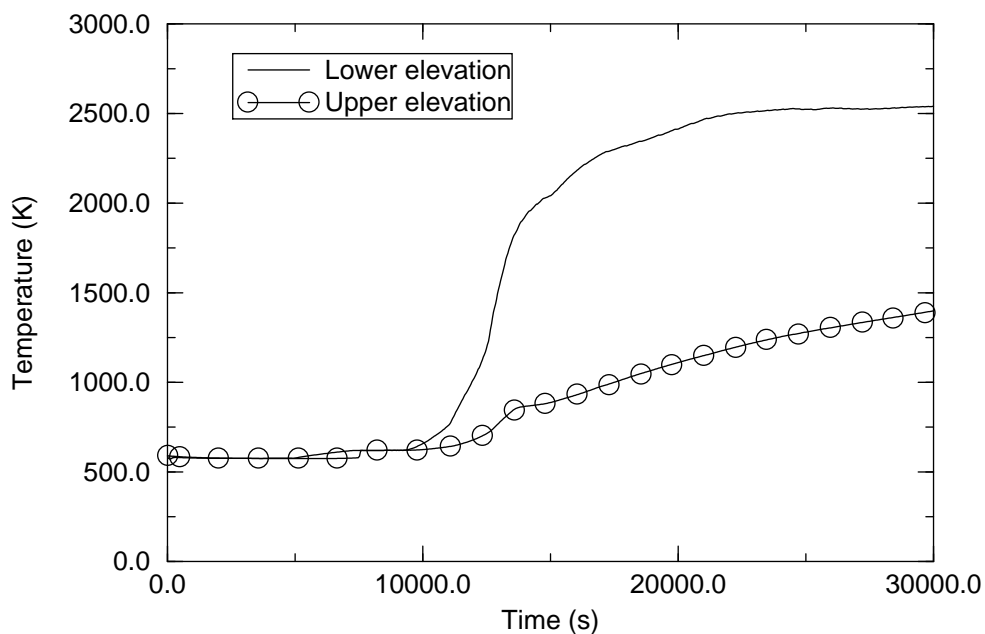


Figure B-15. Temperatures of structures in lower and upper part of upper plenum.

was calculated to increase from 600 K to 1,300 K in the period from 11,000 to 13,035 seconds. The surge line was then calculated to fail due to creep rupture, however, a breach in the surge line was not modeled.

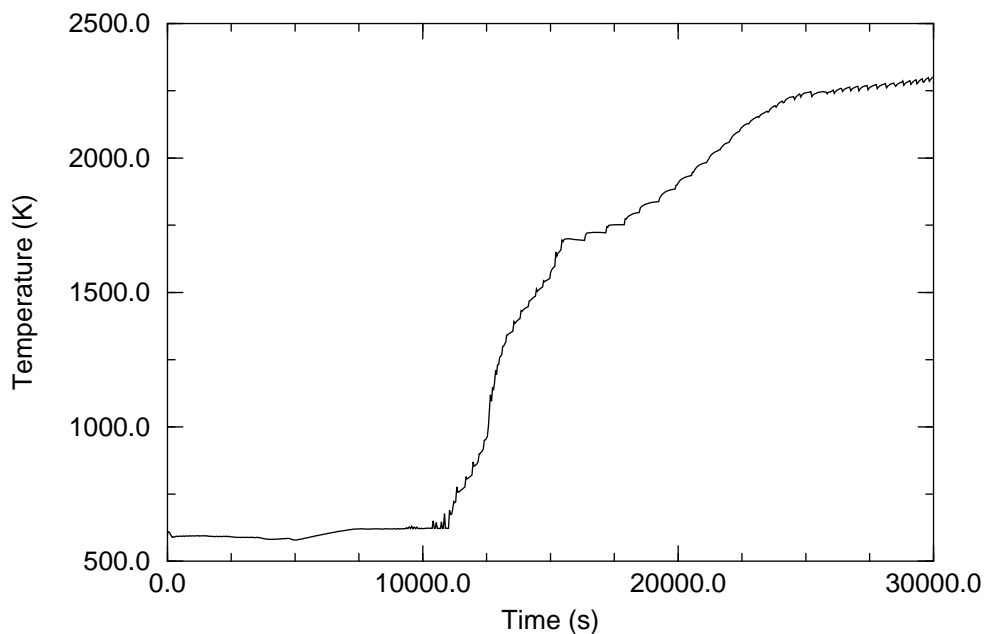


Figure B-16. Temperature history of surge line.

The effective radius of the pool of molten core material was calculated to have a maximum value of 1.6 m. The history of the calculated effective radius is shown in Figure B-17. The effective radius is the

radius of a hemisphere that has a volume equal to the volume of molten material. Core material is calculated to become molten at 12,860 seconds. The effective radius gradually increases from 0.8 m to 1.6 m in the period from 12,860 to 31,000 seconds. The increase in the value of the effective radius is terminated by the slumping of molten material from the core region to the lower head.

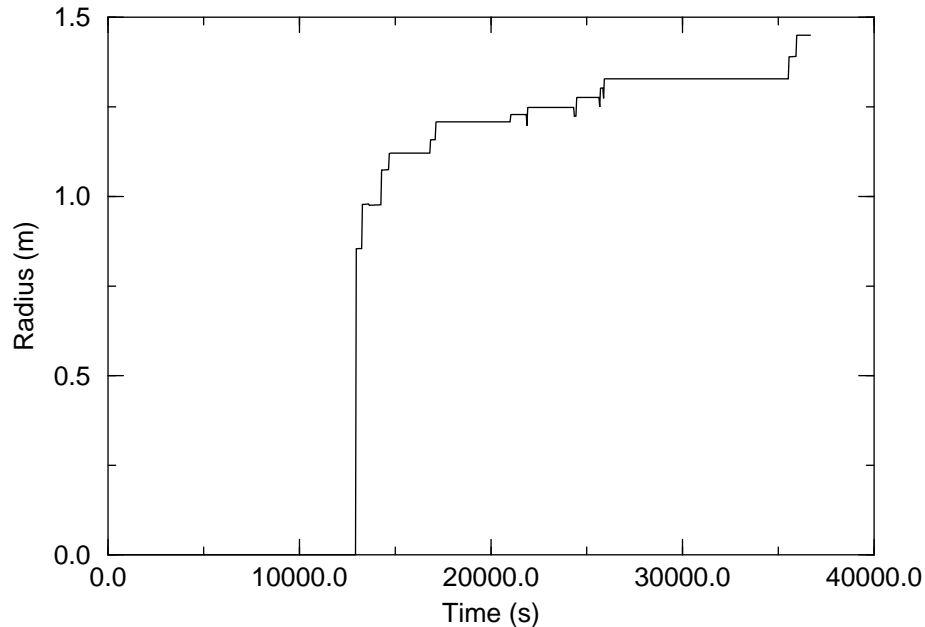


Figure B-17. Effective radius of molten pool.

The evolution of the molten pool is next described. At 14,372 seconds, the molten pool was confined to the middle channel in the elevation interval of 1.5 m to 2.0 m. The center flow channel had a plane blockage due to metallic meltdown at an elevation of 0.4 m. At 20,000 seconds the molten pool is still confined to the middle flow channel and has propagated downward to the elevation of 1.1 m. At 22,000 seconds molten material has formed in the upper part of the center flow channel. The molten materials in the center and middle flow channel did not form a coplanar blockage. At 26,000 seconds molten material has formed in the upper part of the outer flow channel. At 28,000 seconds the plane blockage in the center flow channel had slumped to an elevation of 0.0 m. At 36,275 seconds, the time the lower head is calculated to fail due to creep rupture, the molten pool is still in the core region of the reactor. The molten material is continuing to slump downward, but at a slow rate.

The calculated rate of melt progression is considered to be significantly slower than that calculated in a best estimate calculation. Four factors contribute to the calculated rate of melt progression being slower than reality: (1) the depressurization of the reactor due to rupture of the surge line was not modeled. As a result, the steam pressure stayed near a value of 16 MPa. Steam at this pressure can absorb significantly more heat from the reactor core than steam at a much lower pressure, (2) structures in the upper plenum were calculated to stay in place even after they were calculated to melt. As a result, the capacity of the upper plenum to absorb heat from the reactor core was overpredicted, (3) the possibility for material from the upper plenum slumping to the core region and blocking the circulation of steam was not modeled, and, (4) cooling of the molten pool was overpredicted due to deficient modeling of the heat capacity of a mixture of UO_2 and ZrO_2 during the period of melting of these materials due to eutectic reaction. This

deficiency caused the molten pool to be modeled as being cooled by natural convection of its material during the long periods where the heat of fusion of UO_2 and ZrO_2 were being accounted for.

The calculation required 49 hours of Cray X-MP/216 time. The cumulative CPU time is shown in Figure B-18. The CPU time accumulated at a rate of 1.5 seconds of CPU per seconds of problem time out to 12,500 seconds. After this time, the CPU accumulated at a rate of about 7 seconds of CPU per second of problem time. The time step in the period from 0.0 to 12,500 seconds was about 0.2 seconds. After this period, the time step averaged about 0.06 seconds. The time step of 0.06 seconds is considerably less than the Courant time step.

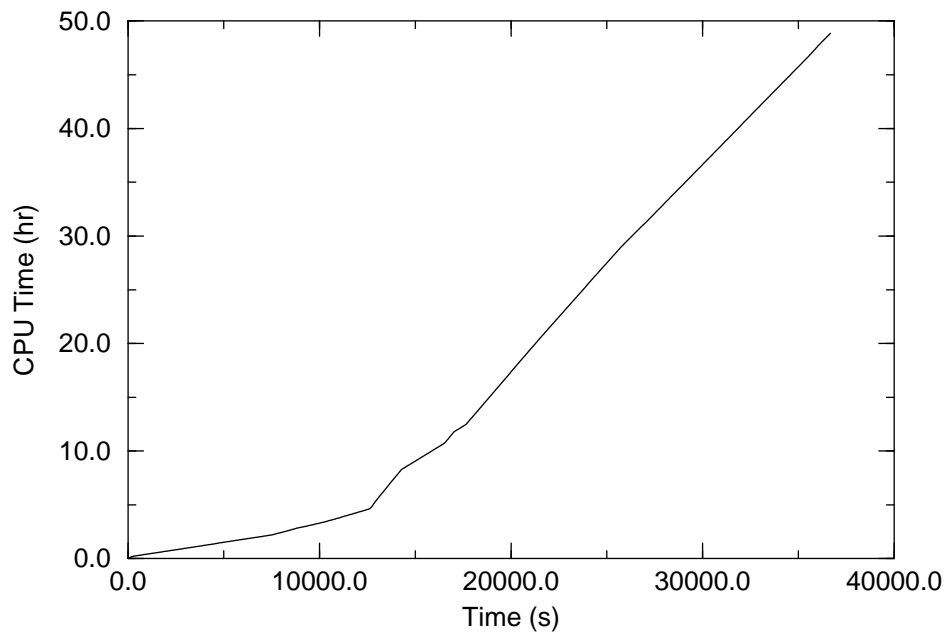


Figure B-18. Accumulated amount of CPU time on CRAY X-MP/216 computer.

B.3. RADIAL AND AXIAL NODALIZATION SENSITIVITY STUDY

The sensitivity of SCDAP/RELAP5 results to the radial and axial nodalization of the reactor core are presented in this section. Analyses of a TMLB' severe accident in the Surry reactor with three different nodalizations of the reactor core are performed. The extent and rate of damage progression calculated by these analyses are compared to determine the sensitivity of code results to nodalization.

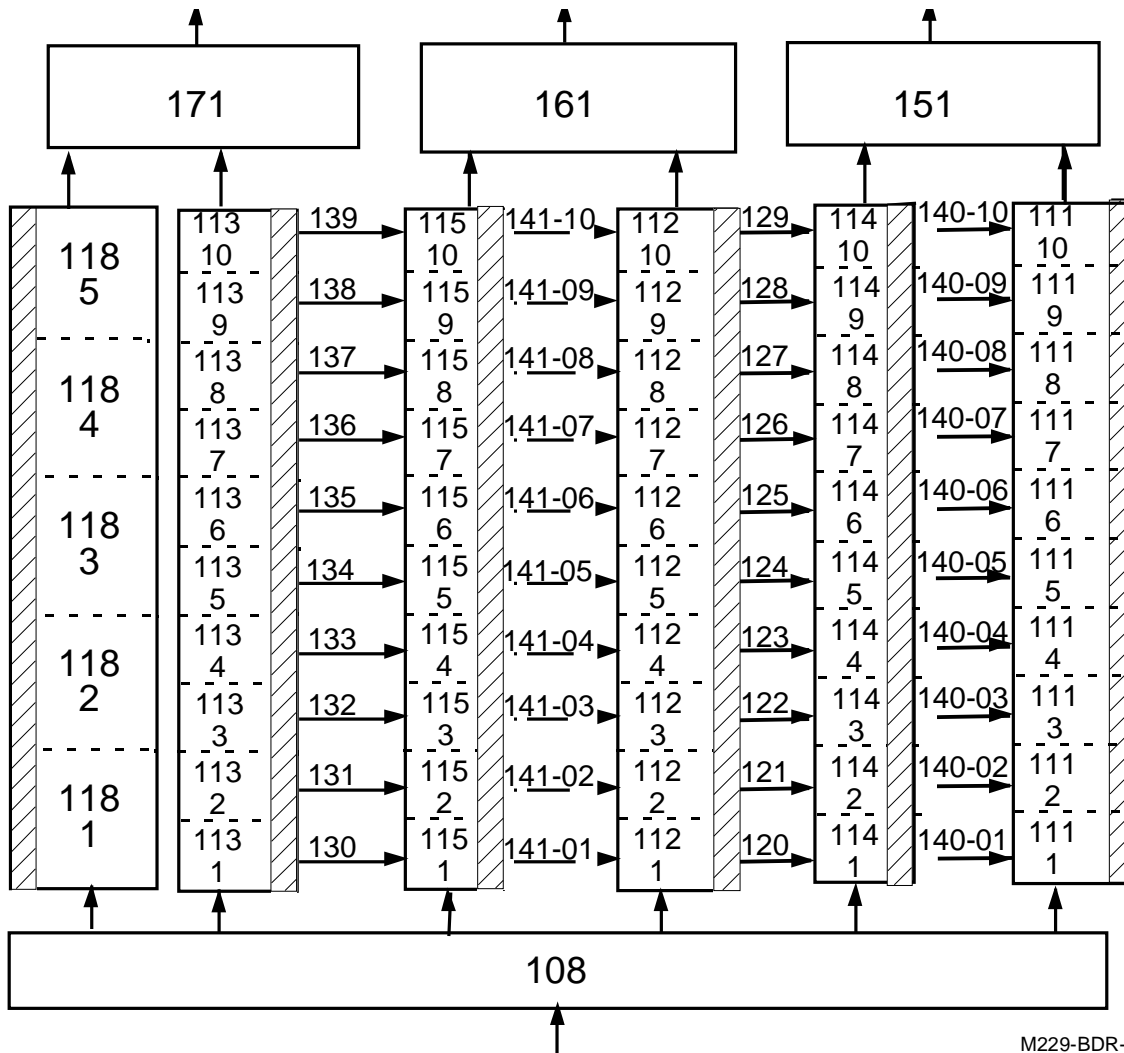
The following three nodalizations of the reactor core were performed. The first nodalization, identified as the 3x10 case, divided the reactor core into three flow channels with ten axial nodes for each flow channel. The second nodalization, identified as the 5x10 case, divided the reactor core onto five flow channels with ten axial nodes for each flow channel. The third nodalization, identified as the 5x20 case, divided the reactor core into five flow channels with twenty axial nodes for each flow channel.

The nodalization of the reactor core for the 5x10 case is shown in Figures B-19 and B-20. A cross-section in the axial direction of the reactor core is shown in Figure B-19 and a radial cross-section of the reactor core is shown in Figure B-20. The center flow channel is represented by control volume number 111 and the outer flow channel by control volume number 113. The three middle flow channels are represented by control volumes 114, 112, and 115, respectively. The five flow channels are connected to each other by crossflow junctions, thus, flow in the lateral direction through the core is modeled. The center flow channel represented 5 fuel assemblies, the channel next to it represented 20 fuel assemblies, the next channel represented 36 fuel assemblies, the next channel represented 60 fuel assemblies, and the outermost flow channel represented 36 fuel assemblies. For the 5x10 and 5x20 cases, the reactor core was represented by a total of ten SCDAP components, namely a fuel rod and control rod component for each of the five flow channels.

The nodalization for the 5x20 case divided the reactor core into twenty evenly spaced nodes instead of ten evenly spaced nodes. The nodalization in the radial direction is the same as for the 5x10 case.

The variation in rod power in the radial direction for the five channel cases is shown in Table B-3. For the five channel cases, the power was almost uniform within the two inner most channels and within the next two flow channels outside of the two inner most channels. The power in the outer flow channel is significantly less than that in the other flow channels. The variation in power in the axial direction was the same for all of the flow channels. The peak power is 1.15 times the average power in the axial direction.

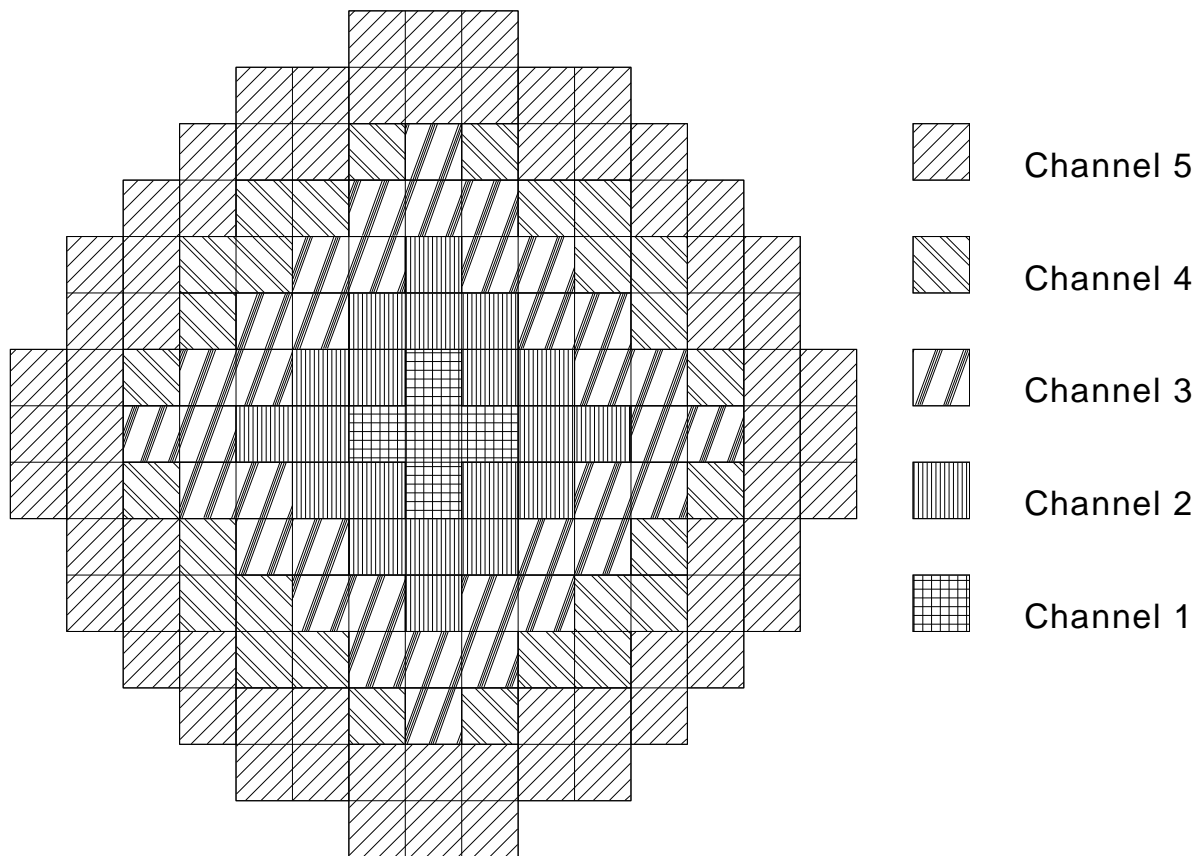
The calculated progression of damage for the three cases is shown in Table B-4. Damage progression begins with rupture of the fuel rods. The earliest calculated time of fuel rod rupture is 11,678 seconds for the 5x20 case and the latest calculated time of rupture is 12,066 seconds for the 3x10 case. These differences in rupture time are small enough to indicate that the nodalization does not significantly effect the calculated time of rupture of fuel rods. The next threshold of damage is the melting and slumping of spacer grids. The timing for this threshold is nearly the same for the 3x10 and 5x10 cases. The time for beginning of spacer grid slumping for the 5x20 case was not available due to part of the output file for the calculations not being saved. The next damage threshold is the melting of fuel rod cladding due to heat up, not liquefaction due to eutectic melting. The timing of this threshold is also almost the same for the three cases. The next damage thresholds are the creep rupture of the surge line and the hot leg with the pressurizer. Again, the timing for these thresholds of damage is nearly the same for the three cases. The next threshold is the beginning of ceramic melting and thus the beginning of a pool of molten material in



M229-BDR-1293-001

Figure B-19. Axial cross-section showing nodalization of vessel for case of five flow channels and ten axial node.

the reactor core. The greater the extent of nodalization, the later the calculated time for this threshold. The time for this threshold ranged from 12,860 seconds for the 3x10 case to 17,040 seconds for the 5x20 case. The time for melting the first 20,000 kg of UO_2 was about 3,000 seconds earlier for the three channel case than it was for the two five channel cases. The time for melting the first 20,000 kg of UO_2 was almost identical for the 5x10 and 5x20 cases. The last threshold of damage is the melting of UO_2 in the outer part of the core and thus the formation of a molten pool is spread across the entire core in the radial direction. The time for this threshold of damage is nearly the same for the 3x10 and 5x10 cases. The time of this damage threshold for the 5x20 case was not available due to the calculations being performed out to the maximum time of 20,000 seconds, when the molten pool had spread through the inner four channels but not through the outer most flow channel. The molten pool size and extent of downward propagation are nearly the same for the 3x10 and 5x10 cases at 30,000 seconds. For both of these cases at this time, the effective radius of the molten pool is 1.33 m and the bottom of the molten pool is at an elevation of 1.1 m. The latest time at which the 5x10 and 5x20 cases can be compared is 20,000 seconds. At this time, the effective radius of the molten pool for the 5x10 case was 1.1 m and for the 5x20 case was 1.05 m. In the



M229-BDR-1293-002

Figure B-20. Radial cross-section of nodalization for five channel case.**Table B-3.** Radial power distribution for five channel case.

Flow channel	Average fuel rod power at start of transient (kW/m)	Ratio of power to average core power
1	24.35	1.169
2	24.32	1.167
3	21.85	1.048
4	21.84	1.048
5	15.81	0.759

5x10 case the bottom of the molten pool was at an elevation of 1.1 m and in the 5x20 case it was at an elevation of 2.0 m. These differences in calculated evolution of the molten pool are due to differences calculated in the time of initial molten pool formation. As discussed in more detail below, these differences in calculated time of initial molten pool formation are due to small differences in the calculated time at which the cladding is completely oxidized. The calculated time to creep rupture of the lower head was

Table B-4. Comparison of the timing of damage progression for the 3x10, 5x10, and 5x20 cases.

Event or threshold in damage progression	3x10	5x10	5x20
	time (s)	time (s)	time (s)
Beginning of rupture of fuel rods	11,950	12,066	11,678
Beginning of slumping of spacer grids	12,196	12,361	-
Beginning of melting of fuel rod cladding (temperature > 2,200 K)	12,560	12,650	12,360
Beginning of ceramic melting (beginning of molten pool)	12,860	13,328	17,040
Ceramic melting of 20,000 kg of UO ₂	17,100	20,060	20,000
Ceramic melting spread across entire core	28,770	28,600	-
Rupture of lower head	36,275	36,600	-

almost the same for the 3x10 and 5x10 cases. In both of these cases, the lower head was calculated to fail due to creep rupture before slumping of the molten pool in the core region. The heatup of the lower head by natural circulation of hot steam was sufficient to weaken the strength of the lower head where the high steam pressure in the vessel caused it to fail by creep rupture. Although the calculated time to failure is not available for the 5x20 case, the calculated conditions of the steam in this case are similar to the other two cases and thus indicate that the lower head would predict rupture at about the same time as was calculated for these cases.

The history of the maximum temperature in the reactor core for the three cases is shown in Figure B-21. In the period from 13,000-20,000 seconds the maximum core temperature for the 5x20 case is 100-300 K less than that for the other two cases. In all three cases the maximum core temperature approached the ceramic melting temperature of a mixture of UO₂ and ZrO₂, but the maximum core temperature did not quite exceed the ceramic melting temperature for the 5x20 case. The ceramic melting temperature is about 2,870 K for the mixture of UO₂ and ZrO₂ at the location of maximum core temperature. The temperature driven oxidation excursion was not quite completed at the time that the maximum core temperature exceeded the ceramic melting temperature for the 3x10 and 5x10 cases. However, for the 5x20 case, however, the maximum temperature at any location in the core never exceeded 2,800 K before that location was completely oxidized. As a result of a blockage developing in the 3x10 and 5x10 cases before the completion of oxidation of the fuel rod cladding, a relatively uncoolable blockage developed in the core for these cases that caused decay heat to heat the blockage region up to the temperature at which the heat of fusion of UO₂ is accounted for. After this temperature is attained, which is about 3,130 K, the temperature remained constant for a long period of time. On the other hand, for the 5x20 case the core maintained an intact and coolable geometry after heatup from oxidation had ceased due to the complete oxidation of fuel rod cladding. Also, no metallic meltdown with the result of plane blockage was calculated to occur for the 5x20 case, while for the 3x10 and 5x10 cases, a metallic meltdown of the fuel rods in the center flow channel with a resulting plane blockage was calculated to occur. For the 5x20 case a core geometry was maintained that resulted in natural circulation being calculated to remove a significant portion of the decay heat from the core and limit the heatup of the core to a rate of about 0.1 K/s. At 20,000

seconds ceramic melting was calculated to begin for the 5x20 case. After this time, the maximum core temperatures for the three cases were similar.

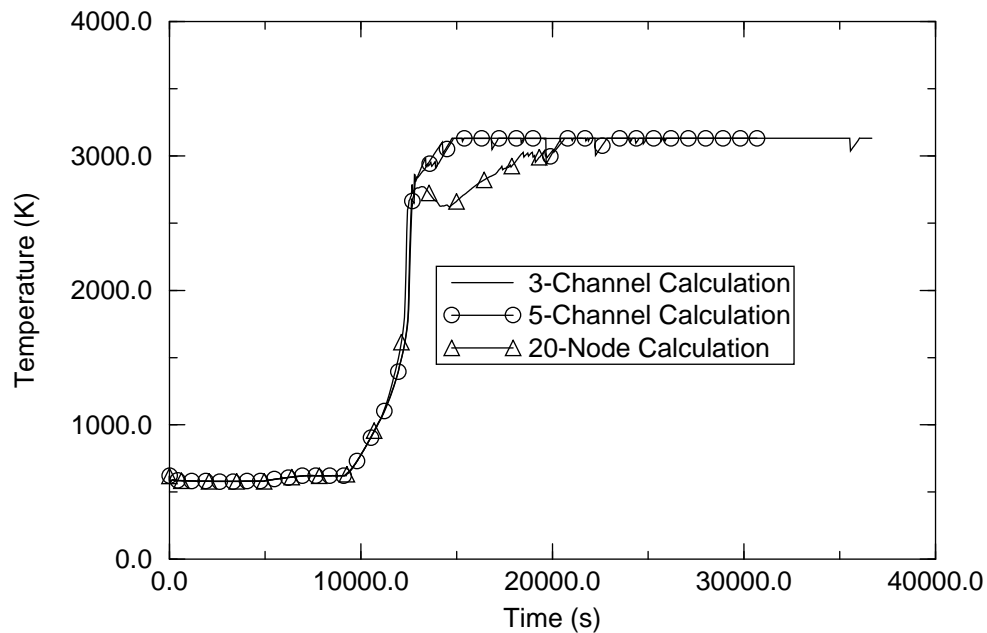


Figure B-21. Comparison of maximum core temperature for the 3x10, 5x10, and 5x20 cases.

The temperatures at an elevation of 2.7 m for the center flow channel during the period of the oxidation excursion are significantly different for the three cases. The 2.7 m elevation was selected because it is near the elevation at which the maximum temperature in the reactor core occurs during the period in which the reactor core heats up rapidly due to oxidation. The temperature history for the three cases is shown in Figure B-22. For the 3x10 case, blockage due to ceramic melting occurred first in the middle flow channel. As a result, the fuel rods in the center flow channel were cooled by steam diverted from the middle flow channel to the center flow channel. For the 5x10 case, ceramic melting and the resulting blockage occurred first in the two inner most flow channels, then the rods in the center channel at the 2.7 m elevation heat up significantly more rapidly than those in the center channel of the 3x10 case. For the 5x20 case the cladding was completely oxidized at 12,500 seconds, when its maximum temperature was 2,600 K. After complete oxidation of the cladding at this location, the rate of heatup decreased significantly. For the 3x10 and 5x10 cases, however, the cladding did not approach complete oxidization until its temperature approached the ceramic melting temperature. There is the possibility that the finer the degree of axial nodalization the more rapidly heat may be calculated to be transferred by axial heat conduction from the hot spot of the fuel rod. This effect may be the reason why meltdown was not calculated for the 5x20 case during the oxidation excursion and thus why the cladding was calculated to be completely oxidized before reaching the temperature at which ceramic melting occurs, ~2,870 K.

Figure B-22 shows that a more rapid heatup was calculated for the 5x20 case than for the other two cases after oxidation began when the cladding temperature exceeded 1,000 K. This difference in heatup may be due to differences in time step between the 5x20 case and the 3x10 and 5x10 cases. Since the heights of the RELAP5 control volumes in the core region are half the size of those for the 3x10 and 5x10 cases, this difference in nodalization results in a Courant time step limit for the 5x20 case that is half the

size of that for the other two cases. As a result, for conditions where the time step is limited by the Courant limit in the core region, the time step for the 5x20 case is half that for the other two cases.

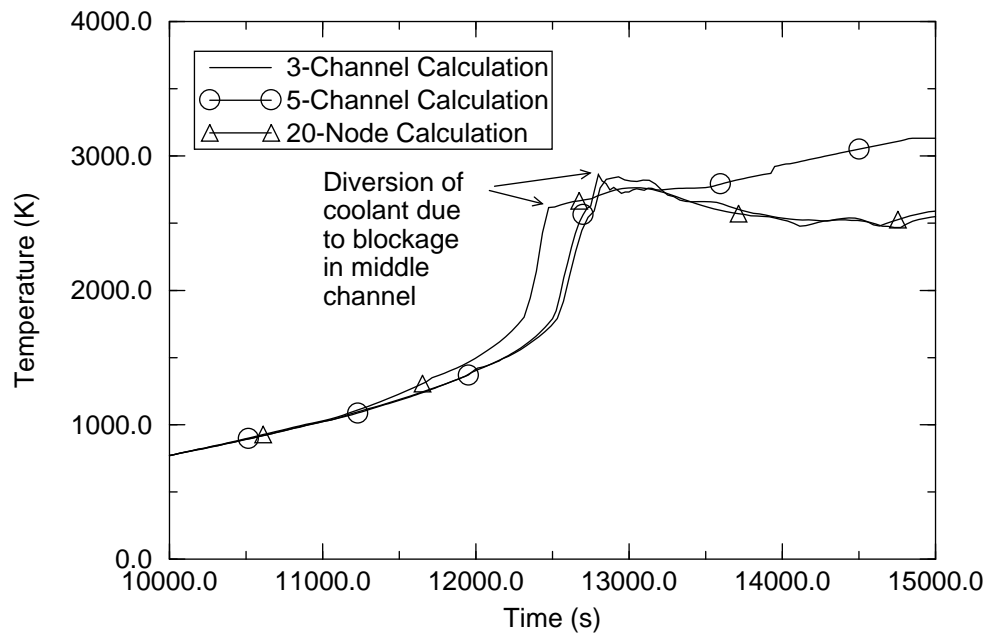


Figure B-22. Comparison of temperatures at the 2.7 m elevation in the center flow channel for the three cases.

The temperature of the fuel rods in the outer most flow channel at an elevation of 2.7 m for the three cases are shown in Figure B-23. The calculated temperature histories for the three cases are somewhat different. The 5x20 case calculated the most rapid rate of heatup at this location during the oxidation excursion. For this case, the cladding at this location was calculated to be completely oxidized by the time that its temperature had attained a value of 2,200 K during the oxidation driven heatup. For the 5x10 case, the cladding was calculated to be completely oxidized by the time that its temperature had attained a value of 2,800 K, which is 70 K less than the ceramic melting temperature at that location. After the cladding was calculated to be completely oxidized at this location, the temperature at this location was calculated to not significantly increase until ceramic melting and the blockage was calculated to occur at 13,328 seconds in the flow channel at a location above 2.0 m. For the 3x10 case, the calculated temperature shows the influence of a flow blockage due to ceramic melting occurring in the middle flow channel at 12,860 seconds. This blockage in the middle channel is calculated to divert a significant amount of flow of steam into the outer channel and to significantly increase the cooling of the fuel rods in outer channel. The fuel rods in the center channel at the elevation of 2.0 m are calculated to heatup at the slow rate of 0.06 K/s in the period from 13,000-20,000 seconds.

The temperature at the 2.0 m elevation for the 3x10 and 5x10 cases are shown in Figure B-24. The differences in temperature between the two cases are due to differences in calculated blockage. The center flow channel for the 3x10 case was calculated to have a blockage due to ceramic melting at a much later time than calculated for the 5x10 case. Both the 5x10 and 5x20 cases calculated that ceramic melting begins in the center flow channel, while the 3x10 case calculates that it begins in the middle channel. The temperature for the 5x10 case at the elevation of 2.0 m is calculated to escalate from 2,600 to 3,100 K at

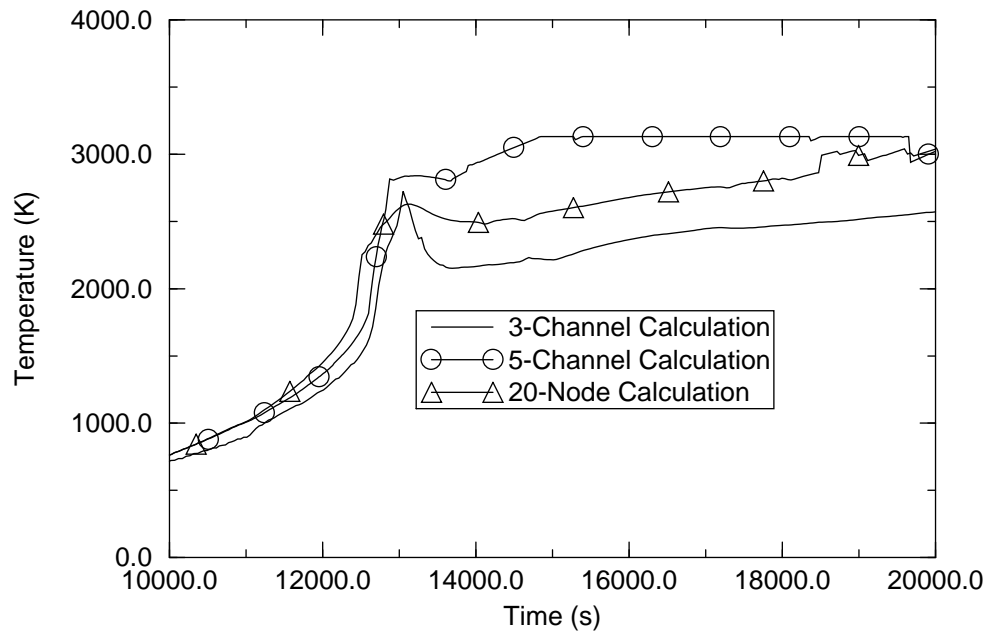


Figure B-23. Temperatures at 2.7 m elevation in outer flow channel for the 3x10, 5x10, and 5x20 cases.

15,000 seconds. This escalation is due to the molten pool propagating down to the 2.0 m elevation. Before 15,000 seconds, the molten pool was located above the 2.0 m elevation for the center flow channel.

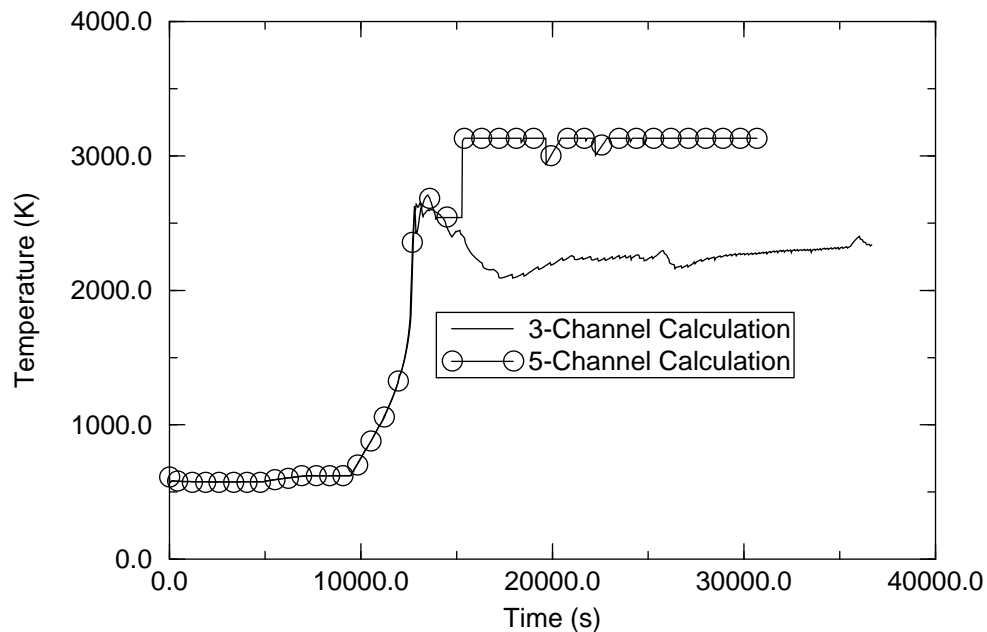


Figure B-24. Temperatures at 2.0 m elevation in center flow channel for the 3x10 and 5x10 cases.

The hydrogen production for the three cases has a similar history. Figure B-25 shows the hydrogen production for the three cases. All three cases show rapid oxidation beginning at 11,000 seconds and

continuing to ~15,000 seconds. Most of the hydrogen produced during the accident was produced during this period. After 20,000 seconds, the hydrogen production for the 3x10 case is 5-10% less than that for the 5x10 and 5x20 cases. At 30,000 seconds, the amount of hydrogen produced for the 5x10 case is 440 kg and for the amount for the 3x10 case is 420 kg.

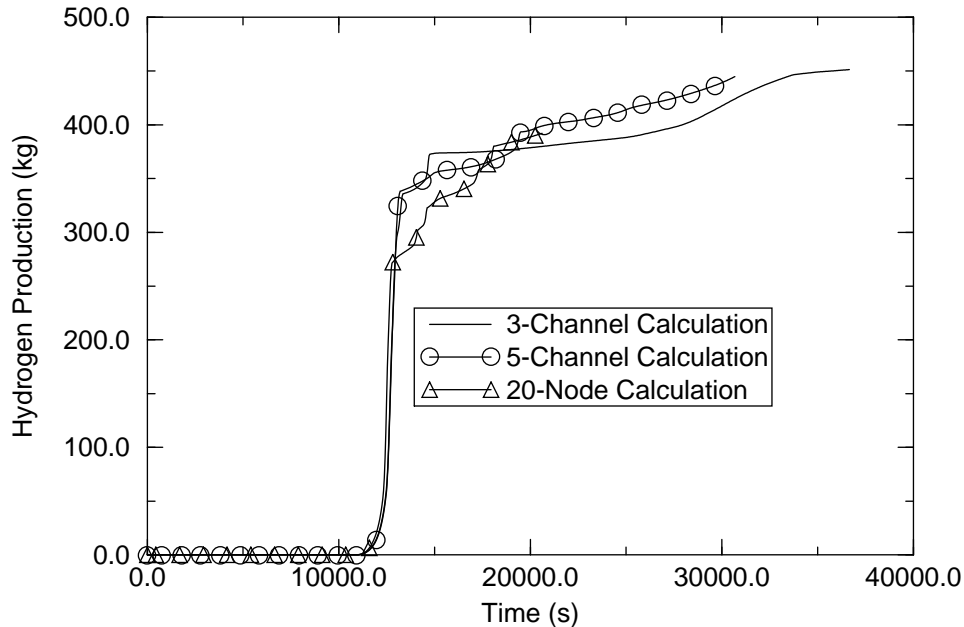


Figure B-25. Accumulated hydrogen production for the 3x10, 5x10, and 5x20 cases.

The distribution in steam velocity at the top of the reactor core was approximately the same for the three nodalizations. Figure B-26 shows the steam velocity for each of the five flow channels for the 5x10 case. The velocity is upward in the four inner flow channels and downward in the outer flow channels. For the four inner flow channels, the velocity is highest in the inner channel and then decreases with respect to distance from the center of the reactor core. This distribution in velocity shows that the 5x10 case calculates a natural circulation pattern where the steam flows upward the center ~80% of the core, flows through the upper plenum, and then flows down the outer 20% of the core. This natural circulation pattern is the same as that calculated by the 3x10 case. The 5x20 case calculated a similar natural circulation pattern. The steam velocity for each of the five channels for the 5x20 case is shown in Figure B-27.

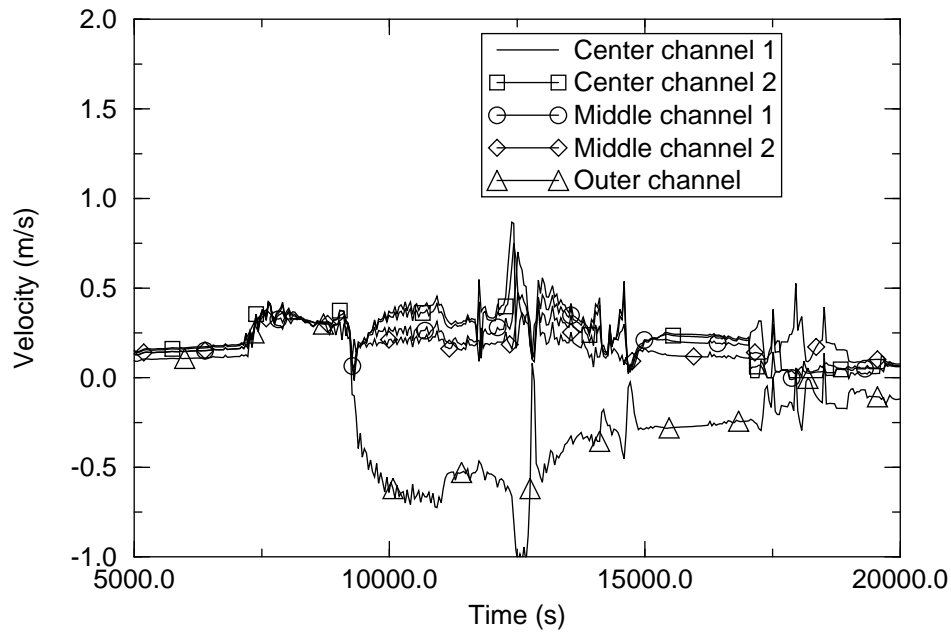


Figure B-26. Radial distribution in velocity of steam at top of core for 5x10 case.

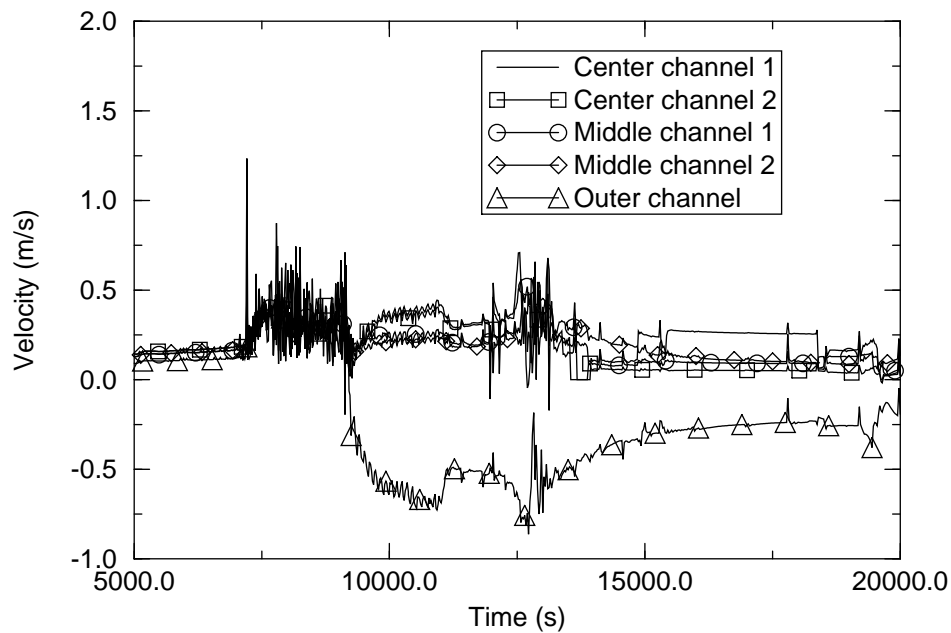


Figure B-27. Radial distribution in velocity of steam at top of core for 5x20 case.

The temperature of the heat structures in the lower plenum for the three cases were almost identical for the three cases. Figure B-28 shows the calculated temperature of the structures in the lower part of the upper plenum for the three cases.

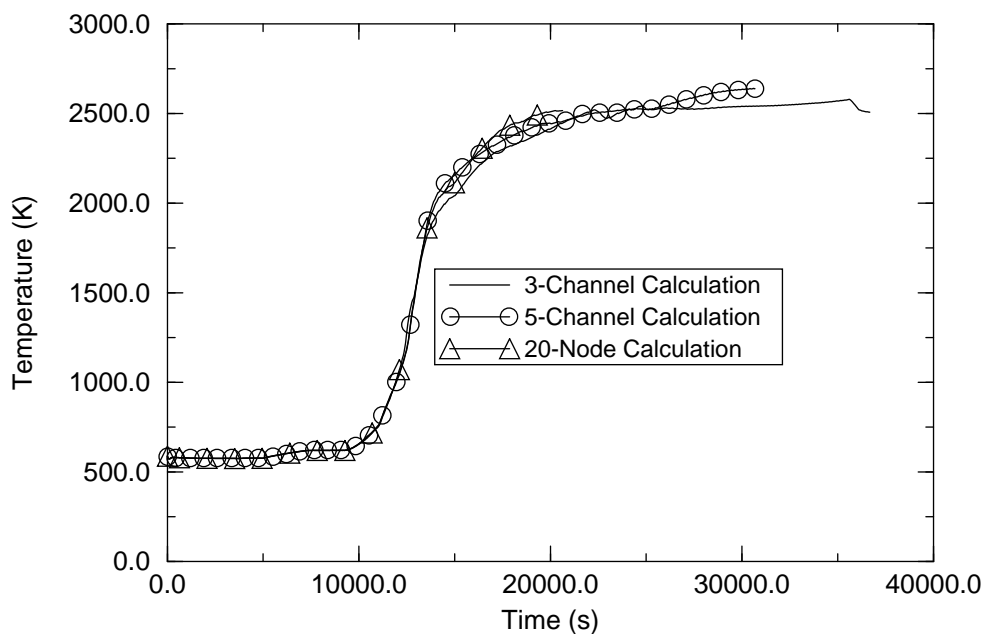


Figure B-28. Temperatures of structures in lower part of upper plenum for the 3x10, 5x10, and 5x20 cases.

The calculated temperature of the surge line for the three cases was almost identical. Figure B-29 shows the calculated temperature for the three cases.

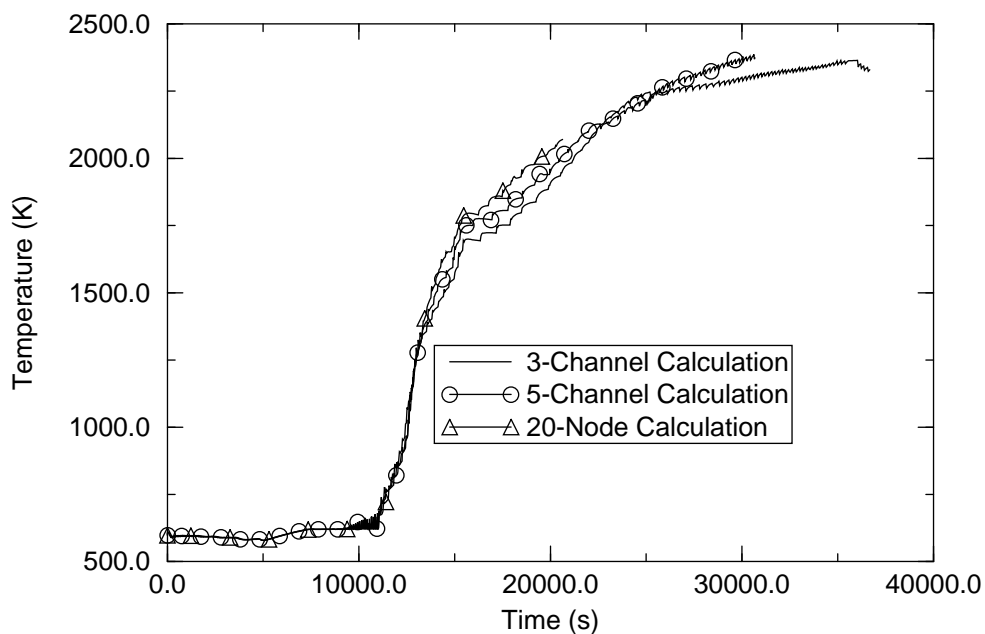


Figure B-29. Temperature of surge line for the 3x10, 5x10, and 5x20 cases.

The calculated effective radius of the molten pool for the three cases is similar in the later period of the accident but has variations between the three cases for the earlier period of the accident. Figure B-30

shows the calculated effective radius for the three cases. Before 30,000 seconds the 3x10 case calculates a 5-15% larger effective radius than the 5x10 case. At 30,000 seconds, however, the two cases calculate an identical size of molten pool. The 5x20 case calculates a significantly smaller effective radius than the other two cases for times earlier than 20,000 seconds.

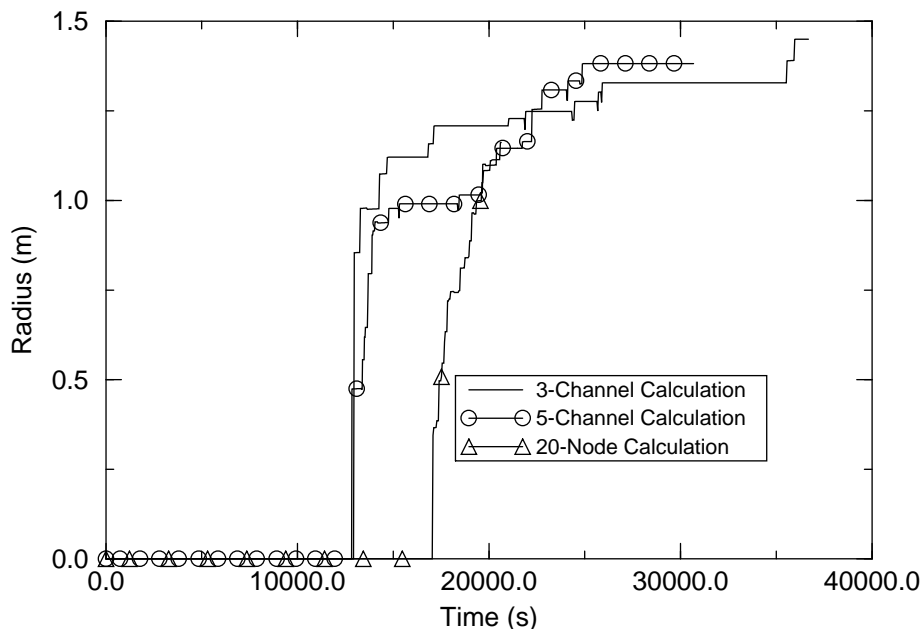


Figure B-30. Effective radius of molten pool for the 3x10, 5x10, and 5x20 cases.

The evolution of core degradation for each of the three cases was somewhat different. Maps showing the evolution of degradation for the 3x10 case are shown in Figures B-31, B-32, and B-33. Figure B-31 shows the evolution from 14,372 to 20,000 seconds. Figure B-32 shows the evolution from 22,000 to 30,000 seconds. Figure B-33 shows the evolution from 31,000 to 38,000 seconds. Figures B-34, B-35, and B-36 show the evolution of the core degradation for the 5x10 case. Figure B-37 shows the evolution of the core degradation for the 5x20 case. The 5x20 case calculated that no metallic meltdown of the fuel rods occurred anywhere in the core. Both the 3x10 and 5x10 cases calculated a metallic meltdown for the fuel rods in the center flow channel and the formation of a plane blockage due to this meltdown. The 5x20 case calculated the formation of a molten pool in the core at a significantly later time than the 3x10 and 5x10 cases calculated. It also calculated a higher location in the reactor core for the molten pool than the other two cases. For times greater than 20,000 seconds, the differences in calculated melt progression between the three cases decrease with time.

The CPU time consumed in the analyses of the three cases was proportional to the extent of nodalization of the reactor core. The time for calculations out to 20,000 seconds for all three cases were 17 hours, 33 hours, and 42 hours, respectively. The CPU time out to 36,000 seconds, near the time of calculated creep rupture of the lower head, was 49 hours and 83 hours for the 3x10 and 5x10 cases, respectively. The CPU time for the 5x20 case at 36,000 seconds was not available. The 3x10 and 5x10 cases were calculated on a CRAY X-MP computer, while the 5x20 case was performed on a DEC alpha computer with a speed about the same as that of the CRAY X-MP. In order to correctly calculate the

core degradation map

I = intact fuel component	underscore indicates	<u>I</u> x's indicate
P = porous debris	metallic or planar	<u>V</u> that total or bulk
M = molten or frozen ceramic pool	blockage in volume at bottom	xxPxx blockage occurs
V = Relap fluid volume now void of fuel	of indicated node	xxMxx in the volume

conditions of in-core molten pool at time = 14372. sec

Axial node #			
10	I	I	I
9	I	I	I
8	I	V	I
7	I	V	I
6	I	V	I
5	I	xxMxx	I
4	I	P	I
3	I	I	I
2	<u>I</u>	I	I
1	I	I	I
Relap vol. at bottom	111010000	112010000	113010000

conditions of in-core molten pool at time = 16372. sec

Axial node #			
10	I	I	I
9	I	I	I
8	I	V	I
7	I	V	I
6	I	V	I
5	I	xxMxx	I
4	I	P	I
3	I	I	I
2	<u>I</u>	I	I
1	I	I	I
Relap vol. at bottom	111010000	112010000	113010000

conditions of in-core molten pool at time = 18000. sec

Axial node #			
10	I	I	I
9	I	I	I
8	I	V	I
7	I	V	I
6	I	V	I
5	I	xxMxx	I
4	I	xxMxx	I
3	I	P	I
2	<u>I</u>	I	I
1	I	I	I
Relap vol. at bottom	111010000	112010000	113010000

conditions of in-core molten pool at time = 20000. sec

Axial node #			
10	I	I	I
9	I	I	I
8	I	V	I
7	I	V	I
6	I	V	I
5	I	xxMxx	I
4	I	xxMxx	I
3	I	P	I
2	<u>I</u>	I	I
1	I	I	I
Relap vol. at bottom	111010000	112010000	113010000

Figure B-31. Evolution of melt progression for 3x10 case in period 14,372 to 20,000 seconds.

transient power of the reactor core, the reactor kinetics subroutines needed to be compiled on the DEC alpha computer with optimization turned off.

```

conditions of in-core molten pool at time =    22000.    sec

  Axial node #
    10          V      I      I
     9          V      I      I
     8        xxMxx    V      P
     7          P      V      I
     6          I      V      I
     5          I      xxMxx    I
     4          I      xxMxx    I
     3          I      P      I
     2        _I_      I      I
     1          I      I      I
Relap vol. at bottom    111010000 112010000 113010000

conditions of in-core molten pool at time =    24000.    sec

  Axial node #
    10          V      I      I
     9          V      I      I
     8        xxMxx    V      P
     7          P      V      I
     6          I      V      I
     5          I      xxMxx    I
     4          I      xxMxx    I
     3          I      P      I
     2        _I_      I      I
     1          I      I      I
Relap vol. at bottom    111010000 112010000 113010000

conditions of in-core molten pool at time =    26000.    sec

  Axial node #
    10          V      I      I
     9          V      I      V
     8        xxMxx    V      V
     7          P      V      xxMxx
     6          I      V      P
     5          I      xxMxx    I
     4          I      xxMxx    I
     3          I      P      I
     2        _I_      I      I
     1          I      I      I
Relap vol. at bottom    111010000 112010000 113010000

conditions of in-core molten pool at time =    28000.    sec

  Axial node #
    10          V      I      I
     9          V      I      V
     8        xxMxx    V      V
     7          P      V      xxMxx
     6          I      V      P
     5          I      xxMxx    I
     4          I      xxMxx    I
     3          I      P      I
     2          I      I      I
     1        _I_      I      I
Relap vol. at bottom    111010000 112010000 113010000

conditions of in-core molten pool at time =    30000.    sec

  Axial node #
    10          V      I      I
     9          V      I      V
     8        xxMxx    V      V
     7          P      V      xxMxx
     6          I      V      P
     5          I      xxMxx    I
     4          I      xxMxx    I
     3          I      P      I
     2          I      I      I
     1        _I_      I      I
Relap vol. at bottom    111010000 112010000 113010000

```

Figure B-32. Evolution of core degradation in 3x10 case for period from 22,000 to 30,000 seconds.


```

conditions of in-core molten pool at time = 31000. sec

Axial node #
10      V      I      I
9       V      I      V
8      xxxxxx  V      V
7       P      V      xxxxxx
6       I      V      P
5       I      xxxxxx I
4       I      xxxxxx I
3       I      P      I
2       I      I      I
1      _I_     I      I
Relap vol. at bottom 111010000 112010000 113010000

conditions of in-core molten pool at time = 33000. sec

Axial node #
10      V      I      I
9       V      I      V
8      xxxxxx  V      V
7       P      V      xxxxxx
6       I      V      P
5       I      xxxxxx I
4       I      xxxxxx I
3       I      P      I
2       I      I      I
1      _I_     I      I
Relap vol. at bottom 111010000 112010000 113010000

conditions of in-core molten pool at time = 35000. sec

Axial node #
10      V      I      I
9       V      I      V
8      xxxxxx  V      V
7       P      V      xxxxxx
6       I      V      P
5       I      xxxxxx I
4       I      xxxxxx I
3       I      P      I
2       I      I      I
1      _I_     I      I
Relap vol. at bottom 111010000 112010000 113010000

conditions of in-core molten pool at time = 36000. sec

Axial node #
10      V      V      I
9       V      V      V
8      xxxxxx  V      V
7       P      V      xxxxxx
6       I      V      P
5       I      xxxxxx I
4       I      xxxxxx I
3       I      P      I
2       I      I      I
1      _I_     I      I
Relap vol. at bottom 111010000 112010000 113010000

conditions of in-core molten pool at time = 38000. sec

Axial node #
10      V      V      V
9       V      V      V
8      xxxxxx  V      V
7       P      V      xxxxxx
6       I      V      P
5       I      xxxxxx I
4       I      xxxxxx I
3       I      P      I
2       I      I      I
1      _I_     I      I
Relap vol. at bottom 111010000 112010000 113010000

```

Figure B-33. Evolution of core degradation for 3x10 case for period from 31,000 to 36,000 seconds.

Appendix B

core degradation map

I = intact fuel component underscore indicates
P = porous debris metallic or planar
M = molten or frozen ceramic pool blockage in volume at bottom
V = Relap fluid volume now void of fuel of indicated node

I x's indicate
V that total or bulk
xxPxx blockage occurs
xxMxx in the volume

conditions of in-core molten pool at time = 14500. sec

Axial node #					
10	V	I	V	I	I
9	V	V	V	I	I
8	V	V	V	I	I
7	xxMxx	V	xxMxx	I	I
6	P	xxMxx	P	I	I
5	I	xxMxx	I	I	I
4	I	P	I	I	I
3	I	I	I	I	I
2	I	I	I	I	I
1	_I_	_I_	I	I	I
Relap vol. at bottom	111010000	114010000	112010000	115010000	113010000

conditions of in-core molten pool at time = 16500. sec

Axial node #					
10	V	I	V	I	I
9	V	V	V	I	I
8	V	V	V	I	I
7	V	V	xxMxx	I	I
6	xxMxx	xxMxx	P	I	I
5	xxMxx	xxMxx	I	I	I
4	P	P	I	I	I
3	I	I	I	I	I
2	I	I	I	I	I
1	_I_	_I_	I	I	I
Relap vol. at bottom	111010000	114010000	112010000	115010000	113010000

conditions of in-core molten pool at time = 18500. sec

Axial node #					
10	V	I	V	I	I
9	V	V	V	I	I
8	V	V	V	I	I
7	V	V	xxMxx	I	I
6	xxMxx	V	P	I	I
5	xxMxx	xxMxx	I	I	I
4	P	xxMxx	I	I	I
3	I	P	I	I	I
2	I	I	I	I	I
1	_I_	_I_	I	I	I
Relap vol. at bottom	111010000	114010000	112010000	115010000	113010000

conditions of in-core molten pool at time = 20000. sec

Axial node #					
10	V	I	V	I	I
9	V	V	V	I	I
8	V	V	V	I	I
7	V	V	xxMxx	V	I
6	V	V	P	xxMxx	I
5	xxMxx	xxMxx	I	P	I
4	xxMxx	xxMxx	I	I	I
3	P	P	I	I	I
2	I	I	I	I	I
1	_I_	_I_	I	I	I
Relap vol. at bottom	111010000	114010000	112010000	115010000	113010000

Figure B-34. Evolution of molten pool for 5x10 case from 14,500 to 20,000 seconds.

```

conditions of in-core molten pool at time =    22000.    sec

  Axial node #
    10          V      V      V      I      I
    9           V      V      V      I      I
    8           V      V      V      I      I
    7           V      V      xxxxxx V      I
    6           V      V      P      xxxxxx I
    5          xxxxxx xxxxxx I      P      I
    4          xxxxxx xxxxxx I      I      I
    3           P      P      I      I      I
    2           I      I      I      I      I
    1          _I_    _I_    I      I      I
Relap vol. at bottom  111010000 114010000 112010000 115010000 113010000

conditions of in-core molten pool at time =    24000.    sec

  Axial node #
    10          V      V      V      V      I
    9           V      V      V      V      I
    8           V      V      V      V      I
    7           V      V      xxxxxx xxxxxx P
    6           V      V      P      xxxxxx I
    5          xxxxxx xxxxxx I      P      I
    4          xxxxxx xxxxxx I      I      I
    3           P      P      I      I      I
    2           I      I      I      I      I
    1          _I_    _I_    I      I      I
Relap vol. at bottom  111010000 114010000 112010000 115010000 113010000

conditions of in-core molten pool at time =    26000.    sec

  Axial node #
    10          V      V      V      V      I
    9           V      V      V      V      I
    8           V      V      V      V      V
    7           V      V      xxxxxx xxxxxx V
    6           V      V      P      xxxxxx xxxxxx
    5          xxxxxx xxxxxx I      P      P
    4          xxxxxx xxxxxx I      I      I
    3           P      P      I      I      I
    2           I      I      I      I      I
    1          _I_    _I_    I      I      I
Relap vol. at bottom  111010000 114010000 112010000 115010000 113010000

conditions of in-core molten pool at time =    28000.    sec

  Axial node #
    10          V      V      V      V      I
    9           V      V      V      V      I
    8           V      V      V      V      V
    7           V      V      xxxxxx xxxxxx V
    6           V      V      P      xxxxxx xxxxxx
    5          xxxxxx xxxxxx I      P      P
    4          xxxxxx xxxxxx I      I      I
    3           P      P      I      I      I
    2           I      I      I      I      I
    1          _I_    _I_    I      I      I
Relap vol. at bottom  111010000 114010000 112010000 115010000 113010000

conditions of in-core molten pool at time =    30000.    sec

  Axial node #
    10          V      V      V      V      I
    9           V      V      V      V      I
    8           V      V      V      V      V
    7           V      V      xxxxxx xxxxxx V
    6           V      V      P      xxxxxx xxxxxx
    5          xxxxxx xxxxxx I      P      P
    4          xxxxxx xxxxxx I      I      I
    3           P      P      I      I      I
    2           I      I      I      I      I
    1          _I_    _I_    I      I      I
Relap vol. at bottom  111010000 114010000 112010000 115010000 113010000

```

Figure B-35. Evolution of molten pool for 5x10 case from 22,000 to 30,000 seconds.

```

conditions of in-core molten pool at time =   30686.   sec

  Axial node #
    10         V         V         V         V         I
     9         V         V         V         V         I
     8         V         V         V         V         V
     7         V         V      xxxxxx      xxxxxx      V
     6         V         V         P      xxxxxx      xxxxxx
     5      xxxxxx      xxxxxx         I         P         P
     4      xxxxxx      xxxxxx         I         I         I
     3         P         P         I         I         I
     2         I         I         I         I         I
     1      _I_      _I_         I         I         I
Relap vol. at bottom  111010000 114010000 112010000 115010000 113010000

```

Figure B-36. State of core degradation for 5x10 case at 30,656 seconds.

core degradation map

I = intact fuel component underscores indicate
P = porous debris metallic or planar
M = molten or frozen ceramic pool blockage in volume at bottom
V = Relap fluid volume now void of fuel of indicated node

— I — x's indicate
— V — that total or bulk
xxPxx blockage occurs
xxMxx in the volume

conditions of in-core molten pool at time = 17675. sec

axial node #					
20	I	V	xxMxx	I	I
19	V	V	P	I	I
18	V	V	I	I	I
17	V	xxMxx	I	I	I
16	xxMxx	P	I	I	I
15	P	I	I	I	I
14	I	I	I	I	I
13	I	I	I	I	I
12	I	I	I	I	I
11	I	I	I	I	I
10	I	I	I	I	I
9	I	I	I	I	I
8	I	I	I	I	I
7	I	I	I	I	I
6	I	I	I	I	I
5	I	I	I	I	I
4	I	I	I	I	I
3	I	I	I	I	I
2	I	I	I	I	I
1	I	I	I	I	I

Relap vol. at bottom 111010000 114010000 112010000 115010000 113010000

conditions of in-core molten pool at time = 19675. sec

Axial node #					
20	I	V	V	I	I
19	V	V	V	I	I
18	V	V	V	I	I
17	V	V	V	V	I
16	V	V	xxMxx	V	I
15	V	xxMxx	xxMxx	V	I
14	xxMxx	xxMxx	P	xxMxx	I
13	xxMxx	xxMxx	I	xxMxx	I
12	xxMxx	P	I	P	I
11	P	I	I	I	I
10	I	I	I	I	I
9	I	I	I	I	I
8	I	I	I	I	I
7	I	I	I	I	I
6	I	I	I	I	I
5	I	I	I	I	I
4	I	I	I	I	I
3	I	I	I	I	I
2	I	I	I	I	I
1	I	I	I	I	I

Relap vol. at bottom 111010000 114010000 112010000 115010000 113010000

conditions of in-core molten pool at time = 21675. sec

Axial node #					
20	I	V	V	I	I
19	V	V	V	I	I
18	V	V	V	I	I
17	V	V	V	V	I
16	V	V	V	V	I
15	V	V	xxMxx	V	P
14	V	V	xxMxx	V	P
13	xxMxx	xxMxx	xxMxx	xxMxx	I
12	xxMxx	xxMxx	P	xxMxx	I
11	xxMxx	xxMxx	P	P	I
10	P	P	I	I	I
9	I	I	I	I	I
8	I	I	I	I	I
7	I	I	I	I	I
6	I	I	I	I	I
5	P	I	P	P	I
4	I	I	I	I	I
3	I	I	I	I	I
2	I	I	I	I	I
1	I	I	I	I	I

Relap vol. at bottom 111010000 114010000 112010000 115010000 113010000

Figure B-37. Evolution of core degradation for 5x20 case.

B.4. CONCLUSIONS

Five conclusions can be drawn from the analysis of the calculated behavior of the Surry reactor during a TMLB' accident: (1) natural circulation within the reactor vessel can result in a significant amount of heat being transferred from the region of the reactor core to structures in the upper plenum and to the vessel itself, (2) the representation of the reactor core with just three flow channels may not be adequate for a realistic representation of the initial stages of molten pool formation, (3) two important parameters for severe accident analysis are the extent of oxidation of fuel rod cladding and its peak temperature during the period of its temperature excursion due to oxidation, (4) the modeling of the heatup and spreading of a molten pool may require some extensions, and, (5) the numerics in SCDAP/RELAP5 are robust. Each of these conclusions is explained in more detail below. These conclusions are applicable to a severe accident in which the coolant pressure remains high, as is the case for a TMLB' accident in which the surge line and hot legs are assumed to never rupture.

The calculations showed that natural circulation within the reactor vessel can result in a transfer of a significant amount of the decay heat in a reactor core to structures in the upper plenum region and to the reactor vessel itself. This transfer of heat from the core region to other structures is indicated by the hot temperature calculated for the structures in the upper plenum, in the reactor vessel, and by the correspondingly slow rate of heatup and of melt progression in the reactor core region. During the period in which the reactor core is oxidizing, the heat generation in the reactor core is more rapid than that which can be removed by natural circulation. But after the reactor core is completely oxidized, then natural circulation can remove a significant amount of heat. Even during the period of rapid oxidation of the reactor core, natural circulation is important in that it may cause enough cooling of the oxidizing parts of the reactor core that these parts are not heated above the ceramic melting temperature. In the case that molten material in the core region stays in the core region, natural circulation will cause enough heatup of the reactor vessel that it will fail due to creep rupture.

The representation of the reactor core with just three flow channels (three nodes in the radial direction), may result in an inaccurate calculation of the evolution of melt progression. In the analysis of the Surry TMLB' performed with the 3x10 nodalization, the initial location of the molten pool was calculated to be in the middle flow channel. This initial location of the molten pool was partly due to natural circulation. The flow of steam in the reactor core was calculated to be upward in the center of the core and downward in the periphery of the core. As a result of this natural circulation pattern, the velocity of the steam in the middle channel was less than that in the center and outer channels, which resulted in less cooling of this portion of the core relative to the center portion. But the calculation of the initial location of the molten pool being in the second (middle) flow channel was also partly due to coarse nodalization. In the analyses performed with the 5x10 and 5x20 nodalizations, the initial formation of the molten pool was in the center flow channel. For these analyses, a natural circulation pattern was also calculated that resulted in the slowest steam velocities occurring in the portion of the core between the center and periphery regions. But in these analyses, the power in the center flow channel was slightly higher than that for the center flow channel for the 3x10 case. This slightly higher power was sufficient to cause the initial location of the molten pool to occur in the center flow channel, where the initial formation of the molten pool is expected to occur. The large flow area represented by the middle (second) flow channel for the 3x10 case also caused an unrealistic amount of cooling of the fuel rods in the center flow channel after the formation of a molten pool in the middle channel. The blockage of this relatively large channel caused a large amount of steam to be diverted to the center channel and to thus significantly

increase the cooling of these fuel rods. This cooling is considered an artifact of the large differences in flow area of the center and middle flow channels and thus an artifact of the coarse radial nodalization of the reactor core.

Two important parameters for severe accident analysis are the extent of oxidation of fuel rod cladding and its peak temperature during the period of its temperature excursion due to oxidation. In the 3x10 and 5x10 cases, the fuel rods were heated by heat generation from oxidation to the point of ceramic melting and molten pool formation just before the cladding was completely oxidized. For the 5x20 case, the cladding was calculated to be completely oxidized just before the fuel rods would have been heated to the point of ceramic melting and molten pool formation. After oxidation is complete, a sharp reduction in heat generation occurs. If the fuel rod cladding had been thicker, the 5x20 case would also have calculated heatup to molten pool formation during the oxidation excursion period of the accident. If the cladding had been thinner, then the 3x10 and 5x10 cases would have calculated the temperature excursion to completion due to complete oxidation of the cladding and thus before the creation of a blockage due to ceramic melting of the fuel rods. In summary, these results show that the time to beginning of ceramic melting and the formation of a molten pool is sensitive to the thickness of the cladding of the fuel rods. For oxidation excursions at low pressure the possibility is less likely of the cladding being completely oxidized before heatup to the temperature where meltdown occurs due to the less heat capacity and thus less cooling for low pressure steam relative to high pressure steam.

The possibility for a molten pool being cooled by vigorous natural circulation within the reactor vessel makes it important to correctly model the heatup of the molten pool and the spreading of the molten pool. Two modeling deficiencies contributed to the calculated heatup of the molten pool being slower than reality. The first deficiency is that of modeling steady state natural convection to begin immediately at the time of molten pool formation, when in reality, a significant amount of time may be required before steady state natural convection develops. The other deficiency is in the modeling of the temperature range at which the heat of fusion of UO_2 and ZrO_2 are accounted for. This deficiency caused the molten pool to be modeled as being cooled by natural convection of its material before the heat of fusion of UO_2 had been accounted for. Until the heat of fusion is accounted for, the mixture of UO_2 and ZrO_2 is a slush, even though it is being liquefied by eutectic reaction. Natural convection will not occur while it is in a slushy state. Other models required for an accurate calculation of molten pool behavior include: (1) modeling of behavior of molten pool after it has spread to edge of the reactor core, and (2) modeling of the structural strength and failure of the crust on top and at the sides of the molten pool.

The calculations for all three cases were performed without encountering numerical instabilities or water property failures. The code was able to maintain a steady time step of about 0.05 seconds through rapid oxidation and through the period when melt progression is occurring in the core region. During the period of melt progression in the reactor core was the period in which the bulk of the computer time was expended. The time step size was not limited by the Courant limit but by mass error or some other cause. It may be productive to investigate the reason for the time step limit and develop the capability to expand this limit so that it is not significantly less than the Courant limit.

The results of these calculations do not clearly indicate what is the minimum acceptable nodalization of the reactor core. All three cases of nodalization calculate about the same time of occurrence of early phase events such as the beginning of rapid oxidation of the reactor core and failure of the surge line. All three cases calculate a different time for beginning of molten pool formation and a different location of the

molten pool during the initial stage of the evolution of the molten pool. For a time significantly later than the initial formation of the molten pool, the calculated size and location of the molten pool appear to converge.

Since the timing of melt progression and the formation of blockages is the behavior that is primarily affected by nodalization, it is expected that the calculated behavior of a reactor is more sensitive to nodalization for high pressure than for low pressure scenarios. For low pressure scenarios, the cooling may be so deficient that blockages may not result in a significantly more rapid heatup of the reactor core than would be the case if blockages do not occur.